Institut für Geowissenschaften, Universität Potsdam, Deutschland
Laboratoire de Géologie, Ecole Normale Supérieure de Paris, France

Doctoral Thesis

Presented to obtain the Academic Degrees
"Doktor der Naturwissenschaften an der Universität Potsdam"
and
"Docteur de l'Université d'Orsay – Paris Sud (PARIS XI)"
under the convention of
"Gemeinsam betreute Promotion"
"Cotutelle de thèse"

Speciality: Geology

STRUCTURAL AND METAMORPHIC EVOLUTION OF THE LYCIAN NAPPES AND THE MENDERES MASSIF (SOUTHWEST TURKEY): GEODYNAMIC IMPLICATIONS AND CORRELATIONS WITH THE AEGEAN DOMAIN

by

Gaëtan RIMMELÉ

Defended in Potsdam, 30th October 2003

Joined German-French examination committee:

Roland OBERHÄNSLI, Universität Potsdam	**PhD supervisor**, Reviewer
Bruno GOFFÉ, Ecole Normale Supérieure, Paris	**PhD supervisor**
Olivier VIDAL, Université Joseph Fourier, Grenoble	Reviewer
Manfred STRECKER, Universität Potsdam	Reviewer
Laurent JOLIVET, Université Pierre et Marie Curie, Paris	Examination
Patrick O'BRIEN, Universität Potsdam	Examination
Bernard BONIN, Université Orsay-Paris Sud	Examination
Frank SCHERBAUM, Universität Potsdam	Examination

“Her yiğidin bir yoğurt yeyişi vardır”

(“Every man has his own style of eating yogurt”, Turkish proverb)

ACKNOWLEDGEMENTS

During these last three and a half years, my PhD thesis under the German-French convention of “Gemeinsam betreute Promotion” / “Cotutelle de these” allowed me to share my time between the University of Potsdam and the Ecole Normale Supérieure of Paris. There are therefore many persons to warmly thank for their contribution to the progress of my PhD thesis.

First of all, I would like to particularly address grateful thanks to my supervisors Roland Oberhänsli (Universität Potsdam) and Bruno Goffé (ENS Paris). I thank them for their ability to be there every time I needed their help, in the field, in Potsdam or in Paris. I also thank them a lot for all fruitful discussions on metamorphic petrology and accretionary wedge processes, for their strong support all along the period of my PhD, and to have accorded me their full confidence in my work.
Many thanks to you, Roli and Bruno, for your scientific supervising and for your great humaneness.

Special thanks go to Laurent Jolivet (Université Pierre et Marie Curie, Paris VI), who kindly accepted to be part of field investigations in Western Turkey, and greatly helped at understanding its tectonic evolution in the whole geodynamic context of the Aegean-Anatolian region. Eight years ago, at my first steps in the world of Geology, Laurent transmitted me his deep interest in the fascinating build up of mountain belts, which in a certain way led me at this stage today. For that reason, this work is partly dedicated to him.

Osman Candan (Dokuz Eylül Universitesi, Izmir, Turkey) is gratefully thanked for the warm welcome in Izmir, for his assistance in the field, and for many fruitful discussions on the geology of the Menderes Massif and the Lycian Nappes. I also thank him for millions of small things which were made easier with his help, and for his permanent kindness and generosity towards us. Sevgili büyük Profesor Osman bey, benim Arkadaşım, çok Teşekkur ederim!

Many thanks are particularly addressed to Teddy Parra (ENS), who led me to dive into the world of chlorites and micas, and friendly helped me to understand how these minerals are precious tools for well-constrained PT calculations in a multi-equilibrium approach.

I would also like to gratefully acknowledge Olivier Vidal (Université Joseph Fourier, Grenoble), Manfred Strecker (Universität Potsdam) who kindly accepted to review this work. Bernard Bonin (Université d’Orsay, Paris XI), Patrick O’Brien (Universität Potsdam), Laurent Jolivet (Université Paris VI), and Frank Scherbaum (Universität Potsdam) are also thanked for being part of the examination committee. Olivier Vidal, Bernard Bonin and Laurent Jolivet are particularly warmly acknowledged to have travelled from France to Potsdam for the PhD defense.

Christian Chopin, Özcan Dora, Erdin Bozkurt, Cemal Göncüoğlu, Alistair Robertson, Romain Bousquet, Jean-Paul Cadet, Michel Bonneau, André Poisson, José-Miguel Azañón, Donna Whitney, Cecile Robin, Christophe Durlet, and Aral Okay are thanked for fruitful discussions or comments about metamorphic, stratigraphic and tectonic processes and the regional geology of Western Turkey.

I am indebted to many persons who gave their technical assistance all along the period of my PhD work at Potsdam University and at the ENS of Paris. Christine Fischer is greatly thanked for quality and number of rock thin sections, as well as Carsten for his punctual help at cutting strong rocks in Potsdam. Roland Caron is also thanked for preparing a few samples in Paris. Many thanks to Max Wilke, Robert Schmid, Astrid Riemann and Ulrike Raulien for their help at performing XRAY analyses in Potsdam. Silvia Sprottii and Annett Junging are also thanked for their great help at preparing samples for fission track thermochronology and Edward Sobel is gratefully acknowledged for the same reasons and for his analyses under microscope. Electron microprobe analyses were performed in three different institutes and the following persons are all thanked for their helpful assistance: Oona Appelt from the GeoForschungsZentrum Potsdam, Roald Tagle and Philippe Claeys from the Museum für Naturkunde in Berlin, and Michel Fialin and Hubert Remy from Université Pierre et Marie Curie of Paris. I also thank Olivier Beyssac for performing few RAMAN spectroscopic analyses. Ines Münch and Peter Koch at Potsdam University, as well as François Farcy and Patrick Chassevent at the ENS Paris are acknowledged for computer and network assistance. Frau Horst, Alex, Nicole and Sabine in Potsdam, as well as Marie-Pierre, Françoise, Mireille and Isabelle in Paris are

thanked for their help at finding clues to many complex enigma of our German-French administration system.

The Deutsche ForschungGemeinschaft (D.F.G.-project OB80/21-2), the Volkswagen Stiftung, and the C.N.R.S. are gratefully acknowledged for financial support.
The Deutsch-Französische Hochschule (D.F.H.) is also thanked for supporting the German-French cooperation.

Great thanks go to many people who belong to the two institutes I used to frequent these last years. Although these persons were not directly involved in this work, I would like to address them many thanks for many small things which were made easier with many small helps, and simply because they contributed to create an essential nice and pleasant atmosphere within both institutes: Thousands of thanks to the Institut für Geowissenschaften in Potsdam: Manfred Strecker, Pady O'Brien, Uwe Altenberger, Julius Partzsch, Andreas Möller, Maria Mutti, Peter Blisniuk, Anke Friedrich, Barbara Carrapa, Estelle Schissele, Ed Sobel, Frank Scherbaum, Matthias Ohrnberger, Masafumi Sudo, Martin Timmerman, Max Wilke, Robert Schmid, Antje Müller, Daniel Vollmer, Christine Fischer and Birgit Fabian. And again thousands of thanks to the mineralogy team of the ENS in Paris: Nicole Catel, Julia de Sigoyer, Marie-Pierre Serot-Almeras, Dominique Janots, Françoise Vivent, Christian Chopin, Christian Robert, Fabrice Brunet, Bruce Velde, Guy Marolleau and Roland Caron. Many thanks to Nicole for the delicious cake specially brought from France for the PhD buffet! Friendly thoughts to Lucile Mamou and Jacques Cassareuil who recently retired.

I would also like to address lots of thanks to all the PhD students who used to bear me during the time of my PhD! Thanks to you to have shared such a nice time with me! In Potsdam, the Baracke'team: mein Grosser Rasmus, der Rote Gunnar, Bodo the freak, Taaaaaadash!, la pequeñita Mónica y Mauricio el flaco, Andres siempre soñando, le bo Paolo, Gudrun, Rob', Nanni, Friederike and Carsten. Thanks also for the nice hat! Special friendly thoughts to my two Turkish friends Fatma and Serhat from Middle East Technical University (Ankara), and to other invited persons who had the great privilege to know the Baracke: Jorge "Que Machera!", Soraya, Dr. Dondovyn Tomurhuu. At the ENS, many thanks to Carboncito, Miiiiillllliiiiie, Kikimimi, J-Pouille, Catherinette, Anne Verlag', Socquette, Anne Loeven', Oliv', Fabien, Victor, Anthony, Sylvain, Guillaume and the others…

Many thanks go to my friends Cüneyt, Ersin, Arzu, Serkan, Bilal and Mete (from the geology department of Dokuz Eylül University, Izmir) for their unforgettable warm welcome and kindness.
I would like to warmly thank all the extremely friendly Turkish people I met in the field when I was working alone in Lycia. Without them, the field seasons would have not been what they were. I particularly thank the persons working in the Nur Motel of Ören, Halis, Eşref, Sabahattin, Ramazan, as well as Halil, Ersan, Recay, Mehmet and many others…

Ulvi Can Ünlügenç, Tamer Rizaoğlu and Osman Parlak are gratefully thanked for the very well organised International Turkish geology symposium in the Çukurova University (Adana, Turkey) and the nice excursion in the Mersin ophiolitic massif.
Tuncay Taymaz and the scientific committee are also warmly acknowledged for giving me the chance to make the keynote speech in the "Exhumation of Metamorphic Terrains" session at the First International Geology Symposium of Istanbul Technical University.
Many thanks to Omar Saddiqi, Rachid Elmamoun, Abdeltif Lahfid, Assia, Samir, Samira, Souad, Lahssen and many other persons for their warm welcome in Casablanca (Morocco) for the "Troisième colloque international sur le magmatisme, métamorphisme et minéralisations associées", at the Hassan II Aïn Chock University. Omar Saddiqi and André Michard are warmly thanked for the beautiful excursion across the Rif Belt. Special friendly thoughts to Mohamed Bouybaouene and Giorgio Martinotti.

Hélène Horen and Christelle Gosselin are gratefully thanked for allowing me to teach in very pleasant conditions at the Versailles University during the three years of my PhD.

Many thanks to Hedi Oberhänsli for her kindness and also for the beautiful flowers!

Thanks to *Teddy's* and *Filou*!

Finally, I address many grateful thanks to my friends who largely supported me all along the period of this work: Thom, Peg, la petite Roxanne, Coralie, Charlie, Rasmus, Miri, Britt' und die kleine Mietzi, Zaz, Hocine, Thomas, Delphine's, Azdine, Etienne, Fleur, Nico, Sandr', Tom and Loic. Special thoughts to my French expatriate friends who also fell in love with Berlin: Isa, Estelle, Anne Cuzol avec un C comme Cuzol, Coralie II and Perrine.

I particularly warmly thank Papa, Maman and Pauline, as well as my friends Thom, Peg, Kikimimi, Cisco, Milie, Julio, and Delphine, who all came from France to assist and support me for the PhD defense in Potsdam. I'll never forget!

Many thanks to Charlotte for everything, and simply for being every time there.

This thesis is dedicated to my parents who contributed to it in a great many ways.

ABSTRACT

Western Anatolia that represents the eastward lateral continuation of the Aegean domain is composed of several tectono-metamorphic units showing occurrences of high-pressure/low-temperature (HP-LT) rocks. While some of these metamorphic rocks are vestiges of the Pan-African or Cimmerian orogenies, others are the result of the more recent Alpine orogenesis.

In southwest Turkey, the Menderes Massif occupies an extensive area tectonically overlain by nappe units of the Izmir-Ankara Suture Zone in the north, the Afyon Zone in the east, and the Lycian Nappes in the south. In the present study, investigations in the metasediments of the Lycian Nappes and underlying southern Menderes Massif revealed widespread occurrences of Fe-Mg-carpholite-bearing rocks. This discovery leads to the very first consideration that both nappe complexes recorded HP-LT metamorphic conditions during the Alpine orogenesis. P-T conditions for the HP metamorphic peak are about 10-12 kbar/400°C in the Lycian Nappes, and 12-14 kbar/470-500°C in the southern Menderes Massif, documenting a burial of at least 30 km during subduction and nappe stacking.

Ductile deformation analysis in concert with multi-equilibrium thermobarometric calculations reveals that metasediments from the Lycian Nappes recorded distinct exhumation patterns after a common HP metamorphic peak. The rocks located far from the contact separating the Lycian Nappes and the Menderes Massif, where HP parageneses are well preserved, retained a single HP cooling path associated with top-to-the-NNE shearing related to the Akçakaya shear zone. This zone of strain localization is an intra-nappe contact that was active in the early stages of exhumation of HP rocks, within the stability field of Fe-Mg-carpholite. The rocks located close to the contact with the Menderes Massif, where HP parageneses are completely retrogressed into chlorite and mica, recorded warmer exhumation paths associated with top-to-the-E intense shearing. This deformation occurred after the southward emplacement of Lycian Nappes, and is contemporaneous with the reactivation of the ‘Lycian Nappes-Menderes Massif’ contact as a major shear zone (the Gerit shear zone) that allowed late exhumation of HP parageneses under warmer conditions. The HP rocks from the southern Menderes Massif recorded a simple isothermal decompression at about 450°C during exhumation, and deformation during HP event and its exhumation is characterized by a severe N-S to NE-SW stretching.

The age of the HP metamorphism recorded in the Lycian Nappes is assumed to range between the Latest Cretaceous (age of the youngest sediments in the Lycian allochthonous unit) and the Eocene (age of the Cycladic Blueschists). A probable Palaeocene age is suggested. The age of the HP metamorphism that affected the cover series of the Menderes Massif is constrained between the Middle Palaeocene (age of the uppermost metaolistostrome of the Menderes ‘cover’) and the Middle Eocene (age of the HP metamorphism in the Dilek-Selçuk region that belongs to the Cycladic Complex). Apatite fission track data for the rocks on both sides of the ‘Lycian Nappes/Menderes Massif‘ contact suggest that these rocks were very close to the paleo-Earth surface in the Late Oligocene-Early Miocene time.

This study in the Lycian Nappes and in the Menderes Massif establishes the existence of an extensive Alpine HP metamorphic belt in southwest Turkey. HP rocks were involved in the accretionary complex related to northward-verging subduction of the Neo-Tethys Ocean, Late Cretaceous obduction and subsequent Early Tertiary continental collision of the passive margin (Anatolide-Tauride block) beneath the active margin of the northern plate (Sakarya micro-continent). During the Eocene, the accretionary complex was made of three stacked HP units. The lowermost corresponds to the imbricated ‘core’ and HP ‘cover’ of the Menderes Massif, the intermediate one consists of the Cycladic Blueschist Complex (Dilek-Selçuk unit), and the uppermost unit is made of the HP Lycian Nappes.

Whereas the basement units of both Aegean and Anatolian regions underwent a different pre-Mesozoic tectonic history, they were probably juxtaposed by the end of the Paleozoic and underwent a common Mesozoic history. Then, the basements and their cover, as well as the Cycladic Blueschists and the Lycian Nappes were involved in similar evolutional accretionary complexes during the Eocene and Oligocene times.

KURZFASSUNG

West Anatolien, welches die östliche laterale Verlängerung der ägäischen Domäne darstellt, besteht aus mehreren tektono-metamorphen Einheiten, die Hochdruck/Niedrigtemperatur (HP/LT) Gesteine aufweisen. Einige dieser metamorphen Gesteine Zeugen der panafrikanischen oder der kimmerischen Orogenese sind, entstanden andere während die jüngere Alpine Orogenese.

Das Menderes Massiv, in der SW Türkei, wird im N von Decken der Izmir-Ankara Suturzone, im E von der Afyon Zone sowie im S von den Lykischen Decken tektonisch überlagert. In den Metasedimenten der Lykischen Decken und dem darunterliegenden Menderes Massiv treten weitverbreitete Vorkommen von Fe-Mg-Carpholith-führenden Gesteinen auf. Diese neue Entdeckung belegt, dass beide Deckenkomplexe während der alpinen Orogenese unter HP/LT Bedingungen überprägt wurden. Die P-T Bedingungen für die HP-Phase liegen bei 10-12 kbar/400°C in den Lykischen Decken und 12-14 kbar/470-500°C im südlichen Menderes Massiv, was eine Versenkung von min. 30 km während der Subduktion und Deckenstapelung dokumentiert.

Die Analyse der duktilen Deformation sowie thermobarometrische Berechnungen zeigen, dass die Lykischen Metasedimente unterschiedliche Exhumierungspfade nach der gemeinsamen HP-Phase durchliefen. In Gesteinen, die weiter entfernt vom Kontakt der Lykischen Decken mit dem Menderes Massiv liegen, lässt sich lediglich ein Hochdruck-Abkühlungspfad belegen, der mit einer „top-NNE“ Bewegung an die Akçakaya Scherzone gebunden ist. Diese Scherzone ist ein Intra-Deckenkontakt, der in den frühen Stadien, innerhalb des Stabilitätsfeldes von Fe-Mg-Carpholith, der Exhumierung aktiv war. Die nahe am Kontakt mit dem Menderes Massiv gelegenen Gesteine weisen wärmere Exhumierungspfade auf, die mit einer „top-E“ Scherung assoziiert sind. Diese Deformation erfolgte nach dem S-Transport der Lykischen Decken und somit zeitgleich mit der Reaktivierung des Kontakts der Lykischen Decken/Menderes Massiv als Hauptscherzone (der Gerit Scherzone), die eine späte Exhumierung der HP-Gesteine unter wärmeren Bedingungen erlaubte. Die Hochdruckgesteine des südlichen Menderes Massiv weisen eine einfache isothermale Dekompression bei etwa 450°C während der Exhumierung nach. Die begleitende Deformation während der Hochdruckphase und der Exhumierung ist durch eine starke N-S bis NE-SW–Dehnung charakterisiert.

Das Alter der Hochdruckmetamorphose in den Lykischen Decken kann zwischen oberster Kreide (jüngste Sedimente in der Lykischen allochthonen Einheit) und Eozän (Kykladische Blauschiefer) festgelegt werden. Ein mögliches Paläozänes Alter kann somit angenommen werden. Das Alter der Hochdruckmetamorphose in den Deckschichten des Menderes Massiv liegt demnach zwischen mittlerem Paläozän (oberste Metaolistostrome der Menderes „Cover“-Einheit) und dem mittleren Eozän (HP-Metamorphose in der Dilek-Selçuk Region des Kykladenkomplex). Apatit-Spaltspur-Daten von beiden Seiten des Kontakts der Lykischen Decken/Menderes Massiv lassen darauf schließen, daß diese Gesteine im späten Oligozän/frühen Miozän sehr nahe der Paläo-Oberfläche waren.

Die hier dargestellten Arbeiten in den Lykischen Decken und im Menderes Massiv lassen auf die Existenz eines ausgedehnten alpinen HP-Metamorphose-Gürtels im SW der Türkei schließen. Die Hochdruckgesteine wurden im Akkretionskomplex einer N-wärtigen Subduktion des Neo-Tethys Ozeans gebildet, der spät-Kretazisch obduziert und dann in die früh-Tertiäre Kontinentalkollision des passiven Randes (Anatolid-Taurid Block) mit der nördlichen Platte (Sakarya Mikrokontinent) miteinbezogen war. Im Eozän bestand der Akkretionskomplex aus drei gestapelten Hochdruckeinheiten. Die Unterste entspricht dem eingeschuppten Kern und Hochdruck-„Cover“ des Menderes Massivs. Die Mittlere besteht aus dem Kykladischen Blauschiefer-Komplex (Dilek-Selçuk Einheit) und die oberste Einheit wird von den Hochdruck Lykischen Decken gebildet.

Während die Basiseinheiten der ägäischen und anatolischen Region tektonisch unterschiedliche Prä-mesozoische Geschichten durchliefen, wurden sie wahrscheinlich am Ende des Paläozikums zusammengeführt und durchliefen dann ein gemeinsame mesozoische Geschichte. Dann wurden die Basis und ihre Deckschichten, ebenso wie die Kykladischen Blauschiefer und Lykischen Decken, in ähnlich entstandene akkretionäre Komplexe während des Eozäns und Oligozäns involviert.

RÉSUMÉ

L'Anatolie occidentale, prolongement vers l'est du domaine égéen, est constituée de plusieurs unités tectono-métamorphiques au sein desquelles affleurent des roches de haute-pression/basse température (HP-BT). Si certaines d'entre elles sont des vestiges des orogenèses Pan-Africaine et Cimmérienne, d'autres témoignent de l'orogenèse Alpine.

Au Sud-Ouest de la Turquie, le massif du Menderes forme un large domaine chevauché au Nord par les unités de la zone de suture d'Izmir-Ankara, à l'Est par la Zone d'Afyon, et au Sud par les nappes lyciennes. Ce travail de thèse a permis de mettre en évidence l'existence de paragenèses à Fe-Mg-carpholite largement distribuées dans les sédiments des nappes lyciennes, ainsi que dans les séries de couverture de la partie la plus méridionale du massif du Menderes. Cette découverte révèle que ces deux complexes de nappes ont enregistré des conditions de HP-BT pendant l'orogenèse Alpine. Les conditions P-T du pic de métamorphisme sont de 10-12 kbar/400°C pour les nappes lyciennes, et de 12-14 kbar/470-500°C pour le massif du Menderes, ce qui correspond à un enfouissement d'au moins 30 km pendant le processus de subduction et d'empilement de nappes.

L'analyse de la déformation ductile couplée à des calculs thermobarométriques basés sur la notion d'équilibres multiples indique que les métasédiments des nappes lyciennes ont enregistré des chemins d'exhumation distincts après le pic de métamorphisme. Les roches situées loin du contact entre les nappes lyciennes et le massif du Menderes, là où les paragenèses de HP sont préservées, ont enregistré des chemins froids (décompression en refroidissement) accompagnés de cisaillements vers le NNE liés à la zone de cisaillement d'Akçakaya. Cette zone de localisation de la déformation est un contact intra-nappe qui a fonctionné pendant les premiers stades d'exhumation des roches de HP, dans le champ de stabilité de la Fe-Mg-carpholite. En revanche, les roches situées au contact avec le massif du Menderes, là où les paragenèses de HP sont totalement rétromorphosées en chlorite et mica, ont enregistré des chemins d'exhumation plus chauds (décompression avec réchauffement) associés à un cisaillement intense vers l'est. Cette déformation s'est produite postérieurement à la mise en place des nappes lyciennes vers le sud, et est contemporaine de la réactivation du contact 'massif du Menderes/nappes lyciennes' en une zone de cisaillement majeure (la zone de cisaillement de Gerit) le long de laquelle se sont exhumées les paragenèses de HP sous des gradients plus chauds. Les roches de HP rencontrées dans les unités de couverture de la partie sud du massif du Menderes ont enregistré une simple décompression isotherme à 450°C pendant leur exhumation, et la déformation associée au métamorphisme de HP et à l'exhumation des roches de HP est caractérisée par un étirement intense orienté N-S à NE-SW.

L'âge du métamorphisme de HP des nappes lyciennes est compris entre le Crétacé terminal (âge des sédiments les plus jeunes des unités allochtones lyciennes) et l'Eocène (âge des schistes bleus cycladiques). Un âge paléocène est envisagé. L'âge du métamorphisme de HP ayant affecté les séries de couverture du massif du Menderes est contraint entre le Paléocène moyen (âge du métaolistostrome de la couverture du massif du Menderes) et l'Eocène moyen (âge du métamorphisme du HP dans la région de Dilek-Selçuk appartenant au complexe cycladique). Des données de traces de fission pour les roches situées de chaque côté du contact 'massif du Menderes/nappes lyciennes' indiquent que ces roches étaient très proche de la paléosurface à la période Oligocène supérieur-Miocène inférieur.

Cette étude menée dans les nappes lyciennes et la partie sud du massif du Menderes établit l'existence d'une large ceinture métamorphique de HP Alpine au Sud-Ouest de la Turquie. Les roches de HP ont été impliquées dans un complexe d'accrétion lié à la subduction vers le nord de l'océan Néo-Téthysien, l'obduction Crétacé supérieur suivie de la collision Tertiaire inférieur entre la marge passive du bloc Anatolides-Taurides au Sud et la marge active de la plaque septentrionale du bloc de Sakarya. Pendant l'Eocène, le complexe d'accrétion était constitué de trois unités de HP : l'unité la plus basse constituée du socle et de la couverture de HP du Menderes, tous deux imbriqués l'un dans l'autre, l'unité intermédiaire correspondant au complexe des schistes bleus cycladiques (unité de Dilek-Selçuk), et l'unité la plus haute composée des nappes de HP du complexe Lycien.

Si les unités de socle des domaines égéen et anatolien ont connu une histoire tectonique ante-Mésozoïque différente, elles ont probablement été juxtaposées vers la fin du Paléozoïque et ont connu une histoire Mésozoïque commune. Ensuite, les unités de socle et leur couverture, ainsi que les schistes bleus cycladiques et les nappes lyciennes ont été impliquées dans des complexes d'accrétion évolutifs similaires pendant l'Eocène et l'Oligocène.

ÖZ

Ege'nin doğu yanal devamını temsil eden Batı Anadolu, yüksek basınç/düşük sıcaklık (YB/DS) kayaç oluşumları içeren birçok tektono-metamorfik birimden meydana gelmektedir. Bu metamorfik kayaçların bir kısmı Pan-Afrikan veya Kimmeriyen orojen kalıtları iken bir kısmı ise Alpin orojenezi sonucu oluşmuştur.

Güneybatı Türkiye'de, Menderes Masifi, kuzeyden İzmir-Ankara Sütur Zonu, doğudan Afyon Zonu Napları ile güneyden Likya Naplarınca tektonik olarak üzerlenen geniş bir alanı kaplamaktadır. Bu çalışmada, Likya Naplarındaki meta-sedimanlarla, bunları altlayan güney Menderes Masifi'nde yapılan araştırmalar, Fe-Mg karfolit içeren kayaçların yaygın biçimde varlığını ortaya koymuştur. Bu bulgu, her iki nap kompleksinde de Alpin orojeni sırasında YB/DS metamorfik koşullarının varlığına ilişkin fikrin ilk kez ortaya çıkışını sağlamıştır. Likya Napları'nda 10-12 kbar/400ºC ve Menderes Masifi güneyinde 12-14 kbar/470ºC-500ºC civarında olan YB metamorfik piklerine karşılık gelen basınç-sıcaklık koşulları, dalma-batma ve nap istiflenmesi olayları sırasında en az 30 km derinliğe gömüldüğünü göstermektedir.

Çoğul-dengeli termobarometrik hesaplamalarla uyumlu olan plastik deformasyon analizleri, ortak yüksek basınç metamorfik pik evresi sonrasında Likya Napları metasedimanlarının farklı yükselme (eksümasyon) modelleri kaydettiğine işaret etmektedir. Likya Napları ve Menderes Masifi dokanağının uzağında bulunan, YB parajenezlerinin iyi korunduğu kayaçlar, Akçakaya makaslanma zonuyla ilgili üstten KKD'ya makaslanmasına ilişkin tek bir YB soğuma eğrisi sunmaktadır. Bu gerilme odaklaşması zonu, Fe-Mg karfolit duraylılık limitleri içerisindeki YB kayaçlarının yükseliminin erken evrelerinde aktif olan bir nap-içi dokanaktır. Menderes Masifi dokanağına yakın YB parajenezlerinin tamamen klorit ve mikaya geriletildiği kayaçlar, üstten doğuya şiddetli makaslanmayla ilintili daha sıcak yükselme eğrileri kaydetmektedir. Bu deformasyon, Likya Naplarının güney yönlü yerleşimi sonrasında oluşmuş olup, "Likya Napları-Menderes Masifi" dokanağının, YB parajenezlerinin daha sıcak koşullardaki geç yükselimine izin veren, ana makaslanma zonu (Gerit makaslanma zonu) olarak reaktivasyonu ile eşzamanlıdır. Menderes Masifi'nin güneyindeki YB kayaçları, yükselme sırasında 450ºC civarındaki basit izotermal dekompresyonu ve YB olayı sırasındaki deformasyonu kaydetmekte olup, yükselimi K-G'den KD-GB'ya şiddetli gerilmelerle karakterize edilmektedir.

Likya Naplarında kaydedilen YB metamorfizmasının yaşının, En Geç Kretase (Likya allokton birimindeki en genç sedimanların yaşı) ve Eosen (Siklat Mavişistlerinin yaşı) arasında olduğu kabul edilmektedir. Olası Paleosen yaş önerilmektedir. Menderes Masifi'nin örtü birimlerini etkileyen YB metamorfizmasının yaşı, Orta Paleosen (Menderes 'örtüsü'nün en üst olistostromunun yaşı) ve Orta Eosen (Dilek-Selçuk bölgesindeki Siklat Kompleksi'ne ait YB metamorfizmasının yaşı) arasında sınırlandırılmıştır. Likya Napları/Menderes Masifi dokanağının her iki tarafındaki kayaçlardan elde edilen apatit fizyon-iz (fission-track) verileri, bu kayaçların Geç Oligosen-Erken Miyosen zamanda paleo-yer yüzeyine çok yakın olduğuna işaret etmektedir.

Likya Napları ve Menderes Masifindeki bu çalışma Türkiye'nin güneybatısında yaygın bir Alpin metamorfik kuşağının varlığını ortaya koymuştur. YB kayaçları, Neo-Tetis Okyanusu'nun kuzey-yönlü dalması, Geç Kretase bindirmesi ve bunu takiben pasif kenarın (Anatolid-Torid bloğu) kuzeydeki plakanın (Sakarya mikro-kontinent) aktif kenarı altına Erken Tersiyer kıtasal çarpışmasıyla ilgili karışım kompleksi içerisinde yeralmaktadır. Eosen döneminde, karışım kompleksi istiflenmiş üç YB biriminden oluşmaktadır. En alttaki, bindirilmiş 'çekirdek' ve Menderes Masifi'nin YB 'örtüsü'ne karşılık gelirken, ortadaki birim Siklat Mavişist Kompleksi (Dilek-Selçuk birimi)'ni içermekte, en üst birim ise YB Likya Napları'ndan oluşmaktadır.

Ege ve Anadolu bölgelerinin temel birimleri, farklı Mesozoyik-öncesi tektonik tarihçeler geçirmiş olmalarına rağmen, muhtemelen Paleozoyik sonunda bitişmiş ve ortak bir Mesozoyik tarihçe geçirmişlerdir. Bu temeller ve örtüleri de, Siklat Mavişistleri ve Likya Naplarının yanısıra, Eosen ve Oligosen dönemlerinde benzer karışım kompleksleri oluşumunda yeralmışlardır.

TABLE OF CONTENTS

TABLE OF CONTENTS

INTRODUCTION

High Pressure-Low Temperature (HP-LT) rocks are widely exposed in the Alpine-Himalayan Belt. Plate tectonic can account for HP-LT metamorphism by fast burial during subduction and crustal thickening. Nevertheless, the processes responsible for the return of these metamorphic rocks back to the surface are far less understood. Exhumation is no longer considered the result of erosion alone. Wernicke (1981), Coney and Harms (1984), then Platt (1986) emphasized that extension can generate large shallow-dipping shear zones (detachments), and that extension along these tectonic contacts can efficiently remove the overburden and could therefore be one major cause of exhumation. However, other authors argued that exhumation of buried rocks could be mainly achieved in compressional regime (Burg et al., 1997; Aerden, 1998; Matte et al., 1998). The active debate on the role of compression and extension in the process of exhumation is often confused because of a tendency to mix syn- and post-orogenic mechanisms (Jolivet and Goffé, 2000). Syn-orogenic extension, restricted to the upper part of the accretionary complex, is contemporaneous with shortening in the lower parts during the build up of a mountain belt. Post-orogenic extension, which affects the whole lithosphere, occurs once mountain building processes have stopped, and contributes to the collapse of the chain. It is generally observed that the early compressional deformation is intensely obliterated by later extension. This intimate interplay between compression and extension (and erosion) results in the complete exhumation of metamorphic rocks (Jolivet and Goffé, 2000).

Distinguishing syn- and post-orogenic mechanisms during the build up and subsequent collapse of a mountain belt is therefore essential to understand how high-pressure (HP) rocks were exhumed. Metamorphic studies and thermobarometric approaches can give good constraints on the distinction of tectonic structures related to these two mechanisms. Particularly, PT paths are good tools to characterize tectonic processes because they depict the way HP metamorphic units returned back to the surface. During the last decade, such tectono-metamorphic method has provided crucial information on the tectonic evolution of the Tethyan-Alpine Belt, for instance in the Betico-Rifan chain (Goffé et al., 1989; Azañon, 1994; Bouybaouene et al., 1995; Azañon and Goffé, 1997; Balanyá et al., 1997; Martínez-Martínez and Azañon, 1997; Michard et al., 1997; Azañon and Crespo-Blanc, 2000; Negro, in prep.), in the Alps (e.g. Bousquet et al., 1998; Agard, 1999; Bousquet et al., 2002), in the Tyrrhenian Sea (Avigad et al., 1997; Jolivet et al., 1998a; Jolivet et al., 1999), in the Aegean Sea (Jolivet et al., 1996; Patriat and Jolivet, 1998; Jolivet and Patriat, 1999; Ring et al., 1999b; Trotet, 2000; Trotet et al., 2001a; 2001b; Parra et al., 2002b), as well as in Oman (Goffé et al., 1988; Michard et al., 1994a).

For many years, the Aegean region that offers excellent conditions of observation has been largely investigated. Extensive metamorphic domains exposing blueschist- to eclogite-facies rocks have been described (Blake et al., 1981; Mposkos and Perdikatsis, 1984; Okrusch et al., 1984; Okrusch and Bröker, 1990; Mposkos and Liati, 1991; Theye and Seidel, 1991; Franz and Okrusch, 1992; Theye et al., 1992; Forster and Lister, 1999b; Trotet et al., 2001b). It has been claimed that exhumation of these HP rocks involves a significant role of major flat-lying extensional shear zones (Avigad and Garfunkel, 1989; Gautier et al., 1993; Gautier and Brun, 1994b; Jolivet et al., 1994a; Jolivet et al., 1996; Forster and Lister, 1999a; Jolivet and Patriat, 1999; Trotet, 2000; Trotet et al., 2001a). However, whereas kinematics of post-orogenic extension during collapse of the mountain belt are quite well studied, the mechanisms of early syn-orogenic exhumation of HP rocks still remain enigmatic. Indeed, most of the structures contemporaneous with subduction and crustal thickening have been obscured by more recent severe extensional episodes. Although some tectonic works devoted to the better understanding of these syn-orogenic HP episodes have been led in the Aegean Sea domain (e.g. Trotet, 2000; Trotet et al., 2001a; 2001b), they only concern local areas. Any representation of the accretionary complex in which the rocks recorded such HP-LT conditions is therefore difficult to establish. It is thus necessary to look for syn-orogenic structures in regions that have been less intensely affected by post-orogenic extension.

Western Turkey, which represents the eastward lateral continuation of the Aegean domain, displays similar occurrences of HP-LT rocks (Okay, 1984; Okay and Kelley, 1994; Candan et al., 1997; Oberhänsli et al., 1997; Candan et al., 1998; Oberhänsli et al., 1998; Okay et al., 1998; Sherlock et al., 1999; Okay and Satir, 2000b; Candan et al., 2001; Oberhänsli et al., 2001; Çetinkaplan, 2002; Candan et al., 2002; Okay et al., 2002). Some of these metamorphic rocks are vestiges of the Pan-African or Cimmerian orogenies. Others are related to the more recent northward subduction of the Neo-Tethyan Ocean and resulting Late Cretaceous-Early Tertiary continental collision between the active margin of the northern plate (Sakarya Zone of the Pontides) and the passive margin of the southern plate (Anatolide-Tauride platform) (Şengör and

Yılmaz, 1981). As in the Aegean domain, Alpine extensional shear zones have been recognised in western Anatolia (Bozkurt and Park, 1994; Hetzel, 1995; Hetzel et al., 1995; Hetzel and Reischmann, 1996; Hetzel et al., 1998; Bozkurt and Satir, 2000; Gessner, 2000; Gessner et al., 2001c; Lips et al., 2001; Okay and Satir, 2000a). However, in this region, post-orogenic extension apparently occurred at slower rate than in the Aegean Sea, as attested by a much thicker crust. This should thus allow a better recognition of early syn-orogenic stages.

In the present study, investigations in the metasediments of the Lycian Nappes and the Menderes Massif, which cover an extensive domain in southwest Turkey, have revealed widespread occurrences of HP-LT parageneses. This discovery, presented herein, leads to reconsider the tectono-metamorphic evolution of western Anatolia during the Alpine orogenesis, and has strong implications on correlations, debated for many years, between western Anatolia and the nearby Aegean domain. The aim of this study is to give the characteristics of these newly reported HP rocks from the Lycian Nappes and the Menderes Massif, and to constrain the exhumation processes using a similar tectono-metamorphic approach as described above.

This manuscript is composed of five chapters:

Chapter I presents the geodynamic context of the whole Aegean-Anatolian region, focuses on the different tectono-metamorphic units forming both the Aegean domain and western Anatolia, and exposes in detail the objectives and the different methods used in this study.

Then, Chapters II and III aim at presenting and discussing metamorphic and structural data respectively from the Lycian Nappes and from the southern Menderes Massif.

Chapter IV focuses on the exhumation of these metamorphic rocks from both complexes, which is constrained by a multi-equilibrium approach and fission track data.

Finally, Chapter V highlights the main results of this work, presents a tectono-metamorphic model for the Alpine evolution of the Lycian Nappes and the Menderes Massif, and proposes tentative correlations between western Anatolia and the Aegean domain.

CHAPTER I

THE AEGEAN-ANATOLIAN REALM: PRESENTATION, OPEN QUESTIONS, OBJECTIVES AND METHODS

Map realized by the geographer Saint Janvier (Paris, middle of 18th Century)

The Menderes Massif and Lycian Nappes belong to the Alpine Belt of western Anatolia. In order to understand the tectono-metamorphic history of this area, first of all, Part A of this chapter highlights the geodynamic features of the Aegea-Anatolia region. Parts B and C present the different units forming both the Aegean domain and the Anatolian domain. Then Part D focuses on the open questions motivating this study and displays the objectives and the different methods used in this work.

A. GEODYNAMIC CONTEXT OF THE AEGEAN-ANATOLIAN DOMAIN

The present geodynamic context of the eastern Mediterranean involves four major tectonic plates: Eurasia, Africa, Arabia and Anatolia. It is dominated by two major phenomena: the subduction of the African Plate under Eurasia and the fast southwestward escape of Anatolia guided by the motion of the Arabian block towards the north (Figure I-1). Observing the high seismicity in the whole region, McKenzie (1972) established a model founded on rigid micro-plates. This model is based on the existence and the movement of the Anatolian micro-plate and the Aegean micro-plate between Africa and Eurasia (Figure I-2). The northward motion of Arabia produced the westward extrusion of Anatolia, this escape being responsible for the southwestward motion of the Aegean micro-plate.

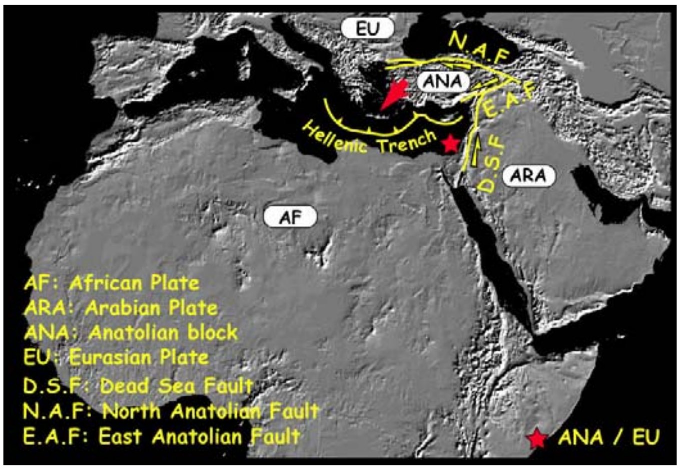

Figure I-1. Map showing the major tectonic plates and their movements in the eastern Mediterranean region.

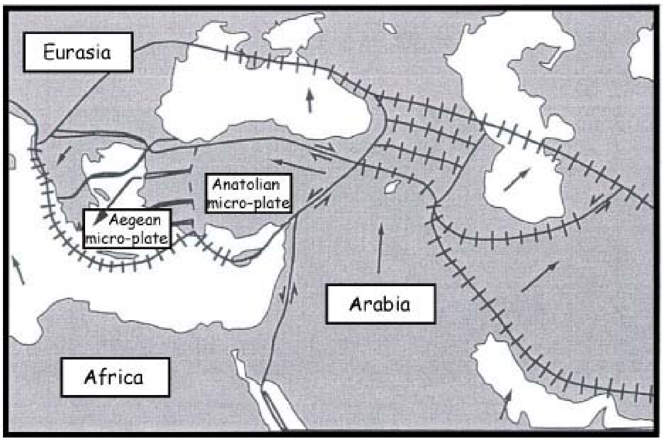

Figure I-2. Model involving Anatolian and Aegean rigid micro-plates (McKenzie, 1972).

1. The Hellenic subduction

The Hellenic trench extends from the Ionian Islands in the west (between Italy and continental Greece) to Rhodes in the east (Figure I-3). The convergence between Africa and Eurasia has a N-S direction and has been considered for many years as a constant motion for 80 Ma (Figure I-4; Olivet et al., 1982). The result of this convergence was the progressive disappearance of the Tethyan Ocean induced by the subduction of the African Plate.

Due to the combination of the motions of Anatolia and Africa, subduction of the African lithosphere proceeds at rates about 30 to 35 mm/yr (Figure I-3). The direction of convergence is about N20°E (Taymaz et al., 1990; Jackson, 1994) and is compatible with that obtained by geodetic data (Le Pichon et al., 1995).

Tomographic studies for more than ten years have led to obtain various pictures of the Hellenic subduction (Spakman et al., 1988; De Jonge et al., 1994). The images revealed a 'cold' zone, 200 km further north from the trench, interpreted as the down-going African slab under the Aegean arc, with a mean dip of 45° and a length of at least 500 km (Figure I-5).

Hatzfeld (1994) proposed a model of subduction, based on a seismicity dataset. This model shows on a profile from Peloponnese towards the northeast that the slab slightly dips under Peloponnese (less than 15°) whereas it is steeper under the Cyclades (30-40°C) (Figure I-6). This double geometry of the slab, which might be acquired over the last 5 Ma, has been interpreted as the result of an increase of the Aegean Plate velocity during extrusion of Anatolia.

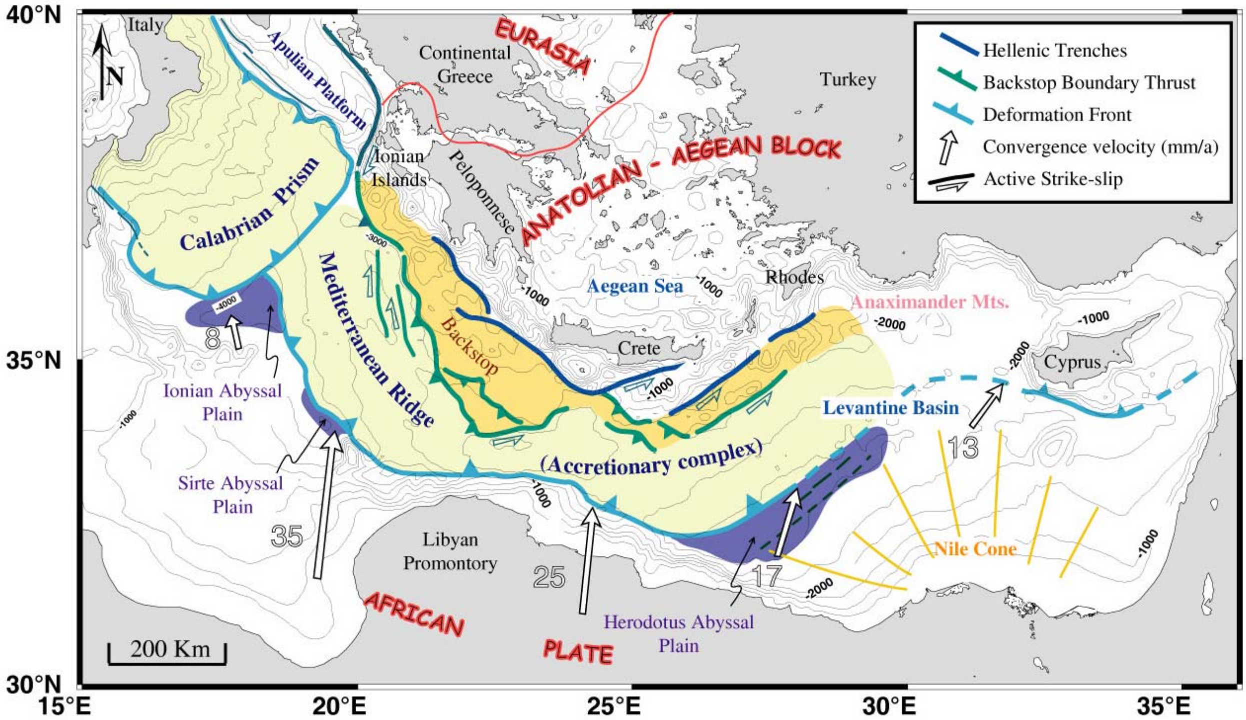

Figure I-3. Simplified tectonic and kinematic sketch of the Eastern Mediterranean (modified after Loubrieu et al., 2000 and Nielsen dit Christensen, 2003).

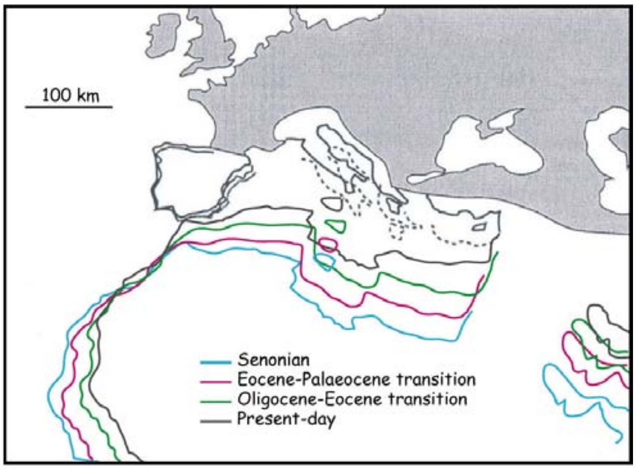

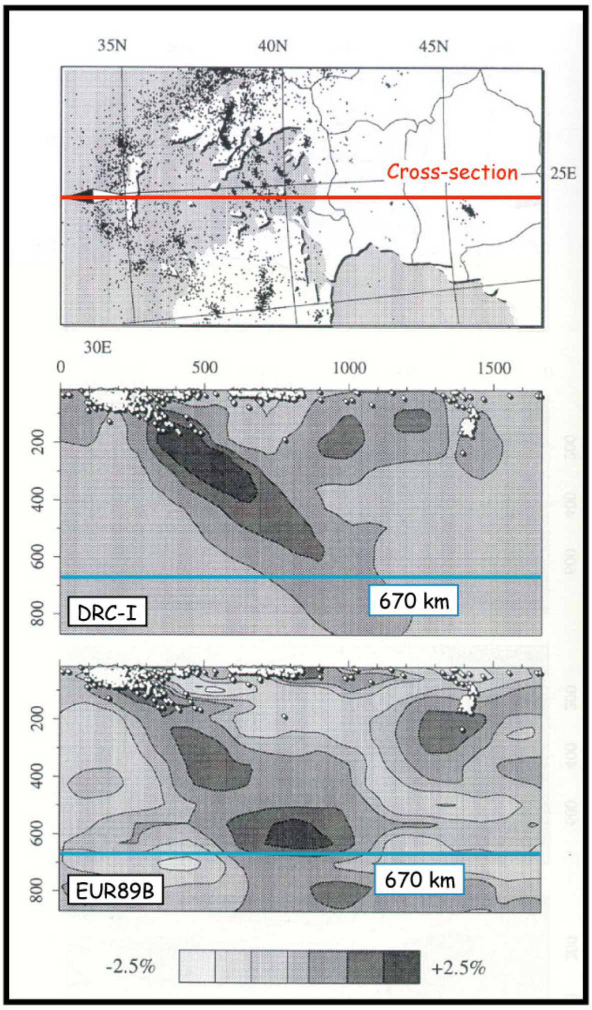

Figure I-4. Above: relative movements of the African and Eurasian plates from the Senonian to the present-day, showing the subduction-related progressive closure of the Mediterranean Sea (Olivet et al., 1982).

Figure I-5. Right: N-S tomographic cross-sections (P-wave anisotropy) across the Aegean domain, highlighting the existence of the down-going African slab under the Aegean arc [DCR-I and EUR89B correspond to pictures obtained by a forward method and a backward method (classical inversion) respectively] (De Jonge et al., 1994).

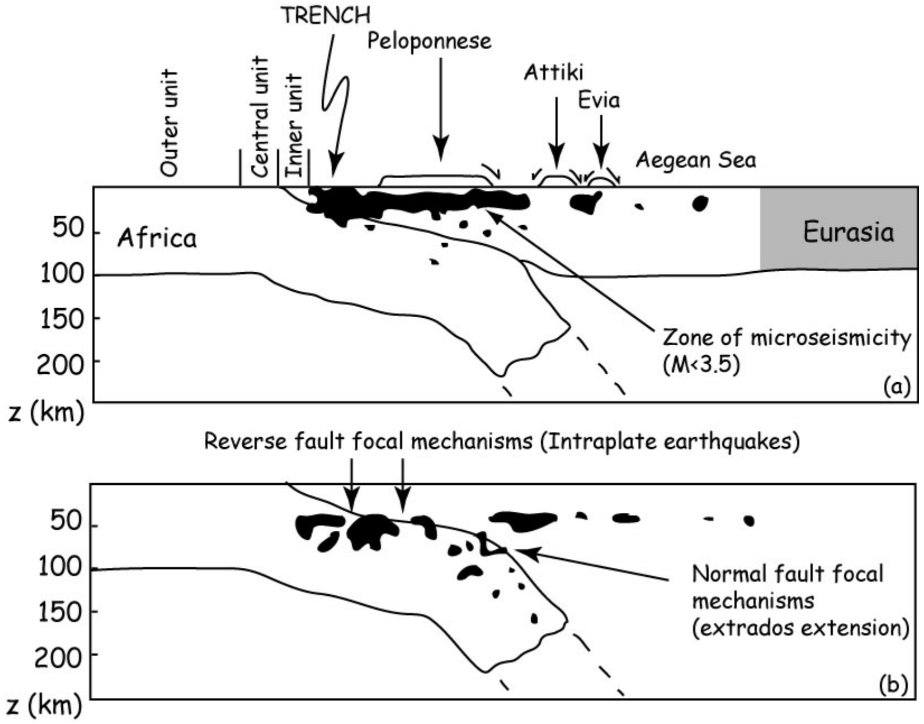

Figure I-6. Double geometry of the slab under Peloponnese (dip<15°) and Aegean Sea (dip~40°) deduced from (a) a microseismicity dataset (M<3.5) represented by the black zone, and (b) the repartition of normal fault and reverse fault focal mechanisms along the slab (modified after Hatzfeld, 1994).

2. Extrusion of Anatolia

Westward extrusion of the Anatolian-Aegean block is a major phenomenon in the eastern Mediterranean realm. As said before, it is related to the northward motion of Arabia with respect to Eurasia. The latter, which began between 12 and 15 Ma (Dercourt et al., 1986), has a velocity of about 6 mm/yr along the Dead Sea Fault. The escape of Anatolia towards the SW is guided by major active faults: the dextral North Anatolian Fault (NAF) and the sinistral East Anatolian Fault (EAF). The motion along the EAF is about 10 mm/yr (McClusky et al., 2000). The NAF constitutes the boundary between the Anatolian block and Eurasia. It is a recent feature formed some 2-5 Ma ago (Barka, 1992; Armijo et al., 1999), which propagated in the Aegean domain not earlier than 2-3 Ma ago (Le Pichon et al., 1995). This dextral fault extends over 1000 km in regular segments, producing a series of important earthquakes (such as Izmit and Duzce, in 1999). Le Pichon et al. (1995) described the motion of the Anatolian-Aegean block with respect to Eurasia as an anticlockwise quasi-rigid block rotation with a pole of rotation located around the Nile Cone (Figure I-7). The 24-25 mm/yr measured for the rotation of Anatolia, are compatible within errors with the 60-80 km of finite displacement along the NAF over 2 Myrs (Le Pichon et al., 1995; McClusky et al., 2000) (compare Figure I-7 and Figure I-8). Based on GPS (Global Positioning System) and SLR (Satellite Laser Ranging) velocities in the Aegea-Anatolia region, Le Pichon et al. (1995) claimed that the block rotation is rigid, similar to that described by McKenzy (1972). They also noticed a westward increase of velocity from Anatolia to Aegea, and concluded to a second order deformation in this area. However, based on a reoccupation of a 100-year-old first order triangulation network with GPS receivers, Davies et al. (1997) illustrated a more complex displacement strain pattern for the Aegean-Anatolian block. They interpreted it as compatible with a sheet of fluid moving towards the Hellenic trench, between two moving rigid blocks. The recent geodetic studies (McClusky et al., 2000) have led to confirm the first order rigid behaviour of Anatolia and introduced a rigid Aegean block (Figure I-9).

While the propagation of the NAF in the Aegean domain is recent (2-3 Ma), extension is much older and started around 25-30 Ma (Jolivet et al., 1994a,b; Gautier et al., 1999; Jolivet and Patriat, 1999; Jolivet and Facenna, 2000).

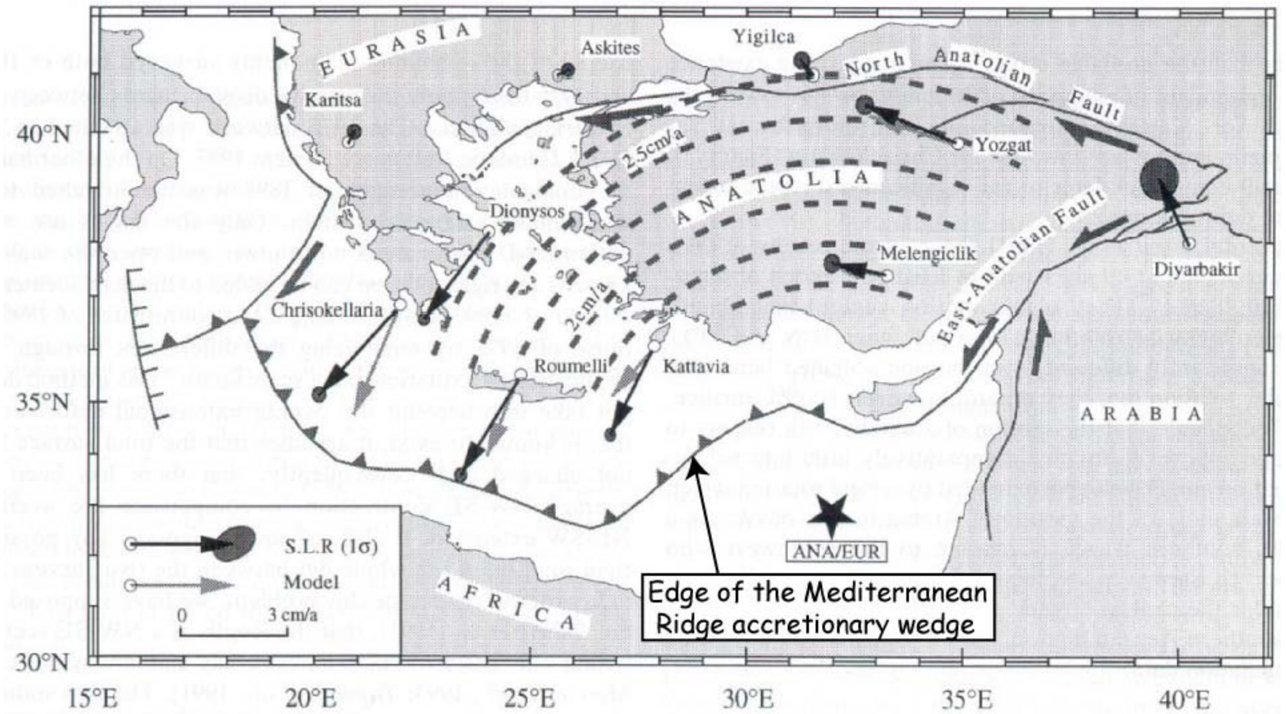

Figure I-7. Kinematic model deduced from geodetic data (Le Pichon et al., 1995). Solid arrows are SLR vectors with respect to Europe and shaded arrows are computed vectors corresponding to the rigid rotation best fitting the Anatolian extrusion. Dashed lines represent small circles which correspond to this rigid rotation. The star (ANA/EUR) locates the pole of rotation.

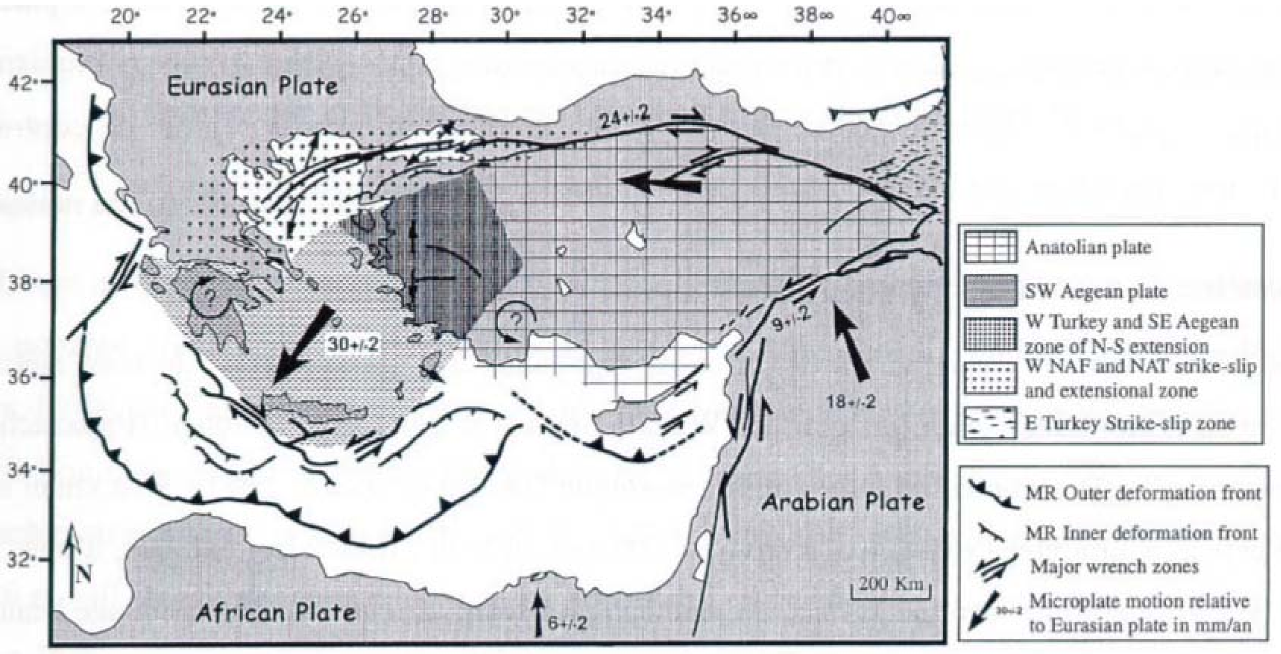

Figure I-8. Kinematic model of McClusky et al. (2000) confirming the rigid behaviour of Anatolia. This model mainly differs from that of Le Pichon et al. (1995) with the presence of a rigid Aegean block introduced in the kinematic model.

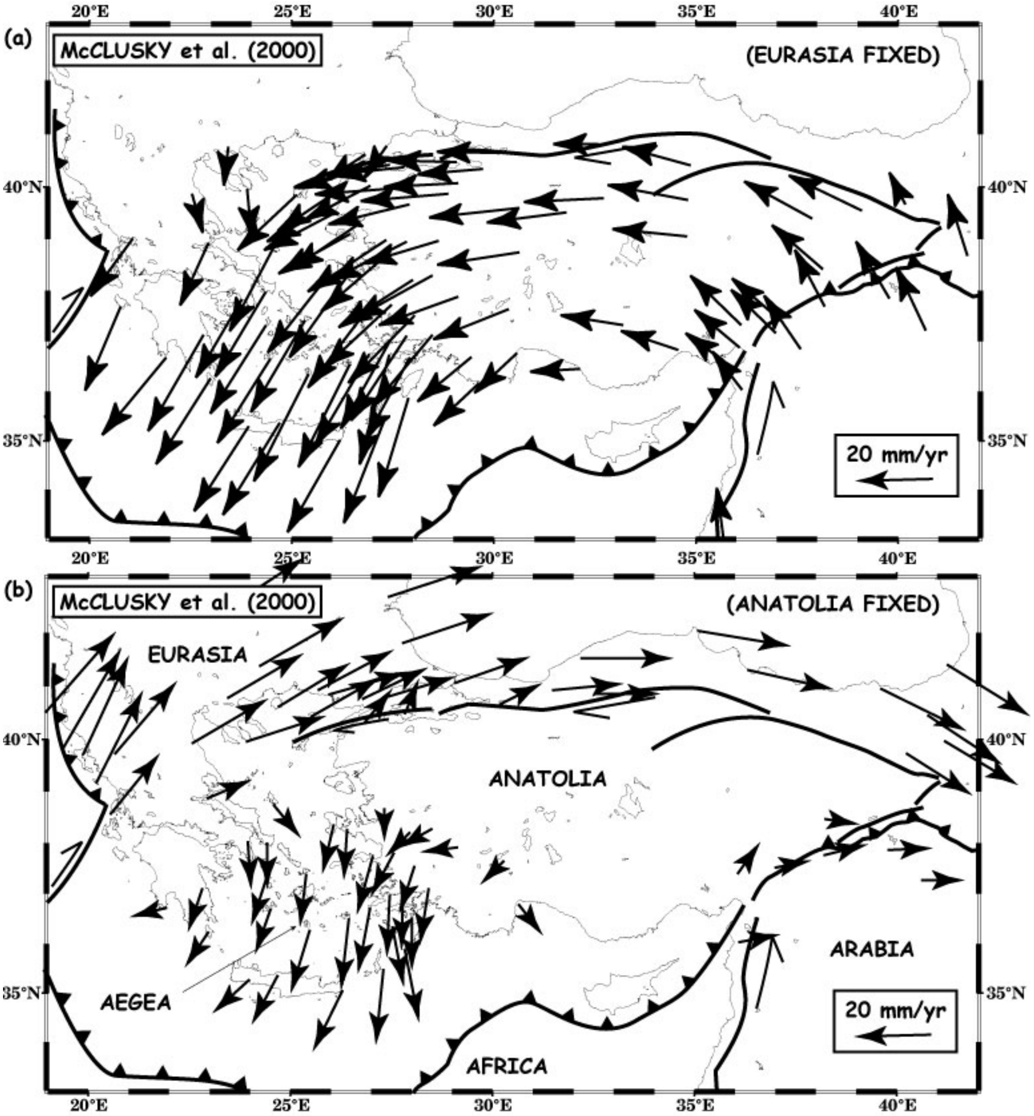

Figure I-9. GPS velocity field after McClusky et al. (2000): (a) GPS horizontal velocities with respect to Eurasia; (b) GPS horizontal velocities with respect to Anatolia (modified after Jolivet, 2001).

3. Aegean extension

The present-day extension in the Aegean domain is kinematically controlled by the extrusion of Anatolia along the NAF. However, as said before, this escape tectonics did not start before the Late Miocene, and the finite displacement along the NAF amounts to a maximum of 85 km (Barka, 1992; Armijo et al., 1999). In consequence, the fast westward migration of Anatolia cannot explain the major part of the Aegean extension which occurred much earlier (Seyitoğlu et al., 1992; Gautier et al., 1999; Seyitoğlu et al., 2002). The Aegean Sea formed in the back-arc region of the Hellenic trench during Late Oligocene until present. Subduction of the African Plate beneath the Anatolian block proceeds at a fast rate (30-40 mm/yr; Le Pichon et al., 1995). Extension has taken place on a previously thickened continental crust, the deep parts of which being now exhumed at the surface (Lister et al., 1984). Subduction of oceanic lithosphere began at least 40 Ma ago, as attested by seismic tomographic studies (Spakman, 1990). Extension has migrated southward continuously from the Early Miocene to the Present (Jolivet et al., 1998a). During the migration, arc volcanism has migrated at the same rate, around 30 mm/yr (Fytikas et al., 1984; Jolivet et al., 1998a). The thrust front has migrated with the slab retreat of the subduction zone. It was at the latitude of Crete during the Early Miocene time and is now south of the Mediterranean ridge.

a. Active and recent extension in the Aegean-Anatolian domain

Extension is mainly active along the eastern and western boundaries of the Aegean block (Figure I-10). Western Turkey shows large E-W-trending grabens (Seyitoğlu and Scott, 1996; Seyitoğlu et al., 2002). Extension is also active in Crete and Peloponnese and trends roughly parallel to the arc. The Corinth-Patras rift zone exposes E-W normal faults which are connected to a shallow north-dipping shear zone at or near the brittle-ductile transition, and shown at depth by many micro-earthquakes (Rigo et al., 1996; Sorel, 2000).

The southward motion of the Aegean block is responsible for 1 to 1.5 cm/yr of extension both in the Corinth-Patras rift and in western Turkey. The quasi-absence of seismicity in the central part of the Aegean Sea favours to a rigid behaviour of the Aegean block (McClusky et al., 2000). Angelier et al. (1982) and Mercier et al. (1987) recognized a succession of stress regimes during the Neogene time. A change in the direction of extension is described after the Lower Pleistocene. While the Pliocene and the Lower Pleistocene are characterized by a NNE-SSW to N-S extension in the Aegean Sea and E-W in Peloponnese, extension in the more recent times is NNW-SSE to N-S in the Aegean and roughly E-W in Crete and Peloponnese. This change has been interpreted as the result of the incipient collision between the Hellenic arc and the Lybian margin, or simply to the recent increase of convergence velocity.

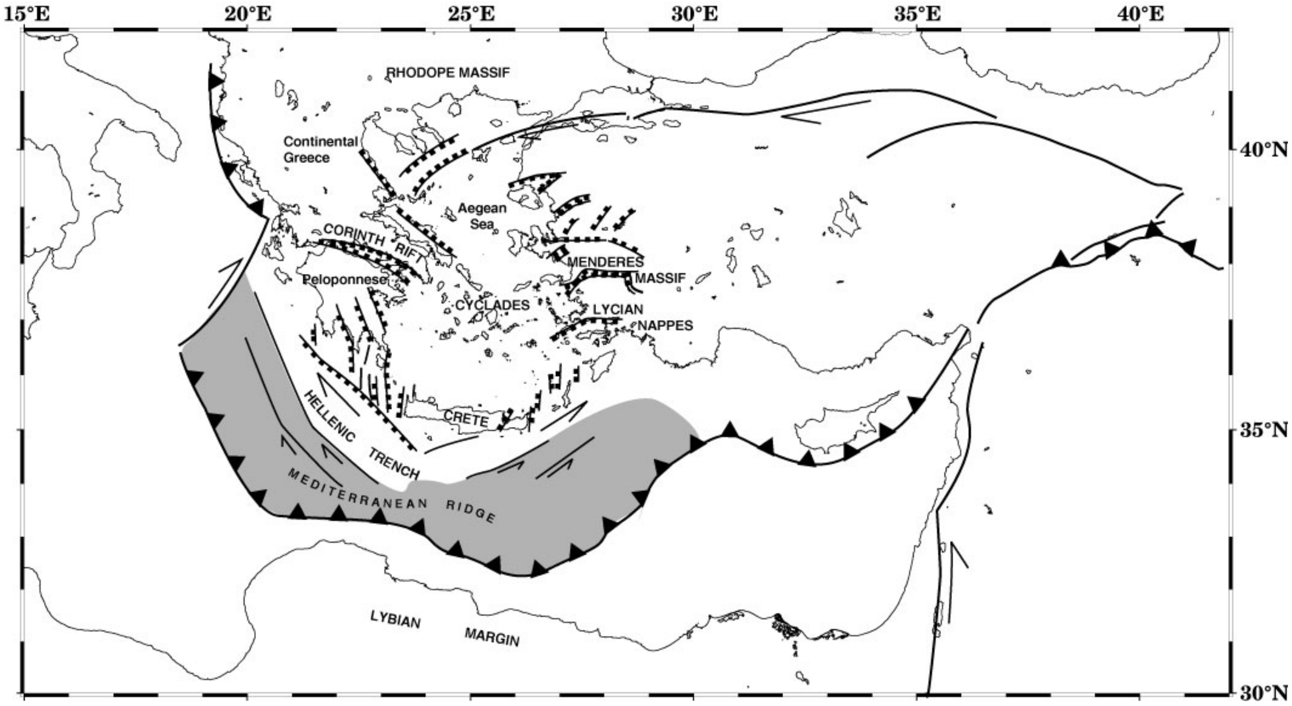

Figure I-10. Location of active deformation in the Aegean domain (modified after Jolivet, 2001). The shaded zone corresponds to the Mediterranean Ridge accretionary wedge.

b. Oligo-Miocene extension

Although extension is presently localized in a few areas of the Aegean-Anatolian region, it was distributed over a wider zone during the Oligocene-Miocene time (Jolivet, 2001; Figure I-11). Consequently to the Late Cretaceous closure of the Neo-Tethyan Ocean in the northern part of the Aegean domain, continuing convergence led to shortening of the Apulian continental crust (Bonneau, 1982; Dercourt et al., 1986; Figure I-12). This event is responsible for the formation and exhumation of high-pressure rocks, such as the Cycladic Blueschist (Bonneau and Kienast, 1982). Shortening and syn-orogenic exhumation occurred during the Late Cretaceous until the Eocene. High-pressure/low-temperature (HP-LT) metamorphic rocks, which underwent blueschist- to eclogite-facies conditions, were brought in the upper crust.

An acceleration of slab retreat changed the subduction regime and caused the collapse of the thickened Hellenic mountain belt and the formation and crustal thinning of the Aegean Sea from the Late Oligocene to the Present (Figure I-12; Jolivet and Faccenna, 2000). Gautier et al. (1999) claimed that the initiation of Aegean extension did not result from the lateral escape of Anatolia. Instead, extension started owing to a process of gravity spreading of the continental lithosphere that had previously been thickened during Alpine collision. Extension is recorded in metamorphic core complexes which crop out in the Cyclades, in western Turkey, as well as in the Rhodope Massif. Post-orogenic extension is characterized by large-scale detachments which allowed the final exhumation of metamorphic core complexes along a warmer geotherm (Lister et al., 1984; Avigad and Garfunkel, 1989; Avigad, 1990; Faure et al., 1991; Lister and Baldwin, 1993; Gautier and Brun, 1994a; Jolivet et al., 1994b; Jolivet and Patriat, 1999). Detachments are found in almost all the Cycladic islands, in the Rhodope as well as in the Menderes Massif (Hetzel et al., 1995). This post-orogenic extensional event is associated with a high-temperature/low-pressure (HT-LP) metamorphic

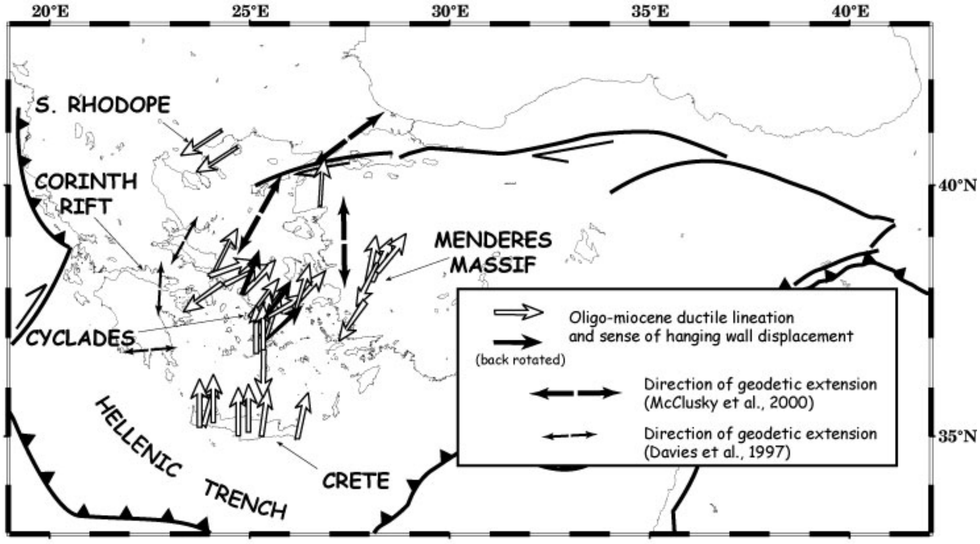

Figure I-11. Comparison between the direction of Oligo-Miocene finite deformation and the direction of active extension derived from GPS velocity field (modified after Jolivet, 2001). White arrows correspond to the stretching lineations with their present strike and black arrows are the same lineations back-rotated accounting for paleomagnetic rotations.

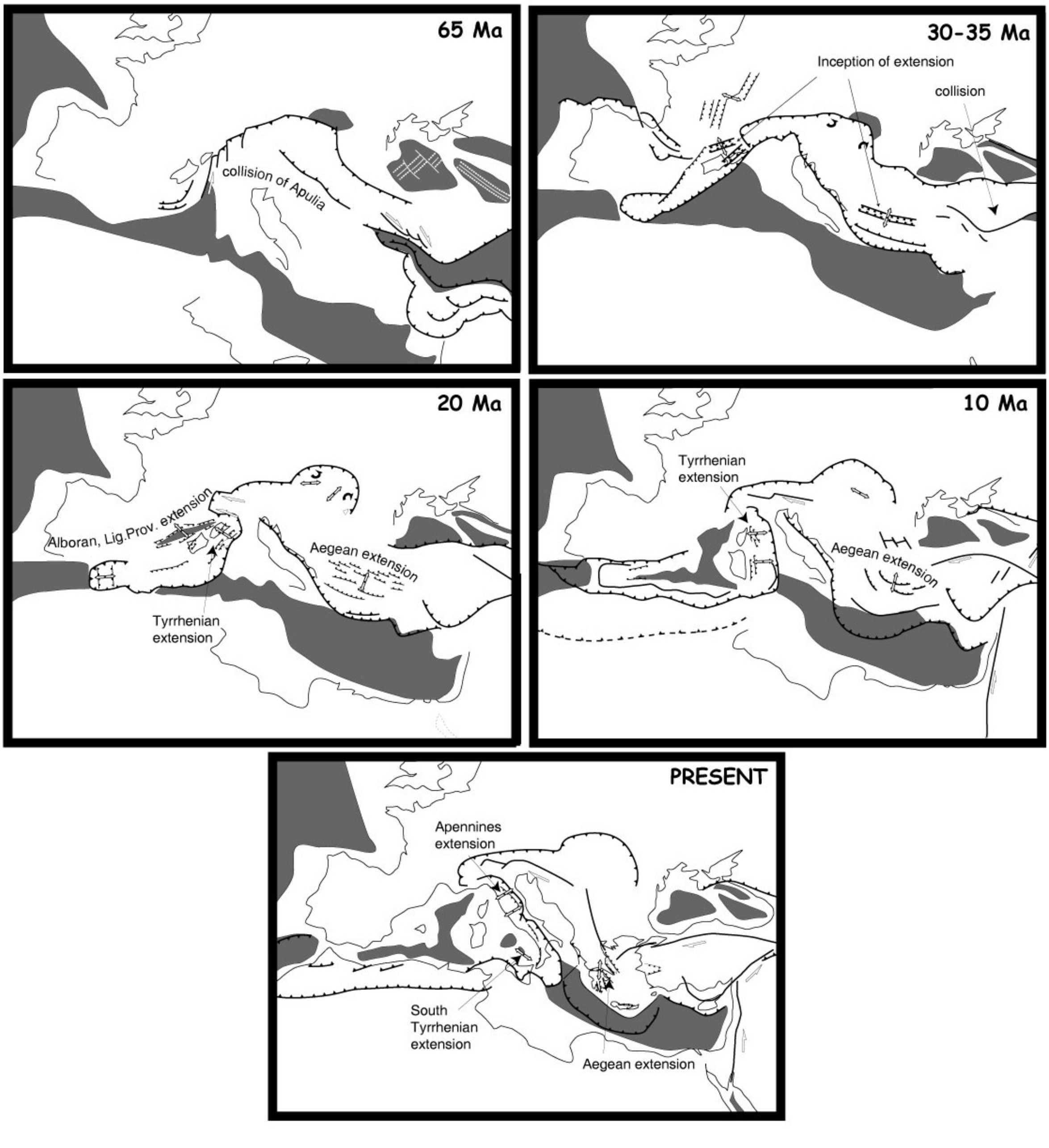

Figure I-12. Paleotectonic reconstructions of the Mediterranean region (modified after Dercourt et al., 1986; Jolivet and Facenna, 2000). Shaded zones represent the oceanic crust.

gradient and the rocks which had not been sufficiently exhumed during the syn-orogenic stage to escape from reheating show evidence of HT recrystallisation and partial melting (Jolivet and Patriat, 1999).

While the back-arc region was extending (Cyclades, Menderes Massif), the frontal part of the orogen was still experiencing syn-orogenic thickening and formation of HP-LT rocks and their exhumation (Crete and Peloponnese) (Fassoulas et al., 1994; Jolivet et al., 1994a; Doutsos et al., 2000; Ring et al., 2001a).

Exhumation of those more recent high-pressure units was mainly achieved by N-S extension along shallow north-dipping shear zones evolving into brittle detachments with a similar shallow dip at the top of the accretionary complex. Post-orogenic extension in the back-arc region is also N-S or NE-SW. Displacement of the hanging wall is consistently towards the north or northeast in the Cyclades, towards the southwest in the southern in the Rhodope Massif and bivergent in the Menderes Massif (Figure I-11).

As a synthesis, Figure I-13 locates the domains of syn-orogenic and post-orogenic Oligo-Miocene extension and crustal collapse, and the domains of recent extension and collapse.
This succession of events has given rise to various tectono-stratigraphic domains which are presented in detail in the next parts (Part B and Part C).

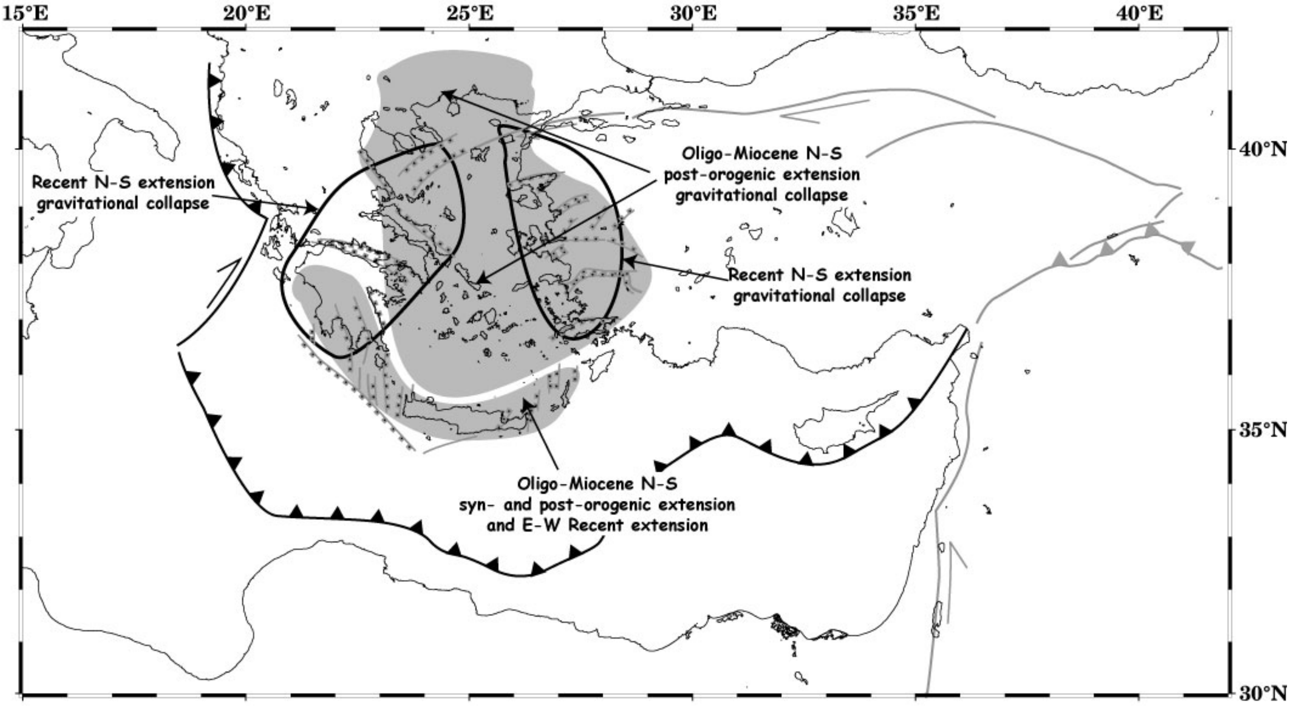

Figure I-13. Domains of syn- and post-orogenic Oligo-Miocene extension and gravitational collapse (shaded areas) and recent extension and collapse (unshaded areas with bold lines) (modified after Jolivet, 2001).

c. Crustal thickness

Differential extension is indicated by the fact that the Aegean domain, especially the Cretan Sea, is underlain by intensely attenuated continental crust whereas the peripheral regions (Greece and Western Turkey) are not. Figure I-14, which highlights the relief in the Aegean-Anatolian region, shows two high-elevated domains separated by a deep basin: the Greece-Evia-Cyclades-Mederes Massif domain in the north, and the external arc domain (Peloponnese-Crete-Dodecanese-Lycian Taurus) in the south, the Cretan Sea forming the deep zone (2000-2500 metres deep) in between. It seems reasonable to correlate these topographic variations with crustal thickness. Based on seismic refraction and gravimetric data (Makris, 1978), Le Pichon and Angelier (1979) calculated the crustal thickness (Figure I-15). A correlation between both maps can be made. It shows a thick continental domain comprising continental Greece and Peloponnese (>40 km) evolving thinner towards Crete. The crustal thickness in the Menderes Massif-Lycian Taurus region is about 35-40 km, around 25-30 in the Cyclades, and less than 20 km in the Cretan Sea. About 45-50 km is a fair minimum estimation of the pre-extension thickness of the crust under the Cretan Sea by comparison to the Hellenic Chain farther west (Jolivet and Patriat, 1999).

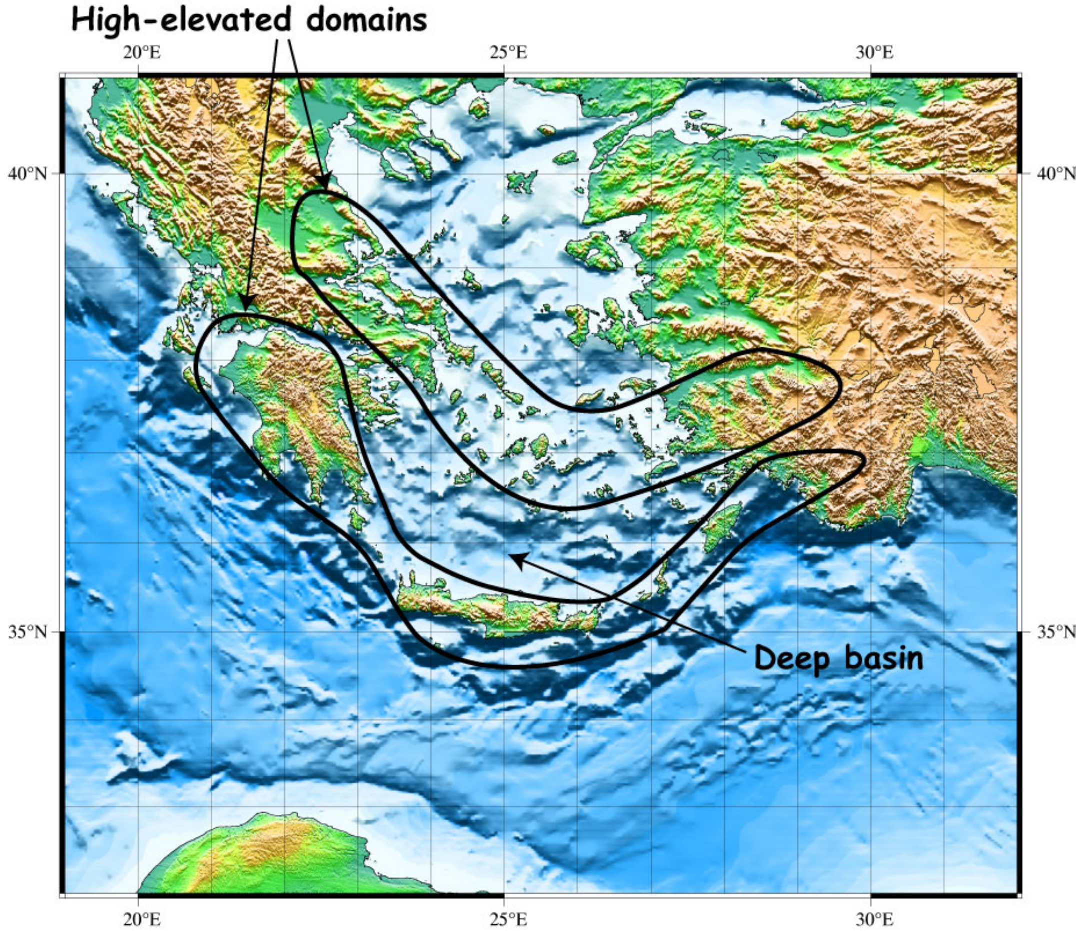

Figure I-14. Topographic map (GTOPO30) showing two high-elevated zones (Greece-Evia-Cyclades-Menderes Massif in the north, and Peloponnese-Crete-Dodecanese-Lycian Taurus in the south) separated by a deep basin (Cretan Sea).

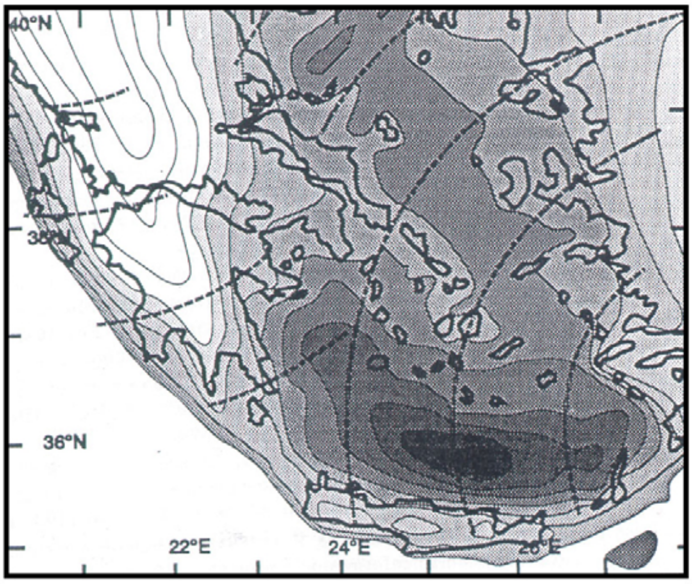

Figure I-15. Map showing the crustal thickness of the Aegean domain (after Makris, 1978 and Le pichon and Angelier, 1979; extracted from Jolivet et al., 1994a). White zones correspond to crustal thickness greater than 40 km and black zones lower than 18.5 km (intervals of 2.5 km).

d. Block rotations

The direction of the Oligo-Miocene extension is shown in the Aegean Sea and in western Turkey by N-S to NE-SW trending stretching lineations (Sokoutis et al., 1993; Jolivet et al., 1994a; Hetzel et al., 1995) (Figure I-11). Some of the lineations have been rotated around vertical axes. Recent vertical axis rotations have been documented by paleomagnetic data on Neogene rocks of the Aegean-Anatolian region (continental Greece, Crete and Turkey; Kissel and Laj, 1988). These data indicate that NE-SW-trending stretching directions are located in a domain showing clockwise rotation, whereas N-S-trending directions are found in a domain that shows no rotation (Figure I-16).

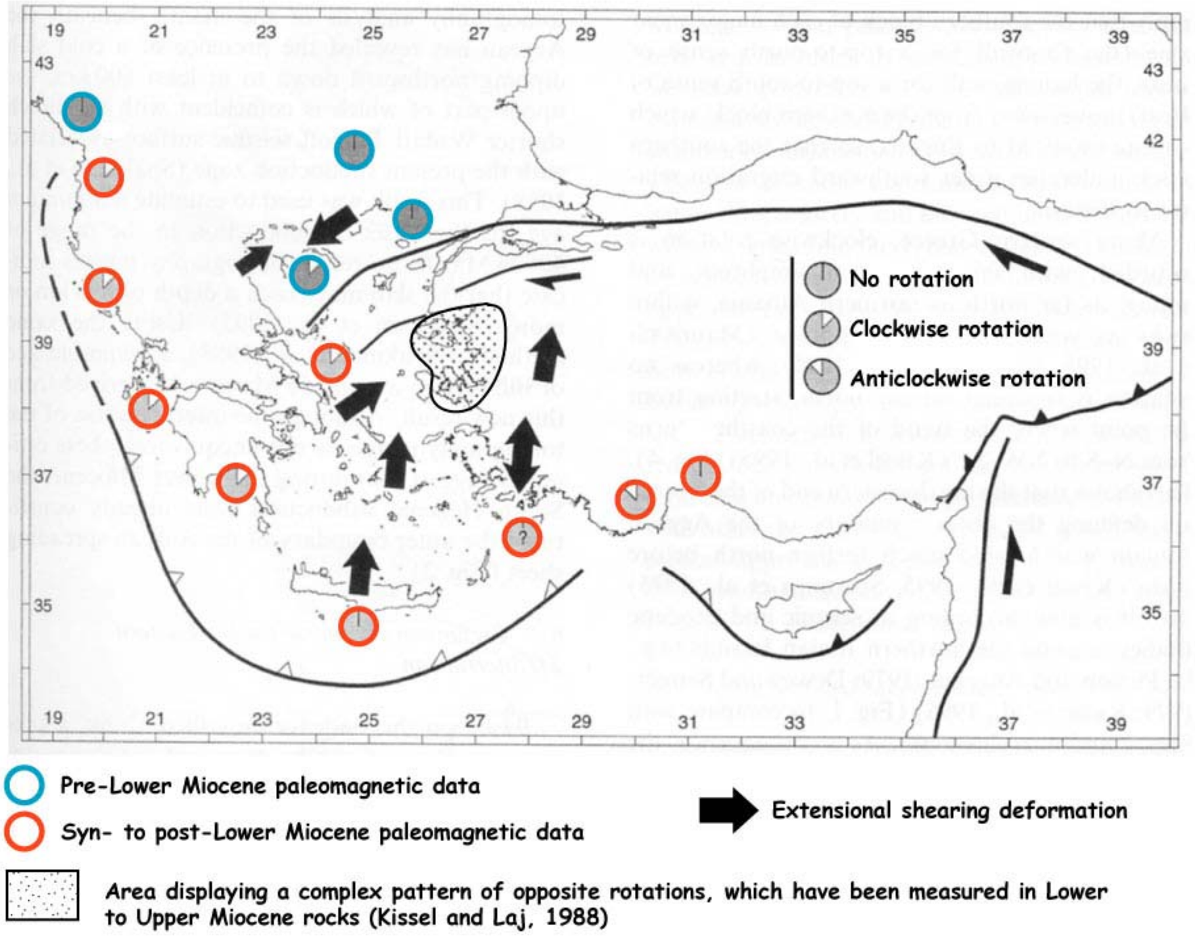

Figure I-16. Map highlighting the relation between extensional shearing deformation and paleomagnetic rotations in the Aegean domain (mainly after Kissel and Laj, 1988; map modified after Gautier et al., 1999). Only a qualitative report of rotation is shown.

In continental Greece, clockwise rotation is recorded whereas the eastern Aegean realm shows a more complex pattern with clockwise and anticlockwise rotations (Figure I-16). Along western Greece, clockwise rotation shows fairly constant amplitude (~20-25°) and timing (Middle Pliocene) whereas no rotation is recorded farther north, in Albania and in the Rhodope Massif (Kissel and Laj, 1988; Kissel et al., 1995). This is consistent with a reconstitution of the Aegean domain at its 10 Ma-position from Le Pichon and Angelier (1979), on the basis of rotation data (Figure I-17).

Paleomagnetic measurements in central and eastern Anatolia document a significant 15-20° anticlockwise rotation interpreted as the evidence for a rigid block rotation of the whole Anatolian block by the same amount (Gürsoy et al., 1998; Platzman et al., 1998; Kissel et al., 2003). This rotation is compatible with the recent motion of Anatolia along the NAF constrained by geodetic data (McClusky et al., 2000; Kissel et al., 2003). However, western Anatolia does not show a consistent rotation pattern. As seen in Figure I-16, the western margin of the Antalya gulf shows a 20° anticlockwise rotation measured in the Bey Dağları platform but the eastern margin does not show any rotation (Kissel and Laj, 1988). The Aegean margin of Anatolia (around Izmir and Chios) shows an area displaying a complex pattern of opposite rotations, measured in Lower to Upper Miocene rocks (Kissel and Laj, 1988). In Rhodes, no or only slight anticlockwise rotations have been detected (Duermeijer et al., 2000). In Turkey, rotations have been largely documented but unfortunately no data are reported from the Lycian Nappes and Menderes Massif.

In the Cyclades, anticlockwise rotation of about 30° and clockwise rotation around 20° have been described respectively in Naxos and Mykonos (Morris and Anderson, 1996). Avigad et al. (1998) reported a 23° clockwise rotation in Late Miocene volcanic intrusions of Tinos Island. Back-rotations of the lineations reduce the discrepancy between the orientations of stretching in these three islands and show that the direction of extension was uniformly NNE-SSW before rotations (Jolivet, 2001).

For many years, Crete has been considered to have not rotated (Kissel and Laj, 1988). However, Duermeijer et al. (1998) documented a complex rotation system, with a significant post-Messinian series of clockwise and anticlockwise rotations in sedimentary basins, although the direction of stretching lineations is remarkably constant in the whole island (Jolivet et al., 1996). It has been proposed that the Miocene basins developed above large-scale detachment (Jolivet et al., 1996) and that the complex rotations affected only the upper plate, leaving the exhumed ductile part non rotated (Jolivet, 2001).

A very recent paleogeographic reconstruction of the eastern Mediterranean region from the Paleocene time to present, deduced from paleomagnetic data, is shown as a synthesis in Figure I-18 (Kissel et al., 2003).

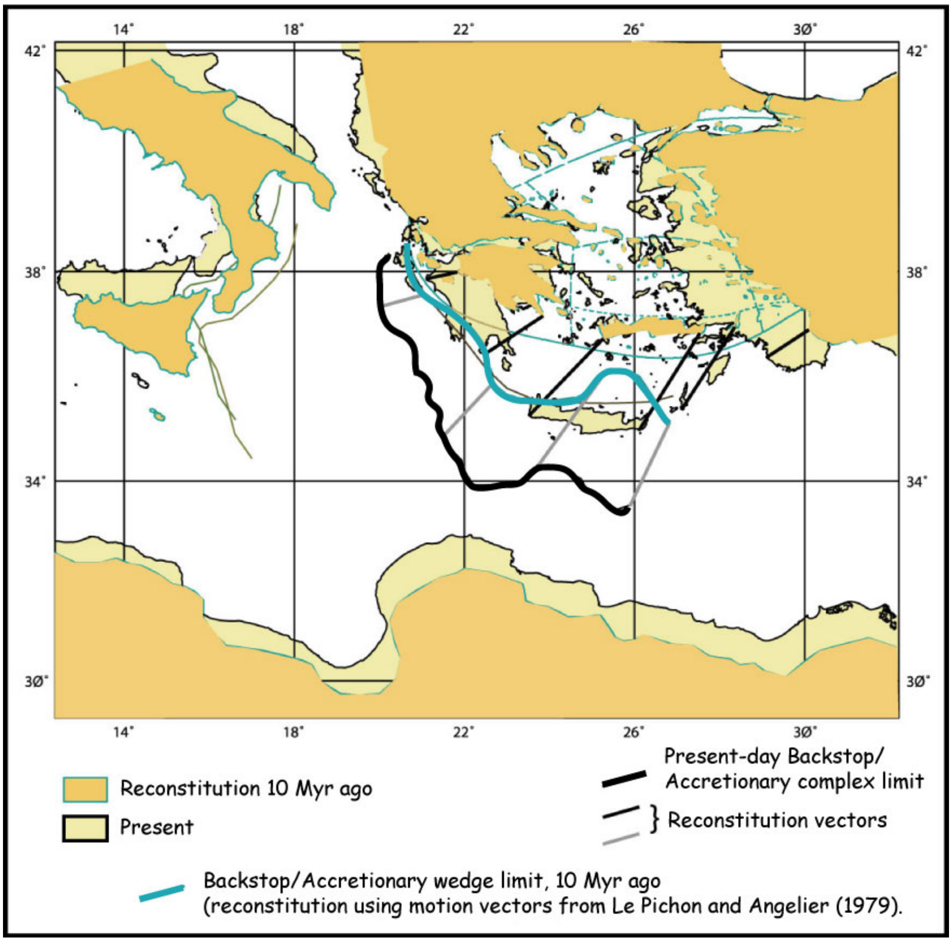

Figure I-17. Reconstitution of the Aegean domain at 10 Ma illustrating the movements of Crete and Peloponnese (modified after Le Pichon and Angelier, 1979; Nielsen dit Christensen, 2003).

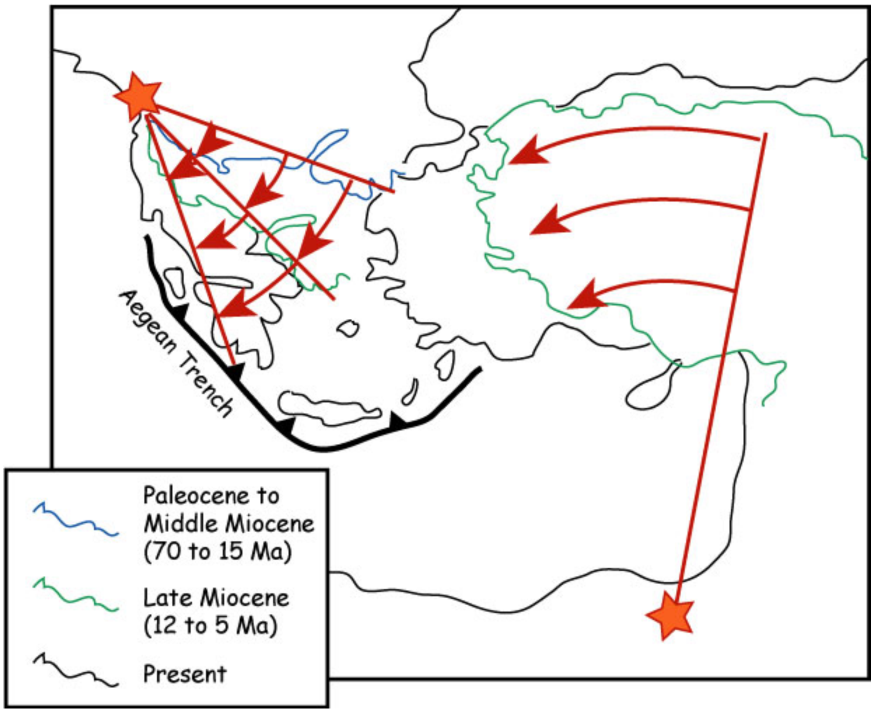

Figure I-18. Schematic evolution of the Eastern Mediterranean deduced from paleomagnetic data and showing two rotations in opposite senses in western Greece and in Turkey (modified after Kissel et al., 2003).

B. TECTONIC AND METAMORPHISM IN THE AEGEAN DOMAIN

In this part, I present the main geological features of each unit that forms the Aegean domain. Then, I summarize the present knowledge of the tectono-metamorphic history of the Aegean region, highlighting the tight relations between deformation and metamorphism.

1. A complex region made of various tectono-metamorphic units

From the northern part of the Aegean Sea to Crete, the Aegean domain is composed of the following distinct units.

a. The Rhodope Massif

The Rhodope Massif is located in the northernmost part of the Aegean domain (Figure I-19), at the north of the Vardar Suture Zone. It partly forms the northern active continental margin of the Tethyan Ocean (Ricou, 1994; Ricou et al., 1998). A Cretaceous-Eocene compressional episode led to nappe stacking, later reworked by post-orogenic extension. In the whole massif, Tertiary granitoids have emplaced in extensional regime that is related to the collapse of the Hellenic Orogen and, more particularly, to the crustal thinning that the Aegean region suffered since the mid-Tertiary (Jones et al., 1992). The Strymon detachment extends in the northern Aegean Sea. Extensional deformation and metamorphic core complex structures have been identified as far south as the island of Thasos (Dinter and Royden, 1993; Sokoutis et al., 1993; Wawrzenitz and Krohe, 1998; Moriceau, 2000). Up to the recent discovery of ultra-high-pressure parageneses in the southern part of the massif (Mposkos and Kostopoulos, 2001), the massif was considered to have undergone eclogite-facies conditions, based on the findings of eclogites within preserved basic boudins in high-temperature gneisses (Liati and Seidel, 1996; Liati and Gebauer, 1999). The age of this high-pressure event is not clearly ascertained. Liati and Gebauer (1999) interpreted U/Pb SCHRIMP ages on zircons between 73 and 42 Ma as HP ages. These ages were later discussed considering other geological data and it has been concluded that the eclogitic stage occurred at 50 Ma or earlier, followed by a progressive exhumation until ~30-35 Ma (Moriceau, 2000). Similar ages have been obtained on the extension of the Rhodope Massif in the island of Thasos (Wawrzenitz and Krohe, 1998; see location in Figure I-19). In the western part of the Rhodope massif (Circum-Rhodope), HP-LT parageneses have been described and correlated with the Late Jurassic event recorded in the Vardar zone (Michard et al., 1994b) within the far-travelled upper units of Crete (Bonneau, 1982).

b. The Vardar Suture Zone

The Vardar suture zone marks the boundary between the Rhodope continental block and the Pelagonian zone further southwest (Figure I-19). It crops out in Yugoslavia and in continental Greece. From west to east, three units form the Vardar zone: the Almopias unit, the Paikon unit and the Peionas unit. The succession is made of Triassic to Jurassic neritic carbonates and volcano-sedimentary formations (mainly in the Paikon and Peionas units). The Jurassic period is characterized by magmatic formations comprising serpentinites, gabbros and lavas (Almopias unit). In the eastern part of the Paikon unit, these rocks are cut by granodioritic plutons of Late Jurassic to Early Cretaceous age (Ricou et al., 1998). Jurassic and Cretaceous rocks comprise a detrital sequence and limestones (Almopias and Paikon) topped by a flysch-type unit (Almopias). This region partly belongs to the active margin once located north of the Tethyan Ocean that is represented by ophiolitic units. Several ophiolitic massifs were attributed to two distinct ophiolitic basins separated by a platform-type unit or to a single ophiolitic nappe resting on top of the platform (Godfriaux and Ricou, 1991a).

c. The Pelagonian Zone

The Pelagonian zone as well as the Vardar zone forms the internal parts of the Hellenides (Figure I-19). It is characterized by a tectono-stratigraphic succession consisting of a Permian detrital sequence overlain by a Mesozoic platform sequence topped by a Late Jurassic chaotic sequence below the Vourinos ophiolite (Celet and Ferrière, 1978). The best and simplest way to characterize the Pelagonian domain is to refer to the Late Jurassic ophiolite obduction and associated deformation (Bonneau, 1982). Pelagonian units crop out in continental Greece and Peloponnese where they have been first defined, but also as far-travelled small slices in the Cyclades (ophiolitic and gneiss units resting on top of extensional metamorphic complexes) or in Crete (Asteroussia nappe) (Bonneau, 1973; Reinecke et al., 1982; Bonneau, 1984; Papanikolaou, 1987) (Figures I-19 and I-20).

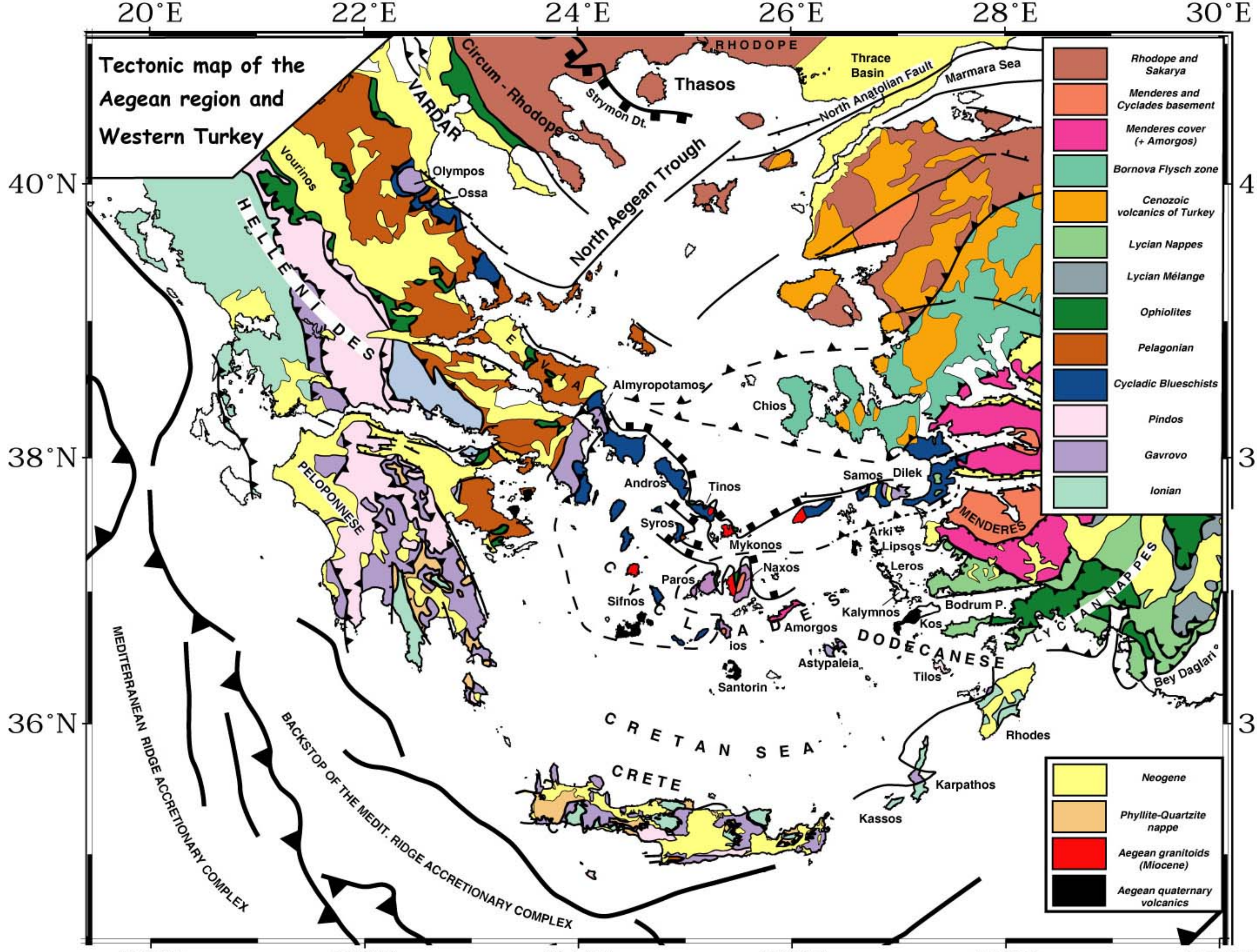

Figure I-19. Tectonic map of the Aegean-Anatolian region (compiled after Creutzburg, 1977; Bonneau, 1982; 1984; Collins and Robertson, 1997; 1998; 1999; Okay and Tüysüz, 1999; Bozkurt and Satir, 2000; Okay and Satir, 2000a; Okay et al., 2001a).

In the Cycladic arc, these outliers of the Pelagonian domain are observed as small units of ophiolitic material in Tinos or Paros, or as high-temperature metamorphic rocks in Syros, Nikouria or Donoussa where Late Cretaceous radiometric ages have been obtained (Jansen, 1977; Dürr et al., 1978; Maluski et al., 1987; Patzak et al., 1994; Katzir et al., 1996). The Pelagonian nappe is also found as clasts in Early Miocene conglomerates deposited above the flat-lying detachments of Paros and Mykonos in the central Cyclades, suggesting that it once covered an extensive area of the Aegean domain (Sanchez-Gomez et al., 2002). In Crete, the Asteroussia nappe contains various lithologies, a Late Jurassic ophiolite similar to the Pelagonian, HP metamorphic rocks such as blueschists, which also provided Late Jurassic ages (Bonneau, 1984; Koepke, 1986). Below the Asteroussia nappe, the Arvi nappe is made of Late Cretaceous pillow-lava and sediments (Bonneau, 1973). It has no equivalent in the Cyclades or in the Hellenides. It has been correlated with the Late Cretaceous ophiolitic thrust sheets of the Lycian Nappes, which widely extend in southwestern Turkey (Bonneau, 1973).

d. The Cycladic Blueschist unit

The Cycladic Blueschists are tectonically overlain by the Pelagionian nappe (Figure I-20). They crop out in continental Greece (Olympos, Ossa and Pelion tectonic windows; Godfriaux, 1965; Ferrière, 1982; Schermer, 1990; Schermer et al., 1990; Godfriaux and Ricou, 1991b; Schermer, 1993), in Evia Island and in the Cyclades (Blake et al., 1981; Bonneau and Kienast, 1982) (Figure I-19). One major characteristic of this unit is the high-grade metamorphism and associated severe deformation, preventing to easily establish its lithostratigraphy. The Blueschist Belt comprises an alternation of metapelites, metabasites and marbles. The metabasites are ancient flows, tuffs or basic blocks in a mélange as described in Syros Island (Bonneau et al., 1980). The vertical succession differs from one island to another one. This is mainly due to strong isoclinal folding. However, a general picture can be given as following (Bonneau et al., 1978; 1980). (1) The deepest unit probably corresponds to the anatectic basement of Ios, Naxos and Paros and the associated post-Variscan sedimentary cover that comprises marbles and chloritoid-kyanite schists, intruded by Triassic granitoids (Engel and Reischmann, 1997; Reischmann, 1997). The marbles contain emery in Naxos and the geochemistry of the metabauxites closely matches that of Jurassic bauxites found elsewhere in the Hellenides and Dinarides (Feenstra, 1985). (2) The blueschist and eclogite series of alternating marbles, metapelites and metabasites, cropping out in Tinos for instance, probably overlie this basal unit. (3) An ophiolitic mélange, which is well exposed in the western part of Syros, is the upper metamorphic unit.

All units underwent HP-LT metamorphism under blueschist- to eclogite-facies conditions (Pmax = 20 kbar, Tmax = 600°C), the age of the HP metamorphic event ranging from 78 Ma to 35 Ma, with a mean age of Early Eocene (50-45 Ma) (Andriessen et al., 1979; Altherr et al., 1979; Maluski et al., 1987; Bröcker, 1990; Okrusch and Bröcker, 1990; Schermer et al., 1990; Bröcker et al., 1993; Brown et al., 1998; Bröcker and Enders, 1999; Parra et al., 2002b). A severe HT-LP overprint occurred during the Late Oligocene-Early Miocene time, coeval with the Aegean post-orogenic extension (Andriessen et al., 1979; Altherr et al., 1982; Wijbrans and McDougall, 1986; Keay et al., 2001). The degree of preservation of the HP-LT assemblages is variable from one island to another one. It is excellent in Sifnos and Syros, especially in the upper units (Schliestedt, 1980; Matthews and Schliestedt, 1984; Schliestedt and Okrusch, 1988; Avigad et al., 1992; Trotet et al., 2001a; 2001b), and intermediate in the southern part of Tinos far from the main Oligo-Miocene extensional shear zone (Jolivet and Patriat, 1999; Parra et al., 2002b). A quasi-complete retrogression of HP parageneses is observed elsewhere. Naxos shows only badly preserved blueschists and eclogites in a very small area in the southeastern part of the island, which corresponds to the upper part of the dome (Jansen, 1977; Avigad, 1998). The eastern part of Amorgos Island shows a good preservation of HP-LT parageneses in the form of Fe-Mg-carpholite in metabauxites included in a marble sequence (Minoux et al., 1980) while the lower part of the sequence has been more extensively retrograded.

e. The Pindos Nappe

The more external Pindos nappe is exposed in continental Greece, Peloponnese and Crete (Figures I-19 and I-20). It is in similar tectonic position as the Cycladic blueschists, immediately above the Gavrovo-Tripolitza nappe (see below). The Pindos unit consists of a Late Triassic-Eocene pelagic and siliceous deposits sequence, overlain by a Late Eocene flysch (Brunn, 1956; Aubouin, 1959). It is unmetamorphosed and the series never exceed 1000m. It has been suggested that the Pindos nappe represents the non-metamorphosed equivalent of the Cycladic Blueschists, which would have escaped from subduction (Bonneau, 1982; Papanikolaou, 1987). In the Dodecanese, it has been claimed that the Kreati sequence of Tilos Island (Figure I-19) belongs to the Pindos Nappe (Bonneau, pers. comm.), although its resemblance with some lithologies of the Lycian Nappes has also been evoked (Roussos and Bonneau, 1979).

f. The Gavrovo-Tripolitza Nappe

The Gavrovo-Tripolitza nappe crops out in continental Greece, in Peloponnese, in Crete, in Santorin (Bonneau, 1984), and in the Dodecanese (Kassos, Karphathos, Rhodes and Astypaleia; Bonneau, 1984) (Figures I-19 and I-20). It consists of a platform sequence from the Triassic to the Eocene with a Late Eocene (Prianonian)-Early Miocene (Aquitanian) flysch in the most external domain (Aubouin, 1959). Most of this unit is unmetamorphosed. However, in the internal parts of the Hellenides where the Gavrovo-Tripolitza crops out in tectonic windows (Olympos, Ossa, Almyropotamos, Figure I-19), just below the Pelagonian nappe and the Cycladic Blueschists (Godfriaux, 1962; 1965; Godfriaux and Pichon, 1980; Godfriaux and Ricou, 1991b), evidence of HP-LT metamorphism has been reported (Schermer, 1990; Avigad et al., 1997; Shaked et al., 2000). Based on Nummulite fauna occurrences in the metamorphic part of the flysch or in a hard ground at the top of the carbonate sequence, it has been suggested that the underthrusting and HP metamorphism is younger than, at least, the Early Eocene (Dubois and Bignot, 1979; Godfriaux and Pichon, 1980; Godfriaux and Ricou, 1991b). Because there is no physical continuity between the unmetamorphosed Gavrovo in the external Hellenides and its HP-LT equivalent in the Olympos-Ossa tectonic windows, it has been claimed that they could represent different tectonic units although they were once part of a single paleogeographic domain (Jolivet et al., in press). It is likely that parts were deeply buried whereas others stayed in more superficial parts of the accretionary complex.

In the Dodecanese Archipelago, the islands of Tilos, Kos, Kalymnos, Leros, Lipsos and Arki extend along the Turkish coast, between Rhodes in the south and Samos in the north (Figure I-19). Geologically, Arki Island can be seen as the northern continuation of the larger islands of Kalymnos, Leros and Lipsos, which are formed by a complex system of nappes (Franz, 1991). From base to top, the nappe pile is made of the Temenia Nappe (the “Temenia unit” of Dürr, 1975), a sheet of pre-Alpidic basement rocks, and the Marina Nappe (upper part of the “Marina unit” of Dürr, 1975). It has been proposed that this nappe pile is an equivalent to the Lycian nappe complex of SW Turkey (Dürr, 1975). The Temenia Nappe mainly consists of young Palaeozoic phyllites, quartzites, micaschists and marbles. On Arki Island, aragonite-bearing blueschists have been described in this lower nappe, suggesting a subduction-related metamorphism with PT conditions of about 7-10 kbar/300-400°C (Franz and Okrusch, 1992). The overlying basement rocks suffered Variscan metamorphism under upper greenschist- to lower amphibolite-facies conditions, later overprinted by greenschist-facies conditions during the Alpine episode (Franz, 1991). The uppermost Marina Nappe that crops out in Leros and Kalymnos is composed of a clastic sequence and carbonaceous series, containing chloritoid-chlorite-muscovite-quartz assemblages (Franz, 1991). It has been considered that the HP metamorphic Temenia nappe does not belong to the external Hellenides but might be connected with the nearby Cycladic complex, although any correlation with the Lycian nappe complex cannot be safely excluded (Franz and Okrusch, 1992). Tentative correlations between the tectonic units of the Dodecanese Archipelago and the surrounding units of the Cycladic or Lycian nappe complexes thus remain an open question.

g. The Phyllite-Quartzite Nappe

The Phyllite-Quartzite nappe is an allochthonous unit, metamorphosed during the Neogene time. It crops out in Peloponnese, in Crete and probably on Santorin Island (Bonneau, 1984) below the low-grade Gavrovo-Tripolitza nappe and above the high-pressure Ionian nappe (Figures I-19 and I-20). It consists of schists, quartzitic phyllites, metaconglomerates, metavolcanics, marbles and limestones. The sequence has been biostratigraphically dated from the Late Palaeozoic to the Middle Triassic. The nappe also contains rare basement units such as in Sitia in eastern Crete (Creutzburg, 1977; Greilling, 1982; Krahl et al., 1983; Hall et al., 1984). HP-LT parageneses occurrences, involving Fe-Mg-carpholite assemblages, have been reported in the Phyllite-Quartzite nappe. The HP peak has been dated around 25 Ma and the final exhumation around 15 Ma (Seidel, 1978; Seidel et al., 1982; Theye and Seidel, 1991; Theye et al., 1992; Theye and Seidel, 1993; Bassias and Triboulet, 1994; Jolivet et al., 1996; Thomson et al., 1998).

h. The Ionian and Paxos Nappes

The most external domain of the Hellenides is made of the Ionian-Paxos nappes. The Ionian nappe is composed of an Upper Triassic-Middle Liassic neritic calcareous sequence, covered by a pelagic sequence until the Late Eocene. The carbonate series are overlain by a Late Eocene-Early Miocene flysch (Aubouin, 1959). The Ionian unit is exposed in the western part of continental Greece and in Karpathos and Rhodes where it does not show any record of metamorphic imprint (Bonneau, 1982; Bonneau and Kienast, 1982; Bonneau, 1984). On the contrary it is more severely affected by metamorphism in Peloponnese and Crete where it crops out below the Gavrovo-Tripolitza and Phyllite-Quartzite nappes (equivalent to the Ida nappe or Plattenkalk) (Figures I-19 and I-20). While only a greenschist-facies metamorphism has been described in Peloponnese (Thiébault, 1982), HP-LT conditions were recorded in the Cretan Plattenkalk, documented by aragonite in marbles and Fe-Mg-carpholite in the metabauxites (Theye et al., 1992; Theye and Seidel, 1993).

The Paxos nappe is only exposed in the western parts of the Aegean domain, where it shows a continuous carbonate platform until the Miocene, topped by a Miocene-Pliocene flysch-type formation.

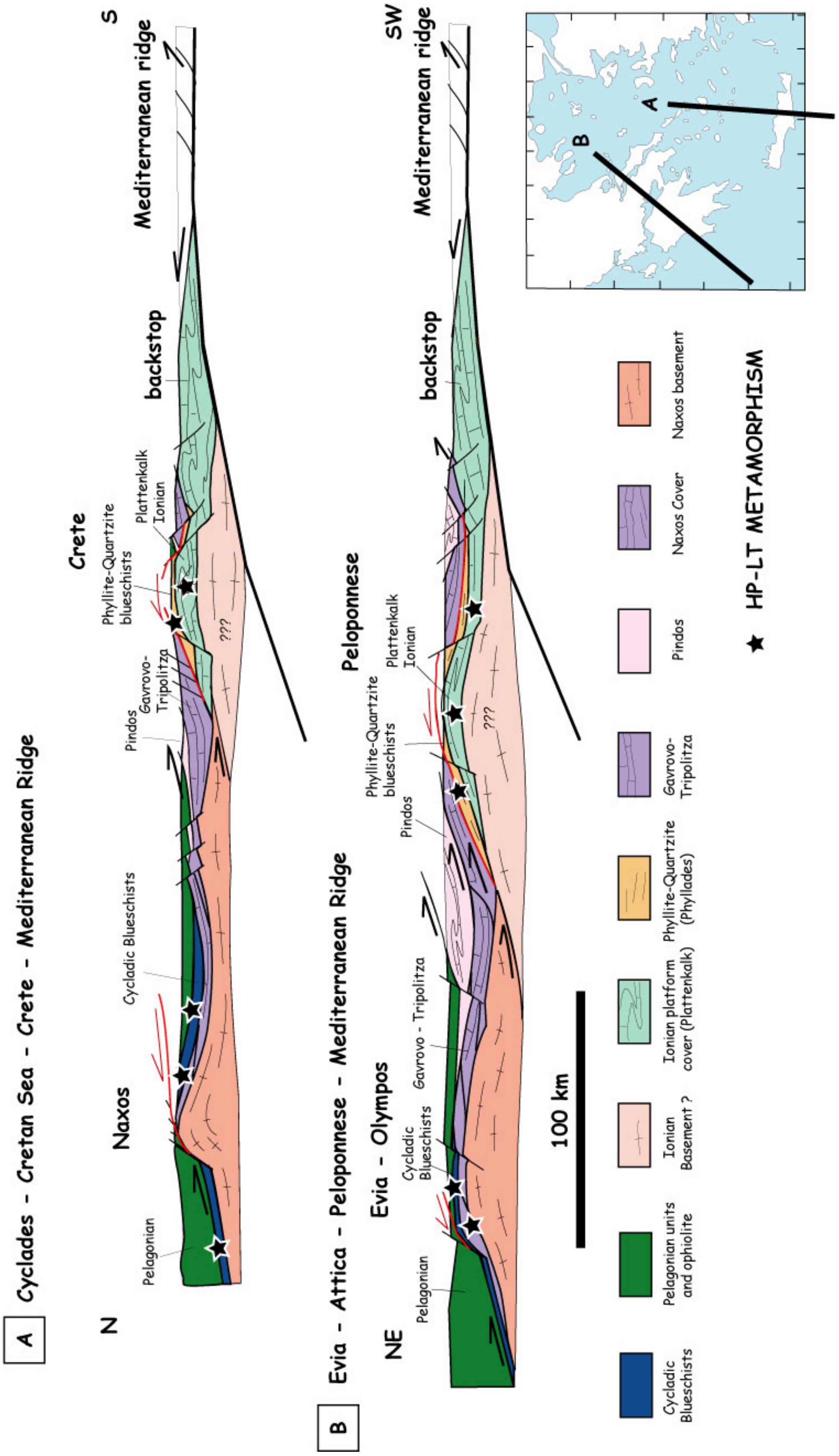

Figure I-20. Schematic cross-sections through the Aegean Sea (a) and Hellenides (b) showing the position of the different tectono-metamorphic units in the nappe stack as well as the major detachment zones (in red) [modified after Jolivet et al., in press].

2. Deformation related to metamorphism in the Aegean Domain

For many years, tectonic studies in the metamorphic zones of the Aegean domain led to a simple kinematic pattern, concerning both compressional and extensional episodes. NE-SW-trending stretching lineations in the western part of the Aegean Sea and N-S directions of stretching in the central and eastern parts document a deformation roughly perpendicular to the arc (Jolivet et al., 1994b; Walcott, 1998; Walcott and White, 1998) (Figure I-21).

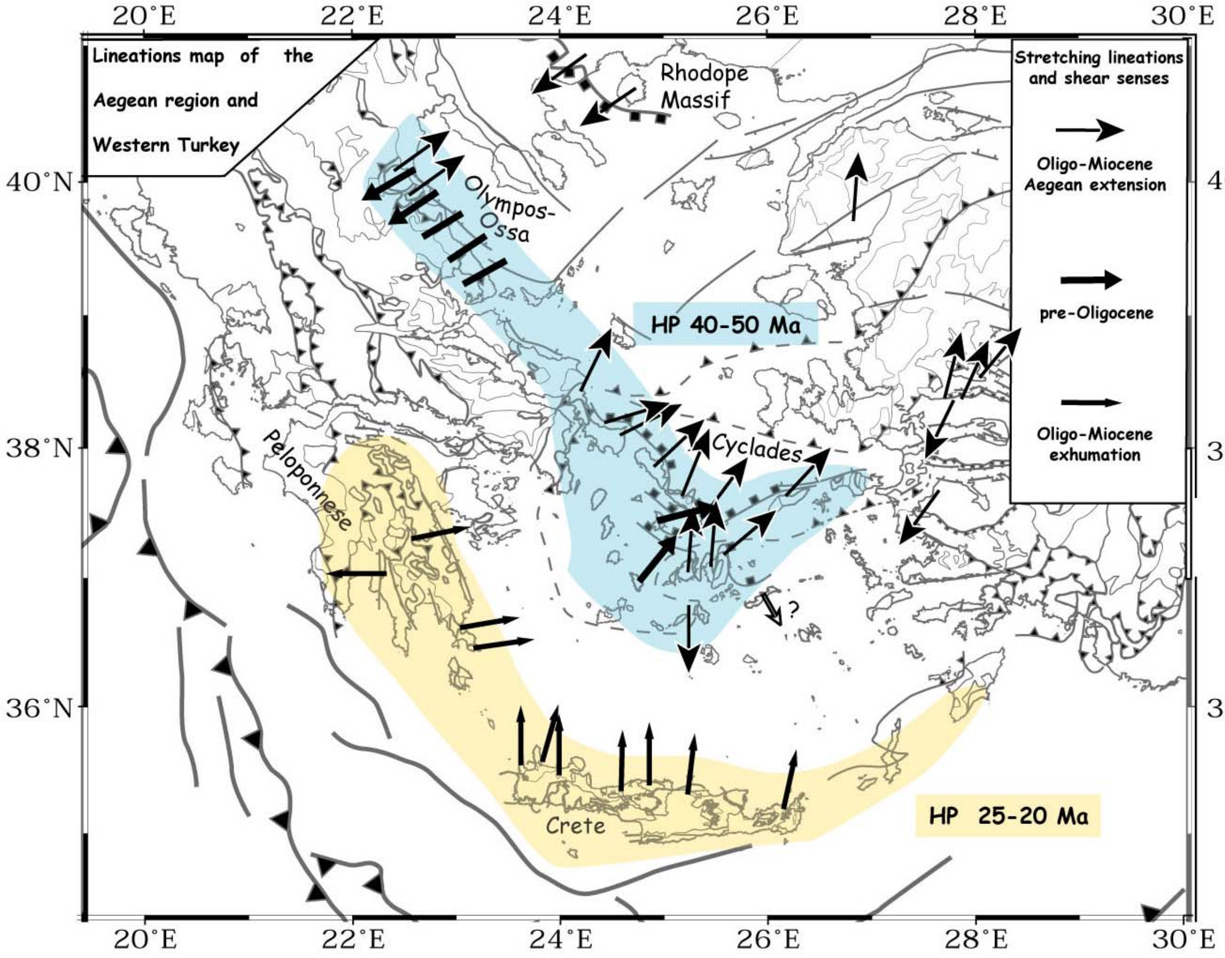

Figure I-21. Stretching lineations and senses of shear in the Aegean domain and Western Turkey (Dinter and Royden, 1993; Gautier et al., 1993; Schermer, 1993; Sokoutis et al., 1993; Gautier and Brun, 1994b; Jolivet et al., 1994b; Hetzel et al., 1995; Jolivet et al., 1996; Bozkurt and Park, 1997a; 1997b; Walcott, 1998; Walcott and White, 1998; Wawrzenitz and Krohe, 1998; Jolivet et al., 1998a; 1998b; Jolivet and Patriat, 1999; Okay and Satir, 2000a; Trotet, 2000; Lips et al., 2001; Trotet et al., 2001a; 2001b). The two Aegean HP belts are represented: The Cycladic Cretaceous-Eocene HP belt in the north (blue) and the Oligo-Miocene HP belt of Crete and Peloponnese in the south (yellow).

a. In the Rhodope Massif

In the northern part of the Aegean region (Thasos Island and Strymon detachment), kinematic indicators show a NE-SW direction of extension (Dinter and Royden, 1993; Sokoutis et al., 1993; Wawrzenitz and Krohe, 1998). This deformation is related to the post-orogenic episode, which corresponds to the Aegean extension. The sense of shear is top-to-the-southwest in this region. The NE-SW direction of extension is similar to that observed in the central parts of the Cycladic arc (for instance Tinos and Andros) but the sense of shear is opposite.

b. In the Olympos-Ossa Area

In the Olympos-Ossa area, the Eocene shortening as well as the Oligo-Miocene extension has a NE-SW orientation, top-to-the-SW for the syn-orogenic nappe stacking and top-to-the-NE for the late extension (Godfriaux and Ricou, 1991b; Schermer, 1993; Walcott and White, 1998). The top-to-the-SW kinematic indicators related to the southwestward emplacement of the Pelagonian above the Cycladic blueschists and Gavrovo-Tripolitza platform (Figure I-21) are associated with the crystallization of blue amphibole (Godfriaux and Ricou, 1991b; Schermer, 1993). The Aegean extensional episode is mostly represented by brittle structures and a few brittle-ductile shear zones (Schermer et al., 1990).

c. In the Cyclades

In the Cyclades, ductile deformation analysis revealed a NE-SW direction of extension in the north (Andros, Tinos, Mykonos) and N-S in the south (Paros and Naxos), with top-to-the-NE and top-to-the-N senses of shear respectively (Lister et al., 1984; Faure et al., 1991; Gautier et al., 1993; Sokoutis et al., 1993; Gautier and Brun, 1994a; 1994b; Jolivet et al., 1994b; Dinter, 1998; Patriat and Jolivet, 1998; Forster and Lister, 1999a; Gautier et al., 1999; Jolivet and Patriat, 1999). This deformation postdates the HP metamorphism and corresponds to the post-orogenic episode (Gautier and Brun, 1994a). A NW-SE-trending lineation with top-to-the-SE sense of shear has been described in Amorgos but its relation with the HP episode is not ascertained (Figure I-21).

Although the post-orogenic deformation in the Cyclades is highly pronounced, the syn-orogenic stage is preserved to various degrees:

- In Tinos, the southwestern part of the island, less affected by the large-scale ductile shear zone that encompasses most of the northeastern half, shows well-preserved blueschists and eclogites (Bröcker, 1990; Jolivet and Patriat, 1999). However the degree of preservation is not sufficient to allow a reliable study of the syn-orogenic kinematics. The rare interpretable outcrops suggest an ENE-WSW direction of stretching during the blueschist episode. Moreover, a study of the magnetic fabric in the northwestern part of the island revealed the existence of two stretching directions. The most obvious one, which trends NE-SW, corresponds to the main extensional event. The older one trends ENE-WSW and is preserved only far from the main extensional shear zone (Aubourg et al., 2000). This older stretching direction might correspond to the syn-orogenic episode as suggested by the occurrence of fresh HP-LT assemblages in this part of the island.
- On Ios Island, well-preserved blueschist and eclogite occurrences have been reported in the uppermost units above the main detachment (Forster and Lister, 1999b).
- Naxos and Paros do not show any significant relics of the HP-LT deformation although some relics of the HP parageneses can be found in the southeast of Naxos (Avigad, 1998). The Oligo-Miocene extensional shear zones erased most of pre-existing structures.
- However, in Sifnos and Syros islands, the syn-orogenic episode is very well preserved. Retrogression in the greenschist-facies is less intense compared to other islands, except in the lowest units of Syros (Trotet et al., 2001a; 2001b). Ar-Ar radiometric ages yielded an Eocene age (in Sifnos: Altherr et al., 1979; in Syros: Maluski et al., 1987) showing that the exhumation occurred before that the Aegean extension started. Only the highly retrograded outcrops show Miocene Ar-Ar radiometric ages (Maluski et al., 1987; Bröcker et al., 1993). The deformation, active during syn-orogenic exhumation, has thus been recently studied in detail. A continuum of extension from ductile to brittle, and from blueschist to greenschist is observed in both islands (Trotet et al., 2001a; 2001b). The direction of stretching is NE-SW in Sifnos and ENE-WSW in Syros and senses of shear are top-to-the-NE everywhere (Figure I-21).

d. In Crete and Peloponnese

- Crete Island shows a very clear and simple kinematic pattern. Stretching lineations trend roughly N-S (Jolivet et al., 1996) and most of the deformation features are associated to the exhumation of high-pressure rocks, coeval with post-orogenic extension further north in the Cyclades (Jolivet et al., 1994b; Jolivet and Patriat, 1999).
- In Peloponnese, the tectonic units are similar to those of Crete. However, the direction of stretching and shear is around E-W (Trotet, 2000). Considering the post-orogenic tectonic movements that affected the geometry of the southern Peloponnese, a rotation back to its Oligo-Miocene position would show directions of shear roughly similar to those described in the Cyclades (Figure I-21).

As a synthesis:

- The Oligo-Miocene deformation is characterized by a stretching that trends NE-SW in the northern Cyclades and more N-S in the southern Cyclades and in Crete.
- The pre-Oligocene (Eocene in Syros and Sifnos islands) deformation shows NE-SW to ENE-WSW directions of shear. N-S direction has not been reported for this episode.

C. WESTERN ANATOLIA: AN AMALGAMATION OF DISTINCT TECTONO-METAMORPHIC UNITS

Western Turkey encompasses several continental fragments which are characterized by distinct stratigraphic, metamorphic and structural criteria. The juxtaposition of these fragments is related to northward subduction of the Neo-Tethyan oceanic lithosphere and resulting Late Cretaceous-Early Tertiary continental collision between the active margin of the northern plate (Sakarya Zone of the Pontides) and the passive margin of the southern plate (Anatolide-Tauride platform) (Şengör and Yılmaz, 1981). Major boundaries, which correspond to the main sutures in western Turkey, define four large domains: the Istanbul Zone, the Sakarya Zone, the Central Anatolian Crystalline Complex and the Anatolide-Tauride block. The suture zones are marked by Ophiolitic fragments and mélanges. From north to south, the Intra-Pontide Suture, the Izmir-Ankara Suture and the Inner Tauride Suture separate the four major units (Okay and Tüysüz, 1999; Figure I-22).

Figure I-22. Simplified tectonic map showing the location of the main tectono-metamorphic units of western Turkey (modified after Okay and Tüysüz [1999] & Bozkurt and Oberhänsli [2001]). The main sutures and thrusts separating the different units are represented on the map.

1. The Istanbul Zone

The Istanbul Zone (Okay, 1989a) is made of a Cadomian basement and an unmetamorphosed Palaeozoic sedimentary cover (Kaya, 1973). This basal material has been called the Istanbul Nappe (Şengör et al., 1984a) and later the Istanbul Fragment (Ustaömer and Robertson, 1993). This Palaeozoic sequence is overlain by unconformable Mesozoic to Cenozoic sediments. The Palaeozoic series are composed of Lower Ordovician-Lower Silurian quartzites and shales, Upper Silurian-Lower Devonian limestones and fossil-rich shales, Upper Devonian limestones topped by Lower Carboniferous radiolarian cherts and marine flysch. Recently, the Istanbul Zone was divided into two tectonic units (Göncüoğlu and Kozur, 1998): The Istanbul unit made of the Palaeozoic sequence which underwent only Hercynian deformation, and the Zonguldak unit made of Palaeozoic sediments that underwent Caledonian deformation.

The Bolu massif (Figure I-23) mainly forms the Cadomian basement of the Istanbul Zone. It is composed of three main tectonic units (Ustaömer and Rogers, 1999). The first one is composed of rocks which underwent an amphibolite-facies metamorphism followed by a retrograde greenschist-facies overprint. The second unit is made of metagranitoids (volcanic-arc and calc-alkaline types) which intrude the third unit that consists of volcanoclastics and metavolcanics. The volcanic series show a greenschist-facies metamorphic imprint. Based on the observation of metamorphic blocks within the overlying unconformable Ordovician clastics, these authors suggested a pre-Early Ordovician age for the metamorphic event that affected the Bolu Massif. Later, Satır et al. (2000) reported Pb/Pb (single zircon) and Nd/Sr (on biotite) ages, all indicating a Precambrian event for the magmatic and metamorphic evolution of the Bolu Massif.

To the west, the Intra-Pontide Suture separates the Istanbul Zone from the Strandja Massif (Figure I-22). The Strandja Massif forms a long NW-SE-trending metamorphic massif at the boundary with Bulgaria (Figure I-23). This massif was regionally metamorphosed during the Late Variscan and the Late Jurassic-Early Cretaceous orogenies (Okay et al., 2001b). The Early Permian orogeny involved amphibolite-facies metamorphism and crustal anatexis (~271 Ma, single zircon ages; Okay et al., 2001b). During the Late Jurassic-Early Cretaceous orogeny, the massif underwent intense deformation and regional greenschist-facies metamorphic imprint (~155 Ma, Rb/Sr biotite-whole rock age; Okay et al., 2001b).

To the south, the Intra-Pontide Suture marks the boundary between the Istanbul Zone and the Sakarya Zone (Figure I-22).

2. The Sakarya Zone

The Sakarya Zone consists of a series of tectonic units made of volcanics and clastic rocks with mainly Late Palaeozoic and Late Triassic metamorphic overprints, covered with unconformable Jurassic and Cretaceous sediments. Most of the metamorphic massifs belonging to the Sakarya Zone expose metamorphosed rocks that were buried into the greenschist-facies to the eclogite-facies conditions during the Triassic time (Figure I-23).

a. The Karakaya Complex

Initially called the Karakaya formation (Bingöl et al., 1973), the Karakaya Complex constitutes an orogen that was formed by the Late Triassic northward obduction of subduction-accretion units of the Palaeotethys (Tekeli, 1981; Okay et al., 1996). This latter was a wide oceanic domain separating Laurasia from Gondwana from Late Ordovician/Silurian to Late Triassic times (e.g. Stampfli and Borel, 2002). In the Ankara region, various outcrops of the Karakaya Complex have been described and named the Karakaya Nappes (Koçyiğit, 1991). Two main units have been described (Okay et al., 1996). The first one (called the Nilüfer formation) is made of metabasites with marble and phyllite intercalations. Eclogite relics have been found in this unit (Okay et al., 1996). Based on Ar/Ar data on phengite, this HP-LT metamorphism has been dated latest Triassic-earliest Jurassic (203-208 Ma; Okay and Monié, 1997). Greenschist-facies assemblages overprinted the eclogite-facies metamorphism. The second unit that tectonically overlies the Nilüfer formation consists of deformed Triassic greywacke with conglomerate, chert, limestone, shale and siltstone intercalations (Orhanlar Greywacke). More recently, along the Izmir-Ankara suture (east of Bursa), Okay et al. (2002) reported Ar/Ar ages between 215 and 205 Ma also indicating a Late-Triassic age for the high-pressure metamorphism of NW Turkey (Figure I-23).

b. The Kargı Massif

To the northeast of the Karakaya Complex, the Kargı Massif crops out in the central Pontides (Figure I-23). The rocks of the Kargı Massif are considered to be the remnants of the northward-subducted Palaeotethys Ocean (Ustaömer and Robertson, 1993). It is composed of three tectonic units. The basal unit is made of highly deformed metamorphic rocks, mainly gneisses, amphibolite, quartzite and marble. The protoliths have been considered to be Precambrian and Early Palaeozoic. The uppermost levels of this unit consist of unconformable Upper Jurassic limestones. The second unit is made of metaophiolite slices and an imbricated stack of metavolcanics and volcanoclastics metamorphosed under the greenschist-facies (Şengör et al., 1984a; Ustaömer and Robertson, 1993). The third unit is composed of sediments and ophiolite intercalations. Evidence for blueschist-facies and eclogite-facies metamorphism has been described in the ophiolites forming the second and third units, and is probably related with their Late Triassic emplacement. These HP rocks are covered by a thick unconformable sequence of Late Jurassic to Upper Cretaceous sediments. These latter are overlain by an unmetamorphosed ophiolite which emplaced during the Late Cretaceous time and caused a second metamorphic event that affected the Kargı massif.

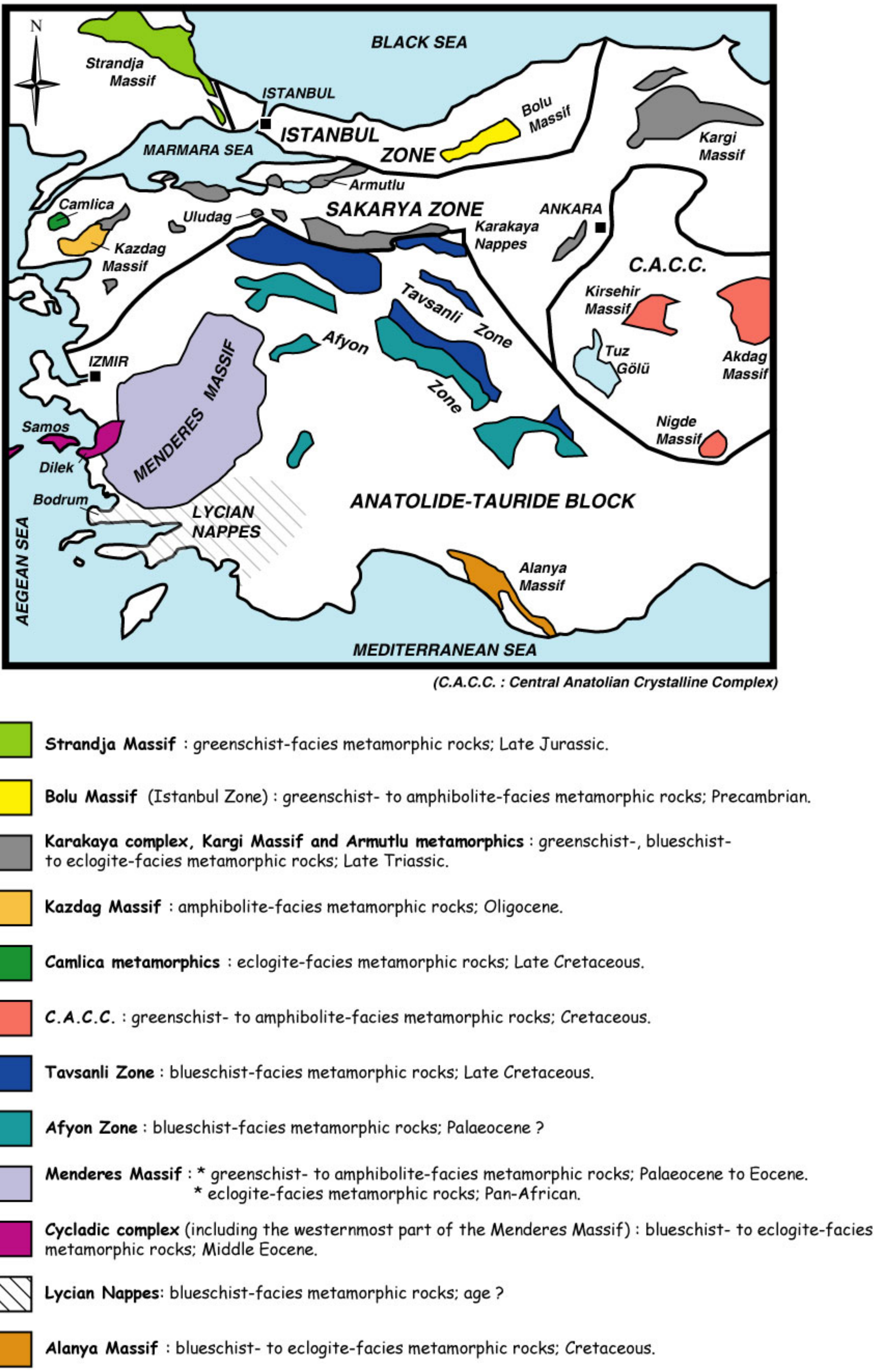

	🟩	**Strandja Massif** : greenschist-facies metamorphic rocks; Late Jurassic.
ISTANBUL ZONE	🟨	**Bolu Massif** (Istanbul Zone) : greenschist- to amphibolite-facies metamorphic rocks; Precambrian.
SAKARYA ZONE	■	**Karakaya complex, Kargi Massif and Armutlu metamorphics** : greenschist-, blueschist- to eclogite-facies metamorphic rocks; Late Triassic.
	🟧	**Kazdag Massif** : amphibolite-facies metamorphic rocks; Oligocene.
	🟩	**Camlica metamorphics** : eclogite-facies metamorphic rocks; Late Cretaceous.
C.A.C.C.	🟥	**C.A.C.C.** : greenschist- to amphibolite-facies metamorphic rocks; Cretaceous.
ANATOLIDE-TAURIDE BLOCK	🟦	**Tavsanli Zone** : blueschist-facies metamorphic rocks; Late Cretaceous.
	🟦	**Afyon Zone** : blueschist-facies metamorphic rocks; Palaeocene ?
	🟪	**Menderes Massif** : * greenschist- to amphibolite-facies metamorphic rocks; Palaeocene to Eocene. * eclogite-facies metamorphic rocks; Pan-African.
	🟪	**Cycladic complex** (including the westernmost part of the Menderes Massif) : blueschist- to eclogite-facies metamorphic rocks; Middle Eocene.
	▨	**Lycian Nappes**: blueschist-facies metamorphic rocks; age ?
	🟧	**Alanya Massif** : blueschist- to eclogite-facies metamorphic rocks; Cretaceous.

Figure I-23. Map showing the distribution of metamorphic rocks in western Turkey (modified after Bozkurt and Oberhänsli, 2001). The main Tethyan sutures are represented with heavy lines. See text for references.

c. The Armutlu Peninsula

On the southern coast of the Marmara Sea, near the Iznik Lake, the Armutlu peninsula (Figure I-23) comprises several tectonic slices which underwent different metamorphisms. Four tectonic units can be distinguished. The first unit corresponds to the basement composed of pre-Triassic schists intercalated with metabasites and limestone lenses metamorphosed under greenschist-facies conditions (Göncüoğlu and Erendil, 1990). The second unit is composed of Triassic low-grade metamorphic rocks. They consist mainly of volcanics, shales, sandstones and recrystallized limestone lenses (Göncüoğlu and Erendil, 1990). The third unit is a Cretaceous metaolistostrome comprising limestone, shale and ophiolite blocks. Finally, the fourth tectonic slice is made of low-grade Palaeozoic metaquartzite and metapelite, amphibolitic metavolcanics and metagreywackes.

d. The Uludağ Massif

The Uludağ Massif, located to the southwest of the Armutlu peninsula (Figure I-23), exposes high-grade Palaeozoic metamorphic rocks under the amphibolite-facies (Okay et al., 1996; Göncüoğlu et al., 2000). Granitoid intrusions within the metamorphic rocks have been dated Oligocene (Ar/Ar ages, 25-27 Ma; Delaloye and Bingöl, 2000).

e. The Kazdağ Massif

In the western part of the Sakarya Zone, the Kazdağ Massif (Figure I-23) has a core and cover structure. It is tectonically overlain on its northern flank by low-grade metamorphic rocks belonging to the Karakaya Complex. The massif, which has a typical dome shape, gives a regional exposure of highly metamorphosed rocks. The core comprises gneisses, amphibolites, metagabbros and marbles. The cover sequence is made of marbles and felsic gneisses with amphibolite intercalations (Bingöl, 1969; Okay and Satır, 2000a). Isotopic ages for this high-grade amphibolite-facies metamorphism yielded about 24 Ma (Rb/Sr on mica; Okay and Satır, 2000a). The exhumation of these rocks started in the latest Oligocene along north-dipping ductile shear zone and were led to the surface during the Pliocene-Quaternary (after 5 Ma) in brittle regime along faults linked to the North Anatolian Fault Zone (Okay and Satır, 2000a). The top-to-the-north sense of shear associated with the Oligo-Miocene amphibolite-facies metamorphism is represented in Figure I-21.

f. The Çamlıca Metamorphic Rocks

The Çamlıca metamorphic rocks crop out in the westernmost part of the Sakarya Zone (Figure I-23). They consist of schists, marbles, quartzites, amphibolites and garnet-bearing metabasites (Okay and Satır, 2000b). Evidence of retrogression textures from the eclogite-facies to the amphibolite-facies has been documented. Rb/Sr analyses on phengite have revealed a Maastrichtian age for the high-pressure metamorphic event (69-65 Ma; Okay and Satır, 2000b), overprinted by greenschist-facies conditions. A correlation between the Çamlıca area and the Rhodope metamorphic massif has been suggested mainly based on metamorphic and stratigraphic similitude between both massifs (Okay and Satır, 2000b).

3. The Central Anatolian Crystalline Complex

To the southeast of the Sakarya Zone and more precisely south of the Kargı Massif, plutonic and metamorphic rocks making up what is commonly called the Central Anatolian Crystalline Complex (CACC; Figure I-22) are exposed (Göncüoğlu et al., 1991). Local outcrops form various massifs in the CACC: the Akdağ Massif in the northeast (Vache, 1963), the Kirşehir Massif in the northwest (Seymen, 1982) and the Niğde Massif in the south (Göncüoğlu, 1977) (Figure I-23). The Inner Tauride suture zone wraps around the southern margin of the CACC. Following emplacement of Neo-Tethyan ophiolites onto the Tauride platform to the south during the Late Cretaceous time, the CACC and the Tauride platform collided along this Inner Tauride zone. The massifs that form the CACC were metamorphosed during Alpine orogenesis, but the Kirşehir and Akdağ massifs differ from the southern massif (Niğde) in metamorphic PT history, timing of metamorphism, magmatism and mechanisms of exhumation. The metamorphic rocks of the CACC consist of ortho- and paragneisses, metasediments with metabasites intercalations, marbles and a metaophiolitic sequence comprising metagabbros, amphibolites, serpentinites and metamorphosed mafic and ultramafic rocks (Göncüoğlu et al., 1991). Based on U/Pb dating method on zircon from the paragneissic lithologies of the Niğde Massif, Göncüoğlu (1982) reported a Proterozoic age (2059±77 Ma) for the protolith of the metamorphic rocks. Two metamorphic events which affected the whole crystalline complex have been described in the literature: a first one characterized by MP-HT conditions associated with severe deformation (Göncüoğlu, 1977; Göncüoğlu, 1982) and a second LP-HT metamorphic event recorded by many recrystallization around pluton intrusions related to crustal extension and partial melting (Göncüoğlu, 1982; Göncüoğlu et al., 1991; Whitney and Dilek, 1997). Göncüoğlu (1986) suggested that the age of the main metamorphism and ophiolite emplacement is pre-Cenomanian (Rb/Sr and K/Ar methods). The Niğde Massif has a more complicated tectonic and metamorphic history compared to the other massifs of the CACC. It has been claimed that the Niğde Massif formed by internal imbrication and crustal thickening followed by erosion and exhumation in a bivergent extensional regime with a consequent magmatic event. The Kirşehir Massif contains rocks which have undergone greenschist-facies- to upper-amphibolite-facies conditions. Relics of granulite have also locally been found in the rocks from the Kirşehir area. Finally, the Akdağ Massif gives the exposure of highly metamorphosed rocks. These two northern massifs experienced thrusting and folding during collision and were slowly exhumed by erosion (Whitney et al., 2001).

4. The Anatolide-Tauride Block

The Izmir-Ankara Suture and the Inner Tauride Suture mark the northern boundaries of the Anatolide-Tauride block. This fragment, also called the Anatolide-Tauride platform, is made of several mega-units separated by major thrusts: the Bornova Flysch Zone, the Tavşanlı Zone, the Afyon Zone, the Menderes Massif, the Lycian Nappes and the Bey Dağları platform (Figure I-22).

a. The Bornova Flysch Zone

The Bornova mélange extends between the Karaburun Belt and the Menderes Massif (Erdoğan, 1990a). This unit is made of large Triassic to Cretaceous limestone blocks (more than 20 km in length) within a matrix of flysch-like sedimentary rocks and spilites (Erdoğan, 1990b). The greywacke-shale matrix is separated by strongly sheared serpentinite slices in a few areas. Based on paleontological and geochronological data, the flysch has been dated latest Cretaceous-Palaeocene (Özer and Irtem, 1982; Okay and Siyako, 1993; Okay et al., 1996).

b. The Tavşanlı Zone

The Tavşanlı Zone is the northernmost unit of the Anatolide-Tauride block (Figures I-22 and I-23) and underlies the unmetamorphosed ophiolites of the Neotethyan Izmir-Ankara Suture in the north (Okay, 1984). To the south, the rocks are thrust onto the metamorphic Afyon Zone (Okay, 1986). The Tavşanlı Zone forms a large domain (40 km wide and over 250 km long) that underwent a HP-LT metamorphism during the Alpine history (Okay, 1984). Two tectonic units have been defined: the Ovacık unit and the Orhaneli unit, the former tectonically overlying the latter.

- The Ovacık unit consists of a disrupted volcano-sedimentary formation underneath massive peridotites. This unit contains reddish-greenish pelagic shales, radiolarian cherts, pelagic limestones, greywackes, syn-sedimentary breccias, manganese deposits and neritic limestone olistoliths (Okay, 1982; 1984; 1986). The rocks are free of penetrative deformation and the sequence appears to be unmetamorphosed in the field. Okay (1984; 1986) reported occurrence of talc and serpentinite outcrops marking thrusts within the volcano-sedimentary sequence, and described the presence of lawsonite and aragonite within veins of volcanic rocks, and aragonite appearing as coarse grains in pelagic limestones. This thus suggests an incipient HP-LT metamorphism (5-8 kbar and 250-300°C; Okay, 1982).
- The Orhaneli unit is characterized by a thick metaclastic sequence overlain by massive white marbles. The metaclastic sequence is made of grey graphite-rich schists, metapelites with metabasite and marble intercalations (Okay, 1984; Okay and Kelley, 1994). The foliation is penetrative and the rocks are completely recrystallized. Lawsonite, glaucophane, garnet, jadeite and aragonite form various mineral assemblages in this unit and indicate a HP-LT metamorphism (Okay, 1982; 1984; 1986). Okay and Kelley (1994) reported PT conditions of about 20 kbar and 430°C. Rb/Sr and Ar/Ar dating revealed a Campanian age for the HP-LT event (83-80 Ma; Sherlock et al., 1999). It has been suggested that the exhumation of the metamorphic rocks from the Tavşanlı Zone was achieved in a compressive regime (Okay et al., 1998).

The close spatial association of the Triassic and Cretaceous blueschists along the Izmir-Ankara suture (in both Karakaya complex and Tavşanlı zone) suggests that the suture constitutes a long-lived plate boundary of Late Paleozoic to Early Tertiary age (Okay et al., 2002).

c. The Afyon Zone

The Afyon Zone is tectonically bounded by the Tavşanlı Blueschist Zone and the Menderes Massif at the north and south respectively (Figures I-22 and I-23). Şengör et al. (1984b) interpreted the Afyon Zone as a structurally higher unit than the rest of the Menderes Massif to the south. The Afyon Zone trends NW-SE and extends over a distance of 600 km. Okay et al. (1996) reported that the stratigraphy of the Afyon Zone is similar to that of the Tavşanlı Zone and the Mesozoic-Early Tertiary cover series of the Menderes Massif. The rock succession can be separated into two units: a Pan-African (?) lower unit and a Mesozoic–Early Tertiary upper unit.

- The lower unit, forming the basement of the Afyon Zone is made up of a sequence of medium-grade schists containing mafic and felsic meta-igneous rocks. Pre-Alpine metamorphism under upper greenschist-facies conditions with quartz + albite + chlorite + white mica ± garnet ± biotite is documented for the schists. Various outcrops of metabasites appear locally as deformed lenses in the schist succession. Numerous glaucophane-bearing gabbroic rocks have been described and suggest that a HP/LT metamorphism under blueschist-facies conditions affected the whole lower unit (Candan et al., 2002). Leucocratic metagranites also occur as veins within the schist sequence and are attributed to Triassic intrusions (Candan et al., 2002), considering similar Early Triassic leucocratic orthogneisses in the Menderes Massif (Koralay et al., 2001). Based on regional correlations, particularly with the Menderes Massif, Candan et al. (2002) suggested a Pan-African age for the protoliths of the metapsammite-metapelite series.
- The upper unit unconformably overlies the former. The whole sequence extends from the Triassic to the Early Palaeocene. A quartzite and/or carbonate basal conglomerate is gradually overlain by phyllites with marble layers in the upper part. This sequence of metasediments, which represents terrestrial to shallow water environment, grades upward to thick platform-type carbonate series (Candan et al., 2002). Fe-Mg-carpholite occurrences have been described in the Triassic conglomerates and metapelites: it appears as rock-forming mineral with a rosetta-like shape associated with chloritoid and pyrophyllite or as intergrowth in quartz segregations (Candan et al., 2002). Pseudoaragonite fibres have been documented in the lowermost levels of the overlying metacarbonate sequence (Candan et al., 2002). Finally, in the uppermost levels of the sequence lies a Late Maastrichtian-Early Palaeocene olistostromal formation that contains limestone, blueschist, ophiolite and serpentinite blocks related to the obducted ophiolite onto the northern margin of the platform. Unmetamorphosed Upper Paleocene-Lower Eocene shallow-water sediments unconformably overlie all units.

The Afyon Zone was considered for many years to have recorded only a low-grade greenschist-facies metamorphism (Okay, 1984; Okay et al., 1996). This recognition of Fe-Mg carpholite and its associated breakdown products leads one to consider a low-grade HP-LT metamorphism under blueschist facies conditions (7-9 kbar, 350-400°C; Candan et al., 2002) which correspond to a burial of the Mesozoic passive margin of about 30 km. It is suggested that the underlying Pan-African (?) basement also underwent this burial. The age of this HP-LT metamorphism is constrained between Late Maastrichtian-Early Palaeocene (ages of the youngest known rocks of the upper unit) and Late Palaeocene-Early Eocene (ages of the oldest known unconformable sediments). Candan et al. (2002) envisaged a continuous process involving internal imbrication of the Anatolide-Tauride platform, burial of the continental tectonic slices beneath the obducted oceanic lithosphere, high-pressure metamorphism and exhumation of the rocks from the Afyon Zone during the Early Paleocene-Late Paleocene time.

N.B. Although the Tavşanlı Zone and the Afyon Zone have been described in this chapter as two distinct mega-units, some authors included both zones in a single belt, termed Kütahya-Bolkardağ Belt (Özcan et al., 1988; Göncüoğlu et al., 1996-1997).

d. The Menderes Massif and the "Menderes-Cycladic" complex

The Menderes Massif, the Lycian Nappes and the Bey Dağları platform cover most of southwest Turkey. The Menderes Massif, with its long NE-SW-trending axis, occupies a large part of western Turkey. It is tectonically overlain by nappes of the Izmir-Ankara Suture Zone (Şengör and Yılmaz, 1981) on its northern flank (including the Bornova Flysch Zone), the Afyon Zone on its eastern border (Şengör et al., 1984b), and the Lycian Nappes (Brunn et al., 1970; de Graciansky, 1972; Poisson, 1977) on its southern flank (Figure I-22). Although the Menderes Massif presents a nappe-pile structure (Dora et al., 1995; Partzsch et al., 1997; Partzsch et al., 1998; Ring et al., 1999a; Gessner, 2000; Gessner et al., 2001a,b; Ring et al., 2001b), its stratigraphy is generally described as an augen gneiss core and an overlying sedimentary cover which were imbricated by late Alpine contractional deformation (Schuiling, 1962; de Graciansky, 1966; Dürr, 1975; Şengör et al., 1984b; Satır and Friedrichsen, 1986).

Core rocks are composed of augen gneiss, deformed metagranite, migmatites, gabbro with some granulite and eclogite relics, and medium- to high-grade metamorphic schists (Şengör et al., 1984b; Satır and Friedrichsen, 1986; Candan et al., 1994; Candan, 1995; Candan, 1996; Oberhänsli et al., 1997; Candan et al., 1998; Candan et al., 2001). They form the Pan-African basement of western Turkey (Schuiling, 1962; Şengör et al., 1984b; Satır and Friedrichsen, 1986; Konak et al., 1987, Hetzel and Reischmann, 1996; Hetzel et al., 1998; Loos and Reischmann, 1999). In the central submassif, eclogite-facies metamorphism occurred (Candan et al., 1994; Candan, 1995; Candan, 1996; Oberhänsli et al., 1997; Candan et al., 1998; Candan et al., 2001) and was later overprinted by a regional amphibolite-facies metamorphism (Candan et al., 2001). This HP metamorphism has been dated Pan-African and is considered to result from crustal thickening during the Late Precambrian-Early Palaeozoic orogeny (Oelsner et al., 1997; Partzsch et al., 1997; Candan et al., 1998; Partzsch et al., 1998; Warkus et al., 1998; Candan et al., 2001; Warkus, 2001; Oberhänsli et al., 2002a) (Figure I-23).

Cover rocks consist of a Palaeozoic schist envelope and a Mesozoic to Cenozoic marble envelope. The schist envelope is made of garnet-, kyanite-, staurolite-, chloritoid-, and sillimanite-bearing micaschists, graphite-rich quartzitic phyllite-schists, garnet amphibolites, and marble intercalations (Dürr, 1975; Akkök, 1983; Ashworth and Evirgen, 1984a; Şengör et al., 1984b; Satır and Friedrichsen, 1986; Konak et al., 1987; Bozkurt, 1996; Hetzel et al., 1998). The schist sequence is overlain by a thick marble envelope. A Late Triassic conglomerate containing dolomite, quartzite pebbles and micaschist lies at the base of the marble series. This formation is overlain by Upper Triassic to Liassic marbles, Jurassic to Lower Cretaceous massive dolomitic marbles with metabauxite containing corundum and diaspore (Konak et al., 1987; Yalçın, 1987), Late Cretaceous (Santonian-Campanian) Rudist-bearing marbles (Dürr, 1975; Konak et al., 1987; Özer, 1998; Özer et al., 2001), and Late Campanian-Late Maastrichtian reddish pelagic cherty marbles (Konak et al., 1987; Özer, 1998; Özer et al., 2001). A Middle Palaeocene metaolistostromal unit comprising metaserpentinite and marble blocks within a pelitic matrix unconformably overlies the marble sequence (Dürr, 1975; Gutnic et al., 1979; Çağlayan et al., 1980; Konak et al., 1987; Özer et al., 2001). This detrital formation marks the end of sedimentation in the Menderes Massif. In the southern submassif, this unit has been described as slightly metamorphosed (Gutnic et al., 1979).

On the contrary, in the area of the Dilek peninsula (Figure I-23), relics of eclogite and eclogitic metagabbro were found in a similar olistostromal unit (the 'Selçuk formation' of Güngör, 1995), near the locality of Selçuk (Candan et al., 1997; Oberhänsli et al., 1998; Çetinkaplan, 2002; Oberhänsli et al., 2002b). Candan et al. (1997) correlated the Selçuk formation with a similarly metamorphosed olistostromal unit in Syros Island (Ridley and Dixon, 1984; Okrusch and Bröker, 1990). In the same region, this eclogite-bearing olistostrome tectonically overlies Mesozoic marble series (Kayaaltı formation of Güngör, 1995) intercalated with mafic metapelites and metavolcanites containing well-preserved blue amphiboles (Candan et al., 1997; Oberhänsli et al., 1998). This blueschist-facies metamorphism (10 kbar min./470°C; Candan et al., 1997) dated Middle Eocene (40 Ma, Ar/Ar on phengite; Oberhänsli et al., 1998) was overprinted by a Barrovian-type metamorphism under greenschist-facies conditions during the Late Eocene-Early Oligocene (Candan et al., 1997). A correlation with the blueschists of Samos Island (Mposkos and Perdikatsis, 1984; Okrusch et al., 1984) belonging to the Cycladic complex has been proposed (Candan et al., 1997; Oberhänsli et al., 1998). Because of similar eclogite and blueschist metamorphic imprints described in the Aegean domain, many authors have argued that the Dilek region forms the eastward lateral continuation of the Cycladic complex, and have excluded it from the geological definition of the Menderes Massif (Oberhänsli et al., 1998; Ring et al., 1999a; Ring et al., 1999b; Gessner et al., 2001a,b; Okay, 2001), the Cycladic complex resting on top of the Menderes Massif (Figure I-23).

As a synthesis:

- The whole Menderes Massif ('core' and the 'cover' rocks) is considered to have suffered a Paleocene to Eocene Barrovian-type metamorphism during its alpine history (the so-called MMM, Main Menderes Metamorphism of Şengör et al., 1984b) showing upper amphibolite-facies conditions in the lower levels of the massif and greenschist-facies conditions in the uppermost parts of the cover series (Dürr, 1975; Akkök, 1983; Ashworth and Evirgen, 1984a; Şengör et al., 1984b; Satır and Friedrichsen, 1986; Konak et al., 1987; Okay, 2001; Whitney and Bozkurt, 2002).
- The Dilek region forming the westernmost part of the Menderes Massif recorded an Eocene blueschist- to eclogite-facies metamorphism and is correlated with the Cycladic Blueschist Belt (Figure I-23).

e. The Lycian Nappes

At the south of the Menderes Massif, the Lycian Nappes tectonically overlie the metasediments of the Menderes cover sequence (de Graciansky, 1972) (Figure I-22). Their origin has been the subject of many controversies. While some authors argued that the tectonic slices originated from north of the Menderes Massif (de Graciansky, 1972; Dürr, 1975; Dürr et al., 1978; Gutnic et al., 1979; Şengör and Yılmaz, 1981; Okay, 1989b; Collins and Robertson, 1997, 1998, 1999, 2003; Güngör and Erdoğan, 2001), others considered a dual origin (Poisson, 1977; Poisson, 1985; Özkaya, 1990; Ersoy, 1993). A recent tectono-stratigraphic study suggested that the Lycian Taurides represent an allochthonous Late Palaeozoic-Mesozoic rift/passive margin succession that was detached from its autochthon and translated towards the southeast between Upper Cretaceous and Late Miocene times (Collins and Robertson, 1997, 1998, 1999, 2003). These latter defined the Lycian nappe complex as being made of three main units: the 'Lycian Thrust Sheets' composed of Upper Palaeozoic to Tertiary sediments, a thick chaotic mélange unit (the 'Lycian Mélange'), tectonically overlain by the 'Lycian Ophiolites' which consist of serpentinized peridotites with a metamorphic sole. At the south of the Menderes Massif, the basal 'Lycian Thrust Sheets' widely crop out on the Bodrum peninsula. They are composed of Upper Permian-Lower Triassic reddish to greenish metapelites (the Karaova formation of Phillippson, 1910-1915) overlain by a thick succession of Middle Triassic-Middle Jurassic massive limestones and dolomites, grading upward to Upper Jurassic-Upper Cretaceous cherty limestones. This thick limestone succession is overlain by the Campanian to Maastrichtian Karaböğürtlen wildflysch (de Graciansky, 1972; Bernoulli et al., 1974; Çakmakoğlu, 1985; Okay, 1989b). This sequence records a continuous sedimentation from Late Palaeozoic to Late Cretaceous. Recent investigations in this area revealed the occurrence of a widespread HP metamorphism documented by Fe-Mg-carpholite in the metasediments of the basal Karaova formation, which involves pressure of about 8 kbar and maximum temperature of 400°C (Oberhänsli et al., 2001) (Figure I-23). HP-LT relics have also been found in klippen of Lycian Nappes located at the top of the Menderes Massif. Up to this discovery of HP parageneses in the Karaova formation, the base of the Lycian Nappes was thought to have recorded only a weak low-grade metamorphism under greenschist-facies conditions (Ashworth and Evirgen, 1984b).

The Menderes Massif and the Lycian Nappes constitute the investigation terrains of this work. The study area is located in the southern part of the Menderes Massif and in the Lycian Nappes, mainly on the Bodrum peninsula. Because these two massifs form an extensive area which was largely investigated for many years and is still the subject of many controversies, a more precise and detailed tectono-metamorphic framework of this region will be displayed at the beginning of the next chapters (Chapters II. and III.).

f. The Bey Dağları Platform and the Alanya Massif

Finally, an "autochthonous" external sequence, occurring along the Mediterranean coast, culminates in the calcareous massif of the Bey Dağları (Brunn et al., 1970). The Bey Dağları platform, also named the Lycian Basement (Collins and Robertson, 1998), is tectonically overlain by the extensive Lycian Nappes in its westernmost part (Figure I-22). It has been suggested that the Bey Dağları platform was overthrust by the Lycian Nappes from NW (Poisson, 1977). The sequence is composed of Lower Jurassic to Lower Miocene shallow-water limestones, overlain by Lower Miocene-Upper Miocene arenites and shales (Bernoulli et al., 1974; Poisson, 1977; Gutnic et al., 1979; Hayward, 1984). Up to now, no older rocks have been reported but it is commonly thought that they exist at depth. Hayward (1984) identified an increase in the sediment thickness within the Middle Miocene succession of the Bey Dağları platform and interpreted it as the development of a foreland basin in front of the advancing Lycian Nappes. The Bey Dağları sequence also occurs in a number of tectonic windows below the pile of the Lycian Nappes, to the north of the small town of Göcek (Göcek windows; de Graciansky, 1972). The rocks which are exposed in the tectonic windows comprise Cenomanian to Lower Burdigalian carbonate rocks, and Upper Burdigalian and possibly somewhat younger clastics (Bernoulli et al., 1974). On the eastern flank of the Bey Dağları platform, flysch deposits of Paleocene-Early Eocene age are closely associated with the emplacement of the Antalya Nappes and are not present in western Lycia (Brunn et al., 1970). While Özkaya (1990) claimed that the Bey Dağları unit and the Menderes Massif form two distinct units, other authors correlated the Bey Dağları platform and the Menderes Metamorphic Complex as a single, laterally continuous basement (Collins and Robertson, 1997-1998-1999-2003). These latter based their correlation on the overthrust relationship of the Lycian Nappes to both the Menderes Massif and the Bey Dağları platform, and on the similar Mesozoic sequences of shallow-water limestones in both units. The relatively autochthonous rocks of the Bey Dağları do not show any metamorphic imprint. On the contrary, the Alanya Massif in the Antalia nappe complex (Figure I-23) shows occurrence of high-grade metamorphic rocks. The Alanya massif forms a high topographic dome in the

Taurides. It is made of a nappe pile which emplaced over the Bey Dağları platform during the Late Cretaceous-Tertiary time (Brunn et al., 1970). Eclogite and blueschist occurrences have been described in the stack of the Alanya nappes (Okay, 1989c). They appear as intercalations or boudinaged blocks of metabasites. The HP-LT metamorphism was overprinted by Barrovian-type greenschist-facies conditions. Structural and metamorphic relations suggest that the HP metamorphism was followed by nappe stacking and consequent regional greenschist-facies metamorphism (Okay, 1989c).

D. OPEN QUESTIONS, OBJECTIVES AND METHODS

1. Open questions motivating this study

We have seen that the whole Aegean-Anatolian domain consists of many units which underwent similar or different histories during its Alpine tectono-metamorphic evolution. The Aegean Sea and western Turkey show widespread occurrence of HP-LT metamorphic rocks which were exhumed during a succession of syn-orogenic and post-orogenic episodes from the Late Cretaceous to the Early Miocene. Although the geometry and kinematics of post-orogenic extension are quite well studied (Avigad and Garfunkel, 1989; Gautier and Brun, 1994a; Hetzel et al., 1995, 1998; Jolivet et al., 1998a, b; Jolivet and Patriat, 1999; Ring et al., 1999b), the syn-orogenic stages are far less understood. Most of the Cretaceous-Eocene structures of the Cycladic blueschists, contemporaneous with subduction and crustal thickening, have been obscured by more recent extensional episodes, and therefore the kinematics and overall geometry of the accretionary complex where these rocks were equilibrated in HP-LT conditions, are still poorly known in the Aegean domain. Nevertheless, syn-orogenic extension has been documented in islands where blueschists and eclogites have been best preserved (Syros and Sifnos islands; Trotet, 2000; Trotet et al., 2001a, b). As said before, a NE-SW or ENE-WSW direction of extension with top-to-the-NE shear senses has been described. Constraining a model of high-pressure exhumation in the Aegean-Anatolian region requires a better understanding of the syn-orogenic episodes. The Oligo-Miocene Aegean extension is recognized in western Turkey but apparently occurred at a slower rate than in the Aegean Sea as shown by a much thicker crust, and thus should allow one a better recognition of early stages. It is thus necessary to look for syn-orogenic structures in the eastward lateral continuation of the Aegean Sea, in domains which were less intensely affected by post-orogenic extension.

The recent discovery of HP-LT parageneses in the Lycian Nappes south of the Menderes Massif (Oberhänsli et al., 2001; this study) as well as the first finding of ascertained Alpine HP-LT parageneses in the rocks from the 'cover' series of the southern Menderes Massif (this study) have strong implications on the tectonic evolution of SW Turkey and on the correlations with the Aegean Sea. The study area encompasses the westernmost part of the Lycian Nappes and the southern Menderes Massif, in the Milas-Bodrum region (on the Bodrum peninsula), and three regions where small klippen of Lycian Nappes crop out on top of the Menderes metamorphic rocks (Figure I-24 for location).

2. Objectives and methods

While Oberhänsli et al. (2001) documented the first occurrence of HP-LT metamorphism in the Lycian Nappes, only a few outcrops containing HP minerals such as Fe-Mg-carpholite were described. A first objective was therefore to expand on this work by providing the first detailed distribution of HP parageneses on the Bodrum peninsula and in the klippen of Lycian Nappes. Furthermore, because structural data have never been so far reported in this area, a second objective of this work was to focus on the characteristics of ductile deformation associated to the Lycian HP metamorphism. A field-based study in the Lycian metasediments which widely crop out on the Bodrum peninsula was essential to understand the tectono-metamorphic history of the Lycian Nappes and their relation to the Menderes Massif in the geodynamic context of the Aegean region.

During our investigations in the HP metamorphic terrains of the Lycian Nappes, we also found HP relics within the 'cover' of the southern Menderes Massif which was considered to have undergone only a Barrovian-type metamorphism during its Alpine evolution. A same kind of study as for the Lycian Nappes (distribution of HP parageneses, structural data associated to the high-pressure, P-T estimates…) had therefore to be led in the southern Menderes Massif in order to understand its tectono-metamorphic evolution.

Three fieldwork seasons (about one month each) were thus led in the Lycian Nappes and the southern Menderes Massif. About 300 outcrops were sampled and 900 thin sections were observed for both structural and metamorphic studies. Many samples collected in the field-area were oriented in order to observe the structures at the thin section scale (S-C relations, shear bands, asymmetric pressure-shadows, microscopic-scale folds…).

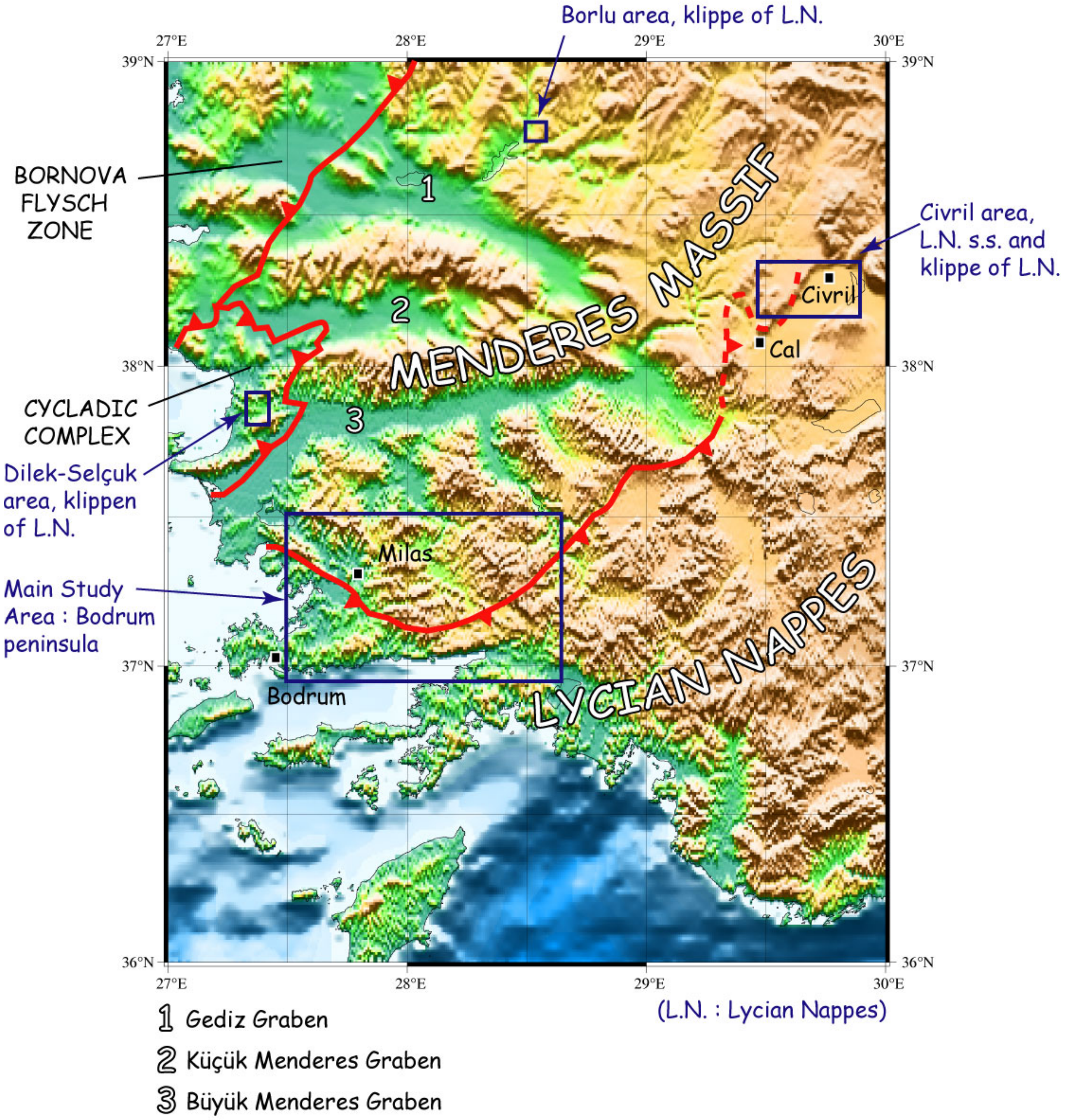

Figure I-24. Topographic map (GTOPO30) of SW Turkey showing location of the study areas in the Menderes-Lycian region. The main thrust contacts are represented with red heavy lines.

Whereas P-T conditions of the metamorphic peaks for the Lycian HP metasediments and the Menderes HP rocks can be easily estimated from the composition of the metamorphic index minerals, detailed and precise retrograde P-T paths reflecting the tectonic mechanism responsible for exhumation are rather difficult to constrain. However, recent studies have shown that in low- to medium-grade garnet-free metapelites, K-white mica (KWM) and chlorite local equilibria are good candidates to constrain the retrograde P-T evolution of exhumed metamorphic rocks (Vidal and Parra, 2000). The method that consists of multi-equilibrium P-T estimates relying on local equilibrium (see detailed explanations in Appendix A) has recently been used to obtain a detailed picture of retrograde P-T paths for exhumed rocks in the Aegean domain (Trotet, 2000; Trotet et al., 2001b; Parra et al., 2002b). These studies have led to distinguish a syn-orogenic exhumation stage characterized by a cold P-T path (decrease of temperature and pressure) during construction of the Hellenides, whereas the subsequent post-orogenic exhumation occurred along warmer conditions (isothermal decompression) during formation of the Aegean Sea, a thermal re-equilibriation of the crust being envisaged between the two exhumation episodes (Parra et al., 2002b).

In the present study, another objective was to use the multi-equilibrium calculation method in order to get precise information on the exhumation pattern of the Lycian and Menderes HP-LT rocks, and to try to relate the deformation observed in both massifs with the intensity of retrogression in the high-pressure metapelites.

As said above, constraining a model of exhumation of HP rocks requires a detailed structural work in concert with a metamorphic study. However, reconstructing the tectono-metamorphic history of any HP belt also needs age constraints. In this work, two methods were envisaged: ^{40}Ar/^{39}Ar age determination on phengite, and apatite fission track ages.

- The use of Ar/Ar dating has the objective to get precise ages of the HP events responsible for the HP-LT metamorphism discovered at the base of the Lycian Nappes, as well as in the ‘cover’ of the Menderes Massif. A serious campaign of sampling was therefore led in both massifs for isotope geochronology. Twenty samples collected in areas where HP relics crop out were selected on the basis of various criteria deduced from thin section observations. Because phengite can occur as associated with Fe-Mg-carpholite or chloritoid at HP conditions, or can be associated with chlorite as part of the retrograde assemblages, it is a good candidate to estimate ages of the HP metamorphic peak as well as cooling ages corresponding to the exhumation of HP parageneses. Therefore, we distinguished several samples by observation of different textural habits of phengites (depicting different generations of phengites) in order to get constraints on the P-T-t history. Twenty rock sections, corresponding to the thin sections in which phengites were analysed with electron microprobe, were meticulously prepared for *in situ* laser ablation Ar/Ar technique. Rock sections are of about 1 mm thickness and 1 cm^2 surface. Photographs of the surface and the corresponding thin section were taken in order to have accurate reference frame during laser probe experiments.

However, many significant technical problems with the Ar/Ar Laser probe of the University of Montpellier (France) prevented to perform the analyses. This work that is in progress will therefore not be presented in this manuscript.

- Apatite fission track data from buried and subsequently exhumed rocks may provide several different general types of information, depending on the maximum paleo-burial temperature (T_{max}) experienced by the samples in question just prior to exhumation. Where rocks were buried to sufficient depth, which is the case for HP rocks of SW Turkey, this T_{max} exceeded the total annealing temperature (Ketcham et al., 1999). As a sample passed through the apatite fission-track partial annealing temperature window of approximately 125° to 60°C during exhumation, the fission track clock is reset to zero and fission track data record information on the time-temperature cooling path of the sample (e.g. Green et al., 1989a, 1989b). This method was therefore used to constrain the late exhumation of HP rocks from both Lycian Nappes and Menderes Massif. Principles of the fission track dating method are explained in details in Appendix B.

Whereas a fast burial in subduction zones explains the HP-LT event recorded in these rocks, as highlighted before, the exhumation mechanisms are far less understood. The whole method described above has for objective to devote much effort for the understanding of the way these HP rocks returned back to the surface.

3. Analytical tools

a. Electron Microprobe

Electron microprobe is the most frequently tool used to make chemical analyses of minerals. About one hundred thin sections were selected from the 900 thin sections and were polished for microprobe analyses. About 3500 analyses were performed on three different microprobes (see Appendix C for examples of microprobe analyses). The three units operated under standard conditions (15 kV, 10 to 20 nA, PAP correction procedure), using natural and synthetic standard minerals.

- CAMECA SX50 at the University Pierre et Marie Curie, Paris VI (Paris, France)
  Standards : Fe_2O_3 [Fe], $MnTiO_3$ [Mn, Ti], diopside [Mg, Si], CaF_2 [F], orthoclase [Al, K], anorthite [Ca], albite [Na].

- CAMECA SX100 at GeoForschungsZentrum (Potsdam, Germany)
  Standards : Fe_2O_3 [Fe], rhodonite [Mn], rutile [Ti], MgO [Mg], wollastonite [Si, Ca], fluorite [F], orthoclase [Al, K], albite [Na].

- JEOL 8800 in the Museum fuer Naturkunde-Humboldt Universität (Berlin, Germany)
  Standards : anorthoclase [Si, Al, Na, K], ilmenite [Ti, Mn], magnetite [Fe], Cr-augite [Mg, Ca], apatite [F], tugtupite [Cl].

The analytical spot diameter was set between 3 and 5 µm keeping the same current conditions.

Note: For a few analyses on carbonate rocks performed at the G.F.Z. (Potsdam), standard conditions were of 15 kV and 10 nA, using the standard minerals which follow: rhodonite [Mn], siderite [Fe], $CaCO_3$ [Ca], $BaAl_2Si_2O$ [Ba], dolomite [Mg], albite [Na], celestite [Sr]. The analytical spot diameter was set at 20 µm.

b. X-Ray diffraction

This technique is commonly used to detect mineral phases which cannot be distinguished under a classical optical microscope, such as different types of micas (phengite, paragonite). Each analysis was made on a powder of sample, using a Siemens-D5005 model (University of Potsdam, Germany).

c. Apatite Fission Tracks

Samples were collected in the HP lithologies of the Lycian Nappes and the southern Menderes Massif. 11 samples come from the Lycian Nappes and 6 from the Menderes Massif. Between 5 and 10 kg of material were collected in the field area for each sample. Sample preparation was made following the methodology exposed in Sobel and Strecker (in press). Each of the 17 samples was crashed for mineral separation. Then Apatite was separated from the samples using standard magnetic and density methods. The apatite fraction resulting from separation was mounted on glass slides with araldite epoxy. After a long stage of grinding and polishing which provides the exposure of an internal surface, the apatites were etched with 5.5 molar nitric acid, at 21°C for 20 seconds. Only half of the samples was sent for irradiation at Oregon State University for reasons which will be exposed later with the results of fission track analysis. Following irradiation, the mica external detectors were etched with 40% hydrofluoric acid, at 21°C for 45 minutes. Samples were analysed with a Leica DMRM microscope with drawing tube located above a digitizing tablet and a Kinetek computer-controlled stage driven by the FTStage program (Dumitru, 1993). Analyses were performed with reflected and transmitted light at 1250x magnification. For this thermochronology technique, I prepared all the samples for fission track analysis, and Edward Sobel (Potsdam University) performed the complete analysis under microscope (see details in Appendix B).

CHAPTER II

METAMORPHIC AND STRUCTURAL DATA IN THE LYCIAN NAPPES

Fe-Mg-carpholite fibres within quartz, Karaova formation of the Lycian Nappes (locality of Demirciler, Bodrum peninsula)

The objective of this part is to present a field-based study that encompasses the region of the Lycian Nappes where pelitic metasediments widely crop out. This chapter exposes tectono-metamorphic data collected mainly in the Bodrum peninsula region. Metamorphic and structural features are also presented for klippen of Lycian Nappes located on top of the Menderes Massif and for the Karaböğürtlen region (east of the Bodrum peninsula) (Figure II-1).

Part of the structural data (from the Bodrum peninsula region) belongs to a paper published in **'Tectonics'** and entitled **"Deformation history of the high-pressure Lycian Nappes and implications for tectonic evolution of SW Turkey"** (by Rimmelé G., Jolivet L., Oberhänsli R., and Goffé B., 2003).

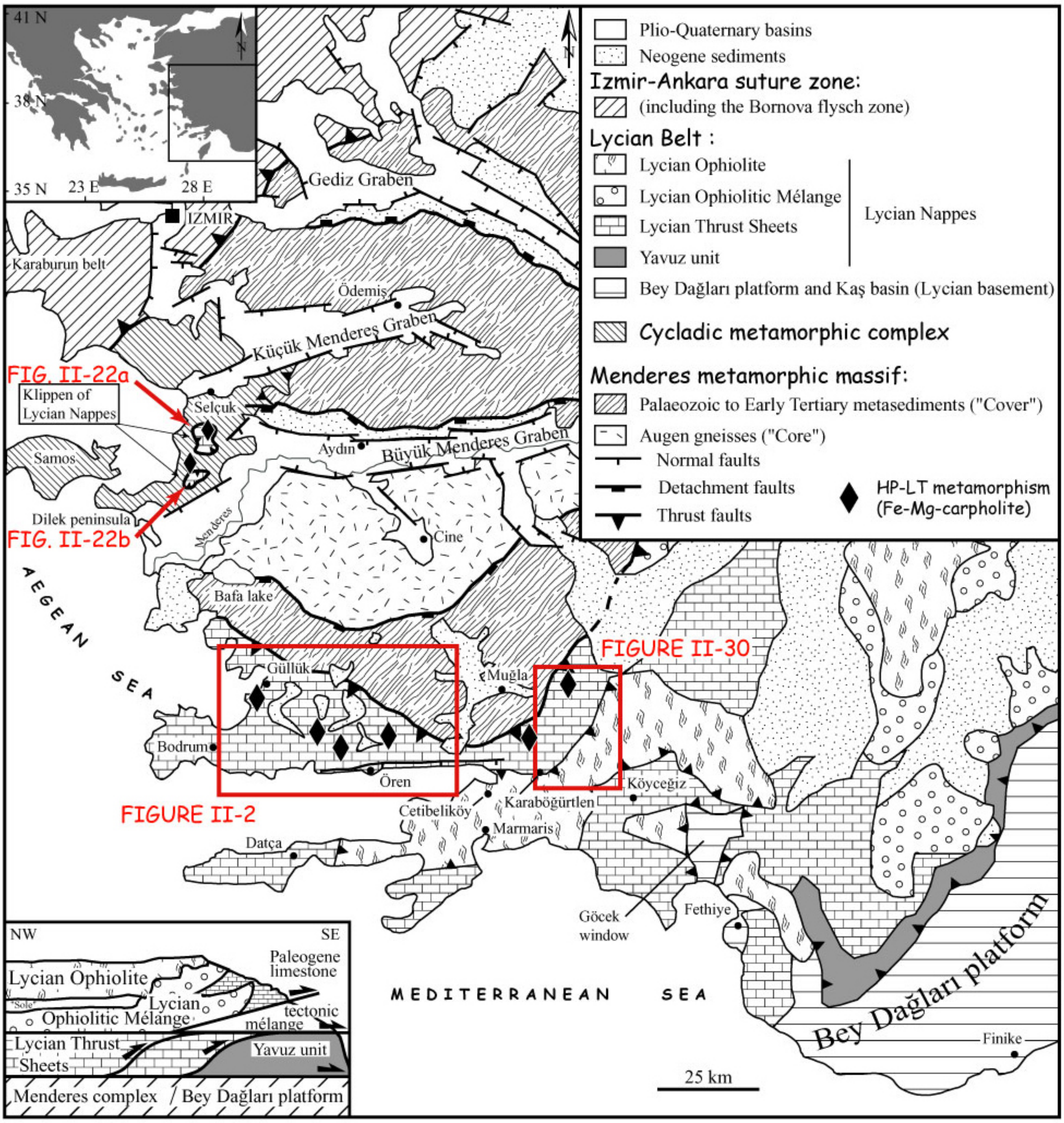

Figure II-1. Simplified geological map of southwest Turkey with location in the Aegean domain (modified after Collins and Robertson, 1999; Bozkurt and Satır, 2000; Okay, 2001). The diagram below the map shows the position of the Lycian Thrust Sheets within the Lycian nappe complex (modified after Collins and Robertson, 1997).

A. GEOLOGICAL SETTING OF THE LYCIAN NAPPES

1. Tectonic Framework – Where did the Lycian Nappes come from?

The origin of the Lycian Nappes in the Lycian Belt has been the subject of controversy for many years. Some authors considered that the tectonic slices came from north of the Menderes Massif; others argued that they originated from south of it. Most of the studies led in the Lycian Taurides for more than thirty years were stratigraphic works. While de Graciansky (1972) restored the Lycian thrust slices to a root zone north of the Menderes Massif, Poisson (1977) considered a dual origin, with sedimentary units associated to the overlying peridotitic nappe derived from the north, and other sedimentary thrust sheets considered to have originated from an intra-continental rift basin located between the Bey Dağları platform and the Menderes Massif (the "intra-Tauric trough", [Poisson, 1985]). Ersoy (1993) also advocated this same dual origin concept but supported the idea that the units which derived from areas to the north of the Menderes Massif were only the ophiolitic slices which were transported southward by Upper Cretaceous-Middle Miocene thrusts. The other units consist mainly of carbonate nappes originated from a trough located south of the Menderes Massif as described before by Poisson (1985). Based on the observation of distinct stratigraphic sequences in the Lycian allochthons, Özkaya (1990) also claimed that the Lycian allochthonous units were derived from two distinct tectonic terrains. At the same time, Okay (1989b) confirmed the differences in the age of deposition within the Lycian allochthonous units observed by Özkaya (1990), but contradicted the hypothesis of Özkaya (1990), affirming that all the thrust sheets were transported only from northwest to southeast. Other studies have suggested that the Lycian Nappes originally formed the northern margin of the Menderes Massif and were tectonically transported southward (Dürr, 1975; Dürr et al., 1978; Gutnic et al., 1979; Şengör and Yılmaz, 1981; Collins and Robertson, 1997, 1998, 1999, 2003). Şengör and Yılmaz (1981) suggested that the Lycian Allochthon belonged to the southern margin of the Neotethyan oceanic basin, located north of the Menderes platform. On the basis of a tectono-stratigraphic analysis, Collins and Robertson (1997, 1998, 1999, 2003) concluded that the Lycian Taurides consist of an allochthonous Mesozoic passive margin succession that was detached from its autochthon with a complex thrusts system and translated southeastward to its present position between Late Cretaceous and Late Miocene.

In the Söke-Selçuk region (Figure II-1 for location) a few klippen of Lycian Nappes were identified at the top of the Menderes Massif (Güngör, 1998; Güngör and Erdoğan, 2001). At the base of these tectonic slices, these authors described top-to-the-SSW sense of shear in red-green phyllites, and thus confirmed the southward emplacement of the Lycian Nappes over the Menderes metamorphic massif (Güngör and Erdoğan, 2001). I describe in Part B many structural data observed mainly in equivalent reddish to greenish lithologies widespread on the Bodrum peninsula, south of the Menderes Massif.

2. General stratigraphy of the Lycian Nappes in SW Turkey

On the southern flank of the Menderes Massif, the stratigraphic sequence of the Lycian Nappes was first described on the Bodrum peninsula by Brinkmann (1967). These series were first considered to be the cover sequence of the Menderes Massif. The tectonic contact characterized by serpentinites separating the Lycian Nappes from the Menderes Massif was later defined by Brunn et al. (1970).

In this southwestern part of Turkey (Figure II-1), three different tectonic units were distinguished by de Graciansky (1972) and Bernoulli et al. (1974). They described from base to top:

(1) a parautochthonous unit, outcropping in the calcareous massif of the Bey Dağları (Brunn et al., 1970; Poisson, 1977) and in a few tectonic windows below the pile of the Lycian Nappes (the two next tectonic units) to the north of Göcek. This parautochthonous sequence is composed of shallow-water and pelagic limestones from Late Cretaceous to Early Miocene age;

(2) an intermediate complex consisting of thrust-sheets and imbricated wedges composed of the widespread Köyceğiz series and the Diabase nappe. The stratigraphic sequence of the Köyceğiz unit that extends from Fethiye to Bodrum comprises Middle Triassic to Middle Liassic shallow-water limestones and dolomites (Gereme limestones), late Liassic to Cenomanian pelagic and turbiditic cherty limestones (Çal Dağ limestones) overlain by a thick breccia with chert fragments (Sirna Breccia). The sequence is topped by regularly stratified flysch sediments (Çamova formation) grading into the Karaböğürtlen formation that is a typical wildflysch with exotic blocks not younger than Maastrichtian in age. The Karaböğürtlen wildflysch is overlain by the Diabase Nappe, an assemblage of basaltic pillow-lavas in primary association with red cherty

limestones, radiolarites, white calcarenites and limestone breccias (Bernoulli et al., 1974). The Diabase Nappe was emplaced on the Karaböğürtlen wildflysch during the Late Cretaceous or Early Tertiary;

(3) a large peridotite nappe which is the uppermost thrust unit of western Lycia. Serpentinites and fragments of doleritic dykes derived from the Peridotite Nappe and are in turn imbricated and mixed with the rocks of the Diabase Nappe.

Later, Collins and Robertson (1997) defined the Lycian nappe complex (Figure II-1) as consisting of three main units which can be regionally correlated:

(1) the “Lycian Thrust Sheets”, composed mainly of Upper Palaeozoic to Tertiary carbonates with radiolarian cherts, shales and Paleogene clastic rocks (Yavuz unit);

(2) the “Lycian Mélange” unit, that corresponds to thick chaotic lithologies, unconformably overlain by Paleogene transgressive marine sediments; these authors interpreted this regionally overlying mélange unit as an emplaced subduction-accretion complex;

(3) the “Lycian Ophiolites”, dominantly composed of serpentinized peridotites with amphibolite-facies sole rocks. During the Cretaceous, the Lycian Peridotite formed within the northerly Neotethyan oceanic basin, probably above a northward-dipping subduction zone (Collins and Robertson, 1998). Protoliths of the amphibolites are chemically of “Mid-Ocean Ridge Basalt” and “Within-Plate Basalt” affinities (Collins and Robertson, 1997; Çelik and Delaloye, 2001). The amphibolite facies sole rocks are inferred to have formed by underplating of oceanic crust or seamounts to the base of the hot over-riding ophiolitic slab, prior to obduction onto the continental margin (Collins and Robertson, 2003).

B. THE BODRUM PENINSULA REGION

1. Stratigraphy of the Lycian Nappes on the Bodrum peninsula

On the Bodrum peninsula (Figure II-2) the exposed basal units of the Lycian nappe complex correspond to the “Lycian Thrust Sheets” (Collins and Robertson, 1997). These series tectonically overlie the metasediments of the Menderes cover sequence (de Graciansky, 1972). The basal levels of the Lycian sediment pile are composed of Permo-Triassic pelitic to quartzose shales, mostly red, purple, bluish-grey in colour (Figure II-3). This lowermost unit of the Lycian nappe complex, called Karaova formation, was first described and named by Phillippson (1910-1915) from the Bodrum peninsula. It constitutes a typical widespread lithology along the southern flank of the Menderes Massif. This unit is overlain by a thick sequence of Middle Triassic to Middle Jurassic massive limestones and dolomites, the Gereme unit. These lithologies are overlain by intermediate to thin layers of cherty limestones from Malm to Late Cretaceous. The highest levels of the calcareous sequence contain cherty limestones with calcite forming rosetta, called the Rosetta Limestone formation. These Middle Triassic to Cretaceous carbonate series are covered by the Campanian to Maastrichtian Karaböğürtlen wildflysch (de Graciansky, 1972; Bernoulli et al., 1974; Çakmakoğlu, 1985; Okay, 1989b). Thus continuous sedimentation from Late Palaeozoic to Late Cretaceous is recorded in the Lycian nappe complex (Figure II-3).

On the Bodrum peninsula, the tectonic contact between the Lycian Thrust Sheets and the Menderes metamorphic massif has a northwest-southeast strike (Figure II-2). In the Milas region, to the north of the contact, the Menderes cover sequence is mainly composed of Mesozoic metapelites, emery-bearing massive marbles and rudist-bearing marbles. The rudist fossils give a Late Cretaceous age to this part of the section (Dürr, 1975) and more precisely Santonian-Campanian (Özer et al., 2001). The uppermost marble layers from these Menderes "cover" units are recognised by the occurrence of reddish cherty marbles containing Late Campanian-Late Maastrichtian Globotruncana species (Özer et al., 2001). However, nummulites have been reported from the “Kızılağaç” marbles indicating an Early Eocene age (Gutnic et al., 1979). This marble sequence is unconformably overlain by a detrital sequence comprising blocks of metaserpentinite, emery-bearing marble and metapelite. It has been proposed that this formation was deposited during the Palaeocene-Middle Eocene times in the Kızılca/Alakaya basin located between the Menderes Massif to the north and the Bey Dağları platform to the south (Poisson and Sarp, 1977; Poisson, 1985; Özkaya, 1991). This slightly metamorphosed metaolistostromal unit (Gutnic et al., 1979) with Middle Palaeocene planktonic foraminifera (Özer et al., 2001) marks the end of sedimentation in the Menderes Massif. These rocks that separate the Lycian Nappes from the Menderes Massif are widespread all along the contact between both complexes (Figure II-2).

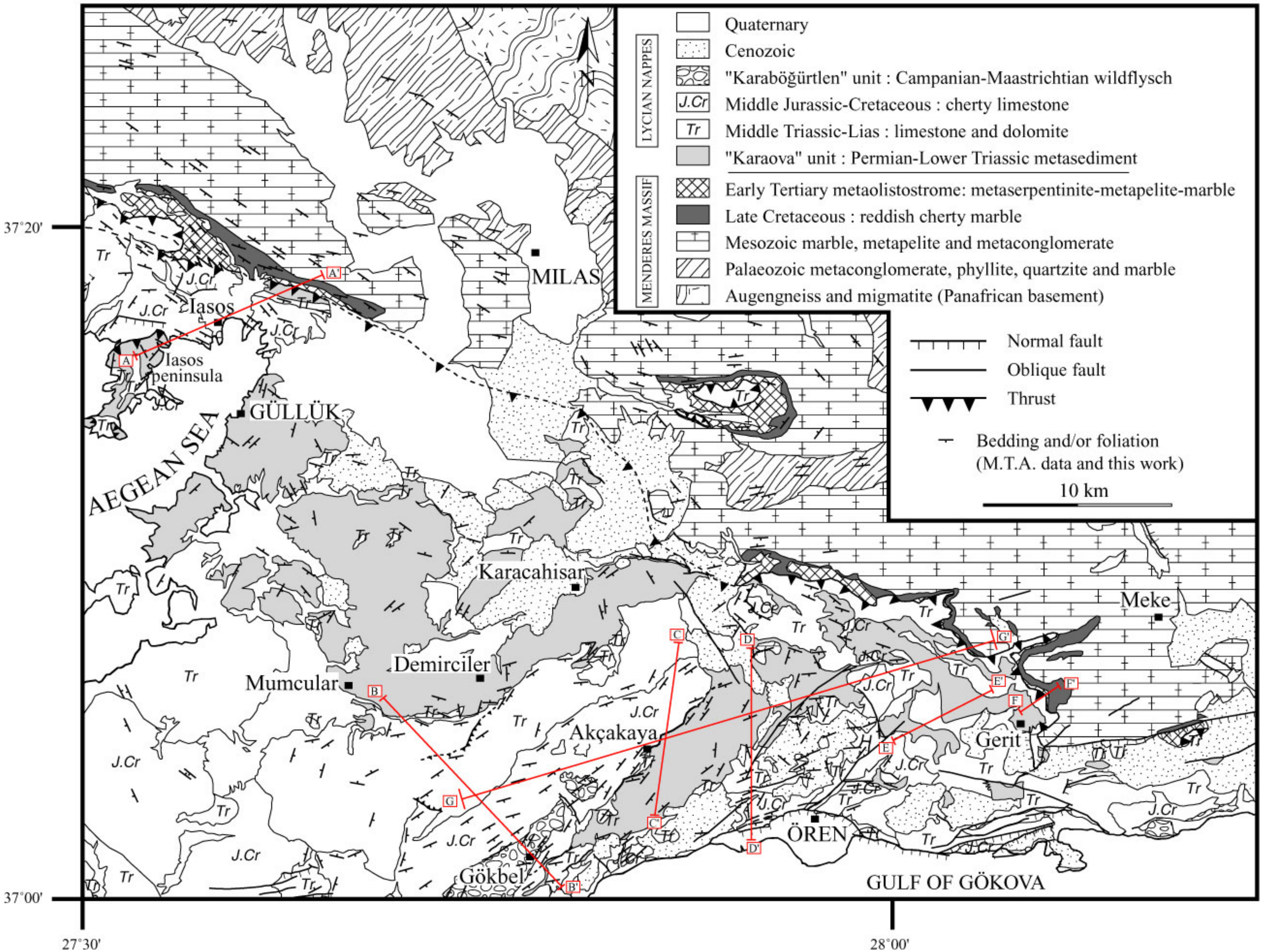

Figure II-2. Geological map of the Bodrum peninsula, south of the Menderes crystalline Massif (modified after M.T.A. preliminary maps; Konak and Akdeniz).

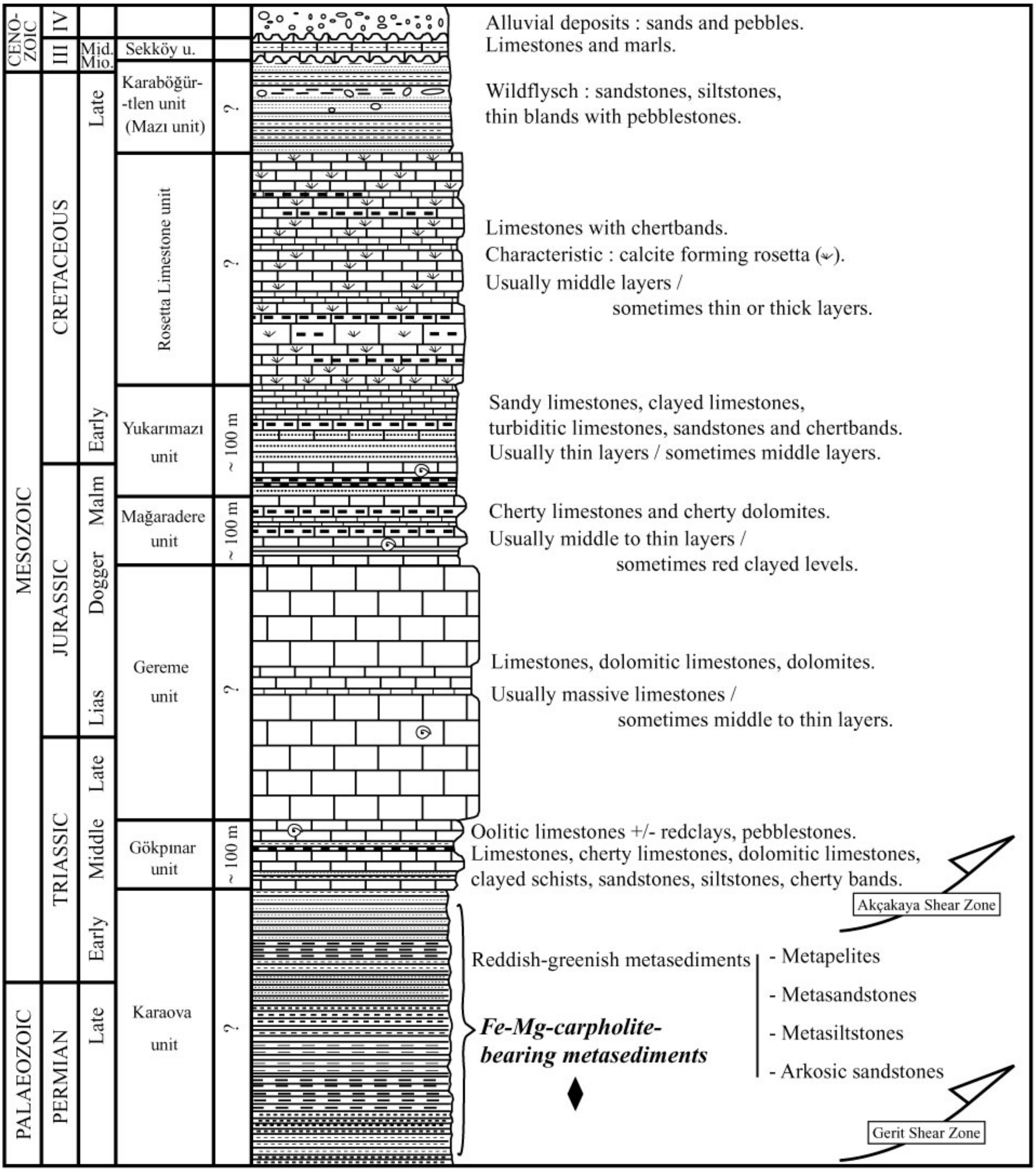

Figure II-3. Lithologies of the Lycian Thrust Sheets on the Bodrum peninsula (modified after Çakmakoğlu, 1985). The two major shear zones described in this chapter are reported on the figure (Note: Akçakaya Shear Zone is a décollement within the same stratigraphic sequence and not a nappe contact).

2. Characteristics of HP metamorphism on the Bodrum peninsula

a. Distribution of the low-grade high-pressure assemblages on the Bodrum peninsula

While Oberhänsli et al. (2001) reported the first description of HP-LT metamorphism documented by Fe-Mg-carpholite and chloritoid occurrences in the Lycian Nappes, only a few outcrops containing HP minerals were described. We expand on this work by providing the first detailed distribution of Fe-Mg-carpholite and its relics on the Bodrum peninsula located south of the Menderes crystalline massif.

This area contains terrains with widely distributed Fe-Mg-carpholite assemblages (Figure II-4). These high pressure-low temperature parageneses have been identified only in these lowermost lithologies (the Karaova unit) of the Lycian Thrust Sheets. Between Güllük and Muğla, the basal Permian to Lower Triassic sediments expose Fe-Mg-carpholite that can be found frequently with decimetre-scale fibres (Figure II-5a). HP-LT relics have not been found south of the peridotitic nappe between the Fethiye and Köyceğiz localities (Figure II-1).

Fe-Mg-carpholite and its breakdown products form veins within the metapelites and are also observed within the metacarbonates. The main vein assemblage observed in these levels is Fe-Mg-carpholite+quartz (Figure II-5b,c). The systematic association at the micrometer- to centimetre-scale of Fe-Mg-carpholite and quartz in massive quartz segregation suggests that carpholite and quartz were produced by the same reaction. The intimate association of carpholite and quartz is a common feature in Western Alps (Goffé, 1982; Goffé, 1984; Goffé and Velde, 1984; Goffé and Chopin, 1986), Central Alps (Goffé and Oberhänsli, 1992; Oberhänsli et al., 1995; Goffé and Bousquet, 1997), Crete (Theye et al., 1992; Jolivet et al., 1996) and Betic Cordillera (Goffé et al., 1989; Azañon and Goffé, 1997).

Fe-Mg-carpholite has also been observed within large crystals of calcite (Figure II-5d). Other parageneses involving Fe-Mg-carpholite in this area include: Fe-Mg-carpholite+pyrophyllite+chlorite (Figure II-5e), Fe-Mg-carpholite+chloritoid+quartz, Fe-Mg-carpholite+kaolinite+chlorite and Fe-Mg-carpholite+phengite+chlorite. While sudoite (di-trioctahedral chlorite) has commonly been observed in the thin sections, cookeite (Li-rich di-trioctahedral chlorite) has not been found. Chloritoid commonly occurs within the mineral foliation throughout the peninsula (Figure II-5f). It has also been found associated with Fe-Mg-carpholite in quartz segregations in the area of Ören. Whereas occurrences of very well preserved Fe-Mg-carpholite+quartz or Fe-Mg-carpholite+chloritoid+quartz assemblages have been found between Demirciler and Ören, Fe-Mg-carpholite only appears as being partly to totally retrogressed into chlorite and pyrophyllite or into chlorite and phengite near Güllük, Gerit or Ula. This might indicate various retrograde paths during exhumation of HP metamorphism. This is discussed in Part 2c.

b. Chemistry of the metamorphic index minerals

In the whole region of the Bodrum peninsula, many samples were collected and analyzed under electron microprobe (microprobe analysis procedure described in Chapter I.D.3) in order to determine the HP mineral chemistry.

- Fe-Mg-carpholite:

Fe-Mg-carpholite structural formula, $(Fe,Mn,Mg)Al_2Si_2O_6(OH, F)_4$, is calculated on the basis of 5 cations for the calculation of Si and 3 cations for Al, Fe, Mn and Mg, in order to account for the contribution of surrounding quartz when analyzing fibers smaller than the microprobe beam diameter (Goffé and Oberhänsli, 1992). The Fe^{3+} ($Fe^{3+} = 2 - Al$) and Fe^{2+} contents are calculated after Goffé and Oberhänsli (1992). Analyses showing an oxide sum lower than 85 wt% or greater than 90 wt% were rejected. Compositions of Fe-Mg-carpholite from the Lycian metasediments of the Bodrum peninsula are reported in Figure II-6a.

On the Bodrum peninsula, Fe-Mg-carpholite composition is variable as attested by X_{Mg} [$X_{Mg} = Mg/(Mg + Fe^{(2+)} + Mn)$] values ranging from 0.4 to 0.7. The X_{Mg} values vary from 0.55 to 0.60 in the area of Demirciler, from 0.6 to 0.7 near the locality of Ula, and from 0.4 and 0.65 (mean value of 0.55) in the region of Ören (see Figure II-4 for location). The Mn content in Fe-Mg-carpholite is very low ($0<X_{Mn}<0.03$) for all samples.

- Chloritoid:

Chloritoid formula, $(Fe,Mn,Mg)_2Al_4Si_2O_{10}(OH)_4$, is calculated on the basis of 12 oxygens. Fe^{3+}/Fe^{2+} ($Fe^{3+} = 4 - Al$) is calculated after Chopin et al. (1992). Analyses showing an oxide sum lower than 90 wt% or greater than 94 wt% were rejected.

Chloritoid from the Karaova formation of the Bodrum peninsula shows X_{Mg} [$X_{Mg} = Mg/(Mg + Fe^{(2+)} + Mn)$] values roughly comprised between 0.1 and 0.2 in the whole region. As for Fe-Mg-carpholite, the X_{Mn} of chloritoid does not exceed 3% (Figure II-6b).

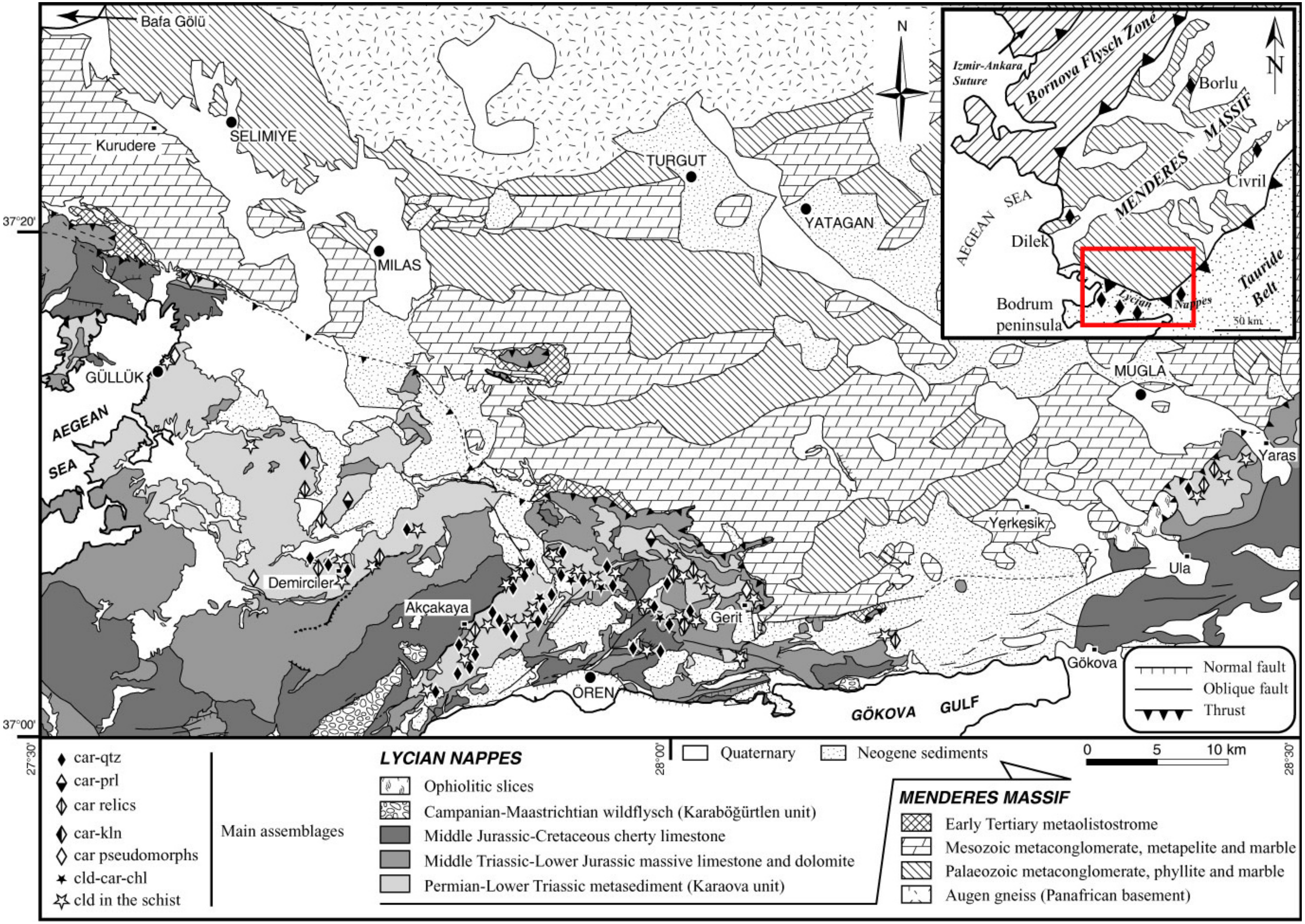

Figure II-4. Distribution of Fe-Mg-carpholite and its relics on the Bodrum peninsula (Abbreviations: car=carpholite, cld=chloritoid, chl=chlorite, prl=pyrophyllite, kln=kaolinite, qtz=quartz).

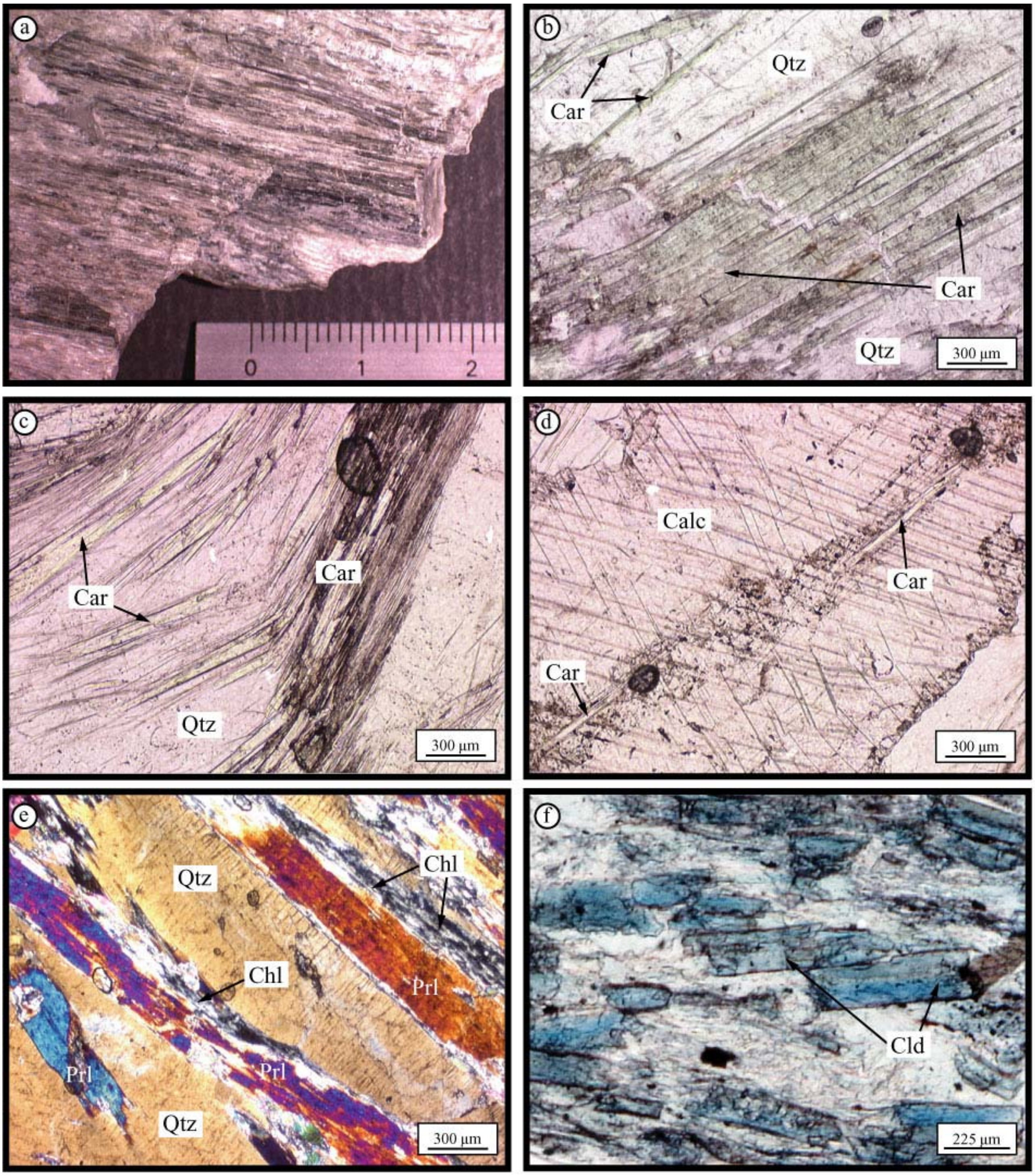

Figure II-5. Occurrence of Fe-Mg-carpholite and its relics near Ören: (a) Centimetre-scale fibres of Fe-Mg-carpholite in a quartz vein; (b) (c) Photomicrographs showing fibres of Fe-Mg-carpholite in a quartz matrix (plane polarized light); note the typical prismatic shape of Fe-Mg-carpholite; (d) Photomicrograph showing Fe-Mg-carpholite fibres within a crystal of calcite (plane polarized light); (e) Photomicrograph illustrating the retrogression of Fe-Mg-carpholite into pyrophyllite and chlorite (crossed polars); (f) Photomicrograph of chloritoid occurrence in quartzose phyllites from the Permo-Triassic Karaova formation (plane polarized light). Abbreviations: Car=Fe-Mg-carpholite, Cld=chloritoid, Chl=chlorite, Prl=pyrophyllite, Qtz=quartz, Calc=calcite.

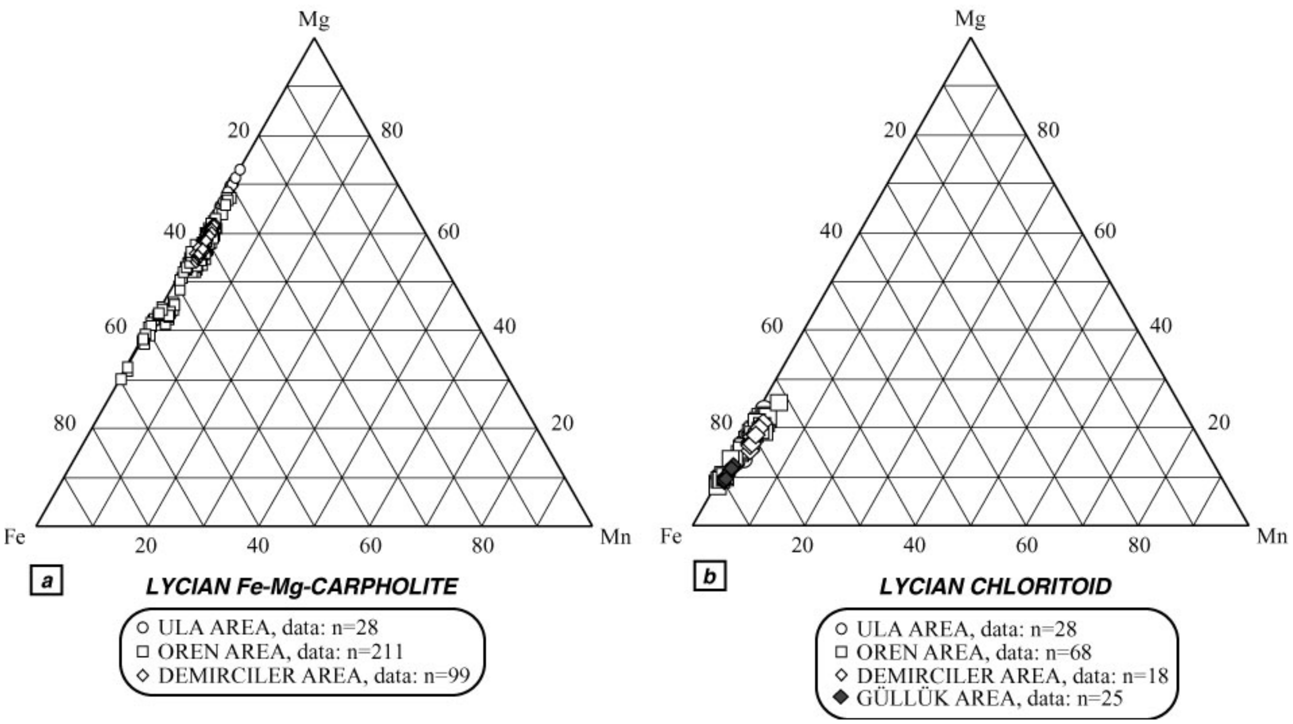

Figure II-6. Fe-Mn-Mg-ternary diagrams showing compositions of Fe-Mg-carpholite (a) and chloritoid (b) from the Lycian metasediments located on the Bodrum peninsula.

c. PT metamorphic conditions for Fe-Mg-carpholite-bearing rocks

Up to the discovery of high-pressure relics in the basal pelitic terrains, the base of the Lycian Nappes was considered to have undergone only a weak low-grade metamorphism under the greenschist facies (Ashworth and Evirgen, 1984b). Based on the coexistence of calcite and dolomite with chloritoid and pyrophyllite in the widespread chloritoid-bearing Karaova metapelites (Figure II-5f), these authors gave a temperature estimate of 350±30°C, calculations being carried out for P = 3 kbar. Oberhänsli et al. (2001) estimated a P-T domain implied from the paragenesis Fe-Mg-carpholite+chloritoid+quartz showing minimum pressures around 8 kb and maximum temperatures around 400°C, therefore indicating a low-grade high-pressure metamorphic event (Figure II-7). Because Fe-Mg-carpholite+kyanite assemblages have not been found, this P-T domain is

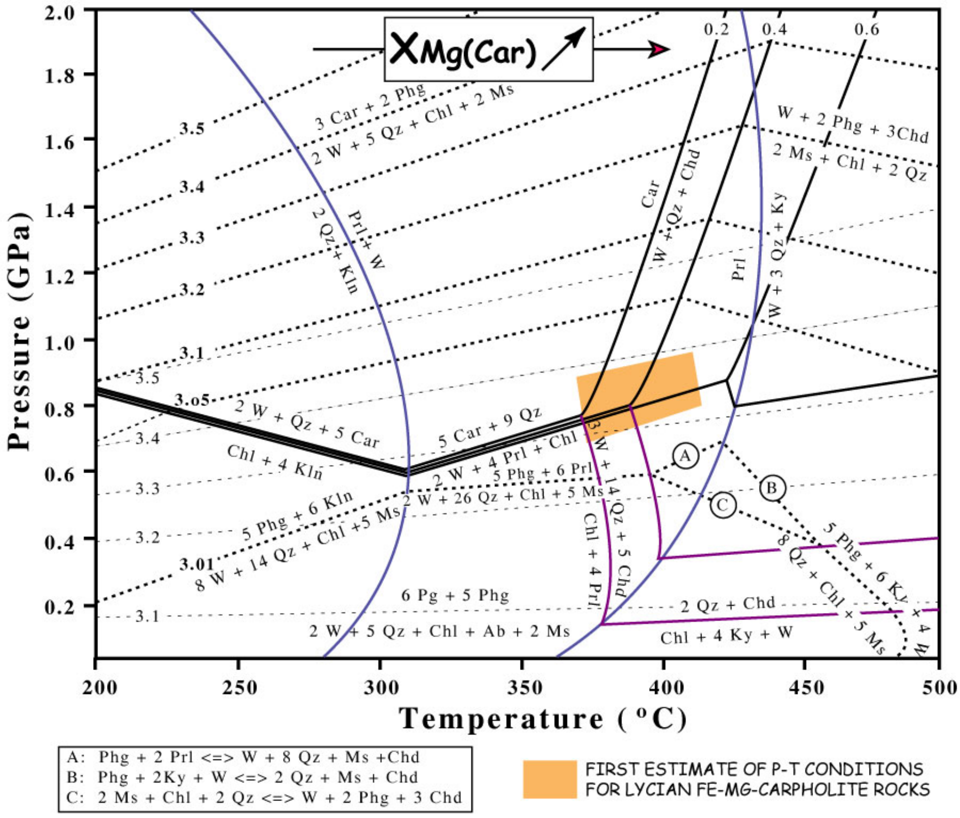

Figure II-7. Petrogenetic grid calculated for Fe-Mg-carpholite-bearing metapelitic assemblages (after Oberhänsli et al., 1995) showing the PT domain implied from paragenesis Fe-Mg-carpholite + chloritoid + quartz (Oberhänsli et al., 2001).

limited to the pyrophyllite stability field. Using the chemical compositions of Fe-Mg-carpholite+chloritoid+quartz assemblages from the Ören area (Figure II-6), the same ranges of PT conditions as those reported by Oberhänsli et al. (2001) were obtained.

The distribution of Fe-Mg-carpholite and its breakdown products throughout the peninsula (Figure II-4) reveals various retrograde metamorphic histories after a probable common HP-LT metamorphic peak. Between Demirciler and Ören, occurrences of very well preserved Fe-Mg-carpholite+quartz and Fe-Mg-carpholite+chloritoid+quartz assemblages suggest a HP cooling path. On the contrary, in the lowermost parts of the pelitic sequence, close to the contact with the Menderes Massif, Fe-Mg-carpholite only appears as being partly to totally retrogressed into chlorite and pyrophyllite or into chlorite and phengite (e.g. near Güllük, Gerit or Ula), which documents a more isothermal decompression (Figure II-8). Chapter IV will show better-constrained PT paths for the exhumation of the Lycian HP rocks, which can be obtained with a multi-equilibrium approach.

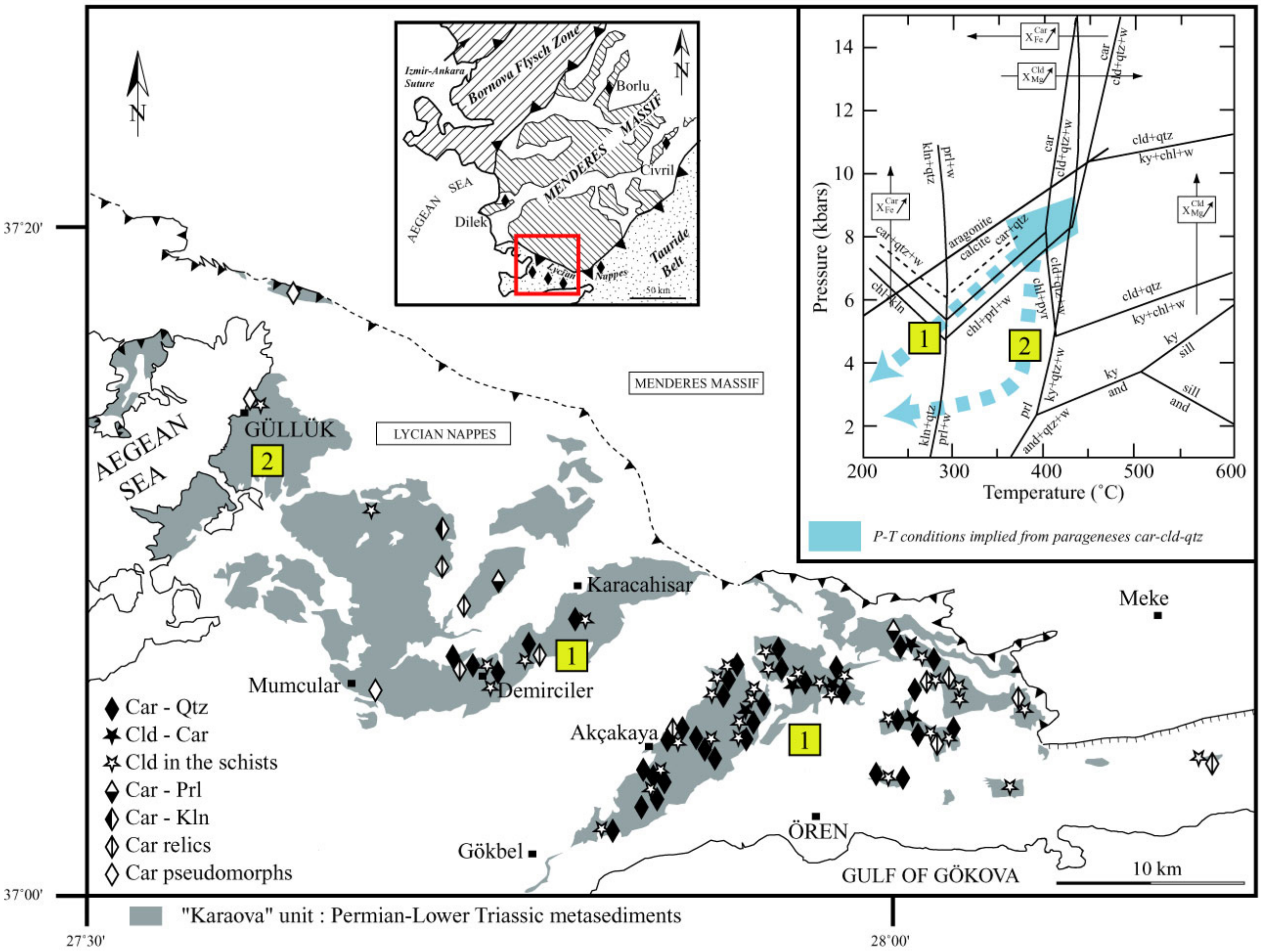

Figure II-8. Simplified map of the distribution of Fe-Mg-carpholite throughout the Bodrum peninsula and associated P-T diagram showing the main reactions involving Fe-Mg-carpholite and its breakdown products, P-T conditions for the Fe-Mg-carpholite-bearing rocks from the Bodrum peninsula, and P-T paths reflecting the exhumation of these HP rocks.

d. Significance of the "Rosetta limestones"

During our investigations in this area of the Lycian Nappes, we found widespread occurrences of decimetre- to meter-scale crystals of calcite forming rosetta (Figure II-9) in Cretaceous cherty limestones, which are part of the thick carbonate sequence that overlies the Karaova formation (Figure II-3). These rosetta occur everywhere in the limestone bedding (Figure II-9).

A few samples containing these long crystals forming radial structures have been analyzed using X-ray diffraction (Siemens diffractometer of Potsdam University) and Raman spectrometry methods (Raman Spectrometer, C.N.R.S. Villetaneuse, France) which showed only calcite spectra. No aragonite relics have been found in these Lycian carbonate rocks.

However, microprobe analyses were performed on one sample (MUM7) from the Rosetta limestones which was collected close to the locality of Akçakaya (Figure II-2 for location of Akçakaya). Analyses show relatively low Fe-, Mn-, and Mg- contents (a few ppm) whereas the Sr-content ranges between 400 and 1500 ppm (Figure II-10). For calcite free of Fe-, Mn-, and Mg- contents (e.g. MUM7-5), such relatively high values of Sr-content suggest that these carbonate rocks underwent PT conditions allowing growth of aragonite before its total retrogression into calcite. Similar values have already been reported for aragonite-bearing HP rocks from the western Alps and the Alpujarride complex of the Betic Chain (Gillet and Goffé, 1988; Goffé et al., 1989; Azañon and Goffé, 1997).

As seen in Figure II-8, the PT conditions implied from Fe-Mg-carpholite+chloritoid+quartz assemblages-bearing Karaova metasediments are located below the aragonite stability field. This finding of the probable existence of aragonite before its total retrogression into calcite in the overlying Rosetta limestone could therefore suggest higher-pressure condition for the HP metamorphism that affected the Lycian Thrust Sheets. This is discussed farther in Chapter IV.

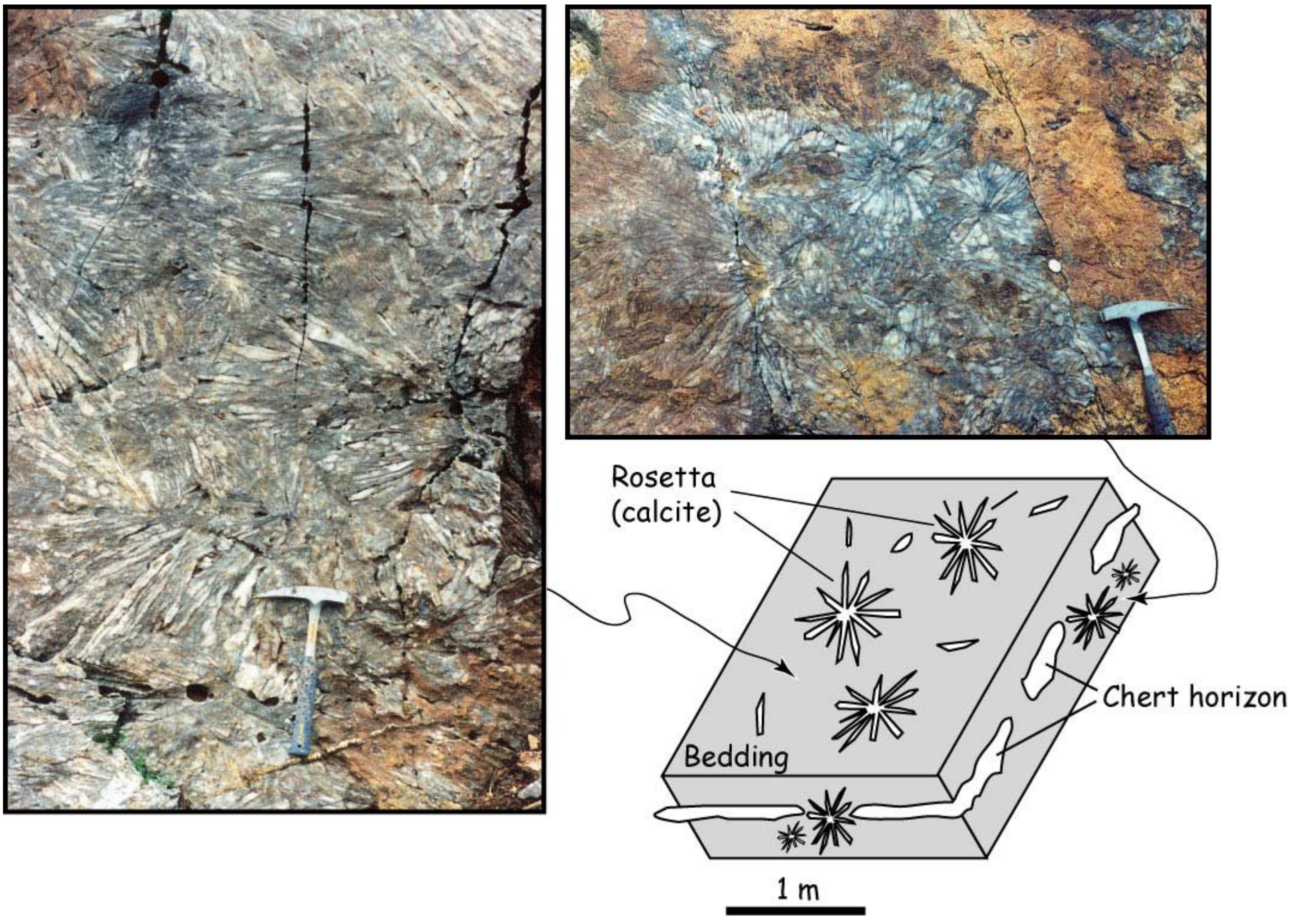

Figure II-9. Calcite crystals forming radial structures in the Cretaceous "Rosetta limestones" of the Lycian Thrust Sheets (Bodrum peninsula, north of Akçakaya, Figure II-2 for location).

Sample	MUM7-1	MUM7-2	MUM7-3	MUM7-4	MUM7-5
Mg(CO3)	0.000	0.000	0.000	0.000	0.000
Ca(CO3)	99.930	99.859	99.790	99.811	99.831
Mn(CO3)	0.000	0.000	0.012	0.000	0.000
Sr(CO3)	**0.038**	**0.074**	**0.132**	**0.076**	**0.150**
Ba(CO3)	0.015	0.042	0.011	0.044	0.000
Fe(CO3)	0.000	0.024	0.005	0.045	0.000

Figure II-10. Microprobe analyses of calcite fibers-bearing 'Rosetta limestones' (sample MUM7, west of Akçakaya).

3. Structural data in the metasediments of the Bodrum peninsula

a. Foliation

In the area of Milas, the main foliation of the Palaeozoic to Mesozoic metapelites and marbles, the overlying reddish cherty marble and the uppermost Tertiary metaolistostromal unit of the Menderes Massif strikes NW-SE and mainly dips to the SW (Figure II-2). The contact between the Menderes complex and the Lycian Nappes has also roughly the same orientation.

In the Lycian metasediments of the Bodrum peninsula, kilometre-scale folds constitute major large-scale structures in this area. Two main fold axes orientations (NW-SE in the Güllük region and between Ören and Meke; NE-SW between Demirciler and Ören) exist in this region (Figure II-2). To the west of Meke (area of Gerit), close to the contact between the Lycian Nappes and the Menderes Massif, the geological map (based on M.T.A. preliminary maps; Konak and Akdeniz, unpubl.) highlights large-scale folded structures that trend NW-SE and have undergone a later deformation phase responsible for folds trending NE-SW (Figure II-2).

The Permo-Triassic levels (the so-called Karaova unit) that are widely exposed throughout the Bodrum peninsula form very deformed lithologies composed of phyllites and interbedded conglomerates. The two main fold phases are also observed at a smaller scale in these "Karaova" metapelites. In several areas, metre-scale P1 folds with axes trending N090 to N120 associated with an early S1 axial plane schistosity have been deformed by later phase P2 folds which are characterized by NS to N060 axes. Figure II-11 illustrates how in these cases the earlier S1 schistosity appears to be overprinted by the S2 axial plane schistosity related to the P2 folds. The distribution of these folds is described in detail in the following paragraphs.

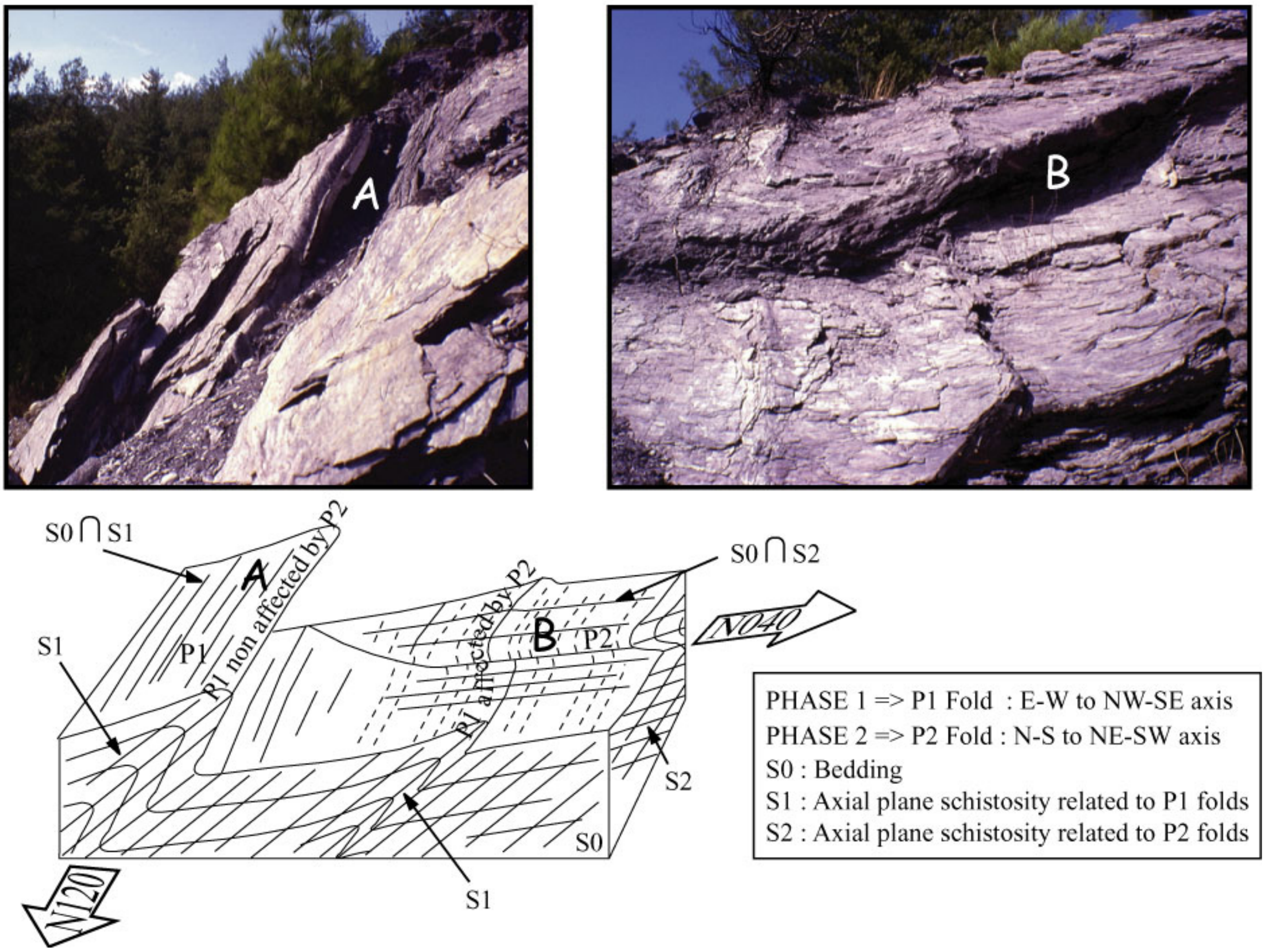

Figure II-11. Sketch showing the two P1 and P2 fold phases and the associated S1 and S2 axial plane schistosities (area of Ören).

b. Structures in the Iasos-Güllük area

To the northeast of Iasos (see location in Figure II-12) pelagic marbles from the metasedimentary cover sequence are highly deformed with northward-vergent overturned folds (Figures II-13 and II-14a). The development of asymmetric boudins of cherty material intercalated with reddish marble horizons is observed. The stretching lineation trends N090 to N120 and the orientation of shear bands indicates a top-to-the-east sense of shear (Figures II-12a and II-13). The metaolistostrome-type formation that constitutes the uppermost lithology of the Menderes Massif is composed of metapelite, metaserpentinite, marble lenses and metre-scale dolomitic blocks. The sub-vertical foliation of the schists is defined by muscovite, biotite and altered chlorite. The stretching lineation trends approximately E-W in the Palaeocene metaolistostrome,

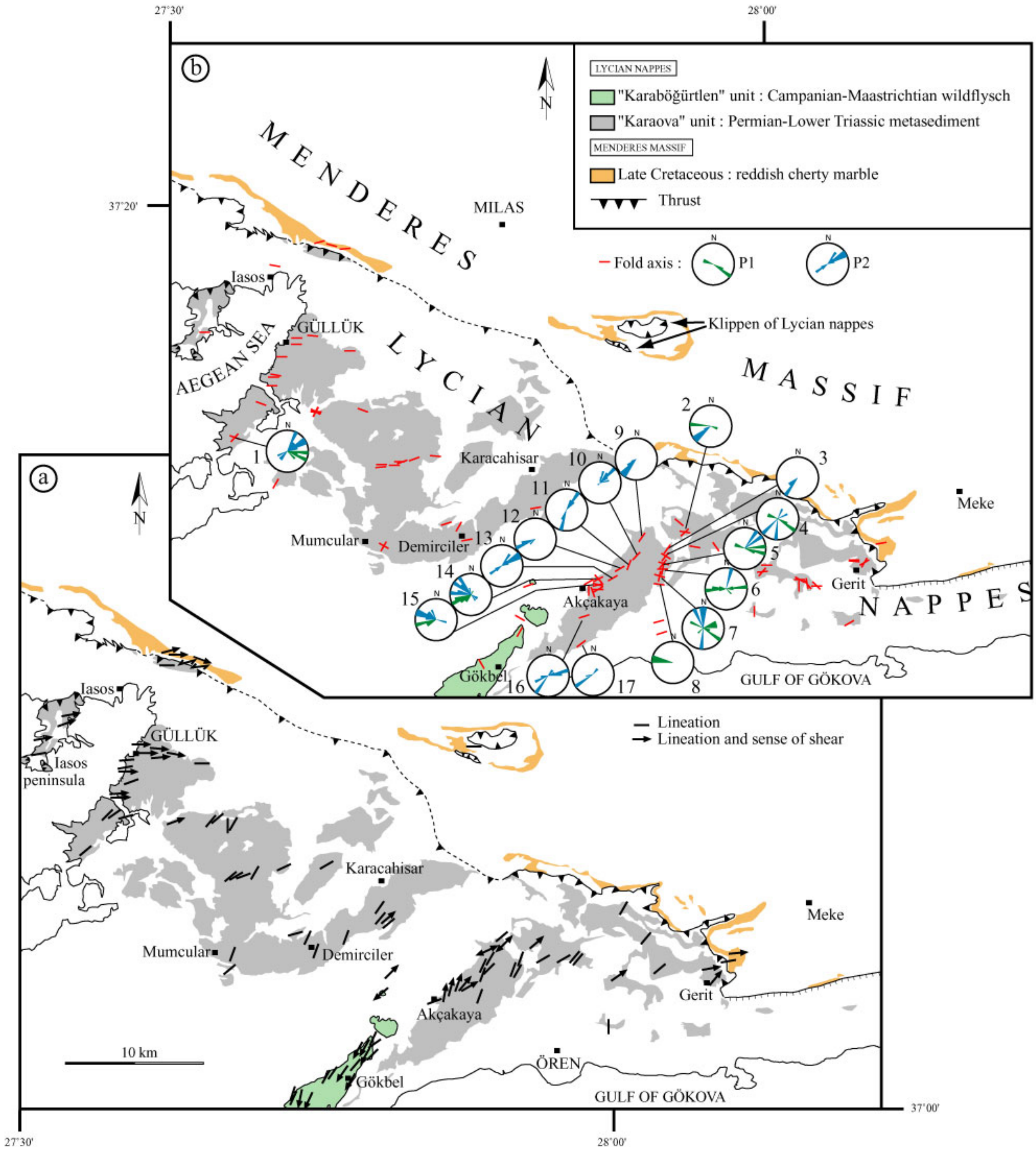

Figure II-12. Maps presenting the structural data in the Lycian Nappes (Karaova unit and Karaböğürtlen wildflysch) and in the uppermost series of the Menderes Massif (reddish marbles and metaolistostrome): (a) map of the stretching lineations and senses of shear; (b) map of the fold axes. The rose diagrams correspond to fold axes measured in different outcrops: the numbers beside the diagrams allow to refer to Figure II-17 for the more detailed stereograms.

similar to the Menderes marbles. Quartz appears as long fibres in asymmetric pressure shadows around hematite crystals (Figure II-15a). The S-C'-type shear band foliation and asymmetric quartz crystals, feldspar or tourmaline porphyroclasts all indicate sinistral shearing (Figure II-15b).

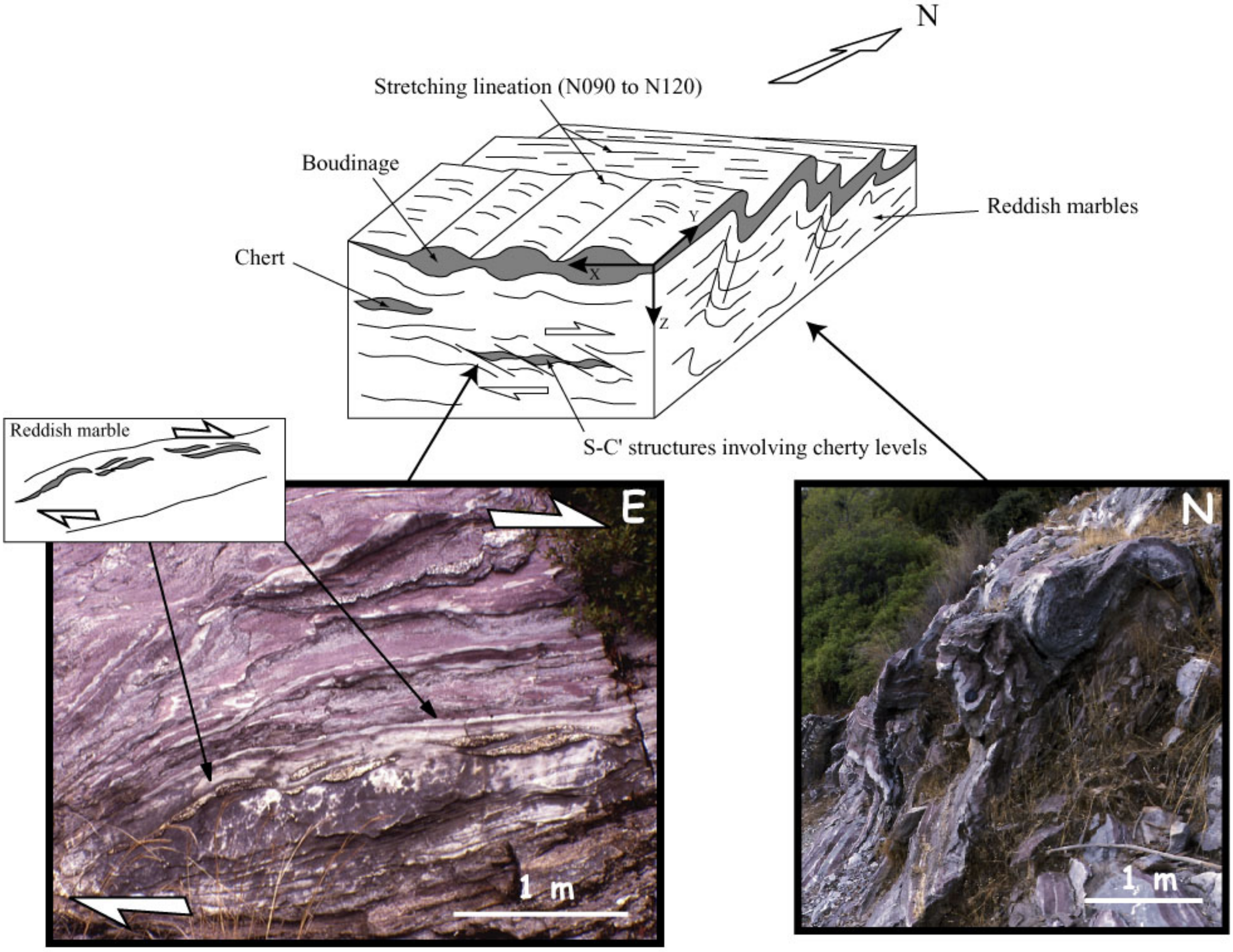

Figure II-13. Diagram showing the characteristics of the deformation observed in the uppermost levels of the Menderes Massif (NE of the locality of Iasos, Menderes reddish marbles).

To the south of the contact between the Menderes Massif and the Lycian Nappes, where the Karaova reddish metapelites are locally exposed, the orientation of the stretching lineation is similar to that observed in the uppermost levels of the Menderes series. The Middle Triassic to Jurassic carbonate sedimentary sequence that slightly dips towards the southwest overlies the Karaova unit (Figure II-14a). Folds in chert-bearing dolomitic limestones also trend N100, as observed in the reddish marbles from the Menderes Massif. To the southwest of the locality of Iasos, the Karaova unit overrides these limestones along a low-angle tectonic contact (Figures II-12 and II-14a). The Iasos peninsula primarily consists of a thrust sheet of Lycian material (mostly Permo-Triassic) emplaced over the Lycian Nappes themselves. On this small peninsula the same tectonic features were observed including the stretching lineation with N070-N080 trend, asymmetric quartz veins and S-C' structures that indicate senses of shear towards the N080 (Figure II-14a and Figure II-15c).

On the opposite side of the gulf, in the Güllük area, the reddish schists of the Karaova unit are severely deformed. To the east of Güllük, the foliation is folded with E-W-trending axes predominantly oriented roughly parallel to the stretching lineation (Figure II-12a and Figure II-12b). Numerous quartz and calcite veins have undergone strong stretching, folding and shearing documenting eastward movements. In the XZ plane of the finite strain ellipsoid, several stretched veins are folded and involved in S-C' shear bands indicating top-to-the-east ductile shearing (Figure II-16). In the YZ plane, early P1 decimetre-scale folds with N090-trending axes are responsible for a sub-horizontal S1 axial plane schistosity. This latter foliation underwent a second fold phase recorded by P1' folds with the same E-W axes which engendered a vertical crenulation schistosity (S1'). In this zone, several outcrops give the exposure of late shear bands cutting the P1' folds and the induced S1' crenulation schistosity. This deformation also shows top-to-the-east shearing although probably in more brittle conditions (Figure II-16). In massive conglomerates belonging to the Karaova formation which have also undergone extreme stretching, the horizontal foliation surrounds asymmetric quartzitic pebbles indicating movements towards the N100 (Figure II-15d).

More to the south, the stretching lineation rather strikes NE-SW (Figure II-12a) and the two fold orientations NW-SE (P1) and NE-SW (P2) described in the previous paragraph are exposed (Figures II-12b and II-17, stereogram [1]). This polyphased deformation supports the conclusion that the schists near Güllük have undergone a severe strain in ductile regime.

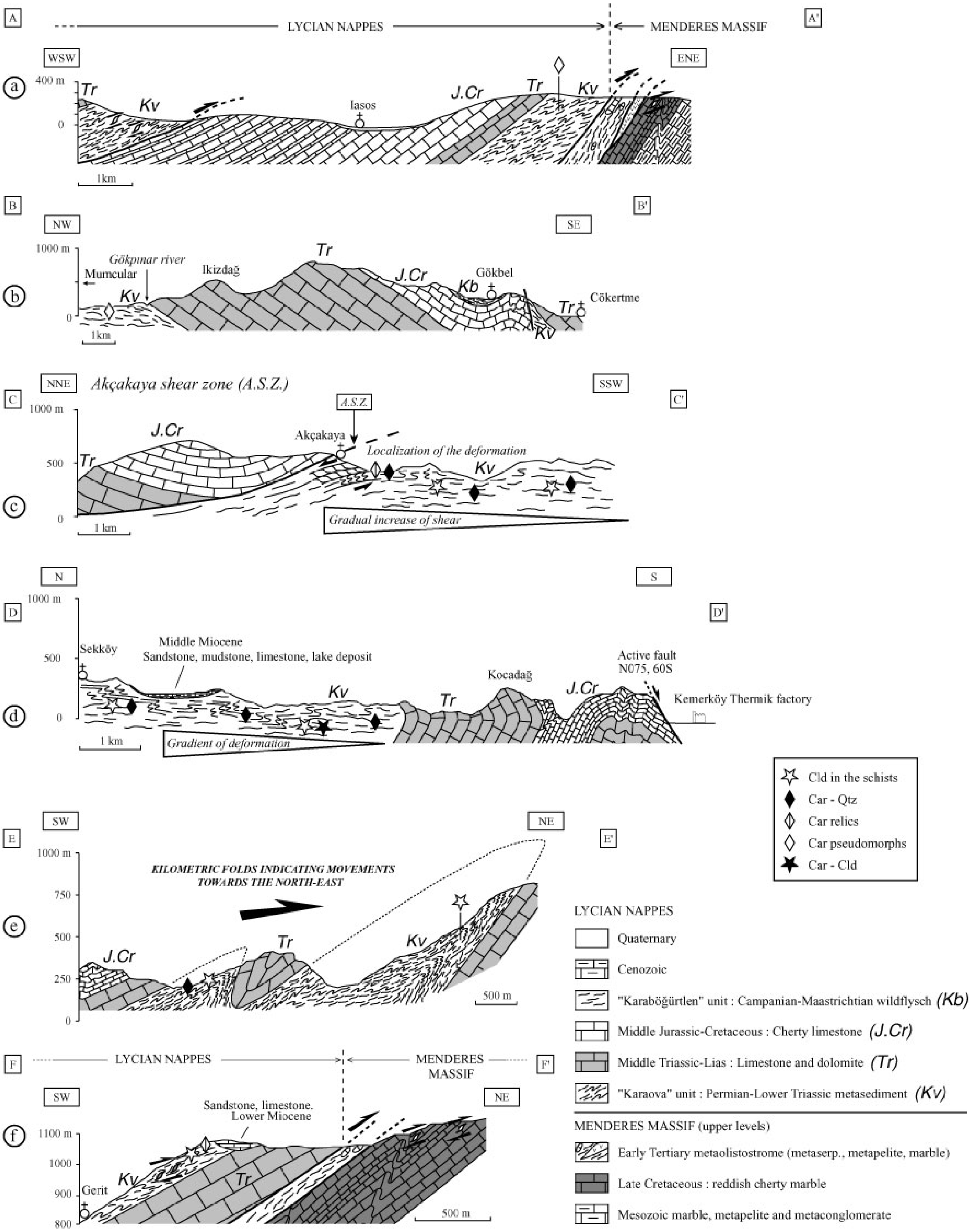

Figure II-14. Cross-sections exposing the main structures observed on the Bodrum peninsula (refer to Figure II-2 for the location of each cross-section).

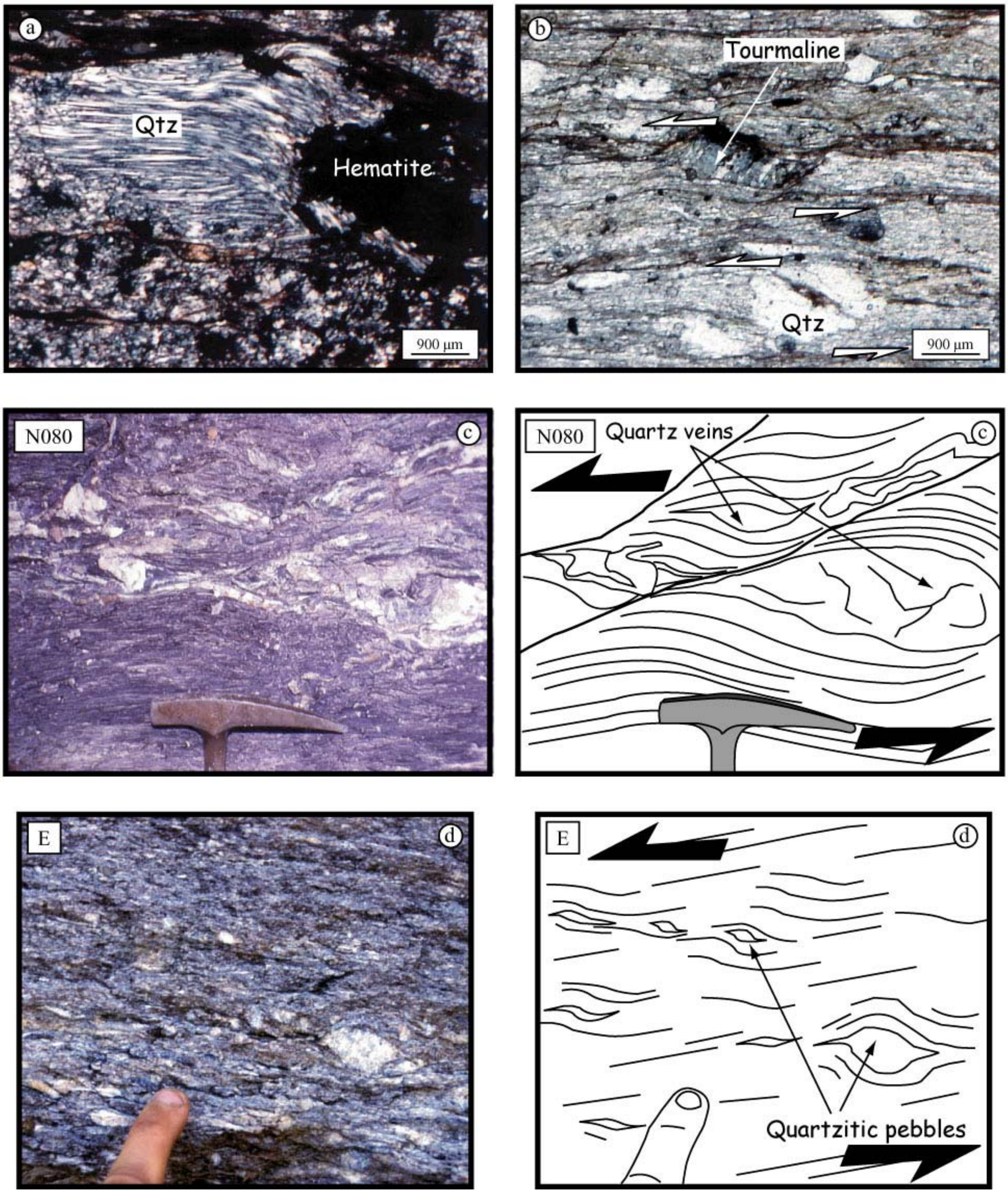

Figure II-15. (a) Photomicrograph of hematite crystal surrounded by intensely stretched quartz appearing as long fibres in the foliation mainly composed of muscovite, biotite and altered chlorite; the sample belongs to the metaolistostromal unit on top of the Menderes Massif, NE Iasos (crossed polars); (b) Photomicrograph showing S-C'-type shear band foliation and asymmetric quartz and tourmaline crystals indicating both a sinistral shear in the metaolistostrome of the Menderes Massif, NE Iasos (plane polarized light); (c) Asymmetric quartz veins documenting eastward shearing (in the Karaova formation from the Iasos peninsula); (d) Asymmetric quartz pebbles indicating movements towards the east (in a massive conglomerate from the Karaova unit, east of Güllük).
N.B. (a) and (b): Thin sections are prepared from oriented samples where sections are cut parallel to the lineation and perpendicular to the foliation.

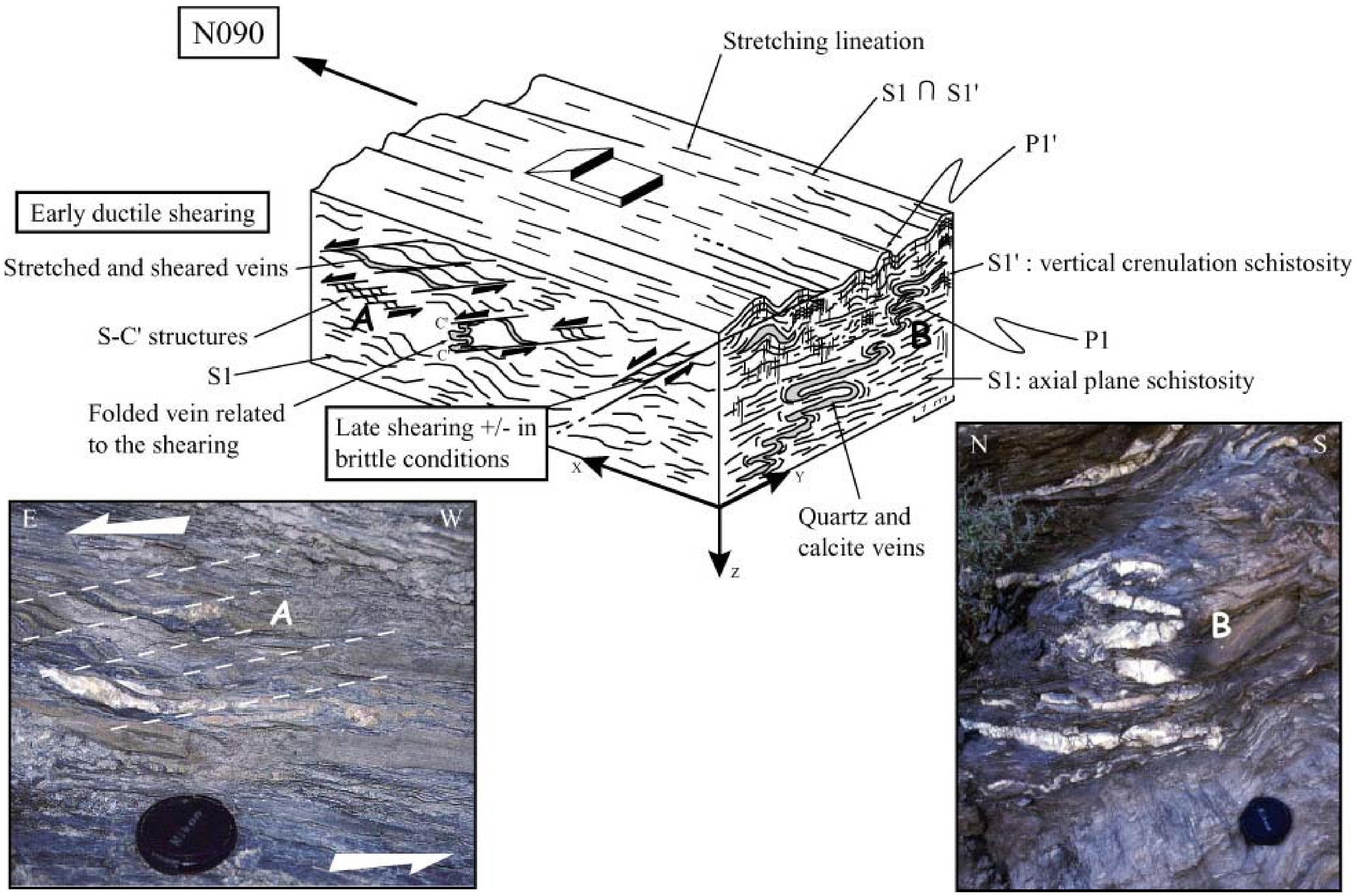

Figure II-16. Diagram showing the deformation observed in the area of Güllük (Karaova formation).

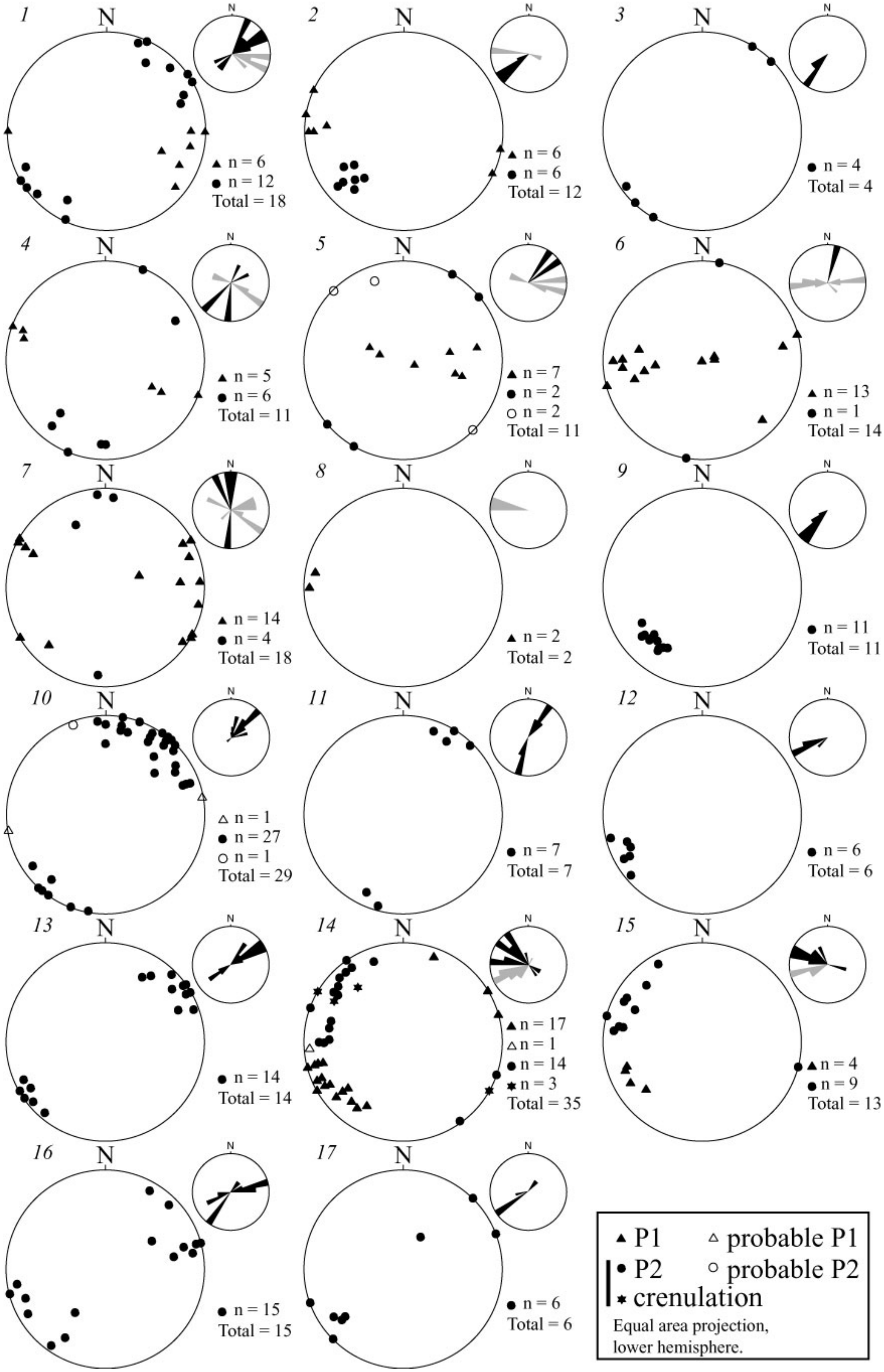

Figure II-17. Stereograms (lower hemisphere, equal area projection) of fold axes measured on the Bodrum peninsula: the numbers associated to the rose diagrams are reported on the fold axes map (Figure II-12b). ***In the rose diagrams, gray areas=P1 and black areas=P2.***

c. Structures in the Karaböğürtlen wildflysch

The "Karaböğürtlen wildflysch" crops out on the top of the Lycian sedimentary series that form a syncline, one of the main NE-SW folded structure (Figure II-14b). This formation consists of a dark greenish schistose matrix including limestone pebbles, sandstone pebbles and chert pebbles. On the Bodrum peninsula, no traces of HP metamorphism have been found in this wildflysch-type formation. Near Gökbel, these pebbles of various lithologies show a constrictional fabric with a strong N025 stretching (Figure II-12a). At the outcrop scale, shear criteria in these stretched pebbles is not often obvious, whereas in thin section asymmetric kinematic indicators favour top-to-the-SSW non coaxial flow (Figure II-18a). Contrarily, in the underlying Cretaceous limestones series, interbedded cherty levels are deformed into book-shelf-like structures that indicate northeastward displacements as observed in the Karaova unit (Figure II-18b).

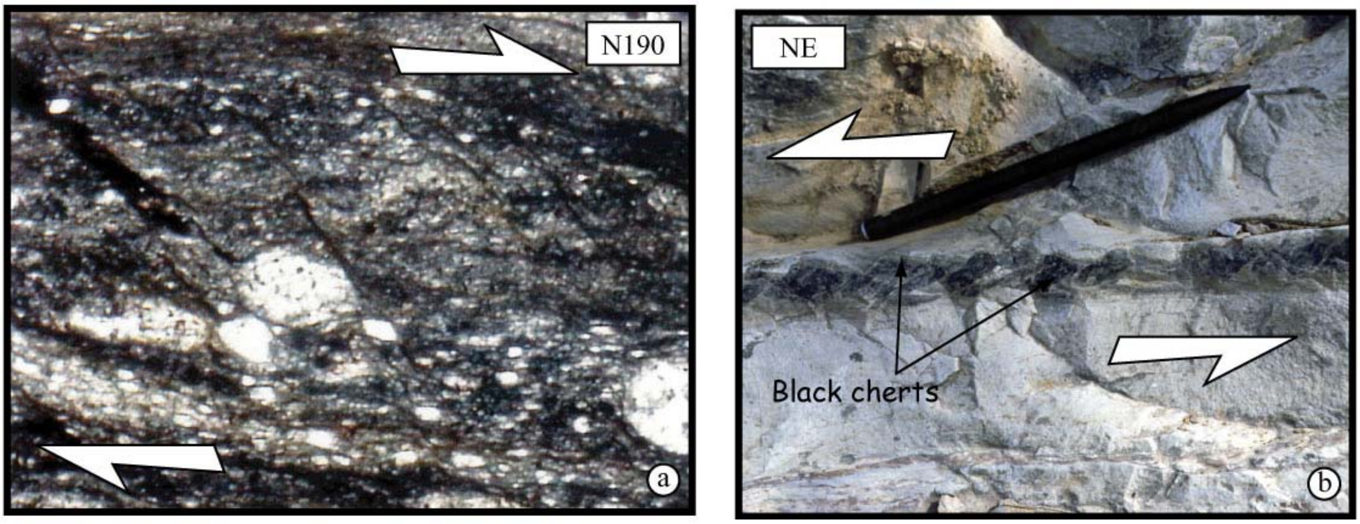

Figure II-18. (a) Photomicrograph showing S-C'-type shear bands in the Karaböğürtlen wildflysch (area of Gökbel); (b) Black cherty layer that forms book-shelf structures indicating movements top-to-the-NE (from Lycian Cretaceous limestones).

d. The "Akçakaya shear zone"

Close to the locality of Akçakaya (Figure II-2 for location), the thick Jurassic limestone series directly overlies the Permo-Triassic schists of the metamorphic Karaova unit (Figure II-14c). A breccia horizon sampled along this contact between both lithologies supports a tectonic nature for this boundary. This is also confirmed by a northward gradient of shear: close to this contact, the stretching lineations trend N015 to N030 and the pervasively sheared foliation clearly indicates intense shearing deformation towards the north (Figure II-12a). In contrast, the metapelites are weakly to non-deformed away from this tectonic boundary. Therefore, the upper part of the Karaova formation in this area shows a shear zone ("Akçakaya shear zone") strongly localizing the ductile deformation (Figures II-14c and II-19a). In this region where fresh Fe-Mg-carpholite is well preserved, the two main fold phases discussed previously have an uneven distribution. Far from the contact (around 5 km to the east of Akçakaya) the Karaova schists are characterized by metre-scale P1 and P2 folds (Figures II-12b and II-17, stereograms [2] to [8]). The sketch shown in Figure II-11 illustrates this polyphased deformation frequently observed along a north-south-trending transect (Figure II-14d). This area is characterized by the preservation of the NW-SE-trending P1 folds that decrease in number towards the south approaching the strongly folded Triassic to Cretaceous sedimentary series (Figures II-12b and II-14d). Stretching is not well recorded in the Karaova dark-reddish schists and sandstones and the shearing appears to be less intense than near the Akçakaya shear zone (Figure II-12a). To the northeast of Akçakaya, only P2 folds with NE-SW-trending axes have been observed (Figures II-12b and II-17, stereograms [9] to [13]). Within the Akçakaya shear zone, synfolial acute fold axes trend roughly parallel to the stretching lineation suggesting that P1 folds have been rotated parallel to the stretching direction. P1 folds are very sharp and the S1 axial plane schistosity is strongly sheared top-to-the-NNE (Figure II-19b). Quartz veins with Fe-Mg-carpholite relics also have undergone stretching, P1 folding and then a severe shearing towards the northeast (Figure II-19c). The occurrence of late P2 centimetre-scale folds (Figure II-19b) contemporaneous with the shear, or related to a late crenulation at the end of the shear, documents a component of constriction along the Akçakaya shear zone (Figures II-12b and II-17, stereograms [14] and [15]). To the south of the Akçakaya shear zone, metapelites are less deformed and folds decrease gradually in number towards the south (Figures II-12b and II-17, stereograms [16] and [17]). As seen in Figure II-19c, the deformation indicating northeastward movements in the Akçakaya region and more largely throughout the Bodrum peninsula is contemporaneous with the retrogression of high pressure-low temperature parageneses and therefore corresponds to the exhumation of these low-grade high-pressure rocks.

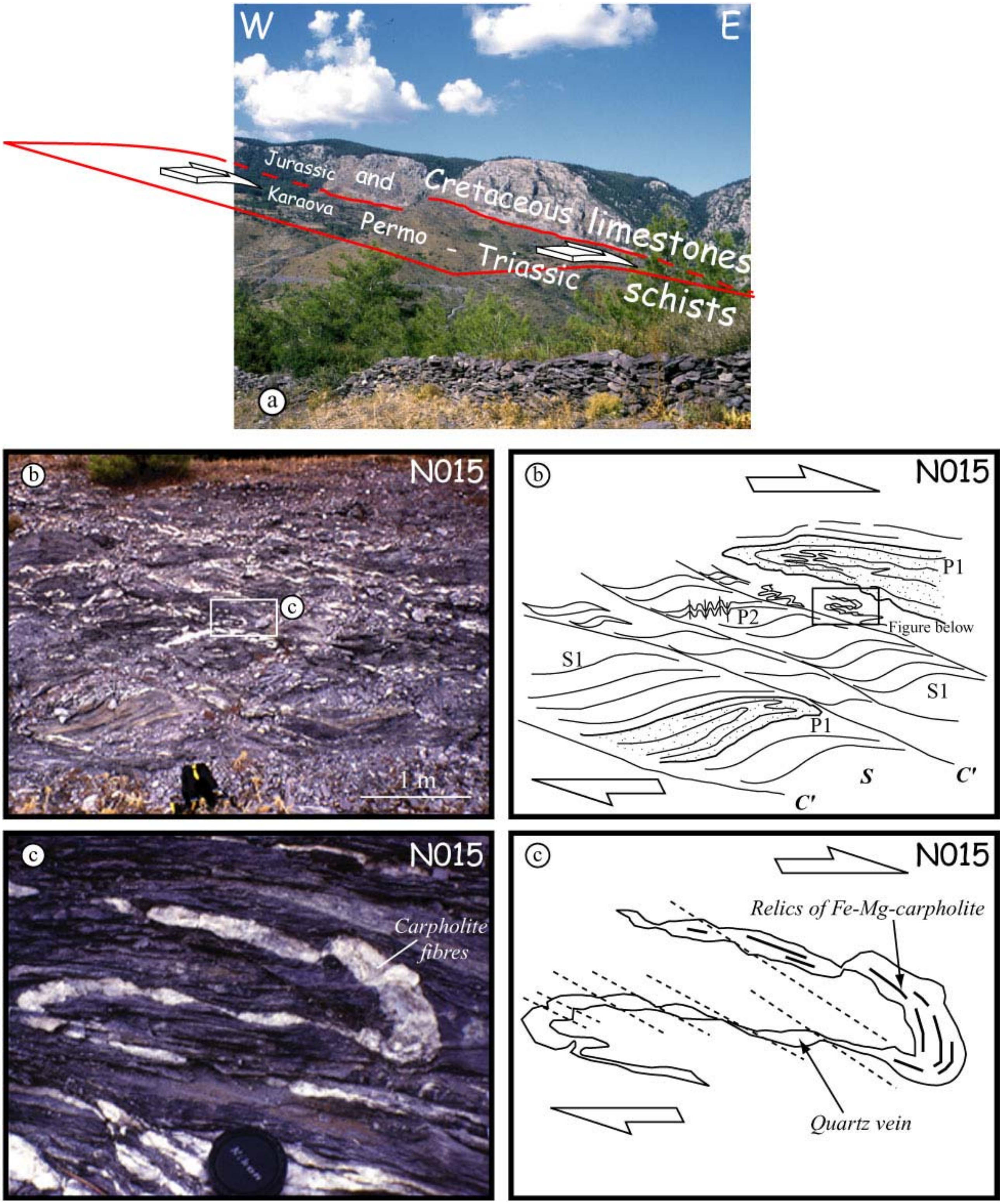

Figure II-19. (a) Picture representing a major tectonic contact in the Akçakaya area: the "Akçakaya shear zone"; (b) S-C' shear bands documenting movements top-to-the-NNE (Akçakaya area), refer to the text for more details; (c) Fe-Mg-carpholite fibres-bearing a folded and sheared quartz vein also suggesting northward displacements (detail of Figure II-19b).

e. Structures between Ören and Meke, the "Gerit shear zone"

To the northeast of Ören (Figures II-2 and II-12), cross-sections EE' and FF' (Figures II-14e and II-14f) show the main structures observed in the area of Gerit.

The first cross-section EE' shows kilometre-scale overturned folds involving the Karaova formation and the Middle Triassic to Liassic massive limestones. These large folded structures, similar to the ones described in the previous section, document movement towards the northeast. The Karaova unit consists of alternating pelitic levels, carbonaceous levels and sandy levels. The foliation is folded by axes mainly trending NW-SE (Figure II-12b).

The second cross-section FF' that cuts the contact between the Lycian Thrust Sheets and the Menderes Massif highlights the same deformation as shown on cross-section AA' (Figure II-2 for location of cross-sections). Near Gerit, stretching lineations observed in polygenic conglomerates of the Karaova formation trend between N045 and N080 (Figure II-12a). Asymmetric clasts in the conglomerates indicate top-to-the-NE to top-to-the-E shear (Figure II-20a). Approaching the contact with the Menderes Massif, the deformation appears to be more intense. In the Palaeocene dark-greenish metaolistostrome that forms the uppermost level of the Menderes Massif, some boudins of marble are elongated with a N065 to N080 orientation. Underlying reddish to greyish marbles, typical of the "Menderes cover", show northeast-vergent overturned folds. Cherty levels are folded around N080 axis and asymmetric boudins of cherty material display top-to-the-east senses of shear as previously observed to the north of Iasos (Figure II-20b). These observations suggest that the contact between the Lycian units and the cover of the Menderes Massif is a zone of strain localization, the "Gerit shear zone".

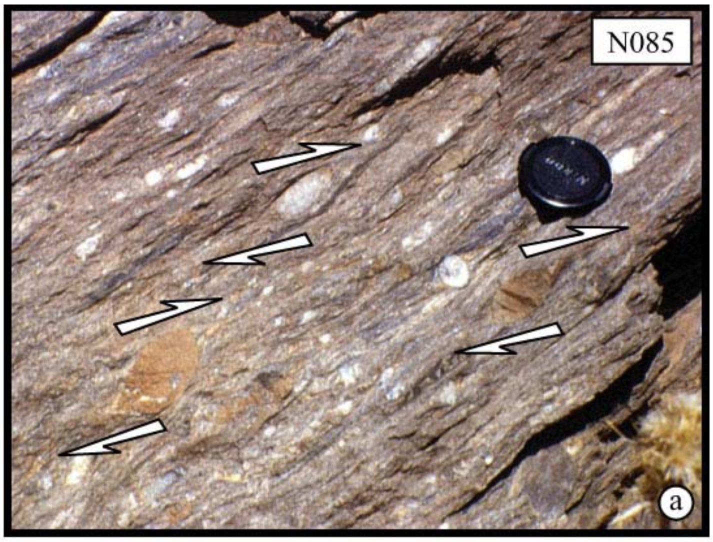

Figure II-20. (a) Polygenic conglomerate from the Karaova formation; pebbles are sheared top-to-the-east (area of Gerit); (b) Sketch showing the deformation observed in the uppermost reddish cherty marbles of the Menderes series.

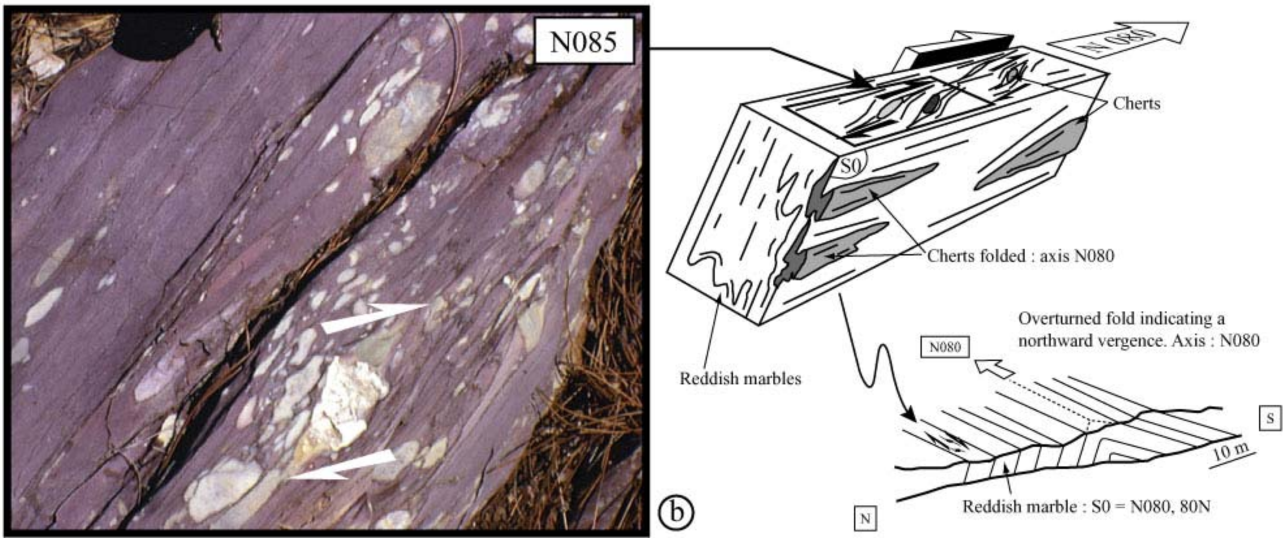

f. Synthesis

Our investigation in HP-LT metasediments of the basal Lycian Thrust Sheets that widely crop out on the Bodrum peninsula reveals the existence of severe ductile deformation associated with top-to-the-northeast to top-to-the-east shearing. This deformation corresponds mainly to the exhumation of the basal Lycian high-pressure sediments. In the underlying cover series that belong to the Menderes Massif, close to the contact with the Lycian Nappes, similar eastward displacements are observed and trajectories of the stretching lineations are continuous from the Lycian Nappes to the Menderes Massif across the contact. Two zones of strain localization are observed. The upper one is at the top of the metapelitic Karaova unit (in the area of Akçakaya), below the more massive limestones (Akçakaya shear zone) and the lower one corresponds to the contact between the Lycian units and the cover of the Menderes Massif (Gerit shear zone, Figure II-21). Strain gradients are observed approaching both shear zones with less intense finite deformation in between. Both shear zones display top-to-the-NE or top-to-the-E kinematic indicators seen at the scale of the outcrop or expressed as overturned folds especially along the basal shear zone. The superposition of NW-SE P1 folds and NE-SW P2 folds is probably due to the constrictional component of this deformation. A component of NW-SE shortening is probable.

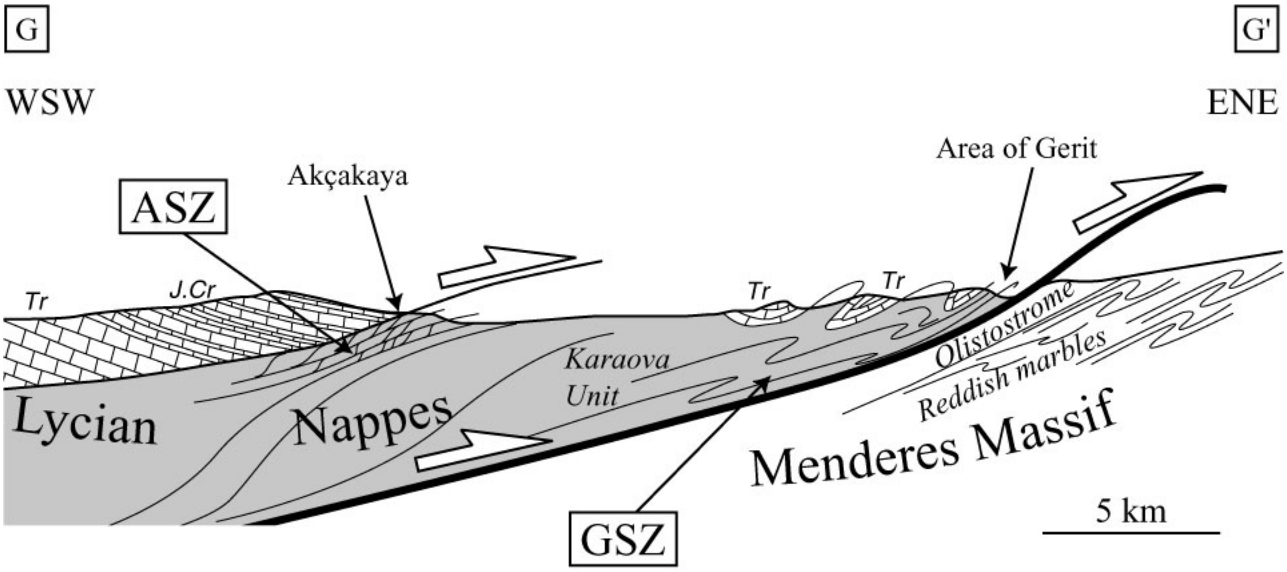

Figure II-21. Synthetic cross-section roughly parallel to the stretching observed in the Lycian Nappes (Bodrum peninsula). The two zones of strain localization are represented: (1) the "Akçakaya shear zone" (ASZ) located at the top of the metapelitic Karaova unit and (2) the "Gerit shear zone" (GSZ) corresponding to the contact between the Lycian units and the cover of the Menderes Massif. Refer to Figure II-2 for the location of the cross-section.

C. THE KLIPPEN OF LYCIAN NAPPES

1. The Milas klippen

Southeast of Milas, two small klippen of Lycian Nappes crop out on top of the Menderes metamorphic rocks (Figure II-2). The Middle Triassic-Lower Jurassic limestones and dolomites of the Lycian Nappes directly lie on the metaolistostromal formation of the Menderes Massif. The Karaova HP metamorphic formation of the Lycian Nappes does not crop out in this area. Therefore, we could not find any traces of Fe-Mg-carpholite at the base of both klippen. Below the limestones of the Lycian Nappes, the metaolistostromal unit of the Menderes Massif shows intense deformation. The foliation is sub-vertical and stretching lineations trend N090 (Figure II-12a), similar to those of Güllük, farther west. In this area, metamorphic features and particularly blue amphibole occurrences within this metaolistostrome are presented in Chapter III.

2. The Dilek-Selçuk klippen

In the Dilek peninsula region, south of Selçuk (Figure II-1), the Lycian Nappes are found as tectonic slices which are far remote parts of the Lycian Nappes relative to the Ören-Milas region (Bodrum peninsula region) (Güngör, 1998; Güngör and Erdoğan, 2001). Whereas the Karaova formation does not crop out at the base of both klippen from the Milas region, the sole of the two Dilek-Selçuk tectonic slices is marked by rare outcrops of the typical red-green phyllites of this Karaova formation (Figure II-22).

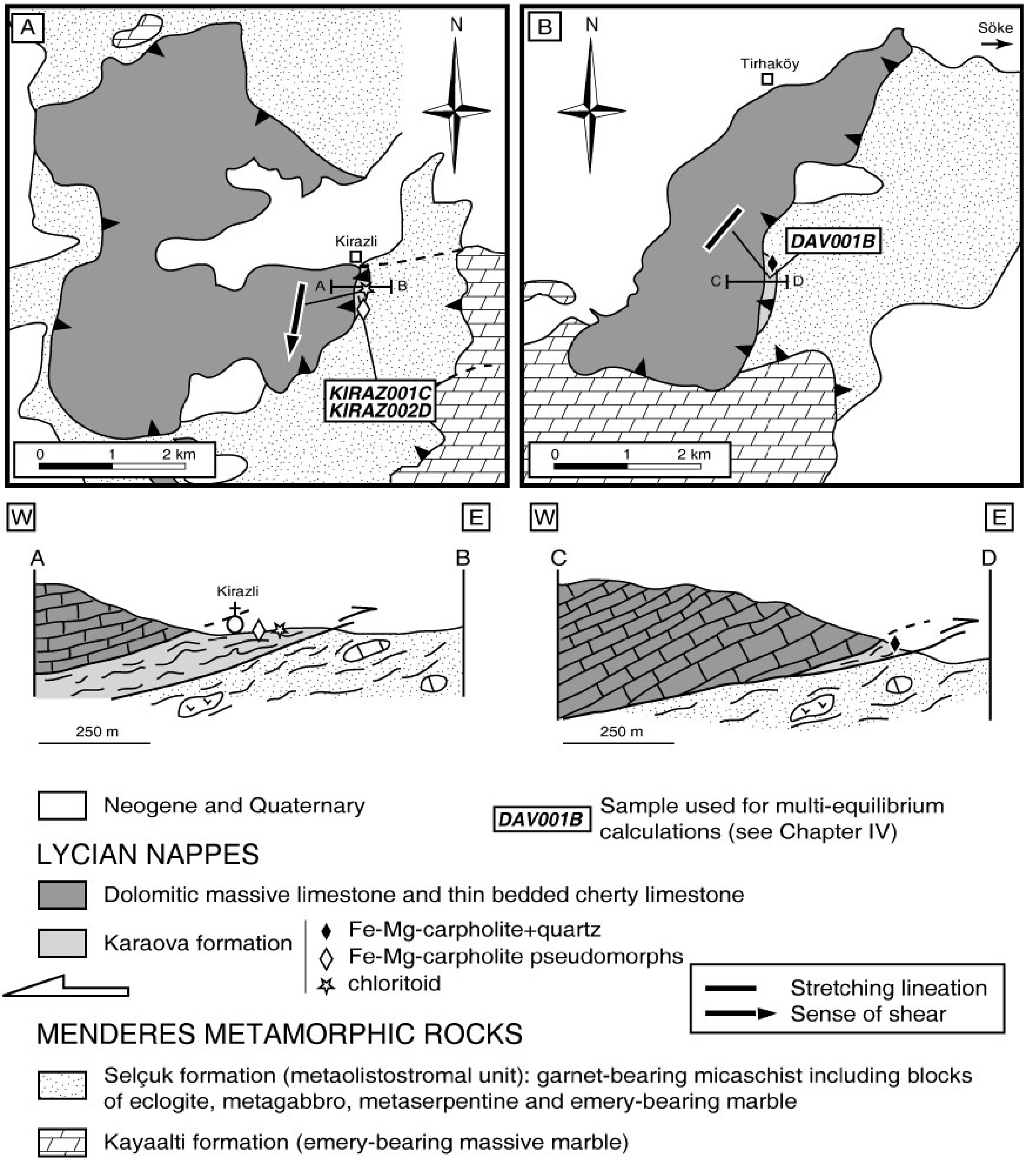

Figure II-22. Simplified geological maps of the two klippen of Lycian Nappes located in the Dilek-Selçuk region (map modified after Güngör and Erdoğan, 2001): (a) map of the northern klippe (Kirazli area) and (b) map of the southern klippe (Tirhaköy area). Location of HP relics is reported on the maps as well as on the two schematic cross sections across each HP metamorphic unit. Location of both klippen is reported in Figure II-1.

The northern klippe of Lycian metasediments is the largest one (Figure II-22a). It mainly consists of grayish and yellowish limestones and dolomites resting tectonically on top of the Selçuk metaolistostromal formation (Güngör, 1995) which is made of garnet-bearing micaschist including blocks of metaophiolitic rocks and emery-bearing massive marbles (Güngör, 1995; 1998), as well as blocks of eclogite and smaragdite-omphacite metagabbros (Candan et al., 1997; Oberhänsli et al., 1998; Çetinkaplan, 2002; Oberhänsli et al., 2002b).

The red-green phyllites of the Karaova formation are only exposed south of the Kirazli village (Figure II-22a). Pseudomorphs after Fe-Mg-carpholite have been found (Figure II-23a). They show a total retrogression of Fe-Mg-carpholite into chlorite. The foliation is made of chlorite and phengite, and small (~100 µm long) chloritoids have been recognized in thin sections (Figure II-23b). Pyrophyllite and kaolinite have also been observed in quartz segregations that contain the pseudomorphs after Fe-Mg-carpholite. The phyllites are intensively deformed. The stretching lineations trend N010 and shear senses are top-to-the-SSW. This structural feature has also been observed by Güngör and Erdoğan (2001).

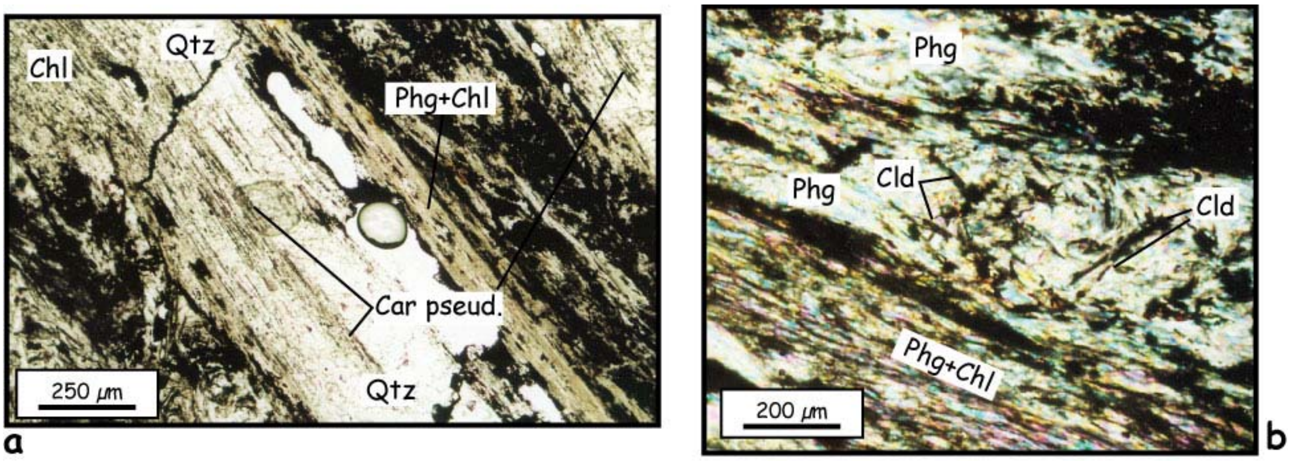

Figure II-23. Photomicrographs showing the occurrence of pseudomorphs after Fe-Mg-carpholite (a; *plane polarized light*) and chloritoid (b; *crossed polars*) within the red-green phyllites of the northern klippe of Lycian Nappes located south of Selçuk (Dilek peninsula region) (Sample KIRAZ002D). Abbreviations: Car pseud.=pseudomorph after Fe-Mg-carpholite, Cld=chloritoid, Chl=chlorite, Phg=phengite, Qtz=quartz.

The southern klippe is located east of the Dilek peninsula (southwest of Söke) (Figures II-1 and II-22b). The same lithologies of Lycian Nappes as for the northern klippe crop out in this region, south of the Tirhaköy village. The red-green phyllites of the Karaova formation are also exposed in a very small area (few hundreds square-metres), in the eastern part of the klippe (Figure II-22b). As for the Kirazli klippe, they also tectonically overlie the Selçuk formation. Centimetre-scale fibres of Fe-Mg-carpholite have been recognized within quartz segregations (Figure II-24a). At the microscopic-scale, Fe-Mg-carpholite appears as hair-like fibres in quartz (Figure II-24b) or forms assemblages with phengite and chlorite (Figure II-24c). Whereas pyrophyllite and sudoite occur in the metapelites, chloritoid has not been found in the metapelites. In this area, the foliation is sub-vertical and stretching lineations roughly trend N030.

Composition of Fe-Mg-carpholite from the Dilek-Selçuk klippen is given by X_{Mg} values ranging between 0.6 and 0.7 (Figure II-25a), very similar to that of the Ula area (eastern part of the Bodrum peninsula; refer to Figure II-6a for ternary plots). Chloritoid compositions show X_{Mg} values about 0.15 (Figure II-25b), also very similar to these from the Bodrum peninsula (refer to Figure II-6b). For both minerals, the Mn-content is also very low ($X_{Mn}<0.03$).

This similitude in the compositions of Fe-Mg-carpholite as well as chloritoid between both regions suggests roughly similar PT conditions for the HP metamorphic rocks of the Dilek-Selçuk area to these estimated for the Bodrum peninsula region.

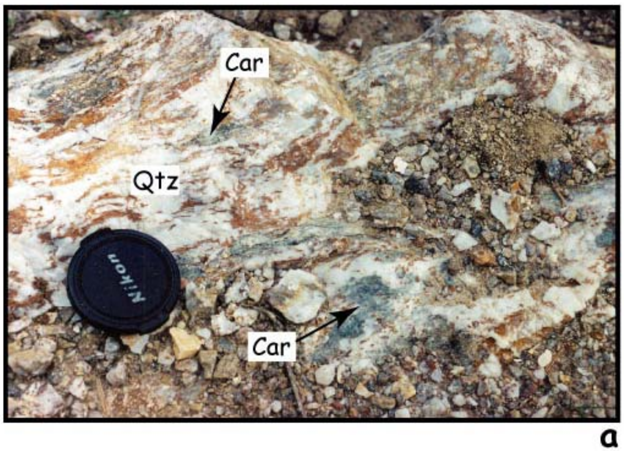

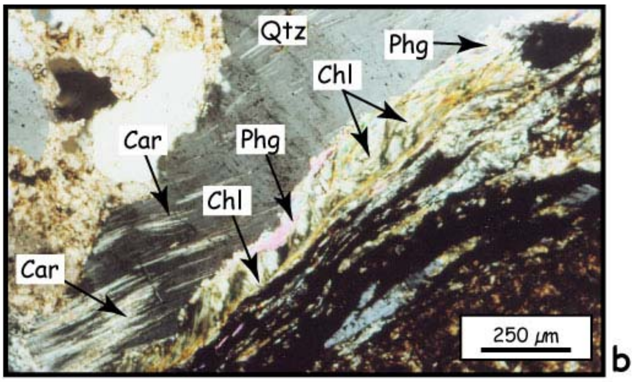

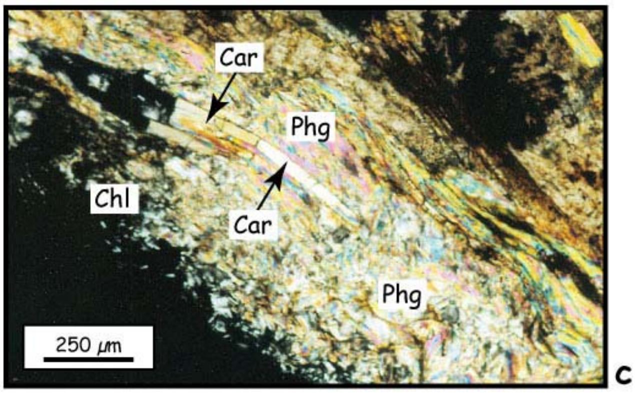

Figure II-24. (a) Fe-Mg-carpholite-bearing quartz segregation in the Karaova formation of the southern klippe of Lycian Nappes, south of Tirhaköy (Dilek peninsula region). (b) Photomicrograph showing hair-like fibres of Fe-Mg-carpholite within quartz (crossed polars). (c) Photomicrograph showing Fe-Mg-carpholite + phengite + chlorite assemblages (crossed polars). Both photomicrographs are from the sample DAV001B (location in Fig. II-22b). Abbreviations: Car = Fe-Mg-carpholite, Chl = chlorite, Phg = phengite, Qtz = quartz.

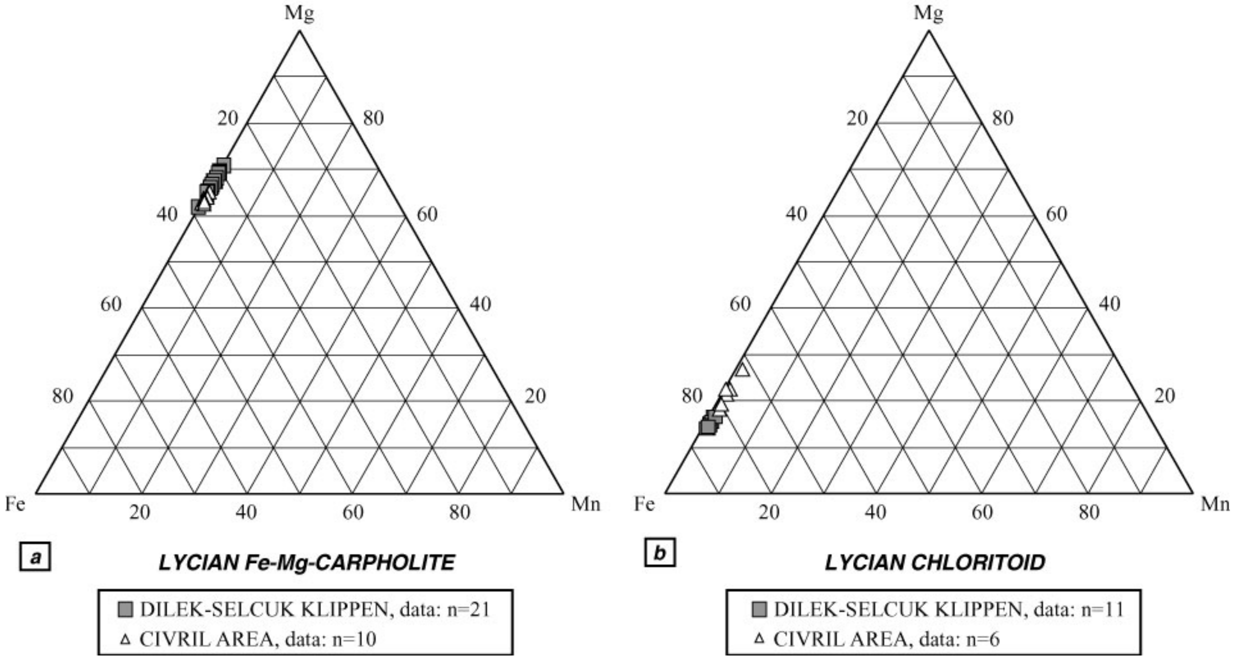

Figure II-25. Fe-Mn-Mg-ternary diagrams showing compositions of Fe-Mg-carpholite (a) and chloritoid (b) from the klippen of Lycian Nappes located in the Dilek-Selçuk region, as well as in the Çivril region.

3. The Borlu klippe

In the northern Menderes Massif, a small relic of Lycian metasediments was identified (Oberhänsli et al., 2001), northeast of the Borlu locality (see location in Figure I-24). This klippe is the northernmost known tectonic slice of Lycian Nappes. In this area, grayish-bluish schists of the Karaova formation and thin beds of Triassic limestones of the Lycian Nappes overlie thin slices of Menderes 'cover' sequences on high-grade garnet-staurolite-kyanite-bearing schists of the Menderes 'core' (Figure II-26a). Deformation in the Karaova formation is severe. Stretching lineations trend N120 and metre-scale quartz segregations as well as S-C structures in the chloritoid-bearing schists attest for top-to-the-ESE shearing deformation (Figure II-26b). Fe-Mg-carpholite has been recognized as hair-like fibres in the quartz segregations (Figure II-26c).

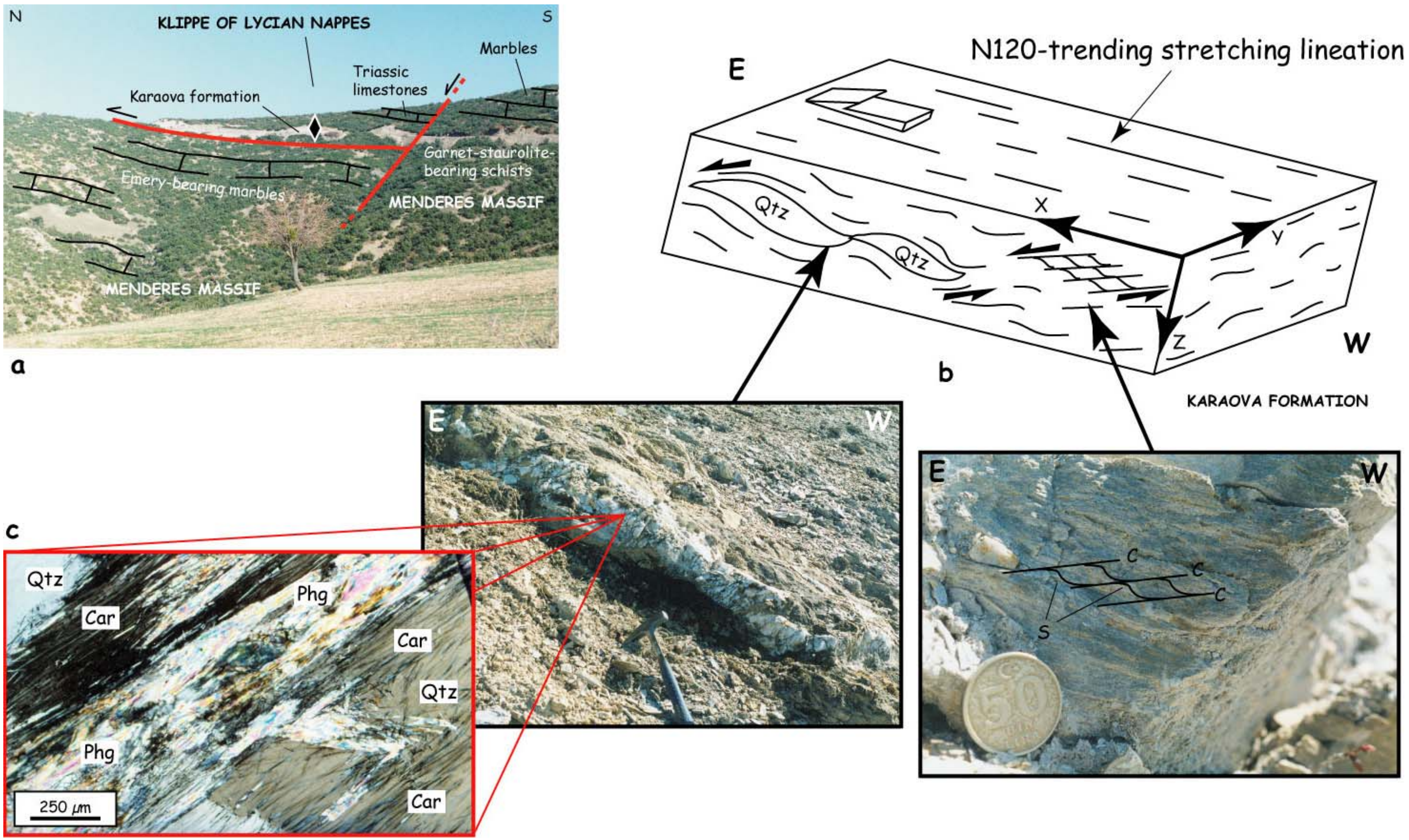

Figure II-26. (a) Panorama showing the klippe of Borlu (northern Menderes Massif). (b) Scheme showing the characteristics of the deformation in the Karaova metapelites. (c) Photomicrograph showing hair-like fibres of Fe-Mg-carpholite within quartz (crossed polars, sample BORLU001B).

4. The Çivril area

In the eastern part of the Menderes Massif, in the region of Çivril (map of Figure II-27), the Lycian Nappes s.s. and a small klippe of Lycian metasediments crop out (Figure I-24 for location of Çivril). In this area, the Lycian Nappes are composed of the Karaova formation and the overlying Jurassic to Cretaceous limestones. They tectonically overlie the uppermost metasedimentary sequence of the Menderes Massif.

Southwest of Çivril, near Gömce, a small slice of Lycian Nappes overlies the thick Jurassic to Cretaceous marbles, as well as the typical Upper Cretaceous reddish marbles of the Menderes Massif (Figure II-27, cross section AB). The basal Karaova formation contains HP-LT assemblages such as Fe-Mg-carpholite+quartz. Fe-Mg-carpholite was also found in calcite crystals (Figure II-28a). The latter show in various parts some square sections, tabular and needle-like shapes, suggesting occurrence of aragonite in relict which has not been found elsewhere in the Karaova metasediments. However, up to now, no quantitative analysis could be performed on these crystals. This observation of probable aragonite within the Karaova formation therefore needs further studies. Chloritoid occurs abundantly within the schists of the Karaova formation (Figure II-28b).

South of the small Lycian slice, an underlying metaolistostrome of the Menderes Massif crops out. As on the Bodrum peninsula, it comprises blocks of cherty marbles and metavolcanics lenses surrounded by a schist matrix in which blue and green amphiboles occur (detailed in Chapter III). The whole formation is highly deformed. Stretching lineations trend N020-N030 and S-C structures show top-to-the-north sense of shear (Figure II-27, cross section CD). This metaolistostromal unit unconformably overlies the Upper Cretaceous reddish marbles which show eastward overturned folds. These folded structures, roughly trending N-S, were observed at the kilometre-scale (Figure II-27, cross section AB), as well as at the metre-scale (Figure II-27, cross section CD; and Figure II-28c). Southwest of the Çivril region, similar kilometre-scale eastward overturned folds have been described by Okay (1989b) who interpreted them as a Late Eocene-Oligocene deformation, post-nappe emplacement.

Northeast of Çivril, Fe-Mg-carpholite and chloritoid also occur near the Akdağ and Işıklı villages (map of Figure II-27). West of Işıklı, shearing deformation indicate movements towards the NNE whereas between Işıklı and Akdağ, the Fe-Mg-carpholite-chloritoid-bearing rocks from the Karaova formation display intense deformation characterized NW-SE-trending stretching lineations and top-to-the-NW sense of shear (Figures II-27 and II-28d,e). Chloritoid widely occur in the foliation and Fe-Mg-carpholite is nearly completely retrogressed into chloritoid+quartz (Figure II-28f). The significance of the NW-SE-trending stretching and displacements towards the NW in this area can be questioned regarding the role of surrounding active faults which could have tilted the different blocks (Figure II-29).

Farther south, in the northwest of Çal (not on map Figure II-27; see location in Figure I-24), similar HP assemblages have been found in the Karaova formation. Fe-Mg-carpholite relics occur in quartz segregations within the chloritoid-bearing schists, and Fe-Mg-carpholite is commonly retrogressed into chlorite and pyrophyllite.

Chemical compositions of Fe-Mg-carpholite ($X_{Mg} \sim 0.65$) and chloritoid ($X_{Mg} \sim 0.2$) from the Çivril region are in the same ranges as these from the Dilek-Selçuk klippen (Figure II-25), thus suggesting roughly similar PT conditions.

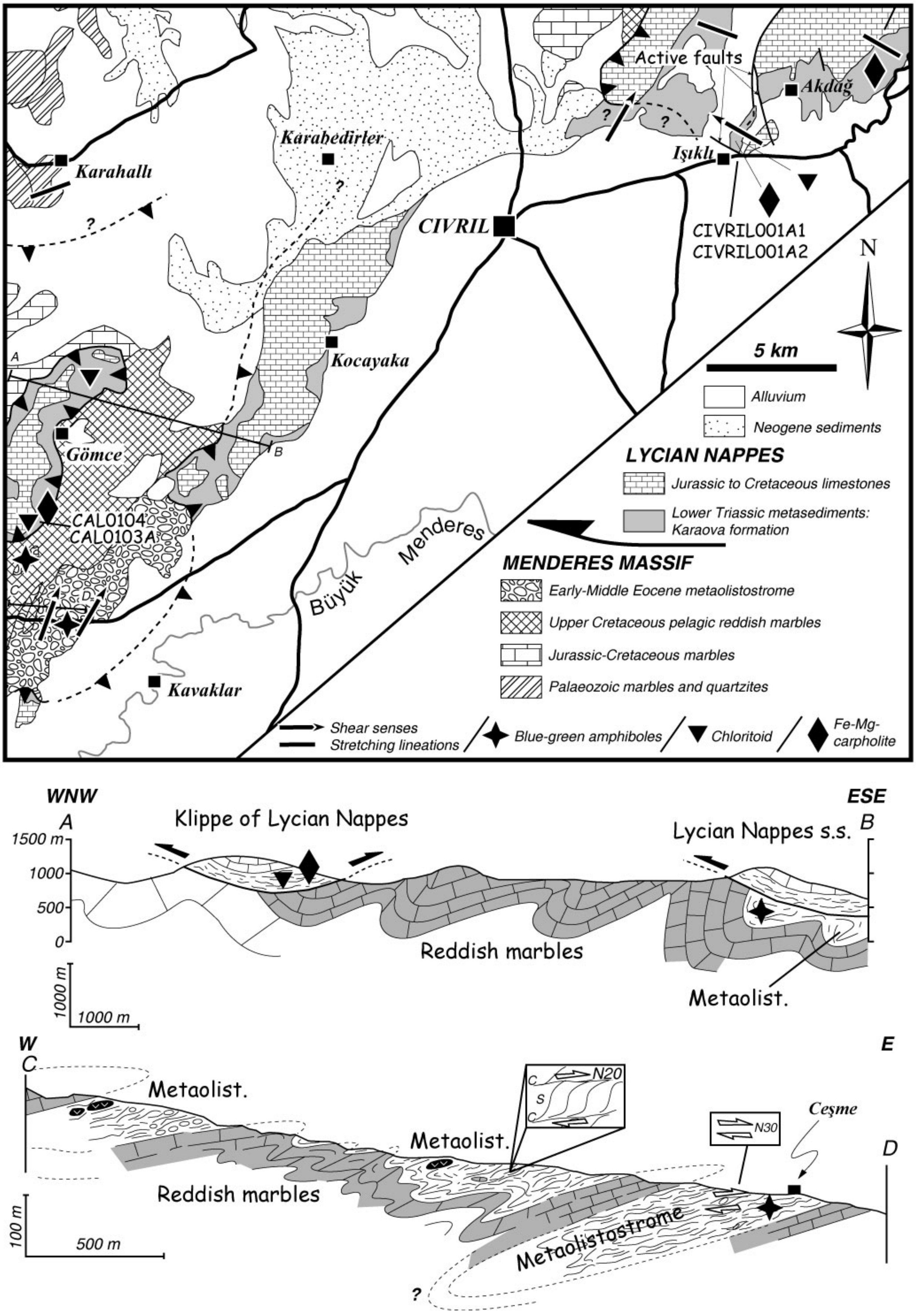

Figure II-27. Above: simplified geological map of the Çivril region (modified after Konak, 1993; and Özer et al., 2001) showing distribution of metamorphic minerals and deformation features. Below: cross sections showing the main structures in the southwestern part of the map (location of cross sections AB and CD are reported on the map). Refer to Figure I-24 for location of the Çivril area.

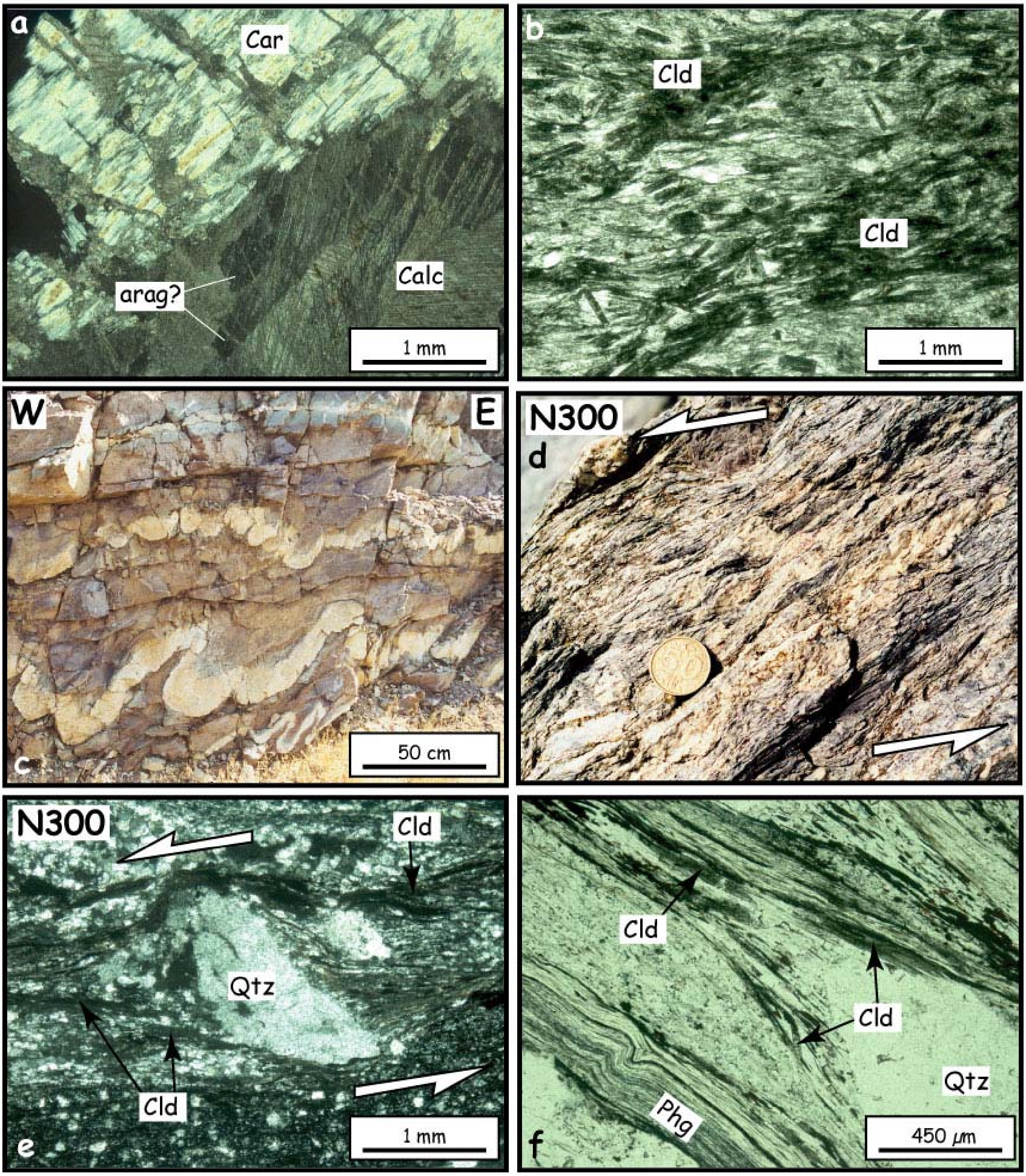

Figure II-28. (a) Photomicrograph showing Fe-Mg-carpholite occurrence within calcite crystals, and probable relics of aragonite in the Karaova metasediments of the small klippe of Lycian nappes (south of Gömce, sample CAL0104, crossed polars); (b) Photomicrograph showing chloritoid occurrence in the Karaova formation (south of Gömce, sample CAL0103A, plane polarized light); (c) Eastward overturned folds in the Upper Cretaceous reddish marbles of the Menderes Massif; (d) S-C structures in the Karaova formation showing top-to-the-NW displacements (north of Işıklı); (e) Photomicrograph of an asymmetric quartz crystal and chloritoid-bearing pressure-shadows showing top-to-the-NW sense of shear (north of Işıklı, sample CIVRIL001A2, crossed polars); (f) Photomicrograph of chloritoid coming from the breakdown of Fe-Mg-carpholite (north of Işıklı, sample CIVRIL001A1, plane polarized light). ***N.B.1: photos (d), (e) and (f) were taken from samples collected at the outcrop shown in Figure II-29. N.B.2: for photos (e) and (f), thin sections are prepared from oriented samples where sections are cut parallel to the lineation and perpendicular to the foliation. N.B.3: Localization of samples is reported in Figure II-27.***

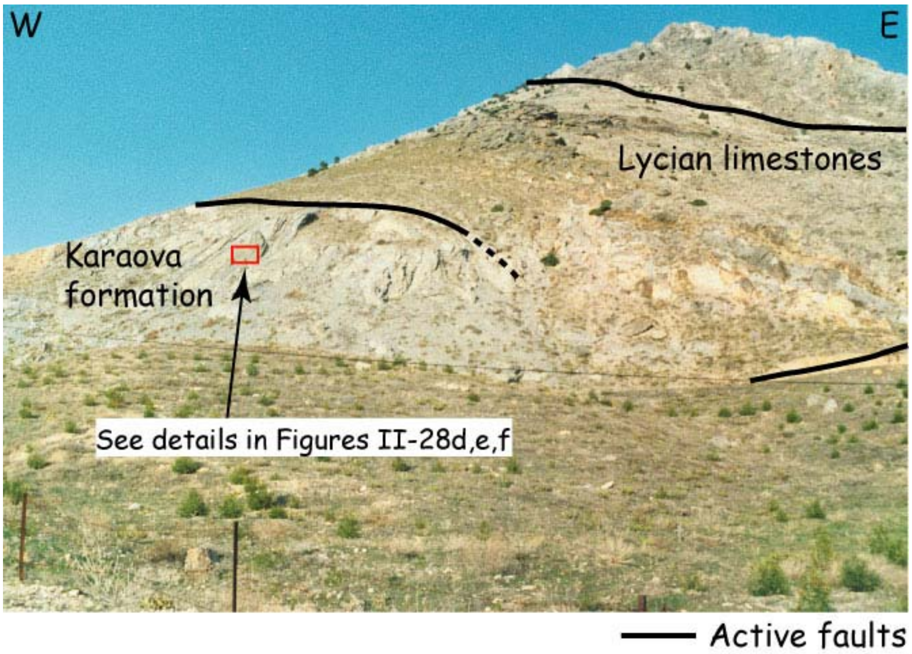

Figure II-29. Panorama showing outcrops of the Fe-Mg-carpholite-chloritoid-bearing Karaova metasediments surrounded by active faults, north of Işıklı (NE of Çivril). Refer to Figure II-27 for location of Işıklı.

D. THE KARABÖĞÜRTLEN REGION (EAST OF THE BODRUM PENINSULA)

In the easternmost parts of the Bodrum peninsula (east of Karaböğürtlen), the extensive Lycian peridotite overlies the metasediments of the Lycian Thrust Sheets (Figure II-30). Collins and Robertson (1997; 1998; 1999; 2003) recently published tectono-stratigraphic data in this region and conclude that the Lycian Nappes (Lycian Thrust Sheets, Lycian Mélange and Lycian Peridotite) were emplaced onto the continental Menderes Massif in stages from latest Cretaceous-Miocene time. They reported structural kinematic evidence, mainly for the Lycian Mélange and Lycian Peridotite Thrust Sheet with its metamorphic sole. All the kinematic fabrics within the main units and especially along major thrust contacts exhibit top-to-the-SE non-coaxial flow, which suggests that the Lycian allochthon was emplaced and successively transported from northwest to southeast (Figure II-31).

Whereas the Late Cretaceous Karaböğürtlen wildflysch that forms the uppermost levels of the Lycian Thrust Sheets appears unmetamorphosed on the Bodrum peninsula, it shows evidence of metamorphic assemblages in the Karaböğürtlen region, below the peridotite nappe (Figure II-30). Sporadic blocks within the wildflysch formation have indeed been described as containing blue amphiboles considered as glaucophane (Kaaden and Metz, 1954; Kaaden, 1966).

During our investigations in this region, Fe-Mg-carpholite was found in quartz segregations within chloritoid-bearing metapelites of the Karaova formation that crops out in the north of the Karaböğürtlen area (SW of the Yemişendere locality; see Figure II-30 for location), which therefore documents another occurrence of HP rocks in the basal sediments of the Lycian Nappes along the contact with the Menderes Massif.

Northeast of Karaböğürtlen, a series of samples were collected in the wildflysch and overlying metamorphic sole of the peridotite nappe which indeed revealed a widespread occurrence of green and blue amphiboles involved in various assemblages (Figure II-30, below the map), and with various chemical compositions (mainly Ca- and Na-amphiboles; Figure II-32).

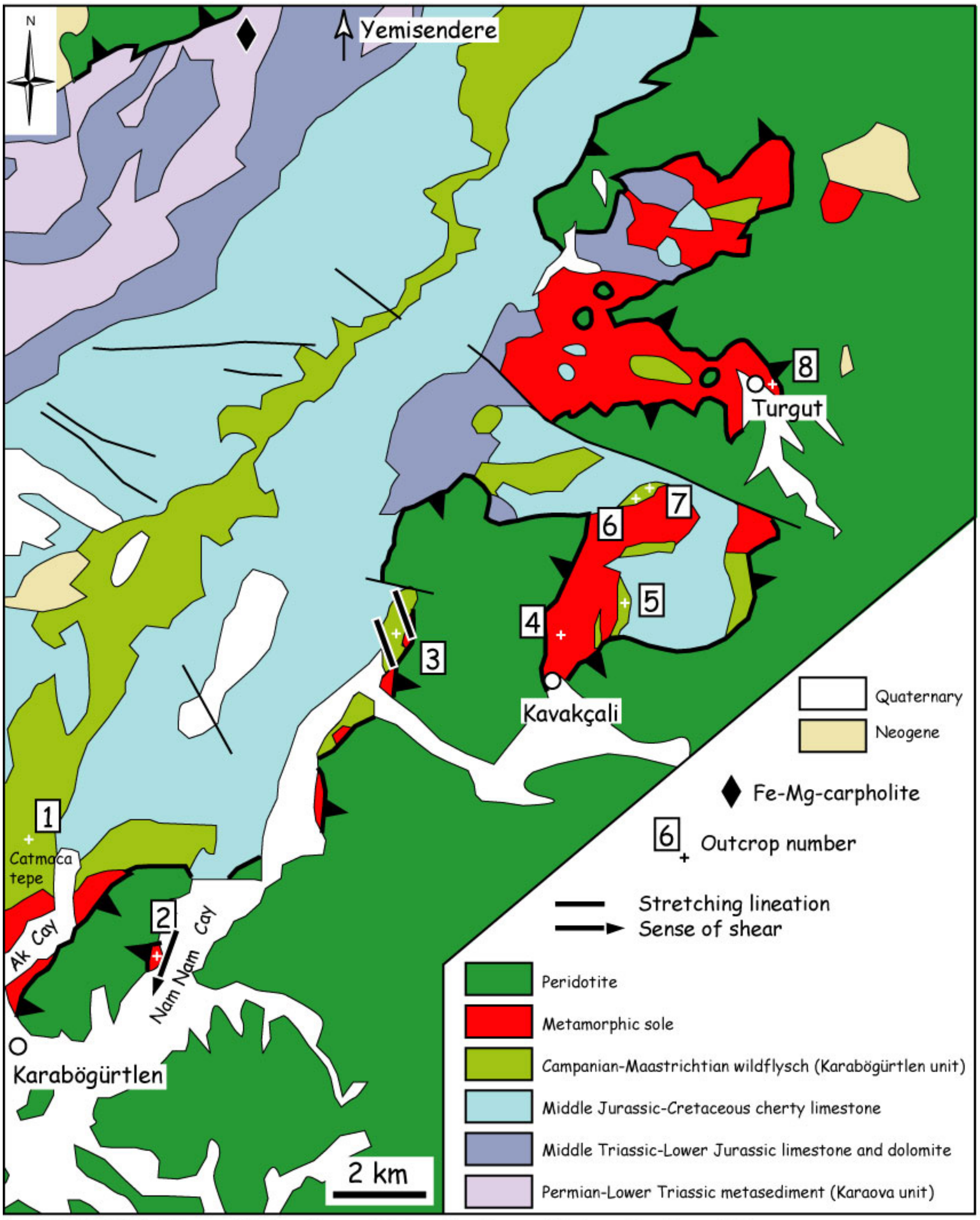

1. KARA-002A4: Na-amphibole + Ca-amphibole + Na-Ca-amphibole + chlorite + albite
   KARA-002B2: muscovite + chlorite + albite
   KARA-002C: Na-amphibole (crossite) + Ca-amphibole + sphene + quartz
   KARA-002D2: Ca-amphibole + epidote + chlorite
2. KARAB-0101B: Ca-amphibole + epidote + chlorite
   KARAB-0102B: Ca-amphibole + epidote + sphene + quartz
   KARAB-0104: garnet + Ca-amphibole + Na-Ca-amphibole + muscovite + chlorite + quartz
4. KARAB-0114A: garnet + epidote + muscovite + biotite + chlorite
5. KARAB-0115C: Ca-amphibole + sphene + albite
6. KARAB-0116B: Ca-amphibole + epidote
   KARAB-0117A: Ca-amphibole + Na-Ca-amphibole + sphene + albite
   KARAB-0117D: garnet + Ca-amphibole + epidote + chlorite + sphene + albite
7. KARAB-0118: garnet + Ca-amphibole + biotite
   KARAB-0120B: Na-amphibole + Ca-amphibole + Na-Ca-amphibole
   KARAB-0121C: garnet + muscovite + biotite + albite + quartz
8. KARAB-0122A: Ca-amphibole + sphene

Figure II-30. Map of the Karaböğürtlen region (modified after de Graciansky, 1972; and M.T.A. unpublished maps, after Konak and Akdeniz) showing location of samples collected in the Karaböğürtlen wildflysch and overlying metamorphic sole of the peridotite nappe. The metamorphic assemblages in the different samples are reported below the map. Refer to Figures II-1 or II-31 for location of the map in SW Turkey.

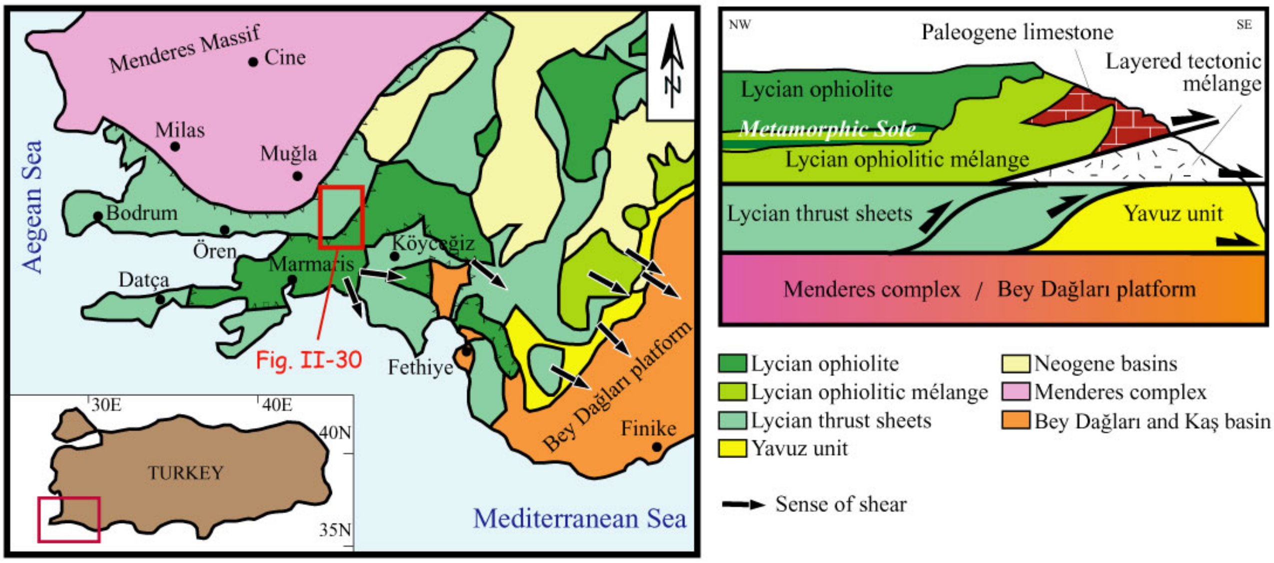

Figure II-31. Left: tectono-stratigraphic map of the Lycian Taurus with location in Turkey. Black arrows show nappe transport directions (after Collins and Robertson, 2003). Right: Rock-relations diagram for major tectonic units within the Lycian Taurus (after Collins and Robertson, 1997; 1998).

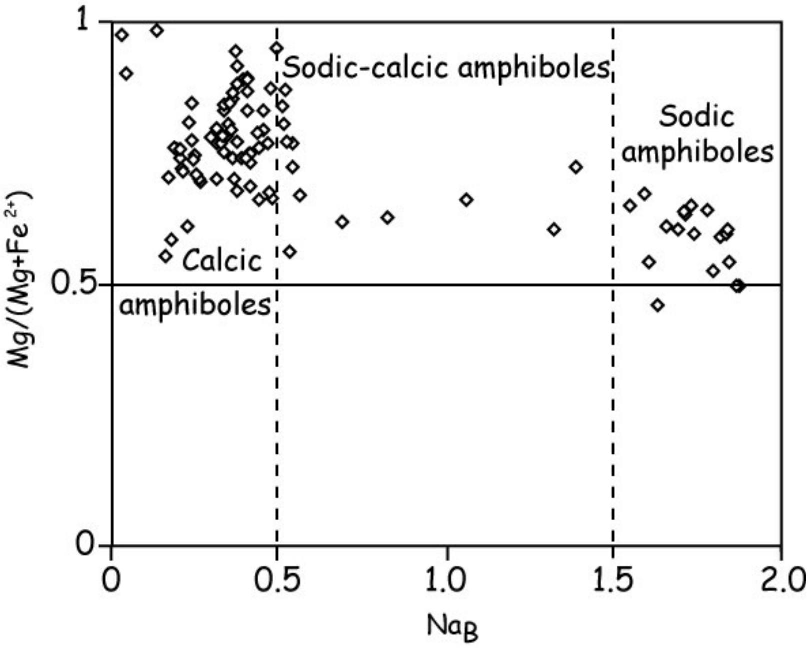

Figure II-32. Composition of amphiboles from the Karaböğürtlen region (wildflysch and metamorphic sole of the peridotite nappe); classification following Leake (1978); Structural formulae of amphibole were calculated on the basis of 23 O; number of data=94.

North of Karaböğürtlen, near Çatmaca Tepe (outcrop 1, see Figure II-30 for location), sporadic metabasite and metaquartzite blocks within the wildflysch were sampled (Figure II-33). Four samples widely contain amphiboles which can be classified (following Leake, 1978 and Leake et al., 1997) as sodic-amphiboles ("crossite" and Mg-riebeckite) and calcic-amphiboles (tschermakite, Mg-hornblende and actinolite), with a few intermediate sodic-calcic compositions (winchite and barroisite) (Figures II-34 and II-35). The samples mainly contain green amphiboles (calcic composition), which are often associated with epidote, chlorite, albite and quartz (Figure II-30), thus documenting greenschist-facies conditions. In very few parts of the thin sections, blue-amphiboles occur as relict, with compositions varying between "crossite" and Mg-riebeckite. Glaucophane compositions have not been observed in any sample. Calculation of activity of crossitic sodic-amphiboles in relict (retrogressed into albite, chlorite and green amphibole, Figure II-33) suggests minimum pressures of 6-8 kbar (group 6 of Evans, 1990), and transition between epidote-blueschist-facies and greenschist-facies is observed in this area (Figure II-36).

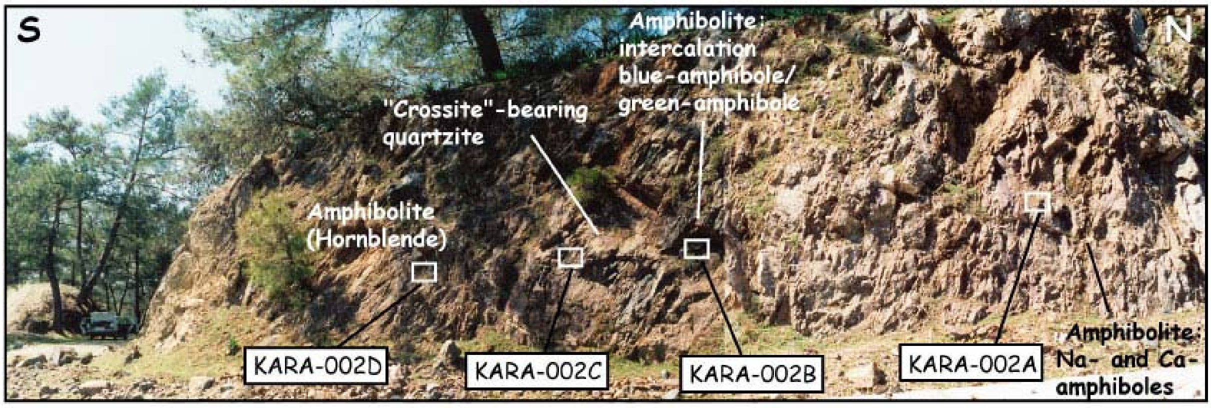

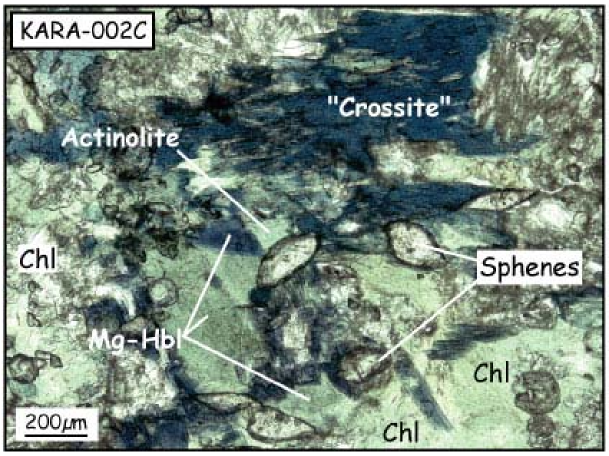

Figure II-33. Above: amphibolite blocks within the Karaböğürtlen wildflysch (Çatmaca Tepe, north of Karaböğürtlen).
Left: photomicrograph of Sample KARA-002C showing a Na-amphibole ("crossite")-Ca-amphibole (tremolite and Mg-hornblende)-chlorite assemblage (plane polarized light). Blue amphibole is retrogressed into green amphibole and chlorite.

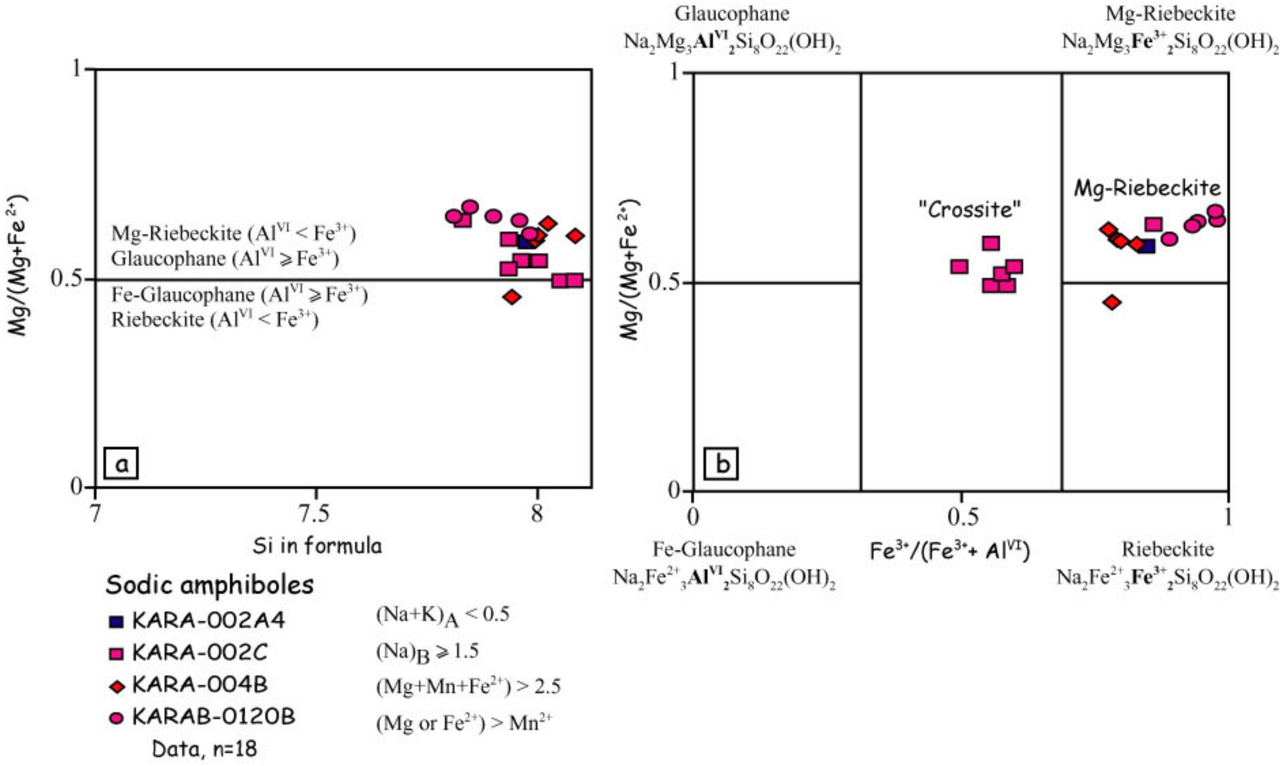

Figure II-34. Si versus X_{Mg} (a) and X_{Fe3+} versus X_{Mg} (b) compositional diagrams (after Leake et al., 1997; the term "crossite" is here not abolished) of sodic-amphiboles from the Karaböğürtlen region (wildflysch and metamorphic sole of the peridotite nappe). Note the "crossitic" composition of amphiboles from Sample KARA-002C. Location of samples is reported on the map Figure II-30.

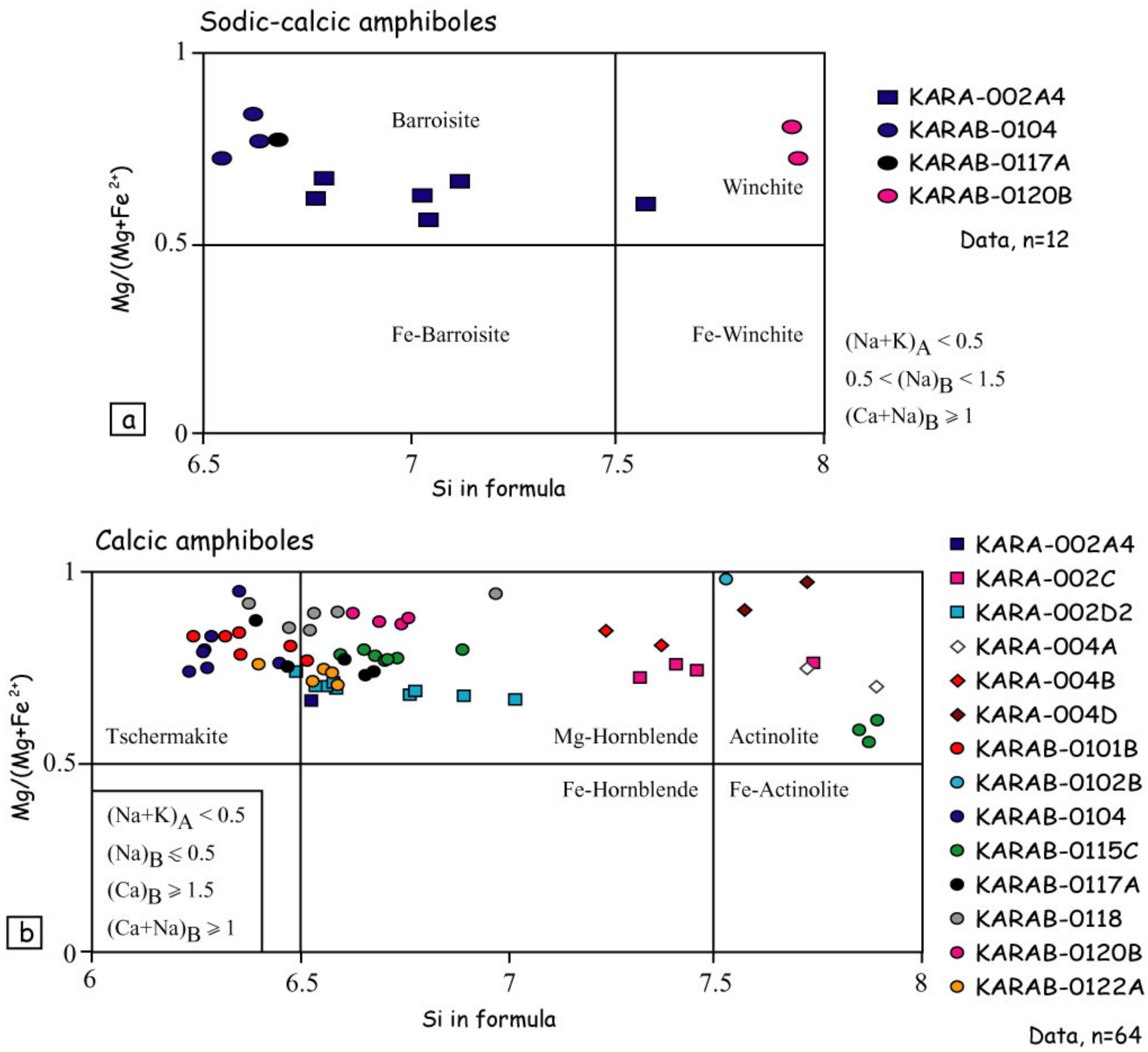

Figure II-35. Si versus X_{Mg} compositional diagrams (after Leake et al., 1997) for sodic-calcic-amphiboles (a) and calcic-amphibole (b) from the Karaböğürtlen wildflysch and the metamorphic sole of the peridotite nappe (area of Karaböğürtlen). Location of samples is reported on the map Figure II-30.

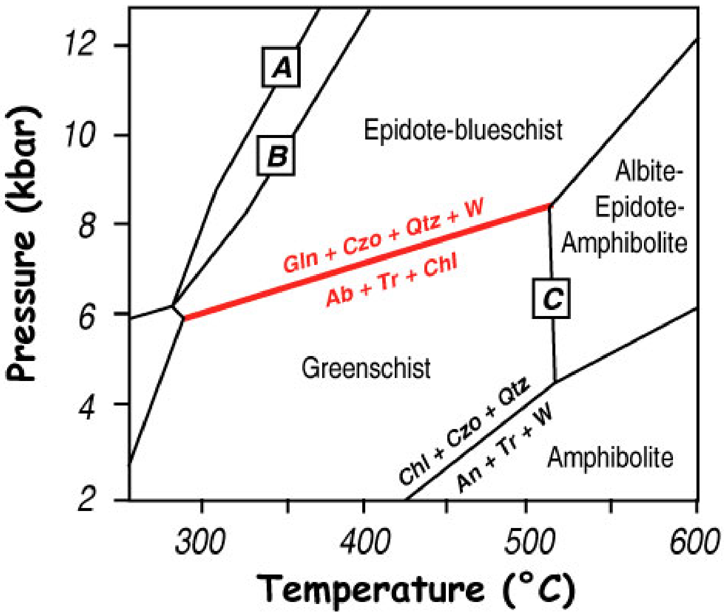

Figure II-36. PT diagram showing transition of epidote-blueschist-facies to greenschist-facies deduced from composition of crossitic sodic-amphiboles (after Evans, 1990) in Sample KARA-002C from a quartzite block occurring in the Karaböğürtlen wildflysch, Çatmaca Tepe.

Northeast of Karaböğürtlen (Nam Nam Çay valley; outcrop 2), the metamorphic sole of the peridotite nappe crops out (Figure II-30). It is made of mafic rocks (basalts and gabbros), carbonate-basalt intercalations grading to quartzites and radiolarites. Mafic rocks mainly contain calcic-amphibole-chlorite-epidote assemblages; radiolarites are characterized by tremolite-epidote-sphene-quartz assemblages (Figure II-37a) and banded quartzite show Ca-amphibole-garnet-chlorite-muscovite-quartz assemblages (Figure II-37b). Garnet is commonly found with an atoll-like structure (Figure II-37b) documenting two generations of growth, or as smaller crystals of second generation.

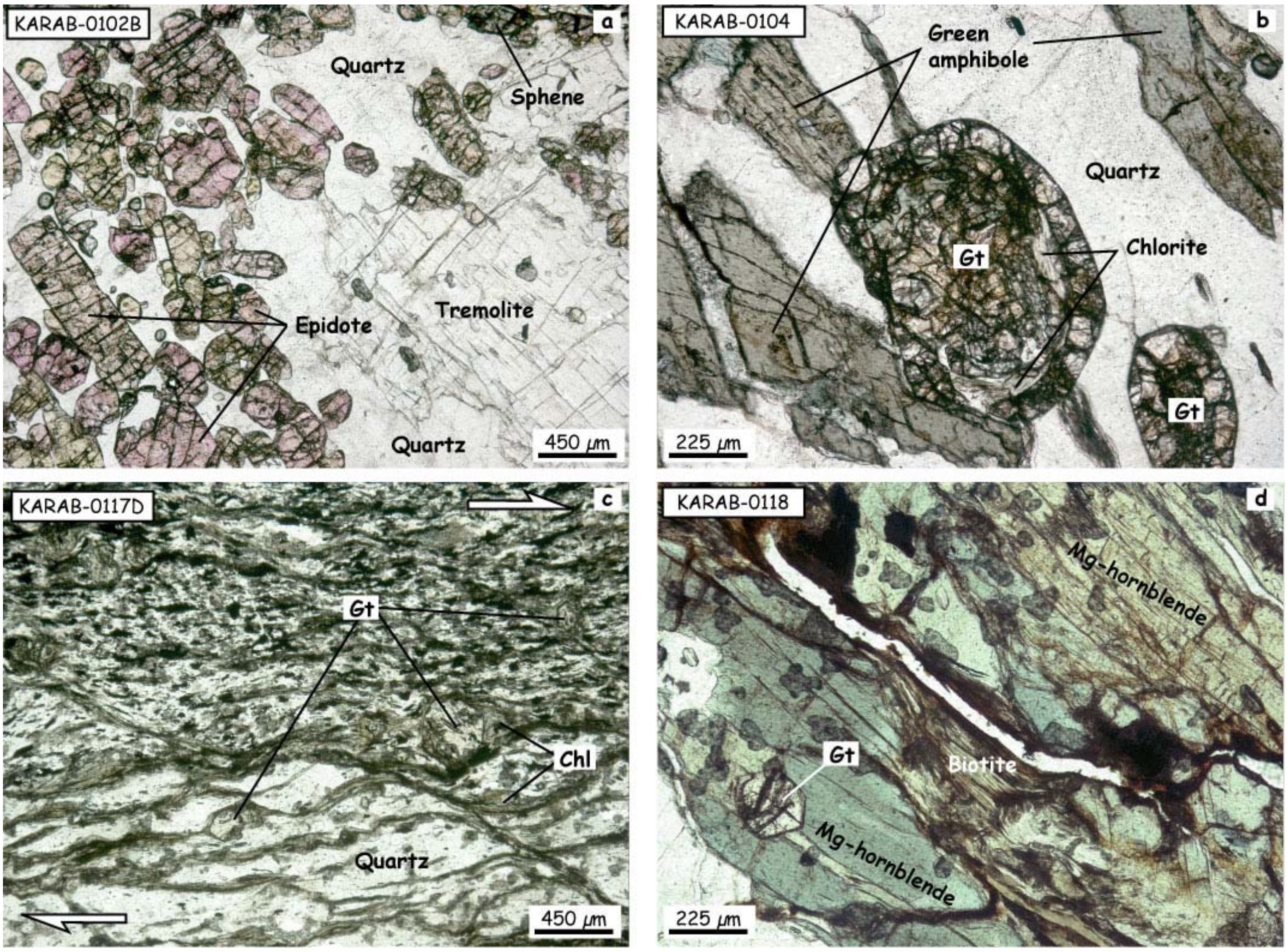

Figure II-37. (a) Photomicrograph of tremolite-epidote-sphene-quartz assemblage-bearing radiolarite from the metamorphic sole of the Lycian peridotite nappe (outcrop 2; Nam Nam Çay valley, NE of Karaböğürtlen); (b) Photomicrograph of Ca-amphibole-garnet-chlorite-quartz assemblage-bearing banded quartzite within the metamorphic sole (outcrop 2; Nam Nam Çay valley). Note the atoll-like structure of garnet documenting two generations of growth; (c) Photomicrograph showing shearing in the matrix of the wildflysch (outcrop 6; north of Kavakçali); (d) Photomicrograph of a Ca-amphibole-garnet-biotite assemblage in the matrix of the Karaböğürtlen wildflysch (outcrop 7; north of Kavakçali). The four photomicrographs were taken with plane polarized light.

Composition of garnet trends between the spessartine and almandine end-members (Figure II-38). Garnets of second generation have similar composition to the external part of the atoll-structure garnets, the internal part of the atolls being Mn-richer. Compositions of Ca-amphiboles (tschermakite) and Ca-Na-amphiboles forming assemblages with the garnets of second generation are reported in Figure II-35. Deformation in the metamorphic sole is intense. Folds and sigmoid structures indicate displacements towards the SSW (Figure II-39). Further north, in the Karaböğürtlen wildflysch (outcrop 3), stretching trends N160 as indicated by deformed pebbles (Figure II-30).

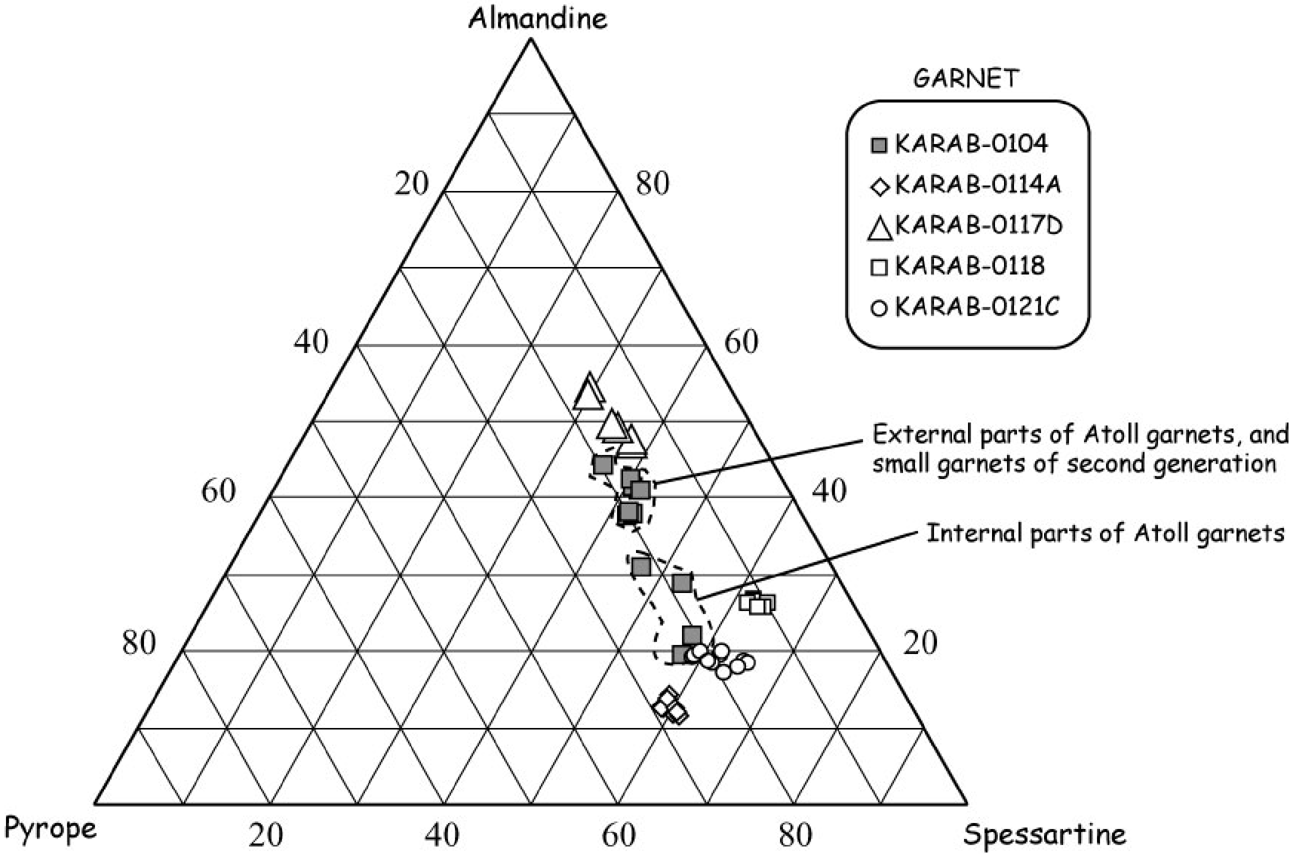

Figure II-38. Almandine-pyrope-spessartine ternary diagram showing composition of garnets from the Karaböğürtlen wildflysch and the metamorphic sole (Karaböğürtlen region).

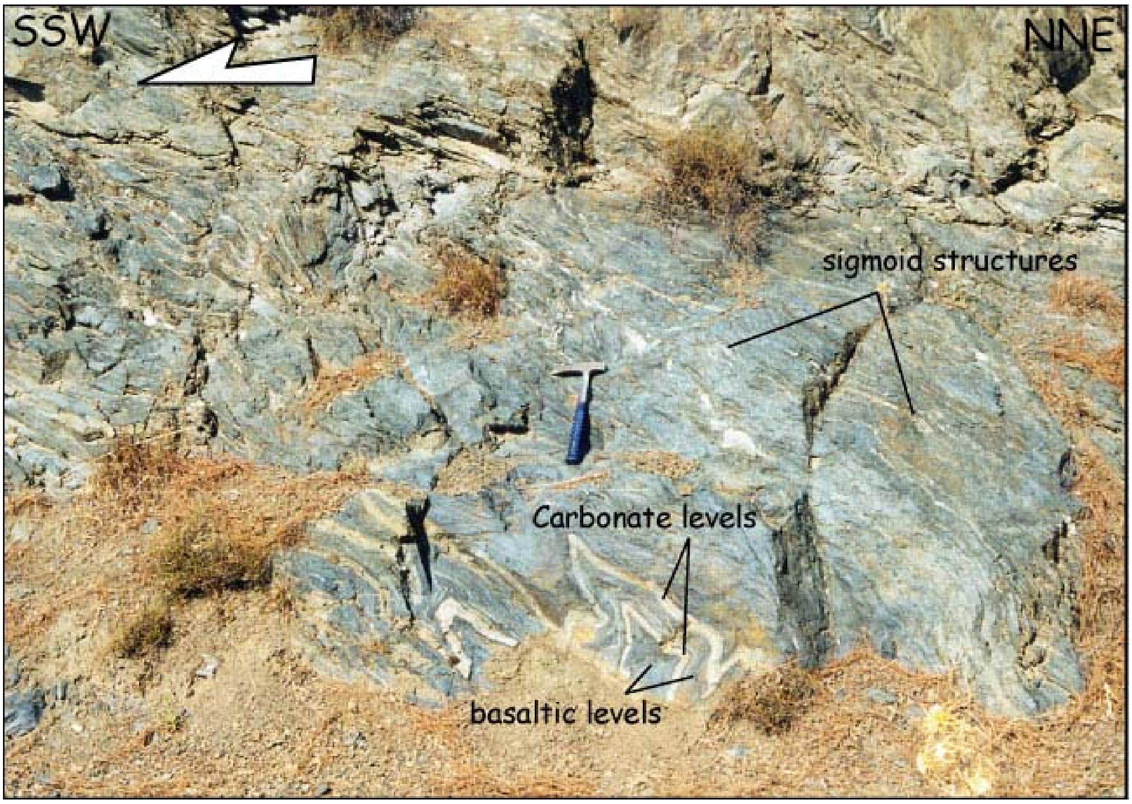

Figure II-39. Folded carbonate-basalt intercalations and sigmoid-structures indicating movements towards the SSW (metamorphic sole; Nam Nam Çay valley, NE of Karaböğürtlen).

At the north of Kavakçali (Figure II-30 for location), similar amphibolite-facies assemblages were recognized within the metamorphic sole, just below the ophiolitic nappe (outcrop 4). Garnet has a composition of about 60% spessartine (Figure II-38). Further NE, approaching the locality of Turgut, amphibolite-facies assemblages have been observed not only in blocks of the Karaböğürtlen wildflysch, but also in its schist matrix (outcrops 5-6-7, see Figure II-30), which clearly differs from that located on the Bodrum peninsula. Mafic blocs contain essentially calcic-amphiboles and epidote and the very deformed matrix is made of Ca-amphibole, epidote, garnet, biotite, muscovite, chlorite, albite, and sphene (Figures II-37c,d and II-40a,b). Garnet compositions cluster between Almandine and spessartine (Figure II-38) and Ca-amphiboles are mainly tschermakite and Mg-hornblende (Figure II-35b). In one sample (KARAB-0120B), relics of Na-amphibole have been recognized and show Mg-riebeckite compositions (Figures II-40c and II-34). The sodic-amphiboles do not show any “crossite” or glaucophane composition. The metamorphic sole that crops out at the locality of Turgut (outcrop 8, Figure II-30) shows widespread occurrences of tschermakite and Mg-hornblende (Figure II-35b).

Finally, in the southwest of the Karaböğürtlen village (outside of the map Figure II-30), the Karaböğürtlen wildflysch contains some mafic blocks which have been described as glaucophane-bearing blocks, although no quantitative analyses have been performed (Kaaden and Metz, 1954) (Çetibeliköy locality, see location on Figure II-1). These sporadic blocks were sampled and microprobe analyses revealed only relics of Mg-riebeckite sodic-amphiboles (Sample KARA004B; Figures II-40d and II-34) in Ca-amphibole-chlorite-diopside assemblages; calcic-amphiboles have a composition trending between Mg-hornblende and actinolite (Samples KARA-004A, B, and D; Figure II-35b).

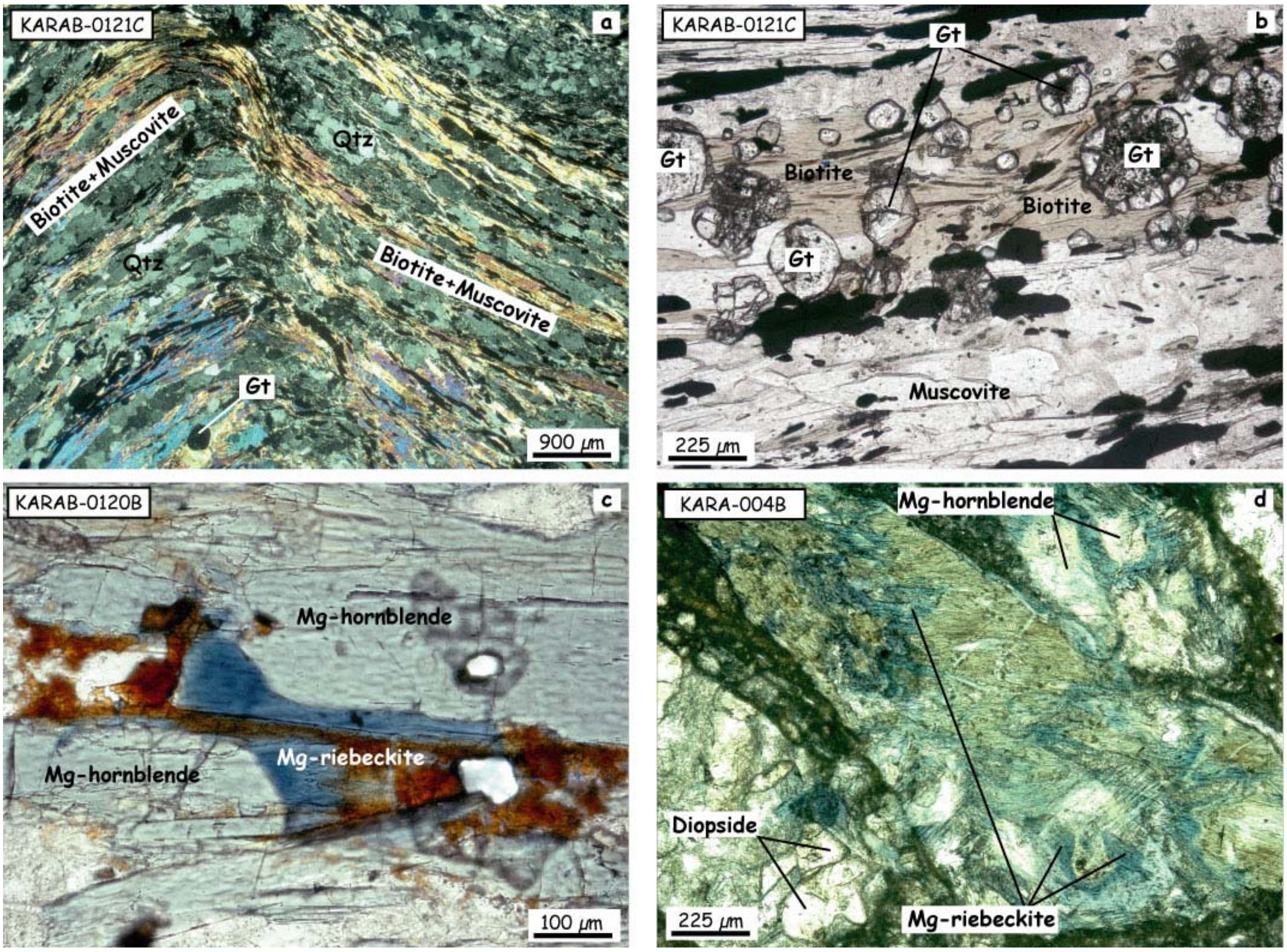

Figure II-40. (a) Photomicrograph of the deformed matrix of the Karaböğürtlen wildflysch, which contains garnet-muscovite-biotite-albite-quartz assemblages (outcrop 7, NE of Kavakçali) [crossed polars]; (b) Photomicrograph of the spessartine garnets within the muscovite+biotite foliation of the Karaböğürtlen wildflysch (outcrop 7, NE of Kavakçali) [plane polarized light]; (c) Photomicrograph showing Mg-riebeckite in relict within crystals of Mg-hornblende from the matrix of the Karaböğürtlen wildflysch (outcrop 7, NE of Kavakçali) [plane polarized light]; (d) Photomicrograph showing relics of Mg-riebeckite in a mafic block that occurs in the Karaböğürtlen wildflysch (Çetibeliköy, SW of Karaböğürtlen) [plane polarized light].

E. DISCUSSION AND CONCLUSIONS

1. Evidence for HP metamorphism

Fe-Mg-carpholite assemblages are widespread in the metasediments of the Karaova formation forming the base of the Lycian Nappes, which widely crop out south of the Menderes crystalline massif. They have been found in the Lycian Nappes s.s. continuously from the Bodrum peninsula region to the region of Çivril along the contact with the Menderes Massif, as well as in klippen of Lycian Nappes located at the top of the Menderes Massif (Dilek-Selçuk region in the west, Borlu area in the north, and Çivril area in the east) (Figure II-41a). Fe-Mg-carpholite-bearing rocks therefore occur over a distance of more than 200 km in the N-S and E-W directions, depicting an extensive metamorphic belt.

Chemical compositions of the metamorphic index minerals are roughly homogeneous over the whole region and point to a HP-LT metamorphism with minimum pressures around 8 kbar and maximum temperatures around 400°C, suggesting an important burial of about 30 km.

The distribution of Fe-Mg-carpholite and its breakdown products throughout the Bodrum peninsula reveals various retrograde metamorphic histories (HP cooling paths versus isothermal decompression patterns) after a probable common HP-LT metamorphic peak.

The rosetta limestones being part of the thick carbonate series that overlie the HP-LT Karaova unit, probably underwent PT conditions allowing growth of aragonite before its total retrogression into calcite. This suggests that high-pressure conditions affected the whole Lycian Thrust Sheets.

2. Deformation related to HP metamorphism

On the Bodrum peninsula, I report here the first field observations on major shear zones which were active during exhumation of the newly reported widespread HP-LT rocks in the Lycian Nappes. Structural data allow to characterize top-to-the-NE to top-to-the-E senses of shear along two major shear zones, one above the metapelitic Karaova sequence near Akçakaya, and one along the contact with the Menderes Massif (Figure II-41b). NE- and ENE-trending stretching is observed throughout the area and is more pronounced within the two shear zones. A component of constriction is shown by fold axes parallel to the stretching. In the Çivril region, similar top-to-the-NE senses of shear are observed in the uppermost metaolistostromal unit of the Menderes Massif and in the Karaova formation (Figure II-41b). In this area, we also observed top-to-the-NW senses of shear, although the significance of these directions can be questioned considering the presence of surrounding active faults which could have tilted several blocks.

This main deformation occurring in the lowermost metapelites of the Lycian Nappes, as well as in the uppermost sedimentary sequence of the Menderes Massif (Figure II-41b), is incompatible with the commonly accepted southward transport of the Lycian Nappes over the Menderes Massif. Along the contact between the Lycian Nappes and the Menderes Massif, the red-green phyllites of the Permo-Triassic Karaova formation expose neither top-to-the-SSW sense of shear as observed in the same basal lithologies from the klippen of the Dilek-Selçuk region, nor top-to-the-SE as deciphered in the Borlu klippe (Figure II-41b). On the Bodrum peninsula, we only observed several similar movements towards the SSW which are only preserved in the Karaböğürtlen wildflysch constituting the upper levels of the Lycian Thrust Sheets (Figure II-41b).

Furthermore, Collins and Robertson (1998; 2003) described pervasive top-to-the-SE shearing in the Lycian Mélange and in the overlying metamorphic sole of the Lycian Peridotite nappe cropping out in the eastern part of the Lycian Belt (Figure II-41b). We also noticed a few kinematic indicators showing movements towards the south and southeast within the Karaböğürtlen wildflysch and the metamorphic sole of the peridotite nappe (east of Karaböğürtlen) (Figure II-41b).

Therefore, we assume that the main northeastward to eastward deformation observed at the base of the Lycian Nappes and in the uppermost levels of the Menderes Massif might have obscured the evidence of the early deformation contemporaneous with the southward transport of the Lycian complex over the Menderes Massif. This earlier deformation is only preserved in the uppermost levels of the Lycian Thrust Sheets (Karaböğürtlen wildflysch), in the Lycian Mélange and in the Lycian Peridotite nappe (Figure II-41c).

Recent structural studies in the metasedimentary 'cover' of the southern Menderes Massif revealed northward movements (Bozkurt, 1995; Bozkurt and Park, 1999; Bozkurt, 2001) also suggesting an opposite direction of shear relative to the nappes southward translation. We therefore claim that the Lycian/Menderes contact has been reactivated as a top-to-the-NE shear zone during exhumation of HP rocks (Figure II-41c).

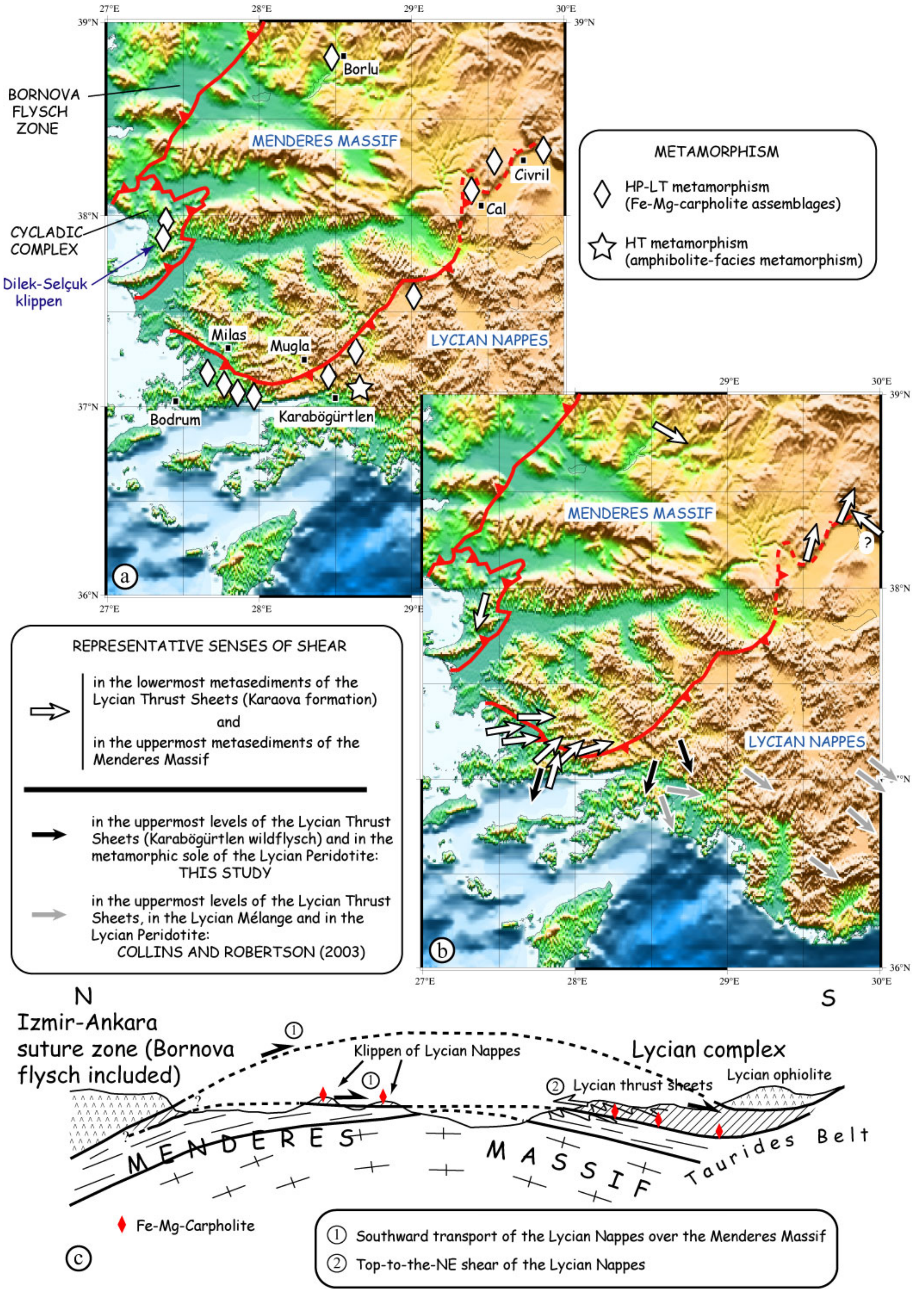

Figure II-41. (a) Synthetic metamorphic map showing the occurrences of HP assemblages at the base of the Lycian Nappes (*stricto sensu* and klippen), and HT assemblages below the peridotite nappe; (b) Synthetic structural map showing the representative senses of shear deciphered in the Lycian nappe complex; (c) Interpretative N-S cross-section across the Menderes Massif.

3. Age of HP metamorphism and its exhumation

As suggested by Oberhänsli et al. (2001), correlation between the Lycian HP metamorphism and the Late Oligocene HP metamorphism in Crete (25 Ma; Jolivet et al., 1996) must be abandoned due to the different paleogeographic provenances of both high-pressure units. Indeed, because the Lycian Nappes originate from northerly regions, it seems reasonable to assume that the age of the HP metamorphism and its exhumation is older than the Oligo-Miocene HP of Crete and probably also older than the Eocene Cycladic HP. Before radiometric ages of the Lycian HP metamorphism are obtained, we conclude that the Lycian Nappes were exhumed in a top-to-the-NE shear context sometime between the Late Cretaceous (age of the youngest sediments involved in the allochthonous units) and the Eocene (age of the Aegean HP metamorphism).

4. HT metamorphism below the Lycian peridotite nappe

Whereas the Late Cretaceous Karaböğürtlen wildflysch of the Lycian Thrust Sheets appears unmetamorphosed on the Bodrum peninsula, it mainly shows greenschist- to amphibolite facies assemblages in the eastern region of Karaböğürtlen, just below the peridotite nappe (Figure II-41a). These traces of HT metamorphism have been found not only in blocks flooding in the wildflysch but also in the matrix itself. The glaucophane-bearing blocks of Kaaden and Metz (1954) do not contain pure glaucophane. Except north of Karaböğürtlen where crossitic amphiboles have been found in relict, blue amphiboles in meta-volcanic or meta-sedimentary blocks generally show Mg-riebeckite compositions documenting greenschist-facies metamorphism. For the "crossite"-bearing block, transition between epidote-blueschist-facies and greenschist-facies is observed in this area.

The amphibolite-facies metamorphic sole of the Karaböğürtlen region, comprising the base of the peridotite nappe and part of the Karaböğürtlen wildflysch is related to the Latest Cretaceous southward obduction of the hot ophiolitic slab onto the continental margin. This HT metamorphic event overprinted the epidote-blueschist-facies assemblages found in an exotic block of the Karaböğürtlen wildflysch, for which the provenance is not ascertained.

CHAPTER III

METAMORPHIC AND STRUCTURAL DATA IN THE SOUTHERN MENDERES MASSIF

Lycian tomb in granitic rocks, southern Menderes Massif (north of Yatağan)

The Menderes Massif occupies a large part of western Turkey. It is tectonically overlain by nappes of the Izmir-Ankara Suture Zone (Şengör and Yılmaz, 1981) on its northern flank (including the Bornova Flysch Zone), the Afyon Zone on its eastern border (Şengör et al., 1984b), and the Lycian Nappes on its southern flank (Brunn et al., 1970; de Graciansky, 1972; Poisson, 1977). Recent investigations in southwest Turkey have reported the occurrence of high-pressure relict mineral assemblages. They have been found in the Afyon Zone (Candan et al., 2002), in the Lycian Nappes (Oberhänsli et al., 2001; and this study), and in the Menderes Massif (Candan et al., 1997; Oberhänsli et al., 1997; Oberhänsli et al., 1998; Candan et al., 2001). Although it is now commonly admitted that the Menderes Massif was affected by a complex polyphase polymetamorphic history, the number and timing of the different tectono-metamorphic episodes is still debated.

I describe in this chapter the first discovered high-pressure relics in the metasedimentary 'cover' of the southern Menderes Massif, underlying the high-pressure Lycian Nappes. This discovery leads one to propose a new tectono-metamorphic history for the Menderes Massif and the Lycian Nappes.

Part of the metamorphic data presented here belongs to a paper in press for **'Lithos'** and entitled **"First evidence of high-pressure metamorphism in the 'cover series' of the southern Menderes Massif. Tectonic and metamorphic implications for the evolution of SW Turkey"** (by Rimmelé G., Oberhänsli R., Goffé B., Jolivet L., Candan O., and Çetinkaplan M., in press).

A. GEOLOGICAL SETTING OF THE MENDERES MASSIF

The stratigraphy of the Menderes Massif is classically divided into two tectono-metamorphic units: an augen gneiss core and an overlying metasedimentary cover imbricated by late Alpine contractional deformation (Schuiling, 1962; de Graciansky, 1966; Dürr, 1975; Şengör et al., 1984b; Satır and Friedrichsen, 1986). Some authors recently described the Menderes Massif as a pile of nappes (Dora et al., 1995; Partzsch et al., 1997; Partzsch et al., 1998; Ring et al., 1999a; Gessner, 2000; Gessner et al., 2001a,b; Ring et al., 2001b). I use here the classical 'core' and 'cover' terminology keeping in mind the allochthonous characteristic of the different units (Figures III-1 and III-2).

1. Core rocks

Core rocks mainly consist of high-grade augen gneisses which have a controversial origin. Whereas some studies have concluded a sedimentary protolith for the augen gneisses (Schuiling, 1962; Şengör et al., 1984b; Satır and Friedrichsen, 1986), other works have suggested a granitic protolith (Konak et al., 1987; Bozkurt et al., 1995). The age of protoliths is also debated. Some authors claimed a Precambrian age for the augen gneisses (Schuiling, 1962; Şengör et al., 1984b; Satır and Friedrichsen, 1986; Konak et al., 1987, Hetzel and Reischmann, 1996; Hetzel et al., 1998; Loos and Reischmann, 1999). Şengör et al. (1984b) initially considered the augen gneiss as the Pan-African basement of western Anatolia. Later Pb/Pb single zircon ages of 550 Ma on average demonstrated that the augen gneisses in the southern Menderes Massif were generated from Pan-African intrusions (Hetzel and Reischmann, 1996; Hetzel et al., 1998; Loos and Reischmann, 1999). On the contrary, mainly based on field observations and particularly on local intrusions of augen gneisses into the overlying schists and marbles, other authors argued that the protoliths of the augen gneisses are Cenozoic in age (Bozkurt and Park, 1994; Bozkurt et al., 1995). It seems, in fact, that multiple generations of magmatic intrusions can be observed.

A major metamorphic event has affected only the core series with intense deformation and metamorphism under high-grade amphibolite-facies conditions with local anatexis (Şengör et al., 1984b; Satır and Friedrichsen, 1986; Dora et al., 1995). Core rocks have yielded Rb/Sr whole rock ages of about 502±10 Ma interpreted as the age of the Pan-African metamorphism, and possible pre-Pan-African sedimentation ages of 550-670 Ma (Satır and Friedrichsen, 1986). Highly deformed intrusive bodies of granitic to tonalitic composition from the northern Menderes Massif have been dated at 471±9 Ma (Rb/Sr whole rock analysis; Satır and Friedrichsen, 1986) that relate them to the end of the Pan-African orogeny, when the last remnants of oceanic material were being subducted (Şengör et al., 1984b). In the central submassif, recently discovered high-pressure (HP) relics within the 'core' consist of eclogites and eclogitic metagabbros (Figure III-1) and suggest P-T conditions around 15 kbar minimum and 640°C (Candan et al., 1994; Candan, 1995; Candan, 1996; Oberhänsli et al., 1997; Candan et al., 1998; Candan et al., 2001). The eclogitic metamorphism was later overprinted by a regional amphibolite-facies metamorphism (7 kbar/620°C; Candan et al., 2001). The eclogite-facies metamorphism as well as associated granulitic parageneses is now considered by most authors to be Pan-African and would have resulted from the crustal thickening during the Late Precambrian-Early Palaeozoic orogeny (Oelsner et al., 1997; Partzsch et al., 1997; Candan et al., 1998; Partzsch et al., 1998; Warkus et al., 1998; Candan et al., 2001; Warkus, 2001; Oberhänsli et al., 2002a). Age determinations on zircons and monazites from eclogitic and granulitic rocks cropping out in the central submassif (Figure III-1) have indeed yielded 600-650 Ma for the high-pressure/high-temperature event (Warkus, 2001, Oberhänsli et al., 2002a). After the Pan-African orogenic event, it has been suggested that the southern part of the Massif was undeformed from the Early Ordovician to the Early (?) Eocene, whereas the northern part of the massif was deformed, intruded by granitic magma and then metamorphosed under greenschist-facies conditions during the Late Triassic. This late deformation would be related to the closure of the Karakaya marginal basin of Palaeotethys (Akkök, 1983; Şengör et al., 1984b; Dannat and Reischmann, 1998; Koralay et al., 1998; Koralay et al., 2001). There was thus, until recently, no evidence for an Alpine HP metamorphic event in the Menderes Massif.

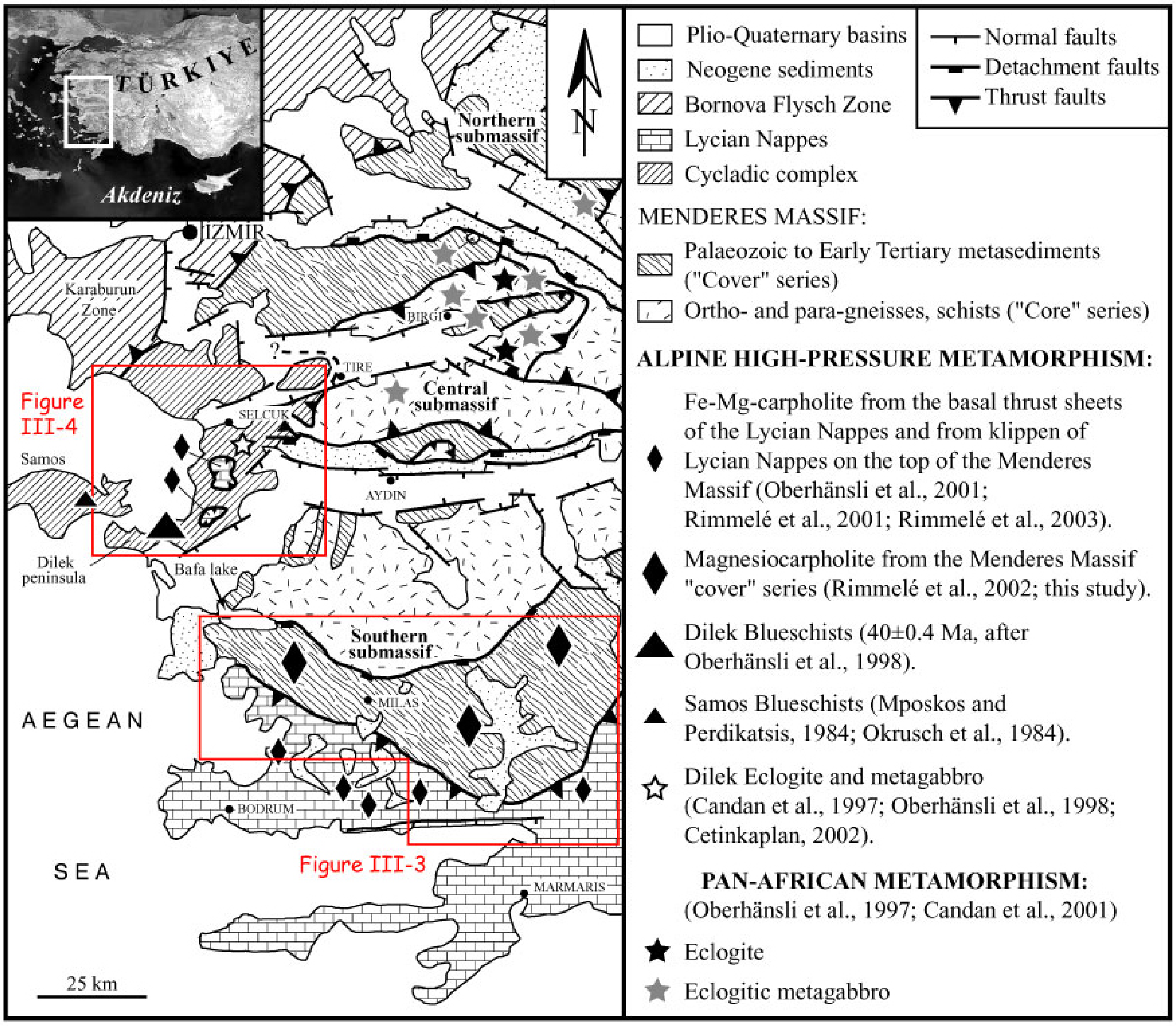

Figure III-1. Geological map showing the regional distribution of HP rocks in southwest Turkey (modified after Bozkurt and Satir, 2000; Candan et al., 2001; Okay, 2001).

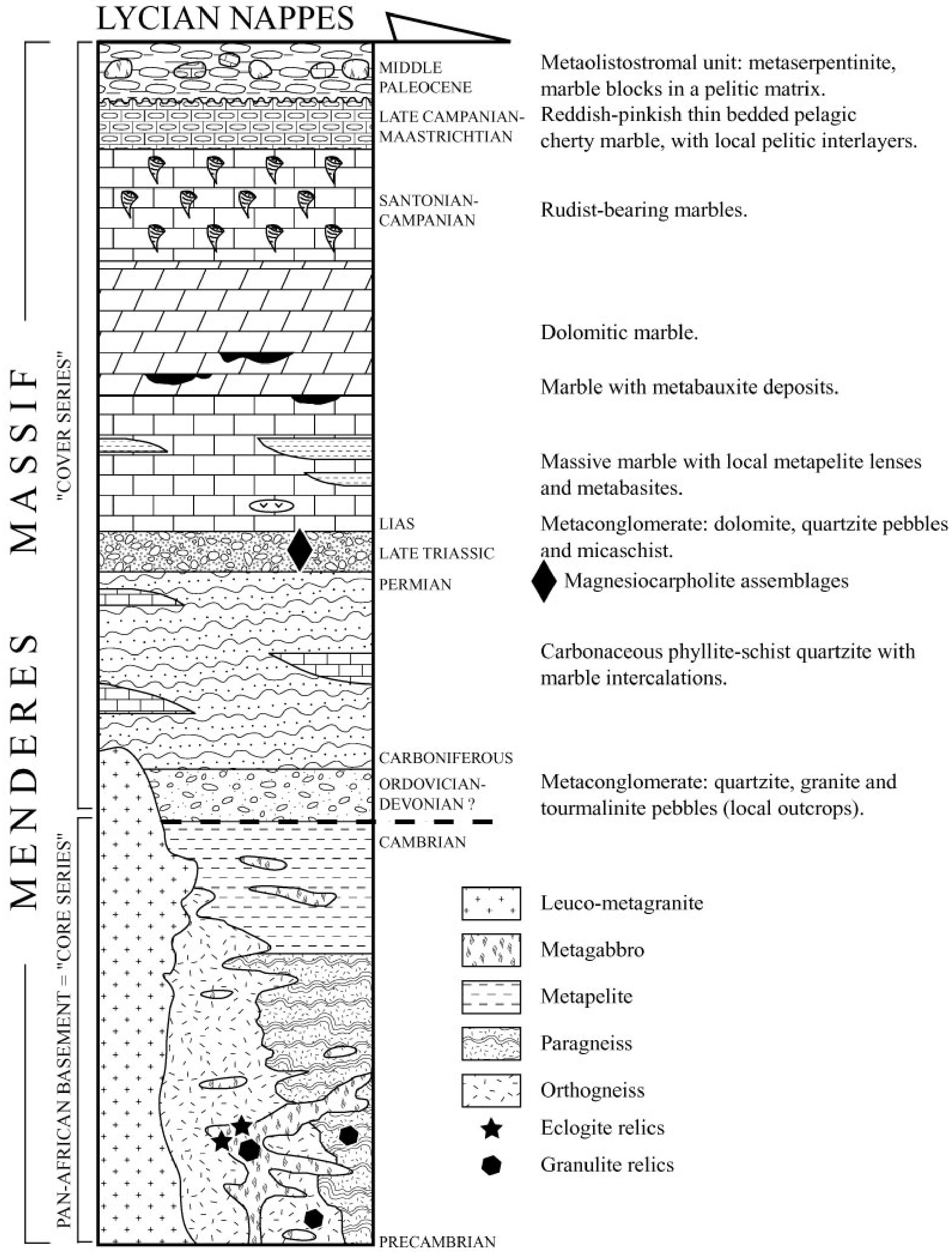

Figure III-2. Generalized stratigraphic section of the Menderes Massif (modified after Dora et al., 2001; and Özer et al., 2001) showing the lithologies which contain HP assemblages (Section not to scale).

2. Cover rocks

Cover rocks roughly consist of two separate units: a Palaeozoic schist envelope and a Mesozoic to Cenozoic marble envelope (Figures III-1 and III-2).

The schist envelope is composed of garnet-, kyanite-, staurolite-, chloritoid-, and sillimanite-micaschists, quartzites, garnet amphibolites, pelitic and psammitic gneisses, with black marble intercalations (Dürr, 1975; Akkök, 1983; Ashworth and Evirgen, 1984a; Şengör et al., 1984b; Satır and Friedrichsen, 1986; Konak et al., 1987; Bozkurt, 1996; Hetzel et al., 1998). In this sequence, metamorphic grade increases from south to north (Bozkurt, 1996). A detailed description of the schist series is reported in Whitney and Bozkurt (2002). Poorly-preserved fossils in the lower parts of the schists have been dated as Late Devonian-Early Carboniferous (Denizli area, Çağlayan et al., 1980; Konak et al., 1987) and zircons from psammites constituting the lowermost levels of the 'cover' have been dated at 526 Ma (Bafa Lake area; Loos and Reischmann, 1999), thus suggesting an Early Palaeozoic protolith age for the lower schist envelope (Figure III-2). The upper levels comprise carbonaceous schists and phyllites with dolomitic marble intercalations ('Göktepe marble'; Önay, 1949) (Figure III-3) and have been dated as Carboniferous to Permian by occurrence of Fusulinids and Bryozoa fossils found in the marble layers (Önay, 1949; Özer, 1998).

The marble envelope constitutes a thick sequence overlying the schist envelope (Figure III-2). The transition between both units is not clear although its stratigraphic character is commonly accepted. Some authors consider that the Göktepe marbles represent the lowermost lithology of the marble envelope (Şengör et al., 1984b; Özer et al., 2001). Others argue that the transition is above the Göktepe marble levels (Dürr, 1975) and that a basal metamorphic conglomerate containing dolomite, quartzite pebbles and micaschist is the lowermost formation of the marble envelope, unconformably overlying the schist envelope lithologies (Çağlayan et al., 1980; Konak et al., 1987; Dora et al., 1995). Above this formation lie Upper Triassic to Liassic marbles with local metapelite lenses, Jurassic to Lower Cretaceous massive dolomitic marbles with metabauxite containing corundum and diaspore (Konak et al., 1987; Yalçın, 1987), Late Cretaceous (Santonian-Campanian) marbles containing Rudist fossils (Figure III-3; Dürr, 1975; Konak et al., 1987; Özer, 1998; Özer et al., 2001), and Late Campanian-Late Maastrichtian reddish pelagic marbles, with chert horizons and local pelitic interlayers (Konak et al., 1987; Özer, 1998; Özer et al., 2001) (Figures III-2 and III-3).

This marble sequence is unconformably overlain by a metaolistostromal formation comprising metaserpentinite and marble blocks within a schist matrix (Dürr, 1975; Gutnic et al., 1979; Çağlayan et al., 1980; Konak et al., 1987). It has been suggested that this unit was deposited during the Palaeocene-Middle Eocene times in the Kızılca/Alakaya basin located between the Menderes Massif to the north and the Bey Dağları carbonate platform to the south (Poisson and Sarp, 1977; Poisson, 1985; Özkaya, 1991). Planktonic foraminifera that occur in this metaolistostrome indicate Middle Palaeocene ages in the southern Menderes Massif (Özer et al., 2001). This lithology constitutes the uppermost levels of the Menderes Massif and therefore marks the end of sedimentation in the massif (Figure III-2).

In the southern Menderes Massif (Milas region), this uppermost unit has been described as slightly metamorphosed (Gutnic et al., 1979) whereas in the central Menderes Massif, in the Dilek peninsula region (east of Selçuk) relics of HP metamorphism were recognised (Candan et al., 1997) within an olistostromal unit (Selçuk formation of Güngör, 1995) which is in the same position as the slightly metamorphosed olistostrome from the southern Menderes Massif (resting at the top of the Marble sequence). Blocks occurring in the Selçuk olistostrome are mainly composed of eclogite and smaragdite-omphacite metagabbro (Figure III-4). The well-preserved HP relics are mostly associated with strongly foliated metaserpentinites (Candan et al., 1997; Oberhänsli et al., 1998; Çetinkaplan, 2002; Oberhänsli et al., 2002b). It has also been suggested that the matrix of the metamorphosed olistostrome, which does not show any evidence of HP relics, has been completely overprinted by later greenschist-facies assemblages whereas the mafic blocks mostly preserved their HP assemblages. A correlation with the similarly metamorphosed olistostromal unit in Syros Island (Ridley and Dixon, 1984; Okrusch and Bröker, 1990) has been proposed (Candan et al., 1997).

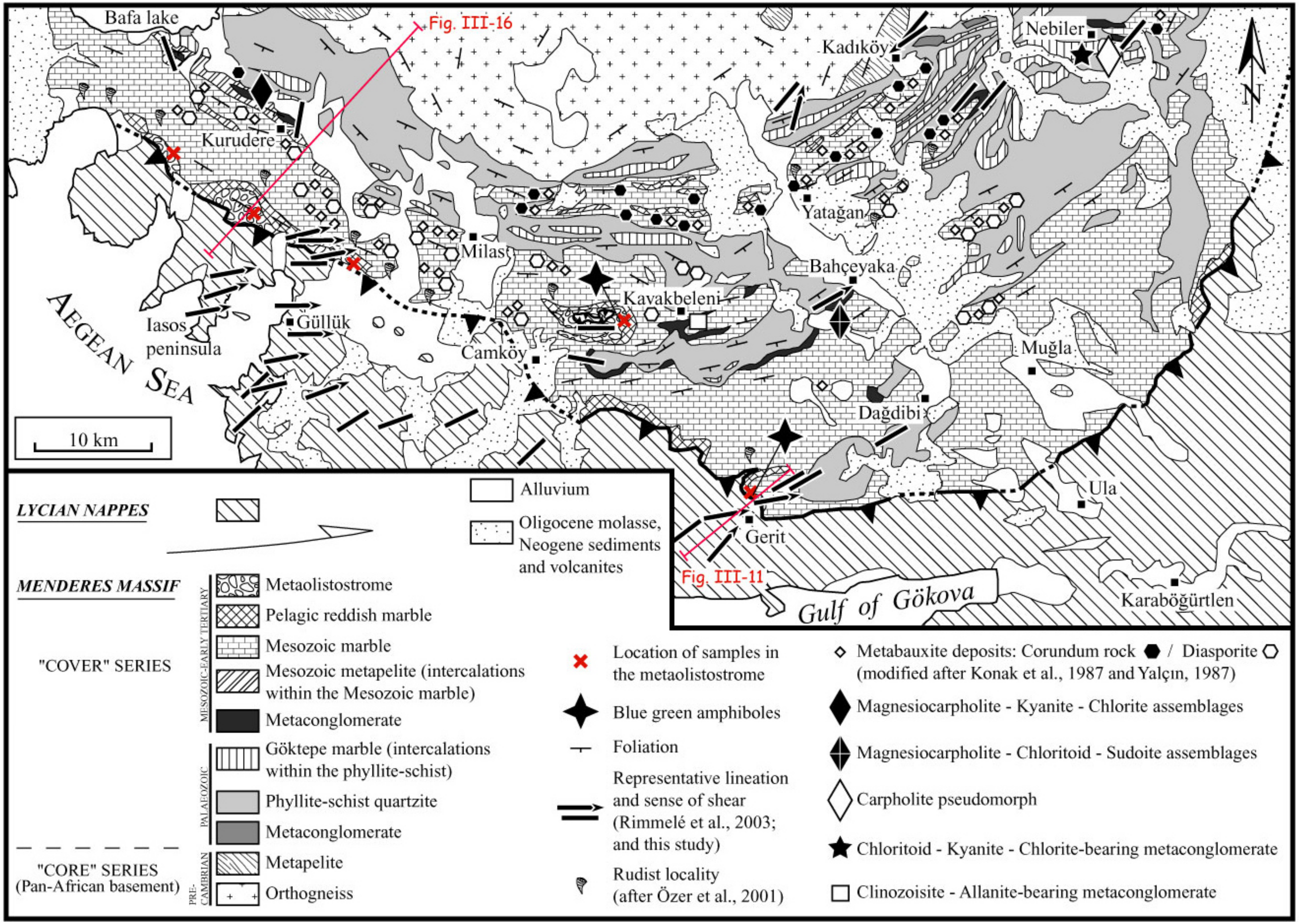

Figure III-3. Tectono-metamorphic map showing the occurrences of HP assemblages and associated stretching in the southern Menderes Massif (geological framework simplified after Çağlayan et al., 1980; Konak et al., 1987; Candan and Dora, 1998; and Konak and Akdeniz [non published geological maps of M.T.A.-Turkey]).

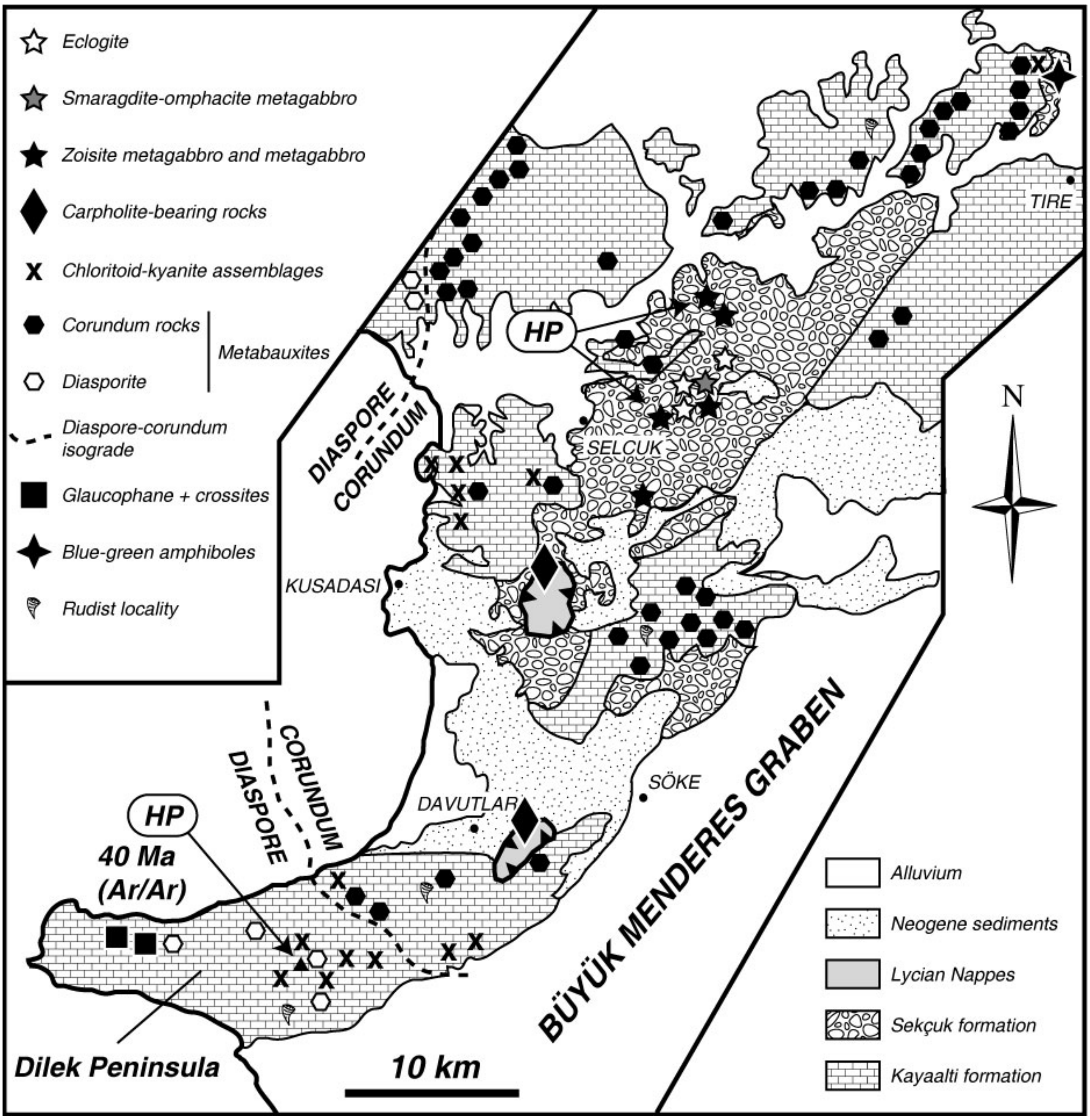

Figure III-4. Geological map showing the Mesozoic units of the westernmost 'Menderes Massif', in the Dilek peninsula region (modified after Oberhänsli et al., 1998). Metamorphic data are from Candan et al. (1997) and Oberhänsli et al. (1998). Location of metabauxites is after Önay (1949) and rudist localities are from Özer (1993).

In the Dilek-Selçuk area, blueschist relics have also been described (Candan et al., 1997; Oberhänsli et al., 1998) within the underlying Mesozoic marble sequence (Kayaaltı formation of Güngör, 1995). The HP metamorphism widespread on the Dilek peninsula (Figure III-4) is characterised by occurrences of well-preserved blue amphiboles in metabasites within thin epidote-crossite-rich layers and lens-shaped bodies, and in carbonate-rich metapelites mixed with volcanic material (Candan et al., 1997). This subduction-related HP metamorphism (conditions about 10 kbar min./470°C max.; Candan et al., 1997) during closure of the Neotethys Ocean has been dated as Middle Eocene on the Dilek peninsula (around 40 Ma, $^{40}Ar/^{39}Ar$ on phengites; Oberhänsli et al., 1998; see Figure III-4). The HP metamorphism was subsequently followed by a regional Barrovian-type overprint under greenschist-facies conditions during Late Eocene-Early Oligocene times (Candan et al., 1997). On Samos island (Figure III-1), which is part of the Cycladic complex, similar HP rocks have been described and estimation of P-T conditions yielded 8 kbar min./470°C (Mposkos and Perdikatsis, 1984; Okrusch et al., 1984).

These traces of a HP event in the Mesozoic Menderes marble sequence of the Dilek peninsula (Figure III-1) led to the interpretation of this region as the eastward lateral continuation of the similar HP Cycladic unit of Samos (Candan et al., 1997; Oberhänsli et al., 1998). It has also been claimed that this unit of the Dilek peninsula does not show any relation to the Menderes Massif and belongs to the Cycladic crystalline complex and should thus be excluded in the geological definition of the Menderes Massif (Oberhänsli et al., 1998; Ring et al., 1999a; Ring et al., 1999b; Gessner et al., 2001a,b; Okay, 2001). On the other hand it has been proposed that the whole Mesozoic marble cover series belong to the Cycladic Complex (the "Dilek nappe", Ring et al., 1999a; Ring et al., 1999b). In fact, the latter consider the southern Menderes Massif as comprising the Çine nappe (orthogneiss of the 'core'), the Selimiye nappe (Paleozoic schist of the 'cover') and the Dilek nappe (mainly Mesozoic marble of the 'cover'; Dilek area and southern submassif). Therefore, they suggest a tectonic contact between the Paleozoic schist sequence and the Mesozoic marbles although there is still no field evidence for it in the southern Menderes Massif. In any case, the Menderes Massif s.s. and the Cycladic complex thus belong to different tectonic units, the Cycladic Blueschists resting on top of the Menderes Massif.

3. The 'Main Menderes Metamorphism' (MMM)

The whole massif suffered a major widespread metamorphism that affected the 'core' and the 'cover' rocks together: the MMM (Main Menderes Metamorphism as termed by Şengör et al., 1984b). This Barrovian-type metamorphism associated with severe deformation reached high-temperature conditions (upper amphibolite-facies conditions) in some nappes of the lower parts of the massif, and only greenschist-facies conditions in the uppermost parts of the Menderes cover series (Dürr, 1975; Akkök, 1983; Ashworth and Evirgen, 1984a; Şengör et al., 1984b; Satır and Friedrichsen, 1986; Konak et al., 1987). In the central submassif, Akkök (1983) estimated pressure-temperature conditions of about 5-6 kbar and 600-660°C in the schist sequence of the Derbent area, and Okay (2001) evaluated pressures and temperatures around 8 kbar and 530°C for garnet-micaschists located north of Aydın (Figure III-1 for location). PT estimates of 2-4 kbar/350-500°C for the cover series, and 5-7 kbar/500-650°C for pelitic rocks of the 'core', have also been reported from the central submassif, north of Birgi (Hetzel, 1995). In the southern submassif, Ashworth and Evirgen (1984a) reported 5 kbar and 530-550°C, and Whitney and Bozkurt (2002) estimated 6 kbar maximum and 430-550°C within the Palaeozoic garnet-biotite schist sequence.

This metamorphic imprint is interpreted as the result of the latest Palaeogene collision across the Neotethys and the consequent internal imbrication of the Menderes-Tauride segment that was formed by burial and intensive shearing within a huge area below the southward-advancing Lycian Nappes. Therefore, it must have been generated during and after the emplacement of the nappes onto the Menderes Massif, at the earliest during Early Eocene times (Şengör and Yılmaz, 1981; Akkök, 1983; Şengör et al., 1984b). Recently published isotopic data fall in the same range and are in remarkable agreement with biostratigraphic evidence that constrained an age for the MMM between Early Eocene and Early Oligocene times (Şengör et al., 1984b). Rb/Sr analyses on white mica and biotite (Satır and Friedrichsen, 1986) have yielded a spread of ages between 63 and 48 Ma (56±1 Ma on average) and 50 and 27 Ma (37±1 Ma on average), respectively. The former ages have been interpreted as crystallisation ages reflecting Alpine metamorphism and the latter as Alpine cooling ages (Satır and Friedrichsen, 1986). New Rb/Sr and Ar/Ar age determinations on mica are consistent with the previous data. Rb/Sr ages slightly post-date the time of major MMM (62-43 Ma; Bozkurt and Satır, 2000) and Ar/Ar data yielded 36±2 Ma for the subsequent cooling (Lips et al., 2001). A subsequent event corresponds to greenschist-facies retrogression and the final exhumation of metamorphic units within low-angle normal-sense ductile shear zones, active between the Eocene and the Early Miocene (Lips et al., 2001). The Menderes Massif was at the surface in the Early Miocene (Bozkurt and Satır, 2000).

4. The 'core-cover' contact

The 'core-cover' contact (augen gneiss/schist contact) has been the subject of controversy for many years. Some authors have considered the contact as a major unconformity (Schuiling, 1962; Şengör et al., 1984b; Satır and Friedrichsen, 1986; Konak et al., 1987). At the base of the schist envelope, a metaconglomerate cropping out locally and made of quartzite, granite and tourmalinite pebbles (Figure III-2) has been interpreted as a basal conglomerate, thus supporting the idea of an unconformity (Konak et al., 1987). Other authors claimed that the 'core-cover' contact is mainly intrusive and that the protoliths of the augen gneiss unit are younger granitoids (Cenozoic in age), this contact later being reactivated as a major shear zone (Bozkurt and Park, 1994; Bozkurt et al., 1995; Bozkurt and Park, 1997a,b). Another interpretation and probably the most realistic is that the 'core-cover' contact is tectonic: it has been described as an Alpine extensional shear zone allowing exhumation of 'core' rocks during top-to-the-south shearing (Bozkurt and Park, 1994; Bozkurt and Park, 1997a,b; Hetzel and Reischmann, 1996; Bozkurt and Satır, 2000; Lips et al., 2001) or as a thrust fault along which the schist sequence was emplaced on top of the augen gneiss unit, either during top-to-the-south Alpine nappe stacking resulting from the collision between Sakarya block and Menderes-Tauride platform (Ring et al., 1999a; Gessner et al., 2001a,b), either during top-to-the-north Alpine contractional deformation, later being reactivated during top-to-the-south Alpine extensional deformation (Lips et al., 2001).

5. The 'Menderes-Lycian' contact

At the south of the Menderes Massif, the Lycian Nappes tectonically overlie the metasediments of the Menderes cover sequence (de Graciansky, 1972). As emphasized in the previous chapter, although their origin has been debated for many years, it is now commonly accepted that they were transported southward over the Menderes Massif between Upper Cretaceous and Late Miocene (de Graciansky, 1972; Dürr, 1975; Dürr et al., 1978; Gutnic et al., 1979; Şengör and Yılmaz, 1981; Okay, 1989b; Collins and Robertson, 1997, 1998, 1999). From base to top, the Lycian Nappes are composed of three main units: the 'Lycian Thrust Sheets' composed of Upper Paleozoic to Tertiary sediments, a chaotic mélange unit (the 'Lycian Mélange'), and a peridotite nappe (the 'Lycian Ophiolites') (Collins and Robertson, 1997). Occurrence of a widespread HP metamorphism documented by Fe-Mg-carpholite has been recently described in the basal metasediments of the 'Lycian Thrust Sheets' which widely crop out in the south of the Menderes Massif (Figure III-1; Oberhänsli et al., 2001; this study). Analysis of the ductile deformation associated with the exhumation of HP rocks indicates shear senses top-to-the-NE to top-to-the-E (Figure III-3). In the uppermost levels of the Menderes 'cover' series, similar eastward displacements are observed and trajectories of the stretching lineations are continuous from the Lycian Nappes to the Menderes Massif across the contact (see Chapter II). It has been proposed that these top-to-the-NE to top-to-the-E movements are probably related to a northward backthrusting of the Lycian Nappes over the Menderes Massif subsequent to their southward translation, reactivating the Menderes/Lycian contact as a top-to-the-NE shear zone allowing exhumation of the Lycian HP rocks. Based on the observation of top-to-the-N fabrics in the metasediments of the southern Menderes Massif, this idea of a northward backthrusting of the Lycian Nappes was also proposed by Bozkurt and Park (1999). The earlier deformation contemporaneous with the southward transport of the nappe complex is only preserved in the uppermost levels of the Lycian Thrust Sheets (Collins and Robertson, 1998; this work), and in the Lycian mélange, as well as in the peridotite nappe (Collins and Robertson, 1998).

The discovery of a high-pressure low-temperature (HP-LT) metamorphic imprint in the Late Triassic (protolith age) metaconglomerate located at the base of the Mesozoic marble envelope of the Menderes Massif brings new constraints for the understanding of the tectono-metamorphic history of the Menderes Massif and its relations with the Lycian Nappes. We describe, in the following paragraphs, the characteristics of this high-pressure metamorphism documented by magnesiocarpholite-kyanite- and/or chloritoid-bearing assemblages (Figure III-3).

B. DISTRIBUTION AND PETROGRAPHY OF HP ROCKS IN THE SOUTHERN MENDERES MASSIF

Occurrences of Fe-Mg-carpholite show a widespread distribution in the Aegean domain (Mposkos and Liati, 1991; Theye and Seidel, 1991; Theye et al., 1992; Jolivet et al., 1996; Trotet, 2000). In southwest Turkey, recent studies led to the first description of Fe-Mg-carpholite-bearing metasediments in the Lycian Nappes (Oberhänsli et al., 2001; this study) extending the distribution of HP metamorphism in the eastern Mediterranean area. During this study, investigations in the so-called 'cover' series of the southern submassif led to the discovery of magnesiocarpholite assemblages that also document for the first time a HP-LT event. The rocks under consideration are located at the base of the Mesozoic marble envelope of the Menderes Massif. They consist of a typical metaconglomerate formation containing quartzite pebbles, yellowish dolomite, quartzite and fine-grained micaschist intercalations (Figure III-2). In the southern part of the Menderes Massif, the metamorphosed conglomerates crop out in a few areas between the Bafa Lake region to the west and the locality of Nebiler to the east (Figure III-3). Our field study in all areas where this metaconglomerate crops out led to the discovery of several occurrences of well preserved HP parageneses. The conglomerate comprises numerous quartz segregations, which appear as synfolial veins containing magnesiocarpholite relics (Figure III-5). The main occurrences of metamorphic index minerals are plotted on Figure III-3 and the main mineral assemblages are summarized in Figure III-6. They mainly consist of the following metamorphic minerals of the FMASH (FeO-MgO-Al_2O_3-SiO_2-H_2O) system: magnesiocarpholite (X_{Mg}=Mg/(Mg+Fe^{2+}+Mn) > 0.5), chloritoid, chlorite, sudoite, kyanite, and pyrophyllite. Four main types of FMASH assemblages observed in the metaconglomerate layer are described below.

Figure III-5. Picture representing a severely stretched synfolial quartz vein within the Late Triassic metaconglomerate, and containing magnesiocarpholite + kyanite HP-LT assemblages (Kurudere area).

1. Kurudere area

In the area of Kurudere (south of Bafa lake, see Figure III-3 for location) *magnesiocarpholite-kyanite-chlorite-quartz* assemblages occur within synfolial quartz veins (Figure III-6). Relic hair-like fibres of magnesiocarpholite (50 to 100 µm long and 1 to 10 µm wide) are preserved in quartz and are found in contact with kyanite (Figures III-7a,b). However, the most common observation in the samples (KURU-0101A, KURU-0110B,C) from this area is the partial to total replacement of magnesiocarpholite by chlorite and kyanite. Kyanite is characterized by long prisms (ranging from 500 µm to 1 cm) running parallel to the micrometer-scale magnesiocarpholite fibres. Up to now, similar magnesiocarpholite occurrences associated with kyanite have only been described in the Alpujarride Complex of the Betic Cordillera (Azañon and Goffé, 1997), in the Sebtides nappes of the Rif (Bouybaouene et al., 1995) and in one pebble from the beach of Psili Ammos in the eastern part of Samos (Okrusch et al., 1984). Pyrophyllite also occurs in the samples but appears as a secondary, retrograde mineral. It coexists only with kyanite. The breakdown of kyanite into pyrophyllite is commonly observed. Phengite is rarely observed in the samples from Kurudere. It is oriented parallel to the kyanite crystals. Chloritoid occurrence was found neither in the quartz segregations, nor in the schist levels.

ASSEMBLAGES	Locality	Sample	Qtz	Car	Cld	Chl	Sud	Prl	Ky	Phg	Czo	Aln	Trm	Rt
Magnesiocarpholite-Kyanite-Chlorite-Quartz	Kurudere	KURU-0101A	+	+		+		X	+	+				"
	Kurudere	KURU-0110B	+	+		+		X	+					"
	Kurudere	KURU-0110C	+	+		+		X	+					"
Magnesiocarpholite-Chloritoid-Sudoite-Quartz	Bahçeyaka	YAT-0107B	+	+	+		+	+	*	+				"
Kyanite-Chloritoid-Chlorite-Quartz	Nebiler	NEBIL-0101B	+		+	+			+	+			"	
	Nebiler	NEBIL-0102A	+		+	+			+	+			"	
Carpholite pseudomorph, Kyanite-Chlorite-Quartz	Nebiler	NEBIL-0103A	+	*		+	X	X	+	+			"	
Clinozoisite-Allanite-Quartz	Kavakbeleni	KAVAKBEL-0103	+			+		+		+	+	+	"	

Figure III-6. Representative metamorphic assemblages observed in the Triassic metaconglomerate of the 'marble envelope'. Names of samples and localities are also reported.
+ Main assemblages / X Secondary retrograde minerals / * Pseudomorphs / " Accessory minerals.
Abbreviations: Qtz, Quartz; Car, Carpholite; Cld, Chloritoid; Chl, Chlorite; Sud, Sudoite; Prl, Pyrophyllite; Ky, Kyanite; Phg, Phengite; Czo, Clinozoisite; Aln, Allanite; Trm, Tourmaline; Rt, Rutile.

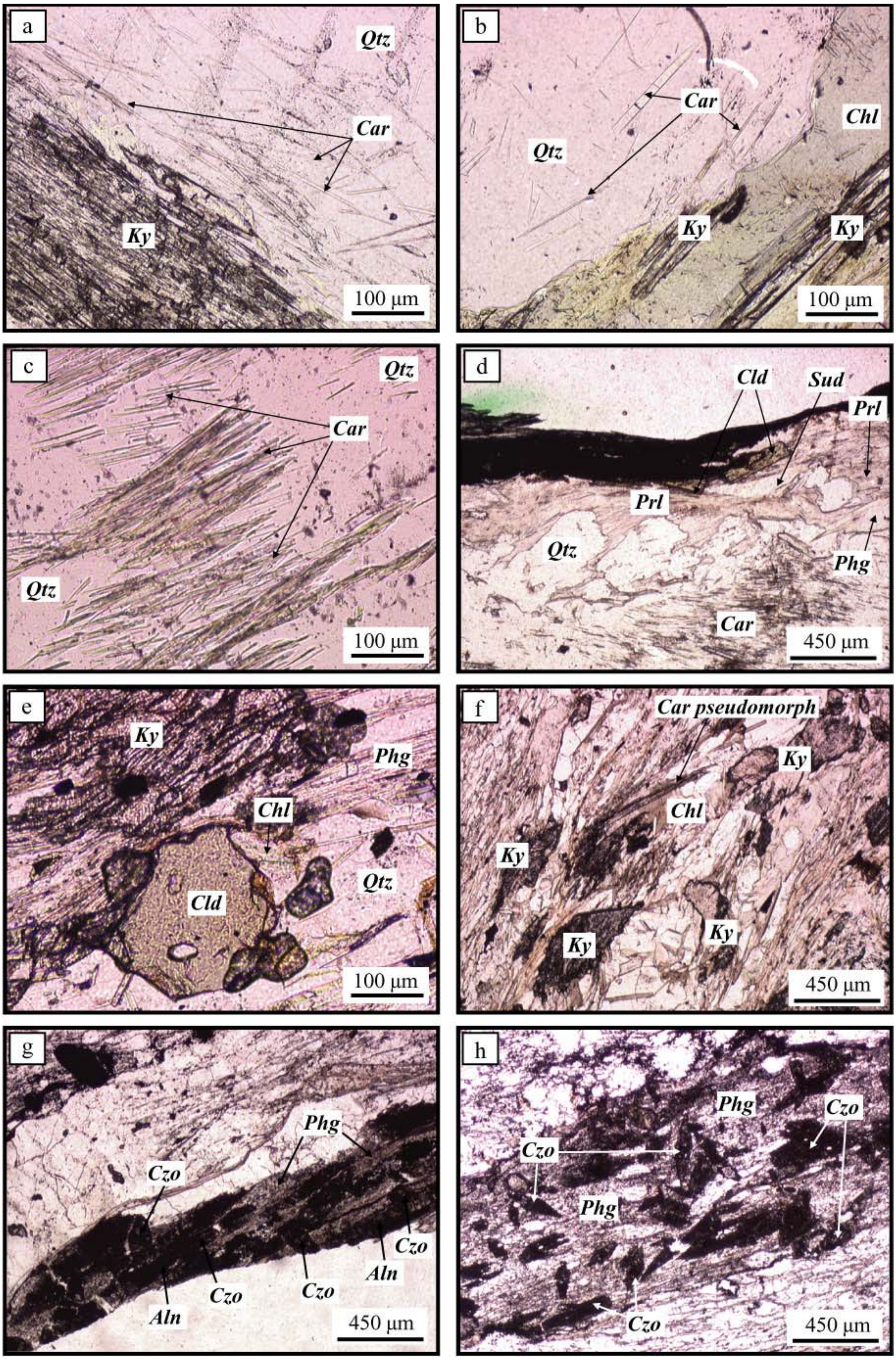

Figure III-7. Photomicrographs showing (a) magnesiocarpholite fibres preserved in quartz, and in contact with kyanite (Kurudere, sample KURU-0110C); (b) the commonly observed retrogression of magnesiocarpholite into chlorite and kyanite (Kurudere, sample KURU-0110C); (c) well preserved magnesiocarpholite in quartz (Bahçeyaka, sample YAT-0107B); (d) a close association of magnesiocarpholite, chloritoid, sudoite and pyrophyllite (Bahçeyaka, sample YAT-0107B); (e) an assemblage of kyanite, chloritoid and chlorite (Nebiler, sample NEBIL-0102A); (f) the total retrogression of carpholite into kyanite and chlorite (Nebiler, sample NEBIL-0103A); (g) (h) allanite-clinozoisite assemblages-bearing schist, south of Kavakbelini (sample KAVAKBEL-0103). Note on picture (g) the retrogression of allanite into clinozoisite. All photomicrographs have been taken under plane polarized light; Mineral abbreviations are reported below Figure III-6.

2. Bahçeyaka area

In a similar metaconglomerate, to the south of the Bahçeyaka (southeast of Yatağan; Figure III-3 for location), *magnesiocarpholite-chloritoid-sudoite-quartz* assemblages (Figure III-6) occur within quartz veins (sample YAT-0107B). Magnesiocarpholite is well preserved within quartz. Prismatic crystals can reach a few hundreds of micrometers (Figure III-7c). It is commonly associated with sudoite, phengite, pyrophyllite and chloritoid (Figure III-7d). Chloritoid crystals, up to 500 µm in length, have a strong pleochroism from greenish-yellowish to colourless. Chloritoid results from the breakdown of magnesiocarpholite, and while kyanite has not been found in the conglomeratic matrix or in quartz segregations, pyrophyllite appears as the result of the retrogression of kyanite (as discussed below).

3. Nebiler area

To the northeast of the investigated region, in the surroundings of Nebiler (Figure III-3), quartzitic schists contain *kyanite-chloritoid-chlorite-quartz* and *magnesiocarpholite pseudomorph-kyanite-chlorite-quartz* assemblages (Figure III-6; samples NEBIL-0101B, -0102A and -0103A). Phengite is also commonly associated to these assemblages. Chloritoid is in contact with kyanite as well as with chlorite (Figure III-7e) and has similar characteristics to chloritoid from the Bahçeyaka area. Only complete pseudomorphs of magnesiocarpholite were observed in this region, as prismatic aggregates of kyanite and chlorite (Figure III-7f).

In all other localities where the metaconglomerate crops out, we could not find any occurrence of these assemblages. The rocks only contain phengite, chlorite and pyrophyllite and sometimes allanite-clinozoisite assemblages (Figures III-6 and III-7g,h) as observed in the area of Kavakbelini (refer to Figure III-3 for location).

C. CHEMISTRY OF THE MAIN METAMORPHIC MINERALS

Mg-Fe-Mn- and amesite-(clinochlore+daphnite)-sudoite ternary plots of the magnesiocarpholite, chloritoid, and chlorite compositions are reported in Figure III-8.

1. Magnesiocarpholite

The composition of magnesiocarpholite is variable, with X_{Mg} ranging from 0.65 to 0.90. In the kyanite-bearing assemblages from the Kurudere metaconglomerate, X_{Mg} values have an average of 0.87 whereas the ones in pyrophyllite-bearing assemblages from Bahçeyaka are about 0.7 (Figure III-8a,b). A similar variation of X_{Mg} values for identical metamorphic assemblages has been described in magnesiocarpholite-bearing metasediments from the HP Alpujarride nappes, south Spain (Azañon and Goffé, 1997). The manganese content in magnesiocarpholite from Kurudere is low ($X_{Mn} \sim 0.03$) but is distinctly high in the lower-grade magnesiocarpholite from Bahçeyaka ($0.15<X_{Mn}<0.25$). Up to now, such Mn-rich magnesiocarpholite compositions have not been described in the Mediterranean Belt.

2. Chloritoid

The chemical compositions of chloritoid from the Nebiler and Bahçeyaka localities are similar in terms of Mg content (Figure III-8c,d; $X_{Mg} \sim 0.4$). On the other hand, the Mn content is clearly higher near Bahçeyaka than near Nebiler (respectively $X_{Mn} = 0.40$ and $X_{Mn} = 0.23$ on average) and may be related to the Mn-rich magnesiocarpholite from the same area (Figure III-8b,d).

3. Chlorite

Chlorite formulae are calculated on the basis of 14 oxygens. Chlorites from Kurudere and Nebiler have roughly the same composition. They are Mg-rich and approach the clinochlore end-member (Figure III-8e). The X_{Mg} values have an average above 0.8 and the Si content varies from 2.6 to 2.85 p.f.u.

4. Sudoite

As for chlorite, sudoite structural formula is calculated on a 14 oxygen basis. It appears as a secondary retrograde mineral in Nebiler whereas it is part of the primary assemblage with magnesiocarpholite and Mn-rich chloritoid in Bahçeyaka (Figure III-6). The X_{Mg} values range from 0.87 to 0.90. Sudoite has a cation sum close to the ideal value of 9.0 but shows a Si content in excess, significantly higher than 3.0 cations p.f.u. (~3.1). This has already been described in sudoite from magnesiocarpholite-bearing rocks (Theye et al., 1992, Azañon and Goffé, 1997, Giorgetti et al., 1998) and is attributed to the Tschermak's substitution Si(Fe^{2+}, Mg)Al_{-2} (Theye et al., 1992). The sudoite compositions are also plotted on the amesite-(clinochlore+daphnite)-sudoite ternary diagram (Figure III-8e).

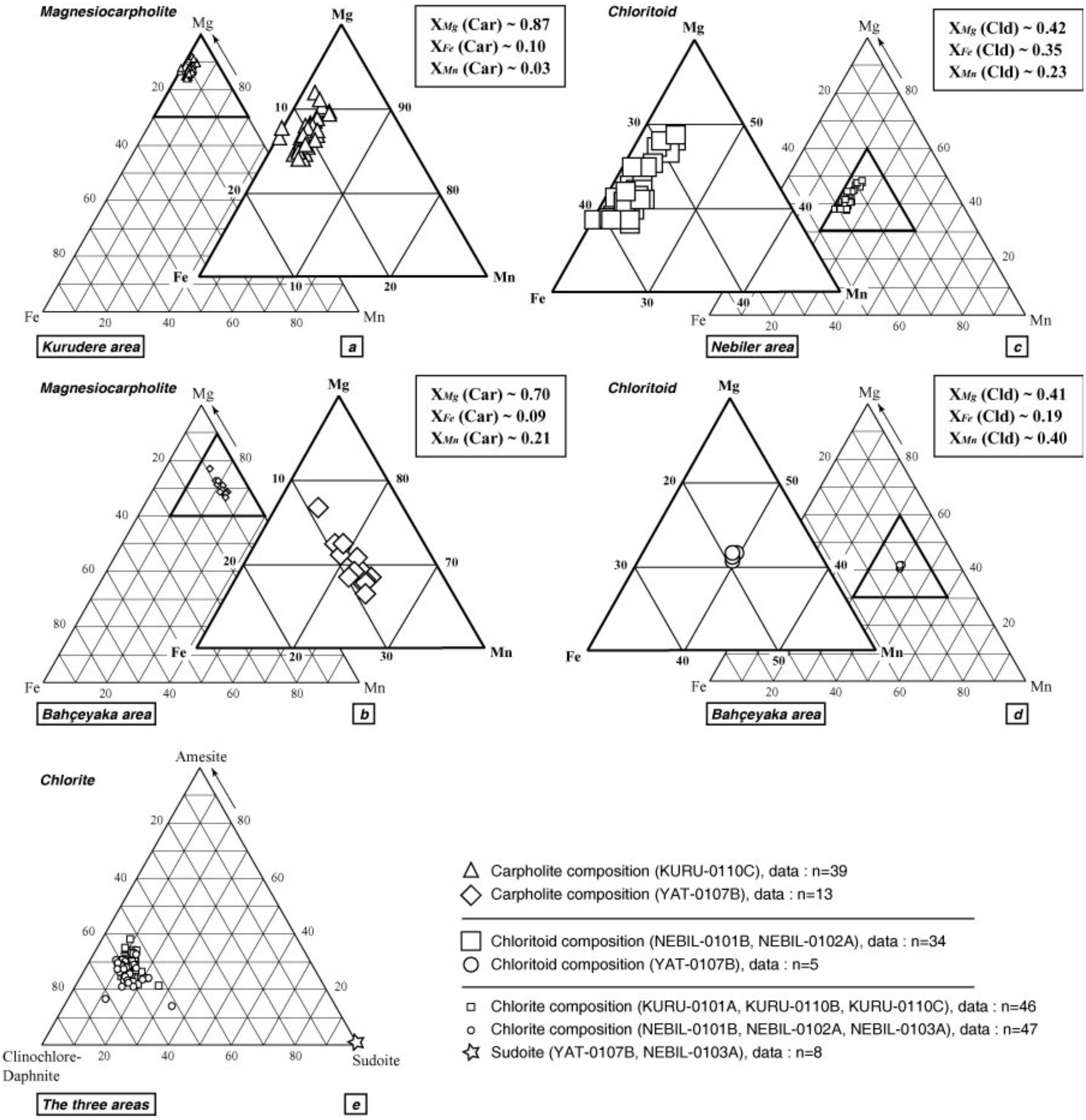

Figure III-8. Mineral compositions for the magnesiocarpholite-bearing rocks from the southern Menderes Massif.

D. PT CONDITIONS OF THE HP METAMORPHISM

P-T conditions were estimated by calculation of phase equilibria using PTAX, a development of GEO-CALC software (Berman and Perkins, 1987) with the internally consistent database of Berman (1988) complemented with thermodynamic properties for magnesiocarpholite and sudoite (Vidal et al., 1992; Vidal and Theye, 1996). The thermodynamic data used for Mg-chloritoid are provisional. They were estimated by Patrick and Berman (unpublished data, 1989) and were used in Oberhänsli et al. (1995), in Jolivet et al. (1996), in Azañon and Goffé (1997), in Goffé and Bousquet (1997), or in Bousquet et al. (2002). These thermodynamic data are listed in Vidal and Theye (1996) and in Vidal et al. (1999). The thermodynamic database used for clinochlore is also reported in Vidal et al. (1999).

For Magnesiocarpholite, the activity is calculated both after Theye et al. (1992) [$a_{(car)} = X_{Mg}$] and Vidal et al. (1992) [$a_{(car)} = (X_{Mg})(X_{Al})^2(X_{OH})^4$ with $X_{Mg} = Mg/(Mg+Fe^{2+}+Mn)$, $X_{Al} = (2\text{-}Fe^{3+})/2$ and $X_{OH} = (4\text{-}F)/4$].

The activity of chloritoid is calculated after Theye et al. (1992) [$a_{(cld)} = X_{Mg},$ with $X_{Mg} = Mg/(Mg+Fe^{2+}+Mn)$].

The activity of chlorite is calculated both after Theye et al. (1992) [$a_{chl} = 0.7(X_{Mg})^5$ with $X_{Mg} = Mg/(Mg+Fe+Mn)$] and Vidal et al. (1992) [$a_{chl} = (X_{Mg})^5(X_{Si})^3(6/5)^5(4/3)^3$ with $X_{Si} = Si/(Si+Al^{IV})$ and $X_{Mg} = Mg/(Mg+Fe+Mn+Al^{VI})$].

The activity of sudoite is calculated after Theye et al. (1992) [$a_{sud} = 0.8(X_{Mg})^2$ with $X_{Mg} = Mg/(Mg+Fe)$].

The curves resulting from the use of these different activity models are represented in Figure III-9 for the three localities that expose magnesiocarpholite assemblages.

1. Kurudere area

The magnesiocarpholite-kyanite-chlorite-quartz assemblages observed near Kurudere correspond to the equilibrium reaction:

magnesiocarpholite = chlorite + kyanite + quartz + water (1)

The breakdown of magnesiocarpholite into kyanite and chlorite as well as the retrogression of kyanite into pyrophyllite are clearly observed in this area and therefore suggest a decompression P-T path without significant heating. The different curves calculated for the equilibrium reaction (1) show minimum temperatures of about 430°C and minimum pressures of 9 kbar on average (Figure III-9a). It is noteworthy that the use of different activity models for the metamorphic index minerals locates reaction curves showing a pressure offset of about 2 kbar for the estimated PT domain. Chloritoid has not been found in this area. Curves corresponding to reactions involving chloritoid have been calculated using a theoretical chloritoid composition deduced from a mean value of magnesiocarpholite-chloritoid partitioning for carpholite-chloritoid-kyanite assemblages from the Alpujarride complex (Betic Cordillera; Azañon and Goffé, 1997). Chloritoid curves appear at minimum values of 15 kbar and therefore are not reported on Figure III-9a. This value corresponds to maximum pressure conditions for the assemblages near Kurudere.

Moreover, occurrences of diaspore- and corundum-bearing metabauxites in overlying Jurassic to Lower Cretaceous marbles (Figure III-3) reflect the equilibrium reaction:

diaspore = corundum + water (2)

It is thus suggested that magnesiocarpholite-bearing rocks from the metaconglomerate have reached the reaction (2) curve during their exhumation (Figure III-9a).

2. Bahçeyaka area

The equilibrium reactions involving magnesiocarpholite, chloritoid and sudoite are:

magnesiocarpholite = quartz + sudoite (3)
magnesiocarpholite = quartz + chloritoid + water (4)
sudoite = quartz + chloritoid + water (5)

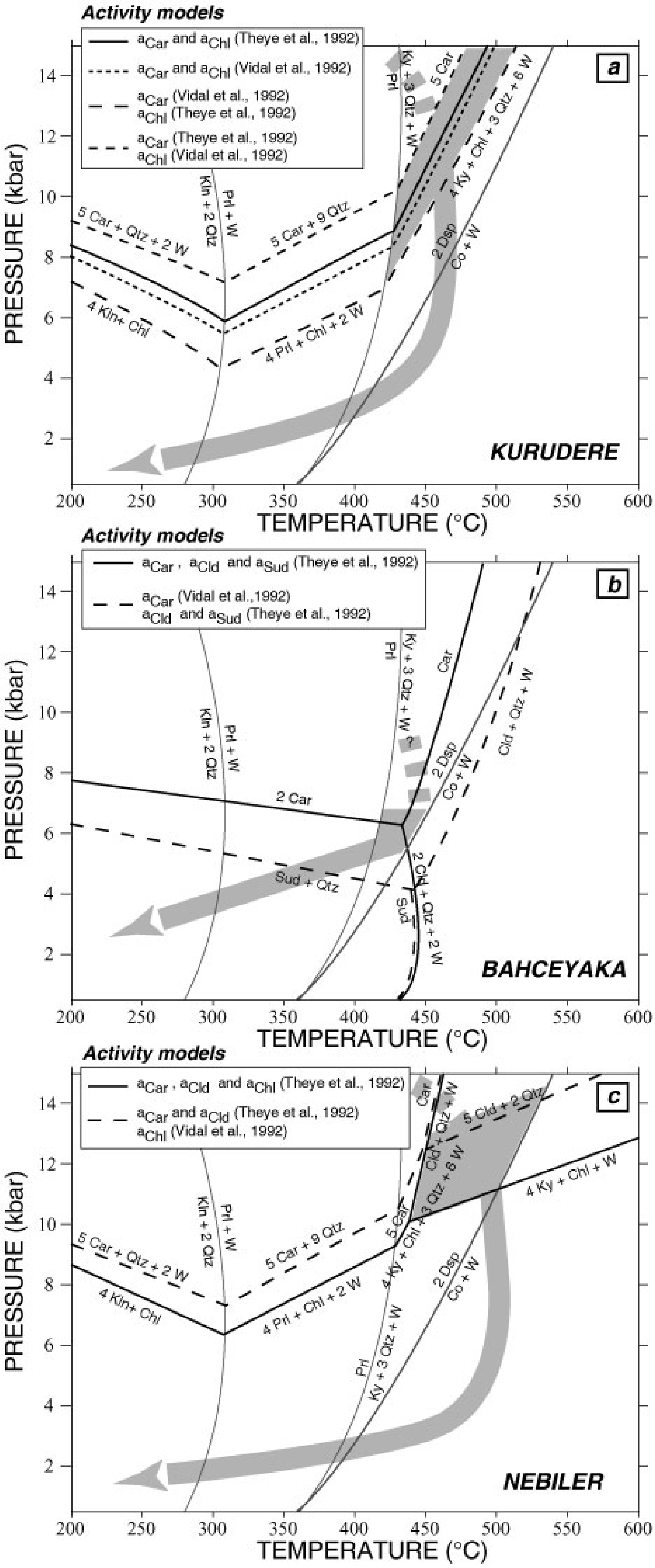

Figure III-9. Calculated Pressure-Temperature conditions and deduced retrograde P-T-paths for magnesiocarpholite assemblages from the Kurudere (a), Bahçeyaka (b) and Nebiler (c) localities. See text for calculation procedures and discussions. Abbreviations are W: Water, Qtz: Quartz, Car: Magnesiocarpholite, Cld: Chloritoid, Chl: Chlorite, Sud: Sudoite, Kln: Kaolinite, Prl: Pyrophyllite, Ky: Kyanite, Dsp: Diaspore, Co: Corundum.

The intersection of the three calculated curves shows pressures between 4.5 and 6.5 kbar and temperatures of about 440°C (Figure III-9b). The similarity in the Mn content of magnesiocarpholite and chloritoid (Figure III-8b,d) suggests a clear phase relation between both minerals. We observed that chloritoid formed by the breakdown of magnesiocarpholite, which suggests that the parageneses describe a retrograde path. The points calculated are located in the kyanite stability field. Although well-preserved kyanite crystals have not been found in the magnesiocarpholite-bearing rocks from this area, pyrophyllite pseudomorphs after kyanite commonly occur. Therefore we assume that the rocks from Bahçeyaka passed into the kyanite stability field during their exhumation before they reached the pyrophyllite stability domain. In the surroundings of Bahçeyaka, only diasporites have been described (Figure III-3). We consider here that the rocks from this metamorphic area did not pass into the corundum domain limited by the equilibrium reaction (2) and therefore were exhumed at slightly lower temperatures than those from Kurudere.

3. Nebiler area

The equilibrium reactions involving kyanite and magnesiocarpholite or chloritoid are mainly:

magnesiocarpholite = chlorite + kyanite + quartz + water (1)
chloritoid + quartz = chlorite + kyanite + water (6)
magnesiocarpholite = chloritoid + quartz + water (4)

Reactions (1) and (6) are the only ones clearly observed in the rocks sampled near Nebiler. The breakdown of magnesiocarpholite through reactions (1) and (4) is complete in this area where the kyanite-chloritoid-chlorite assemblage occurs. For this area devoid of well-preserved magnesiocarpholite, metamorphic conditions (Figure III-9c) were estimated by using a theoretical magnesiocarpholite composition deduced from the magnesiocarpholite-chlorite partitioning calculated for the Kurudere assemblages (K_D[car/chl] = $(Mg/Fe)_{car}/(Mg/Fe)_{chl}$ = 1.23). The log(Mg/Fe^{2+}) graph of coexisting magnesiocarpholite-chlorite is reported in Figure III-10. The points plot in a zone where K_D values are roughly comprised between 1 and 1.5. These K_D values and the mean calculated K_D cluster around 1.2 are similar to those obtained by Theye et al. (1992) for Crete and the Peloponnese ($1.1<K_D<1.4$) and by Azañon and Goffé (1997) for the Betic Cordillera (mean K_D around 1.1 and 1.2). The use of this theoretical magnesiocarpholite composition marks a zone between 10 and 13 kbar (depending on the activity model) and temperatures around 450°C for the kyanite-chloritoid-chlorite assemblage. Considering the total replacement of magnesiocarpholite in the metaconglomerate, the occurrence of preserved corundum-bearing rocks and the absence of diasporites in the overlying marble sequence near Nebiler, we deduce a slightly warmer decompression path than suggested for the HP assemblages from Kurudere (Figure III-9c).

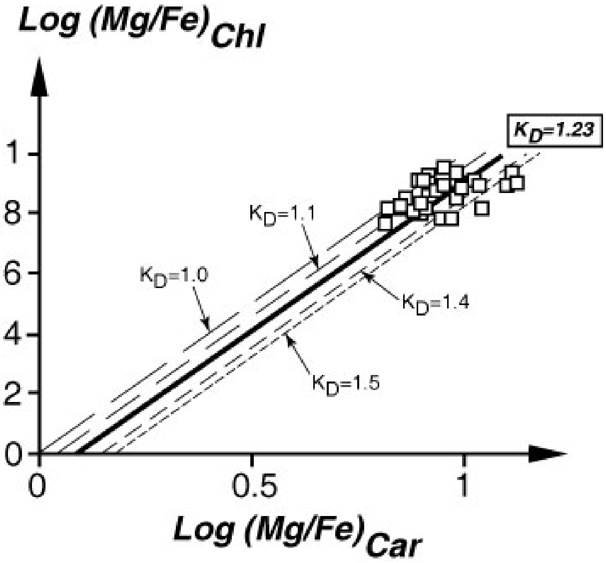

Figure III-10. Logarithmic plot of Mg/Fe^{2+} in coexisting magnesiocarpholite and chlorite from Kurudere. Lines are the constant $K_{D\ (car/chl)}$ values. The thick one corresponds to the calculated K_D value for Kurudere and the other plotted lines are only K_D reference values.

4. Discussion on the PT estimates

The P-T estimates for the Kurudere and Nebiler localities, based on the composition of the metamorphic index minerals, indicate a HP metamorphic peak around 10 to 12 kbar and 450°C. Referring to the petrogenetic grid of Oberhänsli et al. (1995), these P-T conditions are coherent with the Si content (ranging between 3.1 and 3.2) in a few phengites involved in the HP assemblages from both localities. Similar P-T conditions have been estimated for the only other known outcrop of magnesiocarpholite-kyanite assemblages in the Alpujarride Complex of the Betic Cordillera (10-12 kbar/450-500°C; Azañon and Goffé, 1997). Retrograde P-T paths are slightly different between the two areas, with higher temperatures in the Nebiler area during the decompression path than for the exhumation paths for the Kurudere area.

It is noteworthy that the PT estimates for the Bahçeyaka area show lower pressure conditions than for the Kurudere and Nebiler localities. A gap of about 4 kbar (i.e. ~12 km) is observed. In this area, as described above, magnesiocarpholite and chloritoid have a relatively higher Mn-content than in rocks from Kurudere of Nebiler. Recent works have shown that Mn-rich carpholite occurs in low-pressure metamorphic rocks, such as in the Wippra Metamorphic Zone located in Germany, or in the Venn-Stavelot Massif in the Belgian Ardennes (e.g. Theye and Siedel, 1993; Theye et al., 1996). The question arises here of the significance of the Mn-rich sediments of Bahçeyaka. Considering their relative geographic proximity with the two other HP localities, the stratigraphic continuity of the Menderes cover series, and the apparent absence of any major tectonic contact between these localities, such pressure gap of 4 kbar for rocks coming from the same stratigraphic level is difficult to explain. It is emphasized here that the Mn-rich rocks from Bahçeyaka might have probably undergone similar pressure conditions to those from Kurudere and Nebiler, and that the activity models used for PT estimates of these rocks may not be appropriate for such local Mn-rich sediment chemistry.

E. OCCURRENCE OF BLUE-AMPHIBOLES IN THE METAOLISTOSTROME OF THE SOUTHERN MENDERES MASSIF

During our investigations in the southern Menderes Massif region, we found occurrences of blue and green amphiboles in the Middle Palaeocene metaolistostrome of the Menderes Massif that constitutes the uppermost formation of the massif. This metaolistostrome sporadically crops out from the northwest of Güllük (north of the Iasos peninsula; Figure III-3) to the region of Çivril in the eastern part of the massif (refer to Figure II-27), as a thin formation all along the contact between the Menderes Massif and the Lycian Nappes. It is composed of metapelites in which metre-scale dolomitic blocks, marble lenses and metaserpentinite blocks commonly flood. The schist matrix shows amphibole + chlorite ± mica + epidote + albite + quartz assemblages. This formation was sampled north of the Iasos peninsula, in the Milas area where klippen of Lycian Nappes crop out (SE of Milas), north of Gerit (Figure III-3 for these locations), and in the Çivril region (Figure II-27). The schists of the highly deformed metaolistostromal unit only contain chlorite-mica-albite-quartz assemblages in the Iasos peninsula region. Amphibole occurrences were not found in this area. On the contrary, north of Gerit (Figure III-3 and Figure III-11), blue and green amphiboles occur in the schists, generally as small fibres (a few hundreds of micrometers long) associated with albite, chlorite and quartz (Figure III-12a,b).

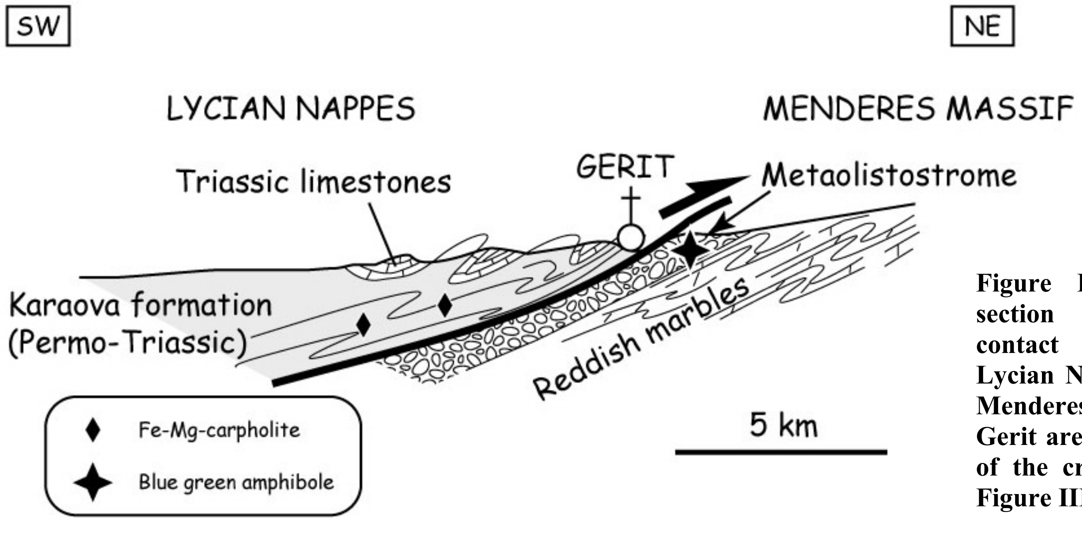

Figure III-11. Cross-section across the contact between the Lycian Nappes and the Menderes Massif in the Gerit area. See location of the cross section in Figure III-3.

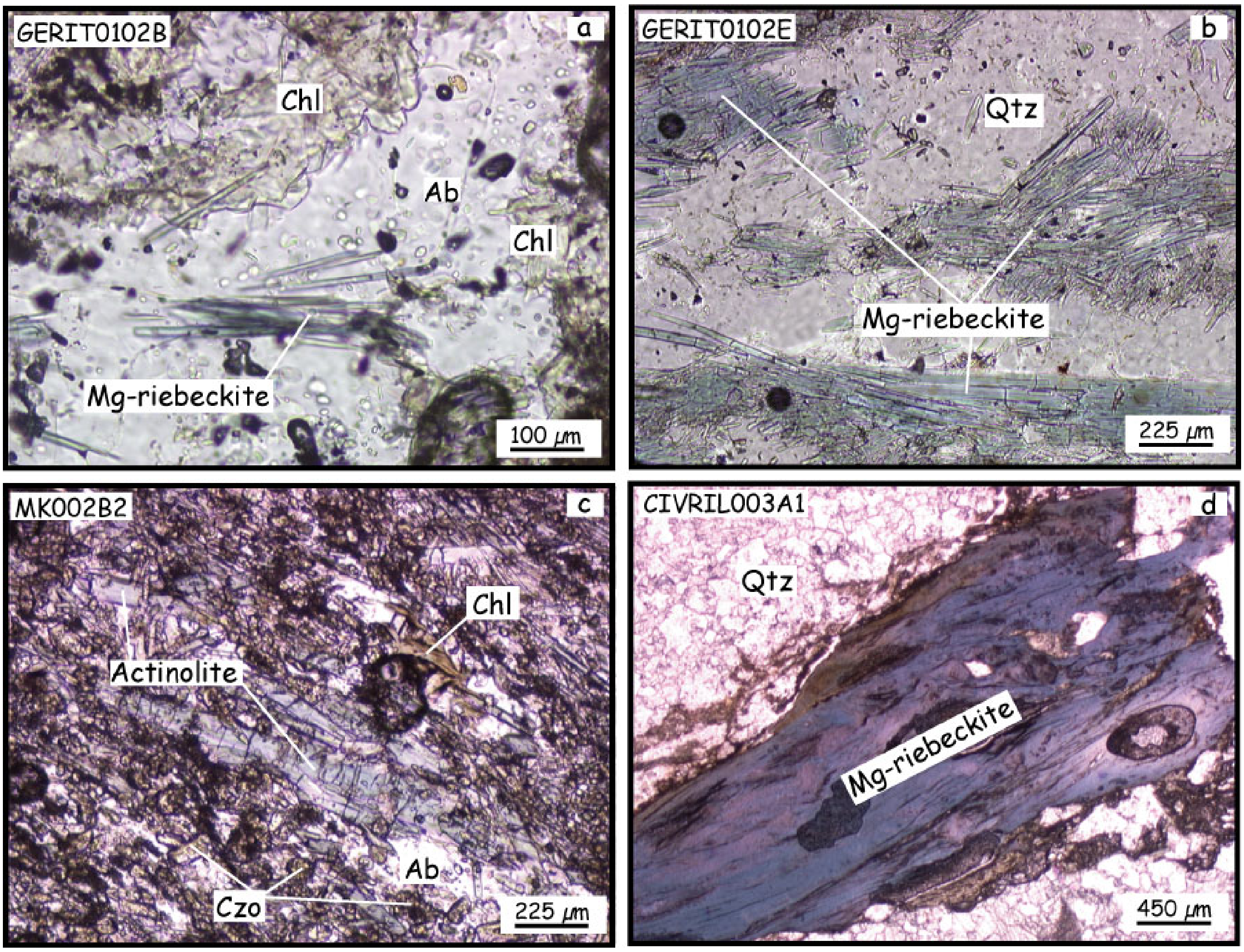

Figure III-12. Photomicrographs showing the main assemblages observed in the metaolistostrome of the Menderes Massif, from the Gerit area (a,b), the Milas area (c), and the Çivril area (d). All photomicrographs were taken under plane polarized light; Mineral abbreviations: Chl, chlorite; Ab, albite; Qtz, quartz; Czo, clinozoisite.

In the Gerit area, amphiboles are essentially either sodic or calcic, with a very few Ca-Na-intermediate compositions (Figure III-13). Sodic-amphiboles have a X_{Mg} higher than 0.5 (Figure III-14a) and the high values of the $X[Fe^{3+}]$ (between 0.8 and 1) document a Mg-riebeckite composition (Figure III-14b). The microprobe analyses revealed neither glaucophane nor "crossite" compositions. Sodic-calcic amphiboles show winchite and barroisite compositions (Figure III-15a) and calcic-amphiboles are essentially tremolites and Mg-hornblendes (Figure III-15b).

Below the klippen of Lycian Nappes located SE of Milas (Figure III-3), the matrix of the metaolistostrome also contains amphiboles which show calcic and few calcic-sodic compositions (Figure III-13). Ca-amphibole is commonly found with epidote, chlorite and albite (Figure III-12c) and shows a composition of actinolite (Figure III-15b). Few winchite compositions are also observed (Figure III-15a).

In the area of Çivril, as mentioned in the previous chapter, the metaolistotromal unit that crops out south of Gömce (see map and cross sections in Figure II-27, Chapter II) contains occurrences of sodic and calcic amphiboles within the schists (Figure III-13). The sodic amphiboles which have a typical very shiny bluish colour (Figure III-12d) are slightly Fe^{2+} -richer than these from the Gerit area, although they all show similar Mg-riebeckite compositions (Figure III-14a,b). As for the Gerit area and the Milas area, the Si-content and the X_{Mg} values in Ca-amphiboles mainly show tremolite compositions (Figure III-15b), and winchite compositions for Ca-Na-amphiboles (Figure III-15a). Ca-amphibole + epidote + chlorite + phengite + albite assemblages are similarly commonly observed.

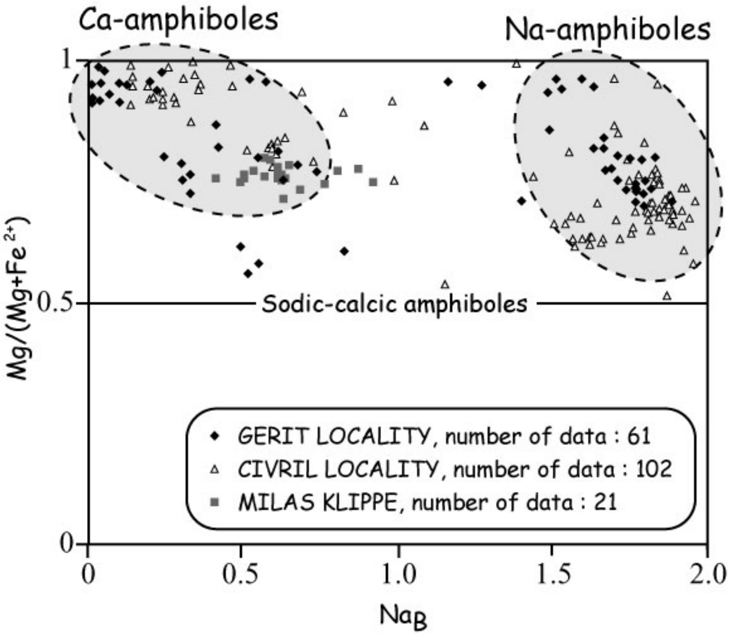

Figure III-13. Composition of the amphiboles from the metaolistostrome of the Menderes Massif; classification follows Leake (1978); Structural formulae of amphiboles were calculated on the basis of 23 O.

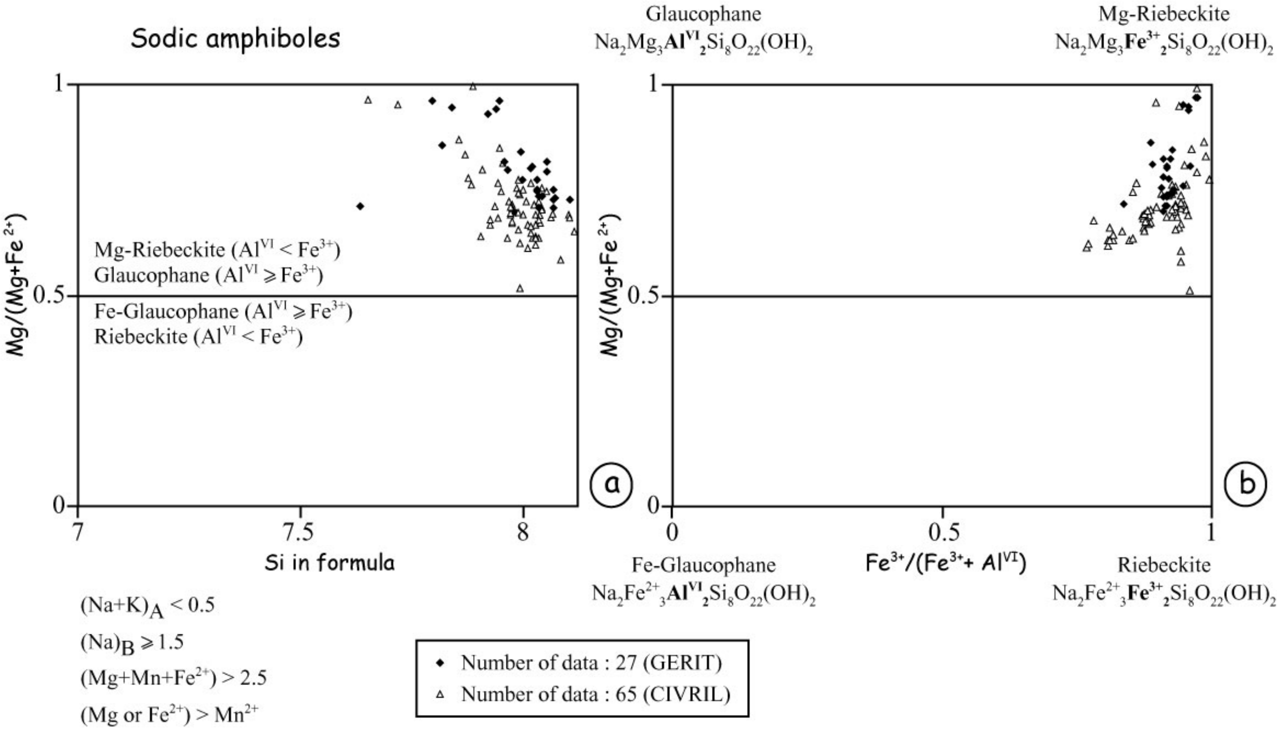

Figure III-14. Si versus X_{Mg} (a) and X_{Fe3+} versus X_{Mg} (b) compositional diagrams (after Leake et al., 1997) of sodic-amphiboles from the metaolistostromal unit of the Menderes Massif.

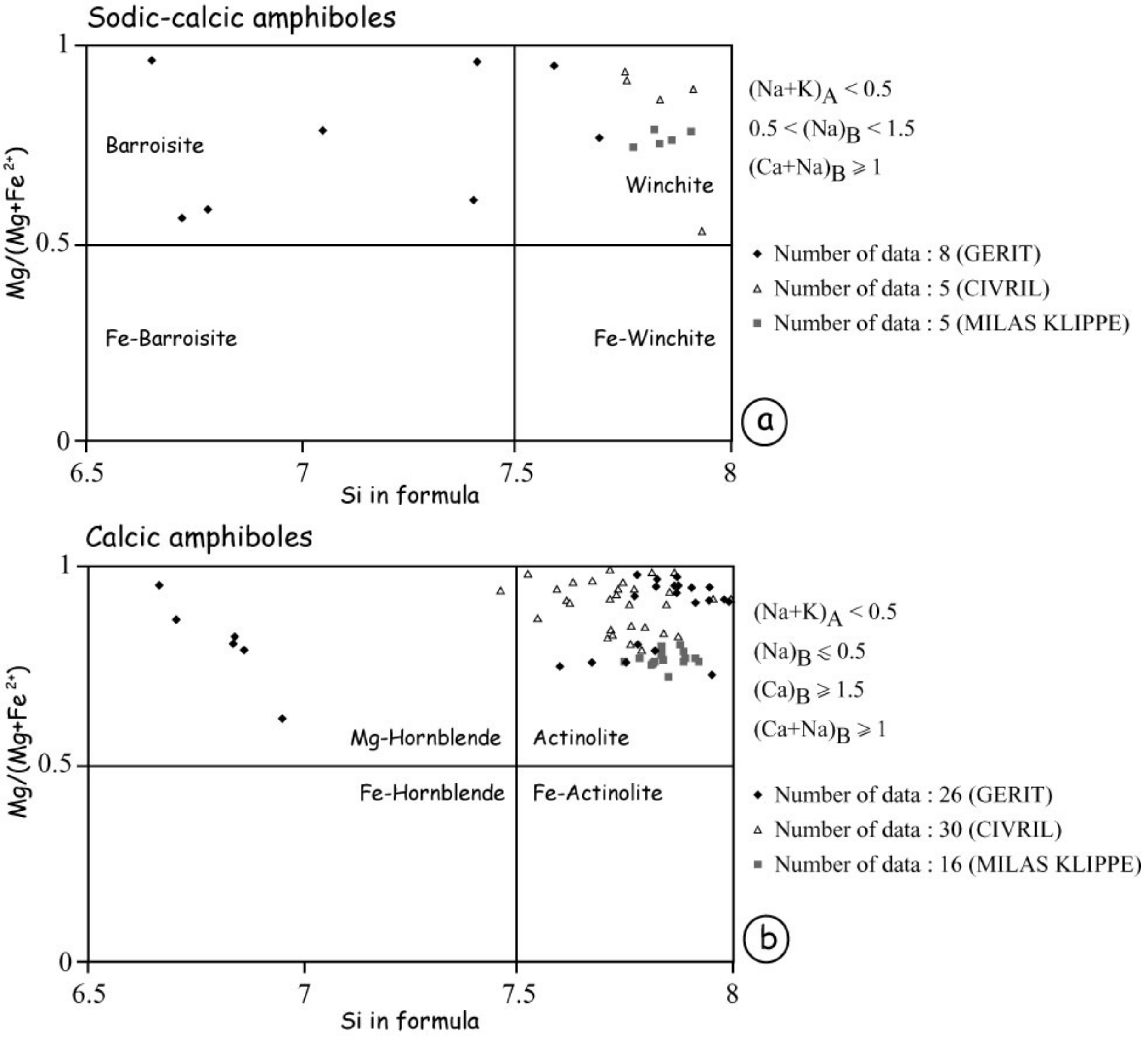

Figure III-15. Si versus X_{Mg} compositional diagrams (after Leake et al., 1997) for sodic-calcic-amphiboles (a) and calcic-amphibole (b) from the metaolistostrome of the Menderes Massif.

Therefore, in the three regions, two groups of amphiboles raise from the classification diagrams (after Leake et al., 1997): a group of sodic amphiboles with a Mg-riebeckite composition and a group of calcic amphiboles which are essentially tremolites. The widespread blue-amphiboles show neither glaucophane nor “crossite” compositions. None of them show compositions corresponding to any amphibole group as defined by Evans (1990) for HP-LT blueschists.

Taking the reaction Na-amphibole+epidote+quartz+water=albite+chlorite+Ca-amphibole, the observed paragenesis of the metaolistostrome schists corresponds to the right hand side, which would indicate greenschist-facies conditions. Calculation of the activities (following Evans, 1990) of Na-amphibole, Ca-amphibole, epidote and chlorite suggests low-pressure conditions (about 3-4 kbar) for temperatures ranging between 400 and 500°C.

F. STRUCTURAL DATA IN THE SOUTHERN MENDERES MASSIF

In this part, I briefly describe a few structural features and also give a short summary of kinematic indicators taken from the literature in order to highlight the consistent orientation of the structures throughout the whole study area.

A regional foliation is well developed in the southern Menderes Massif (Figure III-3). The foliation is penetrative throughout the orthogneisses as well as in the overlying metasedimentary series. In the Milas-Kurudere area, it strikes NW-SE and mainly dips to the SW, whereas between Yatağan and Nebiler it is oriented NE-SW and dips towards the SE. The foliation strikes roughly E-W and dips to the south between the two areas. A mean dip is about 40°S in the whole area. This regional foliation is strongly deformed. The geological map (Figure III-3) highlights major large-scale folded structures within the metasedimentary sequence. They are oriented approximately NW-SE in the westernmost parts of the submassif and trend progressively NE-SW in the easternmost parts. The kilometre-scale folds are mainly asymmetric to overturned and have a northward vergence (Figure III-16). Figure III-3 shows that folded structures trend parallel to the Lycian nappe contact. This has already been described in previous studies (Konak et al., 1987; Bozkurt and Park, 1999; Whitney and Bozkurt, 2002). Associated with the regional foliation, a pronounced stretching observed in the plane of foliation is also well exposed in the southern submassif.

The HP metaconglomerate described above comprises quartz segregations which are mainly synfolial veins containing the HP assemblages. These veins have various sizes from a few centimetres up to several metres long. The observed deformation associated with the HP assemblages is characterised by a stretching roughly oriented N-S to N100 with a mean orientation N50 (Figure III-3). In few places, the rocks are severely stretched but except in a very few areas no clear preferential sense of shear has been observed in the metamorphosed conglomerate (Figure III-16).

In the Palaeozoic schists, we observed a NNE-SSW to NE-SW stretching in a few outcrops with top-to-the-NE kinematic indicators (Figure III-3). Structures within the Palaeozoic schists and underlying augen gneisses have been recently described in the southern submassif (Bozkurt and Park, 1994; Bozkurt, 1996; Hetzel and Reischmann, 1996; Bozkurt and Park, 1999; Gessner, 2000; Gessner et al., 2001a; Whitney and Bozkurt, 2002). It has been claimed that top-to-the-NNE fabrics (Figure III-16) formed during folding and thrusting, and are associated with the MMM (Bozkurt and Park, 1999). Later, top-to-the-south chloritic shear bands overprinted these structures during exhumation (Whitney and Bozkurt, 2002).

In the uppermost levels of the metasedimentary envelope of the massif, we observed an ENE-WSW stretching with senses of shear towards the NE (Figure III-16). These kinematic indicators were observed in the pelagic reddish marbles as well as within the uppermost metaolistostromal unit, just below the contact with the Lycian Nappes (Rimmelé et al., 2001; Arslan et al., 2002; Rimmelé et al., 2003). The basal metasediments of the Lycian Thrust Sheets (as termed by Collins and Robertson, 1997) expose a very clear top-to-the-NE shearing deformation (Figure III-16) contemporaneous with the exhumation of HP parageneses (as seen in Chapter II). This deformation is continuous from the Lycian Nappes towards the Menderes Massif across the contact between the two complexes, with similar direction of stretching and shear sense (Figure III-3). I discuss in the next part the implications of this consistent orientation of kinematic indicators throughout the whole study area.

G. DISCUSSION AND CONCLUSIONS

1. HP metamorphism in the southern Menderes Massif

In the southern submassif, the discovery of a HP metamorphism characterized by magnesiocarpholite assemblages within the Mesozoic 'cover' series shows that the Menderes Massif underwent higher pressure conditions during its Alpine history than previously suggested. Rocks were buried under conditions of about 10-12 kbar and 440°C. The age of this HP-LT metamorphism can be constrained by the paleontological age of the uppermost metaolistostrome of the Menderes 'cover' which has been dated as Middle Palaeocene (Özer et al., 2001). This suggests a probable age between the Middle Palaeocene (age of the youngest metasediments in the Menderes 'cover' unit) and the Eocene (age of the Dilek HP rocks) for the HP metamorphism that affected the 'cover' metasedimentary series of the southern submassif. The age of this metamorphism could indeed be correlated with the Eocene (40±0.4 Ma; Oberhänsli et al., 1998) blueschists described in the Mesozoic marble sequence of the Dilek peninsula (min. 10 kbar/max. 470 °C; Candan et al., 1997). The mechanism responsible for this HP metamorphism is compatible with a burial contemporaneous with Alpine subduction and nappe stacking.

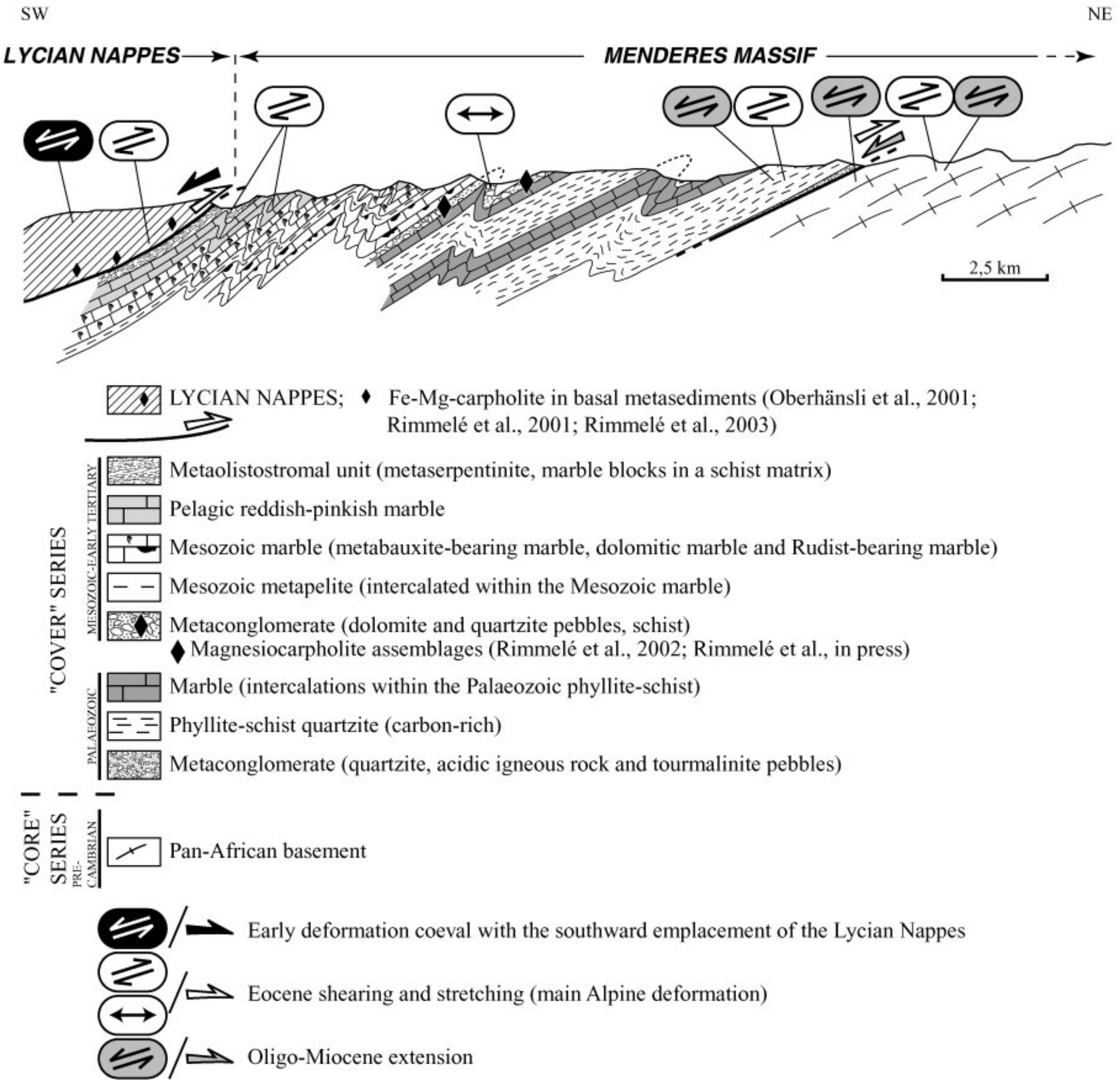

Figure III-16. Synthetic cross-section across the southern submassif roughly parallel to the stretching, and highlighting the different episodes of deformation within the metasedimentary sequence of the massif (see text for references). The location of magnesiocarpholite-bearing rocks from the Lycian Nappes and the Menderes Massif is also reported. Refer to Figure III-3 for the approximate location of cross-section. N.B. Neogene basins and alluvium have not been represented on the cross-section.

2. HP metamorphism on the Dilek peninsula

The HP metamorphic history of the Dilek peninsula region is commonly correlated with that of Samos (Candan et al., 1997; Oberhänsli et al., 1998) and therefore belongs to the Cycladic crystalline complex (Ring et al., 1999a; Ring et al., 1999b; Gessner et al., 2001a,b; Okay, 2001). However, the latter authors also include the Mesozoic 'cover' sequence of the southern Menderes Massif into this Cycladic complex. This interpretation can be questioned because of the absence of a major tectonic contact between the Palaeozoic schists and the Mesozoic series of the Menderes Massif that would exclude the Mesozoic sequence from the Menderes Massif s.s. Therefore, we consider that the Dilek-Selçuk region and the southern Menderes Massif are two different tectonic units (Figure III-1). This interpretation is supported by the fact that the uppermost metaolistostromal formation of the Menderes Massif is a thin slightly metamorphosed unit in the southern submassif (Gutnic et al., 1979) that contains, as seen before, only low-grade metamorphic blue-amphiboles whereas on the Dilek peninsula the stratigraphically similar formation (Selçuk formation) shows evidence of eclogites and blueschists (Candan et al., 1997; Oberhänsli et al., 1998; Çetinkaplan, 2002). All these arguments favour the idea that the HP unit of the Dilek peninsula has to be excluded in the geological definition of the Menderes Massif (as shown in Figure III-1).

3. HP metamorphism in the Lycian Nappes

Recent investigations in the Lycian nappe complex led to the discovery of Fe-Mg-carpholite-chloritoid assemblages (Oberhänsli et al., 2001; this study: Chapter II) similar to those described in this part. However, the absence of kyanite in the parageneses suggests lower P-T conditions (approximately 8 kbar/max. 420°C) than those undergone by the Menderes 'cover' series (min. 10-12 kbar/min. 440°C). These HP assemblages have been found only at the base of the Lycian complex, the upper parts of the nappes appearing unmetamorphosed. If the age of the HP metamorphism in the Menderes 'cover' series can be considered as old as for the Dilek Blueschists (40 Ma, Oberhänsli et al., 2001), the age of the HP metamorphic imprint in the Lycian Nappes is not ascertained. Before radiometric ages are obtained, an age between the Late Cretaceous (age of the youngest sediments in the Lycian allochthonous unit) and the Middle Eocene (age of the Cycladic Blueschists) has been assumed (Rimmelé et al., 2003).

4. Three stacked HP units

It is now clearly admitted that the Menderes Massif has a nappe-pile structure (Dora et al., 1995; Partzsch et al., 1997; Partzsch et al., 1998; Ring et al., 1999a; Gessner, 2000; Gessner et al., 2001a,b). In some places, nappes from the so-called 'core' series tectonically overlie metasedimentary 'cover' sequences (Figure III-1). The Cycladic complex (Dilek-Selçuk area) overlies the Menderes nappes as described in the central submassif, to the east of Selçuk (Okay, 2001). Moreover, near Selçuk, klippen of Lycian nappes overlie the Dilek Blueschists of the Cycladic Complex (Oberhänsli et al., 2001). Therefore, we consider that three stacked HP units were involved in the Alpine continental subduction of the Tauride-Menderes block below the Sakarya micro-continent during the Eocene. The lowermost unit is composed of the imbricated 'core' and HP 'cover' of the Menderes Massif. It is covered by the Cycladic Blueschist complex (Dilek and Samos regions) and finally by the HP Lycian Nappes (Figure III-17a). During the subduction process, the basal part of the Lycian Nappes was dragged deep enough to record HP metamorphism while the upper parts of the nappe complex were too shallow to undergo any significant metamorphic imprint.

5. Alpine HP metamorphism versus Main Menderes Metamorphism (LP-HT) in the southern Menderes Massif

Up to now, evidence for an Alpine HP-LT metamorphism has been described neither in the Menderes 'core' nor in the Paleozoic phyllite-schists of the 'cover'. In the Precambrian basement, all the HP relics found are attributed to the Pan-African orogeny (Candan et al., 2001). Between the earliest Palaeocene and the Middle Eocene (~60 to 45 Ma after Satır and Friedrichsen, 1986; Bozkurt and Satır, 2000) the MMM affected the whole massif (both 'core' and 'cover' rocks), with HT conditions in some nappes of the lower parts of the massif and greenschist-facies conditions in the upper lithologies of the 'cover'. The question arises here of the relationship between the presently described HP-LT metamorphic imprint and the MMM. Assuming the generally accepted description of a stratigraphic continuity between all lithological formations that constitute the 'cover' series, the lack of HP signature in the Palaeozoic schist envelope closer to the core-cover contact has to be discussed. Either HP assemblages (for instance carpholite-bearing assemblages) are preserved in the schist envelope although they have still not been found, or the HP metamorphic history of the schist envelope has been completely overprinted by the MMM characterized by higher temperature conditions approaching the core-cover contact. Another possibility, which is perhaps the most realistic, is to consider rock chemistry restrictions responsible for this lack of HP imprint in the Paleozoic schists. Magnesiocarpholite growth depends on the Al-, Na- and K- contents in metasediments. At the lowest pressure conditions of the Fe-Mg-carpholite stability field, Fe-Mg-carpholite can only appear in rocks containing an Alumino-silicate (kaolinite, pyrophyllite or kyanite). At these conditions ($P<13$ kbar), an Al-poor and/or Na- and K-rich sediment chemistry precludes its growth. This is the case for the Paleozoic garnet-biotite-bearing schists containing for instance pure albite that might have prevented magnesiocarpholite growth. In Al-depleted rocks, Fe-Mg-carpholite can only appear at higher pressure (>13 kbar) for K-rich sediments, and at very high-pressure conditions (>18 kbar) for Na-rich sediments (Agard, 1999).

As seen in Figure III-17b, the HP metamorphism that affected the Menderes 'Cover' and the MMM could have occurred roughly at the same time. If the HP event is post-MMM it can be postulated that the HP was recorded only in rocks in which the Barrovian-type MMM imprint was weak. On the contrary, if HP conditions predate the MMM, as envisaged before, it is possible that they were preserved only in this part of the cover because the MMM was characterized by lower temperature conditions there. In any case, the temporal relations between the HP and the MMM need further studies.

Furthermore, in the HP metaconglomerate, magnesiocarpholite has only been found as relicts in quartz segregations and not in the associated micaschists. Indeed, while magnesiocarpholite appears as relicts in any quartz segregation, it is generally never found in the surrounding schist because its breakdown is instantaneous in this lithology. This is a common observation for carpholite-bearing rocks in HP metamorphic belts (e.g. Goffé and Oberhänsli, 1992), and was particularly well described for the magnesiocarpholite-kyanite assemblages from the Betic Cordillera (Azañon and Goffé, 1997).

Retrogression of HP parageneses from the Menderes Massif indicates an isothermal decompression path. The exhumation of the MMM is well constrained with cooling ages of about 35 Ma (Satır and Friedrichsen, 1986; Lips et al., 2001). Higher in the nappe stack, the high degree of preservation of Fe-Mg-carpholite in the Lycian Nappes suggests a colder retrograde path (Figure III-17b) that is consistent with the exhumation of an orogenic wedge.

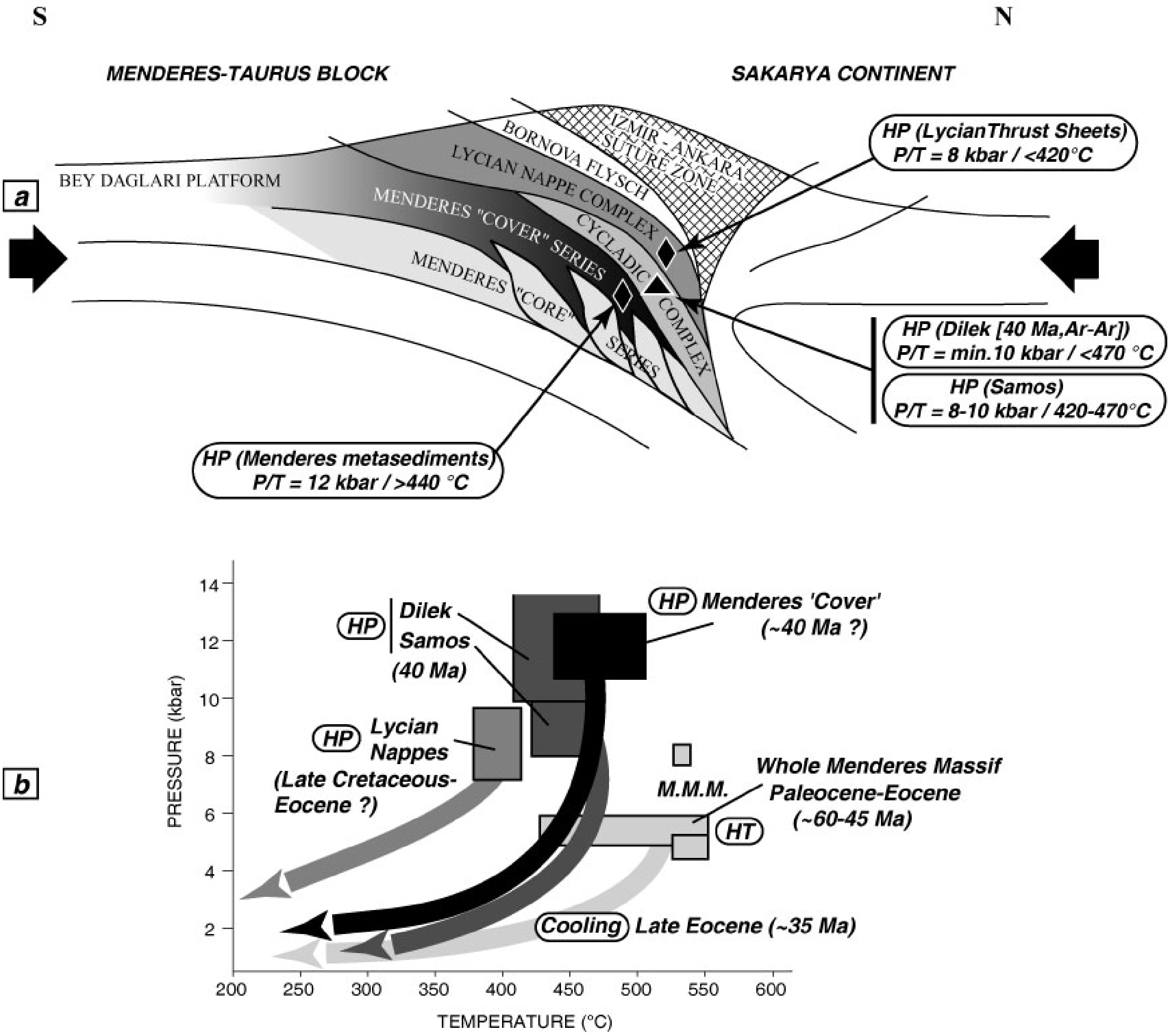

Figure III-17. (a) Schematic interpretative view of the accretionary complex during the Eocene time showing the structural position of the main HP units. The estimated P-T conditions for each HP parageneses are reported. (b) Synthetic P-T-t-diagram showing the pressure-temperature conditions during the metamorphic peaks, and the retrograde paths for each metamorphic unit of SW Turkey (see text for references).

6. Deformation related to metamorphism

Nappe stacking in the Menderes Massif is considered by most authors as the result of N-S contraction coeval with the regional MMM. However, different interpretations have been proposed for the Alpine deformation of the Menderes Massif. Some authors claim that a north-south trending stretching and kinematic indicators showing movements top-to-the-NNE are coeval with folding and thrusting during MMM (Hetzel, 1995; Hetzel et al., 1998; Bozkurt and Park, 1999; Whitney and Bozkurt, 2002) and subsequently cooling (Late Eocene; Lips et al., 2001). It has been proposed that these top-to-the-N fabrics are related to a northward backthrusting of the Lycian Nappes (Bozkurt and Park, 1999). All these syn-metamorphic structures were later overprinted by top-to-the-south greenschist shear bands during exhumation (Whitney and Bozkurt, 2002). In contrast, other studies led to propose that the chloritic top-to-the-south shear bands that crosscut the earlier fabrics in both 'core' and 'cover' units are the main Alpine contractional structures, the top-to-the-north structures being Pan-African in age (Ring et al., 1999a; Gessner et al., 2001a,b).

The deformation during the HP event and its exhumation is characterized by a severe N-S to NE-SW stretching in the HP metaconglomerate. The NE-SW stretching and top-to-the-NE kinematic indicators observed continuously at the base of the Lycian Nappes and in the uppermost levels of the metasedimentary envelope of the massif suggest that the contact between the Menderes Massif and the Lycian Nappes has been reactivated as a top-to-the-NE shear zone during retrogression of HP parageneses (as discussed in Chapter II), subsequently to the southward emplacement of the Lycian nappe complex (Figure III-16). The Menderes/Lycian contact is therefore a syn-metamorphic boundary at least during the retrograde path. The deformation during the prograde path is not well preserved except in the uppermost lithologies of the Lycian Thrust Sheets which display top-to-the-south shearing compatible with the classically admitted southward translation of the Lycian Nappes over the Menderes Massif (de Graciansky, 1972; Dürr, 1975; Dürr et al., 1978; Gutnic et al., 1979; Şengör and Yılmaz, 1981; Okay, 1989b; Collins and Robertson, 1997; 1998; 1999).

7. Towards a tectono-metamorphic model

It seems therefore reasonable to propose a model in three main episodes:

A first stage during which the HP Lycian Nappes were transported southward over the Menderes Massif (Figure III-16), preserving their HP-LT metamorphism, probably generated to the north of the present position of the Menderes Massif during the Late Cretaceous-Eocene (?). The Menderes (and Cycladic) metasediments must have been buried beneath at least 30 km of material during the Eocene to allow HP assemblages such as magnesiocarpholite-kyanite.

The second episode during the continuing Eocene contraction is characterised by top-to-the-N movements (Figure III-16) documented by north-verging folding, shearing, thrusting, imbrication of 'core' and 'cover' series. Top-to-the-north fabrics were recorded in the augen gneisses and in the Palaeozoic metasediments of the massif and are associated with the MMM peak (between the Paleocene and the Eocene) and its progressive cooling (Late Eocene), and an intense N-S to NE-SW stretching was recorded in the HP metaconglomerate of the 'cover' series. All these movements are probably due to a northward backthrusting of the Lycian Nappes over the Menderes Massif, reactivating the Menderes/Lycian contact as a top-to-the-NE shear zone that allowed exhumation of the Lycian HP rocks. The presence of Fe-Mg-carpholite-bearing Lycian units overlying the low-grade metamorphic olistostromal unit of the Menderes Massif implies that the reactivation of the Lycian/Menderes contact postdates the HP metamorphic peak. This favours the idea of a backthrusting of the Lycian Nappes over the Menderes Massif.

Finally, the third stage corresponds to the Oligo-Miocene N-S bivergent extension (Hetzel et al., 1995) during which the final exhumation of the metamorphic rocks occurred along kilometre-scale low-angle detachments. In the southern submassif, the top-to-the-N fabrics were overprinted by top-to-the-south chloritic shear-bands during late exhumation stages (Figure III-16; Whitney and Bozkurt, 2002).

It is here claimed that all these north- to northeast-verging structures have a strongly consistent orientation throughout the whole study area and must have been generated by a northward continuum of deformation (Eocene) during contractional episodes that allowed HP metamorphism in the Menderes Massif and its first stages of exhumation.

CHAPTER IV

EXHUMATION OF THE HP-LT ROCKS FROM THE LYCIAN NAPPES AND THE MENDERES MASSIF: A MULTI-EQUILIBRIUM APPROACH AND FISSION TRACK DATA

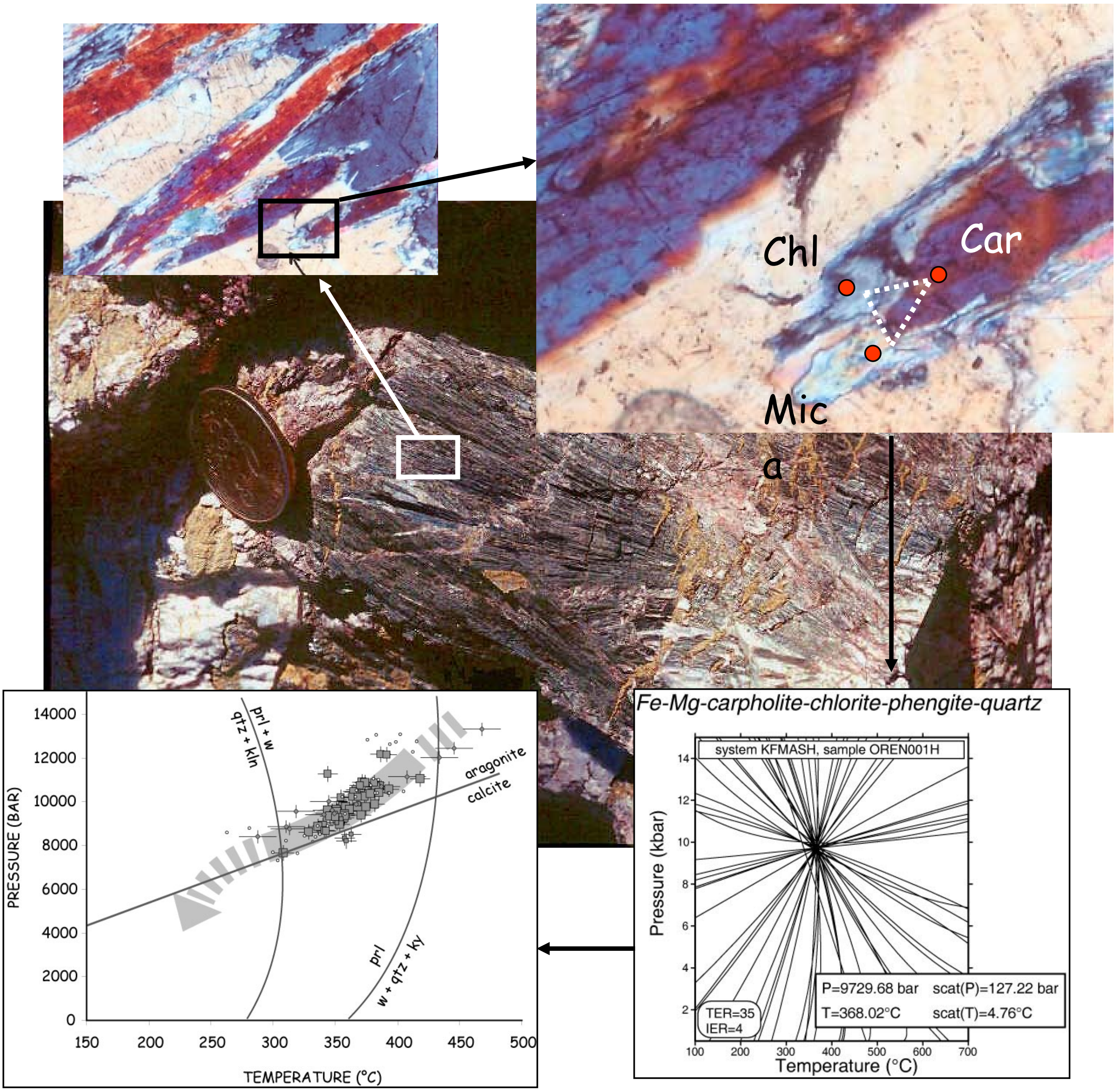

As previously exposed, the recent discovery of HP-LT metamorphic rocks documented by Fe-Mg-carpholite occurrences within the Lycian Nappes and the Menderes Massif led to reconsider the tectono-metamorphic evolution of this region. Evidence for Alpine HP-LT metamorphism in both nappe complexes suggests an important burial (at least 30 km) during formation of the accretionary complex.

Whereas P-T conditions of the metamorphic peaks for the Menderes HP rocks (minimum 10 kbar/minimum 440°C; seen in Chapter III) and the Lycian HP metasediments (minimum 8 kbar/maximum 400°C; seen in Chapter II) can easily be estimated from the composition of metamorphic index minerals (Figure IV-1), detailed and precise retrograde P-T paths reflecting the tectonic mechanisms responsible for exhumation are rather difficult to constrain. Indeed, the determination of P-T conditions of metamorphism is generally based on the presence or absence of index minerals. However, changes in mineralogy are discontinuous processes, and therefore the appearance or disappearance of index minerals can only provide information on the maximal or minimal P-T conditions of metamorphism. The final part of the P-T history (i.e. greenschist-facies conditions) is particularly impossible to constrain because of very few or no mineralogical changes occur. A continuous determination of P-T path must therefore rely on the progressive change of mineral composition with P-T conditions or on the use of different generations of the same minerals showing different compositions, when their relative time of growth can be recognized in a single thin section (local equilibrium). Recent studies have shown that in low- to medium-grade garnet-free metapelites, K-white mica (KWM) and chlorite local equilibria are good candidates to constrain the retrograde P-T evolution of exhumed metamorphic rocks (Vidal and Parra, 2000).

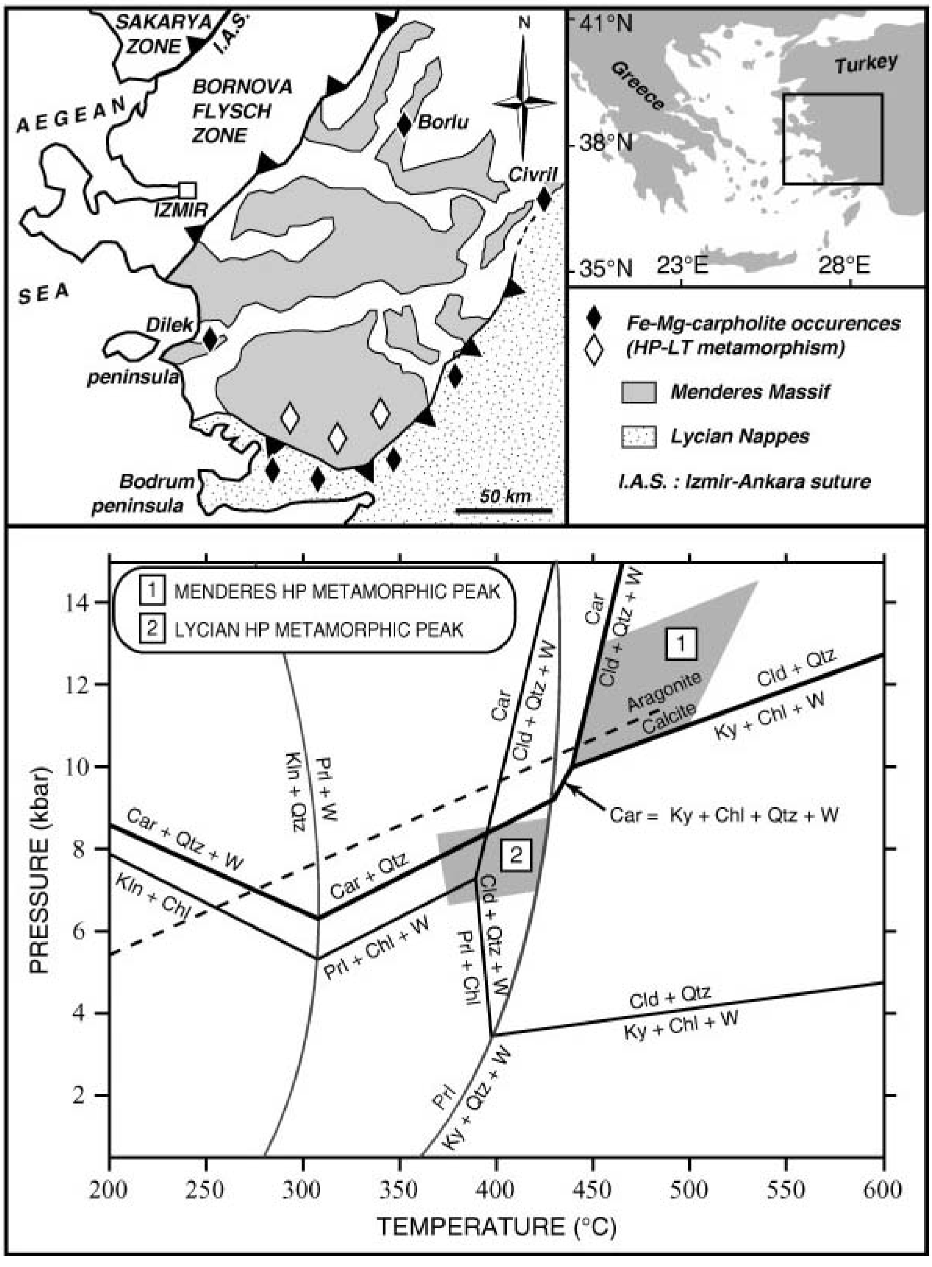

Figure IV-1. Above: simplified map showing the occurrences of Fe-Mg-carpholite-bearing rocks in southwest Turkey. Black diamonds correspond to Fe-Mg-carpholite localities in the Lycian Nappes (s.s. and klippen; Oberhänsli et al., 2001; Rimmelé et al., 2001; Rimmelé et al., 2003) and white diamonds locate magnesiocarpholite occurrences in the Menderes Massif (Rimmelé et al., 2002; Rimmelé et al., in press). Below: PT diagram showing location of metamorphic peak conditions estimated for parageneses involving Fe-Mg-carpholite in the Lycian Nappes (Oberhänsli et al., 2001) and the Menderes Massif (Rimmelé et al., in press). Abbreviations: W, Water; Qtz, Quartz; Car, Fe-Mg-carpholite; Cld, Chloritoid; Chl, Chlorite; Kln, Kaolinite; Prl, Pyrophyllite; Ky, Kyanite.

Furthermore, as the HP rocks of SW Turkey passed through the apatite fission-track partial annealing temperature window of about 125° to 60°C during exhumation, the fission track clock was reset to zero. Fission track data therefore recorded information on the time-temperature cooling path of the exhumed rocks.

In this chapter, I first present the multi-equilibrium calculation method that allowed to get precise information on the exhumation processes of the Lycian and Menderes HP-LT rocks, then I shortly report fission-track data obtained for these rocks.

Part of the data exposed in this chapter belongs to a paper submitted in '**Journal of Petrology**' and entitled **"Exhumation paths of high-pressure low-temperature rocks from the Lycian Nappes and the Menderes Massif (SW Turkey): a multi-equilibrium approach"** (by Rimmelé G., Parra T., Goffé B., Oberhänsli R., Jolivet L., and Candan O.).

A. EXHUMATION PATHS OF THE HP ROCKS FROM THE LYCIAN NAPPES AND THE SOUTHERN MENDERES MASSIF - MULTI-EQUILIBRIUM CALCULATIONS

1. Reminders on the regional distribution of HP assemblages

In the whole region, samples were collected from about 300 outcrops in order to describe the different parageneses involved in these HP rocks. They were mainly collected in the HP Karaova formation of the Lycian Nappes and in the HP metaconglomerate of the Menderes Massif.

a. In the Lycian Nappes

Fe-Mg-carpholite and its retrogression products occur only at the base of the Lycian Nappes, within the metapelitic Karaova formation. They are widespread on the Bodrum peninsula, between Güllük and Yaras (Figure IV-2), and were locally found in a few klippen of Lycian Nappes which crop out at the top of the Menderes metamorphic rocks.

As said in Chapter II, on the Bodrum peninsula, the distribution of HP index minerals is not uniform (Figure IV-2). Well-preserved Fe-Mg-carpholite was widely found between Ören and Demirciler and commonly appears as centimetre to decimetre-scale fibres in quartz segregations. It has also been observed within large crystals of calcite. However, in the lowermost parts of the pelitic sequence, close to the contact with the Menderes Massif, Fe-Mg-carpholite only appears as being partly to totally retrogressed into chlorite and pyrophyllite or into chlorite and phengite (e.g. near Güllük, Gerit or Ula). Chloritoid commonly occurs within the mineral foliation throughout the peninsula. It has also been found associated with Fe-Mg-carpholite in quartz segregations in the area of Ören.

In the Dilek peninsula region (Figure IV-1) where the two klippen of Lycian Nappes crop out on top of the Selçuk formation, local outcrops of the Karaova formation are exposed. At the base of the northern klippe, near the village of Kirazlı (Figure II-22a), the strongly deformed chloritoid-bearing metapelites of the Karaova formation revealed only occurrences of carpholite pseudomorphs, right at the contact with the rocks of the Menderes Massif. On the contrary, in the southern slice of Lycian Nappes (south of Tirhaköy; Figure II-22b), at unknown distance from the Lycian/Menderes contact, fresh Fe-Mg-carpholite occurs in quartz segregations within the reddish-greenish phyllites of the Karaova formation.

b. In the southern Menderes Massif

As described in Chapter III, in the southern Menderes Massif, magnesiocarpholite occurrences have been found in three localities, where the Late Triassic metaconglomerate of the 'cover' series crops out just below a thick marble sequence (Figure IV-2). South of the Bafa Lake, close to the village of Kurudere, magnesiocarpholite-kyanite-chlorite-quartz assemblages were identified within synfolial quartz veins. Magnesiocarpholite is partially preserved as relic hair-like microfibers within quartz in contact with kyanite. Elsewhere, it is commonly replaced by chlorite and kyanite. Chloritoid occurrence was not identified in this area. On the contrary, we found magnesiocarpholite-chloritoid-sudoite-quartz assemblages farther east, southwest of Bahçeyaka. Chloritoid results from the breakdown of magnesiocarpholite which is only preserved within quartz. Finally, east of Nebiler, we found chloritoid-kyanite-chlorite-quartz assemblages and kyanite-chlorite-quartz assemblages. In this area, prismatic aggregates of chlorite and kyanite have been identified as complete pseudomorphs of magnesiocarpholite. In the three areas, pyrophyllite and phengite are commonly associated with these HP-LT assemblages.

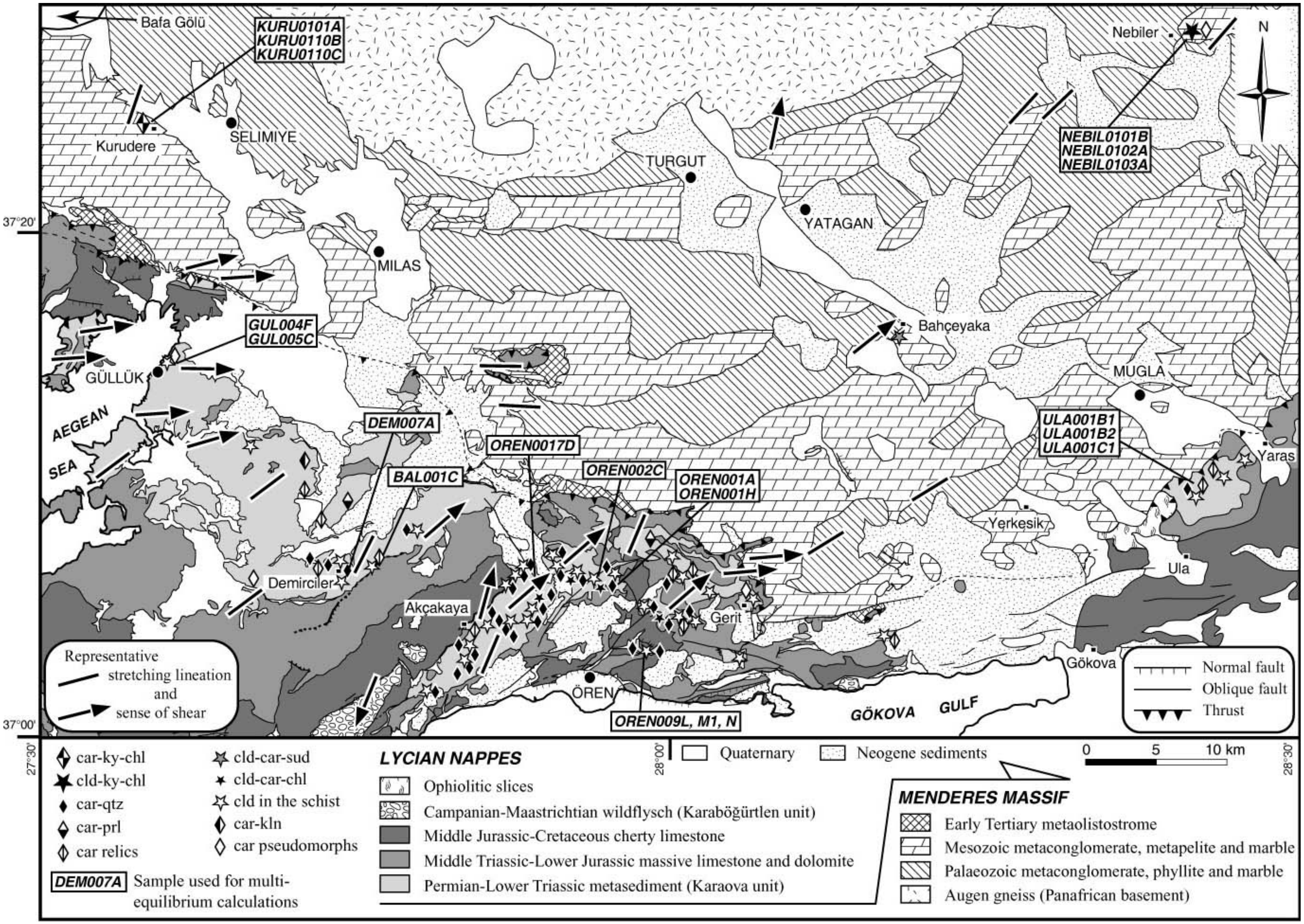

Figure IV-2. Simplified tectono-metamorphic map showing the distribution of HP assemblages and associated deformation in the Bodrum peninsula region (geological setting simplified after Çağlayan et al., 1980; Konak et al., 1987; Candan and Dora, 1998; and Konak and Akdeniz [unpublished geological maps of M.T.A.-Turkey]; tectonometamorphic data after Rimmelé et al., 2003; and Rimmelé et al., in press). Samples used for multi-equilibrium calculation are located on the map. Abbreviations: car, Fe-Mg-carpholite; cld, chloritoid; chl, chlorite; sud, sudoite; kln, kaolinite; prl, pyrophyllite; ky, kyanite; qtz, quartz.

2. Mineral compositions in HP rocks

About 50 samples have been analysed in the whole study area and 23 of them were used for multi-equilibrium calculations. Only the latter are reported in Figures IV-2 and II-22. The 50 samples are from the Karaova formation of the Lycian Nappes and the metaconglomerate of the Menderes 'cover' sequence which both contain HP relics.

a. Fe-Mg-carpholite

Analyses showing an oxide sum lower than 85 wt% or greater than 90 wt% were rejected. The composition domains of Fe-Mg-carpholite from the Lycian Nappes and the Menderes Massif are reported in Figure IV-3a as a synthesis of what was described in more detail in the previous Chapters II and III (Figures II-6a, II-25a and III-8a,b).

In the Lycian Nappes, Fe-Mg-carpholite composition is variable as shown by X_{Mg} [X_{Mg} =Mg/(Mg + Fe$^{(2+)}$ + Mn)] values roughly ranging from 0.4 to 0.7. The Mn content in Fe-Mg-carpholite is very low ($0<X_{Mn}<0.03$) for all samples.

In the Menderes Massif, compositions of magnesiocarpholite are characterized by X_{Mg} values ranging from 0.65 to 0.90, and show a higher Mn-content than in the Lycian Nappes (X_{Mn} reaching 0.25).

b. Chloritoid

Analyses showing an oxide sum lower than 90 wt% or greater than 94 wt% were rejected. As for Fe-Mg-carpholite, chloritoid compositions from the Lycian Nappes and the Menderes Massif are synthesised in Figure IV-3b (for details, refer to Figures II-6b, II-25b, and III-8c,d).

The samples from the Karaova formation of the Lycian Nappes show X_{Mg} [X_{Mg} =Mg/(Mg + Fe$^{(2+)}$ + Mn)] values roughly comprised between 0.1 and 0.2 in the whole region. As for the Lycian Fe-Mg-carpholite, the X_{Mn} does not exceed 3%.

The chemical composition of chloritoid from the Menderes HP rocks is rather different from the latter, showing higher values of X_{Mg} (X_{Mg}~0.45) and X_{Mn} (X_{Mn}~0.25).

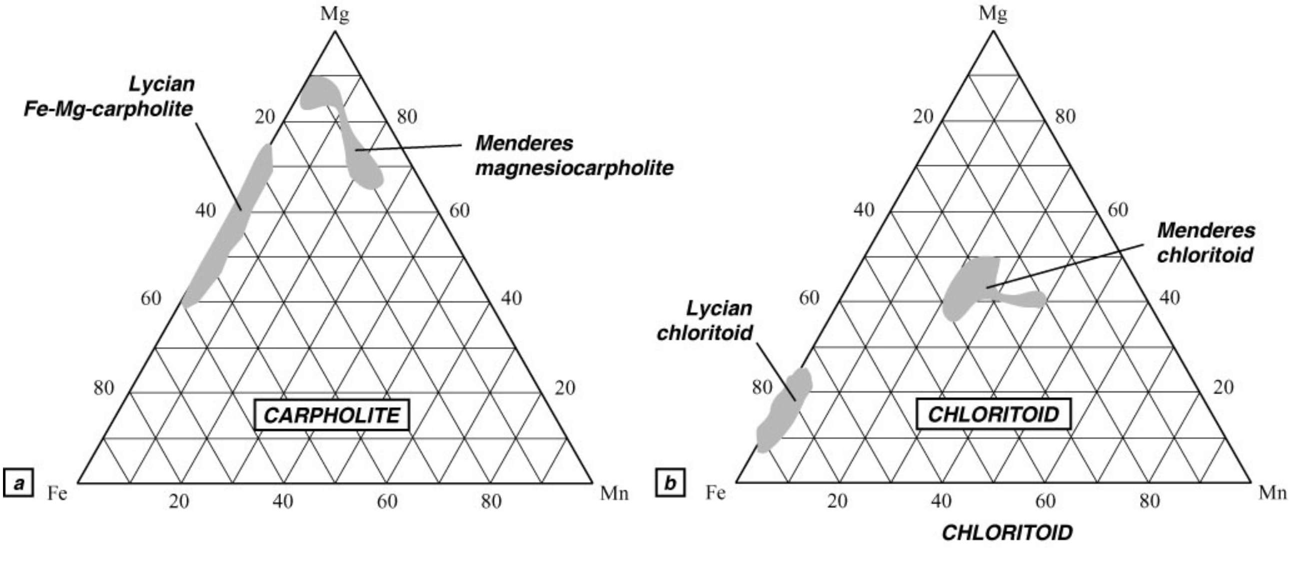

Figure IV-3. Fe-Mn-Mg-ternary diagrams showing composition domains of Fe-Mg-carpholite (a) and chloritoid (b) from the Lycian Nappes and the Menderes Massif.

c. Chlorite, white mica and pyrophyllite

Structural formulae are calculated on the basis of 14 oxygens for chlorite and 11 for white mica. We only retained chlorite and white mica analyses with an oxide sum ranging respectively between 83 wt% and 89.5 wt% and between 92 wt% and 97 wt%. In order to decrease the risk of using KWM and chlorite analyses with significant contaminations or alkali loss, we only retained the analyses which respect chemical criteria reported in Vidal and Parra (2000) [see Appendix A]. Chlorite analyses showing more than 0.5% (Na_2O+K_2O+CaO) and more than 0.1% K_2O were rejected, as well as white mica analyses showing more than 0.5% (MnO+TiO_2+Cl). Finally, only the compositions of chlorites and phengites that could be expressed as linear combinations of the following end-members were retained: clinochlore $Si_3Al_2Mg_5O_{10}(OH)_8$, daphnite $Si_3Al_2Fe_5O_{10}(OH)_8$, (Fe,Mg)-amesite $Si_2Al_4(Mg,Fe)_4O_{10}(OH)_8$, and sudoite $Si_3Al_4(Mg,Fe)_2O_{10}(OH)_8$ for chlorites; and (Fe,Mg)-celadonite $Si_4Al(Mg,Fe)KO_{10}(OH)_2$, muscovite $Si_3Al_3KO_{10}(OH)_2$, paragonite $NaSi_3Al_3O_{10}(OH)_2$, pyrophyllite $Si_4Al_2O_{10}(OH)_2$, and biotite $Si_3Al(Mg,Fe)_3KO_{10}(OH)_2$ for micas.

- Chlorite compositions

Variations of chlorite compositions are mainly due to three major substitutions, the $FeMg_{-1}$ (FM) substitution, the Tschermak (TK) substitution between clinochlore-daphnite and (Mg,Fe)-amesite $[Al^{IV}Al^{VI}Si_{-1}(Mg,Fe)_{-1}]$, and the di-trioctahedral (DT) substitution between clinochlore-daphnite and (Mg,Fe)-sudoite $[(Mg,Fe)_3V_{-1}Al_{-2}$, with V=vacancy] (see Appendix A). The extent of substitutions depends on the metamorphic PT conditions and on the bulk rock chemistry (Vidal et al., 2001). No data are available on the whole rock chemistry of the Lycian HP metasediments and the HP metaconglomerate of the Menderes Massif. However, based on mineralogical observations (assemblages, modes, mineral chemistry), we imply that rocks from the Karaova formation of the Lycian Nappes, as well as the HP metaconglomerate of the Menderes 'cover' series, have a roughly constant chemical composition throughout the study area.

Chlorite and sudoite analyses in samples from the Lycian Karaova formation and the metaconglomerate of the Menderes Massif (Figure IV-4) are plotted in (clinochlore-daphnite)-amesite-sudoite ternary diagrams and in Si versus X_{Mg} diagrams. These representations highlight the extent of the TK, DT and FM substitutions (Figure IV-4a).

Chlorites from the Lycian Nappes have a composition trending between the amesite and the clinochlore-daphnite end-members (Figure IV-4b). The sudoite-content roughly ranges between 10 and 30 mol%, except for some analyses that reach 60 mol%. Figure IV-4c shows X_{Mg} values $[X_{Mg}=Mg/(Mg+Fe^{(2+)}+Mn]$ ranging between 0.35 and 0.75 and Si-contents between 2.5 and 3 a.p.f.u. The chlorite analyses from the Güllük region are Fe-richer than those from other areas ($0.35<X_{Mg}<0.45$).

Sudoite compositions have a Si-content ranging between 3 and 3.2 a.p.f.u. and X_{Mg} values between 0.75 and 0.8 (Figure IV-4d).

In the HP rocks from the Menderes Massif, chlorite compositions exhibit smaller variations of TK, DT and FM substitutions than those from the Lycian Nappes, although the dataset of chlorite analyses in samples from the Menderes Massif is smaller than that of the Lycian Nappes. Compositions are closer to the clinochlore-daphnite end-member, with a smaller sudoite-content (Figure IV-4e). The Si-content ranges between 2.6 and 2.8 a.p.f.u. and the X_{Mg} values cluster between 0.8 and 0.9 (Figure IV-4f).

The very few sudoite analyses show a Si-content around 3.1 a.p.f.u. The X_{Mg} is about 0.9 (Figure IV-4g).

- White mica and pyrophyllite compositions

Variations of K-white mica compositions are essentially a function of the $FeMg_{-1}$ substitution (FM), the Tschermak substitution (TK) between muscovite and (Mg,Fe)-celadonite $[Al^{IV}Al^{VI}Si_{-1}(Mg,Fe)_{-1}]$, the pyrophyllitic substitution (P) between muscovite and pyrophyllite ($KAlSi_{-1}V_{-1}$), and the paragonitic substitution (Pa) between muscovite and paragonite (NaK_{-1}) (see Appendix A). The extent of substitutions in micas also depends on the PT conditions as well as on the rock chemistry (Parra et al., 2002a).

Two white micas have been recognized in the Menderes Massif and the Lycian Nappes: KWM and paragonite. Paragonite has been detected with XRD analyses. X-rays diffractograms revealed very low quantities of this sodic mica in only a few samples. Pyrophyllite also occurs in the samples collected in both Lycian Nappes and Menderes Massif.

Analyses of white mica and pyrophyllite in samples from the Lycian Nappes and the Menderes Massif are plotted in pyrophyllite-celadonite-muscovite and pyrophyllite-paragonite-muscovite ternary diagrams showing the extent of the TK, P and Pa substitutions (Figure IV-5a).

For the Karaova formation of the Lycian Nappes, Figure IV-5b shows that the pyrophyllite-content in KWM can reach high values (~40 mol%) while the celadonite-content [Si- and (Fe+Mg)- contents) is not higher than 10 mol%. The paragonitic-content in KWM is always low (mainly <20 mol%) (Figure IV-5c). Pyrophyllite compositions are also reported in Figure IV-5c.

In the Menderes metaconglomerate, phengites have a lower pyrophyllite-content than in the Lycian Nappes (between 0 and 30 mol%) whereas the celadonite- and muscovite-contents are higher (Figure IV-5d). As for the Lycian Nappes, phengites have a low paragonitic-content (between 10 and 20 mol%) (Figure IV-5e). Compositions of pyrophyllite are also plotted in Figure IV-5e.

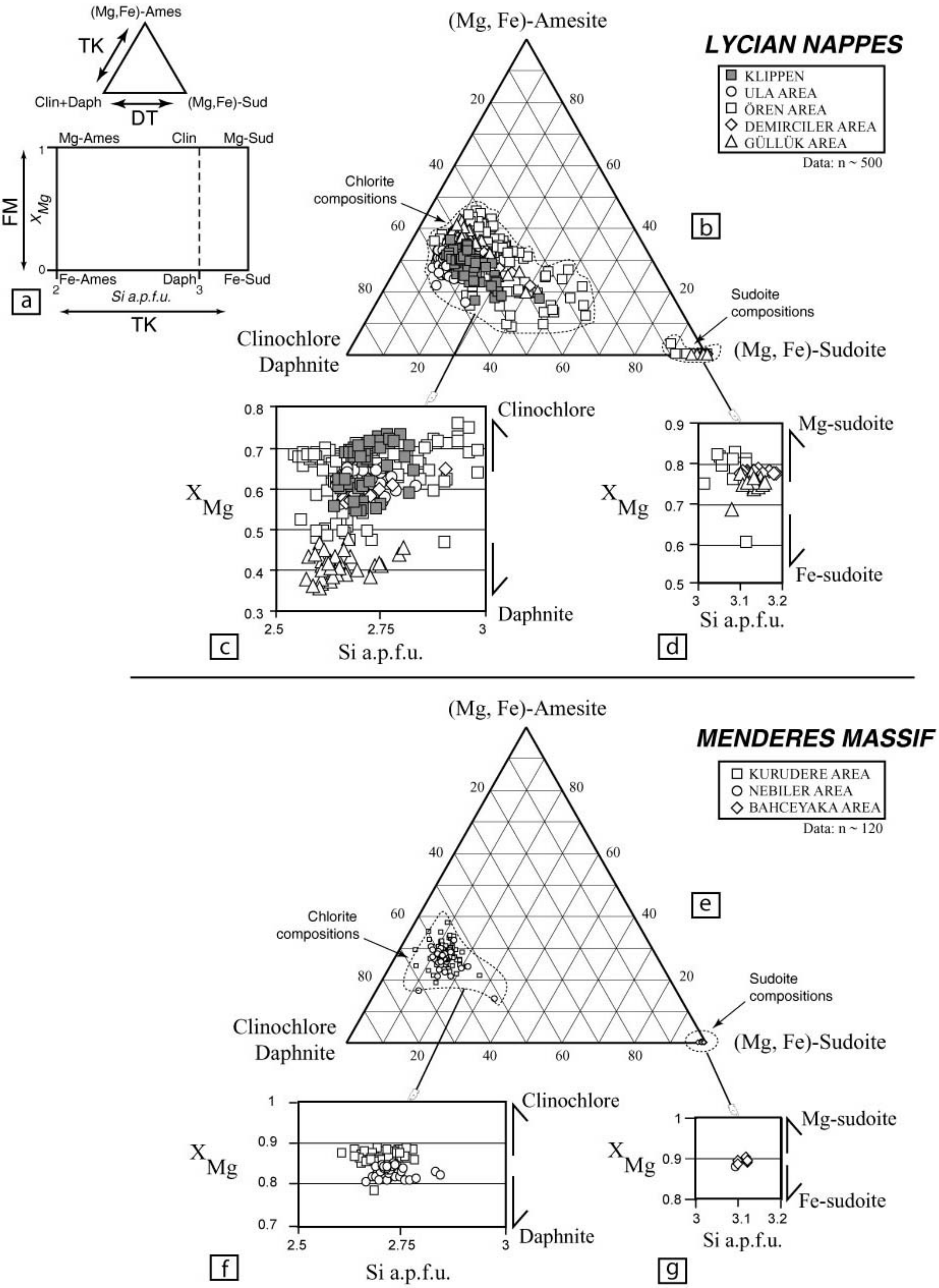

Figure IV-4. (a) Diagrams showing the three systematic main substitutions between the chlorite end-members (TK, Tschermak substitution; DT, di-trioctahedral; FM, $FeMg_{-1}$ substitution). (b) Chemical variability of chlorite and sudoite from the Lycian Nappes due to the TK and DT substitutions. Compositional variability of chlorite (c) and sudoite (d) from the Lycian Nappes due to the TK and FM substitutions. (e) Compositional variability of chlorite and sudoite from the Menderes Massif due to the TK and DT substitutions. Compositional variability of chlorite (f) and sudoite (g) from the Menderes Massif due to the TK and FM substitutions.

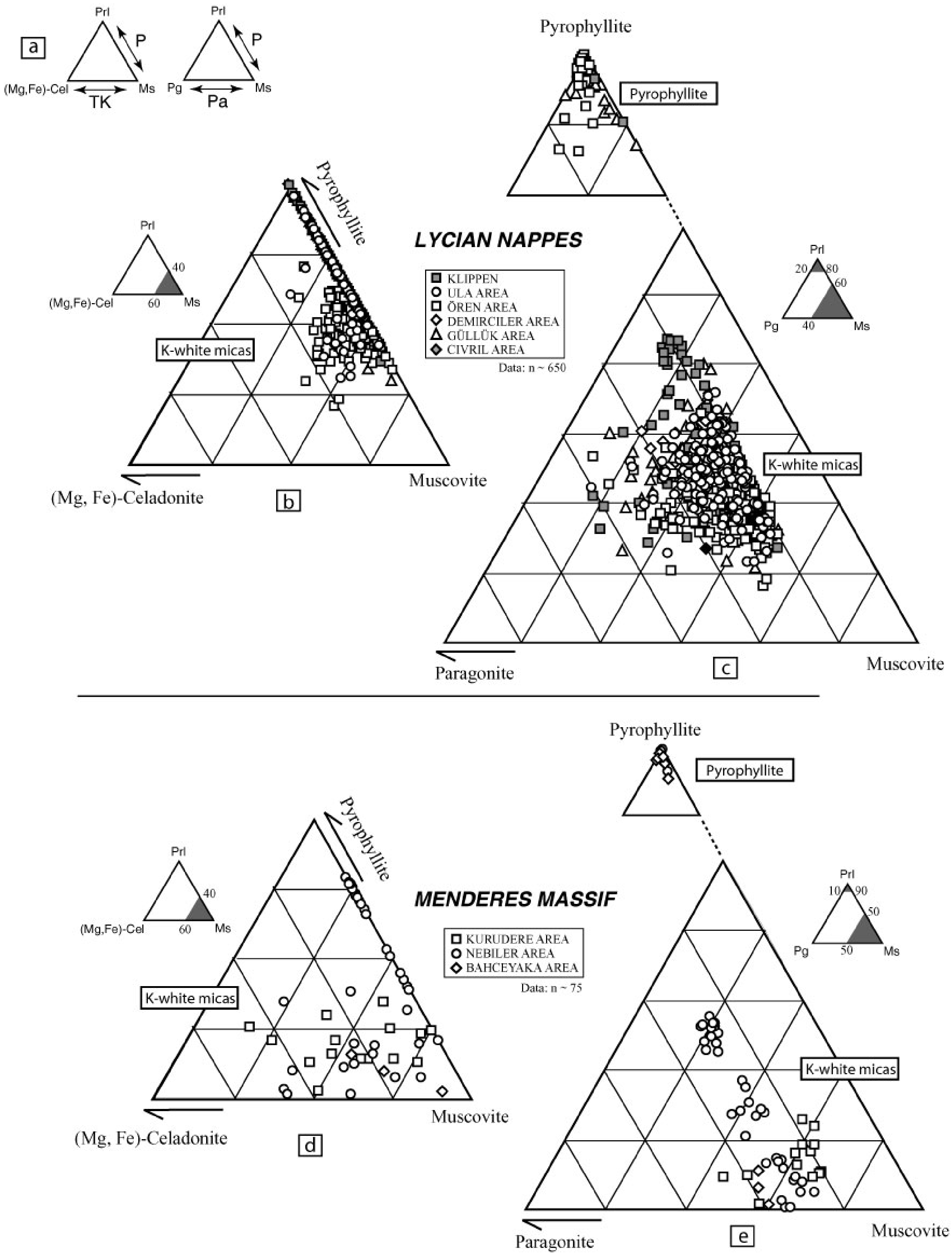

Figure IV-5. (a) Ternary diagrams showing the systematic Tschermak (TK), pyrophyllitic (P) and paragonitic (Pa) substitutions in K- and Na-white micas (abbreviations: Prl, pyrophyllite; Ms, muscovite; (Mg-Fe)-Cel, celadonite; Pg, paragonite). Compositional variability of K-white micas from the Lycian Nappes due to the TK and P substitutions (b) and to the P and Pa substitutions (c). Pyrophyllite compositions from the Lycian Nappes are also reported in Figure (c). Compositional variability of K-white micas from the Menderes Massif due to the TK and P substitutions (d) and to the P and Pa substitutions (e). Pyrophyllite compositions from the Menderes Massif are also plotted in Figure (e).

3. Interpretation in terms of P-T evolution

As said above, Fe-Mg-carpholite and chloritoid compositions in the Lycian Nappes show lower X_{Mg} values than in the Menderes Massif (Figure IV-3), which document higher P-T conditions in the Menderes Massif than in the Lycian Nappes. Furthermore, in the Lycian Nappes, Fe-Mg-carpholite is mainly associated with pyrophyllite whereas it forms assemblages with kyanite in the Menderes Massif, which also suggests higher temperature conditions. The sudoite-content in chlorite from the Lycian Nappes is higher than in those from the Menderes Massif (Figure IV-4), which also documents lower temperature conditions for the Lycian HP metamorphism. The higher pyrophyllite-content and lower muscovite-content in phengites of the Lycian Nappes than in those from the Menderes Massif also suggests lower PT conditions for the Lycian Nappes (Figure IV-5). Furthermore, the TK substitution between muscovite and celadonite has a slightly wider extend in the Menderes metaconglomerate than in the Lycian metasediments (Figures IV-5b,d), thus indicating higher pressure conditions for the Menderes HP rocks than for the Lycian metamorphic rocks. These differences in the mineral compositions from the Lycian Nappes and the Menderes Massif clearly point to different metamorphic conditions in the two massifs. However, the combination of these mineral composition variations at the local equilibria-scale provides a better-constrained picture of the PT conditions reached during HP metamorphism and its exhumation.

4. Sampling for PT estimates based on multi-equilibrium calculations

In the study area, 23 samples collected in the HP Karaova formation of the Lycian Nappes and in the HP metaconglomerate of the Menderes Massif were used to constrain PT estimates based on multi-equilibrium calculations. Locations of these samples are reported in Figures IV-2 and II-22. All samples have been analysed by X-ray diffraction method (Siemens, D5005 model, University of Potsdam, Germany). The different parageneses and relict minerals for each thin section are listed in Figure IV-6.

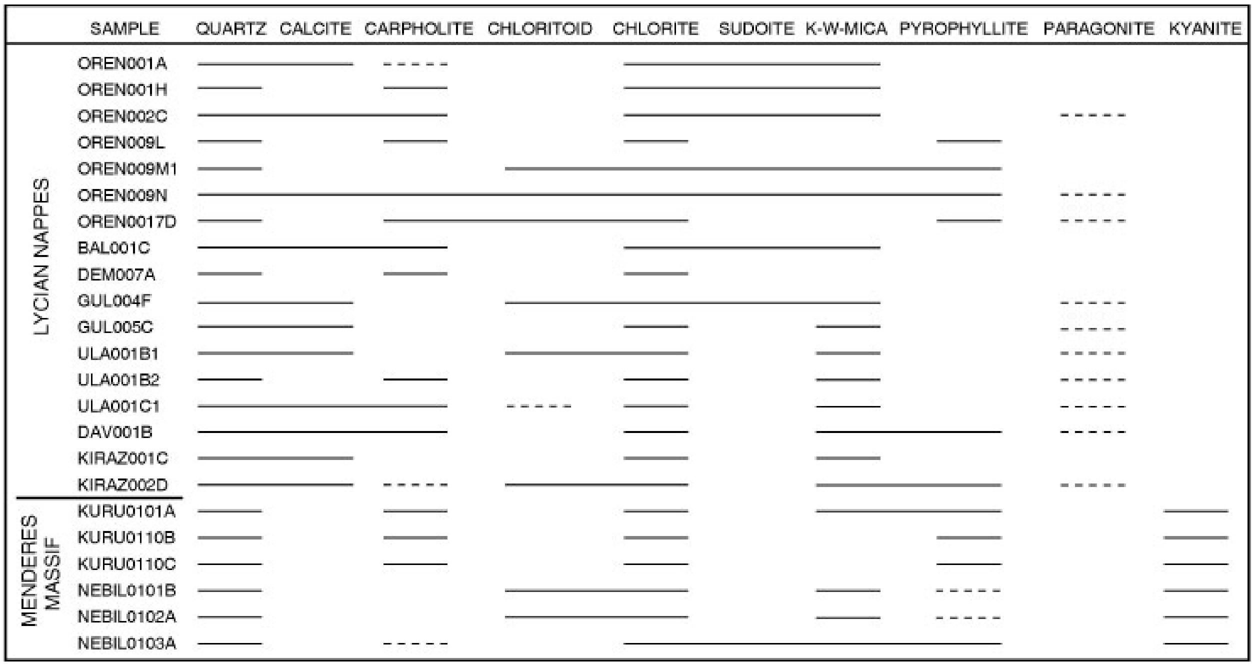

Figure IV-6. Parageneses and relict minerals in the samples used for multi-equilibrium calculations.

5. Thermodynamic data and solid-solution properties

The thermodynamic dataset and solid-solution properties used in this work are from the TWEEQ (Thermobarometry With Estimation of EQuilibration state; Berman, 1991) updated database of Berman (1988). For the following minerals, external data were included: chlorite (Vidal et al., 2001), sudoite (Vidal et al., 1992), KWM (Parra et al., 2002a), Fe-Mg-carpholite (Vidal et al., 1992), and chloritoid (Mg-chloritoid from Vidal et al., 2001; Fe-chloritoid from Vidal et al., 1994). Activities of Fe-Mg-carpholite were calculated after Vidal et al. (1992) [$a_{(car)}=(X_{Mg})(X_{Al})^2(X_{OH})^4$ with $X_{Mg}=Mg/(Mg+Fe^{2+}+Mn)$, $X_{Al}=(2-Fe^{3+})/2$ and $X_{OH}=(4-F)/4$]. The X_{Mg} and X_{Fe} of chloritoid were calculated considering the Mn content

[$X_{Mg}=Mg/(Mg+Fe^{2+}+Mn)$ and $X_{Fe}=Fe/(Mg+Fe^{2+}+Mn)$], and activities are from Vidal et al. (1994) ($a_{[Mg\text{-}Cld]}=X_{Mg}$ and $a_{[Fe\text{-}Cld]}=X_{Fe}$). Since thermodynamic data for Fe-amesite are unpublished and still provisory (Vidal and Parra, pers. comm.), I did not take into account this end-member for calculations.

6. Method of the multi-equilibrium calculations

This paragraph sums up the principles of the method that are exposed in more detail in Appendix A.

The calculation procedure is a systematic method that allows to obtain simultaneous estimates of P and T using a small number of phases which are systematically present in the studied thin sections, and to check for equilibrium. It is based on the notion of "multi-equilibrium calculations" (Berman, 1991), which requires the assumption of local equilibrium and the use of solid-solution models and thermodynamic data for minerals characterized by compositional variations. The method consists in the plot of all the equilibrium reactions (TER, Total Equilibrium Reactions) calculated with the end-members (EM) used for example to describe the composition of chlorite and phengite (often associated with other minerals). Increasing the number of EM to express the compositional variability of chlorite, KWM and other associated minerals allows one to increase the number of TER that can be computed for a given paragenesis involving these minerals, and therefore the number of linearly independent equilibrium reactions (IER) (Vidal and Parra, 2000; Vidal et al., 2001; Parra et al., 2002a; Parra et al., 2002b) (Figure IV-7).

The pairs or triplets used to perform the calculations were first selected using classical microtextural criteria suggesting equilibrium state. In particular, the assemblage-forming minerals must be in contact and be involved in the same microstructure as shown in Figure IV-7. In this case, pairs or triplets of minerals are thought to have grown at the same time.

Assuming that the standard state thermodynamic data as well as the activity-composition relationships are well calibrated, all the reactions computed for a given paragenesis should intersect at a single point in the PT field if equilibrium is achieved (Figure IV-7). However, cumulated errors on each equilibrium reaction involve scatters in the intersection points. The InterSX (Berman, 1991) program included in TWEEQ package allows to calculate P, T and the scatters, scat(P) and scat(T), between intersections.

Even if the thermodynamic database was perfect, imprecision in the mineral analyses places limits on the relative precision of the PT estimates. The precision of the microprobe analysis induces scatter related to variations of mica, chlorite and other mineral compositions, which can be calculated using a Monte Carlo simulation (Lieberman and Petrakakis, 1991; Vidal and Parra, 2000; Parra et al., 2002b). This calculation was made for each paragenesis used for PT estimates and led to determine paragenesis-dependant maximum permissible scatters above which the minerals are considered to be out of equilibrium (Vidal and Parra, 2000).

For each paragenesis, we first chose the assemblages showing mineral compositions that were 'perfectly' equilibrated (i.e. all equilibria intersect at a single point). As an example, for a paragenesis Fe-Mg-carpholite-phengite-chlorite, we took the three compositions which showed the best equilibrium between each mineral. A Gaussian error distribution with $2\sigma=1\%$ relative for all major oxides was randomly sampled about the nominal weight percentage for each oxide in phengite, chlorite and Fe-Mg-carpholite (except for volatile Na_2O and K_2O in phengite where $2\sigma=2\%$ relative). Minor elements were not considered because even large relative variations have a negligible influence on the Monte Carlo simulation. A hundred permutations allowed simulating 100 mineral compositions. The set of a hundred simulated chlorite-phengite-carpholite triplets was used to calculate 100 separate PT points, as well as their associated scatters in P and T [scat(P) and scat(T)] with the InterSX program. These best PT estimates (Pi and Ti, i=1 to 100) are defined as a solid weighted average. Because the distribution of these best estimates can be approximated by a Gaussian distribution (Lieberman and Petrakakis, 1991), we calculated an average pressure $\overline{P}=[\sum Pi]/100$ and an average temperature $\overline{T}=[\sum Ti]/100$ for the 100 Pi and Ti, as well as the 95% confidence standard deviations (σP and σT) and the correlation coefficient $\rho(P,T)$. These values are used to estimate a PT ellipsoid depicting the precision of any P and T calculation for the given paragenesis. The size is calculated with σP and σT. The orientation of the ellipsoid is constrained by the correlation coefficient $\rho(P,T)$ (Powell and Holland, 1988; 1994). We also calculated the average scatters $\overline{scat(P)}=[\sum scat(Pi)]/100$ and $\overline{scat(T)}=[\sum scat(Ti)]/100$, and their standard deviations $\sigma_{scat(P)}$ and $\sigma_{scat(T)}$ in order to determine the maximum permissible scatter [$scat(P)_{max}= \overline{scat(P)}+2\sigma_{scat(P)}$ and $scat(T)_{max}= \overline{scat(T)}+2\sigma_{scat(T)}$] of any PT estimate with a 95% confidence level (2σ). For more details, refer to Appendix A.

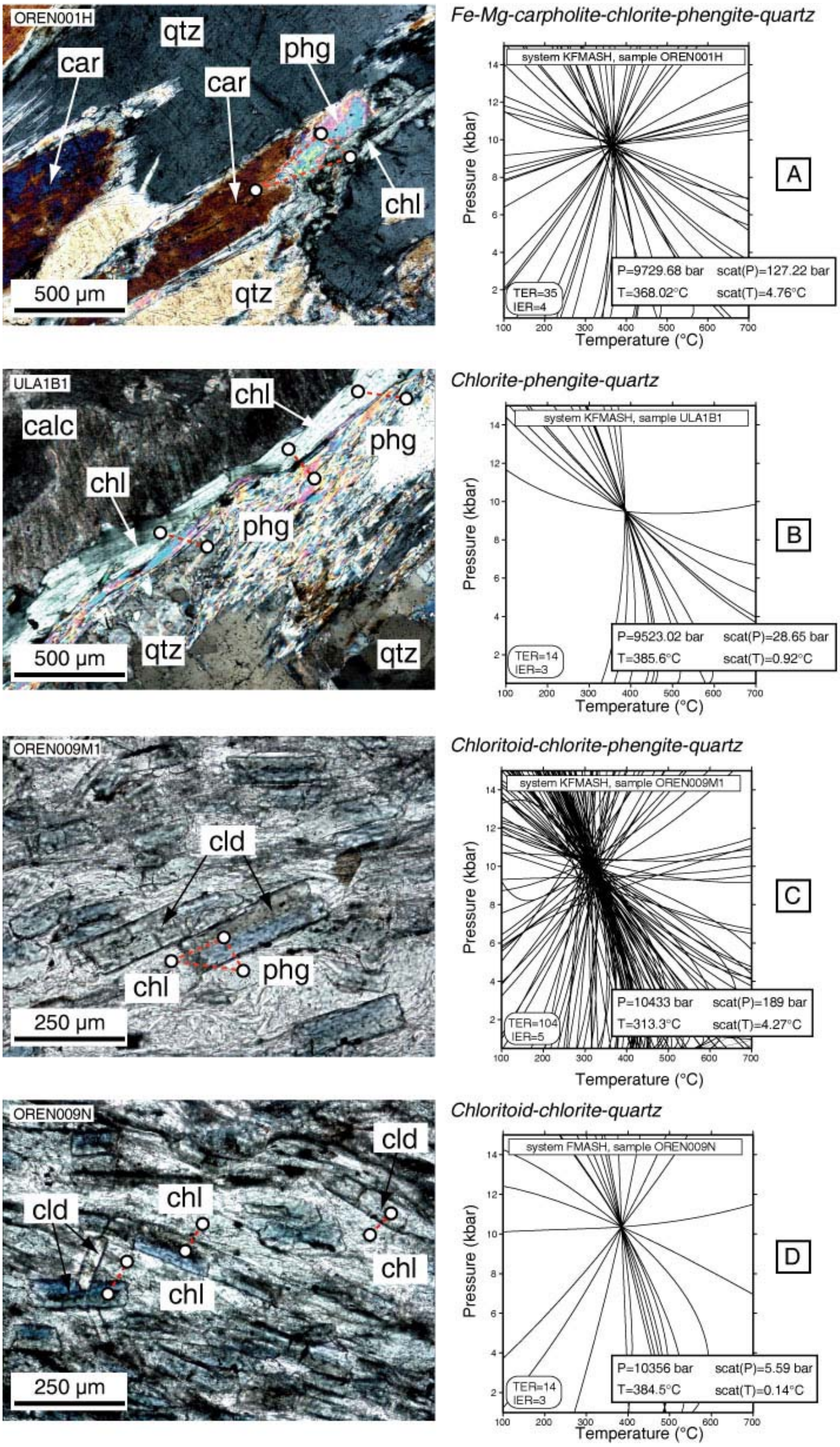

Figure IV-7. Photomicrographs showing location of mineral analyses (left) and P-T diagram showing the plot of all equilibrium reactions (right) computed for a paragenesis Fe-Mg-carpholite-chlorite-phengite-quartz (a), chlorite-phengite-quartz (b), chloritoid-chlorite-phengite-quartz (c) and chloritoid-chlorite-quartz (d). P-T estimates and the scatters between intersections [scat(P), scat(T)] reported on each PT diagram are calculated with the InterSX (Berman, 1991) program included in TWEEQ package. In these examples, calculations were made in the KFMASH (K_2O-FeO-MgO-Al_2O_3-SiO_2-H_2O) system (a,b,c) and in the FMASH (FeO-MgO-Al_2O_3-SiO_2-H_2O) system (d). Abbreviations: car, Fe-Mg-carpholite; phg, phengite; cld, chloritoid; chl, chlorite, qtz, quartz; calc, calcite; TER, total equilibrium reactions; IER, number of independent equilibrium reactions. Photos (a) and (b) were taken under crossed polars, (c) and (d) under plane polarized light.

For any other PT estimate from the same paragenesis, we then compared the scatters scat(P) and scat(T) to the maxima defined previously. If $scat(P)>scat(P)_{max}$ or $scat(T)>scat(T)_{max}$, the minerals involved in the paragenesis were considered to be out of equilibrium and the calculated PT conditions were rejected.

In the following, I present only PT conditions which were estimated from six different parageneses observed in the study area: Fe-Mg-carpholite-chlorite-phengite-quartz, magnesiocarpholite-chlorite-kyanite-quartz, Fe-Mg-carpholite-chlorite-quartz, chlorite-phengite-quartz, chloritoid-chlorite-phengite-quartz, and chloritoid-chlorite-quartz.

For each paragenesis, the Monte Carlo simulation was performed in order to estimate the analytical uncertainties and the paragenesis-dependent maximum permissible scatters (different from one paragenesis to the other one) (Figure IV-8). The amount of rejected PT estimates is large and may result from calculations performed with non-equilibrated minerals. However, as already described in Parra et al. (2002b), a significant proportion of rejected mineral pairs or triplets showing $scat(P)>scat(P)_{max}$ or $scat(T)>scat(T)_{max}$ revealed PT conditions within the PT trend defined by the equilibria which showed $scat(P)<scat(P)_{max}$ or $scat(T)<scat(T)_{max}$. This is probably due to an underestimation of the maximum scatter (i.e. $scat(P)_{max}$ and $scat(T)_{max}$ being to low) that causes rejection of pairs and triplets of minerals being actually in equilibrium.

PARAGENESES	$\overline{P}$ (bar)	$\overline{T}$ (°C)	$\overline{scat(P)}$ (bar)	$\overline{scat(T)}$ (°C)	σP (bar)	σT (°C)	$\sigma_{scat(P)}$ (bar)	$\sigma_{scat(T)}$ (°C)	ρ(P,T)	$scat(P)_{max}$ (bar)	$scat(T)_{max}$ (°C)
Fe-Mg-carpholite-chlorite-phengite-quartz	9961	369.8	213.9	8.1	346.5	7.9	78.3	3.1	0.87	370.4	14.2
Mg-carpholite-chlorite-kyanite-quartz	13767.2	485.9	224.2	7.9	648.2	7.2	133.7	4.4	0.99	491.7	16.7
Fe-Mg-carpholite-chlorite-quartz	10108.5	325.2	3.3	0.1	278.1	14.8	1.9	0.05	0.98	-	-
chlorite-phengite-quartz	8756.8	405.7	177.4	5.6	640.5	26.9	88	2.9	-0.76	353.3	11.3
chlorite-phengite-chloritoid-quartz	10472.3	315.7	505.6	9.5	57	5.9	225.9	4.5	-0.13	957.4	18.5
chlorite-chloritoid-quartz	10592	390.6	313.5	14	264.5	9.7	179.3	10.4	0.84	672.2	34.9

Figure IV-8. Results of the Monte Carlo simulation accounting for analytical uncertainties for each paragenesis used in the PT calculations. See text for explanations.

After the selection of all PT estimates by the Monte Carlo method, those considered to be in equilibrium can be reported on a PT field. We present in the following various PT paths resulting from multi-equilibrium calculations performed from samples collected in different regions (see Figures IV-2 and II-22 for location of samples). For each sample, the calculated PT conditions and their paragenesis-dependent error bars (±1σ) resulting from the Monte Carlo simulation are plotted on a PT diagram. The 95% confidence ellipsoids and the number of independent equilibrium reactions (IER) for each calculation are reported with the PT diagram. It is noteworthy that achievement of equilibrium is not certified for PT results calculated with only two IER. However, most of PT calculations with two IER show PT points located within the trend defined by those calculated with more than two IER, except for PT conditions estimated from pyrophyllite-chlorite-quartz paragenesis. Several PT points were indeed calculated with pyrophyllite and chlorite pairs, coming from the retrogression of Fe-Mg-carpholite. These PT calculations (only with 2 IER) showed pressure conditions of about 14-16 kbar for temperatures ranging between 250 and 400°C. These pressure values are not reasonable considering location of the reaction curve Fe-Mg-carpholite+quartz=pyrophyllite+chlorite+water deduced from the composition of Fe-Mg-carpholite, and might result from calculations performed with non-equilibrated minerals.

7. PT results in the Lycian Nappes

a. The region of Ören-Demirciler

In the region located between Ören and Demirciler (Figure IV-2), the trends defined by the PT estimates from different mineral pairs or triplets are reported in Figure IV-9. Each PT diagram corresponds to PT calculations made in samples from the same outcrop. Depending on the parageneses, calculations were made either with Fe-Mg-carpholite-chlorite-phengite and chloritoid-chlorite-phengite triplets, or with Fe-Mg-carpholite-chlorite, chlorite-phengite and chloritoid-chlorite pairs. Chlorite and phengite commonly come from the retrogression of Fe-Mg-carpholite. They form typical triple HP mineral assemblages. Chloritoid-chlorite pairs are observed in the foliation. Chloritoid-chlorite-phengite triplets could rarely be used in the PT calculations because of contaminated analyses of phengite due to its very small size within the foliation.

North of Ören, in the Karaova metasediments where well-preserved Fe-Mg-carpholite occurs, PT conditions estimated from different thin sections are shown in Figures IV-9a, b, c, and d. The best-constrained PT estimates (with IER>2) locate in a domain from 12 kbar/420°C to 8-9 kbar/300°C. Other PT points calculated with only two independent reactions are located in this PT trends and show a wider range of PT conditions from 13-14 kbar/470°C to 8 kbar/250°C, which are not significantly different to the formers considering the 95% confidence ellipsoids. In the Demirciler area, the two samples DEM007A and BAL001C revealed the same range of metamorphic conditions for the same parageneses (Figures IV-9e,f).

Altogether, the PT conditions estimated in the well-preserved Fe-Mg-carpholite-bearing metasediments of the Ören-Demirciler region indicate a high-pressure metamorphic peak of about 12-13 kbar/400-420°C followed by a progressive decrease of temperature at HP conditions. As shown in Figure IV-9, the 'cold' retrogression paths are located in the aragonite stability field. As described in Chapter II, during our investigations in this region, we found widespread occurrences of calcite forming metre-scale rosetta in the Cretaceous limestones of the carbonate sequence that overlies the Karaova unit. Although no aragonite relicts have been found, the microprobe analyses revealed very low Fe-, Mn-, and Mg- contents and high Sr-content suggesting that these carbonate rocks underwent PT conditions allowing growth of aragonite before its total retrogression into calcite. Furthermore, in the Karaova formation which crops out in the Çivril area, I reported probable occurrence of aragonite in relicts associated with Fe-Mg-carpholite. The fact that the multi-equilibrium PT calculations locate HP cooling paths within the aragonite stability domain is coherent with these proofs of aragonite relics occurrences. It is here therefore proposed that the HP rocks from the Karaova formation might have passed into the calcite stability domain after their HP cooling path (Figure IV-9). Because aragonite is totally retrogressed into calcite, the HP rocks might have crosscut the aragonite-calcite equilibrium-curve at temperatures greater than ~200°C, precluding preservation of aragonite (see Figure 8b of Gillet and Goffé, 1988).

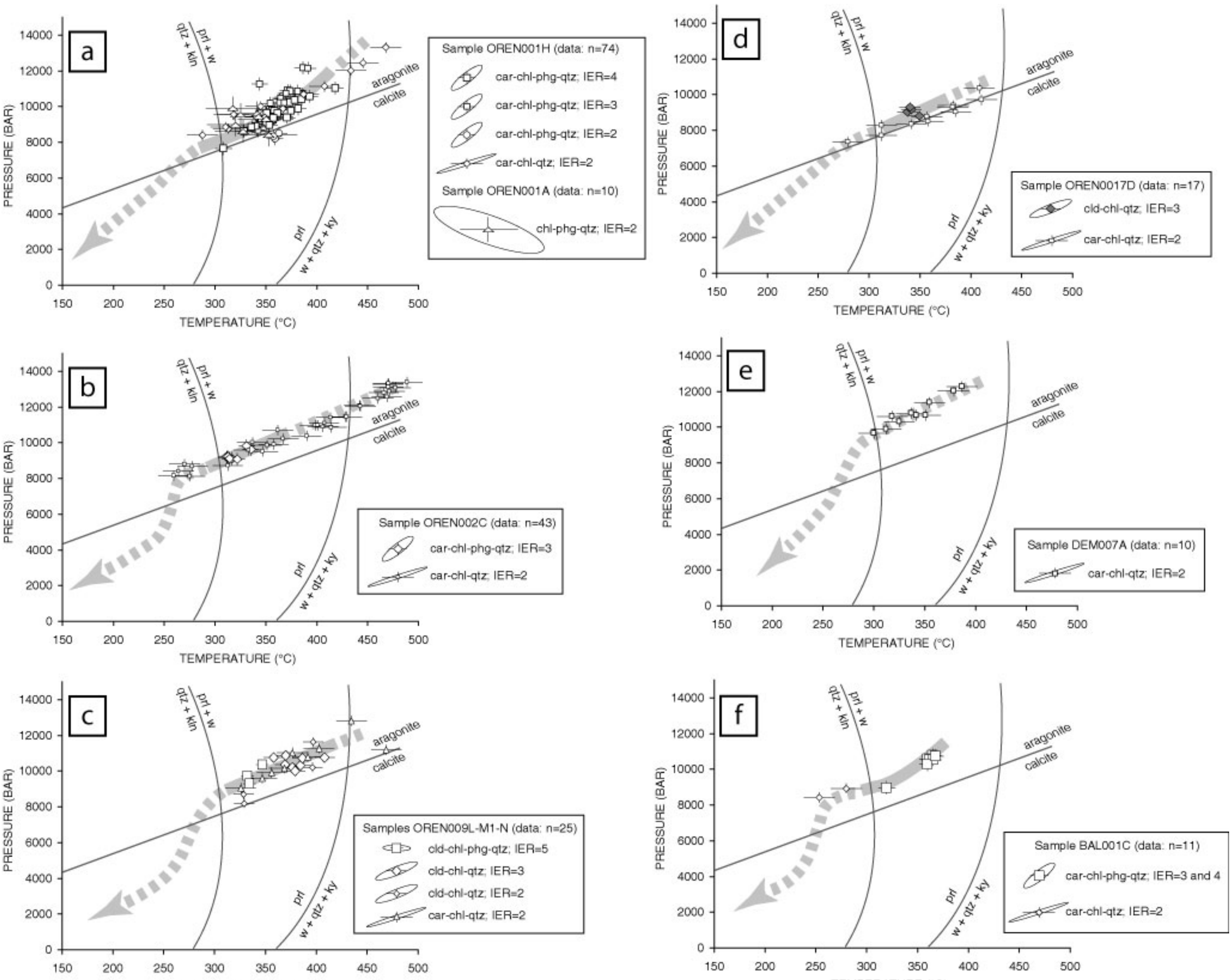

Figure IV-9. PT estimates for samples from the Ören area (a, b, c, d) and the Demirciler area (e, f) [Lycian Nappes]. The paragenesis-dependent error bars (±1σ) and 95% confidence ellipsoids are calculated with the Monte Carlo simulation. The number of independent equilibrium reactions (IER) for each calculation is reported in the legend.

b. The region of Ula

Close to the contact that separates the Lycian Nappes from the Menderes Massif, in the eastern part of the Bodrum peninsula, PT estimates have been made from three samples collected at the same outcrop in the lowermost levels of the Karaova formation (Figure IV-2).

In the sample ULA001B1, PT estimates using several chloritoid-chlorite-phengite triplets and chloritoid-chlorite pairs from the metamorphic foliation cluster between 9 and 11.5 kbar at temperatures ranging between 330 and 400°C. PT calculations with chlorite-KWM pairs which are not associated with chloritoid show higher temperature and slightly lower pressure conditions, thus indicating a warmer exhumation than that for the Ören-Demirciler area (Figure IV-10a).

In the sample ULA001B2 which contains highly retrogressed Fe-Mg-carpholite into chlorite and phengite, a similar pattern is observed. PT calculations have been performed from Fe-Mg-carpholite-chlorite-KWM triplets which draw a HP cooling path whereas chlorite-phengite pairs located in later textural habits reveal lower pressure and higher temperature conditions (Figure IV-10b). This suggests an exhumation process in two parts: (i) a 'cold' retrogression path from 13-14 kbar at 400°C to 10 kbar at 320°C, (ii) a thermal overprint from 320°C to 470°C at pressures of about 9-10 kbar, before a late cooling and decompression path.

For sample ULA001C1 in which Fe-Mg-carpholite associated with phengite and chlorite has been observed, the calculated PT conditions depict the same 'cold' HP cooling path, from 13kbar at 380°C to 10 kbar at ~300°C. Because phengite-chlorite pairs in later habits have not been recognized within this thin section, we cannot constrain the exhumation path following the cold retrogression. However, the fact that sample ULA001C1 comes from the same outcrop as the two latter supports the idea of a similar PT pattern for it (Figure IV-10c).

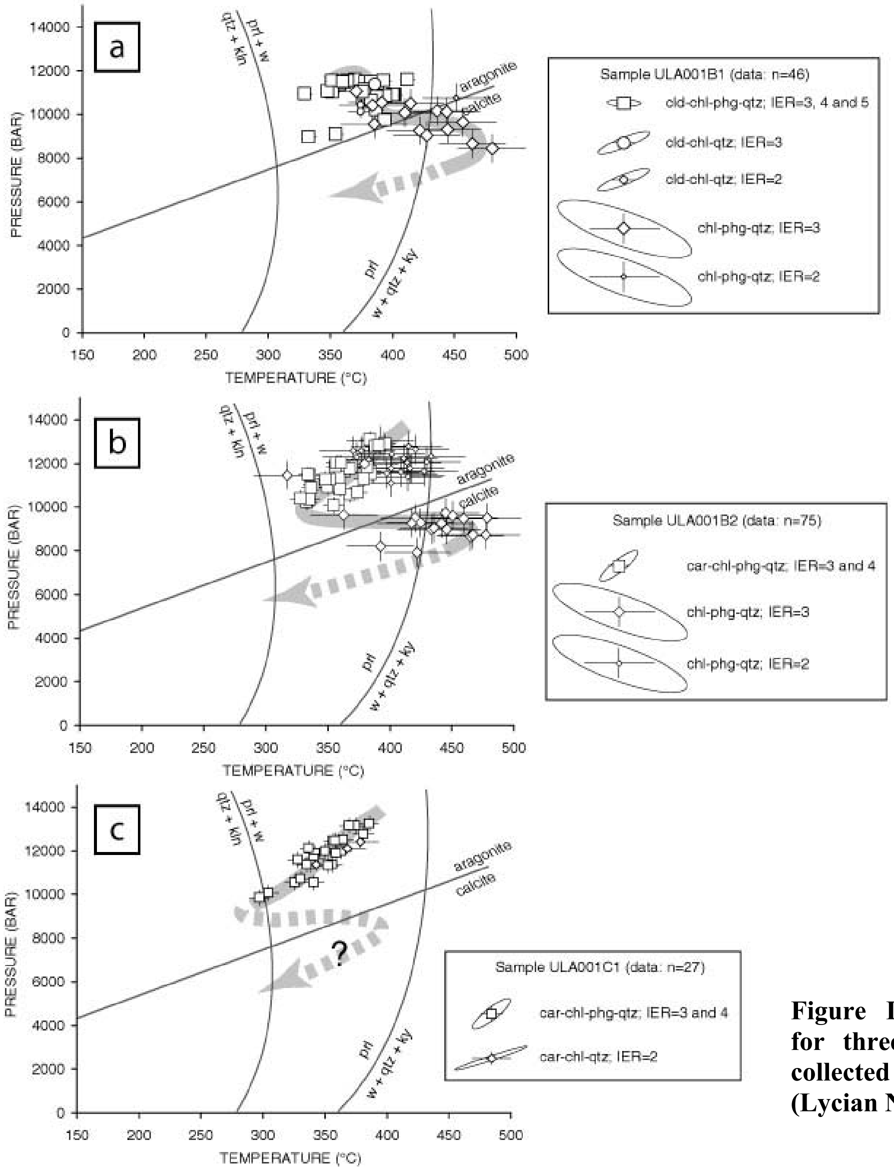

Figure IV-10. PT estimates for three samples (a, b, c) collected in the Ula region (Lycian Nappes).

c. The region of Güllük

In the area of Güllük (Figure IV-2), Fe-Mg-carpholite is completely retrogressed into mica and chlorite. The foliation shows many phengite and chlorite pairs, rarely in contact with chloritoid. PT conditions have been estimated from two samples (GUL004F and GUL005C). A same PT trend depicted by the two samples shows a decompression path in warm conditions, from 12-13 kbar at 350-400°C to 7-8 kbar at 450-470°C (Figure IV-11). This pattern is significantly different compared to that of the Ören-Demirciler or Ula regions. A HP cooling path preceding a thermal overprint such as in the samples from Ula is not observed in rocks from the region of Güllük, but is eventually possible.

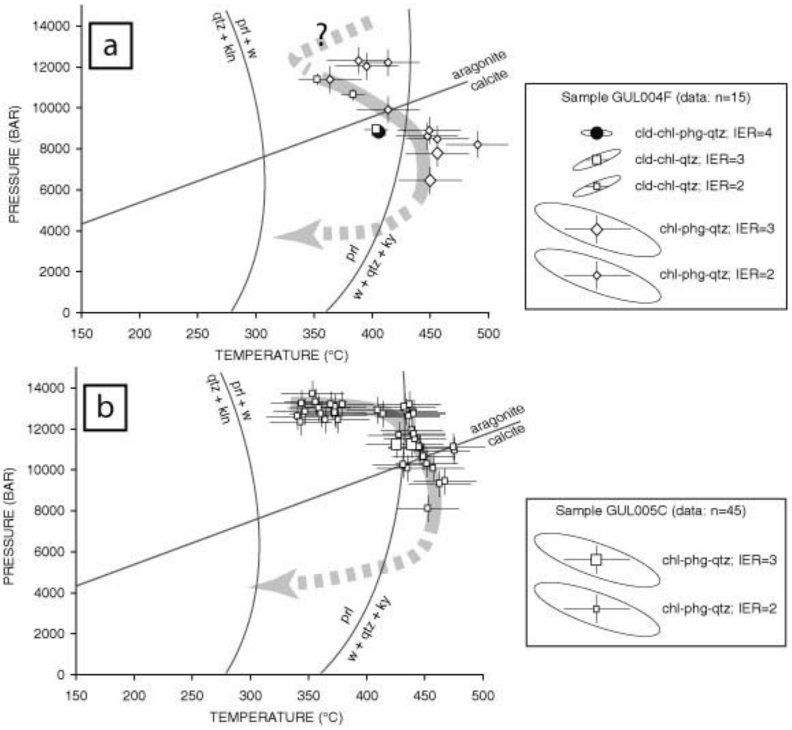

Figure IV-11. PT estimates for two samples (a, b) collected in the area of Güllük (Lycian Nappes).

d. Klippen of Lycian Nappes

In Figure IV-12, I have compiled all the PT estimates from three samples collected in the two tectonic slices of Lycian Nappes on the Dilek peninsula (Figure II-22 for location). In the southern klippe (south of Tirhaköy) where fresh Fe-Mg-carpholite occurs in quartz segregations, the thin section DAV001B allowed PT estimates of 10-11 kbar/350-380°C using Fe-Mg-carpholite-chlorite pairs. At the base of the northern klippe (east of Kirazlı) where chloritoid and carpholite pseudomorphs have been observed, PT and T estimates were made, respectively with chlorite-phengite and chlorite-quartz assemblages from samples KIRAZ001C and KIRAZ002D. The results depict a similar PT trend to that of the Ula area. A cold retrogression path from 12 kbar/350°C to 9.5-10 kbar/280°C is followed by a thermal overprint which reaches 450°C at 9 kbar.

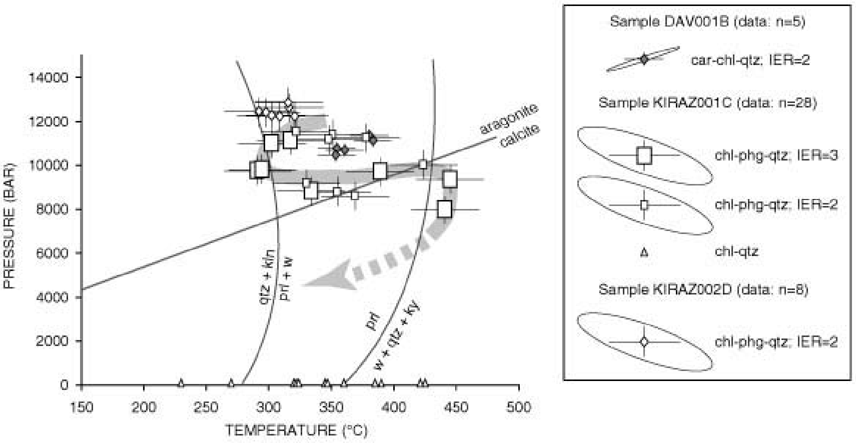

Figure IV-12. PT estimates for samples collected at the base of the two klippen of Lycian Nappes located in the Dilek-Selçuk region.

8. PT results in the southern Menderes Massif

In the southern Menderes Massif, PT estimates have been calculated with samples coming from two localities where HP parageneses-bearing metaconglomerate crops out (Figure IV-2).

Near the locality of Kurudere, the HP metamorphic peak is constrained with magnesiocarpholite-chlorite-kyanite triplets from two samples (KURU0110B and KURU0110C). They indicate PT conditions of 12-14 kbar and 470-500°C (Figure IV-13a), higher than those of the Lycian HP peak. These PT conditions are similar to those already exposed in Chapter III. Furthermore, an isothermal decrease of pressure during exhumation of HP metamorphism has been proposed by these latter, based on the existence of corundum-bearing rocks in the overlying rocks. In the samples from the Kurudere area, the absence of chlorite-phengite pairs did not allow us to constrain this pattern with the multi-equilibrium method. However, temperatures have been estimated using compositional variations of chlorite within the sample KURU0101A, and depict a wide range between 260 and 530°C, which correspond to their temperatures of crystallization during retrogression.

While retrogression of HP parageneses could not be constrained in the Kurudere area with the multi-equilibrium method, phengite-chlorite pairs within the foliation of the sample NEBIL0103A collected near Nebiler (Figure IV-2) have been used to show the exhumation pattern of the Menderes HP rocks. The PT points cluster in two domains, one located between 400 and 500°C at 9-10 kbar, and a narrower one between 420 and 470°C at pressures around 6-7 kbar (Figure IV-13b). The large 95% confidence ellipsoid associated to the chlorite-phengite pairs does not permit to define a detailed pattern for exhumation of these HP rocks. However, it seems reasonable to suggest an isothermal decompression path passing through the two PT domains. Temperatures deduced from chlorite compositions range between 400 and 520°C, which is compatible with the PT estimates obtained with chlorite-KWM pairs.

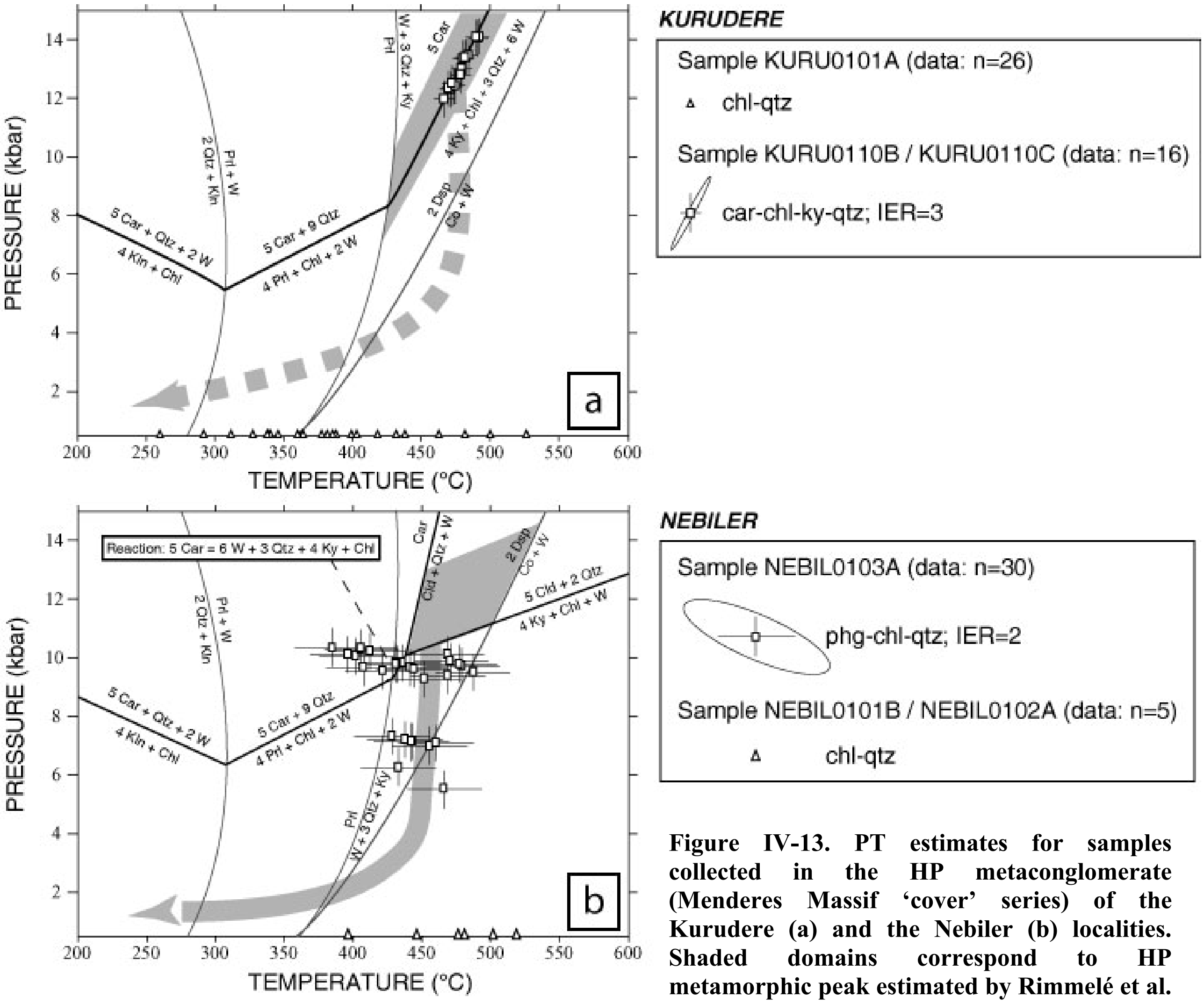

Figure IV-13. PT estimates for samples collected in the HP metaconglomerate (Menderes Massif 'cover' series) of the Kurudere (a) and the Nebiler (b) localities. Shaded domains correspond to HP metamorphic peak estimated by Rimmelé et al. (in press).

9. Regional-scale interpretation and conclusions

HP rocks from both Lycian Nappes and Menderes cover series reveal metamorphic peak conditions of about 10-12 kbar/400°C and 12-14 kbar/470-500°C respectively, slightly higher than the minimum conditions already reported in Oberhänsli et al. (2001), Rimmelé et al. (2003) and Rimmelé et al. (in press) [previous chapters].

Whereas a simple isothermal decompression at about 450°C is well documented for exhumation of HP parageneses from the southern Menderes Massif, various PT paths are observed in the overlying Lycian Nappes. Between Ören and Demirciler where Fe-Mg-carpholite is well preserved, all PT paths depict a cold retrogression path from 12-13 kbar at 420°C to 8 kbar at 270°C-300°C. Such 'cold' HP cooling paths preserving Fe-Mg-carpholite have already been described for high-pressure rocks from Oman (Goffé et al., 1988) and from the Valaisan domain of the Western and Central Alps (Bousquet et al., 1998; 2002). In this area located between Ören and Demirciler, far away from the contact with the Menderes Massif, these HP cooling paths are associated with top-to-the-NNE movements related to the Akçakaya shear zone (Figure IV-14) at the top of the Karaova unit (as seen in Chapter II). This zone of strain localization is a local intra-nappe contact which was active in the early stages of exhumation of HP rocks, within the stability domain of Fe-Mg-carpholite.

On the contrary, at the base of the Karaova formation, close to the contact with the Menderes Massif, PT estimates revealed warmer exhumation patterns. Near Güllük where Fe-Mg-carpholite is completely retrogressed into chlorite and KWM, PT results suggest an exhumation process from 12 kbar/350°C to 7-8 kbar at 450-470°C and near Ula where a few Fe-Mg-carpholite relics have been recognized, PT estimates calculated from samples collected at the same outcrop depict an exhumation process defined by a cold retrogression path from 13-14 kbar/400°C to 10 kabr/300°C, followed by a thermal overprint reaching 470°C at about 9 kbar. Similar trend has been observed for the exhumation path of HP rocks forming the basal part of the two klippen of Lycian material located on the Dilek peninsula. For the rocks near Güllük, the first part of exhumation corresponding to a HP cooling path from 13-14 kbar/400°C to 11-12 kbar/350°C (as for HP rocks from Ula) has been completely erased by a stronger thermal overprint (Figure IV-11). In these lowermost Lycian metasediments of the Bodrum peninsula, the pervasive deformation associated to the warmer PT paths is characterized by top-to-the-east shear senses. As described in Chapter II, approaching the contact with the Menderes Massif, deformation becomes more severe which suggests that the Lycian/Menderes contact has been reactivated as a major shear zone (the Gerit shear zone; see Figure IV-14) after the southward transport of the Lycian Nappes over the Menderes Massif. This zone of strain localization allowed late exhumation of HP parageneses under warmer conditions.

Although all these PT paths have been depicted from samples collected within the same unit (the Karaova unit), it can be argued that the Lycian metasediments recorded three distinct exhumation patterns. A single decompression-cooling path (I) is observed for the rocks located in the uppermost levels of the Karaova unit, whereas a single decompression pattern with heating (II) or a mixture of paths (I) and (II) depict the exhumation of rocks located at (or towards) the base of the Karaova unit, close to the contact with the Menderes Massif (Figures IV-14 and IV-15).

A rapid exhumation mechanism is needed to explain such a cold PT path (I) for rocks located in the uppermost lithologies of the HP unit. The rocks under consideration must have followed their return back to the surface in a cold environment along the Akçakaya shear zone, shearing deformation allowing the HP rocks to pass through roughly flat isotherms. On the contrary, the rocks located at the Lycian Nappes/Menderes Massif boundary have been exhumed along the Gerit shear zone in a warmer environment, across relatively steeper isotherms to maintain the higher temperature conditions during reactivation of the contact between the Lycian and the Menderes massifs as major shear zone. The two opposite situations are not isochronal and the exhumation processes might have occurred in a large wedge allowing, from top to base, such *HP cooling* (I) and *decompression with heating* (II) patterns.

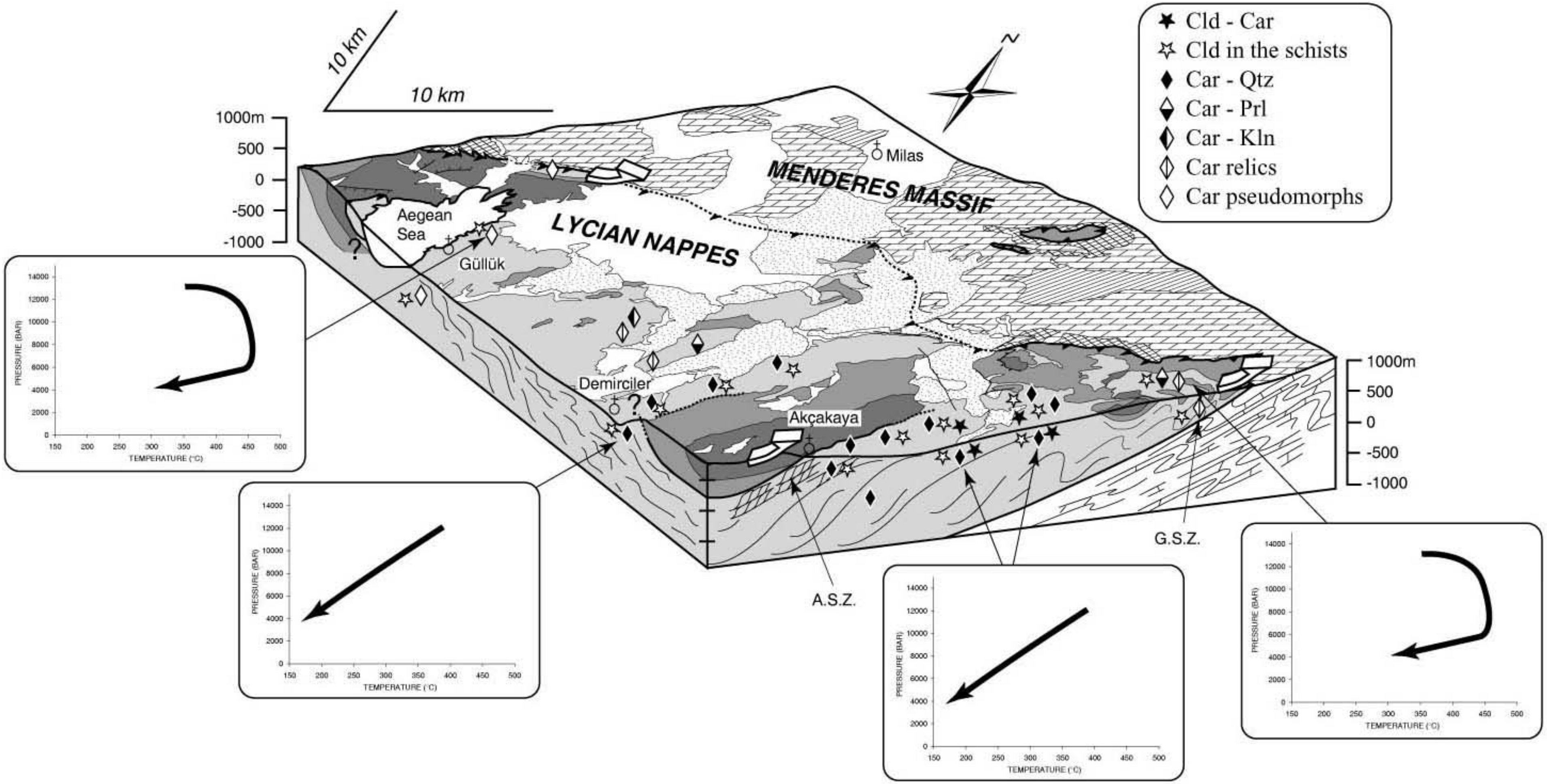

Figure IV-14. 3-D tectono-metamorphic diagram showing the parageneses and the different PT paths in the Lycian Nappes of the Bodrum peninsula, as well as the displacements (white arrows) observed in the Akçakaya shear zone (A.S.Z.) and Gerit shear zone (G.S.Z.). Mineral abbreviations are listed in the caption of Figure IV-2.

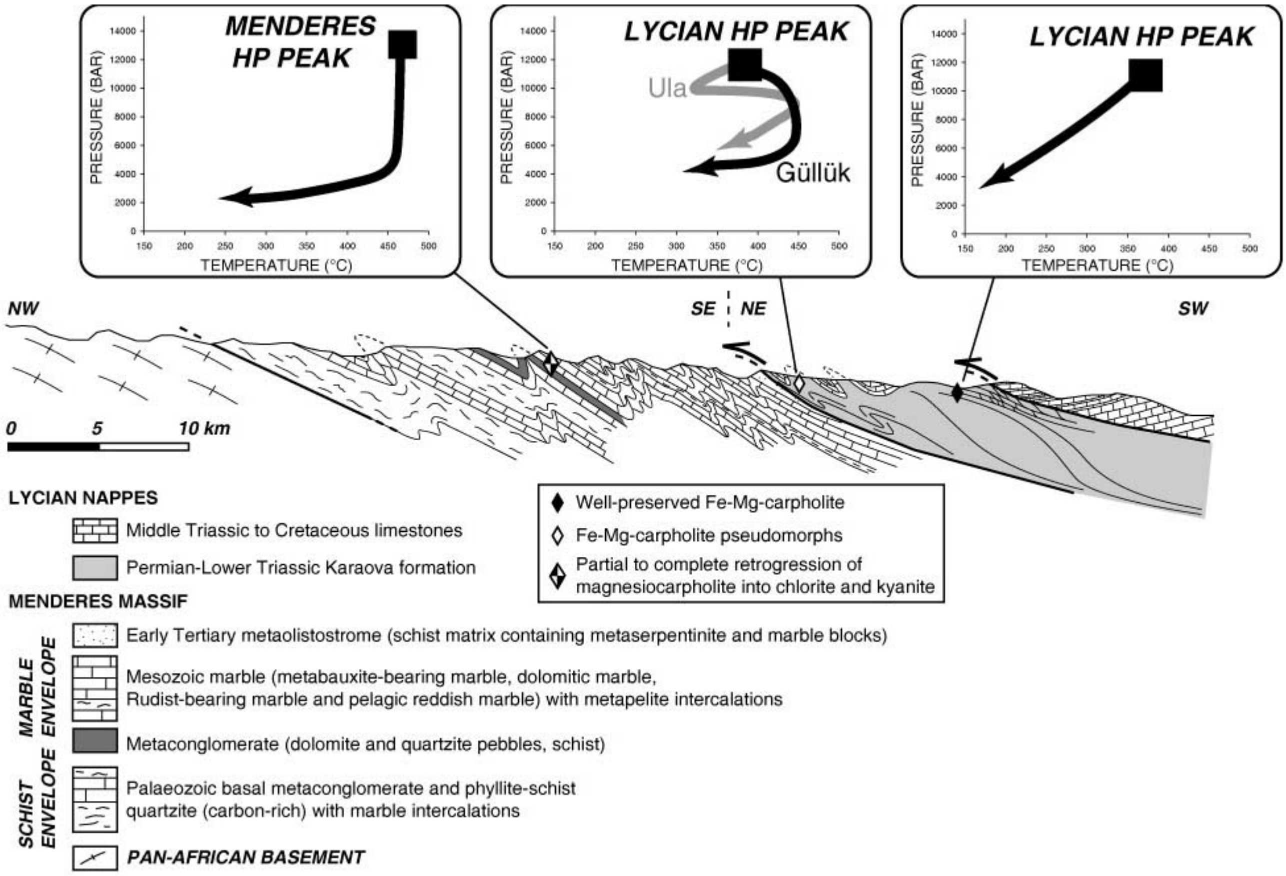

Figure IV-15. Synthetic cross-section across the Lycian Thrust Sheets (Bodrum peninsula region) and the southern Menderes Massif highlighting the HP metamorphic peaks and retrograde PT paths for both massifs.

B. LATE EXHUMATION OF THE LYCIAN NAPPES AND SOUTHERN MENDERES MASSIF - APATITE FISSION TRACK DATA

In order to obtain information on the low-temperature thermal history of the widespread HP rocks of SW Turkey, just before they reached the surface, an apatite fission track study was conducted in collaboration with Edward Sobel. This short part only focuses on the result of this fission track study. Principle, methodology for sample preparation, and analytical details are thoroughly exposed in Appendix B.

1. Apatite fission track data for the HP rocks of SW Turkey

Samples were collected in the lithologies of the Lycian Nappes and the southern Menderes Massif where HP metamorphic rocks were found on the Bodrum peninsula. 11 samples come from the Lycian Nappes and 6 from the Menderes Massif (Figure IV-16).

The results for 8 irradiated samples are shown in Figure IV-17. Only 5 of these samples were countable, the poor quality of apatite crystals (small grain size, many inclusions, too-low Uranium-content…) in the 3 others preventing fission track analysis.

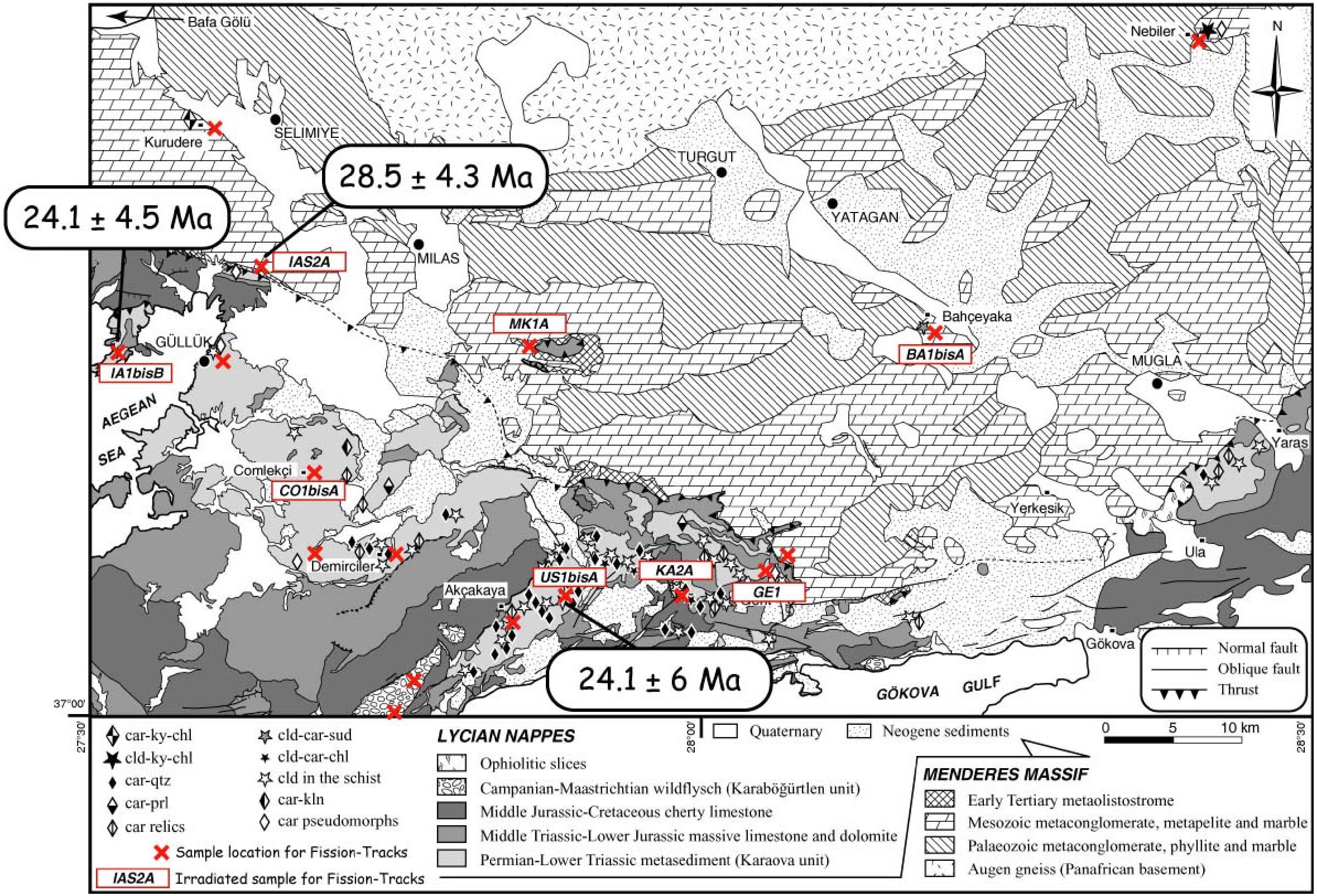

Figure IV-16. Map of the Bodrum peninsula region showing location of the samples collected for apatite fission-track analysis (geological setting simplified after Çağlayan et al., 1980; Konak et al., 1987; Candan and Dora, 1998; and Konak and Akdeniz [unpublished geological maps of M.T.A.-Turkey]). The three fission-track ages for rocks from the metaolistostrome of the Menderes Massif and the Karaova formation of the Lycian Nappes are also reported on the map.

Location of sample	Sample number	Irradiation number	E (m)	Latitude	Longitude	N.G.	Ns	ρS $(x10^6/cm^2)$	Ni	ρI $(x10^6/cm^2)$	ρD $(x10^6/cm^2)$	U (ppm)	$P(\chi^2)$ (%)	Age (Ma)	±1σ	Comments
LN Karaova	KA2A	UP44-7	315	37°05.270'	27°59.685'						1.1694					sample not countable
LN Karaova	**US1bisA**	UP44-8	178	37°05.776'	27°54.877'	3	18	0.2931	161	2.6210	1.1664	28	74	**24.1**	**6.0**	
LN Karaova	CO1bisA	UP44-9	220	37°09.632'	27°41.170'	3	13	0.1710	58	0.7627	1.1634	8	55	48	14.7	very poor quality data
LN Karaova	**IA1bisB**	UP44-10	105	37°14.448'	27°31.091'	5	32	0.2854	285	2.5420	1.1604	27	30	**24.1**	**4.5**	
MM metaolist.	MK1A	UP44-11	635	37°14.5'	27°54.405'						1.1574					sample not countable
LN Karaova	GE1	UP44-12	934	37°05.362	28°04.649'	5	42	0.2659	248	1.5700	1.1544	17	0	42	14.1	very poor quality data
MM metaolist.	**IAS2A**	UP44-13	156	37°17.92'	27°38.321'	13	50	0.2833	373	2.1140	1.1514	23	95	**28.5**	**4.3**	
MM metacongl	BA1bisA	UP44-14	496	37°16.063'	28°10.495'						1.1484					sample not countable

Figure IV-17. Apatite fission track analytical data.

Notes:

-For location of samples, LN=Lycian Nappes, MM=Menderes Massif.

-E is the elevation.

-N.G. is the number of individual grains dated.

-Ns is the number of spontaneous tracks counted on apatite crystals.

-ρS is the spontaneous track density measured in apatite crystals (tracks/cm^2).

-Ni is the number of induced tracks counted on mica crystals (external detector).

-ρI is the induced track density measured in the external detector (tracks/cm^2).

-ρD is the induced track density in the CN5 standard glass.

-U is the Uranium content in ppm.

-$P(\chi^2)$ is the χ-square probability (Galbraith, 1981; Green, 1981). Values greater than 5% are considered to pass this test and therefore represent a single population of ages.

-The pooled age is reported for samples that pass the $P(\chi^2)$ test. The central age is reported for samples that fail the $P(\chi^2)$ test (<5%). Error (1σ) is calculated using zeta calibration method (Hurford and Green, 1983) with zeta of 369.6 ± 7.6 for apatite (E. Sobel, unpublished).

-The number of tracks counted in the external detector adjacent to CN5 dosimetry glass is Nd=4776.

-Sample IA1bisB has a quartzitic lithology. Other samples are schists.

Except for sample GE-1 that shows a $P\chi^2$ value (χ-square probability) lower than 5% (i.e. considered to have not passed this probability test), ages reported in Figures IV-17 and IV-18 are pooled ages which represent a single population of ages. The central age (weighted mean of ages) is reported for sample GE-1.

For sample IAS-2A collected in the metaolistostromal unit of the Menderes Massif (north of Güllük; Figure IV-16) the fission track age (calculated with counting on 13 grains) is 28.5 ± 4.3 Ma (Figures IV-17 and IV-18a). The number of counted grains is statistically reasonable and all data clearly represent a single population of ages, as attested by the high $P(\chi^2)$ value (95%).

The two samples US-1bisA and IA-1bisB, which are both from the Karaova formation of the Lycian Nappes (Figure IV-16 for location), respectively display ages of 24.1 ± 6 Ma and 24.1 ± 4.5 Ma (Figures IV-17 and IV-18b,c). These ages are in the same range as the fission track age for sample IAS-2A, and therefore support the Oligo-Miocene age of the latter. However, these ages have been respectively calculated with only 3 and 5 grains, the other apatites encountered in the samples being very small and of very poor quality which prevented counting. They must therefore be carefully considered in a statistical way.

The two samples GE-1 and CO-1bisA, respectively from the metaolistostrome of the Menderes Massif (near Gerit) and from the Karaova formation of the Lycian Nappes (Çomlekçi area) (Figure IV-16) show poor-quality results in term of statistics. Both samples contain very few grains which were countable.

The five grains counted in sample GE-1 show different population of grains as attested by the $P(\chi^2)$ value of 0. Some of the apatite grains contain very few spontaneous tracks whereas the others have a significantly higher spontaneous track density. The central age estimated 42 ± 14 Ma represents very poor quality data (Figures IV-17 and IV-18d).

Although the ages calculated from 3 grains within sample CO-1bis1 passed the $P(\chi^2)$ test (55%), the very small spontaneous track density in the very-poor quality apatite grains prevent any interpretation of the age of 48 ± 15 Ma (Figures IV-17 and IV-18e).

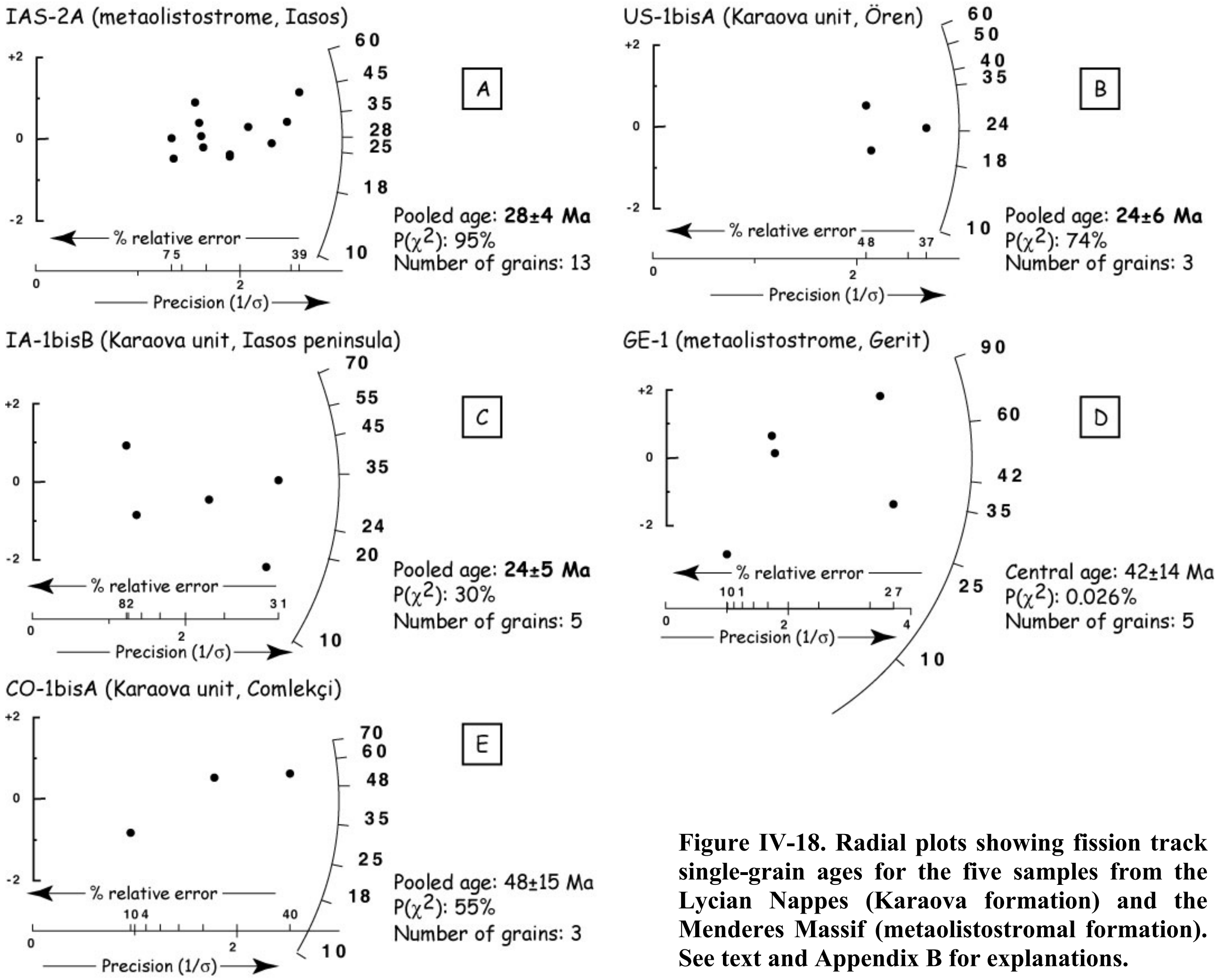

Figure IV-18. Radial plots showing fission track single-grain ages for the five samples from the Lycian Nappes (Karaova formation) and the Menderes Massif (metaolistostromal formation). See text and Appendix B for explanations.

2. Discussion and conclusion

The fission track ages obtained from rocks collected in the Bodrum peninsula region are not as useful as anticipated; many significant encountered obstacles (e.g. poor quality of apatite grains, low uranium content, small grain sizes) preventing fission track analysis for the total of 17 samples.

The three first ages described above, although not statistically very well-constrained, seem to indicate that rocks from the metaolistostrome of the southern Menderes Massif and from the Karaova formation of the Lycian Nappes were at temperatures ranging between 60 and 120°C (see Appendix B) during the Late Oligocene-Early Miocene times (considering errors) (Figure IV-16).

Whereas it has been proposed that the Menderes Massif was unroofed and exhumed by the Early Oligocene (Şengör and Yılmaz, 1981; Şengör et al., 1984b), more recent palynostratigraphic-based studies on Oligo-Miocene molasses (Akgün and Sözbilir, 2001) have revealed that the southern submassif was not at the surface during the Early Oligocene, and that the massif was still buried beneath the Lycian Nappes at least until the Late Oligocene.

It has also been claimed that unroofing of the Menderes Massif was mainly tectonically controlled, associated with normal faulting, rather than erosion (Bozkurt and Satir, 2000). Based on Miocene age data (21 ± 0.4 Ma; Becker-Platen et al., 1977) of the oldest unmetamorphosed sediments above metamorphic rocks of the southern submassif, the latter suggested that the massif was at the surface by the Early Miocene time.

Furthermore, apatite and zircon fission-track thermochronology and cooling histories have suggested a Late Oligocene-Early Miocene extensional exhumation for the southern submassif (Johnson, 1998; Gessner, 2000; Gessner et al., 2001c), ruling out erosional unroofing as the primary exhumation mechanism.

Our few apatite fission track data from metamorphic rocks on both sides of the contact separating the Lycian Nappes from the Menderes Massif show similar ages, suggesting that these rocks were very close to the paleo-Earth surface during the Late Oligocene-Early Miocene times.

CHAPTER V

TECTONO-METAMORPHIC EVOLUTION OF THE EXTENSIVE HIGH-PRESSURE BELT OF SW TURKEY. CORRELATIONS WITH THE NEARBY AEGEAN HIGH-PRESSURE BELT

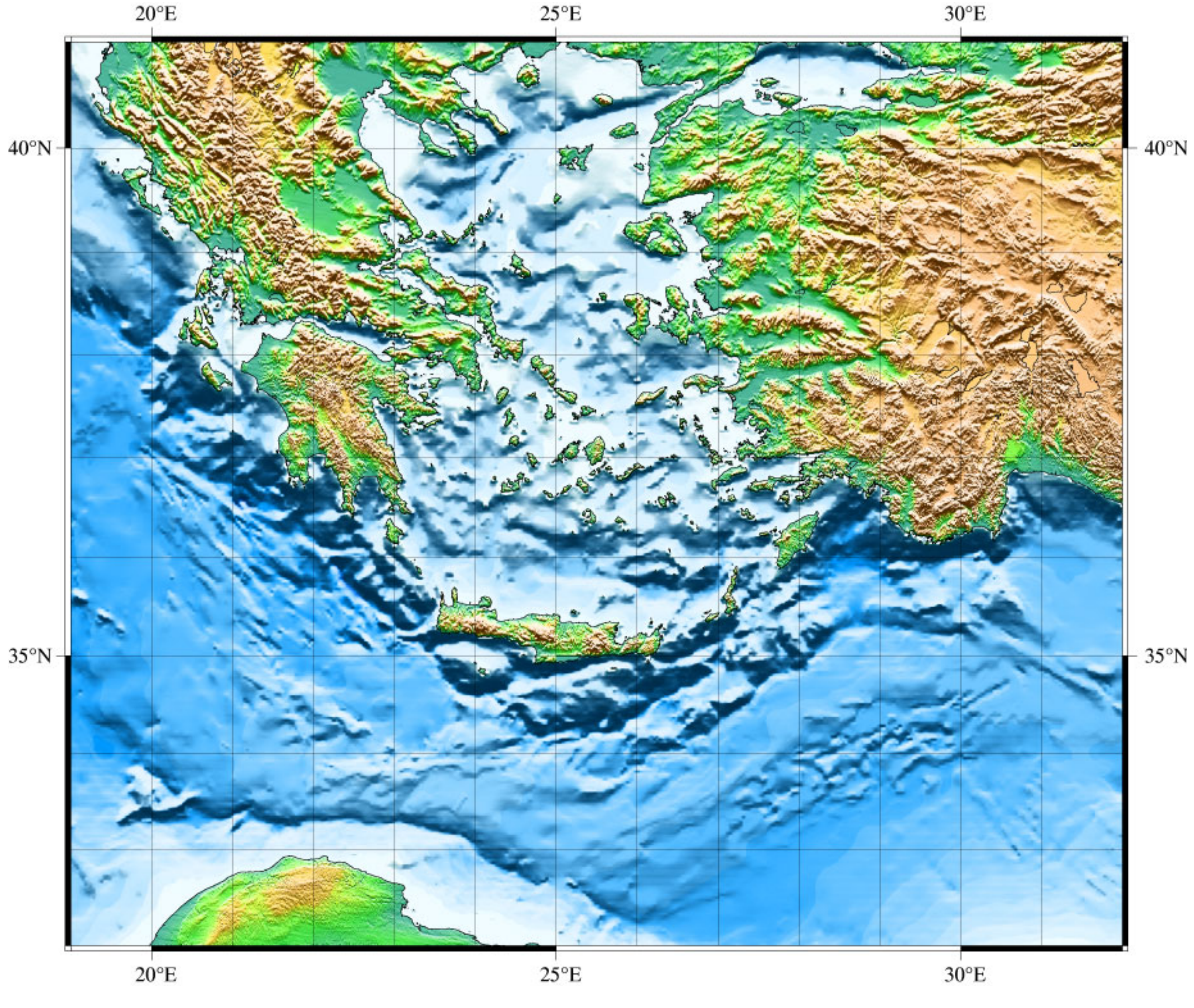

In this last chapter, Part A. summarizes the main results of this study led in the Lycian Nappes and in the Menderes Massif, in order to propose a tectono-metamorphic model for the Alpine evolution of these two nappe complexes in the metamorphic belt of southwest Turkey. Furthermore, the discovery of HP-LT parageneses in southwest Turkey leads to reconsider and discuss the correlations of this region with the nearby collapsed Hellenides Belt of the Aegean domain. Part B. thus focuses on tentative correlations between both Anatolian and Aegean regions.

A. THE LYCIAN NAPPES AND THE MENDERES MASSIF: AN EXTENSIVE HIGH-PRESSURE BELT IN SOUTHWEST TURKEY

1. The Lycian Nappes

Fe-Mg-carpholite assemblages which widely occur in the metasediments of the Karaova formation forming the base of the Lycian Nappes, thus attest for an extensive HP-LT metamorphic belt, over a distance of more than 200 km in the N-S and E-W directions.

The presence of ghosts of aragonite in the rosetta limestones of the overlying carbonate series suggests that the whole metasedimentary sequence of the Lycian Thrust Sheets underwent HP metamorphism.

The parageneses observed in the basal units of the Lycian Nappes imply a quite cold PT gradient, not significantly different from what has been described in the Saih Hatat window below the Semail ophiolite in Oman (Goffé et al., 1988).

Before radiometric ages are obtained, the age of the HP metamorphic event is assumed to range between the Latest Cretaceous (age of the youngest sediments in the Lycian allochthonous unit) and the Eocene (age of the Cycladic Blueschists).

Structural data in the red-green phyllites of the Karaova formation (base of the Lycian nappe complex), as well as in the uppermost levels of the Menderes Massif, allow to characterize top-to-the-NE to top-to-the-E senses of shear along two major shear zones, one above the metapelitic Karaova sequence near Akçakaya (the Akçakaya shear zone), and one that corresponds to the Lycian Nappes/Menderes Massif contact (the Gerit shear zone). These shear zones were active during exhumation of the Lycian HP rocks.

The top-to-the-NE to top-to-the-E movements, which are widespread all along the Lycian/Menderes contact, are not compatible with the southward translation of the Lycian Nappes over the Menderes Massif. Top-to-the-SE to top-to-the-S displacements coeval with the south-southeastward transport of the Lycian Nappes were observed only at the base of klippen of Lycian Nappes located in the northern regions of the Menderes Massif (Dilek-Selçuk and Borlu klippen), as well as in the uppermost levels of the Lycian Thrust Sheets (the Karaböğürtlen wildflysch), in the Lycian Mélange, and in the metamorphic sole of the Lycian peridotite.

It is here claimed that the northeastward to eastward deformation, which represents the main deformation features in the basal metasediments of the Lycian Nappes, might have erased the evidence of the early deformation resulting from the southward transport of the Lycian complex over the Menderes Massif.

PT calculations based on the multi-equilibrium method show that the Lycian Thrust Sheets recorded metamorphic peak conditions of about 10-12 kbar/400°C, suggesting an important burial of more than 30 km. Following the HP metamorphic peak, the Lycian metasediments underwent three distinct exhumation patterns:

-The rocks located in the uppermost levels of the Karaova formation, where Fe-Mg-carpholite is well preserved, retained a single decompression-cooling retrogression path (1) associated with top-to-the-NNE shearing related to the Akçakaya shear zone. This zone of strain localization is an intra-nappe contact that was active in the early stages of exhumation of HP rocks, within the stability field of Fe-Mg-carpholite.

-The rocks located at the base of the Karaova formation, close to the contact with the Menderes Massif, recorded warmer exhumation paths (2) associated with top-to-the-E intense shearing. This deformation occurred after the emplacement of nappes, and is contemporaneous with the reactivation of the Lycian-Menderes contact as a major shear zone (the Gerit shear zone) that allowed late exhumation of HP parageneses under warmer conditions. Where very few relics of Fe-Mg-carpholite have been recognized, exhumation is characterized by a cold retrogression path (1) followed by a thermal overprint (2). Instead, where Fe-Mg-carpholite is completely retrogressed, exhumation is depicted by a single decompression pattern with heating (2). In the latter, the first part of exhumation that corresponds to a HP cooling path (1) has been completely erased by a stronger thermal overprint (2).

The two opposite cases are not isochronal and the exhumation processes might have occurred in a large wedge allowing, from top to base, such HP cooling (1) and decompression with heating (2) patterns.

The apatite fission track data for the rocks on both sides of the Lycian/Menderes contact suggest that these rocks were very close to the paleo-Earth surface in the Late Oligocene-Early Miocene time.

Whereas HP parageneses are found widespread in the basal metasediments of the Bodrum peninsula region, and more largely all along the contact with the Menderes Massif, no traces of HP were found in the sediments of the Lycian Nappes further southeast. On the contrary, the Late Cretaceous Karaböğürtlen wildflysch of the Lycian Thrust Sheets appears unmetamorphosed on the Bodrum peninsula, whereas parts of this formation show greenschist- to amphibolite-facies rocks, in the eastern region of Karaböğürtlen, below the Lycian peridotite nappe.

The fact that the Karaböğürtlen wildflysch of the Bodrum peninsula does not show any HT assemblages such as in the Karaböğürtlen region suggests that parts of the Lycian Thrust Sheets, now located on the Bodrum peninsula, have not been over-ridden by the hot-ophiolite nappe during the Latest Cretaceous southward obduction onto the continental margin.

2. The Menderes Massif

Whereas the Menderes Massif was considered for many years to have undergone only a Barrovian-type metamorphism (the so-called Main Menderes Metamorphism), the finding of magnesiocarpholite-kyanite assemblages in the Mesozoic "cover" series of the southern submassif allows the very first consideration of an Alpine HP metamorphism in this part of the massif. The mechanism responsible for this HP metamorphism is compatible with a burial contemporaneous with Alpine subduction and nappe stacking.

The PT estimates show conditions of about 12-14 kbar/470-500°C for the HP metamorphic peak, higher than these of the Lycian HP metamorphism. Its following exhumation is characterized by a simple isothermal decompression at about 450°C.

The age of this HP metamorphism is constrained between the Middle Palaeocene (age of the uppermost metaolistostrome of the Menderes 'cover') and the Middle Eocene (age of the HP metamorphism of the Dilek peninsula; Oberhänsli et al., 1998).

The HP metamorphic unit of the Dilek peninsula, commonly correlated with that of Samos, belongs to the Cycladic crystalline complex, and must be excluded from the geological definition of the Menderes Massif. The Mesozoic metasedimentary sequence of the Dilek peninsula and that of the southern Menderes Massif cannot be correlated before any major tectonic boundary between the Mesozoic sequence and the underlying Palaeozoic schists of the southern Menderes Massif has been found. Moreover, as described in Chapter III, the uppermost metaolistostromal formation of the Menderes Massif is a thin slightly metamorphosed unit in the southern submassif that contains only low-grade metamorphic Na- and Ca-amphiboles. On the contrary, a stratigraphically similar formation (Selçuk formation) shows evidence of eclogites and blueschists on the Dilek peninsula (Candan et al., 1997; Oberhänsli et al., 1998; Çetinkaplan, 2002). It is therefore reasonable to consider that the Dilek-Selçuk region and the southern Menderes Massif are two different tectonic units. Up to now, evidence for an Alpine HP-LT metamorphism has been described neither in the 'core' of the Menderes Massif, nor in the Paleozoic schists of the 'cover'. In the Precambrian basement, all the HP relics found are attributed to the Pan-African orogeny (Candan et al., 2001).

Assuming the generally accepted description of a stratigraphical continuity between all lithological formations that constitute the 'cover' series, the lack of HP signature in the Palaeozoic schist envelope closer to the core-cover contact could be explained by a strong overprint during the MMM characterized by higher temperature conditions approaching the core-cover contact. Rock chemistry restrictions could also be responsible for this lack of HP imprint in the Paleozoic schists.

Another explanation could consist in two contemporaneous events (HP-LT isochronal with MMM). There is no evidence for an Alpine HP metamorphism in the core of the massif, and no evidence for HT metamorphism in the Mesozoic-Cenozoic part of the Menderes cover. Instead of two separate events, it could be possible to envisage a situation where the upper basement-poor parts of the massif would be in HP-LT conditions and the lower basement-rich part would be in a warmer environment; the difference in thermal gradient being due to the higher content of radioactive material of the basement that would then be internally heated. In fact, recent works have shown that rock type accreted in an accretionary wedge has important effects on the thermal regime of orogenic wedges, which is dominated by radiogenic heat production (Goffé et al., 2003). Material having high radioactive heat production produces HT metamorphism (amphibolitic conditions), whereas material with low radioactive heat production results in low temperature metamorphism of greenschist to blueschist types, depending on the thickness of the wedge (Goffé et al., 2003). The effect of the chemical composition of the crust on the metamorphic evolution of orogenic wedges have been described and thermally modelled for the Central Alps (Bousquet et al., 1997) or for the Himalayas (Henry et al., 1997; Le Pichon et al., 1997).

Nappe stacking in the Menderes Massif is commonly considered as the result of N-S contraction coeval with the regional MMM. It is generally argued that north-south trending stretching and top-to-the-NNE movements are coeval with folding and thrusting during MMM (Bozkurt, 1995; Hetzel et al., 1998; Bozkurt and Park, 1999; Bozkurt, 2001; Whitney and Bozkurt, 2002) and subsequently cooling (Late Eocene; Lips et al., 2001).

The deformation during the HP event and its exhumation is characterized by a severe N-S to NE-SW stretching in the magnesiocarpholite-bearing metaconglomerate.

All these top-to-the-N fabrics observed in the southern submassif show an opposite direction of shear relative to the Lycian Nappes southward translation. A northward backthrusting of the nappes after their emplacement could explain all these movements towards the north, as already proposed by Bozkurt and Park (1999).

During Oligo-Miocene extension, all these syn-metamorphic structures were overprinted by top-to-the-north movements in the northern submassif (Verge, 1995), bivergent movements in the central submassif (Hetzel et al., 1995; 1998), and top-to-the-south greenschist shear bands during exhumation of the southern submassif (Bozkurt and Park, 1994; Whitney and Bozkurt, 2002).

3. Synthesis: a tectono-metamorphic model

All the data presented in this work have strong implications for the tectono-metamorphic Alpine history of the Lycian Nappes and the Menderes Massif. They lead to propose a new model in six major stages, responsible for the present complex structure of the Menderes Massif and the Lycian Nappes in southwest Turkey (Figure V-1).

a. Aptian-Albian initiation of subduction

During the Cretaceous, a northward-dipping intra-oceanic subduction zone formed within the Neotethys Ocean (Collins and Robertson, 1998). The Lycian ophiolitic mélange began to form as an intra-oceanic subduction/accretionary complex during these early stages of convergence, incorporating blocks of basalt of both mid-ocean ridge and within-plate geochemical affinities (Collins and Robertson, 1997). The hot over-riding ophiolite slab caused syn-deformational amphibolite-facies metamorphism in the Aptian-Albian time (102 Ma, K-Ar; Thuizat et al., 1981), prior to the obduction onto the continental margin (Figure V-1a).

The northward root zone of the Lycian Thrust Sheets (relative to the present-day position of the Menderes Massif) was tectonically stable throughout much of the Mesozoic, as attested by the record of a continuous sedimentation from the Permo-Triassic to the Late Cretaceous. The sediments, now forming the Lycian Thrust Sheets, are interpreted to have deposited on a continental slope as part of the Neotethyan passive margin (Figure V-1a). Likewise, the southern Menderes Massif preserved carbonate sedimentation to the end of the Cretaceous, suggesting similar tectonic stability during the Mesozoic time.

b. Campanian-Maastrichtian obduction onto the continental margin

During the Late Cretaceous, the system made of the Lycian ophiolite and the Lycian mélange advanced southward, the Lycian mélange incorporating hot material, probably from seamounts (Collins and Robertson, 1997). In the latest Cretaceous, the ophiolitic complex began to obduct the passive margin and progressively slightly loaded the distal edge of the margin, giving rise to the development of a foredeep in which debris-flow deposits and turbidites accumulated (the Campanian-Maastrichtian Karaböğürtlen wildflysch). This formation that constitutes the uppermost levels of the Lycian Thrust Sheets was locally heated up to amphibolite-facies conditions during southward continuing translation of the hot-enough over-riding ophiolite complex onto the continental margin (Figure V-1b). The obduction-related metamorphic sole rocks are observed at the base of the ophiolitic nappe and locally in the Karaböğürtlen wildflysch. HT metamorphism overprinted the epidote-blueschist-facies assemblages found in an exotic block of the Karaböğürtlen wildflysch, for which the provenance is not ascertained.

c. Middle Palaeocene: initiation of collision (closure of the Neotethys Ocean)

The uppermost metaolistostromal deposits of the Menderes Massif, which is dated Middle Paleocene in the Bodrum peninsula region and Early-Middle Eocene in the Çal-Çivril region (Özer et al., 2001), documents a syn-sedimentary tectonic event. These ages roughly correspond to the range of ages generally given for the Alpine collision between the Menderes-Taurides block and the Sakarya micro-continent (Figure V-1c). In any case, transition from obduction to collision was achieved relatively rapidly (Okay et al., 2001a). The youngest sediment deposit of the Lycian Thrust Sheets (Late Cretaceous Karaböğürtlen wildflysch) suggests that this domain was involved in the nappe stacking shortly after ophiolite obduction. Probably in the Early Palaeogene time, the Lycian Thrust Sheets were buried deep enough below the thick ophiolitic nappe to record their HP-LT metamorphism.

d. Eocene collision

Considering the situation of the Anatolide-Tauride belt during the Eocene time, three stacked HP units were involved in the Alpine continental subduction of the Taurides-Menderes block below the Sakarya micro-continent of the Eurasia margin. The lowermost unit is composed of the imbricated 'core' and HP 'cover' of the Menderes Massif. It is covered by the Cycladic Blueschist complex (Dilek and Samos regions) and finally by the HP Lycian Nappes (Figure V-1d). As said before, the HP-LT metamorphism of the Lycian Nappes might have generated earlier, to the north of the present position of the Menderes Massif, sometime between the Late Cretaceous and the Eocene (Palaeocene?), and was preserved during the southward transport of nappes over the Menderes Massif.

During the Eocene collision, the Menderes metasediments must have been buried beneath at least 30 km of material to allow HP assemblages such as magnesiocarpholite-kyanite (Figure V-1d). The Cycladic blueschist unit also recorded its HP metamorphic conditions (Middle Eocene, 40 Ma; Oberhänsli et al., 1998). Up to now, all the HP parageneses found in the so-called 'core' series of the Menderes Massif are attributed to the Pan-African orogeny. The question of a possible HP Alpine overprint thus remains open.

This contractional episode induced top-to-the-N movements documented by north-verging folding, shearing, thrusting, and imbrication of 'core' and 'cover' series of the Menderes Massif. Top-to-the-north fabrics were recorded in the augen gneisses and in the Palaeozoic metasediments of the massif and are associated with the MMM peak (Paleocene-Eocene) and its progressive cooling (Late Eocene). Intense N-S to NE-SW stretching was recorded in the HP metaconglomerate of the 'cover' series. The very clear deformation pattern of NE-SW stretching and top-to-the-NE kinematic indicators observed continuously at the base of the Lycian Nappes and in the uppermost levels of the metasedimentary 'cover' of the Menderes Massif suggests that the Lycian/Menderes contact has been reactivated as a top-to-the-NE shear zone allowing exhumation of HP metamorphism. The presence of Fe-Mg-carpholite-bearing Lycian units overlying the low-grade metaolistostromal unit of the Menderes Massif implies that the Lycian/Menderes contact postdates HP metamorphism of the Lycian Nappes.

All these movements are probably due to a northward local backthrusting of the HP Lycian Nappes over the Menderes Massif, subsequently to their southward emplacement (Figure V-1d). The deformation during the prograde path is not well preserved except in the uppermost lithologies of the Lycian Thrust Sheets which display top-to-the-south shearing compatible with the southward translation of the Lycian Nappes over the Menderes Massif.

e. Oligo-Miocene extension (collapse of orogen)

The Oligo-Miocene collapse of the HP belt was achieved by several kilometre-scale low-angle detachments along which the final exhumation of the metamorphic rocks occurred. The direction of extension is N-S and all the Eocene syn-metamorphic fabrics were overprinted by top-to-the north sense of shear in the northern submassif, bivergent in the central submassif, and top-to-the-south in the southern part of the Menderes Massif (Figure V-1e).

The rocks of the southern Menderes Massif and the Lycian Nappes were very close to the paleo-Earth surface during the Late Oligocene-Early Miocene time, and unroofing of the Menderes Massif was mainly tectonically controlled.

The final southeastward translation of the Lycian Nappes onto the Bey Dağları occurred until the Late Miocene time (Figure V-1d). It has been envisaged that a new zone of intra-crustal thrusting formed and allowed the final emplacement of the Menderes Massif and the Lycian Nappes during the Miocene (Burdigalian-Serravalian) onto the Bey Dağları parautochthon (Şengör et al., 1984b) (Figure V-1e,f).

f. Neotectonic

This last episode led to high-angle normal faulting and graben formation (Miocene-Pliocene), segmenting the Menderes Massif into northern, central and southern submassifs; the Gediz graben (north) and the Büyük Menderes graben (south) corresponding to the dividing limits (Seyitoğlu et al., 2002; Yilmaz et al., 2000). These high-angle faults crosscut and displace the Oligo-Miocene low-angle detachments (Hetzel et al., 1995; Gessner et al., 2001a; Lips et al., 2001) (Figure V-1f).

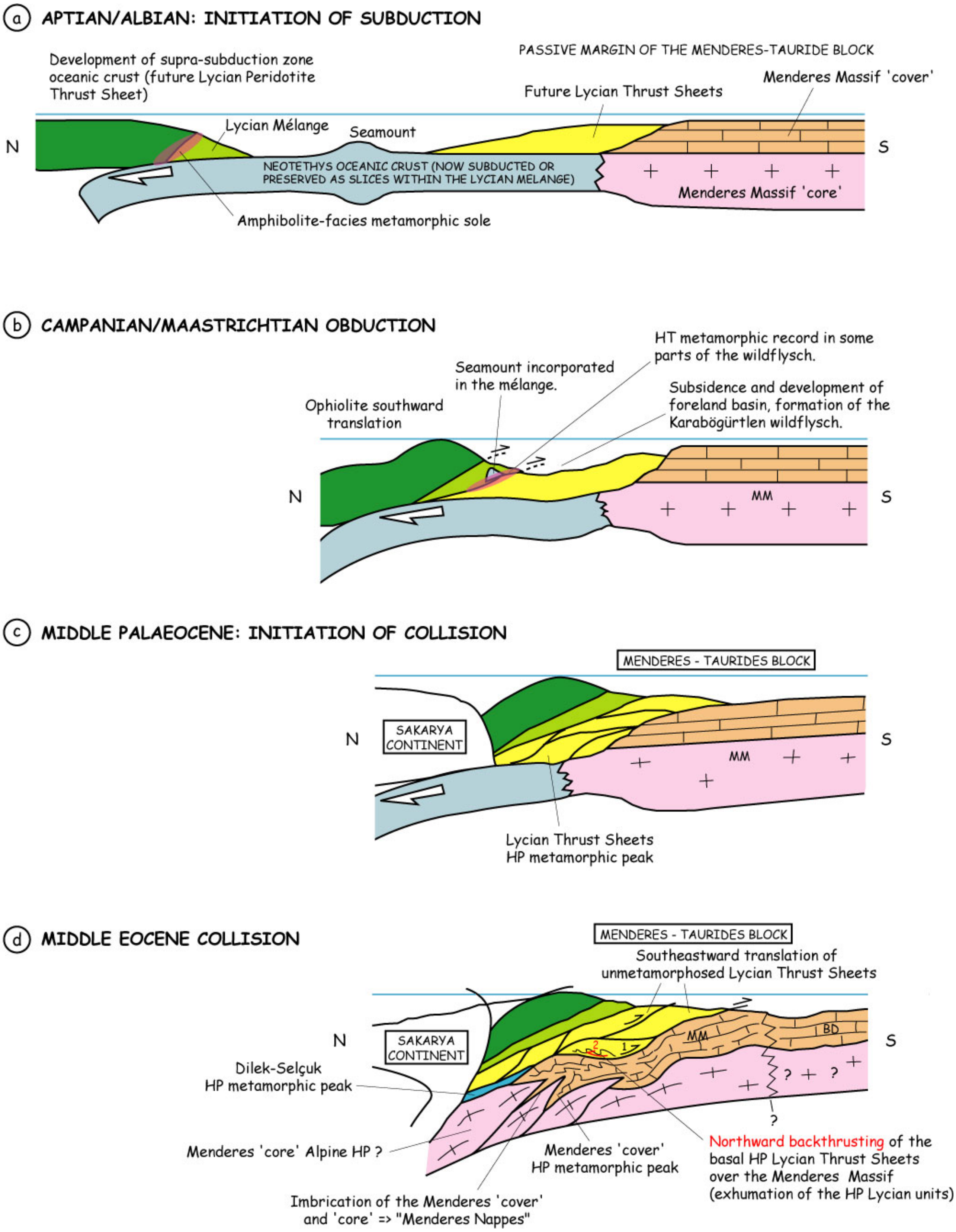

→

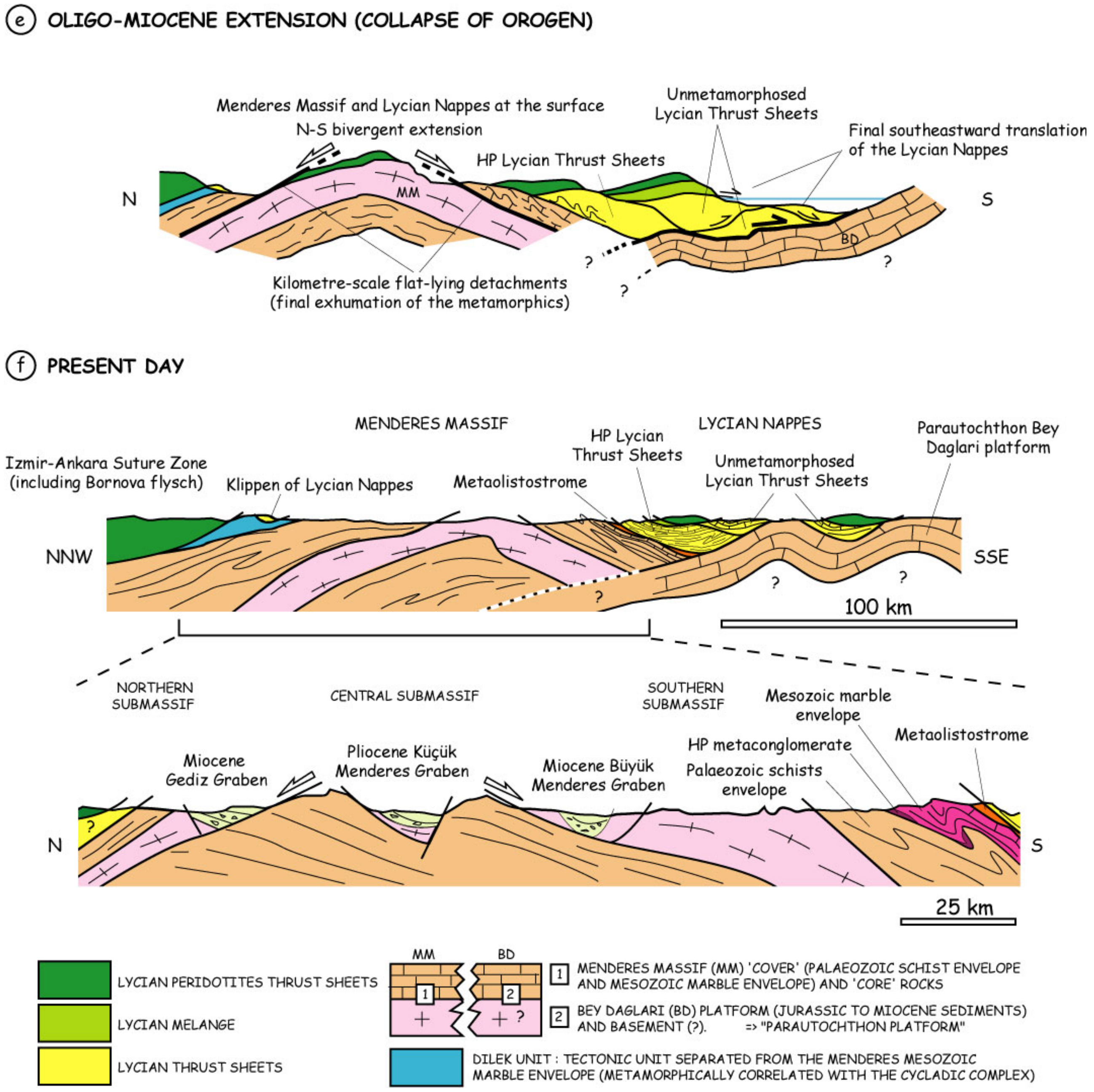

Figure V-1. Synthetic cartoon of the tectono-metamorphic evolution of the Lycian Nappes and the Menderes Massif from the Cretaceous to the present time. See text for explanations.

4. The extensive HP metamorphic terrains of southwest Turkey

This work in the Lycian Nappes and in the Menderes Massif therefore establishes much of the regional zone of HP metamorphism in southwest Turkey (Figure V-2).

North of the Izmir-Ankara suture, the Sakarya Zone constitutes an orogen that was formed by the Late Triassic northward obduction of subduction-accretion units of the Palaeotethys Ocean (Tekeli, 1981; Okay et al., 1996; Okay and Monié, 1997).

South of this long suture, many Alpine HP-LT metamorphic rocks occur:

(1) the Late Cretaceous blueschists of the Tavşanlı Zone (Okay, 1984; Okay and Kelley, 1994; Sherlock et al., 1999),

(2) the newly reported widespread Palaeocene (?) Fe-Mg-carpholite-bearing rocks of the Afyon Zone (Candan et al., 2002; Candan et al., submitted),

(3) the Eocene Cycladic blueschists and eclogites of the Dilek peninsula region (Candan et al., 1997; Oberhänsli et al., 1998; Çetinkaplan, 2002),

(4) the Eocene (?) magnesiocarpholite-kyanite-bearing rocks of the Mesozoic cover of the southern Menderes Massif (Rimmelé et al., 2002; Rimmelé et al., in press),

(5) the Late Cretaceous-Palaeocene (?) Fe-Mg-carpholite-bearing rocks of the Lycian Nappes (Oberhänsli et al., 2001; Rimmelé et al., 2001; Rimmelé et al., 2003).

All these metamorphic rocks were involved in the accretionary complex during northward-verging subduction of the Neo-Tethys Ocean and subsequent collision of the Anatolide-Tauride block beneath the Sakarya micro-continent.

If one replaces the Lycian Nappes in the northern frontal part of the Anatolide-Tauride platform, one could assume a continuous younging in the age of HP-LT metamorphism from north to south, Late Cretaceous in the Tavşanlı Zone and Late Cretaceous-Palaeocene (?) in the Lycian Nappes, Palaeocene in the Afyon Zone, and Eocene in the Menderes Massif. Candan et al. (submitted) envisaged a continental equivalent of a progressive slab roll-back during continuing subduction and subsequent continent-continent collision, corresponding to similar process as observed for the southward migration of HP metamorphism in the Aegean domain.

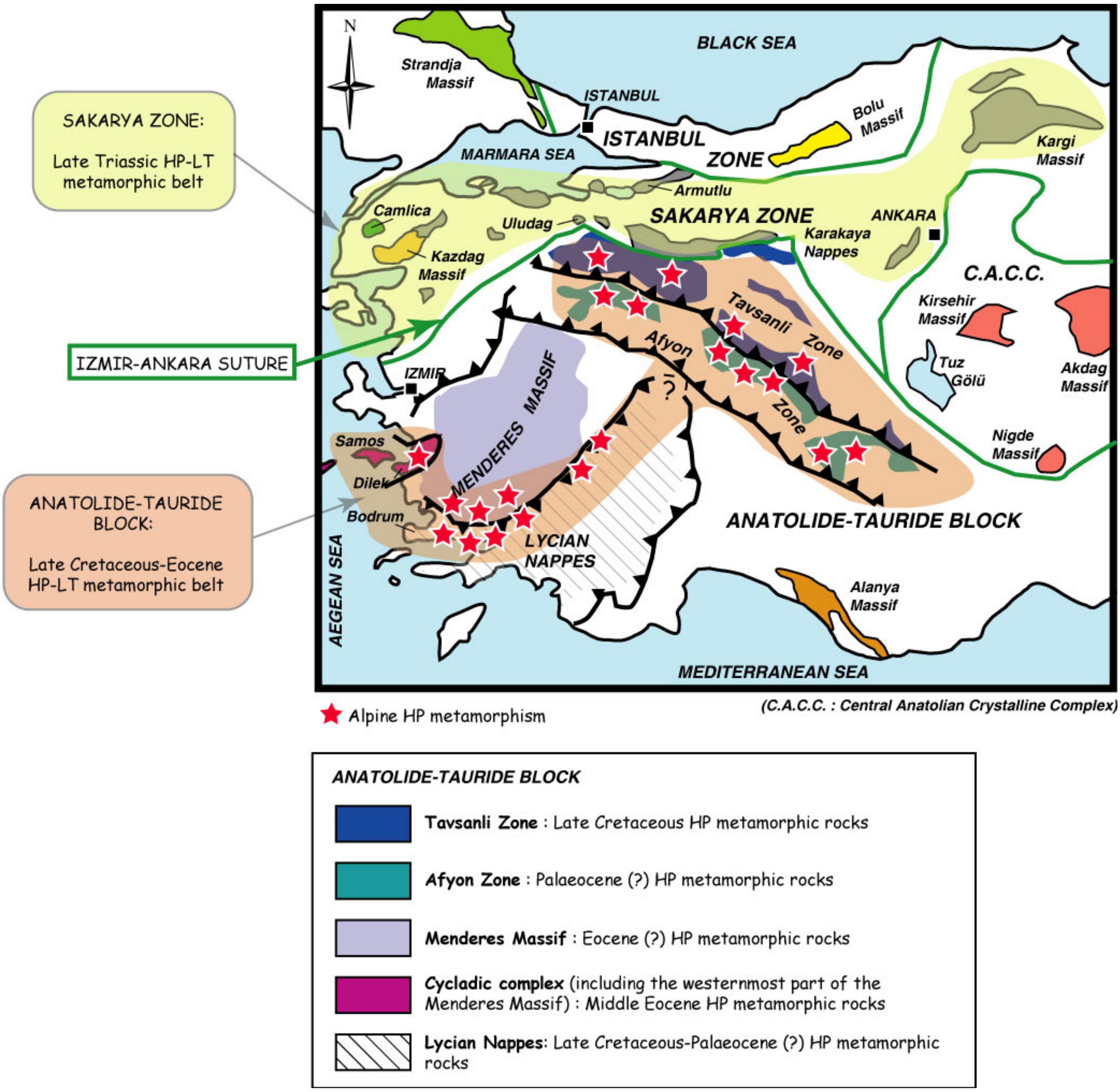

Figure V-2. Simplified map showing the Late Triassic and the Late Cretaceous-Eocene HP-LT metamorphic belts of western Turkey.

B. CORRELATIONS WITH THE NEARBY AEGEAN HIGH-PRESSURE BELT

This part sums up tentative correlations between western Turkey and the nearby Aegean domain that have been proposed in two papers:

- **"Deformation history of the high-pressure Lycian Nappes and implications for tectonic evolution of SW Turkey"** (Rimmelé G., Jolivet L., Oberhänsli R., and Goffé B. - **Tectonics**, 2003).
- **"Correlation of syn-orogenic tectonic and metamorphic events in the Cyclades, the Lycian Nappes and the Menderes Massif. Geodynamic implications"** (Jolivet L., Rimmelé G., Oberhänsli R., Goffé B., and Candan O. – **Bulletin de la Société Géologique de France**, in press).

Although a main link between the Menderes Massif region and the Cyclades can be made through the Cycladic Blueschists which have been recognized in both domains (in the Cyclades and in the Dilek peninsula regions), major significant differences exist between both regions.

1. Menderes and Aegean continental basements

One of the main differences between the two regions is the nature of the continental basement. The continental basement of southwest Turkey is Pan-African (Schuiling, 1962; Şengör et al., 1984b; Satır and Friedrichsen, 1986; Konak et al., 1987, Kröner and Şengör, 1990; Hetzel and Reischmann, 1996; Hetzel et al., 1998; Loos and Reischmann, 1999; Candan et al., 2001) whereas it is Variscan in the Aegean domain (Engel and Reischmann, 1997; Reischmann, 1997; Ring et al., 1999b). No trace of a Pan-African event has been detected in the Cyclades and the Variscan orogeny seems absent from the Menderes Massif.

Whereas in both regions the continental basement has been involved in an accretionary complex and its cover shows HP-LT parageneses, the amount of basement is generally considered quite minor in the Cyclades whereas it represents a significant part of the Menderes massif.

A common point is the occurrence of Triassic intrusions in both domains (Engel and Reischmann, 1997; Reischmann, 1997; Dannat and Reischmann, 1998; Koralay et al., 1998; Koralay et al., 2001). The two basements thus had very different Paleozoic evolutions before these intrusions. Then, the two parts of basement were subjected to a common HP-LT metamorphic episode during formation of the Hellenides-Taurides nappe stack (although up to now only Pan-African HP metamorphism has been identified in the Menderes basement; Oberhänsli et al., 1997; Candan et al., 2001) and to a HT-LP event during the subsequent Aegean extension. During this last stage, the Aegean basement was more intensely reworked.

2. Sedimentary cover

The lowermost sediments of the Menderes cover are Early Palaeozoic in age whereas they are only post-Variscan in the Aegean domain. However, the Mesozoic cover series are quite similar in both regions, with thick sequence of Jurassic and Cretaceous marbles with bauxites. Although the two covers are presently in the same tectonic position (below the Cycladic Blueschists), when looking into more detail, the Mesozoic stratigraphic sequences are different from one place to the other and it is unlikely that these units belonged to a single tectonic unit (Figure V-3).

Both Cycladic Blueschists and Menderes cover underwent HP-LT metamorphism. However, although the Cycladic Blueschist unit is presently above the Menderes cover, it was buried deeper and along a warmer gradient as shown by occurrences of eclogite and garnet-glaucophanites in the Cyclades whereas the Menderes cover only shows magnesiocarpholite-bearing rocks and low-grade blue-amphiboles, attesting for cold gradients. The island of Amorgos (for location, see Figure I-19 in Chapter I) shows a good preservation of HP-LT parageneses in the form of Fe-Mg-carpholite in metabauxites included in a marble sequence (Minoux et al., 1980), thus suggesting similar cold gradients.

Because Amorgos Island is located very close to the inner parts of the Cyclades where the Oligo-Miocene HT-LP intensely overprinted older HP parageneses, its HP-LT metamorphism must have been exhumed earlier than the Oligo-Miocene to be so well preserved, otherwise it would have been highly reworked at higher temperature. The HP-LT unit of Amorgos might have occupied a higher position in the accretionary complex than the metamorphic units of Naxos; the latter being exhumed along a warm gradient during the Oligo-Miocene extension. It is therefore suggested here that the sedimentary cover of Amorgos might represent a lateral equivalent of the cover series of the Menderes Massif (Figure V-3). The Menderes Massif (cover series and probably core) would be originally located above Naxos (basement and cover) but below the Cycladic Blueschists (Figure V-3).

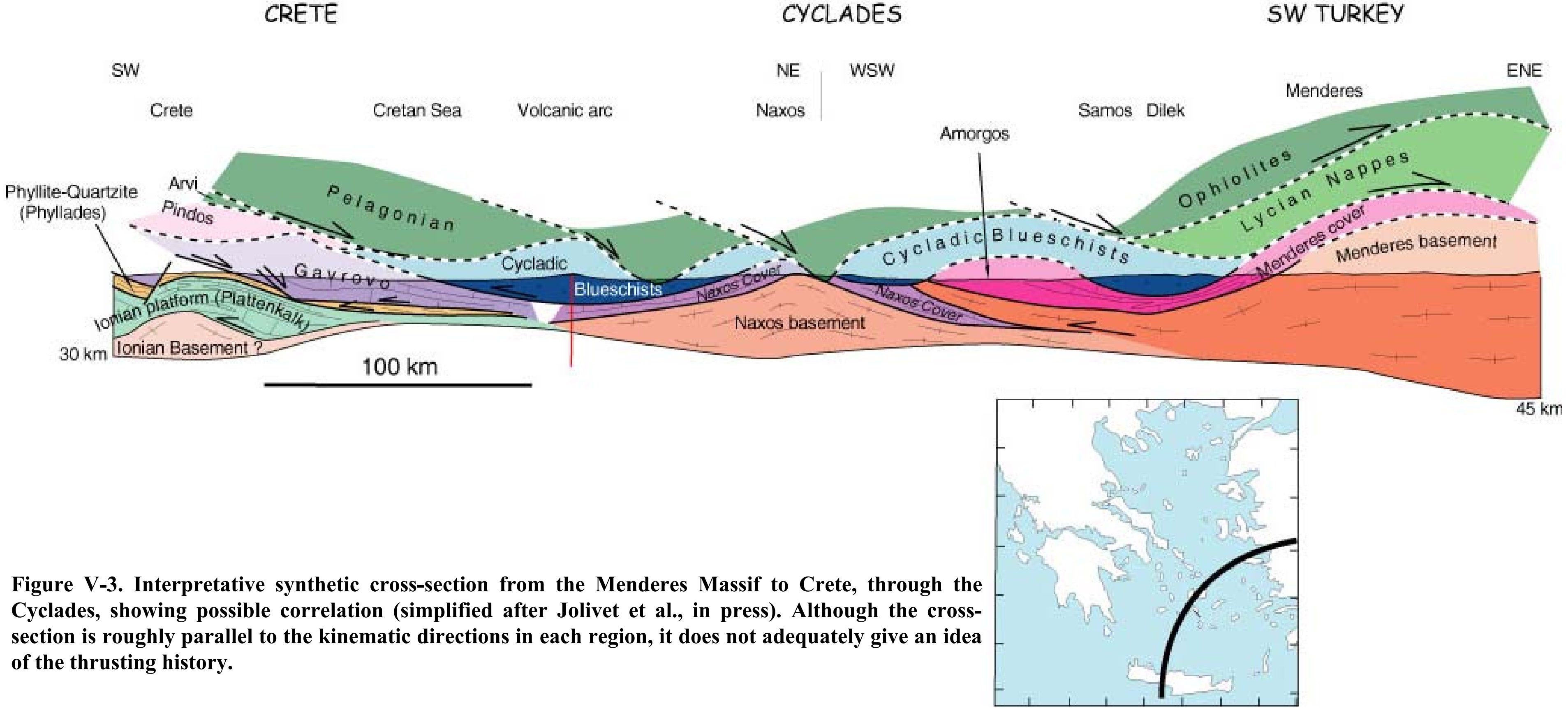

Figure V-3. Interpretative synthetic cross-section from the Menderes Massif to Crete, through the Cyclades, showing possible correlation (simplified after Jolivet et al., in press). Although the cross-section is roughly parallel to the kinematic directions in each region, it does not adequately give an idea of the thrusting history.

However, the presence of Variscan basement on Samos Island (e.g. Ring et al., 1999b) that is considered to belong to the Cycladic Blueschists, still remains problematic with such a representation for the Aegean-Anatolian tectonic units. Moreover, in the Dodecanese Archipelago, as discussed in Chapter I, the Temenia nappe of Arki Island showing aragonite-bearing blueschists has been interpreted to belong either to the Cycladic Blueschists (Franz and Okrusch, 1992), or to the Lycian nappe complex (Gessner et al., 2001b; Ring and Layer, 2003). As for Samos Island, a similar pre-Alpidic basement has been described on Arki, which also raises open questions. Tentative correlations between the tectonic units of the Dodecanese Archipelago and the surrounding units of the Cycladic or Lycian nappe complexes thus need further studies.

In a similar tectonic position, below the Cycladic blueschists, lies the Gavrovo-Tripolitza nappe that widely crops out in the whole Aegean region. Most of this unit is unmetamorphosed, except in the internal parts of the Hellenides (Olympos, Ossa and Almyropotamos tectonic windows; see location on Figure I-19). It has been claimed that this unit forms the basal unit in the Cyclades (Ring et al., 2001a; Ring and Layer, 2003).

In the Cyclades and Western Turkey, the deepest outcropping units are therefore made of a basement, partly Panafrican and partly Variscan with a common Mesozoic sedimentary cover of platform affinity. It includes the core and cover series of the Menderes massif, the basement and cover of Naxos, Paros and Ios, as well as the metamorphic part of the Gavrovo (Figure V-3). These outcrops being now separated from each other, it is difficult to reconstruct the initial geometry of the accretionary complex but the presence of different stratigraphies strongly suggests the presence of several tectonic units, all buried below the Cycladic Blueschists before the Aegean extension started (thus before 30 Ma) (Figure V-4).

In Greece and Crete the external non-metamorphic part of this accretionary complex (Pindos and unmetamorphosed Gavrovo) is thrust above more external units which have been metamorphosed to HP-LT conditions (Phyllite-Quartzites and Ionian nappes). The presence of a basement below these units is probable (Figure V-3), considering the crustal thickness beneath Crete, but it has only been observed as very small units (as near Sitia in Crete).

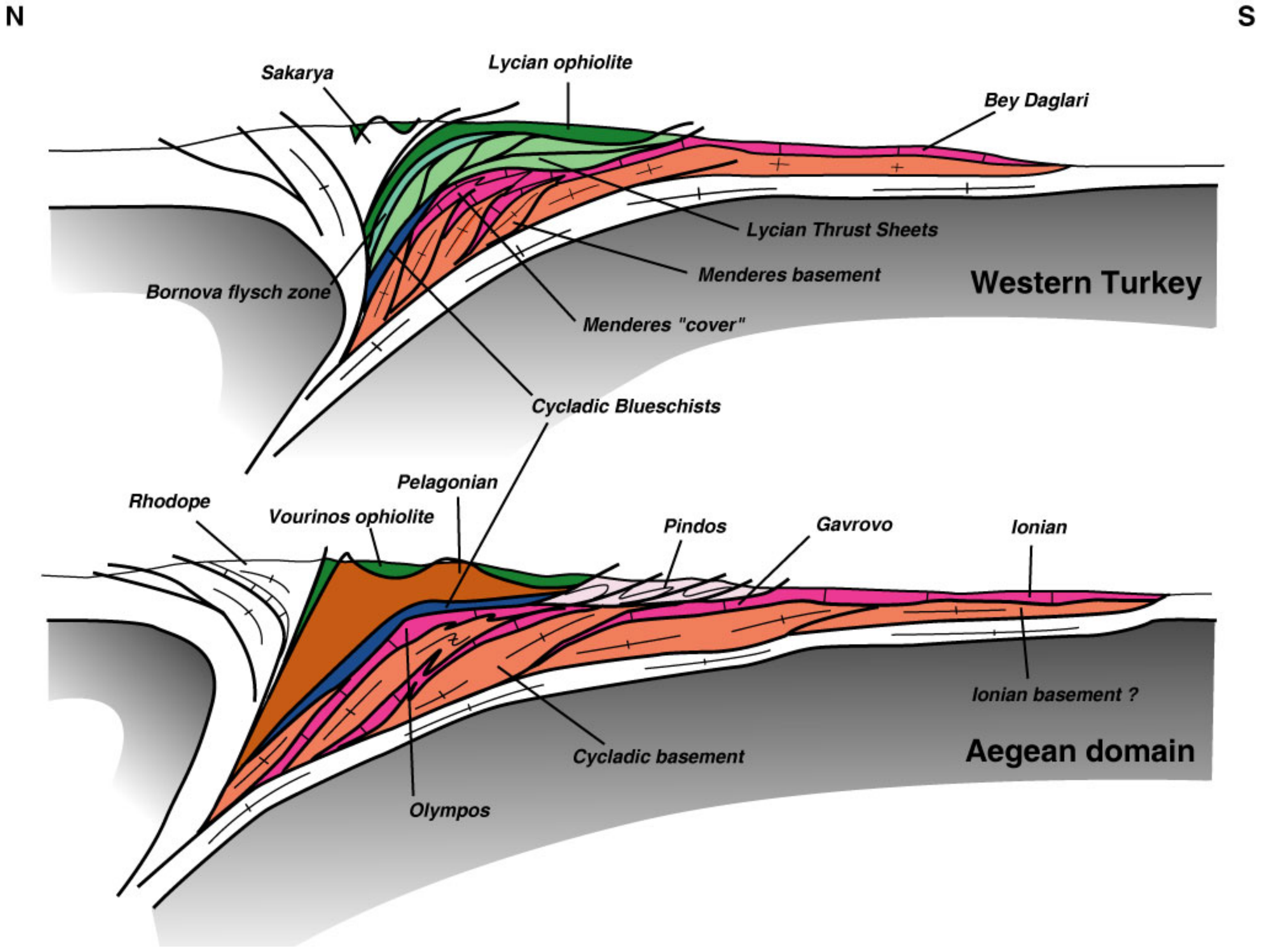

Figure V-4. Interpretative N-S cross-sections of Western Turkey and Aegean domain showing the structure of their accretionary complex some 45 Ma ago (modified after Jolivet et al., in press).

3. The Cycladic Blueschists

The Cycladic blueschist unit widely crops out in the Cyclades, as well as in the westernmost region of the Menderes Massif (Dilek peninsula). This blueschist unit tectonically overlies the basal unit described above (Figure V-3). It comprises all the highly metamorphosed parts of the Cycladic islands, except the Paros-Naxos dome that has been included in the basal unit. Apart from the HP-LT parageneses associated with severe deformation, the main characteristic is the ubiquitous presence of metabasites within the alternating metapelites and marbles, and the olistostrome as observed in Syros (Bonneau et al., 1980).

The age of the HP metamorphic event ranges between 78 and 35 Ma, with a mean age of Early Eocene (50-45 Ma) that is compatible with the age of the youngest sediments involved in the accretionary complex. In the metamorphosed Gavrovo unit of the Olympos, Ossa and Almyropotamos windows (Figure I-19 for location), the occurrence of Nummilites in the uppermost stratigraphic levels attests for a young age of subduction (Godfriaux, 1965). However, the ages clustering between 70-80 Ma in blueschists and eclogites from several regions (Evia, Tinos, Syros) suggest that HP metamorphism in the Cycladic Blueschists certainly began in the Late Cretaceous time.

4. The Lycian Nappes

No clear correlation with the Lycian Nappes has been suggested in the Aegean domain, except its ophiolitic part which has been correlated with the isolated Arvi nappe of Crete, made of Late Cretaceous pillow-lava and sediments (Bonneau, 1973).

Correlation with the Lycian Nappes is in fact problematic considering the differences in the age of ophiolite obduction. It is Late cretaceous for the Lycian Nappes and Late Jurassic in the Hellenides. In both cases, obduction occurred earlier than continental collision, which is Late Cretaceous in the Vardar region and Paleocene in the Izmir-Ankara suture zone. However, the age difference between obduction and collision is very small in Turkey (Okay et al., 2001a). Some Late Cretaceous ages for ophiolites in the northern Cyclades (e.g. Tinos Island) might be related to the age of obduction and these ophiolites could be the extension of the Lycian ophiolite in the Aegean domain. If one assumes that the ophiolite nappes (Jurassic and Cretaceous obduction) all correspond to a single Tethyan oceanic basin, one has to admit the presence of a left-lateral transfer zone separating the two regions allowing non-isochronal obduction.

The Lycian Nappes including the ophiolite are in the same general tectonic position as the Pelagonian domain and its Vourinos ophiolitic nappe (Figure V-3). They are lying above the Cycladic Blueschists in the Dilek peninsula region, and are also in direct contact with the Menderes Massif with an omission of the Cycladic Blueschists further east (Figure V-4). The tectonic contact separating the Lycian Nappes from the Menderes Massif post-dates the Lycian HP metamorphic peak and allows exhumation of the Fe-Mg-carpholite-bearing rocks of the Karaova formation, as described before. This contact formed during subduction of the Menderes Massif below the Cycladic Blueschist and Lycian Nappes and reworked during subsequent exhumation as the HP Lycian Nappes were backthrust onto the massif (Figure V-1d and V-4).

As emphasized in Part A, the age of the magnesiocarpholite-bearing rocks of the Menderes cover could be correlated with the Eocene age of the Dilek HP unit. The age of the HP event in the Lycian nappes cannot be determined with much certainty in the absence of radiometric data. It has to be at least as old as the HP event in the Menderes massif and Cycladic blueschists (Eocene) but it could be quite significantly older as only the exhumation stage is recorded along the ductile contact, as suggested in the previous part (Part A). A reasonable Late Cretaceous-Palaeocene age can be postulated.

As a synthesis, a common tectonic and metamorphic history in the Aegean and Menderes regions starts some 50-45 Ma ago (Eocene) with the main HP event in the Cycladic Blueschists, found in the Cyclades as well as in southwest Turkey. The Cycladic Blueschists and underlying units can be correlated (Figure V-4). Below the Cycladic Blueschists all units have a continental basement and a Permian to Eocene platform cover with bauxite occurrences. Although the pre-Permo-Triassic basements seem to be different in the Menderes Massif and the Cyclades, the more recent history is similar suggesting that they have probably been juxtaposed by the end of the Paleozoic.

5. Eocene versus Oligo-Miocene deformation history

If one tries to compare the kinematic indicators in both Aegean and western Anatolian regions, one observes many similarities (Figure V-5).

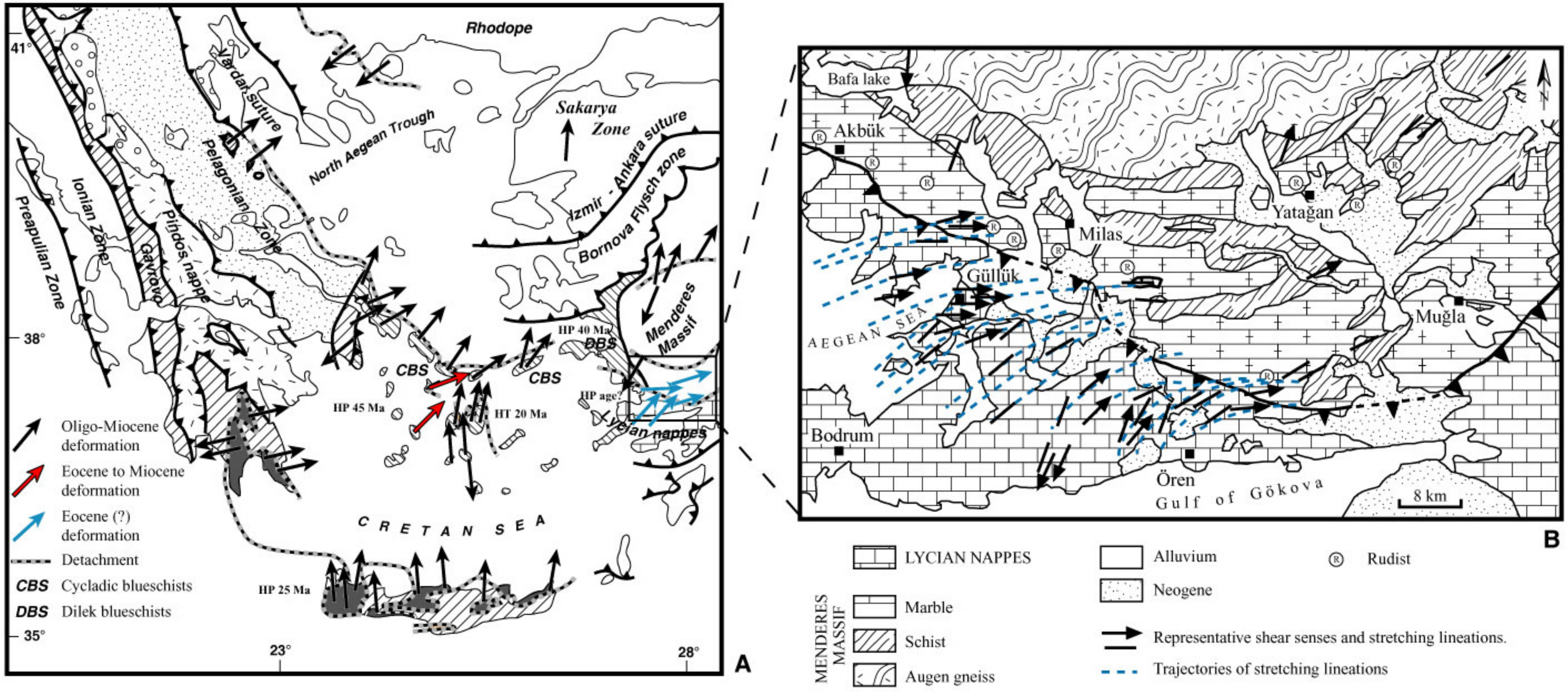

Figure V-5. (a) Stretching lineations and senses of shear in the Aegean domain and Western Turkey (Dinter and Royden, 1993; Gautier et al., 1993; Schermer, 1993; Sokoutis et al., 1993; Gautier and Brun, 1994b; Jolivet et al., 1994b; Hetzel et al., 1995; Jolivet et al., 1996; Bozkurt and Park, 1997a; 1997b; Walcott, 1998; Walcott and White, 1998; Wawrzenitz and Krohe, 1998; Jolivet et al., 1998a; 1998b; Jolivet and Patriat, 1999; Okay and Satir, 2000a; Trotet, 2000; Lips et al., 2001; Trotet et al., 2001a; 2001b; Rimmelé et al., 2001; Rimmelé et al., 2003). (b) Representative stretching lineations and senses of shear on the Bodrum peninsula (modified after Dürr, 1975; Çağlayan et al., 1980; and Konak et al., 1987).

Whereas the Oligo-Miocene deformation is characterized by stretching which trends NE-SW in the northern Cyclades and more N-S in the southern Cyclades and in Crete, the pre-Oligocene (Eocene in Syros and Sifnos islands) deformation shows NE-SW to ENE-WSW directions of shear (Figure V-5a). N-S direction has not been reported for this episode. Considering all the block rotations (described in Chapter I, paragraph A-3-d), the Oligo-Miocene NE-SW-trending stretching directions are located in a domain showing clockwise rotation (e.g. in Peloponese and continental Greece), whereas N-S-trending directions are found in a domain that shows no rotation (e.g. in Crete). Therefore, whereas Eocene directions strike more NE-SW, the Oligo-Miocene ones are more N-S in average.

In the Menderes Massif and Lycian Nappes, the Eocene (?) directions are NE-SW to E-W whereas the Oligo-Miocene directions of extension are more N-S (Figure V-5a,b), which depicts a similar deformation pattern to that of the Aegean domain. It is noticeable that all these kinematic indicators are coeval with exhumation. Rotations in central and eastern Anatolia document a significant 15-20° anticlockwise rotation interpreted as the evidence for a rigid-block rotation of the whole Anatolian block by the same amount (Gürsoy et al., 1998; Platzman et al., 1998; Kissel et al., 2003). This rotation is compatible with the recent motion of Anatolia along the NAF constrained by geodetic data (McClusky et al., 2000; Kissel et al., 2003). However, western Anatolia does not show a consistent rotation pattern. The western margin of the Antalya gulf shows a 20° anticlockwise rotation measured in the Bey Dağları platform but the eastern margin does not show any rotation (Kissel and Laj, 1988). In Rhodes, no rotations have been detected, or a slight anticlockwise rotation (Duermeijer et al., 2000). Unfortunately, no data are reported in the Lycian Nappes and Menderes Massif.

6. Conclusion

The recent discovery of HP-LT in the metasediments of in the Lycian Nappes and the Menderes Massif leads one to reconsider the correlation between the Aegean region (and especially the Cyclades) and western Turkey. Despite significant differences in the early tectonic histories (pre-PermoTriassic) of basement units in the two regions, they belonged to the same paleogeographic units before the Tertiary orogenic events. The two basements were probably juxtaposed by the end of the Paleozoic and underwent a common Mesozoic history. Then, these basements and their cover, as well as the Cycladic Blueschists and the Lycian Nappes were involved in similar evolutional accretionary complexes during the Eocene and Oligocene times. A correlation of the HP metamorphic Menderes cover with some of the Cycladic islands (e.g. Amorgos) that underwent similar HP evolution is possible.

CONCLUSIONS

This study reports widespread occurrences of Fe-Mg-carpholite-bearing rocks in the Lycian Nappes and in the underlying southern Menderes Massif, thus indicating that both nappe complexes underwent HP-LT metamorphism during the Alpine orogenesis. P-T conditions for the HP metamorphic peak recorded in the Lycian Nappes are about 10-12 kbar/400°C. In the southern Menderes Massif, P-T estimates show conditions of about 12-14 kbar/470-500°C for the HP metamorphic peak, higher than these of the Lycian HP metamorphism. These estimates suggest that the metasediments of the Lycian Nappes and the Menderes Massif were buried at depth of about 30-40 km during subduction and nappe stacking.

Following the HP metamorphic peak, the Lycian metasediments underwent three distinct exhumation patterns. The rocks located far from the contact separating the Lycian Nappes and the Menderes Massif, where HP parageneses are well preserved, retained a single HP cooling path (1) associated with top-to-the-NNE shearing related to the Akçakaya shear zone. This zone of strain localization is an intra-nappe contact that was active in the early stages of exhumation of HP rocks, within the stability field of Fe-Mg-carpholite. The rocks located close to the contact with the Menderes Massif recorded warmer exhumation paths (2) associated with top-to-the-E intense shearing. This deformation occurred after the southward emplacement of nappes, and is contemporaneous with the reactivation of the Lycian-Menderes contact as a major shear zone (the Gerit shear zone) that allowed late exhumation of HP parageneses under warmer conditions. Where very few relics of Fe-Mg-carpholite have been recognized, exhumation is characterized by a cold retrogression path (1) followed by a thermal overprint (2). Instead, where Fe-Mg-carpholite is completely retrogressed, exhumation is depicted by a single decompression pattern with heating (2). In the latter, the first part of exhumation that corresponds to a HP cooling path (1) has been completely erased by a stronger thermal overprint (2).

Whereas the rocks of the Lycian Nappes underwent various exhumation patterns, the HP rocks from the southern Menderes Massif recorded a simple isothermal decompression at about 450°C during exhumation. Deformation during HP event and its exhumation is characterized by a severe N-S to NE-SW stretching.

The age of the HP metamorphism recorded in the Lycian Nappes is assumed to range between the Latest Cretaceous (age of the youngest sediments in the Lycian allochthonous unit) and the Eocene (age of the Cycladic Blueschists). A probable Palaeocene age is suggested.

The age of the HP metamorphism that affected the cover series of the Menderes Massif is constrained between the Middle Palaeocene (age of the uppermost metaolistostrome of the Menderes 'cover') and the Middle Eocene (age of the HP metamorphism in the Dilek-Selçuk region that belongs to the Cycladic Complex).

The apatite fission track data for the rocks on both sides of the Lycian/Menderes contact suggest that these rocks were very close to the paleo-Earth surface in the Late Oligocene-Early Miocene time.

The tectono-metamorphic evolution of southwest Turkey can be summarized as following.

During the latest Cretaceous (Campanian-Maastrichtian), the southward-advancing Lycian ophiolite and ophiolitic mélange began to obduct the passive margin and locally heated up to amphibolite-facies conditions the uppermost levels of the Lycian sediments. Transition from obduction to collision occurred relatively rapidly.

During the Middle Palaeocene time, collision between the Menderes-Taurides block and the Sakarya micro-continent initiated. Probably at this stage, the Lycian sediments were buried deep enough (~30 km) below the thick ophiolitic nappe to record their HP-LT metamorphism, to the north of the present position of the Menderes Massif. Deformation during the prograde path is not well preserved except in the uppermost lithologies of the Lycian metasediments which display top-to-the-south shearing compatible with the southward translation of the Lycian Nappes over the Menderes Massif.

The Eocene time is characterized by the continuing continental subduction of the Tauride-Menderes block below the Sakarya micro-continent. The accretionary complex was composed of three stacked HP units, the lowermost corresponding to the imbricated 'core' and 'cover' of the Menderes Massif, the intermediate one consisting in the Cycladic Blueschist complex (Dilek-Selçuk unit), and the uppermost unit being the Lycian Nappes. The metasediments of the Menderes cover, as well as these from the Cycladic blueschist unit, were buried beneath at least 30 km of Lycian material to record their HP-LT metamorphic conditions. This contractional episode induced top-to-the-N movements documented by north-verging folding, shearing, thrusting, and imbrication of 'core' and 'cover' series of the Menderes Massif. Top-to-the-north fabrics were recorded in the augen gneisses and in the Palaeozoic metasediments of the massif and are associated with the MMM peak (Paleocene-Eocene) and its progressive cooling (Late Eocene). Intense N-S to NE-SW stretching was recorded in the HP metaconglomerate of the ‘cover’ series. NE-SW stretching and top-to-the-NE kinematic indicators observed continuously in the basal metasediments of the Lycian Nappes and in the uppermost levels of the metasedimentary ‘cover’ of the Menderes Massif show that the Lycian/Menderes contact has been reactivated as a top-to-the-NE shear zone, allowing exhumation of HP metamorphism. All these movements might be due to a northward local backthrusting of the HP Lycian Nappes over the Menderes Massif, subsequently to their southward emplacement.

The Oligo-Miocene post-orogenic collapse of the HP belt was achieved by several kilometre-scale detachments along which the final exhumation of the metamorphic rocks occurred. The direction of extension is N-S and all the Eocene syn-metamorphic fabrics were overprinted by top-to-the north sense of shear in the northern submassif, bivergent in the central submassif, and top-to-the-south in the southern part of the Menderes Massif. Rocks from the southern Menderes Massif and the Lycian Nappes were very close to the paleo-Earth surface. The final southeastward translation of the Lycian Nappes onto the Bey Dağları parautochthon occurred until the Late Miocene time, probably above an intra-crustal thrusting zone.

A last episode led to high-angle normal faulting that crosscut and displaced the Oligo-Miocene low-angle detachments. The formation of Graben (Miocene-Pliocene) segmented the Menderes Massif into northern, central and southern submassifs (Gediz graben in the north, and Büyük Menderes graben in the south).

Considering the Alpine HP rocks of the nearby Tavşanlı Zone and Afyon Zone, this study in the Lycian Nappes and in the Menderes Massif establishes the existence of an extensive Alpine HP metamorphic belt in southwest Turkey. All these metamorphic rocks were involved in the accretionary complex during northward-verging subduction of the Neo-Tethys Ocean and subsequent collision of the Anatolide-Tauride block beneath the Sakarya micro-continent. Replacing the Lycian Nappes in the northern frontal part of the Anatolide-Tauride platform, a continuous younging, from north to south, in the age of HP-LT metamorphism could be assumed, Late Cretaceous in the Tavşanlı Zone and Late Cretaceous-Palaeocene (?) in the Lycian Nappes, Palaeocene in the Afyon Zone, and Eocene in the Menderes Massif. A continental equivalent of a progressive slab roll-back during continuing subduction and subsequent continent-continent collision, corresponding to similar process as observed for the southward migration of HP metamorphism in the Aegean domain, could be envisaged.

Although the basement units of both Aegean and Anatolian regions show significant differences in the early tectonic histories (pre-PermoTriassic times), they belonged to the same paleogeographic units before the Tertiary orogenic events. The two basements were probably juxtaposed by the end of the Paleozoic and underwent a common Mesozoic history. Then, the basements and their cover, as well as the Cycladic Blueschists and the Lycian Nappes were involved in similar evolutional accretionary complexes during the Eocene and Oligocene times. A correlation between the HP metamorphic Menderes cover and some of the Cycladic islands (e.g. Amorgos), which underwent similar HP evolution, is envisaged.

PERSPECTIVES

At this stage of the study, major missing features are radiometric ages of the HP metamorphism in both Lycian Nappes and southern Menderes Massif. Obtaining such data would give essential constraints on the tectono-metamorphic evolution of the HP mountain belt of SW Turkey. Although it is argued in this work that HP metamorphic peak in the Lycian Nappes might be older than that of the Menderes metasedimentary cover, a serious campaign of sampling for isotope geochronology is necessary to check this important point. Furthermore, as emphasized in this manuscript, temporal relations between HP metamorphism and MMM still remain enigmatic (HP overprinted by MMM? two contemporaneous events?). Such isotopic data may help to clarify these questions remaining open. This work is in progress.

Recent studies have shown that Raman spectra of carbonaceous material in metasediments can be used as a geothermometer of the maximum temperature conditions reached during a metamorphic event (Beyssac et al., 2002). Temperature can be estimated to ±50°C in the range 330-650°C. Maps of temperatures can therefore be established and have the advantage to highlight regional temperature variations in metamorphic terrains. This method combines the benefits of its easy applicability for all types of rocks, with that of its capacity to establish precise cartography of temperature fields. The irreversibility of carbonaceous material transformation allows the record of temperature peak, in contrast to thermobarometry based on mineral assemblages which are prone to re-equilibration effects during retrogression. In the case of the HP metamorphic belt of SW Turkey, sampling along transects across major shear zones would allow one to obtain precise thermal profiles from one metamorphic unit to the other one, particularly for areas in which the multi-equilibrium method could not be envisaged because of rock-chemistry restrictions.

The recent discovery of HP-LT parageneses in the metasediments of the Afyon Zone (Candan et al., 2002; Candan et al., submitted) has strong implications for the tectonic evolution of SW Turkey. In order to understand the tectono-metamorphic relations of this metamorphic domain with these described in this work, similar structural and geochronological studies related to the HP-LT metamorphic event have to be led in the metamorphic terrains of the Afyon Zone.

Finally, major questions concerning correlations between the HP metamorphic belt of Western Anatolia and that of the Aegean domain still remain open. Extending from Rhodes to Samos, between southwest Turkey and the Cycladic-Cretan region, the Dodecanese Archipelago forms a region that is geologically poorly known. One particular major problem concerns correlations between the tectonic units forming these islands and the surrounding units of the Cycladic complex, Menderes Massif, and Lycian Nappes. This enigmatic region therefore requires many investigations because it could represent a key for the better understanding of the Tertiary tectonic evolution of the Aegean-Anatolian metamorphic belt.

REFERENCES

REFERENCES

Aerden, D., 1998. Tectonic evolution of the Montagne Noire and a possible orogenic model for syncollisional exhumation of deep rocks, Variscan Belt, France. *Tectonics*, 17: 62-79.

Agard, P., 1999. Evolution métamorphique et structurale des métapélites océaniques dans l'orogène Alpin: l'exemple des Schistes Lustrés des Alpes occidentales (Alpes Cottiennes). *PhD Thesis*, Pierre et Marie Curie, Paris, 295 pp.

Agard, P., Vidal, O. and Goffé, B., 2001. Interlayer and Si content of phengites in high-pressure carpholite-bearing metapelites. *J. metamorphic Geol.*, 19: 479-496.

Akgün, F. and Sözbilir, H., 2001. A palynostratigraphic approach to the SW Anatolian molasse basin: Kale-Tavas molasse and Denizli molasse. *Geodin. Acta*, 14: 71-93.

Akkök, R., 1983. Structural and metamorphic evolution of the northern part of the Menderes massif: new data from the Derbent area and their implication for the tectonics of the massif. *J. Geol.*, 91: 342-350.

Altherr, R., Schliestedt, M., Okrusch, M., Seidel, E., Kreuzer, H., Harre, W., Lenz, H., Wendt, I. and Wagner, G.A., 1979. Geochronology of high-pressure rocks on Sifnos (Cyclades, Greece). *Contrib. Mineral. Petrol.*, 70: 245-255.

Altherr, R., Kreuzer, H., Wendt, I., Lenz, H., Wagner, G.A., Keller, J., Harre, W. and Hohndorf, A., 1982. A Late Oligocene/Early Miocene high temperature belt in the anti-cycladic crystalline complex (SE Pelagonian, Greece). *Geol. Jb.*, 23: 97-164.

Andriessen, P.A.M., Boelrijk, N.A.I.M., Hebeda, E.H., Priem, H.N.A., Verdurmen, E.A.T. and Vershure, R.H., 1979. Dating the events of metamorphism and granitic magmatism in the Alpine orogen of Naxos (Cyclades, Greece). *Contrib. Mineral. Petrol.*, 69: 215-225.

Angelier, J., Lyberys, N. and Le Pichon, X., 1982. The tectonic development of the Hellenic Arc and the Sea of Crete: a synthesis. *Tectonophysics*, 86: 159-196.

Armijo, R., Meyer, B., Hubert, A. and Barka., A., 1999. Westward propagation of the North Anatolian Fault into the northern Aegean; timing and kinematics. *Geology*, 27(3): 267-270.

Arslan, A., Erdoğan, B. and Güngör, T., 2002. Transport direction of Lycian Nappes studied by kinematic indicators in Milas region, *First International Symposium of the Faculty of Mine (ITU) on Earth Sciences and Engineering*, Istanbul, Turkey, pp. 109.

Ashworth, J.R. and Evirgen, M.M., 1984a. Garnet and associated minerals in the southern margin of the Menderes Massif, southwest Turkey. *Geol. Mag.*, 121(4): 323-337.

Ashworth, J.R. and Evirgen, M.M., 1984b. Mineral chemistry of regional chloritoid assemblages in the Chlorite Zone, Lycian Nappes, southwest Turkey. *Mineral. Mag.*, 48: 159-165.

Aubouin, J., 1959. Contribution à l'étude de la Grèce septentrionale; les confins de l'Epire et de la Thessalie. *Ann. Géol. Pays Hellén.*, 10: 1-483.

Aubourg, C., Hébert, R., Jolivet, L. and Cartayrade, G., 2000. The magnetic fabric in a detachment shear zone: the example of Tinos island (Greece). *Tectonophysics*, 321: 219-236.

Avigad, D., 1990. The geodynamic evolution of the Cycladic massif (Aegean Sea, Greece) - a contribution to the study of continental collision. *PhD Thesis*, Hebrew University.

Avigad, D., 1998. High-pressure metamorphism and cooling on SE Naxos (Cyclades, Greece). *Eur. J. Mineral.*, 10: 1309-1319.

REFERENCES

Avigad, D. and Garfunkel, Z., 1989. Low angle faults above and below a blueschist belt-Tinos Island, Cyclades, Greece. *Terra Nova*, 1: 182-187.

Avigad, D., Matthews, A., Evans, B.W. and Garfunkel, Z., 1992. Cooling during the exhumation of a blueschist terrane: Sifnos (Cyclades, Greece). *Eur. J. Mineral.*, 4: 619-634.

Avigad, A., Garfunkel, Z., Jolivet, L. and Azañón, J.M., 1997. Back-arc extension and denudation of Mediterranean eclogites. *Tectonics*, 16(6): 924- 941.

Avigad, D., Baer, G. and Heimann, A., 1998. Block rotations and continental extension in the Central Aegean Sea: paleomagnetic and structural evidence from Tinos and Mykonos. *Earth Planet. Sci. Lett.*, 157: 23-40.

Azañon, J.M., 1994. Metamorphismo de alta presion/baja temperatura, baja presion/alta temperatura y tectonica del complejo Alpujarride (cordilleras Bético-Rifeñas). *PhD Thesis*, Granada, 331 pp.

Azañon, J.M. and Crespo-Blanc, A., 2000. Exhumation during a continental collision inferred from the tectonometamorphic evolution of the Alpujarride Complex in the central Betics (Alboran Domain, SE Spain). *Tectonics*, 19: 549-565.

Azañon, J.M. and Goffé, B., 1997. Ferro- and magnesiocarpholite assemblages as record of high-P, low-T metamorphism in the Central Alpujarrides, Betic Cordillera (SE Spain). *Eur. J. Mineral.*, 9: 1035-1051.

Balanya, J.C., Garcia-Dueñas, V., Azañon, J.M. and Sanchez-Gomez, M., 1997. Alternating contractional and extensional events in the Alpujarride nappes of the Alboran Domain. *Tectonics*, 16(2): 226-238.

Barka, A., 1992. The North Anatolian Fault. *Annales Tectonicae Special Issue*, supplement to volume VI: 164-195.

Bassias, Y. and Triboulet, C., 1994. Tectono-metamorphic evolution of blueschist formations in the Peloponnesus (Parnon and Taygetos Massifs, Greece): a model of nappe stacking during Tertiary orogenesis. *J. Geol.*, 102: 697-708.

Becker-Platen, J.D., Benda, L. and Steffens, F., 1977. Litho- und biostratigraphische deutung radiometrischer Alterbestirnmungen aus dem Jungtertiar der Turkei. *Geol. Jb.*, B25: 139-167.

Berman, R.G., 1988. Internally consistent thermodynamic data for minerals in the system Na_2O-K_2O-CaO-MgO-FeO-Fe_2O_3-Al_2O_3-SiO_2-TiO_2-H_2O-CO_2. *J. Petrol.*, 29: 445 - 522.

Berman, R.G., 1991. Thermobarometry using multi-equilibrium calculations: a new technique, with petrological applications. *Can. Mineral.*, 29: 833-855.

Berman, R.G. and Perkins, E.H., 1987. GEO-CALC: Software for calculation and display of pressure-temperature-composition phase diagrams. *Am. Mineral.*, 72: 861-862.

Bernoulli, D., de Graciansky, P.C. and Monod, O., 1974. The extension of the Lycian Nappes (SW Turkey) into the southeastern Aegean Islands. *Eclogae Geol. Helv.*, 67: 39-90.

Beyssac, O., Goffé, B., Chopin, C. and Rouzaud, J.N., 2002. Raman spectra of carbonaceous material in metasediments: a new geothermometer. *J. metamorphic Geol.*, 20: 859-871.

Bingöl, E., 1969. Geology of the central and southeastern parts of Kazdag Massif (in Turkish with English abstract). *Min. Res. Expl. Inst. Turkey Bull.*, 72: 110-123.

Bingöl, E., Akyürek, B. and Korkmazer, B., 1973. Biga Yarimadasinin jeolojisi ve Karakaya formasyonunun bazi özellikleri (in Turkish with English abstract). *Proc. 50th Anniv. Turkish Rep.*, Min. Res. Expl. Inst. Turkey: 70-76.

Blake, M.C., Bonneau, M., Geyssant, J., Kienast, J.R., Lepvrier, C., Maluski, H. and Papanikolaou, D., 1981. A geological reconnaissance of the Cycladic blueschist belt, Greece. *Geol. Soc. Amer. Bull.*, 92: 247-254.

Bonneau, M., 1973. La nappe métamorphique de l'Astéroussia, lambeau d'affinités pélagoniennes charrié jusque sur la zone de Tripolitza de la Crète moyenne (Grèce). *C. R. Acad. Sci. Paris*. 2303-2306.

Bonneau, M., 1982. Evolution géodynamique de l'arc égéen depuis le Jurassique Supérieur jusqu'au Miocène. *Bull. Soc. Géol. France*, 7: 229-242.

Bonneau, M., 1984. Correlation of the Hellenic nappes in the south-east Aegean and their tectonic reconstruction. In: J.E. Dixon and A.H.F. Robertson (Editors), The Geological Evolution of the Eastern Mediterranean. *Spec. Publ. Geol. Soc. London*. Blackwell Scientific Publications, Oxford, pp. 517-527.

Bonneau, M. and Kienast, J.R., 1982. Subduction, collision et schistes bleus: exemple de l'Egée, Grèce. *Bull. Soc. Géol. France*, 7: 785-791.

Bonneau, M., Geyssant, J. and Lepvrier, C., 1978. Tectonique alpine dans le massif d'Attique-Cyclade (Grèce): plis couchés kilométriques dans l'île de Naxos, conséquences. *Rev. Geogr. Phys. Geol. Dyn.*, 20(1): 109-122.

Bonneau, M., Kienast, J., Lepvrier, C. and Maluski, H., 1980. Tectonique et métamorphisme haute pression d'âge Eocène dans les Hellénides: exemple de l'île de Syros (Cyclades, Grèce). *C. R. Acad. Sci. Paris*, 291: 171-174.

Bousquet, R., Goffé, B., Henry, P., Pichon, X.L. and Chopin, C., 1997. Kinematic, thermal and petrological model of the Central Alps: Lepontine metamorphism in the Upper Crust and eclogitisation of the lower crust. *Tectonophysics*, 273: 105-128.

Bousquet, R., Oberhänsli, R., Goffé, B., Jolivet, L. and Vidal, O., 1998. High-pressure-low-temperature metamorphism and deformation in the Bündnerschiefer of the Engadine window: Implications for the regional evolution of the eastern Central Alps. *J. Metamorphic Geol.*, 16: 657-674.

Bousquet, R., Goffé, B., Vidal, O., Oberhänsli, R. and Patriat, M., 2002. The tectono-metamorphic history of the Valaisan domain from the Western to the Central Alps: New constraints on the evolution of the Alps. *Geol. Soc. Amer. Bull.*, 114(2): 207-225.

Bouybaouene, M.L., Goffé, B. and Michard, A., 1995. High-pressure, low-temperature metamorphism in the Sebtides nappes, northern Rif, Morocco. *Geogaceta*, 17: 117-119.

Bozkurt, E., 1995. Deformation during main Menderes metamorphism (MMM) and its tectonic significance: evidence from southern Menderes Massif, western Turkey. *Terra Abstr.*, 7: 176.

Bozkurt, E., 1996. Metamorphism of Palaeozoic Schists in the Southern Menderes Massif: Field, Petrographic, Textural and Microstructural Evidence. *Turkish J. Earth Sci.*, 5: 105-121.

Bozkurt, E., 2001. Late Alpine evolution of the central Menderes Massif, western Turkey. *Int. J. Earth Sci.*, 89(4): 728-744.

Bozkurt, E. and Oberhänsli, R., 2001. Menderes Massif (Western Turkey): structural, metamorphic and magmatic evolution - a synthesis. *Int. J. Earth Sci.*, 89(4): 679-708.

Bozkurt, E. and Park, R.G., 1994. Southern Menderes Massif - an Incipient Metamorphic Core Complex in Western Anatolia, Turkey. *J. Geol. Soc. London*, 151: 213-216.

Bozkurt, E. and Park, R.G., 1997a. Evolution of a mid-Tertiary extensional shear zone in the southern Menderes massif, western Turkey. *Bull. Soc. Géol. France*, 168(1): 3-14.

Bozkurt, E. and Park, R.G., 1997b. Microstructures of deformed grains in the augen gneiss of Southern Menderes Massif and their tectonic significance. *Geol. Rundsch.*, 86: 103-119.

Bozkurt, E. and Park, R.G., 1999. The structures of the Palaeozoic schists in the southern Menderes Massif, western Turkey: a new approach to the origin of the Main Menderes Metamorphism and its relation to the Lycian Nappes. *Geodin. Acta*, 12: 25-42.

Bozkurt, E. and Satir, M., 2000. The southern Menderes Massif (western Turkey): geochronologie and exhumation history. *Geol. J.*, 35: 285-296.

Bozkurt, E., Winchester, J.A. and Park, R.G., 1995. Geochemistry and Tectonic Significance of Augen Gneisses From the Southern Menderes Massif (West Turkey). *Geol. Mag.*, 132(3): 287-301.

Brinkmann, R., 1967. Die Südflanke des Menderes-Massivs bei Milas, Bodrum und Ören, *Scient. Rep. Faculty Sci., Ege Univ.*, Izmir, Turkey.

Brown, D., Juhlin, C., Alvarez-Marron, J., Perez-Estaun, A. and Oslinshi, A., 1998. Crustal scale structure and evolution of an arc-continent collision zone in the southern Urals, Russia. *Tectonics*, 17: 158-171.

Bröcker, M., 1990. Blueschist-to-greenschist transition in metabasites from Tinos island, Cyclade, Greece: compositional control or fluid infiltration. *Lithos*, 25: 25-39.

Bröcker, M. and Enders, M., 1999. U-Pb zircon geochronology of unusual eclogite-facies rocks from Syros and Tinos (Cyclades, Greece). *Geol. Mag.*, 136: 111-118.

Bröcker, M., Kreuzer, H., Matthews, A. and Okrusch, M., 1993. ^{40}Ar/^{39}Ar and oxygen isotope studies of polymetamorphism from Tinos island, Cycladic blueschist belt, Greece. *J. metamorphic Geol.*, 11: 223-240.

Brunn, J.H., 1956. Contribution à l'étude géologique du Pinde septentrional et de la macédoine occidentale. *Ann. Géol. Pays Hellén.*, 7: 358.

Brunn, J.H., de Graciansky, P.C., Gutnic, M., Juteau, T., Lefèvre, R., Marcoux, J., Monod, O. and Poisson, A., 1970. Structures majeures et corrélations stratigraphiques dans les Taurides occidentales. *Bull. Soc. Géol. France*, 12: 515-556.

Burg, J.P., Davy, P., Nievergelt, P., Oberli, F., Seward, D., Zhizhong Diao and Meier, M., 1997. Exhumation during crustal folding in the Namche-Barwa syntaxis. *Terra Nova*, 9: 53-56.

Çağlayan, A.M., Öztürk, E.M., Öztürk, Z., Sav, H. and Akat, U., 1980. Structural observations on the southern Menderes Massif. *Publ. Chamber Geol. Eng. Turkey* (in Turkish with English summary), 10: 9-17.
Çakmakoğlu, A., 1985. Aydin N19-d3, Marmaris O19-a2 ve Denizli M21-d3-c4, *MTA report* ("Paftasina ait genellestirilmis dikme kesit"), MTA enstitüsü Jeoloji, Bornova, Izmir.

Candan, O., 1995. Menderes Masifinde kalinti granulit fasiyesi metamorfizmasi (in turkish with english abstract). *Turkish J. Earth Sci.*, 4: 35-55.

Candan, O., 1996. Çine asmasifindeki (Menderes Masifi) gabrolarin metamorfizmasi ve diger asmasiflerle karsilastirilmasi (in turkish with english abstract). *Turkish J. Earth Sci.*, 4: 123-139.

Candan, O. and Dora, O., 1998. Generalized geological map of the Menderes Massif, Western Turkey, Dokuz Eylül Universitesi Mühendislik Fakültesi, Izmir-Turkey.

Candan, O., Dora, O.Ö., Dürr, S. and Oberhänsli, R., 1994. Erster Nachweis von Granulit- und Eklogit-Relikten im Menderes Massiv / Türkei, *T. S. K. 5th symposium*. Göttinger Arbeiten zur Geologie und Paeontologie, pp. 217-220.

Candan, O., Dora, O.Ö., Oberhänsli, R., Oelsner, F. and Dürr, S., 1997. Blueschist relics in the Mesozoic cover series of the Menderes Massif and correlations with Samos Island, Cyclades. *Schweiz. Mineral. Petrogr. Mitt.*, 77: 95-99.

Candan, O., Dora, O.Ö., Oberhänsli, R., Çetinkaplan, M., Oelsner, F. and Dürr, S., 1998. Two different high-pressure metamorphisms in the Menderes Massif: Pan-African and Tertiary events, *Geol. Congr. Turkey Abstr.*, pp. 52-54.

Candan, O., Dora, O.Ö., Oberhänsli, R., Çetinkaplan, M., Partzsch, J.H., Warkus, F.C. and Dürr, S., 2001. Pan-African high-pressure metamorphism in the Precambrian basement of the Menderes Massif, western Anatolia, Turkey. *Int. J. Earth Sci.*, 89(4): 793-811.

Candan, O., Çetinkaplan, M., Oberhänsli, R. and Rimmelé, G., 2002. Fe-Mg-Carpholite - pyrophyllite - chloritoid-bearing Triassic metapelites from Afyon Zone, Turkey: First evidence for Alpine low-grade, high-P/low-T metamorphism, *First International Symposium of the Faculty of Mines (ITU) on Earth Sciences and Ingineering*, Istanbul, Turkey, pp. 107.

Candan, O., Çetinkaplan, M., Oberhänsli, R., Rimmelé, G. and Akal, C., submitted. Fe-Mg carpholite occurrence as a record of Alpine high-P/low-T metamorphism of Afyon Zone and implication for metamorphic evolution of western Anatolia, Turkey.

Cathelineau, M. and Nieva, D., 1985. A chlorite solid solution geothermometer. The Los Azufres (Mexico) geothermal system. *Contrib. Mineral. Petrol.*, 91: 235-244.

Celet, P. and Ferrière, J., 1978. Les Hellénides internes: le Pélagonien. *Eclogae geol. Helv.*, 71: 467-495.

Çelik, O.F. and Delaloye, M., 2001. Origin of the ophiolite-related metamorphic rocks and their post-kinematic mafic dykes in the Antalya and Lycian ophiolites, *International Symposium on Eastern Mediterranean Geology*, Isparta, Turkey.

Çetinkaplan, M., 2002. Tertiary high pressure/low temperature metamorphism in the Mesozoic cover series of the Menderes Massif and correlation with the Cycladic Crystalline Complex. *PhD Thesis*, Dokuz Eylül Universitesi, Izmir, 323 pp.

Chopin, C., Seidel, E., Theye, T., Ferraris, G., Ivaldi, G. and Catti, M., 1992. Magnesiochloritoid, and the Fe-Mg series in the chloritoid group. *Eur. J. Mineral.*, 4: 67-76.

Collins, A.S. and Robertson, A.H.F., 1997. Lycian melange, southwestern Turkey: An emplaced Late Cretaceous accretionary complex. *Geology*, 25: 255-258.

Collins, A.S. and Robertson, A.H.F., 1998. Processes of Late Cretaceous to Late Miocene episodic thrust-sheet translation in the Lycian Taurides, SW Turkey. *J. Geol. Soc. London*, 155: 759-772.

Collins, A.S. and Robertson, A.H.F., 1999. Evolution of the Lycian Allochthon, western Turkey, as a north-facing Late Palaeozoic to Mesozoic rift and passive continental margin. *Geol. J.*, 34: 107-138.

Collins, A.S. and Robertson, A.H.F., 2003 (in press). Kinematic evidence for Late Mesozoic-Miocene emplacement of the Lycian Allochthon over the Western Anatolide Belt, SW Turkey. *Geol. J.*

Coney, P.J. and Harms, T.A., 1984. Cordilleran metamorphic core complexes, Cenozoic extensional relics of Mesozoic compression. *Geology*, 12: 550-554.

Creutzburg, N., 1977. General geological map of Greece. Crete island. 1:200 000. Institute of Geological and Mining Research, Athens.

Dannat, C. and Reischmann, T., 1998. Geochronological, geochemical and isotopic data on granitic gneisses from the Menderes Massif, SW Turkey, *3rd Int.Turk Geol. Symp.*, Middle East Technical University, Ankara, pp. 282.

Davies, R., England, P., Parsons, B., Billiris, H., Paradissis, D. and Veis, G., 1997. Geodetic strain of Greece in the interval 1892-1992. *J. Geophys. Res.*, 102: 24571-24588.

De Caritat, P., Hutcheon, I. and Walshe, J.L., 1993. Chlorite geothermometry : a review. *Clays and clay minerals*, 41: 219-239.

De Graciansky, P.C., 1966. Le massif cristallin du Menderes (Taurus occidental. Asie Mineure). Un exemple possible de vieux socle granitique remobilisé. *Rev. Géogr. Phys. Géol. Dyn.*, 8: 289-306.

De Graciansky, P.C., 1972. Recherches géologiques dans le Taurus Lycien occidental. *D.S. Thesis*, Univ. Paris Sud, Orsay, 571 pp.

De Jonge, M., Wortel, M. and Spakman, W., 1994. Regional scale tectonic evolution and the seismic velocity structure of the lithosphere and upper mantle. *J. Geophys. Res.*, 99: 12091-12108.

Delaloye, M. and Bingöl, E., 2000. Granitoids from western and northwestern Anatolia: geochemistry and modelling of geodynamic evolution. *Int. Geol. Rev.*, 42: 241-268.

Dercourt, J., Zonenshain, L.P., Ricou, L.E., Kuzmin, V.G., Le Pichon, X., Knipper, A.L., Grandjacquet, C., Sbortshikov, I.M., Geyssant, J., Lepvrier, C., Pechersky, D.H., Boulin, J., Sibuet, J.C., Savostin, L.A., Sorokhtin, O., Westphal, M., Bazhenov, M.L., Lauer, J.P. and Biju-Duval, B., 1986. Geological evolution of the Tethys belt from the Atlantic to the Pamir since the Lias. *Tectonophysics*, 123: 241-315.

Dinter, D.A., 1998. Late Cenozoic extension of the Alpine collisional orogen, northeastern Greece: origin of the north Aegean basin. *Geol. Soc. Amer. Bull.*, 110(9): 1208-1230.

Dinter, D.A. and Royden, L., 1993. Late Cenozoic extension in northeastern Greece: Strymon valley detachment system and Rhodope metamorphic core complex. *Geology*, 21: 45-48.

Dora, O.Ö., Candan, O., Dürr, S. and Oberhänsli, R., 1995. New evidence on the geotectonic evolution of the Menderes Massif, *International Earth Sciences Colloquium on the Aegean Region*, 4 - 14 October 1995, Izmir/Güllük - Turkey, pp. 53-72.

Dora, O.Ö., Candan, O., Kaya, O., Koralay, E. and Dürr, S., 2001. Revision of "Leptite-gneisses" in the Menderes Massif: a supracrustal metasedimentary origin. *Int. J. Earth Sci.*, 89(4): 836-851.

Doutsos, T., Koukouvelas, I., Poulimenos, G., Kokkalas, S., Xypolias, P. and Skourlis, K., 2000. An exhumation model for the south Peloponnesus, Greece. *Int. J. Earth Sci.*, 89: 350-365.

Dubois, R. and Bignot, G., 1979. Présence d'un "hardground" nummulitique au sommet de la série crétacée d'Almyropotamos (Eubée méridionale, Grèce). *C. R. Acad. Sc. Paris*, 289: 993-995.

Duermeijer, C.E., Krigjsman, W., Langereis, C.G. and Ten Veen, J.H., 1998. Post-early Messinian counterclockwise rotations on Crete: implications for Late Miocene to recent kinematics of the southern Hellenic arc. *Tectonophysics*, 298: 177-189.

Duermeijer, C.E., Nyst, M., Meijer, P.T., Langereis, C.G. and Spakman, W., 2000. Neogene evolution of the Aegean arc: paleomagnetic and geodetic evidence for a rapid and young rotation phase. *Earth Planet. Sci. Lett.*, 176: 509-525.

Dumitru, T.A., 1993. A new computer automated microscope stage system for fission track analysis. *Nucl. Tracks*, 21: 575-580.

Dürr, S., 1975. Über Alter und geotektonische Stellung des Menderes-Kristallins/SW-Anatolien und seine Aequivalente in der mittleren Aegaeis. *PhD Thesis*, Univ. Marburg/Lahn, Germany, 106 pp.

Dürr, S., Alther, R., Keller, J., Okrusch, M. and Seidel, E., 1978. The median Aegean crystalline belt: stratigraphy, structure, metamorphism and magmatism. In: H. Closs, D.R. Roeder and K. Schmidt (Editors), Alps, Apennines, Hellenides, *Schweizerbart*, Stuttgart, pp. 455-477.

Engel, M. and Reischmann, T., 1997. Geochronological data on granitoid gneiss from Paros, greece, obtained by single zircon Pb evaporation. *Terra Nova*, 9: 463.

Erdoğan, B., 1990a. Stratigraphy and tectonic evolution of Izmir-Ankara Zone between Izmir and Seferihisar. *Turkish Assoc. Petrol. Geol. Bull.*, 2: 1-20.

Erdoğan, B., 1990b. Tectonic relation between Izmir-Ankara Zone and Karaburun belt. *Min. Res. Exp. Turkey Bull.*, 110: 1-15.

Ersoy, S., 1993. The geological setting of the tectonic units situated on the SW Anatolia (Turkey) and their geodynamic development. *Bull. Geol. Soc. Greece*, 28: 617-628.

Evans, B.W., 1990. Phase relations in epidote-blueschists. *Lithos*, 25: 3-23.

Fassoulas, C., Kilias, A. and Mountrakis, D., 1994. Postnappe stacking extension and exhumation of high-pressure/low-temperature rocks in the island of Crete, Greece. *Tectonics*, 13: 127-138.

Faure, M., Bonneau, M. and Pons, J., 1991. Ductile deformation and syntectonic granite emplacement during the late Miocene extension of the Aegean (Greece). *Bull. Soc. Géol. France*, 162: 3-12.

Feenstra, A., 1985. Metamorphism of bauxites on Naxos, Greece, *PhD Thesis*, Rijksuniversiteit Utrecht, Geologica Ultraiectina 39, 206 pp.

Ferrière, J., 1982. Paléogéographies et tectoniques superposées dans les Hellénides Internes: les massifs de l'Othrys et du Pélion (Grèce continentale). *Soc. Géol. Nord*, 7: 970.

Forster, M.A. and Lister, G.S., 1999a. Detachment faults in the Aegean core complex of Ios, Cyclades, Greece. In: U. Ring, M.T. Brandon, G.S. Lister and S.D. Willett (Editors), Exhumation processes: normal faulting, ductile flow and erosion. *Spec. Publ. Geol. Soc. London*, pp. 305-323.

Forster, M.A. and Lister, G.S., 1999b. Separate episodes of eclogite and blueschist facies metamorphism in the Aegean metamorphic core complex of Ios, Cyclades, Greece. In: C. Mac Niocall and P.D. Ryan (Editors), Continental Tectonics. *Spec. Publ. Geol. Soc. London*, pp. 157-177.

Franz, L., 1991. Die polymetamorphe Entwicklung des Altkristallins auf Kreta und im Dodekanes (Griechenland): eine geologische, geochemische und petrologische Bestandsaufnahme. *PhD Thesis*, Unversität Würzburg, Stuttgart, 389 pp.

Franz, L. and Okrusch, M., 1992. Aragonite-bearing blueschists on Arki Island, Dodecanese, Greece. *Eur. J. Mineral.*, 4: 527-537.

Fytikas, M., Innocenti, F., Manetti, P., Mazzuoli, R., Peccerillo, A. and Villari, L., 1984. Tertiary to Quaternary evolution of volcanism in the Aegean region. In: J.E. Dixon and A.H.F. Robertson (Editors), The Geological Evolution of the Eastern Mediterranean. *Spec. Publ. Geol. Soc. London*, 17: 687-699.

Galbraith, R.F., 1981. On statistical models for fission track counts. *Mathematical Geology*, 13: 471-478.

Galbraith, R.F., 1988. Graphical display of estimates having different standard errors. *Technometrics*, 30: 271-281.

Galbraith, R.F., 1990. The radial plot: graphical assessment of spread in ages. *Nucl. Tracks*, 17: 207-214.

Galbraith, R.F. and Laslett, G.M., 1993. Statistical models for mixed fission track ages. *Nucl. Tracks*, 21: 459-470.

Gallagher, K., Brown, R. and Johnson, C., 1998. Fission track analysis and its applications to geological problems. *Annu. Rev. Earth Planet. Sci.*, 26: 519-572.

Gautier, P. and Brun, J.P., 1994a. Crustal-scale geometry and kinematics of late-orogenic extension in the central Aegean (Cyclades and Evvia island). *Tectonophysics*, 238: 399-424.

Gautier, P. and Brun, J.P., 1994b. Ductile crust exhumation and extensional detachments in the central Aegean (Cyclades and Evvia islands). *Geodin. Acta*, 7(2): 57-85.

Gautier, P., Brun, J.P. and Jolivet, L., 1993. Structure and kinematics of upper Cenozoic extensional detachement on Naxos and Paros (Cyclades Islands, Greece). *Tectonics*, 12: 1180-1194.

Gautier, P., Brun, J.-P., Moriceau, R., Sokoutis, D., Martinod, J. and Jolivet, L., 1999. Timing, kinematics and cause of Aegean extension: a scenario based on a comparison with simple analogue experiments. *Tectonophysics*, 315: 31-72.

Gessner, K., 2000. Eocene nappe tectonics and late-Alpine extension in the central Anatolide belt, western Turkey - structure, kinematics and deformation history. *PhD Thesis*, Johannes -Gutenberg Universität Mainz, Mainz, 74 pp.

Gessner, K., Piazolo, S., Güngör, T., Ring, U., Kröner, A. and Passchier, C.W., 2001a. Tectonic significance of the deformation patterns in granitoid rocks of the Menderes nappes, Anatolide belt, southwest Turkey. *Int. J. Earth Sci.*, 89(4): 766-780.

Gessner, K., Ring, U., Passchier, C.W. and Güngör, T., 2001b. How to resist subduction: evidence for large-scale out-of-sequence thrusting during Eocene collision in western Turkey. *J. Geol. Soc. London*, 158: 769-784.

Gessner, K., Ring, U., Johnson, C., Hetzel, R., Passchier, C.W. and Güngör, T., 2001c. An active bivergent rolling-hinge detachment system: Central Menderes metamorphic core complex in western Turkey. *Geology*, 29(7): 611-614.

Gillet, P. and Goffé, B., 1988. On the significance of aragonite occurrences in the Western Alps. *Contrib. Mineral. Petrol.*, 99: 70-81.

Giorgetti, G., Goffé, B., Memmi, I. and Nieto, F., 1998. Metamorphic evolution of Verrucano metasediments in northern Apennines: new petrological constraints. *Eur. J. Mineral.*, 10: 1295-1308.

Gleadow, A.J.W. and Duddy, I.R., 1981. A natural long term annealing experiment for apatite. *Nucl. Tracks*, 5: 169-174.

Godfriaux, Y., 1962. L'Olympe: une fenêtre tectonique dans les Hellénides internes. *C. R. Acad. Sc. Paris*, 255: 1761-1763.

Godfriaux, Y., 1965. Etude géologique de la région de l'Olympe. *Thèse d'Etat*, Université de Lille, 280 pp.

Godfriaux, Y. and Pichon, J.F., 1980. Sur l'importance des événements tectoniques et métamorphiques d'âge tertiaire en Thessalie septentrionale (L'Olympe, Ossa et Flamburon). *Annales Géol. Soc. Nord*, 99: 367-376.

Godfriaux, Y. and Ricou, L.E., 1991a. Le Païkon, une fenêtre tectonique dans les Hellénides Internes (Macédoine, Grèce). *C. R. Acad. Sc. Paris*, 313: 1479-1484.

Godfriaux, Y. and Ricou, L.E., 1991b. Direction et sens de transport associés au charriage synmétamorphe sur l'Olympe. *Bulletin of the Geological Society of Greece*, 25: 207-229.

Goffé, B., 1982. Définition du faciès à Fe-Mg-carpholite-chloritoïde, un marqueur du métamorphisme de HP-BT dans les métasédiments alumineux. *PhD Thesis*, Paris.

Goffé, B., 1984. Le facies à carpholite-chloritoid dans la couverture briançonnaise des Alpes Ligures: un témoin de l'histoire tectono-métamorphique régionale. *Mem. Soc. Geol. It.*, 28: 461-479.

Goffé, B. and Bousquet, R., 1997. Ferrocarpholite, chloritoid et lawsonite dans les métapélites des unités du Versoyen et du Petit St Bernard (zone valaisanne, Alpes occidentales). *Schweiz. Mineral. Petrogr. Mitt.*, 77: 137-147.

Goffé, B. and Chopin, C., 1986. High-pressure metamorphism in the Western Alps: zoneography of metapelites, chronology and consequences. *Schweiz. Mineral. Petrogr. Mitt.*, 66: 41-52.

Goffé, B. and Oberhänsli, R., 1992. Ferro- and magnesiocarpholite in the "Bündnerschiefer" of the eastern Central Alps (Grisons and Engadine window). *Eur. J. Mineral.*, 4: 835-838.

Goffé, B. and Velde, B., 1984. Contrasted metamorphic evolutions in thrusted cover units of the Briançonnais zone (French Alps): a model for the conservation of HP-LT metamorphic mineral assemblages. *Earth Planet. Sci. Lett.*, 68: 351-360.

Goffé, B., Michard, A., Kienast, J.R. and Mer, O.L., 1988. A case of obduction-related high pressure, low temperature metamorphism in upper crustal nappes, Arabian continental margin, Oman: P-T paths and kinematic interpretation. *Tectonophysics*, 151: 363-386.

Goffé, B., Michard, A., Garcia-Duenas, V., Gonzales-Lodeiro, F., Monié, P., Campos, J., Galindo-Zaldivar, J., Jabaloy, A., Martinez-Martinez, J.M. and Simancas, F., 1989. First evidence of high pressure, low temperature metamorphism in the Alpujarride nappes, Betic Cordillera (SE Spain). *Eur. J. Mineral.*, 1: 139-142.

Goffé, B., Bousquet, R., Henry, P. and Le Pichon, X., 2003. Effect of the chemical composition of the crust on the metamorphic evolution of orogenic wedges. *J. Metamorphic Geol.*, 21: 123-141.

Göncüoğlu, M.C., 1977. Geologie des westlichen Nigde Massivs. *PhD Thesis*, Bonn University, Bonn, Germany.

Göncüoğlu, M.C., 1982. Nigde Masifinde paragnayslarinda zirkon U/Pb yaslari. *Türkiye Jeoloji Kurumu Bülteni*, 25: 61-66.

Göncüoğlu, M.C., 1986. Geochronologic data from the southern part (Nigde area) of the Central Anatolian Massif. *Maden Tetkik ve Arama Dergisi*, 105/106: 83-96.

Göncüoğlu, M.C. and Erendil, M., 1990. Armutlu Yarimadasinin Geç Kretase öncesi tektonik birimleri (in Turkish with English abstract), *Proc. 8th Petrol. Congr.*, pp. 161-168.

Göncüoğlu, M.C. and Kozur, H., 1998. Remarks to the pre-Variscan development in Turkey. *Schr. Stall. Mus. Min. Gel. Dresden*, 9: 137-138.

Göncüoğlu, M.C., Toprak, V., Kusçu, I., Erler, A. and Olgun, E., 1991. Orta Anadolu Mafisi'nin bati bölümünün jeolojisi, Bölüm 1: Güney Kesim (in Turkish), *Turkish Petrol. Coorp. Report*.

Göncüoğlu, M.C., Dirik, K. and Kozur, H., 1996-1997. Pre-Alpine and Alpine terranes in Turkey: explanatory notes to the terrane map of Turkey. *Ann. Géol. Pays Hellén.*, 37: 515-536.

Göncüoğlu, M.C., Turhan, N., Sentürk, K., Özcan, A., Uysal, S. and Yaliniz, M.K., 2000. A geotraverse across northwestern Turkey: tectonic units of the central Sakarya region and their tectonic evolution. In: E. Bozkurt, J.A. Winchester and J.D.A. Piper (Editors), Tectonics and magmatism in Turkey and the surrounding area. *Spec. Publ. Geol. Soc. London*, pp. 139-161.

Green, P.F., 1981. A new look at statistics in fission-track dating. *Nucl. Tracks*, 5: 77-86.

Green, N.P.F., Duddy, I.R., Gleadow, A.J.W. and Lovering, J.F., 1989a. Apatite fission-track analysis as a paleotemperature indicator for hydrocarbon exploration. In: N.D. Naeser and T.H. McCulloh (Editors), Thermal History of Sedimentary Basins: Methods and Case Histories. *Springer-Verlag*, New York, pp. 181-195.

Green, P.F., Duddy, I.R., Laslett, G.M., Hegarty, K.A., Gleadow, A.J.W. and F., L.J., 1989b. Thermal annealing of fission tracks in apatite. Quantitative modelling techniques and extension to geological timescales. *Chem. Geol. (Isotope Geosci. Sec.)*, 79: 155-182.

Greilling, R., 1982. The metamorphic and structural evolution of the Phyllite-Quartzite nappe of western Crete. *J. Struct. Geol.*, 4: 291-297.

Guidotti, C.V., Yates, M.G., Dyar, M.D. and Taylor, M.E., 1994. Petrogenetic significance of the Fe3+ content of muscovite in pelitic schists. *Am. Mineral.*, 79: 793-795.

Gutnic, M., Monod, O., Poisson, A. and Dumont, J.F., 1979. Géologie des Taurides occidentales (Turquie). *Mém. Soc. Géol. France*, 137: 1-112.

Güngör, T., 1995. Stratigraphy and tectonics of the Menderes Massif, *Int. Earth Sci. Coll. on Aegean Region. Excursion guide book*, Izmir, Turkey, pp. 15-22.

Güngör, T., 1998. Stratigraphy and tectonic evolution of the Menderes Massif in the Söke-Selçuk region. *PhD Thesis*, Dokuz Eylül Univ., Izmir, 147 pp.

Güngör, T. and Erdoğan, B., 2001. Emplacement age and direction of the Lycian Nappes in the Söke-Selçuk region, western Turkey. *Int. J. Earth Sci.*, 89(4): 874-882.

Gürsoy, H., Piper, J.D.A., Tatar, O. and Mesci, L., 1998. Palaeomagnetic study of the Karaman and Karapinar volcanic complexes, central Turkey: neotectonic rotation in the south-central sector of the Anatolian block. *Tectonophysics*, 299: 191-211.

Hall, R., Audley-Charles, M.G. and Carter, D.J., 1984. The significance of Crete for the evolution of the Eastern Mediterranean. In: J.E. Dixon and A.H.F. Robertson (Editor). The geological evolution of the Eastern Mediterranean. *Spec. Publ. Geol. Soc. London*, pp. 499-516.

Hatzfeld, D., 1994. On the shape of the subducting slab beneath Peloponnese, Greece. *Geophys. Res. Lett.*, 21: 173-176.

Hayward, A.B., 1984. Miocene clastic sedimentation related to the emplacement of the Lycian Nappes and the Antalya complex. In: J.E. Dixon and A.H.F. Robertson (Editors), The geological evolution of the Eastern Mediterranean. *Spec. Publ. Geol. Soc. London*, pp. 287-300.

Henry, P., Pichon, X.L. and Goffé, B., 1997. Kinematic, thermal and petrological model of the Himalayas: constraints related to metamorphism within the underthrust Indian crust. *Tectonophysics*, 273: 31-56.

Hetzel, R., 1995. The Alpine tectono-metamorphic evolution of the central Menderes Massif, southwestern Turkey. *PhD Thesis*, Johannes-Gutenberg-Universität, Mainz, 77 pp.

Hetzel, R. and Reischmann, T., 1996. Intrusion age of the Pan-African augen gneisses in the southern Menderes Massif and the age of cooling after Alpine ductile extensional deformation. *Geol. Mag.*, 133(5): 565 - 572.

Hetzel, R., Passchier, C.W., Ring, U. and Dora, O.Ö., 1995. Bivergent extension in orogenic belts: The Menderes massif (southwestern Turkey). *Geology*, 23: 455-458.

Hetzel, R., Romer, R.L., Candan, O. and Passchier, C.W., 1998. Geology of the Bozdag area, central Menderes Massif, SW Turkey: Pan-African basement and Alpine deformation. *Geol. Rundsch.*, 87: 394-406.

Holland, T.J.B. and Powell, R., 1990. An enlarged and updated internally consistent thermodynamic dataset with uncertainties and correlations: the system K_2O-Na_2O-CaO-MgO-FeO-Fe_2O_3-Al_2O_3-TiO_2-SiO_2-C-H_2-O_2. *J. Metamorphic Geol.*, 8: 89-124.

Holland, T.J.B., Baker, J. and Powell, R., 1998. Mixing properties and activity-composition relationships of chlorites in the system MgO-FeO-Al_2O_3-SiO_2-H_2O. *Eur. J. Mineral.*, 10: 395-406.

Hurford, A.J. and Carter, A., 1991. The role of fission track dating in discrimination of provenance. In: A.C. Morton, S.P. Todd and P.D.W. Haughton (Editors), Developments in Sedimentary Provenance Studies. *Spec. Publ. Geol. Soc. London*, pp. 67-78.

Hurford, A.J. and Green, P.F., 1983. The zeta age calibration of fission-track dating. *Chemical Geology*, 41: 285-317.

Jackson, J., 1994. Active tectonics of the Aegean region. *Annual Review of Earth Planet. Sci. Lett.*, 22: 239-271.

Jansen, J.B.H., 1977. Metamorphism on Naxos, Greece. *PhD Thesis*, Utrecht University.

Johnson, K., 1998. Cooling, denudation, and pre-extensional configuration of the Menderes Massif, *Abstract of Workshop Türkei*, das Menderes Massiv und seine Randebiete, Mainz, pp. 11.

Jolivet, L., 2001. A comparison of geodetic and finite strain in the Aegean, geodynamic implications. *Earth Planet. Sci. Lett.*, 187: 95-104.

Jolivet, L. and Faccenna, C., 2000. Mediterranean extension and the Africa-Eurasia collision. *Tectonics*, 19(6): 1095-1106.

Jolivet, L. and Goffé, B., 2000. Les dômes métamorphiques extensifs dans les chaînes de montagnes. Extension syn-orogénique et post-orogénique. *C. R. Acad. Sci. Paris*, 330: 739-751.

Jolivet, L. and Patriat, M., 1999. Ductile extension and the formation of the Aegean Sea. In: B. Durand, L. Jolivet, F. Horvàth and M. Séranne (Editors), The Mediterranean Basins; Tertiary Extension within Alpine Orogen. *Spec. Publ. Geol. Soc. London*, pp. 427-456.

Jolivet, L., Daniel, J.M., Truffert, C. and Goffé, B., 1994a. Exhumation of deep crustal metamorphic rocks and crustal extension in back-arc regions. *Lithos*, 33(1/2): 3-30.

Jolivet, L., Brun, J.P., Gautier, P., Lallemant, S. and Patriat, M., 1994b. 3-D kinematics of extension in the Aegean from the Early Miocene to the Present, insight from the ductile crust. *Bull. Soc. Géol. France*, 165: 195-209.

Jolivet, L., Goffé, B., Monié, P., Truffert-Luxey, C., Patriat, M. and Bonneau, M., 1996. Miocene detachment in Crete and exhumation P-T-t paths of high-pressure metamorphic rocks. *Tectonics*, 15(6): 1129-1153.

Jolivet, L., Facenna, C., Goffé, B., Mattei, M., Rossetti, F., Brunet, C., Storti, F., Funiciello, R., Cadet, J.P., d'Agostino, N. and Parra, T., 1998a. Midcrustal shear zones in postorogenic extension: Example from the northern Tyrrhenian Sea. *J. Geophys. Res.*, 103: 12,123-12,160.

Jolivet, L., Goffé, B., Bousquet, R., Oberhänsli, R. and Michard, A., 1998b. Detachments in high-pressure mountain belts, Tethyan examples. *Earth Planet. Sci. Lett.*, 160: 31-47.

Jolivet, L., Faccenna, C., d'Agostino, N., Fournier, M. and Worrall, D., 1999. The Kinematics of Marginal Basins, examples from the Tyrrhenian, Aegean and Japan Seas. In: C. Mac Niocaill and P.D. Ryan (Editors), Continental Tectonics. *Spec. Publ. Geol. Soc. London*, pp. 21-53.

Jolivet, L., Rimmelé, G., Oberhänsli, R., Goffé, B. and Candan, O., in press. Correlation of syn-orogenic tectonic and metamorphic events in the Cyclades, the Lycian Nappes and the Menderes Massif. Geodynamic implications. *Bull. Soc. Géol. France*.

Jones, C.E., Tarney, J., Baker, J.H. and Gerouki, F., 1992. Tertiary granitoids of Rhodophe, northern Greece: magmatism related to extensional collapse of the Hellenic orogen. *Tectonophysics*, 210: 295-314.
Kaaden, G.v.d., 1966. The significance and distribution of glaucophane rocks in Turkey. *Bull. Min. Res. Expl. Inst. Turkey*, 67: 35-67.

Kaaden, G.v.d. and Metz, K., 1954. Beitraege zur Geologie des Raumes zwischen Datça-Mugla-Dalaman çay (SW-Anatolien). *Bull. Geol. Soc. Turkey*, 5(1-2): 71-168.

Katzir, Y., Matthews, A., Garfunkel, Z., Schliestedt, M. and Avigad, D., 1996. The tectono-metamorphic evolution of a dismembered ophiolite (Tinos, Cyclades, Greece). *Geol. Mag.*, 133: 237-254.

Kaya, O., 1973. The Devonian and Lower Carboniferous stratigraphy of the Istinye, Bostanci and Büyükada sub areas. In: O. Kaya (Editor), Palaeozoic of Istanbul. *Ege Univ. Sci. Fac. Publ.*, Izmir, pp. 1-34.

Keay, S., Lister, G. and Buick, I., 2001. The timing of partial melting, Barrovian metamorphism and granite intrusion in the Naxos metamorphic core complex, Cyclades, Aegean Sea, Greece. *Tectonophysics*, 342: 275-312.

Ketcham, R.A., Donelik, R.A. and Carlson, W.D., 1999. Variability of apatite fission-track annealing kinetics: Extrapolation to geological time scales. *Am. Mineral.*, 84: 1235-1255.

Kissel, C. and Laj, C., 1988. The Tertiary geodynamical evolution of the Aegean Arc: a paleomagnetic reconstruction. *Tectonophysics*, 146: 183-201.

Kissel, C., Speranza, F. and Milicevic, V., 1995. Paleomagnetism of external southern Dinarides and northern Albanides: implications for the cenozoic activity of the Scutari-Pec shear zone. *J. Geophys. Res.*, 100(B8): 14999-15007.

Kissel, C., Laj, C., Poisson, A. and Görür, N., 2003. Paleomagnetic reconstruction of the cenozoic evolution of the eastern Mediterranean. *Tectonophysics*, 362: 199-217.

Koçyiğit, A., 1991. First remarks on the geology of Karakaya Orogen and pre-Jurassic nappes in eastern Pontides. *Geol. Romanna*, 27: 3-11.

Koepke, J., 1986. Die Ophiolithe des Südägäischen Inselbrücke, Universität Carolo-Wilhelmina, *Braunschweig*, 204 pp.

Konak, N., 1993. Structural characteristics of the Menderes Massif around Cal-Civril-Karahalli (in Turkish). *Türkiye Jeoloji Kurultayi, Bildiri özleri*.

Konak, N. and Akdeniz, N., 1/100 000 ölçekli N-19 ve N-20 paftalarinin jeolojik haritalari, Maden Tetkik Arama Müdürlügü, Ankara-Türkiye (Yaninlanmamis).

Konak, N., Akdeniz, N. and Öztürk, E.M., 1987. Geology of the south of Menderes Massif. In: M.R.E. Inst (Editor), Correlation of Variscan and pre-Variscan events of the Alpine Mediterranean mountain belt, *field meeting. IGCP project no. 5*, Turkey.

Koralay, O.E., Satir, M. and Dora, O.Ö., 1998. Geochronologic evidence of Triassic and Precambrian magmatism in the Menderes Massif, west Turkey, *3rd Int.Turk.Geol.Symp.*, Middle East Technical University, Ankara, pp. 285.

Koralay, O.E., Satir, M. and Dora, O.Ö., 2001. Geochemical and geochronological evidence for Early Triassic calk-alkaline magmatism in the Menderes Massif, western Turkey. *Int. J. Earth Sci.*, 89(4): 822-835.

Krahl, J., Kauffmann, G., Kozur, H., Richter, D., Förster, O. and Heinritz, F., 1983. Neue Daten zur Biostratigraphie und zur tektonischen Lagerung der Phyllit-Gruppe und der Trypali-Gruppe auf der Insel Kreta (Griechenland). *Geol. Rundsch.*, 72(3): 1147-1166.

Kröner, A. and Sengör, A.M.C., 1990. Archean and Proterozoic ancestry in Late Precambrian to Early Proterozoic crustal elemtens of southern Turkey as revealed by single-zircon dating. *Geology*, 18: 1186-1190.

Laslett, G.M., Green, P.F., Duddy, I.R. and Gleadow, A.J.W., 1987. Thermal annealing of fission tracks in apatite, a quantitative analysis. *Chem. Geol.*, 65: 1-13.

Le Pichon, X. and Angelier, J., 1979. The Hellenic arc and trench system : a key to the neotectonic evolution of the Eastern Mediterranean area. *Tectonophysics*, 60: 1-42.

Le Pichon, X., Chamot-Rooke, N. and Lallemant, S., 1995. Geodetic determination of the kinematics of Central Greece with respect to Europe. Implications for Eastern Mediterranean tectonics. *J. Geophys. Res.*, 100(7): 12675-12690.

Le Pichon, X., Henry, P. and Goffé, B., 1997. Uplift of Tibet: from eclogites to granulites - implications for the Andean Plateau and the Variscan Belt. *Tectonophysics*, 273: 57-76.

Leake, B.E., 1978. Nomenclature of amphiboles. *Amer. Mineral.*, 63: 1023-1053.

Leake, B.E., Wolley, A.R., Arps, C.E.S., Bireh, W.D., Gilbert, M.C., Grice, J.D., Hawthorne, F.C., Kato, A., Kirsch, H.J., Krivovichec, V.G., Linthout, K., Laird, J., Mandarino, J., Maresch, W.V., Nickel, E.H., Rock, N.M.S., Schumacher, J.C., Smith, D.C., Stephenson, N.C.N., Ungaretti, L., Wittaker, E.J.W. and Youxhi, G., 1997. Nomenclature of Amphiboles; report of the subcommitte on Amphiboles of the International Mineralogical Association, commission on new minerals and mineral names. *Am. Mineral.*, 82: 1019-1037.

Leoni, L., Sartori, F. and Tamponi, M., 1998. Compositional variation in K-white micas and chlorites coexisting in Al- saturated metapelites under late diagenetic to low-grade metamorphic conditions (Internal Liguride Units,
Nortern Apennines, Italy. *Eur. J. Mineral.*, 10: 1321-1339.

Liati, A. and Gebauer, D., 1999. Constraining the prograde and retrograde P-T-t path of Eocene HP rocks by SHRIMP dating of different zircon domains: inferred rates of heating, burial, cooling and exhumation for central Rhodope, northern Greece. *Contrib. Mineral. Petrol.*, 135: 340-354.

Liati, A. and Seidel, E., 1996. Metamorphic evolution and geochemistry of kyanite eclogites in central Rhodope, northern Greece. *Contrib. Mineral. Petrol.*, 123: 293-307.

Lieberman, J. and Petrakakis, K., 1991. TWEEQU thermobarometry: Analysis of uncertainties and application to granulites from the western Alaska and Austria. *Can. Mineral.*, 29: 857-887.

Lips, A.L.W., Cassard, D., Sözbilir, H., Yilmaz, H. and Wijbrans, J.R., 2001. Multistage exhumation of the Menderes Massif, Western Anatolia (Turkey). *Int. J. Earth Sci.*, 89(4): 781-792.

Lister, G.S. and Baldwin, S., 1993. Plutonism and the origin of metamorphic core complexes. *Geology*, 21: 607-610.

Lister, G.S., Banga, G. and Feenstra, A., 1984. Metamorphic core complexes of cordilleran type in the Cyclades, Aegean Sea, Greece. *Geology*, 12: 221-225.

Loos, S. and Reischmann, T., 1999. The evolution of the southern Menderes Massif in SW Turkey as revealed by zircon dating. *J. Geol. Soc. London*, 156: 1021-1030.

Loubrieu, B., Satra, C. and Cagna, R., 2000. Cartographie par sondeur multifaisceaux de la Ride Méditerranéenne et des domaines voisins. Ifremer/Ciesm. Ed. *Ifremer, Cartes & Atlas*, 2 cartes pliées au 1/1500000.

Makris, J., 1978. The crust and upper mantle of the Aegean region from deep seismic sounding. *Tectonophysics*, 46: 269-284.

Maluski, H., Bonneau, M. and Kienast, J.R., 1987. Dating the metamorphic events in the Cycladic area: 39Ar/40Ar data from metamorphic rocks of the island of Syros (Greece). *Bull. Soc. Géol. France*, 8: 833-842.

Martinez-Martinez, J.M. and Azañon, J.M., 1997. Mode of extensional tectonics in the southeastern Betics (SE Spain): implications for the tectonic evolution of the peri-Alboran orogenic system. *Tectonics*, 16(2): 205-225.

Massonne, H.J., 1995. Experimental and petrogenetic study of UHPM. In: R.G. Coleman and X. Wang (Editors), Ultrahigh Pressure Metamorphism. *Cambridge University Press*, pp. 33-95.

Massonne, H.J. and Schreyer, W., 1987. Phengite geobarometry based on the limiting assemblage with K-feldspar, phlogopite and quartz. *Contrib. Mineral. Petrol.*, 96: 212-224.

Massonne, H.J. and Szpurka, Z., 1997. Thermodynamic properties of white micas on the basis of high-pressure experiments in the systems K2O-MgO-Al2O3-SiO2-H2O. *Lithos*, 41: 229-250.

Matte, P., Lancelot, J. and Mattauer, M., 1998. La zone axiale de la Montagne Noire n'est pas un "metamorphic core complex" extensif mais un anticlinal post-nappe a coeur anatectique. *Geodin. Acta*, 11: 13-22.

Matthews, A. and Schliestedt, M., 1984. Evolution of the blueschist and greenschist facies rocks of Sifnos, Cyclades, Greece. *Contrib. Mineral. Petrol.*, 88: 150-163.

McClusky, S., Balassanian, S., Barka, A., Demir, C., Ergintav, S., Georgiev, I., Gurkan, O., Hamburger, M., Hurst, K., Kahle, H., Kastens, K., Kekelidze, G., King, R., Kotzev, V., Lenk, O., Mahmoud, S., Mishin, A., Nadariya, M., Ouzounis, A., Paradissis, D., Peter, Y., Prilepin, M., Reilinger, R., Sanli, I., Seeger, H., Tealeb, A., Toksoz, M.N. and Veis, G., 2000. Global positioning system constraints on plate kinematics and dynamics in the eastern Mediterranean and Caucasus. *J. Geophys. Res., B, Solid Earth and Planets*, 105(3): 5695-5719.

McKenzie, D.P., 1972. Active Tectonics of the Mediterranean region. *Geophys. J. R. Astron. Soc.*, 30: 109-185.

Mercier, J., Sorel, D. and Simeakis, P., 1987. Changes in the states of stress of the overrinding plate of a subduction zone: the Aegean Arc from Pliocene to Present. *Annales Tectonicae*, 1: 20-39.

Michard, A., Goffé, B., Saddiqi, O., Oberhänsli, R. and Wendt, A.S., 1994a. Late Cretaceous exhumation of the Oman blueschists and eclogites: a two-stage extensional mechanism. *Terra Nova*, 6: 404-413.

Michard, A., Goffé, B., Liati, A. and Mountrakis, D., 1994b. Découverte du faciès schiste bleu dans les nappes du Circum-Rhodope: un élément d'une ceinture HP-BT éohellénique en Grèce septentrionale ? *C. R. Acad. Sc. Paris*, 318: 1535-1542.

Michard, A., Goffé, B., Bouybaouene, M.L. and Saddiqi, O., 1997. Late Hercynian-Mesozoic thinning in the Alboran domain: metamorphic data from the northern Rif, Morocco. *Terra Nova*, 9: 171-174.

Minoux, L., Bonneau, M. and Kienast, J.R., 1980. L'île d'Amorgos, une fenêtre des zones externes au coeur de l'Egée (Grèce), métamorphisée dans le faciès schistes bleus. *C. R. Acad. Sc. Paris*, 291: 745-748.

Moriceau, R., 2000. Evolution du massif métamorphique du Rhodope (Grèce, Bulgarie) dans le contexte alpin. Structures, cinématique et origine de la déformation ductile. *PhD Thesis*, Université de Rennes I, Rennes, 537 pp.

Morris, A. and Anderson, A., 1996. First paleaomagnetic results from the Cycladic Massif, Greece, and their implications for Miocene extension directions and tectonic models in the Aegean. *Earth Planet. Sci. Lett.*, 142: 397-408.

Mposkos, E.D. and Kostopoulos, D.K., 2001. Diamond, former coesite and supersilicic garnet in metasedimentary rocks from the Greek Rhodope: a new ultrahigh-pressure metamorphic province established. *Earth Planet. Sci. Lett.*, 192: 497-506.

Mposkos, E. and Liati, A., 1991. Fe-carpholite in chloritoid-bearing metapelites-metasandstones of Skopelos Island, N. Sporades, Greece, 5th congress of the Geological Society of Greece. Deltio tes Ellenikes Geologikes Etaireias = *Bulletin of the Geological Society of Greece*, Salonika, Greece, pp. 55-66.

Mposkos, E. and Perdikatsis, V., 1984. Petrology of glaucophane metagabbros and related rocks from Samos, Aegean Island (Greece). *Neues Jahrbuch Miner. Abh.*, 149(1): 43-63.

Nielsen dit Christensen, C., 2003. Etudes des zones de subduction en convergence hyper oblique: Ride Mediterranéenne, Marge Indo-Birmane, *PhD Thesis*, Paris XI, Orsay, 215 pp.

O'Sullivan, P.B. and Parrish, R.R., 1995. The importance of apatite composition and single-grain ages when interpreting fission track data from plutonic rocks: a case study from the Coast Ranges, British Columbia. *Earth Planet. Sci. Lett.*, 132: 213-224.

Oberhänsli, R., Goffé, B. and Bousquet, R., 1995. Record of a HP-LT metamorphic evolution in the Valais Zone: Geodynamic implications. In: B. Lombardo (Editor), Studies on metamorphic rocks and minerals of the western Alps. A Volume in Memory of Ugo Pognante. *Supplemento al Bolletino del Museo Regionale delle Scienze naturali di Torino*, pp. 221-240.

Oberhänsli, R., Candan, O., Dora, O.Ö. and Dürr, S.H., 1997. Eclogites within the Menderes Massif/western Turkey. *Lithos*, 41: 135-150.

Oberhänsli, R., Monié, P., Candan, O., Warkus, F.C., Partzsch, J.H. and Dora, O.Ö., 1998. The age of blueschist metamorphism in the Mesozoic cover series of the Menderes Massif. *Schweiz. Mineral. Petrogr. Mitt*, 78: 309-316.

Oberhänsli, R., Partzsch, J., Candan, O. and Cetinkaplan, M., 2001. First occurrence of Fe-Mg-carpholite documenting a high-pressure metamorphism in metasediments of the Lycian Nappes, SW Turkey. *Int. J. Earth Sci.*, 89(4): 867-873.

Oberhänsli, R., Warkus, F. and Candan, O., 2002a. Dating of Eclogite and Granulite Facies Relics in the Menderes Massif, *First International Symposium of the Faculty of Mine (ITU) on Earth Sciences and Engineering*, Istanbul, Turkey, pp. 104.

Oberhänsli, R., Hamann, E., Partzsch, J., Warkus, F., Cetinkaplan, M. and Candan, O., 2002b. Petrology of manganese-rich eclogite from the Selçuk olistostrome, *First International Symposium of the Faculty of Mine (ITU) on Earth Sciences and Engineering*, Istanbul, Turkey, pp. 108.

Oelsner, F., Partzsch, J., Candan, O. and Oberhänsli, R., 1997. Repeated high-pressure overprint in the Menderes Massif, SW-Turkey, *Terra Abstr.*, pp. 407.

Okay, A.I., 1982. Incipient blueschist metamorphism and metasomatism in the Tavsanli region, North-west Turkey. *Contrib. Mineral. Petrol.*, 79: 361-367.

Okay, A.I., 1984. Distribution and characteristics of the north-west Turkish blueschists. In: J.E. Dixon and A.H.F. Robertson (Editors), The geological evolution of the eastern Mediterranean. *Spec. Publ. Geol. Soc. London*, pp. 455-466.

Okay, A.I., 1986. High-pressure/low-temperature metamorphic rocks of Turkey. *Geol. Soc. Am. Mem.*, 164: 333-347.

Okay, A.I., 1989a. Tectonic units and sutures in the Pontides, northern Turkey. In: A.M.C. Sengör (Editor), Tectonic evolution of the Tethyan region, *Kluwer, Dordrecht*, pp. 109-116.

Okay, A.I., 1989b. Geology of the Menderes Massif and the Lycian Nappes south of Denizli, western Taurides. *Min. Res. Expl. Turkey Bull.*, 109: 37-51.

Okay, A.I., 1989c. An exotic eclogitic/blueschist slice in a barrovian-style metamorphic terrain, Alanya nappes, southern Turkey. *J. Petrol.*, 30: 107-132.

Okay, A.I., 2001. Stratigraphic and metamorphic inversions in the central Menderes Massif: a new structural model. *Int. J. Earth Sci.*, 89(4): 709-727.

Okay, A.I. and Kelley, S.P., 1994. Tectonic Setting, Petrology and Geochronology of Jadeite + Glaucophane and Chloritoid + Glaucophane Schists From North- West Turkey. *J. Metamorphic Geol.*, 12(4): 455-466.

Okay, A.I. and Monié, P., 1997. Early Mesozoic subduction in the Eastern Mediterranean: Evidence from Triassic eclogite in northwest Turkey. *Geology*, 25(7): 595-598.

Okay, A.I. and Satir, M., 2000a. Coeval plutonism and magmatism in a latest Oligocene metamorphic core complex in Northwest Turkey. *Geol. Mag.*, 137(5): 495-516.

Okay, A.I. and Satir, M., 2000b. Upper Cretaceous Eclogite-Facies Metamorphic Rocks from the Biga Peninsula, Northwest Turkey. *Turkish J. Earth Sci.*, 9: 47-56.

Okay, A.I. and Siyako, M., 1993. The new position of the Izmir-Ankara Neo-Tethyan suture between Izmir and Balikesir. In: S. Turgut (Editor), Tectonics and hydrocarbon potential of Anatolia and surrounding regions. *Proc. Ozan Sungurlu Symp.*, pp. 333-355.

Okay, A. and Tüysüz, O., 1999. Tethyan sutures of northern Turkey. In: B. Durand, L. Jolivet, F. Horvath and M. Séranne (Editors), The Mediterranean basins: Tertiary extension within the alpine orogen. *Spec. Publ. Geol. Soc. London*, pp. 475-515.

Okay, A.I., Satir, M., Maluski, H., Siyako, M., Monié, P., Metzger, R. and Akyüz, S., 1996. Palaeo- and Neo-Tethyan events in northwest Turkey: geological and geochronological constraints. In: A. Yin and M. Harrison (Editors), Tectonics of Asia. *Cambridge Univ. Press*, Cambridge, pp. 420-441.

Okay, A.I., Harris, N.B.W. and Kelley, S.P., 1998. Exhumation of blueschists along a Tethyan suture in northwest Turkey. *Tectonophysics*, 285(3-4): 275-299.

Okay, A.I., Tansel, I. and Tüysüz, O., 2001a. Obduction, subduction and collision as reflected in the Upper Cretaceous - Lower Eocene sedimentary record of western Turkey. *Geol. Mag.*, 138(2): 117-142.

Okay, A.I., Satir, M., Tüyüz, O., Akyüz, S. and Chen, F., 2001b. The tectonics of the Strandja Massif: late-Variscan and mid-Mesozoic deformation and metamorphism in the northern Aegean. *Int. J. Earth. Sci.*, 90: 217-233.

Okay, A.I., Monod, O. and Monié, P., 2002. Triassic blueschists and eclogites from northwest Turkey: vestiges of the Paleo-Tethyan subduction. *Lithos*, 64: 155-178.

Okrusch, M. and Bröcker, M., 1990. Eclogites associated with high-grade blueschists in the Cyclades archipelago, Greece: a review. *Eur. J. Mineral.*, 2: 451-478.

Okrusch, M., Richter, P. and Katsikatsos, G., 1984. High-pressure rocks of Samos, Greece. In: J.E. Dixon and A.H.F. Robertson (Editors), The geological evolution of Eastern Mediterranean. *Spec. Publ. Geol. Soc. London*, pp. 529-536.

Olivet, J.L., Bonnin, J., Beuzart, P. and Auzende, J.M., 1982. Cinématique des plaque et paléogéographie: une revue. *Bull. Soc. Géol. France*, 24: 875-892.

Önay, T.S., 1949. Über die Smirgelgesteine SW-Anatoliens. *Schweiz. Min. Petr. Mitt.*, 29: 359-484.

Özcan, A., Göncüoglu, M.C., Turan, N., Uysal, S., Sentürk, K. and Isik, A., 1988. Late Palaeozoic evolution of the Kütahya-Bolkardag belt. *METU J. Pure Appl. Sci.*, 21: 211-220.

Özer, S., 1993. Upper Cretaceous rudists from the Menderes Massif. *Bull. of the Geol. Soc. of Greece*, XXVIII(3): 55-73.

Özer, S., 1998. Rudist bearing Upper Cretaceous metamorphic sequences of the Menderes Massif (Western Turkey). *Geobios*, 22: 235-249.

Özer, S. and Irtem, O., 1982. Geological setting, stratigraphy and facies characteristics of the upper Cretaceous limestones in the Isiklar-Altindag (Bornova-Izmir) area (in Turkish). *Bull. Geol. Soc. Turkey*, 25: 41-47.

Özer, S., Sözbilir, H., Özkar, I., Toker, V. and Sari, B., 2001. Stratigraphy of Upper Cretaceous-Palaeogene sequences in the southern and eastern Menderes Massif (Western Turkey). *Int. J. Earth Sci.*, 89(4): 852-866.

Özkaya, I., 1990. Origin of the allochthons in the Lycian belt, Southwest Turkey. *Tectonophysics*, 177: 367-379.

Özkaya, I., 1991. Evolution of a Tertiary volcanogenic trough in SW Turkey - the Alakaya Basin of the Lycian Belt. *Geol. Rundsch.*, 80(3): 657-668.

Papanikolaou, D., 1987. Tectonic evolution of the Cycladic blueschist belt (Aegean Sea, Greece). In: H.C. Helgeson (Editor), Chemical transport in metasomatic processes. *D. Reidel Publishing Company*, pp. 429-450.

Parra, T., 2001. Les équilibres chlorite-phengite. De l'étude de la lame mince aux calculs des trajets pression-température. *PhD Thesis*, Paris XI, Paris Sud-Orsay, 390 pp.

Parra, T., Vidal, O. and Agard, P., 2002a. A thermodynamic model for Fe-Mg dioctahedral K white micas using data from phase-equilibrium experiments and natural pelitic assemblages. *Contrib. Mineral. Petrol.*, 143: 706-732.

Parra, T., Vidal, O. and Jolivet, L., 2002b. Relation between deformation and retrogression in blueschist metapelites of Tinos island (Greece) evidenced by chlorite-mica local equilibria. *Lithos*, 63: 41-66.

Partzsch, J.H., Oelsner, F. and Oberhänsli, R., 1997. The Menderes Massif, W Turkey: a complex nappe pile recording 1.0 Ga of geological history?, *Terra Abstr.*, pp. 394.

Partzsch, J.H., Warkus, F.C. and Oberhänsli, R., 1998. The evolution of the Central Menderes Massif, West Turkey: A complex nappe pile recording 1.0Ga of geological history? In: *F. Forschungshefte* (Editor), *TSK, Freiberg*, pp. 166-168.

Patriat, M. and Jolivet, L., 1998. Post-orogenic extension and shallow-dipping shear zones, study of a brecciated decollement horizon in Tinos (Cyclades, Greece). *C. R. Acad. Sci. Paris*, 326: 355-362.

Patzak, M., Okrusch, M. and Kreuzer, H., 1994. The Akrotiri unit on the island of Tinos, Cyclades, Greece: witness of a lost terrane of Late Cretaceous age. *N. Jb. Geol. Paläont. Abh.*, 194: 211-252.

Phillippson, A., 1910-1915. Reisen und Forschungen im westlichen Kleinasian, *Pet. Geogr. Mitt. Erg. Hefte*, pp. 167-183 der Petermans Mitteilungen Gotha Justus Perthes.

Platt, J.P., 1986. Dynamics of orogenic wedges and the uplift of high-pressure metamorphic rocks. *Geol. Soc. Amer. Bull.*, 97: 1037-1053.

Platzman, H.S., Tapirdamaz, C. and Sanver, M., 1998. Neogene anticlockwise rotation of central Anatolia (Turkey): preliminary paleomagnetic and geochronological results. *Tectonophysics*, 99: 175-189.

Poisson, A., 1977. Recherches géologiques dans les Taurides occidentales (Turquie). *PhD Thesis*, Univ. Paris Sud, Orsay, 795 pp.

Poisson, A., 1985. The extension of the Ionian trough into southwestern Turkey. In: J.E. Dixon and A.H.F. Robertson (Editors), The Geological Evolution of the Eastern Mediterranean. *Spec. Publ. Geol. Soc. London*, pp. 241-249.

Poisson, A. and Sarp, H., 1977. La zone de Kizilca-Corakgöl : un exemple de sillon intra-plate-forme à la marge externe du Massif du Menderes. In: E. Izdar and E. Nakoman (Editors), *Sixth colloquium on geology of the Aegean region*, Ege University, Izmir, pp. 555-564.

Powell, R. and Holland, T.J.B., 1988. An internally consistent thermodynamic dataset with uncertainties and correlations. III. Application methods, worked examples and a computer program. *J. Metamorphic Geol.*, 6: 173-204.

Powell, R. and Holland, T.J.B., 1994. Optimal geothermometry and geobarometry. *Am. Mineral.*, 79: 120-133.

Reinecke, T., Altherr, R., Hartung, B., Hatzipanagiotou, K., Kreuzer, H., Harre, W., Klein, H., Keller, J., Geenen, E. and Böger, H., 1982. Remnants of a late Cretaceous high temperature belt on the island of Anafi (Cyclades, Greece). *N. Jb. Miner. Abh*, 145(2): 157-182.

Reischmann, T., 1997. Single zircon Pb/Pb dating of tectonic units from the metamorphic core complex of Naxos. *Terra Abstracts*, 9: 496.

Ricou, L.E., 1994. Tethys reconstructed: plates, continental fragments and their boundaries since 260 Ma from Central America to south-eastern Asie. *Geodin. Acta*, 7: 169-218.

Ricou, L.E., Burg, J.P., Godfriaux, I. and Ivanov, Z., 1998. Rhodope and Vardar: the metamorphic and olistostromic paired belts related to the Cretaceous subduction under Europe. *Geodin. Acta*, 11(6): 285-309.

Ridley, J. and Dixon, J.E., 1984. Reaction pathways during the progress deformation of a blueschist metabasite: the role of chemical desequilibrium and restricted range equilibrium. *J. metamorphic Geol.*, 2: 115-128.

Rieder, M., Cavazzini, G., D'Yakonov, Y.S., Franck-Kamenetskii, V.A., Gottardi, G., Guggenheim, S., Koval, P.V., Muller, G., Neiva, A.M.R., Radoslovich, E.W., Robert, J.L., Takeda, H., Weiss, Z. and Jones, D.R., 1998. Nomenclature of the Micas. *Can. Mineral.*, 36: 905-912.

Rigo, A., Lyon-Caen, H., Armijo, R., Deschamps, A., Hatzfeld, D., Makropoulos, K., Papadimitriou, P. and Kassaras, I., 1996. A microseismicity study in the western part of the Gulf of Corinth (Greece): implications for large-scale normal faulting mechanisms. *Geophys. J. Int.*, 126: 663-688.

Rimmelé, G., Oberhänsli, R., Jolivet, L. and Goffé, B., 2001. First structural data related to the low-grade high-pressure metamorphism in the metasediments of the Lycian Nappes, SW Turkey, *Terra Abstr.*, pp. 309.

Rimmelé, G., Oberhänsli, R., Goffé, B., Jolivet, L., Candan, O. and Çetinkaplan, M., 2002. High-pressure rocks from the southern Menderes Massif and the Lycian Nappes: implications for the tectonic evolution of southwest Turkey, *European Geophysical Society, XXVII General Assembly*, Nice, France, pp. 85.

Rimmelé, G., Jolivet, L., Oberhänsli, R. and Goffé, B., 2003. Deformation history of the high-pressure Lycian Nappes and implications for tectonic evolution of SW Turkey. *Tectonics*, 22(2),1007, doi:10.1029/2001TC901041.

Rimmelé, G., Oberhänsli, R., Goffé, B., Jolivet, L., Candan, O. and Cetinkaplan, M., in press. First evidence of high-pressure metamorphism in the "Cover Series" of the southern Menderes Massif. Tectonic and metamorphic implications for the evolution of SW Turkey. *Lithos*.

Rimmelé, G., Parra, T., Goffé, B., Oberhänsli, R., Jolivet, L. and Candan, O., submitted. Exhumation paths of high-pressure low-temperature rocks from the Lycian Nappes and the Menderes Massif (SW Turkey): a multi-equilibrium approach. *J. Petrol.*.

Ring, U. and Layer, P.W., 2003. High-pressure metamorphism in the Aegean, eastern Mediterranean: Underplating and exhumation from the Late Cretaceous until the Miocene to Recent above the retreating Hellenic subduction zone. *Tectonics*, 22(3): doi: 10.1029/2001TC001350, 2003.

Ring, U., Gessner, K., Güngör, T. and Passchier, C.W., 1999a. The Menderes Massif of western Turkey and the Cycladic Massif in the Aegean-do they really correlate? *J. Geol. Soc. London*, 156: 3-6.

Ring, U., Laws, S. and Bernet, M., 1999b. Structural analysis of a complex nappe sequence and late-orogenic basins from the Aegean Island of Samos, Greece. *J. Struct. Geol.*, 21: 1575-1601.

Ring, U., Layer, P.W. and Reischmann, T., 2001a. Miocene high-pressure metamorphism in the Cyclades and Crete, Aegean Sea, Greece: evidence for large-magnitude displacement on the Cretan detachment. *Geology*, 29(5): 395-398.

Ring, U., Willner, A.P. and Lackmann, W., 2001b. Stacking of nappes with different pressure-temperature paths: an example from the Menderes Nappes of western Turkey. *Am. J. Sci.*, 301: 912-944.

Roussos, N. and Bonneau, M., 1979. Stratigraphie et structure de l'île de Tilos (Dodécanèse, Grèce), *Proc. VI Colloq. Geol. Aegean Reg.*, Athènes, pp. 333-343.

Sanchez-Gomez, M., Avigad, D. and Heiman, A., 2002. Geochronology of clasts in allochthonous Miocene sedimentary sequences on Mykonos and Paros islands: implications for back-arc extension in the Aegean Sea. *J. Geol. Soc. London*, 159: 45-60.

Satir, M. and Friedrichsen, H., 1986. The origin and evolution of the Menderes Massif, W-Turkey: a rubidium/strontium and oxygen isotope study. *Geol. Runsch.*, 75: 703-714.

Satir, M., Chen, F., Terzioglu, N., Siebel, W. and Saka, K., 2000. Late Proterozoic crustal accretion in northwestern Turkey: evidence from U-Pb and Pb-Pb dating and Nd-Sr isotopes, *IESCA abstract*, Izmir, Turkey, pp. 106.

Schermer, E.R., 1990. Mechanism of blueschist creation and preservation in a A-type subduction zone, Mount Olympos region, Greece. *Geology*, 18: 1130-1133.

Schermer, E.R., 1993. Geometry and kinematics of continental basement deformation during the Alpine orogeny, Mt. Olympos region, Greece. *J. Struct. Geol.*, 15(3-5): 571-591.

Schermer, E.R., Lux, D.R. and Burchfiel, B.C., 1990. Temperature-time history of subducted continental crust, Mount Olympos region, Greece. *Tectonics*, 9(5): 1165-1195.

Schliestedt, M., 1980. Phasengleichgewichte in Hochdruckgesteinen von Sifnos, Griechenland, *PhD Thesis*, TU, Braunschweig, 142 pp.

Schliestedt, M. and Okrusch, M., 1988. Meta-acidites and silicic metasediments related to eclogite in northern Sifnos. In: D.C. Smith (Editor), Developments in Petrology: Eclogites and Eclogite-facies Rocks. *Elsevier*, pp. 291-334.

Schuiling, R.D., 1962. On petrology, age and structure of the Menderes migmatite complex (SW Turkey). *Min. Res. Expl. Inst. Turkey Bull.*, 58: 71-84.

Seidel, E., 1978. Zur petrologie des Phyllit-Quartzit Serie Kretas. *PhD Thesis*, Braunschweig.

Seidel, E., Kreuzer, H. and Harre, W., 1982. The late Oligocene/early Miocene high pressure in the external hellenides. *Geol. Jb.*, E23: 165-206.

Şengör, A.M.C. and Yilmaz, Y., 1981. Tethyan evolution of Turkey: a plate tectonic approach. *Tectonophysics*, 75: 181-241.

Şengör, A.M.C., Yilmaz, Y. and Sungurlu, O., 1984a. Tectonics of the Mediterranean Cimmerides: nature and evolution of the western termination of the paleo-Tethys. In: J.E. Dixon and A.H.F. Robertson (Editors), The geological evolution of the eastern Mediterranean. *Spec. Publ. Geol. Soc. London*, pp. 77-112.

Şengör, A.M.C., Satir, M. and Akkök, R., 1984b. Timing of tectonic events in the Menderes Massif, western Turkey: implications for tectonic evolution and evidence for Pan-African basement in Turkey. *Tectonics*, 3: 693-707.

Seyitoğlu, G. and Scott, B.C., 1996. The cause of N-S extensional tectonics in western Turkey: tectonic escape vs back-arc spreading vs orogenic collapse. *J. Geodynamics*, 22: 145-153.

Seyitoğlu, G., Scott, B.C. and Rundle, C.C., 1992. Timing of extensional tectonics in west Turkey. *J. Geol. Soc. London*, 149: 533-538.

Seyitoğlu, G., Tekeli, O., Cemen, I., Sen, S. and Isik, V., 2002. The role of the flexural rotation/rolling hinge model in the tectonic evolution of the Alasehir graben, western Turkey. *Geol. Mag.*, 139(1): 15-26.

Seymen, I., 1982. Kaman (Kirsehir) dolayinda Kirsehir masifinin stratigrafisi ve metamorfizmasi (in Turkish with English abstract). *Geol. Soc. Turkey Bull.*, 24: 7-14.

Shaked, Y., Avigad, D. and Garfunkel, Z., 2000. Alpine high-pressure metamorphism of the Almyropotamos window (southern Evia, Greece). *Geol. Mag.*, 137(4): 367-380.

Sherlock, S., Kelley, S.P., Inger, S., Harris, N. and Okay, A.I., 1999. ^{40}Ar-^{39}Ar and Rb-Sr geochronology of high-pressure metamorphism and exhumation history of the Tavsanli Zone, NW Turkey. *Contrib. Mineral. Petrol.*, 137: 46-58.

Sobel, E.R. and Strecker, M.R., in press. Uplift, exhumation, and precipitation: Tectonic and climatic control of Late Cenozoic landscape evolution in the northern Sierras Pampeanas, Argentina. *Basin Research.*

Sokoutis, D., Brun, J.P., Driessche, J.V.D. and Pavlides, S., 1993. A major Oligo-Miocene detachment in southern Rhodope controlling north Aegean extension. *J. Geol. Soc., London*, 150: 243-246.

Sorel, D., 2000. A Pleistocene and still-active detachment fault and the origin of the Corinth-Patras rift, Greece. *Geology*, 28: 83-86.

Spakman, W., 1990. Tomographic images of the upper mantle below central Europe and the Mediterranean. *Terra Nova*, 2: 542-553.

Spakman, W., Wortel, M. and Vlaar, N., 1988. The Hellenic subduction zone: a tomographic image and its geodynamic implications. *Geophys. Res. Lett.*, 15: 60-63.

Stampfli, G.M. and Borel, G.D., 2002. A plate tectonic model for the Paleozoic and Mesozoic constrained by dynamic plate boundaries and restored synthetic oceanic isochrons. *Earth Planet. Sci. Lett.*, 196: 17-33.

Taymaz, T., Jackson, J. and Westaway, R., 1990. Earthquake mechanism in the Hellenic Trench near Crete. *Geophys. J. Int.*, 102: 695-731.

Tekeli, O., 1981. Subduction complex of pre-Jurassic age, northern Anatolia, Turkey. *Geology*, 9: 68-72.

Theye, T. and Seidel, E., 1991. Petrology of low-grade high-pressure metapelites from the External Hellenides (Crete, Peloponnese). A case study with attention to sodic minerals. *Eur. J. Mineral.*, 3: 343-366.

Theye, T. and Seidel, E., 1993. Uplift-related retrogression history of aragonite marbles in western Crete (Greece). *Contrib. Mineral. Petrol.*, 114: 349-356.

Theye, T. and Siedel, H., 1993. Chloritoid, carpholite and sudoite in very low-grade metamorphic rocks of the Wippra Metamorphic Zone (Harz, Germany). *N. Jb. Miner. Mh.*, 2: 73-96.

Theye, T., Seidel, E. and Vidal, O., 1992. Carpholite, sudoite and chloritoid in low-grade high-pressure metapelites from Crete and the peloponnese, Greece. *Eur. J. Mineral.*, 4: 487-507.

Theye, T., Schreyer, W. and Fransolet, A.M., 1996. Low-Temperature, Low-Pressure Metamorphism of Mn-rich Rocks in the Lienne Syncline, Venn-Stavelot Massif (Belgian Ardennes), and the Role of Carpholite. *J. Petrol.*, 37(3): 767-783.

Thiébault, F., 1982. Evolution géodynamique des Hellénides externes en Péloponnèse méridional (Grèce). *PhD Thesis*, Université des sciences et techniques, Lille, France.

Thomson, S.N., Stöckhert, B. and Brix, M.A., 1998. Thermochronology of the high-pressure metamorphic rocks of Crete, Greece: implications for the speed of tectonic processes. *Geology*, 26: 259-262.

Thuizat, R., Whitechurch, H., Montigny, R. and Juteau, T., 1981. K-Ar dating of some infra-ophiolitic metamorphic soles from the eastern Mediterranean: new evidence for oceanic thrusting before obduction. *Earth Planet. Sci. Lett.*, 52: 302-310.

Trotet, F., 2000. Exhumation des roches de haute pression-basse température le long d'un transect des Cyclades au Péloponnèse, implications géodynamiques. *PhD Thesis*, Univ. Paris Sud, Orsay.

Trotet, F., Jolivet, L. and Vidal, O., 2001a. Tectono-metamorphic evolution of Syros and Sifnos islands (Cyclades, Greece). *Tectonophysics*, 338: 179-206.

Trotet, F., Vidal, O. and Jolivet, L., 2001b. Exhumation of Syros and Sifnos metamorphic rocks (Cyclades, Greece). New constraints on the P-T paths. *Eur. J. Mineral.*, 13(5): 901-920.

Ustaömer, T. and Robertson, A.H.F., 1993. A late Paleozoic-Early Mesozoic marginal basin along the active southern continental margin of Eurasia: evidence from the central Pontides (Turkey) and adjacent regions. *Geol. J.*, 28: 219-238.

Ustaömer, P.A. and Rogers, G., 1999. The bolu Massif: remnant of a pre-Early Ordovician active margin in the west Pontides, northern Turkey. *Geol. Mag.*, 136: 579-592.

Vache, R., 1963. Akdagmadeni kontak yataklari ve bunlarin Orta Anadolu Kristalinine karsi olan jeolojik çerçevesi (in Turkish with English abstract). *Min. Res. expl. Inst. Turkey Bull*, 60: 22-36.

Velde, B., 1965. Phengite micas: Synthesis, stability, and natural occurrence. *Am. J. Sci.*, 263: 886-913.

Verge, N.J., 1995. Oligo-Miocene extensional exhumation of the Menderes Massif, western Anatolia. *Terra Abstr.*, 7: 117.

Vidal, O. and Parra, T., 2000. Exhumation paths of high pressure metapelites obtained from local equilibria for chlorite-phengite assemblages. *Geol. Mag.*, 35: 139-161.

Vidal, O. and Theye, T., 1996. Discussion on "Petrology of Fe-Mg-carpholite-bearing metasediments from NE Oman". *J. Metamorphic Geol.*, 14: 381-397.

Vidal, O., Goffé, B. and Theye, T., 1992. Experimental study of the stability of sudoite and magnesiocarpholite and calculation of a new petrogenetic grid for the system FeO-MgO-Al_2O_3-SiO_2-H_2O. *J. Metamorphic Geol.*, 10: 603-614.

Vidal, O., Theye, T. and Chopin, C., 1994. Experimental study of chloritoid stability at high pressure and various fO_2 conditions. *Contrib. Mineral. Petrol.*, 118: 256-270.

Vidal, O., Goffé, B., Bousquet, R. and Parra, T., 1999. Calibration and testing of an empirical chloritoid-chlorite Mg-Fe-exchange thermometer and thermodynamic data for daphnite. *J. metamorphic Geol.*, 17: 25-39.

Vidal, O., Parra, T. and Trotet, F., 2001. A thermodynamic model for Fe-Mg aluminous chlorite using data from phase equilibrium experiments and natural pelitic assemblages in the 100-600°C, 1-25 kbar range. *Am. J. Sci.*, 6(301): 557-592.

Wagner, G. and van den Haute, P., 1992. Fission-track dating. *Kluwer Academic*, Boston, 285 pp.

Walcott, C.R., 1998. The alpine evolution of Thessaly (NW Greece) and Late Tertiary Aegean kinematics. *PhD Thesis*, Utrecht University, 175 pp.

Walcott, C.R. and White, S.H., 1998. Constraints on the kinematics of post-orogenic extension imposed by stretching lineations in the Aegean region. *Tectonophysics*, 298: 155-175.

Warkus, F.C., 2001. Untersuchungen an Hochdruckrelikten im zentralen Menderes Massiv, W Türkei. *PhD Thesis*, Univ. Potsdam, Potsdam, Germany, 87 pp.

Warkus, F.C., Partzsch, J.H., Candan, O. and Oberhänsli, R., 1998. The tectonometamorphic evolution of the Birgi-Tire Nappe in the Menderes Massif, SW-Turkey, *Freiberger Forschungshefte*, Freiberg, pp. 237-238.

Wawrzenitz, N. and Krohe, A., 1998. Exhumation and doming of the Thasos metamorphic core complex (S Rhodope,Greece): structural and geochronological constraints. *Tectonophysics*, 285: 301-332.

Wernicke, B., 1981. Low-angle normal faults in the Basin and Range province: nappe tectonics in an extending orogen. *Nature*, 291: 645-648.

Whitney, D.L. and Bozkurt, E., 2002. Metamorphic history of the southern Menderes massif, western Turkey. *Geological Society of America Bulletin*, 114(7): 829–838.

Whitney, D.L. and Dilek, Y., 1997. Core complex development in central Anatolia, Turkey. *Geology*, 25(11): 1023-1026.

Whitney, D.L., Teyssier, C., Dilek, Y. and Fayon, A.K., 2001. Metamorphism of the Central Anatolian Crystalline Complex, Turkey: influence of orogen-normal collision vs. wrench-dominated tectonics on P-T-t paths. *J. metamorphic Geol.*, 19: 411-432.

Wijbrans, J.R. and McDougall, I., 1986. ^{40}Ar/^{39}Ar dating of white micas from an alpine high-pressure metamorphic belt on Naxos (Greece); the resetting of the argon isotopic system. *Contrib. Mineral. Petrol.*, 93: 187-194.

Worley, B., Powell, R. and Wilson, C., 1997. Crenulation cleavage formation: Evolving diffusion, deformation and equilibration mechanisms with increasing metamorphic grade. *J. Struct. Geol.*, 19: 1121-1135.

Yalçin, Ü., 1987. Petrologie und Geochemie der Metabauxite SW-Anatoliens, *PhD Thesis*, Universitaet Bochum, Bochum, 136 pp.

Yilmaz, Y., Can Genç, S., Gürer, F., Bozcu, M., Yilmaz, K., Karacik, Z., Altunkaynak, S. and Elmas, A., 2000. When did the western Anatolian grabens begin to develop? In: E. Bozkurt, J.A. Winchester and J.D.A. Piper (Editors), Tectonics and Magmatism in Turkey and the Surrounding Area. *Spec. Publ. Geol. Soc. London*, pp. 353-384.

APPENDIX A

PRESSURE-TEMPERATURE ESTIMATES BASED ON MULTI-EQUILIBRIUM CALCULATIONS

For more than ten years, thermodynamic datasets have been established for minerals frequently found in HP-LT metapelites and have yielded more and more precise PT estimates (*Fe-Mg-carpholite:* Holland and Powel, 1990; Vidal et al., 1992 / *chloritoid:* Patrick, 1989 [unpublished]; Vidal et al., 1994; Vidal et al., 1999 / *micas:* Massone, 1995; Parra et al., 2002a / *chlorite:* Berman, 1988; Vidal et al., 1999; Vidal et al., 2001 / *sudoite:* Vidal et al., 1992). It is now accepted that the mineralogy of these metamorphic rocks is sensitive to PT conditions. In the system FMASH, Vidal et al. (1992) showed a PT grid which highlights variations of mineral compositions with PT conditions (Figure 1). However, metapelites commonly expose a poor mineralogical diversity and it is therefore difficult to obtain well-constrained PT estimates. Determination of PT conditions using the 'classical' method of divariant fields bounded by univariant curves is not useful if one wants to constrain a precise PT-path. A detailed picture of the tectonic processes responsible for exhumation of HP rocks is still often impossible, because continuous PT paths for exhumed rocks lack in many cases. Indeed, the determination of metamorphic PT conditions is generally based on the presence or absence of index minerals. Appearance and disappearance of index minerals can only provide information on the maximal and minimal PT conditions. Therefore, a continuous determination of the PT evolution must rely on the progressive change of mineral composition with PT conditions, or on the use of several generations of the same minerals showing different compositions, when their relative time of growth can be identified (local equilibrium). Vidal and Parra (2000) emphasized that chlorite and mica local equilibria can be used to constrain the retrograde PT evolution of rocks which have been exhumed. The concept of local equilibrium is consistent with the chemical variations observed in different grains of the same phase that coexist within the same thin section.

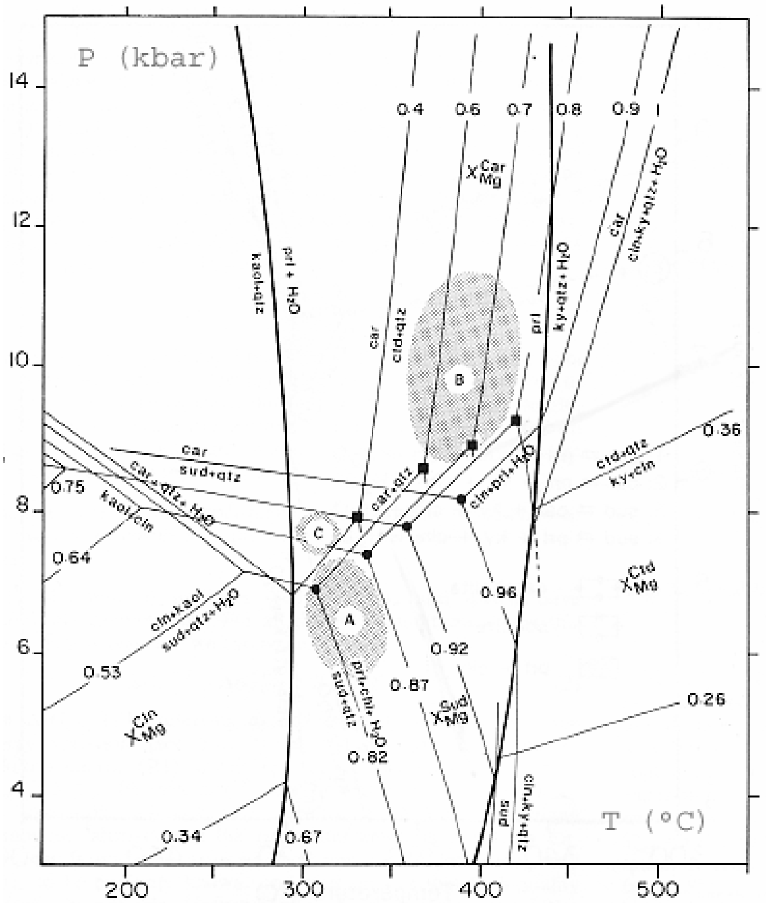

Figure 1. PT-grid for the system FeO - MgO - Al_2O_3 - SiO_2 - H_2O (FMASH). Variations of Fe-Mg-carpholite, sudoite and chloritoid compositions are directly related to metamorphic PT conditions. Estimated PT conditions in eastern Crete, western Crete and Oman correspond to dashed field A, B, and C respectively (after Vidal et al., 1992).

This appendix has the aim at presenting a systematic method that allows obtaining one estimate of both pressure and temperature, with only one calculation. This method of calculation is based on the notion of "multi-equilibrium calculations" (see Berman, 1991), which requires the assumption of local equilibrium, and the use of solid-solution models and thermodynamic data for minerals characterized by compositional variations.

1. Phengite and chlorite multi-equilibrium

Dioctahedral potassic micas (KWM: Rieder et al., 1998) and chlorites are widespread minerals in metapelites. They are found over a wide range of pressure and temperature conditions. Their compositions have been experimentally shown to depend on the thermobarometric conditions (Velde, 1965; Cathelineau and Nieva, 1985; Massone and Schreyer, 1987, Vidal et al., 1994; Leoni et al., 1998; Vidal et al., 2001; Parra et al., 2002a). Therefore, phengite and chlorite are good candidates for estimates of natural PT conditions. Metamorphic pressures are commonly estimated using the Si content of phengites, and temperatures from the Al^{IV} content of chlorites in diagenetic conditions (i.e. <375°C) (Cathelineau and Nieva, 1985; de Caritat et al., 1993).

Strong compositional heterogeneities among phengites and chlorites commonly coexist at the thin section scale. This is mainly due to the lack of equilibrium at distances greater than a few millimetres and the coexistence of several mineral generations which did not re-equilibrate during the thermobarometric evolution.

However, at a smaller scale, local chlorite-phengite equilibrium might be preserved. Recent works have highlighted that these compositional heterogeneities among various generations of phengites and chlorites within the same thin section are strong features for the understanding of metamorphic PT evolution (Vidal and Parra, 2000; Trotet, 2000; Parra, 2001; Trotet et al., 2001a; Trotet et al., 2001b; Parra et al., 2002b).

2. Compositional variability of phengites and chlorites

Variations of phengite and chlorite compositions are mainly due to major substitutions which occur in both minerals:

- The $FeMg_{-1}$ substitution
- The Tschermak substitution $[Al^{IV}Al^{VI}Si_{-1}(Mg, Fe)_{-1}]$
- The di-trioctahedral substitution $[(Mg, Fe)_3V_{-1}Al_{-2}]$, with V=vacancy, $Al=Al^{VI}$

Three additional substitutions are observed in white micas:

- The pyrophyllitic substitution $(KAl^{IV}Si_{-1}V_{-1})$, with V=vacancy
- The paragonitic substitution (NaK_{-1})
- The $Fe^{3+}Al_{-1}$, with $Al=Al^{VI}$

The extent of substitutions in micas depends on the PT conditions and the rock chemistry, or at fixed PT conditions, on the mineralogical assemblage (Massone and Szputka, 1997; Leoni et al., 1998; Agard et al., 2001; Parra et al., 2002a) (Figure 2). Phengite is highly pressure dependent and therefore is a useful theoretical geobarometer. At low PT conditions, phengites are characterized by a low (K+Na) content and contain a significant proportion of pyrophyllite end-member, whereas at high-temperature conditions, the (K+Na) content is high and phengite has a composition trending between muscovite and celadonite. For a fixed mineralogy, the proportion of celadonite (Si content and Fe+Mg content) increases with pressure.

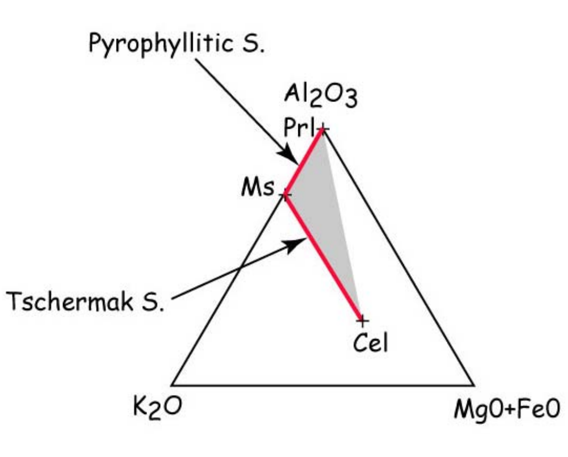

Figure 2. K-Al-(Mg+Fe) ternary diagram showing the different end-members of KWM and major substitutions influencing the composition of KWM.

Abbreviations:
Cel=(Fe,Mg)-celadonite, $Si_4Al(Mg,Fe)KO_{10}(OH)_2$
Ms=muscovite, $Si_3Al_3KO_{10}(OH)_2$
Prl=pyrophyllite, $Si_4Al_2O_{10}(OH)_2$

The extent of substitutions in chlorite also depends on the metamorphic PT conditions and on the bulk rock chemistry (De Caritat et al., 1993; Holland et al., 1998; Leoni et al., 1998) (Figure 3). Chlorite is more temperature dependent. With temperature decreasing, the proportion of amesite decreases whereas sudoite proportions increase. However, variations of compositions have been described with increasing pressure: the Si and (Fe+Mg) contents decrease whereas Al^{IV}, Al^{VI} and V increase (Leoni et al., 1998; Vidal et al., 2001).

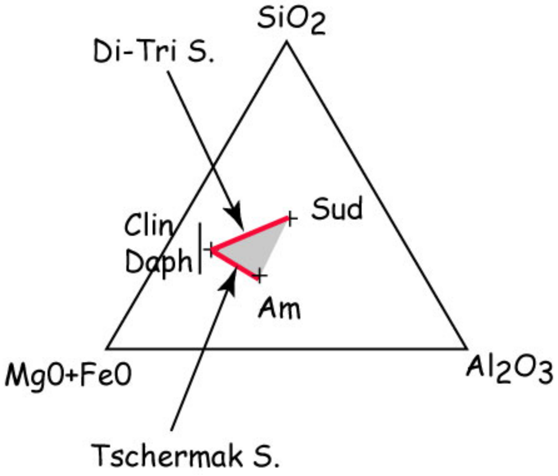

Figure 3. Si-Al-(Mg+Fe) ternary diagram showing the different end-members of chlorite and relevant substitutions responsible for the compositional variability of chlorites.

Abbreviations:
Clin = clinochlore, $Si_3Al_2Mg_5O_{10}(OH)_8$
Daph = daphnite, $Si_3Al_2Fe_5O_{10}(OH)_8$
Am = (Fe,Mg)-amesite, $Si_2Al_4(Mg,Fe)_4O_{10}(OH)_8$
Sud = (Fe,Mg)-sudoite, $Si_3Al_4(Mg,Fe)_2O_{10}(OH)_8$

Vacancies (V) inferred from electron microprobe analyses (EMPA) are not measurable but calculated quantities (see di-trioctahedral and pyrophyllitic substitutions). Vidal and Parra (2000) suggested that they might be an artefact resulting either from inadequate reference used for normalization of the EMPA to the structural formula (e.g. the amount of Fe^{3+} not assessed by EMPA), from contaminated analyses, or from analyses of inter-grown phyllosilicate.

A second problem for phengite analyses has to be taken into account: the possible loss of alkalis during analyses. However, it seems commonly accepted that Fe^{3+} in chlorite has a low content and is controlled by crystallo-chemical properties rather than by fO_2 conditions. It has been claimed that vacancies calculated from EMPA of chlorite with the assumption that $Fe^{2+} = Fe_{total}$ should be realistic, at least at LP-LT conditions (Cathelineau and Nieva, 1985; De Caritat et al., 1993; Leoni et al., 1998). On the contrary, it has been proposed that the Fe^{3+} proportion in mica is controlled by fO_2 conditions (Guidotti et al., 1994).

To avoid this problem and in order to reduce the errors related to the assumption that $Fe^{2+} = Fe_{total}$, Vidal and Parra (2000) consider that the samples used for PT estimates have to contain graphite (Fe^{3+} is low in rocks containing graphite).

3. Method of calculations

The multi-equilibrium calculation method allows one not only to estimate PT conditions, but also to check for equilibrium. It permits simultaneous estimates of P and T using a small number of phases which are always present in the studied thin sections. The method consists in the plot of all the equilibrium reactions (TER, Total Equilibrium Reactions) calculated with the end-members (EM) used to describe the composition of chlorite and phengite.

The number of linearly independent equilibrium reactions (IER, Independent Equilibrium Reactions) can be calculated as following:

$$IER = (EM + 2) - C$$

The term '+2' corresponds to the presence of quartz and water, and C is the number of components forming the chemical system (i.e. the number of oxides).

As an example, for an assemblage chlorite-mica-quartz-water, it is possible to plot 14 equilibrium reactions using chlorite and phengite end-members in the system KFMASH (C=6).

Depending on the chlorite and mica compositions, we use the different end-members of both minerals. In this example, the 4 end-members used for the calculations are sudoite, daphnite, Mg-amesite and clinochlore.

For phengite, we use 3 end-members: Fe-celadonite, pyrophyllite and muscovite. EM total = 7, and therefore IER = (7 + 2) – 6 = 3.

Assuming that the standard state thermodynamic data as well as the activity-composition relationships are well calibrated, all the reactions computed for a given paragenesis should intersect at a single point in the PT field if equilibrium is achieved. This is the case for the assemblage chlorite-mica-quartz-water (Figure 4a). The intersection point represents the stability conditions for the assemblage undertaken. The low dispersion of the different intersections [scat(P)=263 bar and scat(T)=7.5°C] indicates that equilibrium between all mineral phases is achieved.

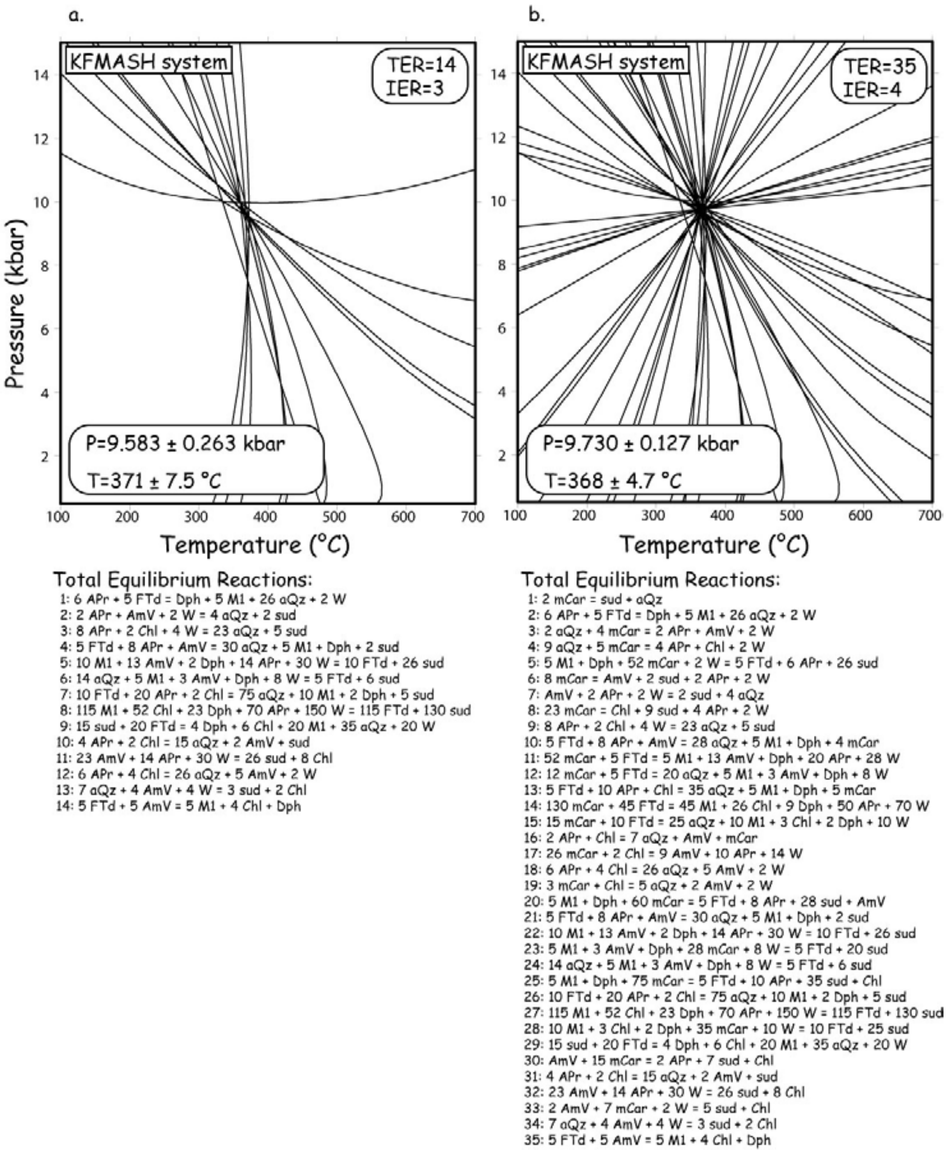

Total Equilibrium Reactions:
1: 6 APr + 5 FTd = Dph + 5 M1 + 26 aQz + 2 W
2: 2 APr + AmV + 2 W = 4 aQz + 2 sud
3: 8 APr + 2 Chl + 4 W = 23 aQz + 5 sud
4: 5 FTd + 8 APr + AmV = 30 aQz + 5 M1 + Dph + 2 sud
5: 10 M1 + 13 AmV + 2 Dph + 14 APr + 30 W = 10 FTd + 26 sud
6: 14 aQz + 5 M1 + 3 AmV + Dph + 8 W = 5 FTd + 6 sud
7: 10 FTd + 20 APr + 2 Chl = 75 aQz + 10 M1 + 2 Dph + 5 sud
8: 115 M1 + 52 Chl + 23 Dph + 70 APr + 150 W = 115 FTd + 130 sud
9: 15 sud + 20 FTd = 4 Dph + 6 Chl + 20 M1 + 35 aQz + 20 W
10: 4 APr + 2 Chl = 15 aQz + 2 AmV + sud
11: 23 AmV + 14 APr + 30 W = 26 sud + 8 Chl
12: 6 APr + 4 Chl = 26 aQz + 5 AmV + 2 W
13: 7 aQz + 4 AmV + 4 W = 3 sud + 2 Chl
14: 5 FTd + 5 AmV = 5 M1 + 4 Chl + Dph

Total Equilibrium Reactions:
1: 2 mCar = sud + aQz
2: 6 APr + 5 FTd = Dph + 5 M1 + 26 aQz + 2 W
3: 2 aQz + 4 mCar = 2 APr + AmV + 2 W
4: 9 aQz + 5 mCar = 4 APr + Chl + 2 W
5: 5 M1 + Dph + 52 mCar + 2 W = 5 FTd + 6 APr + 26 sud
6: 8 mCar = AmV + 2 sud + 2 APr + 2 W
7: AmV + 2 APr + 2 W = 2 sud + 4 aQz
8: 23 mCar = Chl + 9 sud + 4 APr + 2 W
9: 8 APr + 2 Chl + 4 W = 23 aQz + 5 sud
10: 5 FTd + 8 APr + AmV = 28 aQz + 5 M1 + Dph + 4 mCar
11: 52 mCar + 5 FTd = 5 M1 + 13 AmV + Dph + 20 APr + 28 W
12: 12 mCar + 5 FTd = 20 aQz + 5 M1 + 3 AmV + Dph + 8 W
13: 5 FTd + 10 APr + Chl = 35 aQz + 5 M1 + Dph + 5 mCar
14: 130 mCar + 45 FTd = 45 M1 + 26 Chl + 9 Dph + 50 APr + 70 W
15: 15 mCar + 10 FTd = 25 aQz + 10 M1 + 3 Chl + 2 Dph + 10 W
16: 2 APr + Chl = 7 aQz + AmV + mCar
17: 26 mCar + 2 Chl = 9 AmV + 10 APr + 14 W
18: 6 APr + 4 Chl = 26 aQz + 5 AmV + 2 W
19: 3 mCar + Chl = 5 aQz + 2 AmV + 2 W
20: 5 M1 + Dph + 60 mCar = 5 FTd + 8 APr + 28 sud + AmV
21: 5 FTd + 8 APr + AmV = 30 aQz + 5 M1 + Dph + 2 sud
22: 10 M1 + 13 AmV + 2 Dph + 14 APr + 30 W = 10 FTd + 26 sud
23: 5 M1 + 3 AmV + Dph + 28 mCar + 8 W = 5 FTd + 20 sud
24: 14 aQz + 5 M1 + 3 AmV + Dph + 8 W = 5 FTd + 6 sud
25: 5 M1 + Dph + 75 mCar = 5 FTd + 10 APr + 35 sud + Chl
26: 10 FTd + 20 APr + 2 Chl = 75 aQz + 10 M1 + 2 Dph + 5 sud
27: 115 M1 + 52 Chl + 23 Dph + 70 APr + 150 W = 115 FTd + 130 sud
28: 10 M1 + 3 Chl + 2 Dph + 35 mCar + 10 W = 10 FTd + 25 sud
29: 15 sud + 20 FTd = 4 Dph + 6 Chl + 20 M1 + 35 aQz + 20 W
30: AmV + 15 mCar = 2 APr + 7 sud + Chl
31: 4 APr + 2 Chl = 15 aQz + 2 AmV + sud
32: 23 AmV + 14 APr + 30 W = 26 sud + 8 Chl
33: 2 AmV + 7 mCar + 2 W = 5 sud + Chl
34: 7 aQz + 4 AmV + 4 W = 3 sud + 2 Chl
35: 5 FTd + 5 AmV = 5 M1 + 4 Chl + Dph

Figure 4. (a) Example of 'multi-equilibrium calculation' in the system KFMASH for an assemblage chlorite-phengite-quartz-water. Calculation is performed with the TWEEQ software (Berman, 1991) using solid-solution models and thermodynamic datasets. The scatters between the intersections of 14 plotted equilibria are calculated with the InterSX software (Berman, 1991) and show low values (scat[P] and scat[T]) indicating that the mineral phases used in the calculation are most probably in equilibrium around 9.5 kbar/370°C. (b) Same calculation as before, with the addition of Fe-Mg-carpholite to the previous assemblage. The scatters between the intersections of the 35 reactions are lower than in Figure (a) and the curves intersect at a single point located in the same PT area as in the case (a).

Moreover, if chlorite and mica are associated with other(s) mineral(s), a same kind of calculation can be performed. The new assemblage undertaken is Fe-Mg-carpholite-chlorite-phengite-quartz-water involving the same chlorite and phengite compositions from the previous assemblage (Figure 5).

In the system KFMASH (C=6), with the addition of Fe-Mg-carpholite composition to the previous calculation, EM=8 and therefore IER=4. There are 35 equilibrium reactions (TER) plotted in the PT field and as shown in Figure 4b, the dispersion of all intersections (scat[P]=127 bar and scat[T]=4.7°C) is lower than in the case of an assemblage chlorite-phengite-quartz-water. Therefore calculation is better constrained and equilibrium between all mineral phases is achieved.

If one uses the multi-equilibrium method, one should analyse assemblages involving minerals which display variations of compositions (due to several substitutions), in other terms mineral which can be defined as a combination of at least 2 end-members and more if possible. In fact, increasing the number of end-members to express the compositional variability of chlorite and KWM (and other associated minerals) allows one to increase the number of reactions that can be computed for a given paragenesis involving these minerals (Vidal and Parra, 2000; Vidal et al., 2001; Parra et al., 2002a; Parra et al., 2002b), and therefore to decrease the uncertainties of the PT estimates (see paragraph 7).

In the case of the mineral phases would have not been in equilibrium (for instance diachronic mineral crystallization), the pattern within the PT domain would have displayed a high dispersion of intersections and not a single point (Figure 6).

The calculations described above are performed with the TWEEQ software (Thermobarometry With Estimation of EQuilibration state; Berman, 1991).

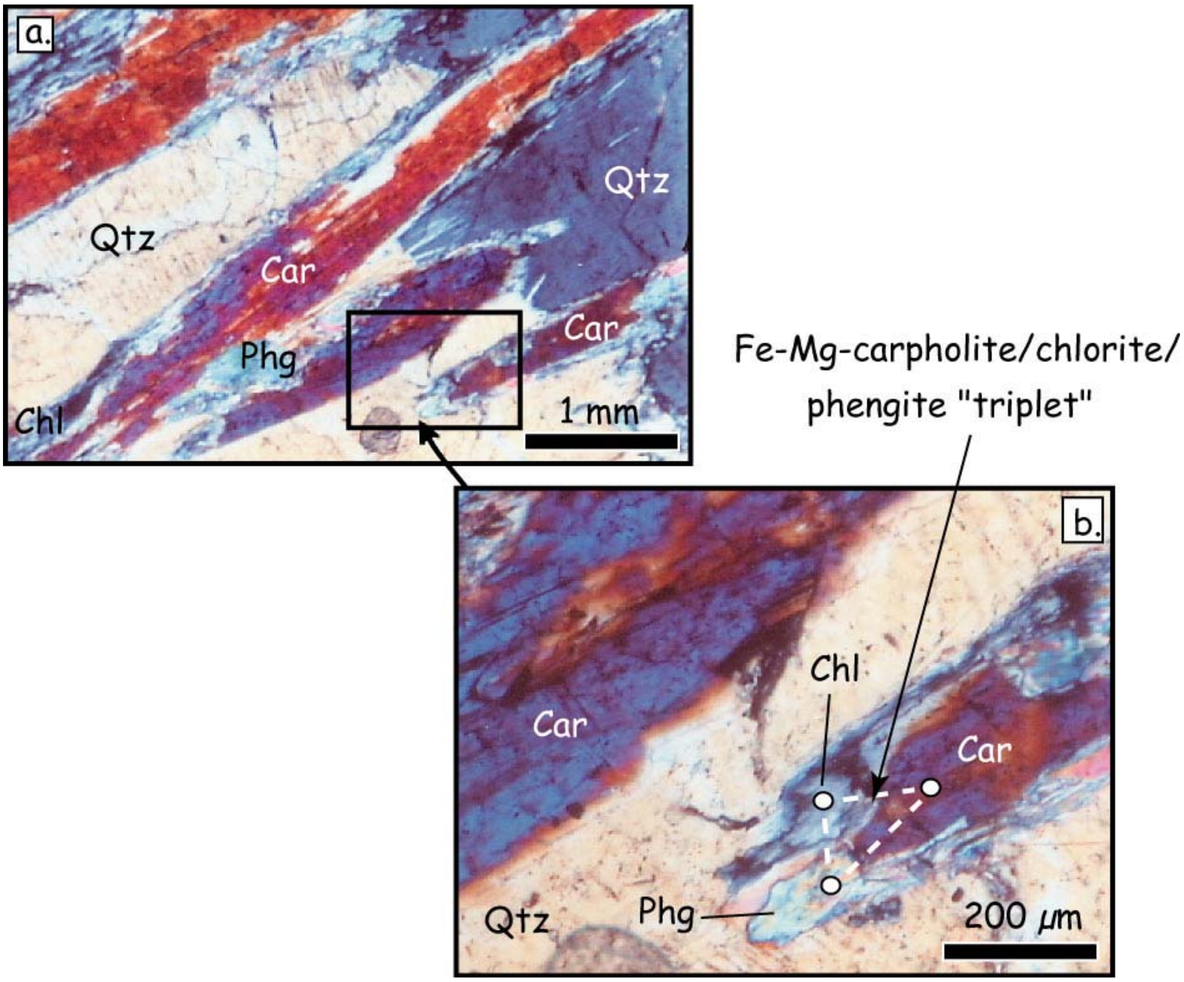

Figure 5. (a) Photomicrograph of a typical paragenesis observed in the Lycian metasediments (sample OREN001H) which is Fe-Mg-carpholite + chlorite + phengite + quartz (Car=Fe-Mg-carpholite, Chl=chlorite, Phg=phengite, Qtz=quartz). (b) Detail of Figure 5a; white dots show the locations of the analyses.

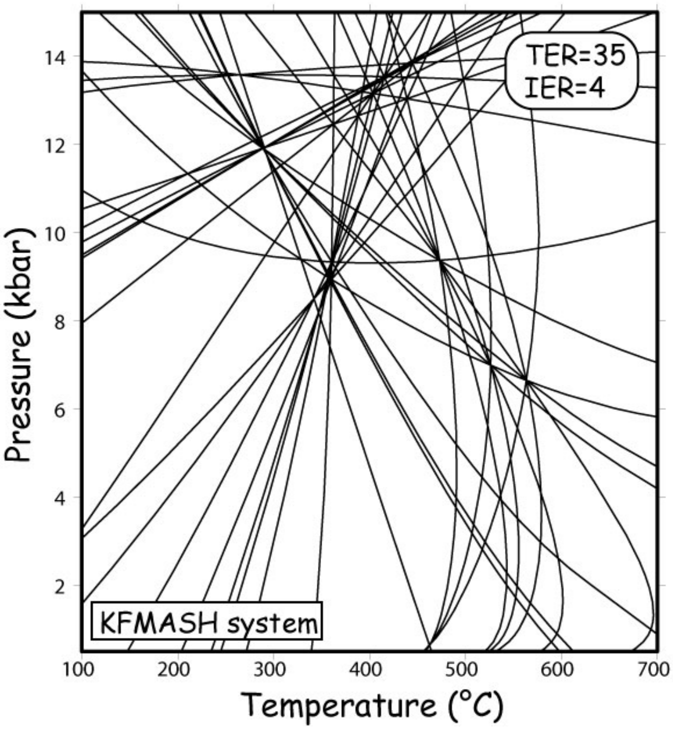

Figure 6. Example of 'multi-equilibrium calculation' in the system KFMASH for an assemblage Fe-Mg-carpholite + chlorite + phengite + quartz + water. The reaction curves do not intersect at one single point; the dispersion of intersections is very high and thus shows that the undertaken minerals are probably not in equilibrium.

4. Equilibrium criteria

The 'chlorite-phengite' pairs or 'chlorite-phengite-other mineral' triplet used to perform the calculations were first selected using classical criteria suggesting equilibrium state. Minerals must be in contact as represented in Figure 5. Pairs or triplets of minerals are thought to have grown at the same time. In addition, the minerals must be involved in the same microstructure, such as schistosity or S-C' band. When zoning was observed, which is commonly seen for phengites, the analysis was made at the rim.

At the thin section scale, the re-homogenisation of compositions involves the removal of matter from grain boundaries by grain boundary diffusion or advection, and chemical changes within grains by re-crystallisation or volume diffusion. It has been shown that volume diffusion in phyllosilicates (micas and chlorites) is not significant at temperatures lower than 550°C (Worley et al., 1997) and that equilibration of mineral composition is mainly controlled by crystallization and re-crystallization process. This is compatible with the large compositional variations of mica and chlorite observed in the same thin section. Therefore, crystallization and re-crystallization of new chlorite and mica seems to be the main processes which act to maintain local equilibrium during PT evolution.

5. Selection of the analyses

Mineral analyses were obtained on three different electron microprobes, Cameca SX50 at University Paris VI (Paris, France), Cameca SX100 at GeoForschungsZentrum (Potsdam, Germany), and JEOL 8800 in the Humboldt Museum (Berlin, Germany), the three units operated under standard conditions (15 kV, 10 to 20 nA, PAP correction procedure), using natural and synthetic standard minerals (in Paris: Fe_2O_3 [Fe], $MnTiO_3$ [Mn, Ti], diopside [Mg, Si], CaF_2 [F], orthoclase [Al, K], anorthite [Ca], albite [Na]; in Potsdam: Fe_2O_3 [Fe], rhodonite [Mn], rutile [Ti], MgO [Mg], wollastonite [Si, Ca], fluorite [F], orthoclase [Al, K], albite [Na]; in Berlin: anorthoclase [Si, Al, Na, K], ilmenite [Ti, Mn], magnetite [Fe], Cr-augite [Mg, Ca], apatite [F], tugtupite [Cl]). The analytical spot diameter was set between 3 and 5 μm keeping the same current conditions.

In order to decrease the risk of using KWM and chlorite analyses with a significant contamination or alkali loss, we only retained the analyses respecting the chemical criteria listed in Vidal and Parra (2000):

❑ Chlorite analyses showing more than 0.5% (Na_2O+K_2O+CaO) and more than 0.1% K_2O were rejected. Analyses which show an oxide sum lower than 83 wt% or greater than 89.5 wt% were also rejected.

❑ Mica analyses showing more than 0.5% ($MnO+TiO_2+Cl$) were also rejected. We kept only the analyses which showed an oxide sum comprised between 92 wt% and 97 wt%.

❑ Only the compositions of chlorite and phengite that could be expressed as a linear combination of the following end-members were retained:

For chlorites,
- clinochlore
- (Fe,Mg)-amesite
- daphnite
- sudoite

For micas,
- (Fe,Mg)-celadonite
- muscovite
- paragonite
- pyrophyllite
- biotite

The compositions that could not be expressed with these end-members involve other substitutions than those described above. Other strict criteria based on relations between the different end-members (listed in Vidal and Parra, 2000) were also used to select the analyses of chlorites and micas.

❑ Structural formulae are calculated on the basis of 14 oxygens for chlorite and 11 for mica.

❑ Incorporation of Fe^{3+} in KWM has a small effect on the PT conditions calculated without the Fe-end-members (Vidal and Parra, 2000). In order to reduce the errors related to the assumption that $Fe^{2+} = Fe_{total}$, PT estimates were performed for samples containing graphite. However, we noticed that the celadonite end-member sometimes showed negative values, probably due to the Fe^{3+} content in the Fe-celadonite end-member. We rejected all KWM analyses showing a negative value greater than 5% of the Fe-celadonite end-member.

In addition, in our samples, chlorites and micas are frequently associated with Fe-Mg-carpholite (or magnesiocarpholite) as well as chloritoid:

❑ Fe-Mg-carpholite and magnesiocarpholite structural formulae, $(Fe, Mn, Mg)Al_2Si_2O_6(OH, F)_4$, are calculated on the basis of 5 cations for the calculation of Si and 3 cations for Al, Fe, Mn and Mg, in order to account for the contribution of surrounding quartz when analysing fibres smaller than the microprobe beam diameter (Goffé and Oberhänsli, 1992). The Fe^{3+} ($Fe^{3+} = 2 - Al$) and Fe^{2+} contents are calculated after Goffé and Oberhänsli (1992). Analyses showing an oxide sum lower than 85 wt% or greater than 90 wt% were rejected.

❑ Chloritoid formula, $(Fe, Mn, Mg)_2Al_4Si_2O_{10}(OH)_4$, is calculated on the basis of 12 oxygens. Fe^{3+}/Fe^{2+} ($Fe^{3+} = 4 - Al$) is calculated after Chopin et al. (1992). Analyses showing an oxide sum lower than 90 wt% or greater than 94 wt% were rejected.

The selection of the analyses is therefore an inevitable stage before to perform any PT estimation. In this study, about 50% of analyses were rejected for PT conditions estimates. This is mainly due to the very small grain size that precludes the procurement of uncontaminated analyses.

6. Thermodynamic data and solid-solution properties

Most of the solid-solution models used in this work are derived from experimental results. The thermodynamic data and solid-solution properties used in the present study are from the TWEEQ software updated database of Berman (1988) for all phases except for chlorite, KWM, carpholite and chloritoid.

✓For chlorite:

The thermodynamic data for daphnite and Mg-Amesite are listed in Vidal et al. (2001). The clinochlore data come from Berman (1988). The Mg-sudoite properties used in the calculations are exposed in Vidal et al. (1992). Since thermodynamic data for Fe-amesite are unpublished and still provisory (Vidal and Parra, pers. comm.), I did not take into account this end-member for calculations.

✓For KWM:

The thermodynamic data for muscovite, paragonite and pyrophyllite are from Berman (1988). Solid-solution parameters and thermodynamic properties for $Fe^{(2+)}$-Al-celadonite and Mg-Al-celadonite are listed in Parra et al. (2002a; 2002b). They are a reappraisal of the Margules parameters and thermodynamic properties exposed in Vidal and Parra (2000). They have been re-estimated using additional natural and experimental data and are in closer agreement with the shape of the paragonite-muscovite, pyrophyllite-muscovite and paragonite-pyrophyllite solvi [see Figures 7 and 8 of Parra et al. (2002a)].

✓For Fe-Mg-carpholite:

The thermodynamic data of Fe-Mg-carpholite and the activity model of the Mg end-member are from Vidal et al. (1992) [$a_{(car)} = (X_{Mg})(X_{Al})^2(X_{OH})^4$ with $X_{Mg} = Mg/(Mg+Fe^{2+}+Mn)$, $X_{Al} = (2-Fe^{3+})/2$ and $X_{OH} = (4-F)/4$].

✓For chloritoid:

The thermodynamic data of Mg-chloritoid are listed in Vidal et al. (2001) and those of Fe-chloritoid come from Vidal et al. (1994). X_{Mg} and X_{Fe} have been calculated considering the Mn content, although very low [$X_{Mg} = Mg/(Mg+Fe^{2+}+Mn)$ and $X_{Fe} = Fe/(Mg+Fe^{2+}+Mn)$], and activities have been calculated after Vidal et al. (1994) (i.e. $a_{[Fe\text{-}Cld]}=X_{Fe}$ and $a_{[Mg\text{-}Cld]}=X_{Mg}$).

7. PT uncertainties resulting from analytical uncertainties

As said before, increasing the number of end-members expressing the compositional variability of chlorite and KWM (and other associated minerals) leads one to increase the amount of the computed reactions involving these minerals. Assuming that the standard state thermodynamic data, as well as the mixing properties of the end-members are correct, all the reactions computed for a given paragenesis should intersect at a single PT point if equilibrium is achieved. However, some scatters in the intersection points result from cumulated errors in each reaction, which stem from (1) the uncertainties in the thermodynamic standard state properties of end-members and solid-solution models, (2) departure of the analysed compositions from equilibrium compositions, and (3) analytical uncertainties.

Uncertainties associated with the thermodynamic data is difficult to estimate, because the uncertainties in the thermodynamic properties of the different end-members were calibrated using experimental and natural data of various levels of confidence and also depend on unreported uncertainties associated with other minerals included in the database of Berman (1988). However, these uncertainties have a systematic effect on the computed positions of the intersection points in the PT field, but not on their relative positions.

Even if the thermodynamic database was perfect, imprecision in the mineral analyses places limits on the relative precision of the PT estimates. The precision of the microprobe analysis induces scatter related to variations of mica, chlorite and other minerals composition. This scatter can be calculated using a Monte Carlo technique (Lieberman and Petrakakis, 1991; Vidal and Parra, 2000; Parra et al., 2002b). This calculation was made for each paragenesis used for PT estimates. It led to determine the paragenesis-dependant maximum permissible scatter [$scat(P)_{max}$ and $scat(T)_{max}$] above which the minerals are considered to be out of equilibrium (Vidal and Parra, 2000).

APPENDIX A

Description of the method:

For each paragenesis involving phengite and/or chlorite with/without other minerals, we first chose the assemblage showing mineral compositions that are 'perfectly' equilibrated (i.e. all equilibria intersect at a single point).

As an example, for a paragenesis carpholite-phengite-chlorite, we took the three compositions which showed the best equilibrium between each mineral (see Figure 7).

A Gaussian error distribution with $2\sigma=1\%$ relative for all major oxides was randomly sampled about the nominal weight percentage for each oxide in phengite, chlorite and Fe-Mg-carpholite (except $2\sigma=2\%$ relative for volatile Na_2O and K_2O in phengite). Minor elements were not considered because even large relative variations have a negligible influence on the Monte Carlo simulation. A hundred permutations allowed simulating 100 mineral compositions.

The set of a hundred simulated chlorite-phengite-carpholite triplets was used to calculate 100 separate PT points, as well as their associated scatters in P and T [scat(P) and scat(T)], with the InterSX program integrated in the TWEEQ package (Figure 7). These best PT estimates (Pi and Ti, i=1 to 100) are defined as a solid weighted average. Although the distribution of single PT points is non-Gaussian, the distribution of these best estimates can be approximated by a Gaussian distribution (Lieberman and Petrakakis, 1991). Therefore, we calculated an average pressure ($\overline{P}=\sum Pi/100$) and an average temperature ($\overline{T}=\sum Ti/100$) for the 100 Pi and Ti, as well as the 95% confidence standard deviations (σP and σT) and the correlation coefficient $\rho(P,T)$.

These values are used to estimate a PT ellipsoid depicting the precision of any P and T calculation for the given paragenesis. The size is calculated with σP and σT (Figure 7). The orientation of the ellipsoid is constrained by the correlation coefficient $\rho(P,T)$ between the hundred estimated PT points (Powell and Holland, 1988; 1994).

We also calculated the average scatters ($\overline{scat}(P)=[\sum scat(Pi)]/100$ and $\overline{scat}(T)=[\sum scat(Ti)]/100$) and their associated 2σ standard deviations ($\sigma_{scat(P)}$ and $\sigma_{scat(T)}$) in order to determine the maximum permissible scatter [$scat(P)_{max}=\overline{scat}(P)+2\sigma_{scat(P)}$ and $scat(T)_{max}=\overline{scat}(T)+2\sigma_{scat(T)}$] of any PT estimate with a 95% confidence level (2σ).

For any other PT estimate from the same paragenesis, we then compared the scatters scat(P) and scat(T) to the maxima defined previously, and if $scat(P)>scat(P)_{max}$ or $scat(T)>scat(T)_{max}$, the minerals involved in the paragenesis were considered to be out of equilibrium and the calculated PT conditions were rejected.

In the study area, PT conditions were estimated from 7 different parageneses:

- Fe-Mg-carpholite-chlorite-phengite-quartz
- Magnesiocarpholite-chlorite-kyanite-quartz
- Fe-Mg-carpholite-chlorite-quartz
- Chlorite-phengite-quartz
- Chloritoid-chlorite-quartz
- Chloritoid-chlorite-phengite-quartz
- Pyrophyllite-chlorite-quartz

For each paragenesis, the Monte Carlo simulation was performed in order to estimate the analytical uncertainties and the paragenesis-dependant maximum permissible scatters (different from one paragenesis to the other one) (Figures 8, 9 and 10). This allowed us to reject mineral pairs or triplets which were considered to be out of equilibrium. The amount of rejected PT estimates is large and may appear to be inconsistent with the assumption of (even local) equilibrium. It is however highlighted in the following paragraph that a significant proportion of rejected mineral pairs or triplets reveals PT conditions within the PT trend, this latter being defined by the equilibria showing $scat(P)<scat(P)_{max}$ or $scat(T)<scat(T)_{max}$. This is probably due to an underestimation of the maximum scatter (i.e. $scat(P)_{max}$ and $scat(T)_{max}$ being to low) that causes rejection of pairs and triplets being actually in equilibrium.

APPENDIX A

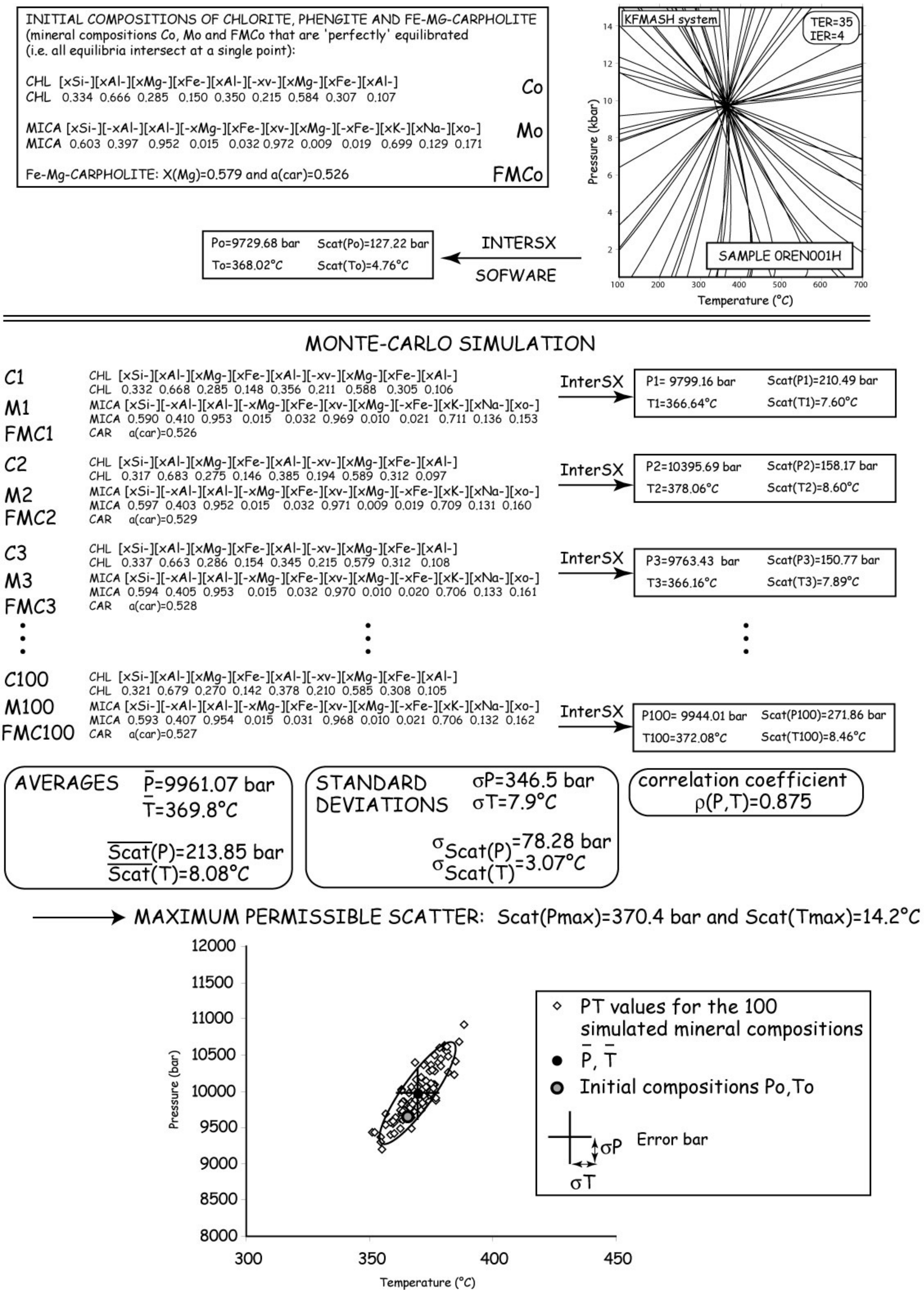

INITIAL COMPOSITIONS OF CHLORITE, PHENGITE AND FE-MG-CARPHOLITE
(mineral compositions Co, Mo and FMCo that are 'perfectly' equilibrated
(i.e. all equilibria intersect at a single point):

CHL [xSi-][xAl-][xMg-][xFe-][xAl-][-xv-][xMg-][xFe-][xAl-]
CHL 0.334 0.666 0.285 0.150 0.350 0.215 0.584 0.307 0.107 **Co**

MICA [xSi-][-xAl-][xAl-][-xMg-][xFe-][xv-][xMg-][-xFe-][xK-][xNa-][xo-]
MICA 0.603 0.397 0.952 0.015 0.032 0.972 0.009 0.019 0.699 0.129 0.171 **Mo**

Fe-Mg-CARPHOLITE: X(Mg)=0.579 and a(car)=0.526 **FMCo**

INTERSX SOFWARE

Po=9729.68 bar Scat(Po)=127.22 bar
To=368.02°C Scat(To)=4.76°C

MONTE-CARLO SIMULATION

C1 CHL [xSi-][xAl-][xMg-][xFe-][xAl-][-xv-][xMg-][xFe-][xAl-]
CHL 0.332 0.668 0.285 0.148 0.356 0.211 0.588 0.305 0.106
M1 MICA [xSi-][-xAl-][xAl-][-xMg-][xFe-][xv-][xMg-][-xFe-][xK-][xNa-][xo-]
MICA 0.590 0.410 0.953 0.015 0.032 0.969 0.010 0.021 0.711 0.136 0.153
FMC1 CAR a(car)=0.526

InterSX → P1= 9799.16 bar Scat(P1)=210.49 bar
T1=366.64°C Scat(T1)=7.60°C

C2 CHL [xSi-][xAl-][xMg-][xFe-][xAl-][-xv-][xMg-][xFe-][xAl-]
CHL 0.317 0.683 0.275 0.146 0.385 0.194 0.589 0.312 0.097
M2 MICA [xSi-][-xAl-][xAl-][-xMg-][xFe-][xv-][xMg-][-xFe-][xK-][xNa-][xo-]
MICA 0.597 0.403 0.952 0.015 0.032 0.971 0.009 0.019 0.709 0.131 0.160
FMC2 CAR a(car)=0.529

InterSX → P2=10395.69 bar Scat(P2)=158.17 bar
T2=378.06°C Scat(T2)=8.60°C

C3 CHL [xSi-][xAl-][xMg-][xFe-][xAl-][-xv-][xMg-][xFe-][xAl-]
CHL 0.337 0.663 0.286 0.154 0.345 0.215 0.579 0.312 0.108
M3 MICA [xSi-][-xAl-][xAl-][-xMg-][xFe-][xv-][xMg-][-xFe-][xK-][xNa-][xo-]
MICA 0.594 0.405 0.953 0.015 0.032 0.970 0.010 0.020 0.706 0.133 0.161
FMC3 CAR a(car)=0.528

InterSX → P3=9763.43 bar Scat(P3)=150.77 bar
T3=366.16°C Scat(T3)=7.89°C

⋮

C100 CHL [xSi-][xAl-][xMg-][xFe-][xAl-][-xv-][xMg-][xFe-][xAl-]
CHL 0.321 0.679 0.270 0.142 0.378 0.210 0.585 0.308 0.105
M100 MICA [xSi-][-xAl-][xAl-][-xMg-][xFe-][xv-][xMg-][-xFe-][xK-][xNa-][xo-]
MICA 0.593 0.407 0.954 0.015 0.031 0.968 0.010 0.021 0.706 0.132 0.162
FMC100 CAR a(car)=0.527

InterSX → P100= 9944.01 bar Scat(P100)=271.86 bar
T100=372.08°C Scat(T100)=8.46°C

AVERAGES $\bar{P}$=9961.07 bar
$\bar{T}$=369.8°C
$\overline{Scat}$(P)=213.85 bar
$\overline{Scat}$(T)=8.08°C

STANDARD DEVIATIONS σP=346.5 bar
σT=7.9°C
$\sigma_{Scat(P)}$=78.28 bar
$\sigma_{Scat(T)}$=3.07°C

correlation coefficient
ρ(P,T)=0.875

→ MAXIMUM PERMISSIBLE SCATTER: Scat(Pmax)=370.4 bar and Scat(Tmax)=14.2°C

Figure 7. Example of the Monte Carlo simulation for a paragenesis Fe-Mg-carpholite-chlorite-phengite-quartz.

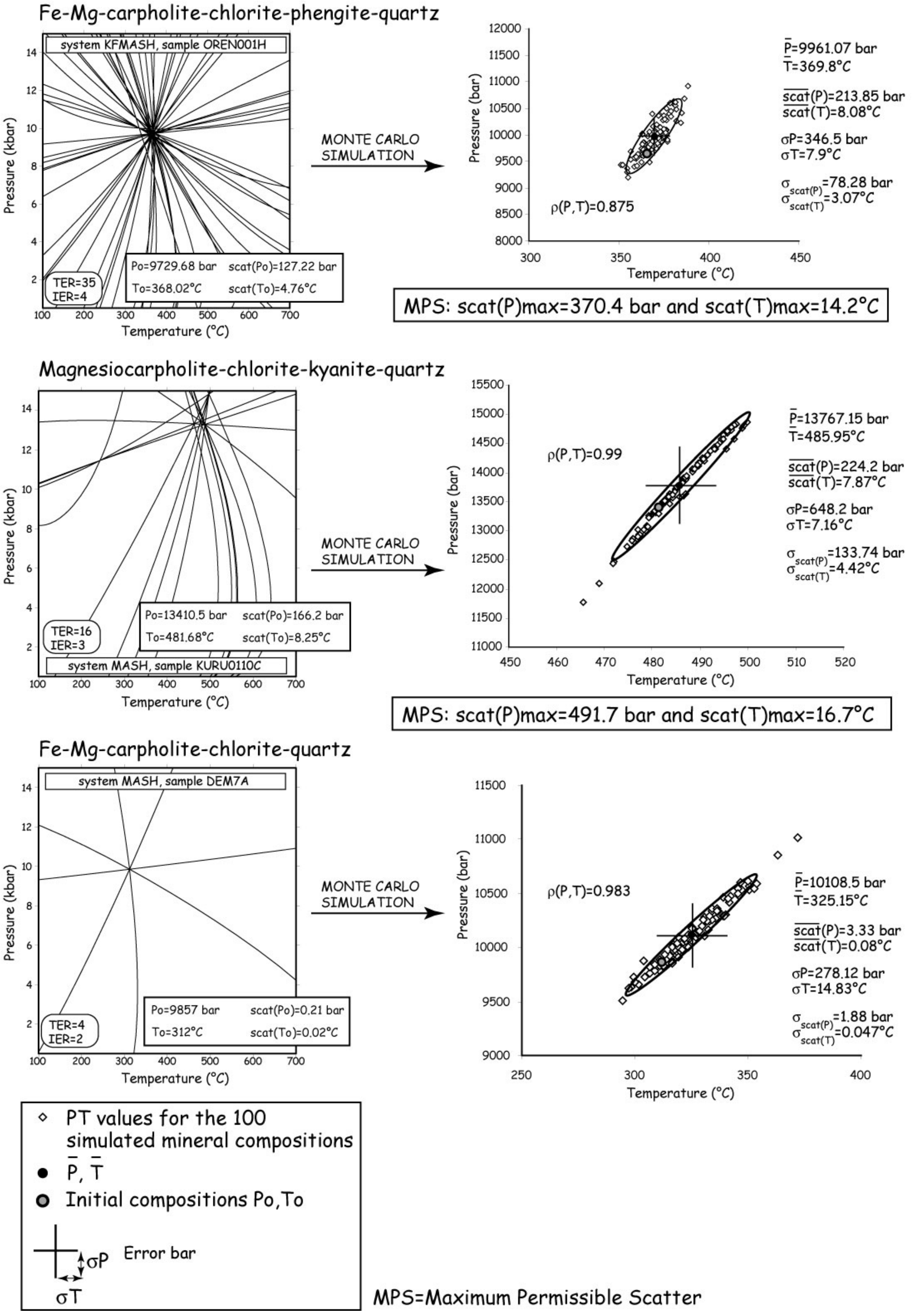

Figure 8. Result of the Monte Carlo simulation for the parageneses Fe-Mg-carpholite-chlorite-phengite-quartz, Magnesiocarpholite-chlorite-kyanite-quartz and Fe-Mg-carpholite-chlorite-quartz.

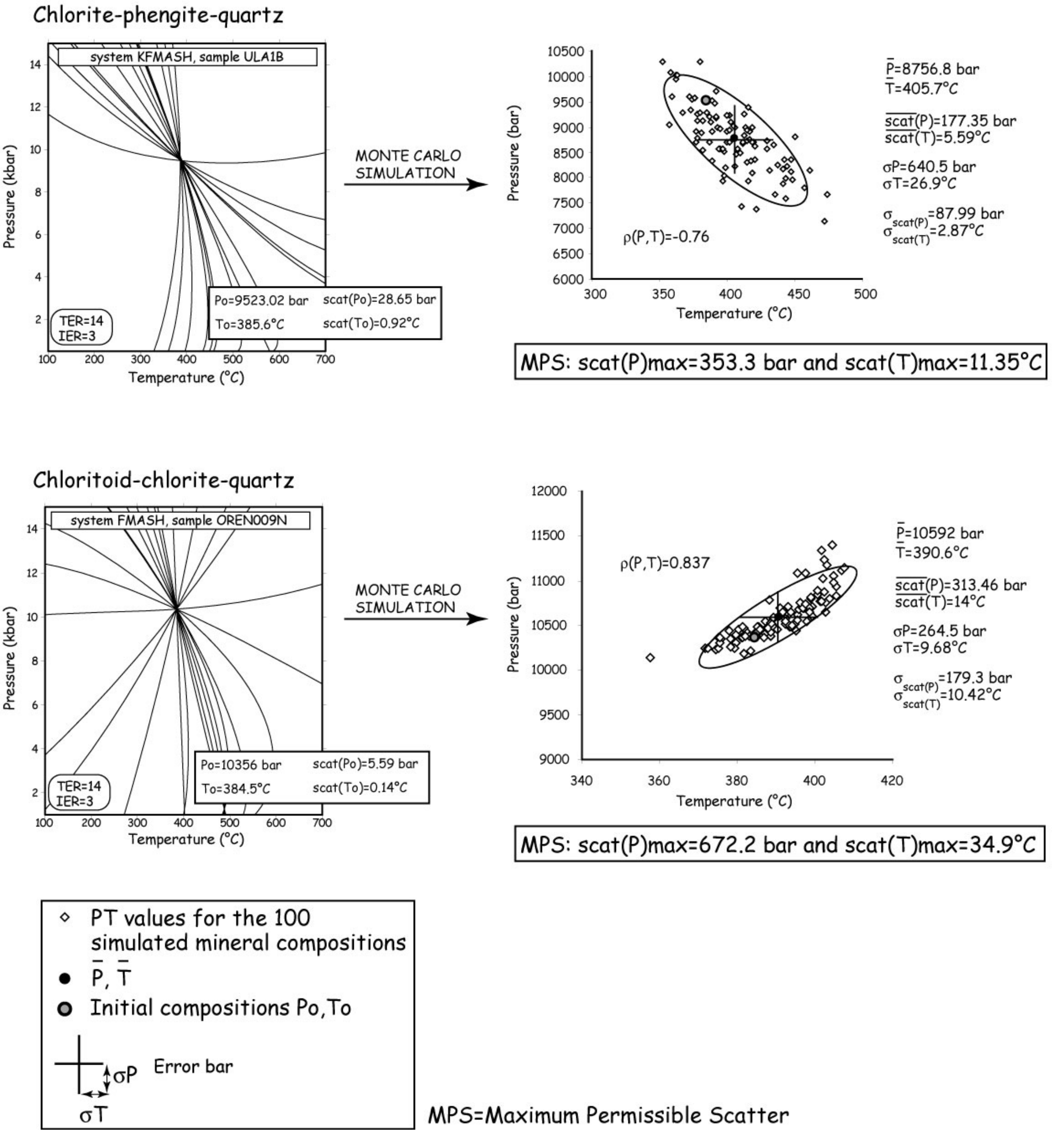

Figure 9. Result of the Monte Carlo simulation for the parageneses chlorite-phengite-quartz and chloritoid-chlorite-quartz.

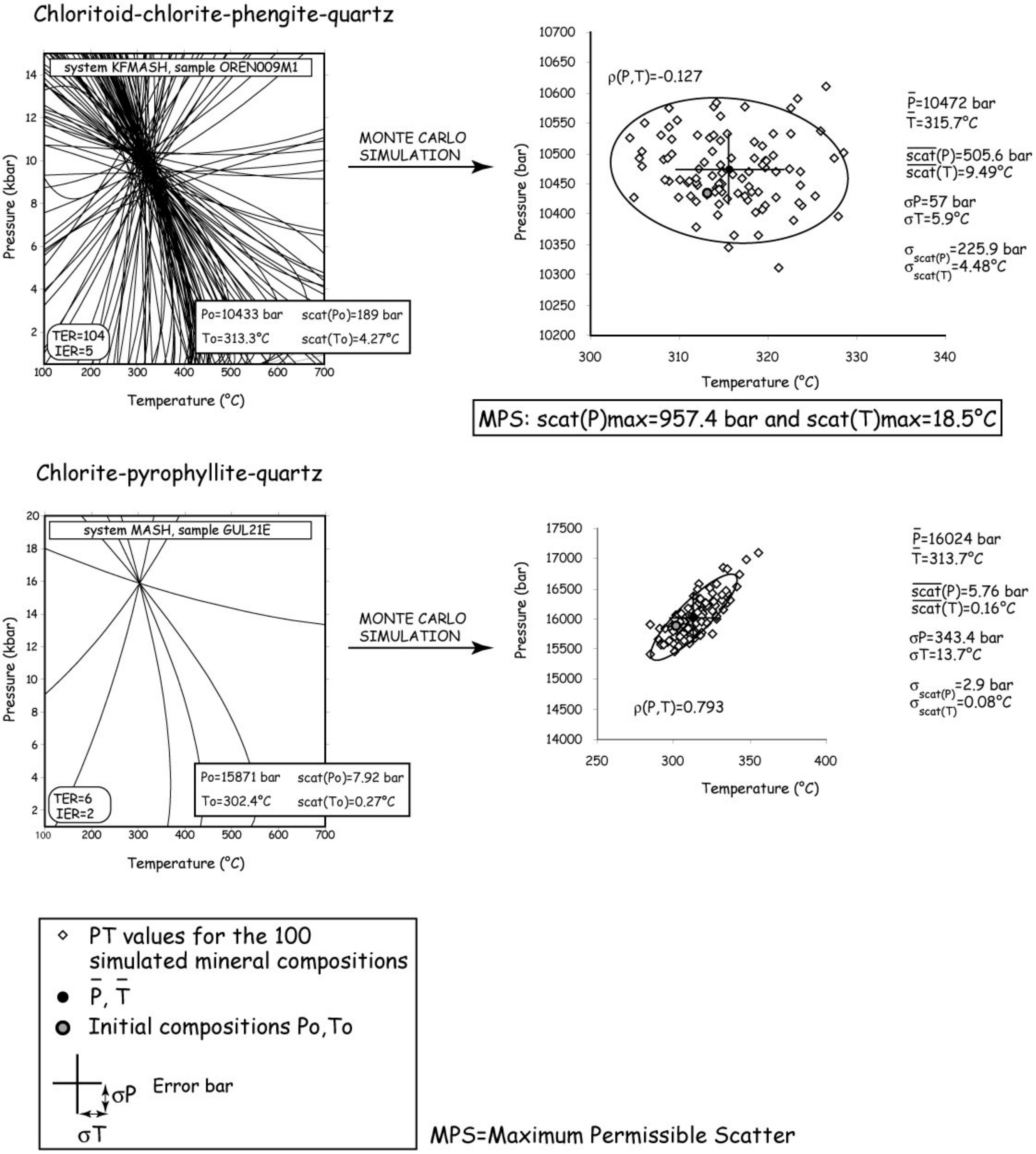

Figure 10. Result of the Monte Carlo simulation for the parageneses chloritoid-chlorite-phengite-quartz and chlorite-pyrophyllite-quartz.

8. Example of multi-equilibrium calculations leading to a PT path

Finally, after the selection of all PT estimates by the Monte Carlo method, those considered to be in equilibrium [i.e. showing $scat(P)<scat(P)_{max}$ and $scat(T)<scat(T)_{max}$] can be reported on a PT field. In this example, the PT conditions have been estimated from parageneses Fe-Mg-carpholite-chlorite-phengite-quartz and Fe-Mg-carpholite-chlorite-quartz (Figure 11) observed in a single thin section (OREN001H). The progressive PT evolution of the sample relies on the chemical composition variations of minerals. In the case of the sample OREN001H, Fe-Mg-carpholite, chlorite and mica actually have a high variability of compositions within the thin section (Figure 12).

I also distinguished in Figure 11 the PT conditions which were calculated with 2, 3 or 4 independent equilibrium reactions (IER). As already said, increasing the number of end-members to express the compositional variability of minerals allows to increase the number of reactions that can be computed for a given paragenesis involving these minerals, and therefore to decrease the uncertainties of the PT estimates. Therefore, the PT points obtained with 3 or 4 IER are better constrained than those obtained with only 2 IER. The paragenesis-dependent error bars corresponding to the σP and σT (±1σ) are calculated with the Monte Carlo simulation described above. It is noteworthy that achievement of equilibrium is not certified for PT results calculated with only two IER. However, most of PT calculations with two IER show PT points located within the trend defined by those calculated with more than two IER.

The PT estimates clearly show a high-pressure cooling path from 13 kbar/450°C to 8 kbar/ 250°C. However, the best-constrained PT conditions (IER>2) are located between 300°C and 400°C (Figure 11).

PT estimates which have been rejected after the Monte Carlo simulation [$scat(P)>scat(P)_{max}$ or $scat(T)>scat(T)_{max}$] are also reported on the PT diagram in order to highlight that these PT results are mainly located in the trend defined by the non-rejected equilibria. Therefore, it can be emphasized that the magnitude of the maximum scatter calculated from the Monte Carlo simulation might be too low, in other terms some of the rejected mineral pairs and triplets might actually be in equilibrium.

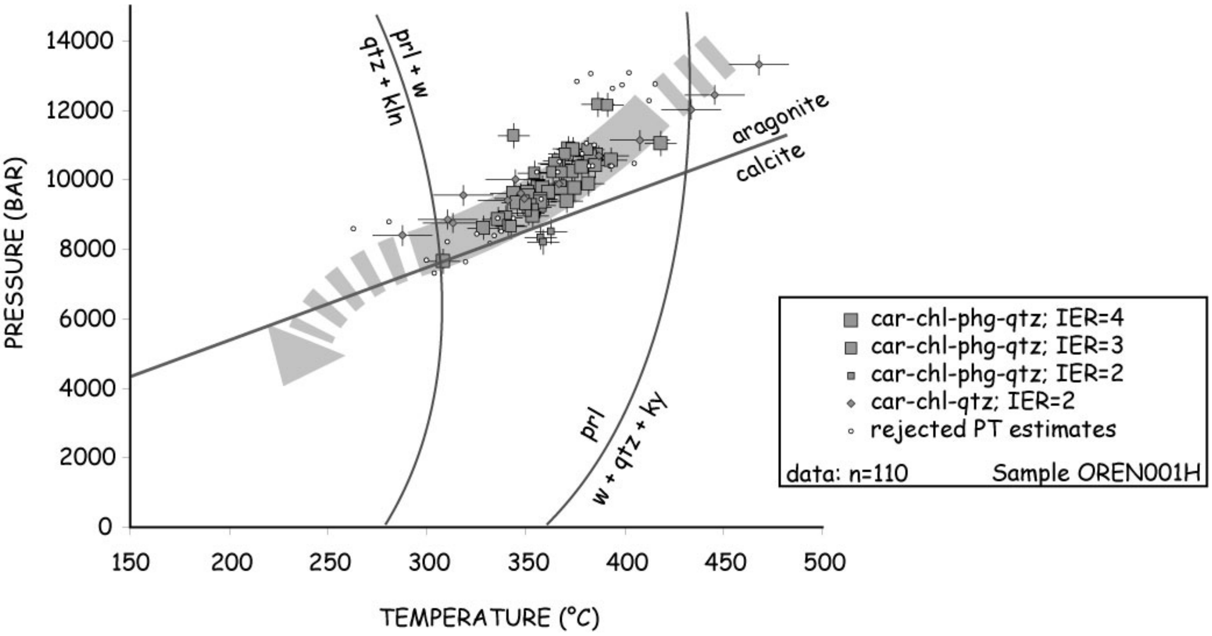

Figure 11. PT path inferred from the multi-equilibrium calculation. PT conditions are estimated from Fe-Mg-carpholite-chlorite-phengite and Fe-Mg-carpholite-chlorite equilibria (sample OREN001H). Error bars are the σP and σT calculated from the Monte Carlo simulation. Rejected PT conditions after the Monte Carlo simulation are also reported (see text for explanations).

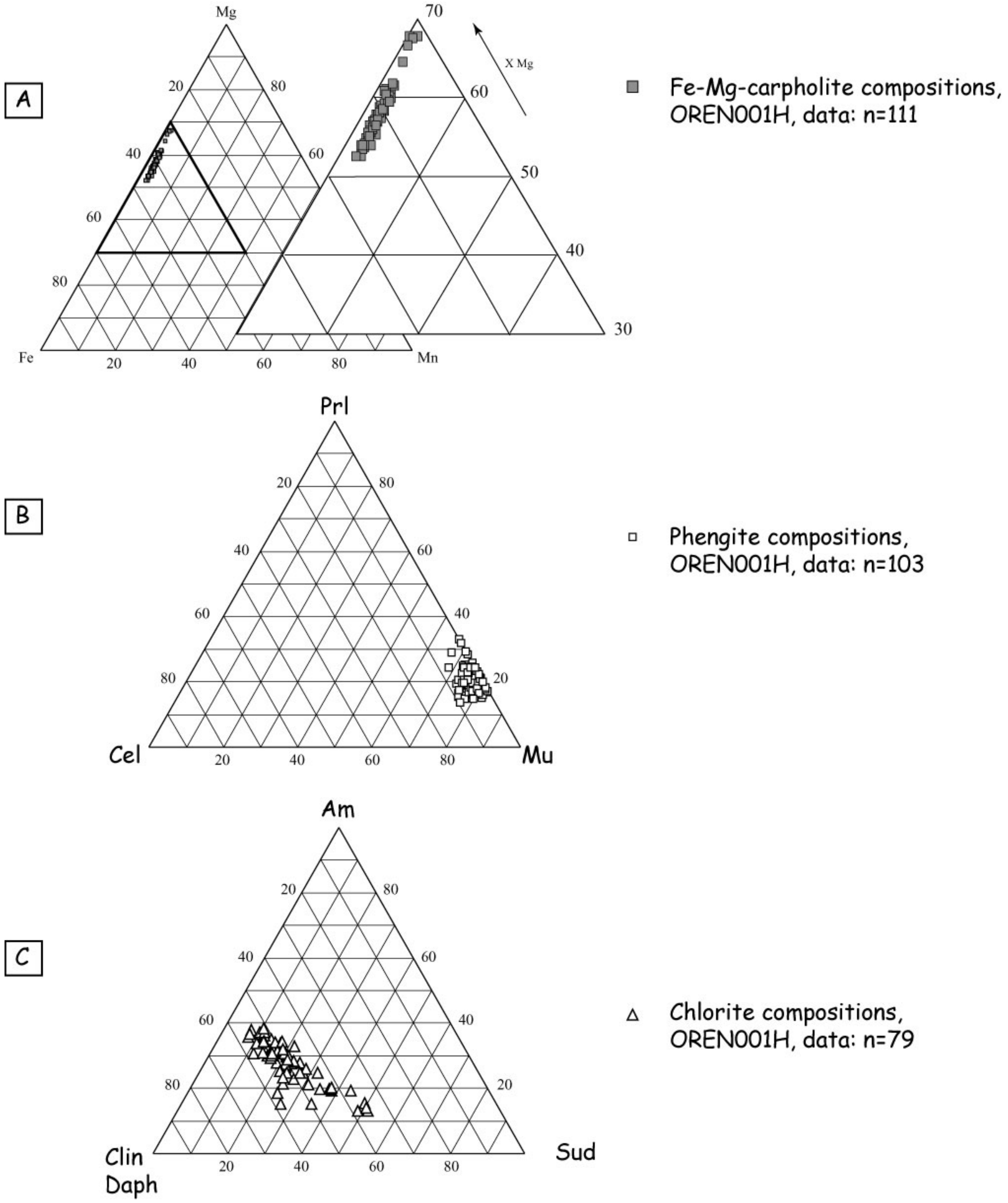

Figure 12. Fe-Mg-Mn-, pyrophyllite-muscovite-celadonite-, and amesite-sudoite-clinochlore/daphnite- ternary diagrams showing the compositional variability of Fe-Mg-carpholite, phengite and chlorite [(A), (B) and (C) respectively] within the same sample (OREN001H).

9. Conclusion

New thermodynamic datasets and solid-solution models for chlorite and mica permit to describe more precisely the variations of their composition within metamorphic rocks. Particularly, they increase the number of end-members defining the composition of these minerals, and thus provide better constraints on PT estimates using the 'multi-equilibrium' method. This method allows simultaneous estimates of pressure and temperature using a small number of phases which are always present in the considered thin sections. In addition, the Monte Carlo simulation permits to establish equilibrium criteria and to estimate error bars on the PT calculations for the different observed parageneses.

Although the retrograde PT evolution of exhumed rocks can be well constrained using this systematic method of calculation, major inconveniences rise. The first problem is that before obtaining a single PT estimate, a series of inevitable stages are necessary and take a long time. Because the selection criteria of analyses are strict, many of chlorite and mica compositions have to be rejected. Furthermore, structural formulae and cationic decomposition are calculated with Excel whereas the composition files within the TWEEQ software must be converted as particular text formats. Determination of the analytical uncertainties using the Monte Carlo method needs simulation of at least 100 mineral compositions, each of the hundred iterations requiring a single calculation in order to estimate the uncertainties on pressure and temperature values (error bars) as well as the maximum permissible scatter above which the minerals are considered to be out of equilibrium [$scat(P)_{max}$ and $scat(T)_{max}$]. Moreover, the Monte Carlo simulation has to be performed for each paragenesis. For instance, in this study, PT calculations were made from seven different parageneses and therefore 700 simulations, i.e. 700 calculations (one by one) had to be performed only to estimate the analytical uncertainties. Realization of single software in which all calculation proceedings are performed is presently being made and will be useful for faster PT estimates (Parra, pers. comm.).

APPENDIX B

FISSION-TRACKS:

PRINCIPLE, SAMPLE PREPARATION, AND ANALYTICAL PROCEDURE

APPENDIX B

This appendix briefly exposes the principle of the fission-track thermochronology, the methodology followed for sample preparation, and analytical details.

1. Principle

When charged nuclear particles travel through a solid, they leave linear trails of disrupted atoms, reflecting intense damage at the atomic scale (e.g. Wagner and Van den Haute, 1992). Fission tracks are such damages, and a fission track analysis consists of the characterization of these damages in minerals.

Spontaneous tracks in rocks are the result of the spontaneous fission of the isotope ^{238}U. Because these natural tracks are too small (a few nm) to be observed optically, a process of chemical etching is needed to open up the "latent" tracks and therefore to allow them to be characterized using an optic microscope (under high-magnification, 1250x).

Given that fission tracks can be observed optically in a grain and that fission processes occur at a statistically constant rate through geological time, fission tracks can provide a useful method of dating minerals. The number of fission events, which occur within a grain during a fixed time interval, depends on the magnitude of the time interval and the uranium content of the grain.

However, the concentration of ^{238}U (parent) to produce a detectable number of tracks (daughters) has to be sufficient if one wants to get reasonable fission track results. In the same way, too-high concentration of ^{238}U would create so many tracks that it would not be possible to distinguish individual tracks. The appropriate range of uranium concentration in apatite for accumulation over geological time scales is between 5 and 100 ppm, typical of relative common minerals such as apatite, zircon and sphene. We use in this study the apatite fission track method.

2. How do fission tracks provide an age?

The fission track dating method relies on the general radioactive decay equation. It requires the estimate of the relative abundance of the parent (number of ^{238}U atoms) and the daughter product (number of spontaneous tracks per unit of volume).

Whereas the abundance of the daughter product can be estimated by counting the number of spontaneous tracks on a given surface of apatite, determining of the relative abundance of ^{238}U is not so straightforward. The sample is irradiated with low-energy thermal neutrons which induce fission in ^{235}U (higher-energy neutrons would induce unwanted fission, for instance, from ^{232}Th and ^{238}U). The number of induced tracks measured after irradiation is therefore indicative of the abundance of ^{235}U, and as the ratio $^{235}U/^{238}U$ is constant in nature, the abundance of ^{238}U can be estimated.

3. What kind of age do apatite fission tracks provide?

Apatite fission track analysis from rocks which were buried and subsequently exhumed provides detailed information on the low-temperature thermal histories of these rocks, just prior to exhumation. Where rocks are buried to sufficient depth, the maximum paleo-burial temperature prior to their exhumation (T_{max}) exceeds the total annealing temperature (Ketcham et al., 1999). As they pass through the apatite fission-track partial annealing temperature window (~120° to 60°C) during exhumation, the fission track clock is reset to zero and fission track data record information on the time-temperature cooling path of these rocks (e.g. Green et al., 1989a, 1989b). The concept of a closure temperature for the fission track system, i.e. the temperature of the system at the time given by its apparent age, is considered to be an oversimplification (Gallagher et al., 1998). For instance, although 110 ± 10°C is commonly adopted for the nominal closure temperature of apatite, some geological examples showed that significant annealing occurs over a temperature range of at least 60°C (e.g. Gleadow and Duddy, 1981). This interval is generally inferred to as the partial annealing zone. It is noteworthy that apatite composition may be an important control on annealing rate, particularly the relative proportions of Cl, F, and OH (e.g. O'Sullivan and Parrish, 1995). For instance, F-apatite is expected to anneal more easily than the Durango apatite of Laslett et al. (1987).

As a synthesis, an apatite fission track age roughly corresponds to temperature ranging between 60 and 120°C, for apatites with commonly measured compositions.

4. Sample preparation and analytical details

For each of the 17 samples collected in the Lycian Nappes and in the Menderes Massif, between 5 and 10 kg of material were collected in the field area.

Because the etchable width and length of a fission track depends on the actual mineral and the nature of the chemical etchant, a well-calibrated and consistent sample preparation is necessary before making a fission track analysis.

Sample preparation was made following the methodology described in Sobel and Strecker (in press). Each of the 17 samples was crushed in a jaw crusher and then ground to sand grade in a rotary disc mill. After a first separation with a water table, the material was washed to remove dust, and dried. Then apatite was separated from the samples using standard magnetic and density methods (conventional heavy liquids). After a last step of sieving, the apatite fraction was mounted on glass slides with araldite epoxy, which were then polished to provide the exposure of an internal surface. Finally, the apatites were etched with 5.5 molar nitric acid (HNO_3), at 21°C for 20 seconds to reveal the fossil spontaneous fission tracks. After etching, all mounts are cut, cleaned in alcohol and distilled water.

The external detector zeta calibration method (Hurford and Carter, 1991) was used in order to date crystals individually (Figure 1). After etching and cleaning the surface of the apatite samples, an essentially uranium-free detector (mica crystal) was sealed in intimate contact with this surface. Each batch of mounts was stacked between two pieces of CN5 uranium standard glass, prepared in similar way. This dosimeter (glass of known uranium concentration) is used to monitor the neutron flux in the reactor. The sandwiches were then insert into an aluminium can for irradiation.

Only 8 of the 17 samples were sent for irradiation at Oregon State University, the other samples containing, either too-low quantities of apatite crystals, very poor quality apatites, or too-low uranium contents as attested by the quasi-inexistence of spontaneous tracks in apatite crystals.

During irradiation, tracks produced from ^{235}U in apatite cross the interface into mica, producing a mirror image of the original grain (Figure 1).

Following irradiation, the mica external detectors were removed from the grain mounts and standard glasses. They were etched with 40% hydrofluoric acid, at 21°C for 45 minutes, to reveal the fission tracks produced by induced fission of ^{235}U in the apatite and standard glass (Figure 1).

By counting the number of induced track in the mica, one estimates the uranium concentration (parent) of the apatite, whereas by counting the number of spontaneous tracks in the apatite, one estimates the concentration of the daughter product.

Samples were analyzed with a Leica DMRM microscope with drawing tube located above a digitizing tablet and a Kinetek computer-controlled stage driven by the FTStage program (Dumitru, 1993). Analyses were performed with reflected and transmitted light at 1250x magnification.

For the external detector method, fission track ages (FTA) are calculated with the standard fission track age equation that uses the zeta calibration (equation 5 of Hurford and Green, 1983):

$$FTA = [1/\lambda_D] \times Ln\,[(\lambda_D \,.\, \zeta \,.\, g \,.\, \rho D \,.\, \rho S\,)/\,\rho I \quad + \quad 1]$$

with

λ_D = α decay constant of ^{238}U
ζ = Zeta calibration factor (related to observation process)
g = Geometry factor (=0.5)
ρS = Spontaneous track density
ρI = Induced track density
ρD = Track density from uranium standard glass (dosimeter)

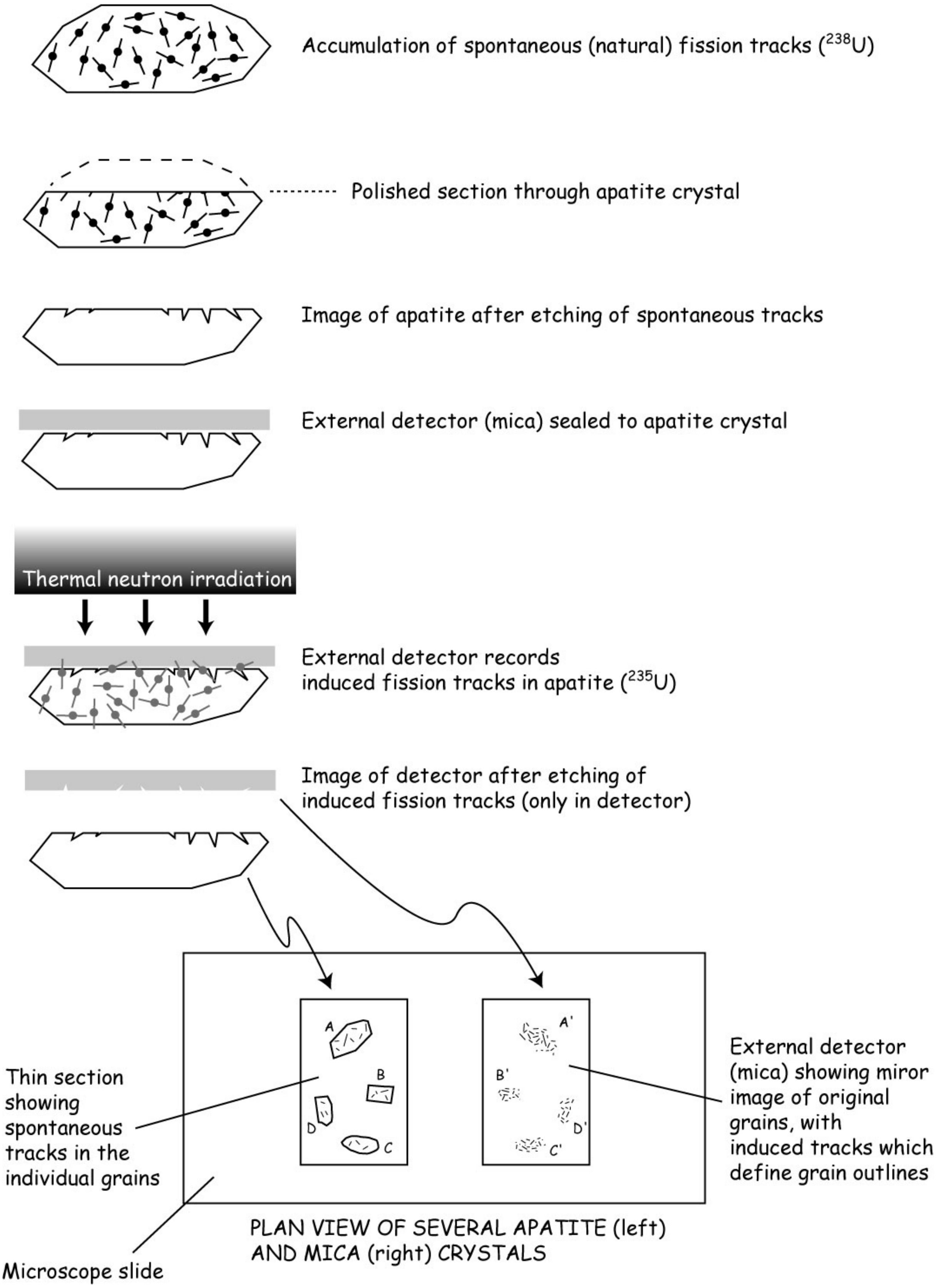

Figure 1. Simplified sketch summarizing the external detector method, after Hurford and Carter (1991). See text for details.

A fission track age is reported as a kind of average estimate of individual single grain ages. There are commonly 3 ways to calculate an age: the pooled, mean, and central ages. Considering the counts, the appropriate probability distribution is Poissonian.

- The pooled age is a simple sum of the spontaneous track counts divided by the sum of the induced track counts. It is only used when the distribution of counts passes a conventional $P(\chi^2)$ test.
- The mean age is the arithmetic mean of the individual ratios of spontaneous to induced track counts. This age is no longer used.
- The central age (Galbraith and Laslett, 1993) is the weighted mean of the log normal distribution of single grain ages ("weighted ages").

The latter is used when the distribution of counts is inconsistent with purely Poissonian variation (assessed with a conventional $P(\chi^2)$ test statistic)

5. How to read a radial plot?

For assessing the distribution of single grain ages, at least in a qualitative sense, we used the radial plot method (Figure 2) introduced by Galbraith (1988, 1990). These representations explicitly display the uncertainties in the single-grain ages so that the 'intergrain' age spread can be more easily assessed. On these plots, the X and Y coordinates are given by

$$X_n=1/\sigma_n$$

$$Y_n=(A_n-\tilde{A})/\sigma_n$$

where A_n is the age of the grain 'n', $\tilde{A}$ is some reference age (the average age of all grains), and σ_n is the standard error on the age of the grain 'n'.

X_n is an index of the precision of the ages and statistically more precise data plot further from the X origin (towards the right).

All data have a common normalized error: the $\pm 2\sigma$ error bars (vertical axis on the left of the radial plot) that have the same physical size for all grains in the radial plot.

The slope (Y_n / X_n) of a line from the plot origin (middle of the y axis, on the left of the radial plot) to a grain's data point indicates the grain's age, and therefore ages may be read from the radial age scale that is an arc-tan transform (right part of the radial plot).

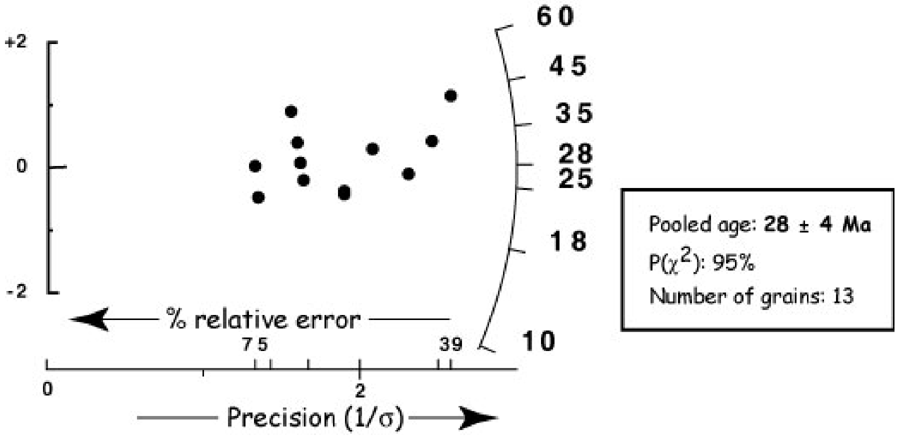

Figure 2. Example of a radial plot representation showing fission track single-grain ages.

APPENDIX C

ELECTRON MICROPROBE ANALYSES

This appendix contains examples of mineral analyses
(extracted from the whole microprobe analysis dataset)

CARPHOLITE FROM THE LYCIAN NAPPES (Ören area)

Sample	OREN001H	OREN001H	OREN001H	OREN001H	OREN001H	OREN001H	OREN001H	OREN001H	OREN001H	OREN002C	OREN002C	OREN002C	OREN002C
SiO2	37.97	37.19	37.35	38.42	37.46	37.98	37.81	38.06	37.62	38.63	38.17	38.63	37.94
Al2O3	30.27	30.16	30.26	30.60	30.01	30.57	30.23	30.58	30.41	32.70	32.69	32.38	31.64
FeO	11.20	11.48	10.81	10.94	11.20	10.06	10.53	10.40	11.14	9.67	9.27	9.36	9.57
MnO	0.62	0.67	0.52	0.56	0.56	0.44	0.56	0.50	0.59	0.39	0.33	0.38	0.40
MgO	6.58	6.41	7.25	7.04	7.10	7.43	7.21	7.43	6.90	7.63	7.73	7.50	7.22
F	0.00	0.00	0.00	0.00	0.00	0.00	0.00	0.00	0.00	0.00	0.00	0.00	0.00
Total	86.64	85.91	86.18	87.56	86.32	86.47	86.33	86.96	86.65	89.02	88.20	88.26	86.76
Si	2.03	2.01	2.00	2.03	2.01	2.02	2.02	2.02	2.01	1.99	1.98	2.01	2.01
Al	1.93	1.93	1.91	1.93	1.90	1.93	1.92	1.92	1.92	1.98	1.99	1.99	1.98
Fe3+	0.07	0.07	0.09	0.07	0.10	0.07	0.08	0.08	0.08	0.02	0.01	0.01	0.02
Fe2+	0.44	0.45	0.40	0.41	0.41	0.39	0.40	0.39	0.42	0.40	0.39	0.40	0.41
Mn	0.03	0.03	0.02	0.03	0.03	0.02	0.03	0.02	0.03	0.02	0.01	0.02	0.02
Mg	0.53	0.52	0.58	0.56	0.57	0.59	0.58	0.59	0.55	0.58	0.59	0.58	0.57
F	0.00	0.00	0.00	0.00	0.00	0.00	0.00	0.00	0.00	0.00	0.00	0.00	0.00
XMg	0.53	0.52	0.58	0.56	0.57	0.59	0.58	0.59	0.55	0.58	0.59	0.58	0.57

Sample	OREN009L	OREN009L	OREN009L	OREN009L	OREN009L	OREN009L	OREN009L	OREN009L	OREN009N	OREN009N	OREN009N	OREN009N	OREN009N
SiO2	38.22	37.79	38.03	37.69	37.40	37.45	37.46	37.73	38.09	38.23	38.10	38.31	38.59
Al2O3	30.60	31.12	31.02	31.34	31.39	31.11	31.57	32.37	30.89	30.67	31.45	31.28	31.49
FeO	12.83	12.54	12.11	11.98	11.74	11.93	11.39	10.87	13.04	14.01	13.18	13.31	11.73
MnO	0.24	0.18	0.19	0.28	0.16	0.14	0.22	0.14	0.58	0.69	0.55	0.54	0.26
MgO	6.74	6.80	6.96	6.68	6.91	7.01	7.03	7.10	5.60	5.31	5.53	5.45	6.45
F	0.00	0.00	0.00	0.00	0.00	0.00	0.00	0.00	0.00	0.00	0.00	0.00	0.00
Total	88.63	88.43	88.31	87.97	87.59	87.63	87.68	88.21	88.20	88.91	88.81	88.90	88.52
Si	2.01	1.98	2.00	1.99	1.98	1.98	1.97	1.97	2.02	2.02	2.01	2.02	2.02
Al	1.90	1.92	1.92	1.94	1.94	1.92	1.94	1.98	1.95	1.92	1.96	1.95	1.96
Fe3+	0.10	0.08	0.08	0.06	0.06	0.08	0.06	0.02	0.05	0.08	0.04	0.05	0.04
Fe2+	0.46	0.46	0.45	0.46	0.45	0.45	0.44	0.45	0.53	0.55	0.54	0.55	0.48
Mn	0.01	0.01	0.01	0.01	0.01	0.01	0.01	0.01	0.03	0.03	0.02	0.02	0.01
Mg	0.53	0.53	0.54	0.52	0.54	0.55	0.55	0.55	0.45	0.42	0.44	0.43	0.51
F	0.00	0.00	0.00	0.00	0.00	0.00	0.00	0.00	0.00	0.00	0.00	0.00	0.00
XMg	0.53	0.53	0.54	0.52	0.54	0.55	0.55	0.55	0.45	0.42	0.44	0.43	0.51

CARPHOLITE FROM THE LYCIAN NAPPES (Ören and Cal-Civril areas)

Sample	OREN009N	OREN009N	OREN009N	OREN009N	OREN009N	OREN009N	OREN009N	OREN005E	OREN005E	OREN005E	OREN005E	OREN005E	OREN005E
SiO2	38.14	38.02	38.17	37.93	38.19	38.30	38.24	38.11	38.51	38.32	38.47	38.29	37.74
Al2O3	30.84	30.72	31.03	30.78	31.20	31.96	32.00	30.77	31.26	30.97	31.72	32.02	31.12
FeO	13.14	14.34	13.37	12.75	13.64	11.32	11.59	11.77	10.92	10.43	10.10	9.83	10.28
MnO	0.59	0.66	0.54	0.43	0.66	0.13	0.22	0.21	0.24	0.29	0.24	0.25	0.15
MgO	5.60	5.20	5.42	6.10	5.22	6.80	6.43	6.64	6.94	6.71	7.41	7.72	6.88
F	0.00	0.00	0.00	0.00	0.00	0.00	0.00	0.45	0.20	0.00	0.35	0.28	0.30
Total	88.31	88.94	88.52	87.99	88.90	88.51	88.48	87.95	88.07	86.72	88.29	88.38	86.47
Si	2.02	2.01	2.02	2.01	2.02	2.00	2.00	2.02	2.03	2.04	2.01	1.99	2.02
Al	1.94	1.92	1.95	1.93	1.95	1.97	1.98	1.94	1.96	1.97	1.97	1.96	1.98
Fe3+	0.06	0.08	0.05	0.07	0.05	0.03	0.02	0.06	0.04	0.03	0.03	0.04	0.02
Fe2+	0.53	0.56	0.55	0.50	0.56	0.46	0.49	0.46	0.44	0.45	0.41	0.39	0.44
Mn	0.03	0.03	0.02	0.02	0.03	0.01	0.01	0.01	0.01	0.01	0.01	0.01	0.01
Mg	0.45	0.41	0.43	0.48	0.41	0.53	0.50	0.53	0.55	0.54	0.58	0.60	0.55
F	0.00	0.00	0.00	0.00	0.00	0.00	0.00	0.08	0.03	0.00	0.06	0.05	0.05
XMg	0.45	0.41	0.43	0.48	0.41	0.53	0.50	0.53	0.55	0.54	0.58	0.60	0.55

Sample	OREN005E	OREN0017B	OREN0017B	OREN0017B	OREN0017D	OREN0017D	OREN0017D	CAL0104	CAL0104	CAL0104	CAL0104	CAL0104	CAL0104
SiO2	37.95	37.55	37.42	37.75	37.78	37.61	37.54	38.74	38.84	38.79	38.44	38.51	38.67
Al2O3	31.25	30.78	30.75	31.35	31.32	30.97	30.95	31.23	31.94	31.83	31.71	31.50	31.64
FeO	10.37	12.21	13.58	12.39	13.71	13.15	13.31	8.44	8.39	7.73	8.70	8.55	8.08
MnO	0.07	0.16	0.13	0.19	0.12	0.17	0.13	0.13	0.12	0.09	0.05	0.08	0.13
MgO	6.93	5.22	5.05	5.51	4.86	5.38	5.42	8.07	7.92	8.23	7.93	7.98	7.87
F	0.00	0.27	0.46	0.42	0.00	0.15	0.46	0.45	0.35	0.47	0.35	0.39	0.32
Total	86.56	86.20	87.40	87.61	87.79	87.43	87.82	87.07	87.56	87.14	87.18	87.01	86.71
Si	2.02	2.04	2.02	2.02	2.02	2.02	2.01	2.04	2.04	2.04	2.02	2.03	2.04
Al	1.98	2.00	1.97	1.99	1.99	1.97	1.96	1.97	2.00	2.00	1.98	1.98	2.00
Fe3+	0.02	0.00	0.03	0.01	0.01	0.03	0.04	0.03	0.00	0.00	0.02	0.02	0.00
Fe2+	0.44	0.56	0.59	0.55	0.60	0.56	0.56	0.35	0.37	0.34	0.37	0.36	0.36
Mn	0.00	0.01	0.01	0.01	0.01	0.01	0.01	0.01	0.01	0.00	0.00	0.00	0.01
Mg	0.55	0.43	0.41	0.44	0.39	0.43	0.43	0.64	0.63	0.65	0.63	0.63	0.63
F	0.00	0.05	0.08	0.07	0.00	0.03	0.08	0.08	0.06	0.08	0.06	0.07	0.05
XMg	0.55	0.43	0.41	0.44	0.39	0.43	0.43	0.64	0.63	0.65	0.63	0.63	0.63

CARPHOLITE FROM THE LYCIAN NAPPES (Demirciler area)

Sample	BALCILAR1C	BALCILAR1C	BALCILAR1C	BALCILAR1C	BALCILAR1C	BALCILAR1C	BALCILAR1C	BALCILAR1C	BALCILAR1C	DEM1A	DEM1A	DEM1A	DEM1A
SiO2	39.23	39.32	38.56	39.37	39.38	39.19	39.21	39.41	39.02	39.44	39.25	39.13	38.88
Al2O3	31.68	31.68	31.56	31.87	31.92	31.87	31.78	32.07	31.63	31.79	31.58	31.37	31.48
FeO	9.47	9.96	9.66	9.47	9.40	9.70	10.00	9.50	9.90	9.23	10.20	10.07	9.41
MnO	0.20	0.20	0.21	0.17	0.23	0.19	0.15	0.20	0.19	0.27	0.28	0.32	0.30
MgO	7.73	7.52	7.53	7.75	7.81	7.53	7.47	7.76	7.43	7.90	7.51	7.52	7.52
F	0.29	0.13	0.15	0.22	0.22	0.16	0.15	0.27	0.17	0.16	0.07	0.12	0.11
Total	88.59	88.80	87.68	88.86	88.96	88.63	88.76	89.21	88.34	88.79	88.89	88.53	87.69
Si	2.04	2.04	2.02	2.04	2.04	2.04	2.04	2.03	2.04	2.04	2.04	2.04	2.04
Al	1.97	1.96	1.97	1.97	1.97	1.97	1.97	1.97	1.97	1.97	1.95	1.95	1.97
Fe3+	0.03	0.04	0.03	0.03	0.03	0.03	0.03	0.03	0.03	0.03	0.05	0.05	0.03
Fe2+	0.38	0.40	0.40	0.39	0.38	0.40	0.41	0.39	0.41	0.37	0.40	0.39	0.39
Mn	0.01	0.01	0.01	0.01	0.01	0.01	0.01	0.01	0.01	0.01	0.01	0.01	0.01
Mg	0.61	0.59	0.59	0.61	0.61	0.59	0.59	0.60	0.58	0.62	0.59	0.59	0.60
F	0.05	0.02	0.03	0.04	0.04	0.03	0.02	0.04	0.03	0.03	0.01	0.02	0.02
XMg	0.61	0.59	0.59	0.61	0.61	0.59	0.59	0.60	0.58	0.62	0.59	0.59	0.60

Sample	DEM1A	DEM1A	DEM1A	DEM1A	DEM1A	DEM1A	DEM7A	DEM7A	DEM7A	DEM7A	DEM7A	DEM7A	DEM7A
SiO2	39.42	39.20	39.02	39.50	38.98	39.35	38.75	38.78	38.82	38.96	39.08	38.98	38.95
Al2O3	31.93	31.59	31.49	31.68	31.40	31.65	31.02	30.82	31.37	31.69	31.33	31.11	31.70
FeO	9.58	9.75	9.47	9.48	9.33	9.31	11.52	11.80	10.78	10.57	10.98	11.12	10.61
MnO	0.29	0.29	0.30	0.24	0.28	0.23	0.43	0.43	0.37	0.35	0.41	0.42	0.39
MgO	7.82	7.60	7.65	7.40	7.69	7.82	6.87	6.86	7.18	7.07	7.03	6.97	6.98
F	0.11	0.11	0.13	0.13	0.14	0.13	0.05	0.11	0.10	0.01	0.06	0.09	0.00
Total	89.14	88.54	88.06	88.43	87.82	88.48	88.64	88.79	88.62	88.66	88.89	88.68	88.62
Si	2.03	2.04	2.04	2.06	2.04	2.04	2.03	2.03	2.03	2.03	2.04	2.04	2.03
Al	1.96	1.96	1.96	1.98	1.96	1.97	1.93	1.92	1.95	1.96	1.95	1.94	1.97
Fe3+	0.04	0.04	0.04	0.02	0.04	0.03	0.07	0.08	0.05	0.04	0.05	0.06	0.03
Fe2+	0.38	0.39	0.38	0.40	0.38	0.38	0.44	0.44	0.42	0.43	0.43	0.43	0.43
Mn	0.01	0.01	0.01	0.01	0.01	0.01	0.02	0.02	0.02	0.02	0.02	0.02	0.02
Mg	0.61	0.60	0.60	0.59	0.61	0.61	0.54	0.54	0.56	0.55	0.55	0.55	0.55
F	0.02	0.02	0.02	0.02	0.02	0.02	0.01	0.02	0.02	0.00	0.01	0.01	0.00
XMg	0.61	0.60	0.60	0.59	0.61	0.61	0.54	0.54	0.56	0.55	0.55	0.55	0.55

CARPHOLITE FROM THE LYCIAN NAPPES (Ula area and Dilek-Selçuk klippen)

Sample	ULA1B2.	ULA1B2.	ULA1B2.	ULA1B2.	ULA1B2.	ULA1B2.	ULA1B2.	ULA1B2.	ULA1B2.	ULA1B2.	ULA1C1.	ULA1C1.	ULA1C1.
SiO2	39.13	39.13	39.34	39.06	39.45	39.67	39.46	39.40	39.49	39.48	39.22	39.43	39.58
Al2O3	31.75	31.23	31.87	31.32	31.91	32.08	31.72	31.29	31.92	31.57	31.59	31.84	31.45
FeO	9.45	9.79	9.29	9.63	8.68	8.23	8.99	9.57	8.90	9.34	8.21	7.41	8.50
MnO	0.24	0.24	0.23	0.24	0.16	0.16	0.20	0.18	0.19	0.23	0.15	0.15	0.11
MgO	8.13	8.05	8.20	8.11	8.41	8.61	8.36	8.09	8.20	8.25	8.65	8.96	8.75
F	0.10	0.00	0.02	0.26	0.07	0.14	0.11	0.00	0.02	0.00	0.23	0.18	0.09
Total	88.80	88.44	88.94	88.61	88.67	88.89	88.84	88.53	88.71	88.86	88.05	87.98	88.49
Si	2.02	2.03	2.03	2.03	2.03	2.04	2.03	2.04	2.04	2.04	2.04	2.04	2.04
Al	1.95	1.93	1.95	1.93	1.96	1.97	1.95	1.94	1.96	1.94	1.96	1.97	1.94
Fe3+	0.05	0.07	0.05	0.07	0.04	0.03	0.05	0.06	0.04	0.06	0.04	0.03	0.06
Fe2+	0.36	0.36	0.36	0.36	0.34	0.33	0.34	0.36	0.35	0.35	0.32	0.29	0.31
Mn	0.01	0.01	0.01	0.01	0.01	0.01	0.01	0.01	0.01	0.01	0.01	0.01	0.01
Mg	0.63	0.63	0.63	0.63	0.65	0.67	0.65	0.63	0.64	0.64	0.68	0.70	0.68
F	0.02	0.00	0.00	0.04	0.01	0.02	0.02	0.00	0.00	0.00	0.04	0.03	0.02
XMg	0.63	0.63	0.63	0.63	0.65	0.67	0.65	0.63	0.64	0.64	0.68	0.70	0.68

Sample	ULA1C1.	ULA1C1.	ULA1C1.	ULA1C1.	DAV1B	DAV1B	DAV1B	DAV1B	DAV1B	DAV1B	DAV1B	DAV1B	DAV1B
SiO2	39.84	39.42	39.62	39.44	39.45	39.49	39.39	38.41	38.32	39.64	39.53	39.46	39.63
Al2O3	31.96	31.79	31.95	32.15	31.65	31.91	31.71	31.24	30.90	32.17	32.12	32.08	32.28
FeO	7.59	7.52	7.55	7.69	8.97	8.50	8.62	7.69	7.65	8.39	8.13	8.19	8.39
MnO	0.17	0.08	0.11	0.11	0.08	0.06	0.13	0.12	0.08	0.07	0.08	0.04	0.06
MgO	9.01	8.88	9.07	8.88	8.47	8.69	8.69	8.22	8.34	8.39	8.45	8.35	8.39
F	0.14	0.07	0.12	0.18	0.64	0.66	0.61	0.54	0.63	0.24	0.30	0.29	0.27
Total	88.71	87.77	88.42	88.44	89.25	89.31	89.15	86.21	85.92	88.89	88.60	88.41	89.01
Si	2.04	2.04	2.04	2.03	2.03	2.03	2.03	2.04	2.05	2.04	2.04	2.04	2.04
Al	1.96	1.97	1.96	1.97	1.95	1.95	1.94	1.99	1.97	1.98	1.98	1.99	1.98
Fe3+	0.04	0.03	0.04	0.03	0.05	0.05	0.06	0.01	0.03	0.02	0.02	0.01	0.02
Fe2+	0.29	0.30	0.29	0.31	0.34	0.32	0.32	0.33	0.32	0.34	0.34	0.34	0.35
Mn	0.01	0.00	0.00	0.00	0.00	0.00	0.01	0.01	0.00	0.00	0.00	0.00	0.00
Mg	0.70	0.70	0.70	0.69	0.66	0.67	0.67	0.66	0.67	0.65	0.66	0.65	0.65
F	0.02	0.01	0.02	0.03	0.11	0.11	0.10	0.09	0.11	0.04	0.05	0.05	0.04
XMg	0.70	0.70	0.70	0.69	0.66	0.67	0.67	0.66	0.67	0.65	0.66	0.65	0.65

CARPHOLITE FROM THE MENDERES MASSIF (Kurudere and Bahçeyaka areas)

Sample	KURU0110C	KURU0110C	KURU0110C	KURU0110C	KURU0110C	KURU0110C	KURU0110C	KURU0110C	KURU0110C	KURU0110C	KURU0110C	KURU0110C	KURU0110C
SiO2	40.47	39.95	40.02	40.56	40.61	40.47	40.06	40.05	39.95	39.81	39.90	40.23	39.76
Al2O3	33.05	31.95	32.35	32.78	33.11	33.65	32.96	31.77	32.36	31.51	32.97	32.80	32.62
FeO	2.42	2.75	3.08	3.13	2.70	2.50	2.95	2.79	2.53	3.21	2.73	2.99	3.57
MnO	0.64	0.58	0.58	0.86	0.71	0.69	0.66	0.69	0.73	0.94	0.54	0.59	0.83
MgO	11.43	11.31	11.21	11.20	11.64	11.53	11.48	11.57	11.02	11.09	11.55	11.37	10.99
F	0.21	0.48	0.21	0.69	0.05	0.32	0.64	0.53	0.59	0.75	0.00	0.53	0.79
Total	88.21	87.03	87.45	89.22	88.82	89.17	88.75	87.39	87.17	87.30	87.68	88.52	88.56
Si	2.04	2.05	2.04	2.04	2.03	2.02	2.02	2.05	2.05	2.05	2.02	2.04	2.02
Al	2.00	1.97	1.98	1.98	1.98	2.00	1.98	1.95	2.00	1.95	1.98	1.98	1.97
Fe3+	0.00	0.03	0.02	0.02	0.02	0.00	0.02	0.05	0.00	0.05	0.02	0.02	0.03
Fe2+	0.10	0.09	0.11	0.11	0.09	0.10	0.10	0.07	0.11	0.09	0.10	0.11	0.12
Mn	0.03	0.03	0.03	0.04	0.03	0.03	0.03	0.03	0.03	0.04	0.02	0.03	0.04
Mg	0.87	0.88	0.87	0.85	0.88	0.87	0.87	0.90	0.86	0.87	0.88	0.87	0.84
F	0.03	0.08	0.03	0.11	0.01	0.05	0.10	0.09	0.10	0.12	0.00	0.09	0.13
X Mg	0.87	0.88	0.87	0.85	0.88	0.87	0.87	0.90	0.86	0.87	0.88	0.87	0.84
X Fe	0.10	0.09	0.11	0.11	0.09	0.10	0.10	0.07	0.11	0.09	0.10	0.11	0.12
X Mn	0.03	0.03	0.03	0.04	0.03	0.03	0.03	0.03	0.03	0.04	0.02	0.03	0.04

Sample	YAT0107B	YAT0107B	YAT0107B	YAT0107B	YAT0107B	YAT0107B	YAT0107B	YAT0107B	YAT0107B	YAT0107B	YAT0107B	YAT0107B	YAT0107B
SiO2	38.50	38.37	38.69	38.64	38.93	38.43	39.09	39.27	39.15	38.74	38.58	39.36	38.40
Al2O3	32.38	32.24	32.47	32.72	32.38	32.73	33.15	32.68	32.90	32.76	31.74	33.04	32.05
FeO	2.68	3.00	2.79	2.67	2.27	2.31	2.27	2.45	2.07	2.18	2.49	1.96	2.51
MnO	5.33	5.48	5.39	5.43	5.05	4.83	4.19	4.98	3.23	4.39	4.80	4.26	5.48
MgO	8.82	9.02	8.96	8.94	9.03	9.31	9.53	9.02	9.93	9.25	8.69	9.39	8.53
F	0.61	1.26	0.61	0.77	0.61	0.83	0.99	0.39	1.46	0.82	0.66	0.72	0.72
Total	88.31	89.36	88.90	89.17	88.26	88.43	89.22	88.79	88.74	88.15	86.95	88.72	87.69
Si	1.99	1.98	1.99	1.98	2.01	1.98	2.00	2.01	2.01	2.00	2.03	2.02	2.01
Al	1.97	1.95	1.96	1.97	1.98	1.98	2.00	1.98	2.00	2.00	1.99	2.01	1.98
Fe3+	0.03	0.05	0.04	0.03	0.02	0.02	0.00	0.02	0.00	0.00	0.01	0.00	0.02
Fe2+	0.09	0.07	0.08	0.08	0.08	0.08	0.09	0.09	0.09	0.09	0.10	0.08	0.09
Mn	0.23	0.24	0.23	0.23	0.22	0.21	0.18	0.22	0.14	0.19	0.22	0.19	0.24
Mg	0.68	0.69	0.68	0.68	0.70	0.71	0.73	0.69	0.76	0.71	0.69	0.72	0.67
F	0.10	0.20	0.10	0.12	0.10	0.13	0.16	0.06	0.24	0.13	0.11	0.12	0.12
X Mg	0.68	0.69	0.68	0.68	0.70	0.71	0.73	0.69	0.77	0.71	0.69	0.73	0.67
X Fe	0.09	0.07	0.08	0.08	0.08	0.08	0.09	0.09	0.09	0.09	0.10	0.09	0.09
X Mn	0.23	0.24	0.23	0.23	0.22	0.21	0.18	0.22	0.14	0.19	0.22	0.19	0.24

CHLORITOID FROM THE LYCIAN NAPPES (Ören area)

Sample	OREN009M1.	OREN009M1.	OREN009M1.	OREN009M1.	OREN009M1.	OREN009M1.	OREN009M1.	OREN009M1.	OREN009M1.	OREN009M1.	OREN009M1.	OREN009M1.
SiO2	24.66	24.70	24.68	24.60	24.74	24.36	24.92	24.59	24.28	24.20	24.50	24.70
TiO2	0.02	0.04	0.00	0.00	0.03	1.22	0.03	0.08	0.06	0.11	0.05	0.01
Al2O3	41.51	40.10	40.84	40.71	41.00	40.56	39.75	40.99	40.71	40.58	39.99	40.66
FeO	23.15	24.57	22.93	22.98	23.25	23.13	24.97	23.54	24.54	25.88	24.00	24.39
MnO	0.82	0.29	0.72	0.71	0.67	0.68	0.36	0.59	0.40	0.28	0.41	0.45
MgO	3.51	3.69	3.43	3.48	3.53	3.55	3.14	3.75	3.10	2.74	3.74	3.10
Total	93.68	93.40	92.63	92.50	93.24	93.53	93.33	93.56	93.10	93.85	92.69	93.30
Si	2.00	2.02	2.02	2.02	2.02	1.98	2.04	2.00	1.99	1.98	2.02	2.02
Ti	0.00	0.00	0.00	0.00	0.00	0.07	0.00	0.00	0.00	0.01	0.00	0.00
Al	3.97	3.87	3.94	3.94	3.94	3.89	3.84	3.93	3.94	3.92	3.88	3.92
Fe3+	0.03	0.13	0.06	0.06	0.06	0.11	0.16	0.07	0.06	0.08	0.12	0.08
Fe2+	1.53	1.55	1.51	1.52	1.52	1.46	1.56	1.53	1.63	1.70	1.53	1.59
Mn	0.06	0.02	0.05	0.05	0.05	0.05	0.03	0.04	0.03	0.02	0.03	0.03
Mg	0.42	0.45	0.42	0.43	0.43	0.43	0.38	0.45	0.38	0.33	0.46	0.38
X(Mg)	0.21	0.22	0.21	0.21	0.21	0.22	0.20	0.22	0.19	0.16	0.23	0.19
X(Fe)	0.76	0.77	0.76	0.76	0.76	0.75	0.79	0.76	0.80	0.83	0.76	0.80
X(Mn)	0.03	0.01	0.03	0.02	0.02	0.02	0.01	0.02	0.01	0.01	0.01	0.02

Sample	OREN009M1.	OREN009M1.	OREN009M1.	OREN009M1.	OREN009M1.	OREN009M1.	OREN009M1.	OREN009M1.	OREN009M1.	OREN009M1.	OREN009M1.	OREN009M1.
SiO2	24.48	24.15	24.43	23.86	24.42	24.51	24.48	24.25	24.41	24.42	24.24	24.63
TiO2	0.06	0.02	0.02	4.32	0.45	0.01	0.05	0.02	0.03	0.00	0.13	0.02
Al2O3	39.74	39.80	39.18	38.53	40.28	40.47	39.26	39.51	39.30	39.53	39.68	40.99
FeO	26.10	25.42	27.08	23.08	23.30	25.00	25.52	25.53	25.12	24.95	25.13	24.03
MnO	0.39	0.32	0.27	0.38	0.33	0.42	0.37	0.39	0.35	0.28	0.30	0.52
MgO	2.68	2.60	2.61	2.75	3.45	3.03	3.26	2.84	2.88	3.07	2.55	2.75
Total	93.47	92.31	93.60	93.13	92.30	93.48	92.95	92.55	92.10	92.27	92.03	92.95
Si	2.02	2.01	2.02	1.96	2.01	2.01	2.03	2.02	2.03	2.03	2.02	2.02
Ti	0.00	0.00	0.00	0.27	0.03	0.00	0.00	0.00	0.00	0.00	0.01	0.00
Al	3.86	3.91	3.82	3.73	3.91	3.91	3.83	3.87	3.86	3.87	3.90	3.96
Fe3+	0.14	0.09	0.18	0.27	0.09	0.09	0.17	0.13	0.14	0.13	0.10	0.04
Fe2+	1.66	1.68	1.70	1.31	1.51	1.62	1.60	1.65	1.61	1.60	1.65	1.61
Mn	0.03	0.02	0.02	0.03	0.02	0.03	0.03	0.03	0.02	0.02	0.02	0.04
Mg	0.33	0.32	0.32	0.34	0.42	0.37	0.40	0.35	0.36	0.38	0.32	0.34
X(Mg)	0.16	0.16	0.16	0.20	0.22	0.18	0.20	0.17	0.18	0.19	0.16	0.17
X(Fe)	0.82	0.83	0.83	0.78	0.77	0.80	0.79	0.81	0.81	0.80	0.83	0.81
X(Mn)	0.01	0.01	0.01	0.02	0.01	0.01	0.01	0.01	0.01	0.01	0.01	0.02

CHLORITOID FROM THE LYCIAN NAPPES (Ören and Gerit areas)

Sample	OREN009N	OREN009N	OREN009N	OREN009N	OREN009N	OREN009N	OREN009N	OREN009N	OREN009N	OREN009N	OREN0016A	OREN0016A
SiO2	24.64	24.38	24.89	24.91	24.98	24.64	24.62	24.37	24.75	24.58	24.34	24.69
TiO2	0.02	0.02	0.01	0.00	0.01	0.02	0.00	0.04	0.00	0.03	0.07	0.00
Al2O3	39.54	39.29	40.27	41.08	40.02	39.20	39.74	38.66	40.81	40.31	39.22	39.55
FeO	26.38	27.39	24.96	23.38	25.03	27.25	25.51	27.29	23.74	25.24	21.62	22.58
MnO	0.33	0.34	0.41	0.71	0.35	0.32	0.36	0.27	0.29	0.43	0.76	0.62
MgO	2.91	2.62	2.89	3.71	2.58	2.49	3.11	2.57	3.49	3.12	3.95	3.17
Total	93.82	94.05	93.53	93.82	93.11	93.96	93.35	93.21	93.09	93.72	90.00	90.70
Si	2.03	2.01	2.04	2.02	2.05	2.03	2.03	2.03	2.02	2.01	2.05	2.06
Ti	0.00	0.00	0.00	0.00	0.00	0.00	0.00	0.00	0.00	0.00	0.00	0.00
Al	3.83	3.82	3.88	3.92	3.88	3.81	3.86	3.80	3.93	3.89	3.88	3.90
Fe3+	0.17	0.18	0.12	0.08	0.12	0.19	0.14	0.20	0.07	0.11	0.12	0.10
Fe2+	1.65	1.71	1.59	1.51	1.60	1.69	1.61	1.70	1.55	1.62	1.40	1.48
Mn	0.02	0.02	0.03	0.05	0.02	0.02	0.02	0.02	0.02	0.03	0.05	0.04
Mg	0.36	0.32	0.35	0.45	0.32	0.31	0.38	0.32	0.42	0.38	0.50	0.39
X(Mg)	0.18	0.16	0.18	0.22	0.16	0.15	0.19	0.16	0.21	0.19	0.25	0.21
X(Fe)	0.81	0.83	0.81	0.75	0.82	0.84	0.80	0.83	0.78	0.80	0.72	0.77
X(Mn)	0.01	0.01	0.01	0.02	0.01	0.01	0.01	0.01	0.01	0.01	0.03	0.02

Sample	OREN0016A	OREN0016A	OREN0017D	GERIT0101.	GERIT0101.	GERIT0101.	GERIT0101.	GERIT0101.	GERIT0101.	GERIT0101.	GERIT0101.	GERIT0101.
SiO2	24.95	24.32	24.42	24.65	24.59	24.35	24.70	24.60	24.25	24.55	24.47	24.23
TiO2	0.12	0.08	0.05	0.00	0.00	0.08	0.00	0.65	0.08	0.00	0.00	0.05
Al2O3	39.16	40.31	40.13	41.49	41.62	41.95	42.01	41.01	38.18	39.58	40.00	39.10
FeO	24.57	23.40	25.64	25.75	26.29	25.72	25.14	25.75	26.14	26.27	26.38	25.53
MnO	0.94	0.72	0.00	0.01	0.12	0.13	0.00	0.24	0.11	0.17	0.22	0.17
MgO	2.98	3.11	2.19	1.38	1.32	1.28	1.47	1.52	1.39	1.44	1.53	1.53
Total	93.10	92.26	92.51	93.29	94.02	93.74	93.50	93.84	90.37	92.07	92.63	90.72
Si	2.05	2.01	2.02	2.02	2.01	1.99	2.01	2.01	2.07	2.05	2.04	2.05
Ti	0.01	0.01	0.00	0.00	0.00	0.01	0.00	0.04	0.01	0.00	0.00	0.00
Al	3.80	3.93	3.92	4.01	4.01	4.03	4.03	3.95	3.84	3.90	3.92	3.90
Fe3+	0.20	0.07	0.08	0.00	0.00	0.00	0.00	0.05	0.16	0.10	0.08	0.10
Fe2+	1.49	1.54	1.70	1.77	1.80	1.75	1.71	1.71	1.70	1.74	1.76	1.71
Mn	0.07	0.05	0.00	0.00	0.01	0.01	0.00	0.02	0.01	0.01	0.02	0.01
Mg	0.36	0.38	0.27	0.17	0.16	0.16	0.18	0.19	0.18	0.18	0.19	0.19
X(Mg)	0.19	0.19	0.14	0.09	0.08	0.08	0.09	0.10	0.09	0.09	0.10	0.10
X(Fe)	0.78	0.78	0.86	0.91	0.91	0.91	0.91	0.89	0.90	0.90	0.90	0.89
X(Mn)	0.03	0.03	0.00	0.00	0.00	0.00	0.00	0.01	0.00	0.01	0.01	0.01

CHLORITOID FROM THE LYCIAN NAPPES (Ula area)

Sample	ULA1B	ULA1B	ULA1B	ULA1B	ULA1B	ULA1B	ULA1B	ULA1B	ULA1B	ULA1B	ULA1B	ULA1B
SiO2	24.61	24.70	24.88	24.64	24.88	24.85	24.87	24.86	24.29	24.68	24.83	24.68
TiO2	0.03	0.00	0.03	0.05	0.03	0.00	0.00	0.05	2.80	0.02	0.14	0.08
Al2O3	39.54	39.61	40.46	39.06	39.79	39.44	40.12	40.61	39.44	39.52	39.76	40.11
FeO	24.45	24.56	24.74	25.77	25.79	25.56	25.01	25.27	23.99	25.11	25.33	25.12
MnO	0.43	0.43	0.46	0.42	0.53	0.40	0.49	0.45	0.49	0.40	0.44	0.46
MgO	3.34	3.42	2.66	2.98	2.64	3.20	3.09	2.74	2.85	3.14	3.12	2.70
Total	92.60	92.95	93.25	92.92	93.69	93.49	93.61	94.04	93.90	92.92	93.66	93.16
Si	2.03	2.03	2.04	2.04	2.04	2.04	2.04	2.03	1.98	2.04	2.03	2.03
Ti	0.00	0.00	0.00	0.00	0.00	0.00	0.00	0.00	0.17	0.00	0.01	0.01
Al	3.85	3.85	3.91	3.82	3.85	3.82	3.87	3.90	3.79	3.85	3.84	3.89
Fe3+	0.15	0.15	0.09	0.18	0.15	0.18	0.13	0.10	0.21	0.15	0.16	0.11
Fe2+	1.54	1.54	1.60	1.60	1.62	1.58	1.58	1.62	1.42	1.58	1.58	1.62
Mn	0.03	0.03	0.03	0.03	0.04	0.03	0.03	0.03	0.03	0.03	0.03	0.03
Mg	0.41	0.42	0.32	0.37	0.32	0.39	0.38	0.33	0.35	0.39	0.38	0.33
X(Mg)	0.21	0.21	0.17	0.18	0.16	0.20	0.19	0.17	0.19	0.19	0.19	0.17
X(Fe)	0.78	0.77	0.82	0.80	0.82	0.79	0.79	0.82	0.79	0.79	0.79	0.82
X(Mn)	0.02	0.02	0.02	0.01	0.02	0.01	0.02	0.02	0.02	0.01	0.02	0.02

Sample	ULA1B	ULA1B	ULA1B	ULA1B	ULA1B	ULA1B	ULA3E	ULA3E	ULA3E	ULA3E	ULA3E	ULA3E
SiO2	24.68	24.71	24.58	24.72	24.82	24.57	24.49	24.17	24.31	24.08	23.67	23.94
TiO2	0.01	0.05	0.04	0.06	0.02	1.38	0.08	0.23	0.00	0.07	0.03	0.00
Al2O3	40.25	39.88	39.86	39.24	39.14	38.68	39.72	39.78	40.42	39.96	40.98	40.90
FeO	25.23	25.14	25.45	26.29	24.79	25.28	23.65	23.16	24.39	25.18	24.49	24.09
MnO	0.50	0.42	0.51	0.46	0.41	0.52	0.47	0.50	0.54	0.54	0.42	0.31
MgO	2.61	2.85	2.53	2.64	3.44	2.74	2.62	2.78	2.27	2.45	2.07	2.36
Total	93.31	93.07	93.02	93.45	92.65	93.29	91.17	90.64	91.98	92.49	91.80	91.77
Si	2.03	2.04	2.03	2.04	2.05	2.03	2.04	2.03	2.02	2.00	1.97	1.99
Ti	0.00	0.00	0.00	0.00	0.00	0.09	0.01	0.01	0.00	0.00	0.00	0.00
Al	3.90	3.87	3.88	3.82	3.81	3.76	3.91	3.94	3.96	3.91	4.02	4.00
Fe3+	0.10	0.13	0.12	0.18	0.19	0.24	0.09	0.06	0.04	0.09	0.00	0.00
Fe2+	1.63	1.60	1.64	1.64	1.53	1.51	1.56	1.56	1.65	1.66	1.71	1.67
Mn	0.03	0.03	0.04	0.03	0.03	0.04	0.03	0.04	0.04	0.04	0.03	0.02
Mg	0.32	0.35	0.31	0.33	0.42	0.34	0.33	0.35	0.28	0.30	0.26	0.29
X(Mg)	0.16	0.18	0.16	0.16	0.21	0.18	0.17	0.18	0.14	0.15	0.13	0.15
X(Fe)	0.82	0.81	0.83	0.82	0.77	0.80	0.81	0.80	0.84	0.83	0.86	0.84
X(Mn)	0.02	0.01	0.02	0.02	0.01	0.02	0.02	0.02	0.02	0.02	0.01	0.01

CHLORITOID FROM THE LYCIAN NAPPES (Dilek-Selçuk klippen and Güllük area)

Sample	KIRAZ2D	KIRAZ2D	KIRAZ2D	KIRAZ2D	KIRAZ2D	KIRAZ2D	KIRAZ2D	KIRAZ2D	KIRAZ2D	GUL4F	GUL4F	GUL4F
SiO2	24.79	24.59	24.72	24.87	24.41	24.76	24.71	24.54	24.71	24.61	24.67	24.92
TiO2	0.03	0.16	0.00	0.00	0.96	0.01	0.02	0.00	0.04	0.01	0.00	0.02
Al2O3	40.11	40.18	40.35	39.90	39.94	40.29	39.85	39.50	39.89	40.12	39.88	40.33
FeO	25.13	25.01	24.58	25.44	24.92	24.46	24.93	25.46	25.23	26.65	26.81	25.88
MnO	0.22	0.25	0.31	0.27	0.26	0.31	0.26	0.27	0.27	0.25	0.19	0.24
MgO	2.67	2.27	2.62	2.47	2.31	2.63	2.60	2.23	2.28	1.83	1.75	1.97
Total	93.00	92.50	92.59	93.04	92.84	92.50	92.40	92.06	92.45	93.54	93.29	93.37
Si	2.04	2.03	2.04	2.05	2.01	2.04	2.05	2.05	2.05	2.03	2.04	2.05
Ti	0.00	0.01	0.00	0.00	0.06	0.00	0.00	0.00	0.00	0.00	0.00	0.00
Al	3.89	3.92	3.92	3.88	3.88	3.92	3.89	3.88	3.90	3.90	3.89	3.91
Fe3+	0.11	0.08	0.08	0.12	0.12	0.08	0.11	0.12	0.10	0.10	0.11	0.09
Fe2+	1.62	1.65	1.62	1.63	1.60	1.61	1.62	1.66	1.65	1.74	1.74	1.69
Mn	0.02	0.02	0.02	0.02	0.02	0.02	0.02	0.02	0.02	0.02	0.01	0.02
Mg	0.33	0.28	0.32	0.30	0.28	0.32	0.32	0.28	0.28	0.22	0.22	0.24
X(Mg)	0.17	0.14	0.16	0.16	0.15	0.17	0.16	0.14	0.14	0.11	0.11	0.12
X(Fe)	0.83	0.85	0.82	0.83	0.84	0.82	0.83	0.85	0.85	0.88	0.88	0.87
X(Mn)	0.01	0.01	0.01	0.01	0.01	0.01	0.01	0.01	0.01	0.01	0.01	0.01

Sample	GUL4F	GUL4F	GUL4F	GUL4F	GUL4F	GUL4F	GUL4F	GUL4F	GUL4F	GUL4F	GUL4F	GUL4F
SiO2	24.55	24.51	24.68	24.78	24.46	24.78	24.77	24.68	24.46	24.57	24.62	24.56
TiO2	0.00	0.03	0.01	0.00	0.11	0.03	0.02	0.02	0.32	0.05	0.03	0.02
Al2O3	40.07	40.16	39.38	39.98	39.68	40.42	40.19	39.98	39.06	40.06	39.84	39.71
FeO	26.34	26.64	27.37	26.32	26.45	25.67	26.24	26.43	26.85	26.92	26.97	27.02
MnO	0.26	0.18	0.18	0.20	0.18	0.19	0.24	0.24	0.22	0.22	0.15	0.21
MgO	1.86	1.68	1.51	1.89	1.72	2.03	1.78	1.64	1.79	1.46	1.60	1.56
Total	93.09	93.22	93.16	93.18	92.65	93.17	93.30	93.07	92.74	93.31	93.26	93.14
Si	2.03	2.03	2.05	2.05	2.04	2.04	2.04	2.04	2.04	2.03	2.04	2.04
Ti	0.00	0.00	0.00	0.00	0.01	0.00	0.00	0.00	0.02	0.00	0.00	0.00
Al	3.91	3.92	3.86	3.89	3.89	3.92	3.91	3.90	3.84	3.91	3.89	3.89
Fe3+	0.09	0.08	0.14	0.11	0.11	0.08	0.09	0.10	0.16	0.09	0.11	0.11
Fe2+	1.73	1.76	1.76	1.71	1.73	1.69	1.72	1.73	1.71	1.77	1.76	1.76
Mn	0.02	0.01	0.01	0.01	0.01	0.01	0.02	0.02	0.02	0.02	0.01	0.01
Mg	0.23	0.21	0.19	0.23	0.21	0.25	0.22	0.20	0.22	0.18	0.20	0.19
X(Mg)	0.12	0.10	0.10	0.12	0.11	0.13	0.11	0.10	0.11	0.09	0.10	0.10
X(Fe)	0.88	0.89	0.90	0.87	0.88	0.87	0.88	0.89	0.88	0.90	0.89	0.89
X(Mn)	0.01	0.01	0.01	0.01	0.01	0.01	0.01	0.01	0.01	0.01	0.01	0.01

CHLORITOID FROM THE LYCIAN NAPPES (Güllük, Demirciler and Civril areas)

Sample	GUL4F	GUL4F	GUL4F	GUL4F	GUL4F	GUL4F	GUL4F	GUL4F	DEM1A	DEM1A	DEM1A	DEM1A
SiO2	24.53	24.81	24.42	24.74	24.30	24.64	23.88	24.88	24.87	25.05	24.62	24.96
TiO2	0.01	0.02	0.00	0.09	0.95	0.03	2.82	0.01	0.00	0.04	0.00	0.00
Al2O3	40.21	39.72	38.83	40.10	39.79	39.45	38.41	40.21	40.32	40.79	39.26	39.98
FeO	26.00	26.85	27.31	26.21	25.74	26.86	26.13	25.78	24.47	23.96	24.92	25.11
MnO	0.23	0.22	0.18	0.24	0.25	0.23	0.19	0.25	0.45	0.39	0.61	0.47
MgO	1.81	1.61	1.57	1.79	1.82	1.45	1.42	1.87	2.72	2.92	2.47	2.67
Total	92.89	93.30	92.37	93.23	92.91	92.71	92.86	93.03	92.83	93.15	91.89	93.22
Si	2.03	2.05	2.05	2.04	2.01	2.05	1.99	2.05	2.05	2.05	2.06	2.05
Ti	0.00	0.00	0.00	0.01	0.06	0.00	0.18	0.00	0.00	0.00	0.00	0.00
Al	3.92	3.87	3.84	3.90	3.88	3.88	3.77	3.91	3.91	3.92	3.86	3.87
Fe3+	0.08	0.13	0.16	0.10	0.12	0.12	0.23	0.09	0.09	0.08	0.14	0.13
Fe2+	1.72	1.73	1.76	1.71	1.67	1.75	1.59	1.69	1.59	1.56	1.60	1.60
Mn	0.02	0.02	0.01	0.02	0.02	0.02	0.01	0.02	0.03	0.03	0.04	0.03
Mg	0.22	0.20	0.20	0.22	0.23	0.18	0.18	0.23	0.33	0.36	0.31	0.33
X(Mg)	0.11	0.10	0.10	0.11	0.12	0.09	0.10	0.12	0.17	0.18	0.16	0.17
X(Fe)	0.88	0.89	0.89	0.88	0.87	0.90	0.89	0.87	0.81	0.80	0.82	0.82
X(Mn)	0.01	0.01	0.01	0.01	0.01	0.01	0.01	0.01	0.02	0.01	0.02	0.02

Sample	DEM1A	DEM1A	DEM1A	CIVRIL001A1.	CIVRIL001A1.	CIVRIL001A1.	CIVRIL001A1.	CIVRIL001A1.
SiO2	24.72	24.92	24.64	24.12	25.32	23.93	24.85	23.76
TiO2	0.01	0.01	0.03	0.79	0.06	1.74	0.14	0.79
Al2O3	39.93	40.37	39.44	39.43	39.95	39.59	39.53	38.31
FeO	23.51	23.55	24.39	24.32	22.16	23.16	23.32	24.21
MnO	0.47	0.45	0.50	0.24	0.15	0.18	0.19	0.25
MgO	2.96	2.99	2.68	2.86	3.23	3.51	2.95	3.39
Total	91.61	92.29	91.68	91.81	90.96	92.15	90.98	90.83
Si	2.05	2.05	2.05	2.01	2.10	1.98	2.07	2.01
Ti	0.00	0.00	0.00	0.05	0.00	0.11	0.01	0.05
Al	3.91	3.92	3.88	3.87	3.90	3.85	3.89	3.81
Fe3+	0.09	0.08	0.12	0.13	0.10	0.15	0.11	0.19
Fe2+	1.54	1.54	1.58	1.57	1.43	1.45	1.51	1.52
Mn	0.03	0.03	0.03	0.02	0.01	0.01	0.01	0.02
Mg	0.37	0.37	0.33	0.35	0.40	0.43	0.37	0.43
X(Mg)	0.19	0.19	0.17	0.18	0.22	0.23	0.19	0.22
X(Fe)	0.79	0.79	0.81	0.81	0.78	0.77	0.80	0.77
X(Mn)	0.02	0.02	0.02	0.01	0.01	0.01	0.01	0.01

CHLORITOID FROM THE MENDERES MASSIF (Nebiler and Bahçeyaka areas)

Sample	NEBILER0101B	NEBILER0101B	NEBILER0102A	NEBILER0102A	NEBILER0102A	NEBILER0102A	NEBILER0102A	NEBILER0102A
SiO2	25.57	24.96	24.90	24.96	24.99	24.91	25.01	25.02
TiO2	0.00	0.02	0.03	0.00	0.00	0.03	0.00	0.02
Al2O3	41.58	40.54	40.48	40.83	41.78	41.07	42.56	41.45
FeO	11.05	12.47	12.67	12.42	12.16	12.22	12.08	12.04
MnO	6.94	7.05	6.92	6.65	6.64	6.46	6.93	6.28
MgO	6.78	6.37	6.35	6.59	6.38	6.24	6.52	6.67
Total	91.98	91.58	91.44	91.43	92.11	90.98	93.15	91.78
Si	2.05	2.02	2.03	2.02	2.00	2.03	1.99	2.01
Ti	0.00	0.00	0.00	0.00	0.00	0.00	0.00	0.00
Al	3.92	3.88	3.88	3.90	3.95	3.94	3.99	3.92
Fe3+	0.08	0.12	0.12	0.10	0.05	0.06	0.01	0.08
Fe2+	0.66	0.72	0.74	0.75	0.77	0.77	0.79	0.73
Mn	0.47	0.48	0.48	0.46	0.45	0.44	0.47	0.43
Mg	0.81	0.77	0.77	0.80	0.76	0.76	0.77	0.80
X(Mg)	0.42	0.39	0.39	0.40	0.39	0.38	0.38	0.41
X(Fe)	0.34	0.37	0.37	0.37	0.39	0.39	0.39	0.37
X(Mn)	0.24	0.25	0.24	0.23	0.23	0.23	0.23	0.22

Sample	NEBILER0102A	NEBILER0102A	NEBILER0102A	YAT0107B	YAT0107B	YAT0107B	YAT0107B	YAT0107B
SiO2	24.79	25.13	25.08	25.02	25.00	25.14	24.80	25.05
TiO2	0.10	0.13	0.05	0.02	0.10	0.00	0.00	0.00
Al2O3	41.07	40.81	40.90	42.45	42.31	42.22	41.41	41.45
FeO	11.81	11.34	12.45	6.35	6.47	6.58	7.19	6.68
MnO	7.10	6.87	6.57	11.87	12.00	12.01	12.03	11.62
MgO	6.47	7.38	6.89	7.07	7.11	6.94	7.08	6.95
Total	91.37	91.72	92.13	92.93	93.20	92.94	92.58	91.78
Si	2.01	2.02	2.02	1.98	1.98	2.00	1.99	2.01
Ti	0.01	0.01	0.00	0.00	0.01	0.00	0.00	0.00
Al	3.93	3.87	3.87	3.97	3.94	3.95	3.91	3.93
Fe3+	0.07	0.13	0.13	0.03	0.06	0.05	0.09	0.07
Fe2+	0.73	0.64	0.71	0.39	0.37	0.39	0.39	0.38
Mn	0.49	0.47	0.45	0.80	0.80	0.81	0.82	0.79
Mg	0.78	0.89	0.82	0.84	0.84	0.82	0.85	0.83
X(Mg)	0.39	0.44	0.42	0.41	0.42	0.41	0.41	0.42
X(Fe)	0.36	0.32	0.36	0.19	0.18	0.19	0.19	0.19
X(Mn)	0.24	0.23	0.23	0.39	0.40	0.40	0.40	0.40

CHLORITE FROM THE LYCIAN NAPPES (Ula area)

Sample	ULA1B	ULA1B	ULA1B	ULA1B	ULA1B	ULA1B	ULA1B	ULA1B2.	ULA1B2.	ULA1B2.	ULA1B2.	ULA1B2.	ULA1B2.	ULA1C1.	ULA1C1.	ULA1C1.	ULA1C1.	ULA1C1.	ULA1C1.	ULA1C1.
SiO2	26.95	27.10	26.81	26.53	26.91	26.49	27.96	27.46	26.85	26.62	26.58	27.39	26.48	27.09	26.94	26.78	26.43	26.26	26.67	26.70
TiO2	0.04	0.03	0.03	0.00	0.03	0.02	0.01	0.03	0.02	0.00	0.02	0.02	0.01	0.02	0.03	0.02	0.02	0.00	0.01	0.01
Al2O3	23.83	24.05	24.36	24.12	24.27	24.60	25.73	23.59	23.77	24.22	24.12	23.85	24.18	24.64	24.56	25.11	24.68	24.73	24.67	24.57
FeO Total	19.03	18.61	19.75	19.65	19.48	18.59	18.89	18.50	18.69	19.38	18.79	18.17	18.90	17.93	18.12	19.26	19.01	19.95	18.04	18.15
MnO	0.10	0.14	0.12	0.16	0.09	0.14	0.06	0.09	0.07	0.11	0.11	0.08	0.11	0.07	0.03	0.04	0.05	0.05	0.07	0.06
MgO	18.03	17.96	18.19	17.67	17.75	17.79	15.37	18.53	18.16	17.83	17.99	18.03	18.22	18.18	18.53	17.35	17.79	17.32	18.48	18.62
CaO	0.01	0.03	0.01	0.03	0.02	0.04	0.03	0.00	0.04	0.03	0.01	0.00	0.01	0.00	0.03	0.06	0.01	0.04	0.04	0.03
Na2O	0.01	0.01	0.03	0.01	0.01	0.01	0.02	0.02	0.01	0.00	0.01	0.00	0.01	0.00	0.00	0.02	0.00	0.03	0.01	0.01
K2O	0.01	0.01	0.04	0.01	0.01	0.00	0.06	0.05	0.05	0.04	0.05	0.03	0.01	0.01	0.01	0.03	0.01	0.02	0.02	0.01
F	0.00	0.00	0.00	0.00	0.00	0.00	0.00	0.00	0.00	0.00	0.00	0.00	0.00	0.00	0.00	0.00	0.00	0.00	0.00	0.00
Cl	0.02	0.00	0.02	0.01	0.01	0.01	0.02	0.00	0.00	0.00	0.00	0.00	0.00	0.01	0.01	0.02	0.00	0.00	0.02	0.00
Total	88.04	87.93	89.35	88.20	88.57	87.67	88.13	88.27	87.65	88.23	87.67	87.56	87.93	87.94	88.27	88.68	88.00	88.41	88.03	88.15
Si	2.71	2.72	2.67	2.68	2.70	2.67	2.79	2.75	2.71	2.68	2.69	2.76	2.67	2.71	2.69	2.68	2.66	2.65	2.67	2.67
Ti	0.00	0.00	0.00	0.00	0.00	0.00	0.00	0.00	0.00	0.00	0.00	0.00	0.00	0.00	0.00	0.00	0.00	0.00	0.00	0.00
Al	2.83	2.85	2.86	2.87	2.87	2.93	3.03	2.78	2.83	2.88	2.87	2.83	2.87	2.91	2.89	2.96	2.93	2.94	2.91	2.90
Fe2+	1.60	1.56	1.65	1.66	1.63	1.57	1.58	1.55	1.58	1.63	1.59	1.53	1.59	1.50	1.51	1.61	1.60	1.68	1.51	1.52
Mn	0.01	0.01	0.01	0.01	0.01	0.01	0.01	0.01	0.01	0.01	0.01	0.01	0.01	0.01	0.00	0.00	0.00	0.00	0.01	0.00
Mg	2.71	2.69	2.70	2.66	2.65	2.68	2.29	2.76	2.73	2.68	2.71	2.70	2.74	2.71	2.76	2.59	2.67	2.60	2.76	2.78
Ca	0.00	0.00	0.00	0.00	0.00	0.00	0.00	0.00	0.00	0.00	0.00	0.00	0.00	0.00	0.00	0.01	0.00	0.00	0.00	0.00
Na	0.00	0.00	0.01	0.00	0.00	0.00	0.00	0.00	0.00	0.00	0.00	0.00	0.00	0.00	0.00	0.00	0.00	0.00	0.00	0.00
K	0.00	0.00	0.00	0.00	0.00	0.00	0.01	0.01	0.01	0.00	0.01	0.00	0.00	0.00	0.00	0.00	0.00	0.00	0.00	0.00
F	0.00	0.00	0.00	0.00	0.00	0.00	0.00	0.00	0.00	0.00	0.00	0.00	0.00	0.00	0.00	0.00	0.00	0.00	0.00	0.00
Cl	0.00	0.00	0.00	0.00	0.00	0.00	0.00	0.00	0.00	0.00	0.00	0.00	0.00	0.00	0.00	0.00	0.00	0.00	0.00	0.00
Total	9.87	9.85	9.90	9.89	9.87	9.86	9.70	9.86	9.88	9.88	9.88	9.83	9.89	9.84	9.86	9.85	9.87	9.89	9.88	9.88
X Mg	0.63	0.63	0.62	0.61	0.62	0.63	0.59	0.64	0.63	0.62	0.63	0.64	0.63	0.64	0.65	0.62	0.62	0.61	0.65	0.65
Amesite	0.28	0.27	0.33	0.32	0.30	0.33	0.21	0.25	0.29	0.32	0.31	0.24	0.33	0.29	0.31	0.32	0.34	0.35	0.33	0.33
Clinochlore	0.59	0.58	0.57	0.57	0.57	0.54	0.49	0.61	0.59	0.56	0.56	0.59	0.56	0.55	0.55	0.52	0.54	0.53	0.54	0.55
Sudoite	0.13	0.15	0.10	0.11	0.13	0.14	0.30	0.14	0.13	0.12	0.13	0.17	0.11	0.16	0.14	0.16	0.13	0.12	0.13	0.12

CHLORITE FROM THE LYCIAN NAPPES (Ören area)

Sample	OREN001a	OREN001a	OREN001a	OREN001a	OREN002c	OREN002c	OREN002c	OREN002c	OREN001H	OREN001H	OREN001H	OREN001H	OREN009L	OREN009L	OREN009L
Analysis	35	38	39	44	95	111	134	148	33	38	39	40	62	64	65
SiO2	26.87	27.37	26.69	27.58	26.95	26.89	27.00	27.19	26.72	27.37	26.68	26.80	26.18	26.49	25.25
TiO2	0.01	0.00	0.02	0.02	0.04	0.00	0.02	0.00	0.07	0.02	0.04	0.00	0.00	0.00	0.03
Al2O3	27.23	27.57	27.22	28.58	27.87	27.54	27.75	28.24	25.44	25.79	25.53	24.79	26.03	25.75	25.04
FeO Total	15.59	16.39	16.05	12.83	14.98	17.07	16.21	15.26	16.92	15.63	16.35	15.64	19.87	18.43	20.55
MnO	0.12	0.07	0.13	0.08	0.17	0.10	0.11	0.10	0.07	0.11	0.06	0.11	0.11	0.10	0.14
MgO	17.39	17.53	18.18	17.83	17.62	16.24	17.14	18.07	17.45	17.25	16.77	18.36	16.43	16.91	16.12
CaO	0.08	0.04	0.04	0.03	0.01	0.09	0.02	0.01	0.06	0.03	0.02	0.01	0.04	0.06	0.00
Na2O	0.06	0.04	0.03	0.12	0.03	0.06	0.03	0.02	0.03	0.01	0.00	0.03	0.04	0.03	0.00
K2O	0.10	0.08	0.04	0.07	0.02	0.09	0.02	0.03	0.01	0.00	0.01	0.04	0.02	0.02	0.00
F	0.00	0.00	0.00	0.00	0.00	0.00	0.00	0.00	0.00	0.00	0.00	0.00	0.00	0.00	0.00
Cl	0.02	0.01	0.01	0.03	0.00	0.01	0.01	0.00	0.01	0.00	0.00	0.01	0.01	0.01	0.00
Total	87.46	89.09	88.41	87.16	87.69	88.08	88.31	88.92	86.77	86.22	85.45	85.79	88.73	87.79	87.12
Si	2.67	2.67	2.63	2.69	2.65	2.67	2.66	2.64	2.69	2.75	2.72	2.72	2.62	2.66	2.60
Ti	0.00	0.00	0.00	0.00	0.00	0.00	0.00	0.00	0.01	0.00	0.00	0.00	0.00	0.00	0.00
Al	3.18	3.17	3.16	3.29	3.23	3.22	3.22	3.23	3.02	3.06	3.07	2.96	3.08	3.05	3.03
Fe2+	1.29	1.34	1.32	1.05	1.23	1.41	1.33	1.24	1.43	1.31	1.39	1.33	1.67	1.55	1.77
Mn	0.01	0.01	0.01	0.01	0.01	0.01	0.01	0.01	0.01	0.01	0.01	0.01	0.01	0.01	0.01
Mg	2.57	2.55	2.67	2.60	2.59	2.40	2.51	2.62	2.62	2.58	2.55	2.78	2.45	2.53	2.47
Ca	0.01	0.00	0.00	0.00	0.00	0.01	0.00	0.00	0.01	0.00	0.00	0.00	0.00	0.01	0.00
Na	0.01	0.01	0.01	0.02	0.01	0.01	0.01	0.00	0.00	0.00	0.00	0.01	0.01	0.01	0.00
K	0.01	0.01	0.00	0.01	0.00	0.01	0.00	0.00	0.00	0.00	0.00	0.00	0.00	0.00	0.00
F	0.00	0.00	0.00	0.00	0.00	0.00	0.00	0.00	0.00	0.00	0.00	0.00	0.00	0.00	0.00
Cl	0.00	0.00	0.00	0.00	0.00	0.00	0.00	0.00	0.00	0.00	0.00	0.00	0.00	0.00	0.00
Total	9.76	9.75	9.80	9.68	9.73	9.74	9.74	9.75	9.79	9.72	9.74	9.81	9.84	9.82	9.88
X Mg	0.66	0.66	0.67	0.71	0.67	0.63	0.65	0.68	0.65	0.66	0.65	0.68	0.59	0.62	0.58
Amesite	0.33	0.33	0.37	0.30	0.34	0.33	0.34	0.36	0.30	0.25	0.28	0.28	0.38	0.34	0.40
Clinochlore	0.41	0.42	0.42	0.35	0.38	0.39	0.39	0.38	0.49	0.47	0.47	0.52	0.46	0.47	0.48
Sudoite	0.26	0.26	0.21	0.34	0.27	0.27	0.27	0.26	0.21	0.28	0.26	0.20	0.16	0.19	0.12

CHLORITE FROM THE LYCIAN NAPPES (Ören area)

Sample	OREN009L	OREN009M1.	OREN009M1.	OREN009M1.	OREN009M1.	OREN009N	OREN009N	OREN009N	OREN009N	OREN0017D	OREN0017D	OREN0017D	OREN0017D
Analysis	66	109	110	111	115	173	175	177	180	4	5	8	9
SiO2	26.55	26.18	26.78	27.43	26.79	26.72	26.51	26.87	25.57	26.04	25.84	25.79	26.05
TiO2	0.01	0.07	0.01	0.08	0.05	0.01	0.04	0.24	0.11	0.00	0.12	0.05	0.03
Al2O3	25.78	24.53	24.58	27.41	24.98	25.86	25.38	25.47	23.48	25.55	26.96	26.64	25.93
FeO Total	20.70	19.50	18.78	15.82	17.32	18.71	17.86	17.51	18.09	20.69	21.18	20.68	20.21
MnO	0.18	0.12	0.15	0.12	0.12	0.11	0.19	0.11	0.08	0.00	0.00	0.00	0.01
MgO	16.11	17.69	18.33	17.13	19.20	17.30	18.88	18.15	18.68	14.14	12.18	12.80	14.48
CaO	0.02	0.01	0.00	0.00	0.00	0.02	0.00	0.02	0.03	0.00	0.03	0.04	0.00
Na2O	0.01	0.00	0.00	0.02	0.02	0.05	0.02	0.04	0.00	0.01	0.03	0.02	0.03
K2O	0.02	0.01	0.02	0.07	0.03	0.08	0.00	0.03	0.02	0.00	0.00	0.00	0.00
F	0.00	0.00	0.00	0.00	0.00	0.00	0.00	0.00	0.00	0.00	0.22	0.22	0.02
Cl	0.01	0.00	0.01	0.00	0.00	0.00	0.00	0.02	0.01	0.00	0.00	0.00	0.00
Total	89.38	88.10	88.64	88.07	88.51	88.87	88.87	88.45	86.05	86.42	86.57	86.24	86.77
Si	2.65	2.64	2.67	2.70	2.66	2.66	2.63	2.67	2.63	2.69	2.67	2.67	2.67
Ti	0.00	0.01	0.00	0.01	0.00	0.00	0.00	0.02	0.01	0.00	0.01	0.00	0.00
Al	3.03	2.92	2.89	3.18	2.92	3.03	2.97	2.98	2.85	3.11	3.28	3.25	3.13
Fe2+	1.73	1.65	1.57	1.30	1.44	1.56	1.48	1.45	1.56	1.79	1.83	1.79	1.73
Mn	0.01	0.01	0.01	0.01	0.01	0.01	0.02	0.01	0.01	0.00	0.00	0.00	0.00
Mg	2.40	2.66	2.73	2.51	2.84	2.56	2.79	2.69	2.87	2.18	1.88	1.98	2.21
Ca	0.00	0.00	0.00	0.00	0.00	0.00	0.00	0.00	0.00	0.00	0.00	0.00	0.00
Na	0.00	0.00	0.00	0.00	0.00	0.01	0.00	0.01	0.00	0.00	0.01	0.00	0.01
K	0.00	0.00	0.00	0.01	0.00	0.01	0.00	0.00	0.00	0.00	0.00	0.00	0.00
F	0.00	0.00	0.00	0.00	0.00	0.00	0.00	0.00	0.00	0.00	0.07	0.07	0.01
Cl	0.00	0.00	0.00	0.00	0.00	0.00	0.00	0.00	0.00	0.00	0.00	0.00	0.00
Total	9.83	9.89	9.88	9.71	9.88	9.84	9.89	9.83	9.93	9.76	9.75	9.77	9.77
X Mg	0.58	0.62	0.63	0.66	0.66	0.62	0.65	0.65	0.65	0.55	0.51	0.52	0.56
Amesite	0.35	0.35	0.32	0.30	0.34	0.34	0.37	0.31	0.36	0.31	0.32	0.33	0.33
Clinochlore	0.48	0.54	0.55	0.41	0.54	0.49	0.52	0.51	0.57	0.45	0.36	0.37	0.43
Sudoite	0.17	0.11	0.12	0.29	0.12	0.17	0.11	0.18	0.07	0.24	0.32	0.30	0.24

CHLORITE FROM THE LYCIAN NAPPES (Demirciler area)

Sample	BALCILAR1C	BALCILAR1C	BALCILAR1C	BALCILAR1C	BALCILAR1C	DEM7A	DEM7A	DEM7A	DEM7A	DEM7A	DEM7A	DEM7A	DEM7A	DEM7A	DEM7A
SiO2	26.90	26.36	26.50	27.62	26.47	26.44	26.95	26.94	26.99	26.88	26.34	26.66	27.25	26.65	26.36
TiO2	0.02	0.02	0.02	0.02	0.00	0.03	0.03	0.03	0.02	0.04	0.02	0.05	0.04	0.03	0.02
Al2O3	26.16	26.10	25.97	27.20	25.97	24.31	25.23	24.89	24.97	25.17	24.82	25.44	24.82	24.41	24.67
FeO Total	18.93	19.92	19.90	18.24	20.43	20.54	19.83	20.13	20.84	20.21	21.45	20.70	19.16	20.01	20.15
MnO	0.05	0.04	0.08	0.08	0.08	0.16	0.10	0.18	0.13	0.13	0.14	0.12	0.14	0.14	0.16
MgO	14.82	15.44	15.49	15.04	15.57	16.64	15.63	16.00	16.09	16.28	15.82	15.74	16.29	15.80	16.11
CaO	0.07	0.09	0.07	0.04	0.05	0.05	0.05	0.03	0.03	0.00	0.04	0.03	0.03	0.04	0.03
Na2O	0.01	0.04	0.03	0.02	0.04	0.04	0.04	0.06	0.03	0.01	0.02	0.01	0.02	0.02	0.03
K2O	0.03	0.03	0.01	0.02	0.03	0.00	0.02	0.00	0.00	0.01	0.02	0.00	0.02	0.02	0.00
F	0.00	0.00	0.00	0.00	0.00	0.00	0.00	0.00	0.00	0.00	0.00	0.00	0.00	0.00	0.00
Cl	0.02	0.01	0.02	0.02	0.01	0.01	0.00	0.01	0.01	0.00	0.00	0.00	0.00	0.00	0.01
Total	87.02	88.05	88.08	88.29	88.64	88.22	87.86	88.26	89.10	88.73	88.67	88.75	87.78	87.10	87.53
Si	2.73	2.66	2.67	2.74	2.66	2.68	2.72	2.72	2.70	2.70	2.67	2.68	2.75	2.72	2.69
Ti	0.00	0.00	0.00	0.00	0.00	0.00	0.00	0.00	0.00	0.00	0.00	0.00	0.00	0.00	0.00
Al	3.12	3.10	3.09	3.18	3.08	2.90	3.00	2.96	2.95	2.97	2.96	3.01	2.95	2.94	2.96
Fe2+	1.60	1.68	1.68	1.51	1.72	1.74	1.67	1.70	1.75	1.69	1.82	1.74	1.61	1.71	1.72
Mn	0.00	0.00	0.01	0.01	0.01	0.01	0.01	0.01	0.01	0.01	0.01	0.01	0.01	0.01	0.01
Mg	2.24	2.32	2.33	2.22	2.33	2.52	2.35	2.40	2.40	2.43	2.39	2.36	2.45	2.41	2.45
Ca	0.01	0.01	0.01	0.00	0.01	0.01	0.00	0.00	0.00	0.00	0.00	0.00	0.00	0.00	0.00
Na	0.00	0.01	0.01	0.00	0.01	0.01	0.01	0.01	0.01	0.00	0.00	0.00	0.00	0.00	0.01
K	0.00	0.00	0.00	0.00	0.00	0.00	0.00	0.00	0.00	0.00	0.00	0.00	0.00	0.00	0.00
F	0.00	0.00	0.00	0.00	0.00	0.00	0.00	0.00	0.00	0.00	0.00	0.00	0.00	0.00	0.00
Cl	0.00	0.00	0.00	0.00	0.00	0.00	0.00	0.00	0.00	0.00	0.00	0.00	0.00	0.00	0.00
Total	9.72	9.79	9.79	9.68	9.81	9.87	9.78	9.81	9.82	9.82	9.85	9.81	9.78	9.81	9.84
X Mg	0.58	0.58	0.58	0.59	0.58	0.59	0.58	0.58	0.58	0.59	0.57	0.57	0.60	0.58	0.59
Amesite	0.27	0.34	0.33	0.26	0.34	0.32	0.28	0.28	0.29	0.30	0.33	0.32	0.25	0.27	0.31
Clinochlore	0.44	0.45	0.46	0.41	0.46	0.55	0.50	0.52	0.53	0.51	0.52	0.49	0.53	0.53	0.52
Sudoite	0.29	0.21	0.22	0.33	0.20	0.13	0.23	0.20	0.18	0.19	0.15	0.19	0.22	0.20	0.17

CHLORITE FROM THE LYCIAN NAPPES (Güllük area)

Sample	GUL005c	GUL005c	GUL005c	GUL005c	GUL005c	GUL005c	GUL005c	GUL005c	GUL005c	GUL005c	GUL005c	GUL005c	GUL005c
SiO2	24.94	24.02	24.80	24.63	24.92	24.45	24.22	25.13	24.79	25.15	24.64	25.06	24.64
TiO2	0.06	0.03	0.02	0.07	0.05	0.02	0.01	0.05	0.02	0.06	0.07	0.03	0.02
Al2O3	24.21	24.31	24.09	23.82	23.91	23.68	23.53	23.73	24.03	23.92	23.79	24.27	23.96
FeO Total	28.10	29.62	28.09	27.94	27.75	28.36	29.97	28.40	27.52	27.43	28.52	28.67	27.99
MnO	0.03	0.08	0.09	0.08	0.08	0.03	0.07	0.06	0.08	0.07	0.10	0.06	0.07
MgO	10.82	10.07	11.21	11.30	11.48	11.04	9.79	10.64	10.34	11.40	11.27	10.61	11.46
CaO	0.01	0.04	0.03	0.02	0.02	0.02	0.10	0.01	0.03	0.05	0.03	0.04	0.10
Na2O	0.02	0.02	0.03	0.00	0.02	0.00	0.04	0.01	0.05	0.03	0.02	0.04	0.04
K2O	0.05	0.02	0.08	0.04	0.08	0.03	0.09	0.08	0.06	0.07	0.05	0.09	0.03
F	0.00	0.00	0.00	0.00	0.00	0.00	0.00	0.00	0.00	0.00	0.00	0.00	0.00
Cl	0.00	0.00	0.00	0.00	0.01	0.00	0.01	0.02	0.04	0.00	0.00	0.00	0.00
Total	88.23	88.19	88.44	87.91	88.32	87.62	87.82	88.13	86.95	88.17	88.49	88.86	88.31
Si	2.64	2.57	2.62	2.62	2.63	2.61	2.61	2.67	2.66	2.65	2.61	2.64	2.61
Ti	0.00	0.00	0.00	0.01	0.00	0.00	0.00	0.00	0.00	0.00	0.01	0.00	0.00
Al	3.02	3.06	3.00	2.98	2.97	2.98	2.99	2.97	3.03	2.97	2.97	3.01	2.99
Fe2+	2.48	2.65	2.48	2.48	2.45	2.53	2.70	2.52	2.46	2.42	2.52	2.52	2.48
Mn	0.00	0.01	0.01	0.01	0.01	0.00	0.01	0.01	0.01	0.01	0.01	0.01	0.01
Mg	1.70	1.60	1.76	1.79	1.81	1.76	1.57	1.68	1.65	1.79	1.78	1.67	1.81
Ca	0.00	0.00	0.00	0.00	0.00	0.00	0.01	0.00	0.00	0.01	0.00	0.00	0.01
Na	0.00	0.00	0.01	0.00	0.00	0.00	0.01	0.00	0.01	0.01	0.00	0.01	0.01
K	0.01	0.00	0.01	0.01	0.01	0.00	0.01	0.01	0.01	0.01	0.01	0.01	0.00
F	0.00	0.00	0.00	0.00	0.00	0.00	0.00	0.00	0.00	0.00	0.00	0.00	0.00
Cl	0.00	0.00	0.00	0.00	0.00	0.00	0.00	0.00	0.01	0.00	0.00	0.00	0.00
Total	9.86	9.90	9.89	9.89	9.89	9.90	9.91	9.86	9.84	9.86	9.91	9.87	9.91
X Mg	0.41	0.38	0.41	0.42	0.42	0.41	0.37	0.40	0.40	0.42	0.41	0.40	0.42
Amesite	0.36	0.43	0.38	0.38	0.37	0.39	0.39	0.33	0.34	0.34	0.39	0.36	0.39
Clinochlore	0.49	0.47	0.50	0.51	0.51	0.51	0.51	0.52	0.48	0.51	0.52	0.49	0.51
Sudoite	0.15	0.10	0.12	0.11	0.12	0.11	0.10	0.15	0.17	0.14	0.10	0.14	0.10

CHLORITE FROM THE LYCIAN NAPPES (Güllük area)

Sample	GUL21E	GUL21E	GUL21E	GUL21E	GUL21E	GUL21E	GUL21E	GUL21E	GUL21E	GUL21E	GUL4F	GUL4F	GUL4F	GUL4F	GUL4F	GUL4F	GUL4F	GUL4F
SiO2	26.01	25.20	25.03	25.03	25.25	24.78	24.98	24.56	26.27	25.11	26.00	25.16	24.84	25.63	24.29	24.66	24.81	25.11
TiO2	0.03	0.03	0.15	0.04	0.01	0.01	0.04	0.00	0.00	0.12	0.03	0.02	0.01	0.03	0.04	0.00	0.03	0.03
Al2O3	25.55	25.19	25.18	24.85	24.94	24.19	24.62	24.48	25.18	24.60	25.72	25.32	24.55	24.53	24.39	24.34	24.41	24.77
FeO Total	27.10	28.33	28.20	28.06	28.41	29.66	28.88	28.98	27.76	28.97	25.93	25.40	27.10	26.43	29.77	28.56	27.02	26.26
MnO	0.08	0.08	0.07	0.13	0.08	0.10	0.12	0.07	0.11	0.10	0.08	0.08	0.07	0.05	0.05	0.04	0.02	0.04
MgO	10.20	10.11	9.99	10.40	10.21	9.90	10.07	10.04	9.68	10.25	11.16	12.63	11.11	12.07	9.40	10.85	11.40	11.33
CaO	0.01	0.03	0.03	0.00	0.00	0.02	0.01	0.00	0.02	0.00	0.02	0.07	0.02	0.00	0.02	0.01	0.03	0.03
Na2O	0.03	0.04	0.07	0.03	0.05	0.01	0.03	0.04	0.03	0.02	0.03	0.00	0.01	0.00	0.00	0.00	0.00	0.01
K2O	0.00	0.04	0.03	0.01	0.02	0.01	0.00	0.02	0.01	0.00	0.08	0.02	0.05	0.02	0.01	0.00	0.02	0.04
F	0.00	0.00	0.00	0.00	0.00	0.00	0.00	0.00	0.00	0.00	0.00	0.00	0.00	0.00	0.00	0.00	0.00	0.00
Cl	0.00	0.01	0.01	0.01	0.02	0.00	0.00	0.02	0.01	0.01	0.03	0.00	0.00	0.00	0.00	0.01	0.00	0.00
Total	88.99	89.06	88.74	88.56	88.97	88.68	88.74	88.20	89.07	89.17	89.09	88.69	87.76	88.76	87.96	88.49	87.75	87.62
Si	2.69	2.63	2.63	2.63	2.64	2.63	2.63	2.61	2.73	2.63	2.68	2.60	2.63	2.66	2.60	2.61	2.62	2.64
Ti	0.00	0.00	0.01	0.00	0.00	0.00	0.00	0.00	0.00	0.01	0.00	0.00	0.00	0.00	0.00	0.00	0.00	0.00
Al	3.12	3.10	3.11	3.08	3.08	3.02	3.06	3.07	3.08	3.04	3.12	3.09	3.06	3.00	3.08	3.03	3.04	3.07
Fe2+	2.35	2.48	2.47	2.47	2.49	2.63	2.54	2.58	2.41	2.54	2.23	2.20	2.40	2.29	2.67	2.52	2.39	2.31
Mn	0.01	0.01	0.01	0.01	0.01	0.01	0.01	0.01	0.01	0.01	0.01	0.01	0.01	0.00	0.00	0.00	0.00	0.00
Mg	1.58	1.58	1.56	1.63	1.59	1.56	1.58	1.59	1.50	1.60	1.71	1.95	1.75	1.87	1.50	1.71	1.80	1.78
Ca	0.00	0.00	0.00	0.00	0.00	0.00	0.00	0.00	0.00	0.00	0.00	0.01	0.00	0.00	0.00	0.00	0.00	0.00
Na	0.01	0.01	0.01	0.01	0.01	0.00	0.01	0.01	0.01	0.00	0.01	0.00	0.00	0.00	0.00	0.00	0.00	0.00
K	0.00	0.00	0.00	0.00	0.00	0.00	0.00	0.00	0.00	0.00	0.01	0.00	0.01	0.00	0.00	0.00	0.00	0.00
F	0.00	0.00	0.00	0.00	0.00	0.00	0.00	0.00	0.00	0.00	0.00	0.00	0.00	0.00	0.00	0.00	0.00	0.00
Cl	0.00	0.00	0.00	0.00	0.00	0.00	0.00	0.00	0.00	0.00	0.00	0.00	0.00	0.00	0.00	0.00	0.00	0.00
Total	9.75	9.82	9.82	9.83	9.83	9.86	9.84	9.86	9.74	9.84	9.77	9.85	9.85	9.84	9.86	9.88	9.86	9.82
X Mg	0.40	0.39	0.39	0.40	0.39	0.37	0.38	0.38	0.38	0.39	0.43	0.47	0.42	0.45	0.36	0.40	0.43	0.43
Amesite	0.30	0.36	0.36	0.36	0.36	0.37	0.36	0.39	0.27	0.36	0.32	0.40	0.37	0.34	0.40	0.39	0.38	0.36
Clinochlore	0.44	0.45	0.44	0.46	0.46	0.49	0.47	0.47	0.46	0.48	0.44	0.46	0.47	0.50	0.46	0.48	0.48	0.46
Sudoite	0.25	0.19	0.19	0.17	0.18	0.14	0.16	0.14	0.27	0.16	0.24	0.15	0.16	0.16	0.14	0.12	0.14	0.18

CHLORITE FROM THE LYCIAN NAPPES (Dilek-Selçuk klippen)

Sample	KIRAZ2D	KIRAZ2D	KIRAZ2D	KIRAZ2D	KIRAZ2D	KIRAZ2D	KIRAZ1C	KIRAZ1C	KIRAZ1C	KIRAZ1C	KIRAZ1C	KIRAZ1C	DAV1B	DAV1B	DAV1B	DAV1B	DAV1B	DAV1B
SiO2	26.81	26.40	26.30	26.37	26.92	26.23	28.25	29.24	28.60	27.26	27.42	27.42	26.31	26.41	26.77	26.91	27.04	26.78
TiO2	0.03	0.05	0.03	0.02	0.07	0.03	0.02	0.02	0.01	0.00	0.00	0.01	0.01	0.02	0.02	0.00	0.02	0.00
Al2O3	25.99	24.84	24.77	25.24	24.85	24.77	25.43	26.93	26.36	25.21	25.69	24.79	25.45	25.52	25.57	25.54	25.56	25.09
FeO Total	20.00	21.25	21.73	21.43	21.29	21.65	13.60	12.77	13.47	16.03	14.71	15.51	19.45	18.60	18.76	19.37	19.05	18.83
MnO	0.08	0.06	0.00	0.02	0.05	0.07	0.12	0.10	0.11	0.15	0.14	0.14	0.01	0.02	0.01	0.05	0.01	0.02
MgO	14.70	14.57	14.46	14.74	14.58	14.60	19.89	19.56	19.16	18.71	19.68	19.87	16.76	17.30	17.35	16.30	16.53	16.71
CaO	0.03	0.01	0.02	0.00	0.02	0.02	0.03	0.01	0.03	0.00	0.00	0.03	0.02	0.02	0.03	0.01	0.05	0.02
Na2O	0.05	0.01	0.01	0.02	0.02	0.01	0.04	0.01	0.03	0.02	0.01	0.03	0.02	0.01	0.03	0.00	0.04	0.01
K2O	0.03	0.02	0.01	0.02	0.02	0.02	0.01	0.03	0.02	0.02	0.04	0.04	0.02	0.03	0.02	0.00	0.05	0.06
F	0.00	0.00	0.00	0.00	0.00	0.00	0.00	0.00	0.00	0.00	0.00	0.00	0.00	0.00	0.00	0.00	0.00	0.00
Cl	0.02	0.01	0.00	0.02	0.02	0.02	0.01	0.01	0.01	0.01	0.00	0.01	0.02	0.00	0.01	0.00	0.01	0.01
Total	87.74	87.20	87.33	87.87	87.83	87.42	87.40	88.68	87.81	87.40	87.69	87.83	88.06	87.92	88.55	88.18	88.36	87.52
Si	2.71	2.71	2.70	2.69	2.74	2.69	2.77	2.80	2.78	2.72	2.70	2.71	2.65	2.65	2.67	2.70	2.70	2.70
Ti	0.00	0.00	0.00	0.00	0.01	0.00	0.00	0.00	0.00	0.00	0.00	0.00	0.00	0.00	0.00	0.00	0.00	0.00
Al	3.10	3.01	3.00	3.03	2.98	3.00	2.94	3.04	3.02	2.96	2.98	2.89	3.02	3.02	3.01	3.02	3.01	2.99
Fe2+	1.69	1.82	1.87	1.83	1.81	1.86	1.12	1.02	1.10	1.34	1.21	1.28	1.64	1.56	1.56	1.63	1.59	1.59
Mn	0.01	0.00	0.00	0.00	0.00	0.01	0.01	0.01	0.01	0.01	0.01	0.01	0.00	0.00	0.00	0.00	0.00	0.00
Mg	2.22	2.23	2.22	2.24	2.21	2.24	2.91	2.79	2.78	2.78	2.89	2.93	2.52	2.59	2.58	2.44	2.46	2.51
Ca	0.00	0.00	0.00	0.00	0.00	0.00	0.00	0.00	0.00	0.00	0.00	0.00	0.00	0.00	0.00	0.00	0.01	0.00
Na	0.01	0.00	0.00	0.00	0.00	0.00	0.01	0.00	0.01	0.00	0.00	0.01	0.00	0.00	0.01	0.00	0.01	0.00
K	0.00	0.00	0.00	0.00	0.00	0.00	0.00	0.00	0.00	0.00	0.01	0.00	0.00	0.00	0.00	0.00	0.01	0.01
F	0.00	0.00	0.00	0.00	0.00	0.00	0.00	0.00	0.00	0.00	0.00	0.00	0.00	0.00	0.00	0.00	0.00	0.00
Cl	0.00	0.00	0.00	0.00	0.00	0.00	0.00	0.00	0.00	0.00	0.00	0.00	0.00	0.00	0.00	0.00	0.00	0.00
Total	9.75	9.79	9.80	9.80	9.77	9.81	9.76	9.68	9.71	9.81	9.81	9.85	9.84	9.84	9.83	9.79	9.80	9.81
X Mg	0.57	0.55	0.54	0.55	0.55	0.55	0.72	0.73	0.72	0.67	0.70	0.69	0.61	0.62	0.62	0.60	0.61	0.61
Amesite	0.29	0.29	0.29	0.31	0.25	0.30	0.23	0.20	0.21	0.28	0.30	0.29	0.35	0.35	0.33	0.30	0.29	0.30
Clinochlore	0.45	0.50	0.50	0.48	0.51	0.50	0.53	0.48	0.49	0.52	0.51	0.55	0.49	0.49	0.50	0.49	0.49	0.51
Sudoite	0.26	0.22	0.21	0.21	0.24	0.20	0.24	0.32	0.30	0.20	0.19	0.16	0.16	0.17	0.17	0.21	0.21	0.20

CHLORITE FROM THE MENDERES MASSIF (Kurudere area)

Sample	KURU0101A	KURU0101A	KURU0101A	KURU0101A	KURU0101A	KURU0101A	KURU0110B	KURU0110B	KURU0110B	KURU0110B	KURU0110B	KURU0110B	KURU0110B
Analysis	36	37	38	42	46	47	5	7	8	9	10	11	14
SiO2	28.11	28.92	28.32	28.64	28.56	28.34	28.00	28.07	28.28	27.99	28.42	27.91	28.00
TiO2	0.10	0.05	0.11	0.00	0.11	0.00	0.12	0.14	0.09	0.04	0.07	0.05	0.11
Al2O3	24.79	24.51	24.48	25.48	24.58	24.87	25.21	25.43	25.28	25.27	25.44	24.73	24.70
FeO Total	5.86	5.78	5.99	5.89	5.55	5.84	7.17	6.91	7.15	7.06	6.61	6.78	7.46
MnO	0.51	0.47	0.56	0.52	0.47	0.51	0.53	0.56	0.40	0.42	0.31	0.57	0.42
MgO	26.47	27.29	26.45	26.57	26.38	26.13	26.12	25.92	25.90	25.65	24.56	25.90	25.33
CaO	0.01	0.03	0.02	0.00	0.01	0.00	0.04	0.02	0.04	0.03	0.07	0.00	0.03
Na2O	0.02	0.01	0.00	0.00	0.00	0.00	0.01	0.00	0.02	0.01	0.02	0.00	0.04
K2O	0.00	0.00	0.02	0.02	0.00	0.03	0.00	0.01	0.02	0.02	0.01	0.00	0.01
F	0.58	0.30	0.39	0.44	0.49	0.20	0.00	0.44	0.10	0.24	0.34	0.29	0.15
Cl	0.01	0.00	0.00	0.00	0.00	0.00	0.02	0.00	0.02	0.01	0.01	0.00	0.04
Total	86.45	87.36	86.33	87.56	86.14	85.91	87.22	87.49	87.29	86.73	85.86	86.23	86.27
Si	2.71	2.75	2.73	2.72	2.76	2.74	2.68	2.69	2.70	2.70	2.75	2.71	2.72
Ti	0.01	0.00	0.01	0.00	0.01	0.00	0.01	0.01	0.01	0.00	0.01	0.00	0.01
Al	2.82	2.75	2.78	2.85	2.80	2.83	2.85	2.87	2.85	2.87	2.91	2.83	2.83
Fe2+	0.47	0.46	0.48	0.47	0.45	0.47	0.57	0.55	0.57	0.57	0.54	0.55	0.61
Mn	0.04	0.04	0.05	0.04	0.04	0.04	0.04	0.05	0.03	0.03	0.03	0.05	0.03
Mg	3.81	3.87	3.81	3.76	3.79	3.76	3.73	3.70	3.69	3.68	3.55	3.74	3.67
Ca	0.00	0.00	0.00	0.00	0.00	0.00	0.00	0.00	0.00	0.00	0.01	0.00	0.00
Na	0.00	0.00	0.00	0.00	0.00	0.00	0.00	0.00	0.00	0.00	0.00	0.00	0.01
K	0.00	0.00	0.00	0.00	0.00	0.00	0.00	0.00	0.00	0.00	0.00	0.00	0.00
F	0.18	0.09	0.12	0.13	0.15	0.06	0.00	0.13	0.03	0.07	0.10	0.09	0.04
Cl	0.00	0.00	0.00	0.00	0.00	0.00	0.00	0.00	0.00	0.00	0.00	0.00	0.01
Total	10.05	9.96	9.99	9.99	9.99	9.91	9.89	10.00	9.90	9.94	9.90	9.97	9.92
X Mg	0.81	0.81	0.80	0.81	0.81	0.80	0.77	0.78	0.77	0.77	0.78	0.78	0.76
Amesite	0.28	0.25	0.26	0.28	0.24	0.26	0.31	0.30	0.29	0.30	0.24	0.29	0.28
Clinochlore	0.59	0.63	0.61	0.57	0.60	0.58	0.58	0.57	0.58	0.56	0.55	0.59	0.59
Sudoite	0.13	0.13	0.13	0.15	0.16	0.15	0.11	0.13	0.14	0.14	0.21	0.12	0.14

CHLORITE FROM THE MENDERES MASSIF (Kurudere area)

Sample	KURU0110B	KURU0110C	KURU0110C	KURU0110C	KURU0110C	KURU0110C	KURU0110C	KURU0110C	KURU0110C	KURU0110C	KURU0110C	KURU0110C	KURU0110C
Analysis	15	96	97	98	100	101	139	140	141	142	143	144	145
SiO2	27.92	27.89	28.11	27.83	28.31	29.00	28.46	28.07	28.62	27.67	28.12	28.03	27.95
TiO2	0.05	0.00	0.09	0.04	0.00	0.04	0.04	0.00	0.00	0.16	0.02	0.02	0.11
Al2O3	24.81	25.24	25.38	25.83	25.10	24.48	25.21	26.14	24.62	26.05	25.90	25.35	25.29
FeO Total	7.36	7.03	7.19	7.63	7.20	6.74	7.06	7.08	6.23	6.55	7.40	7.77	7.26
MnO	0.32	0.39	0.56	0.54	0.45	0.53	0.31	0.50	0.46	0.46	0.48	0.37	0.45
MgO	26.19	25.43	25.53	25.52	25.95	26.34	25.73	26.18	26.18	25.92	25.65	26.02	25.85
CaO	0.01	0.02	0.00	0.00	0.01	0.05	0.00	0.02	0.01	0.01	0.00	0.03	0.02
Na2O	0.01	0.02	0.02	0.05	0.07	0.00	0.05	0.04	0.00	0.05	0.03	0.03	0.00
K2O	0.00	0.00	0.01	0.00	0.00	0.00	0.03	0.00	0.05	0.02	0.04	0.04	0.00
F	0.34	0.15	0.20	0.63	0.29	0.44	0.20	0.15	0.54	0.54	0.20	0.00	0.30
Cl	0.00	0.00	0.01	0.00	0.03	0.03	0.00	0.00	0.04	0.02	0.00	0.01	0.00
Total	87.01	86.14	87.10	88.07	87.40	87.65	87.09	88.18	86.76	87.44	87.85	87.67	87.23
Si	2.69	2.70	2.70	2.66	2.71	2.77	2.73	2.66	2.76	2.65	2.68	2.68	2.68
Ti	0.00	0.00	0.01	0.00	0.00	0.00	0.00	0.00	0.00	0.01	0.00	0.00	0.01
Al	2.82	2.88	2.87	2.91	2.83	2.75	2.85	2.92	2.79	2.94	2.91	2.85	2.86
Fe2+	0.59	0.57	0.58	0.61	0.58	0.54	0.57	0.56	0.50	0.52	0.59	0.62	0.58
Mn	0.03	0.03	0.05	0.04	0.04	0.04	0.03	0.04	0.04	0.04	0.04	0.03	0.04
Mg	3.76	3.67	3.65	3.64	3.71	3.75	3.67	3.70	3.76	3.70	3.64	3.71	3.70
Ca	0.00	0.00	0.00	0.00	0.00	0.00	0.00	0.00	0.00	0.00	0.00	0.00	0.00
Na	0.00	0.00	0.00	0.01	0.01	0.00	0.01	0.01	0.00	0.01	0.00	0.00	0.00
K	0.00	0.00	0.00	0.00	0.00	0.00	0.00	0.00	0.01	0.00	0.00	0.00	0.00
F	0.10	0.05	0.06	0.19	0.09	0.13	0.06	0.04	0.17	0.16	0.06	0.00	0.09
Cl	0.00	0.00	0.00	0.00	0.00	0.00	0.00	0.00	0.01	0.00	0.00	0.00	0.00
Total	10.00	9.91	9.92	10.07	9.97	9.99	9.91	9.93	10.02	10.04	9.93	9.90	9.97
X Mg	0.77	0.77	0.77	0.76	0.77	0.78	0.78	0.78	0.80	0.79	0.76	0.76	0.77
Amesite	0.31	0.30	0.29	0.33	0.29	0.23	0.27	0.34	0.24	0.34	0.32	0.32	0.31
Clinochlore	0.59	0.56	0.56	0.54	0.58	0.62	0.58	0.54	0.60	0.53	0.55	0.57	0.57
Sudoite	0.10	0.14	0.14	0.12	0.13	0.15	0.15	0.12	0.15	0.13	0.13	0.10	0.12

CHLORITE FROM THE MENDERES MASSIF (Nebiler area)

Sample	NEBILER0102A	NEBILER0102A	NEBILER0102A	NEBILER0102A	NEBILER0102A	NEBILER0102A	NEBILER0103A	NEBILER0103A	NEBILER0103A	NEBILER0103A	NEBILER0103A
Analysis	11	16	1	2	7	25					
SiO2	27.45	27.23	27.37	27.20	27.43	27.41	28.53	28.19	28.32	28.39	28.32
TiO2	1.29	0.07	0.21	0.00	0.00	0.00	0.00	0.03	0.04	0.01	0.05
Al2O3	24.10	23.70	23.91	23.75	23.87	23.45	24.38	24.76	24.75	24.90	24.50
FeO Total	8.60	9.13	9.29	9.13	9.73	8.77	7.78	8.24	8.12	8.01	7.72
MnO	0.98	1.29	1.04	1.19	1.10	1.00	0.64	0.69	0.62	0.71	0.65
MgO	23.52	23.35	24.39	24.24	23.91	24.27	25.61	25.43	24.90	25.04	25.54
CaO	0.00	0.02	0.00	0.03	0.08	0.00	0.01	0.01	0.04	0.00	0.01
Na2O	0.03	0.00	0.01	0.05	0.06	0.00	0.01	0.01	0.01	0.01	0.02
K2O	0.02	0.00	0.02	0.00	0.00	0.06	0.01	0.00	0.01	0.01	0.02
F	0.42	0.39	0.31	0.24	0.43	0.22	0.00	0.00	0.00	0.00	0.00
Cl	0.03	0.00	0.00	0.00	0.02	0.00	0.01	0.00	0.01	0.00	0.00
Total	86.43	85.17	86.55	85.84	86.62	85.18	86.98	87.35	86.82	87.08	86.82
Si	2.70	2.72	2.69	2.70	2.71	2.73	2.75	2.71	2.74	2.73	2.73
Ti	0.09	0.01	0.02	0.00	0.00	0.00	0.00	0.00	0.00	0.00	0.00
Al	2.79	2.79	2.77	2.77	2.78	2.75	2.77	2.81	2.82	2.82	2.78
Fe2+	0.71	0.76	0.76	0.76	0.80	0.73	0.63	0.66	0.66	0.64	0.62
Mn	0.08	0.11	0.09	0.10	0.09	0.08	0.05	0.06	0.05	0.06	0.05
Mg	3.44	3.48	3.58	3.58	3.52	3.60	3.68	3.65	3.59	3.59	3.67
Ca	0.00	0.00	0.00	0.00	0.01	0.00	0.00	0.00	0.00	0.00	0.00
Na	0.00	0.00	0.00	0.01	0.01	0.00	0.00	0.00	0.00	0.00	0.00
K	0.00	0.00	0.00	0.00	0.00	0.01	0.00	0.00	0.00	0.00	0.00
F	0.13	0.12	0.10	0.07	0.13	0.07	0.00	0.00	0.00	0.00	0.00
Cl	0.01	0.00	0.00	0.00	0.00	0.00	0.00	0.00	0.00	0.00	0.00
Total	9.95	10.00	10.01	10.00	10.05	9.97	9.87	9.88	9.86	9.86	9.87
X Mg	0.71	0.69	0.70	0.70	0.69	0.71	0.75	0.74	0.74	0.74	0.75
Amesite	0.21	0.27	0.29	0.30	0.29	0.27	0.25	0.29	0.26	0.27	0.26
Clinochlore	0.61	0.60	0.61	0.61	0.61	0.62	0.62	0.60	0.59	0.59	0.61
Sudoite	0.19	0.12	0.09	0.08	0.09	0.10	0.13	0.12	0.15	0.15	0.13

SUDOITE FROM THE MENDERES MASSIF (Bahçeyaka and Nebiler areas)

Sample	YAT 0107B	YAT 0107B	YAT 0107B	YAT 0107B	YAT 0107B	NEBIL 0103A	NEBIL 0103A	NEBIL 0103A
SiO_2	34.190	33.788	33.700	34.231	34.057	34.404	34.205	35.365
TiO_2	0.195	0.000	0.088	0.107	0.123	0.020	0.023	0.023
Al_2O_3	35.191	34.809	34.928	34.807	35.459	35.261	35.802	36.090
FeO	2.776	2.545	2.700	2.868	2.983	3.547	3.310	3.188
MnO	0.158	0.074	0.133	0.118	0.179	0.075	0.082	0.105
MgO	13.661	13.926	14.112	14.178	13.785	13.536	13.697	12.291
Sum.	86.248	85.202	85.697	86.646	86.721	87.006	87.252	87.825
Si	3.113	3.110	3.090	3.116	3.092	3.117	3.088	3.170
Ti	0.013	0.000	0.006	0.007	0.008	0.001	0.002	0.002
Al^{IV}	0.887	0.890	0.910	0.884	0.908	0.883	0.912	0.830
Al^{VI}	2.889	2.885	2.863	2.849	2.886	2.883	2.897	2.983
Fe^{2+}	0.211	0.196	0.207	0.218	0.226	0.269	0.250	0.239
Mn	0.012	0.006	0.010	0.009	0.014	0.006	0.006	0.008
Mg	1.854	1.911	1.929	1.924	1.866	1.829	1.843	1.643
Sum.	8.992	9.005	9.020	9.100	9.035	9.008	9.014	8.969

PHENGITE FROM THE LYCIAN NAPPES (Ören area)

Sample	OREN009N	OREN005E	OREN005E	OREN001H	OREN001H	OREN001H	OREN001H	OREN001H	OREN001H	OREN001H	OREN001H	OREN001H	OREN001H	OREN001H
analysis	191	93	94	90	92	94	95	96	97	98	104	106	107	115
SiO2	46.29	47.57	47.43	46.92	47.31	47.37	47.37	46.82	46.64	46.52	46.78	46.48	47.96	48.20
TiO2	0.05	0.05	0.00	0.04	0.08	0.11	0.02	0.03	0.09	0.07	0.04	0.05	0.02	0.09
Al2O3	34.04	34.81	35.49	34.75	33.07	33.13	32.75	34.87	34.47	34.54	34.32	34.15	34.40	35.03
FeO Total	2.95	1.45	1.49	1.96	2.46	2.53	2.81	2.04	2.04	2.15	1.37	2.25	1.52	1.53
MnO	0.00	0.00	0.04	0.00	0.01	0.00	0.00	0.00	0.00	0.00	0.00	0.00	0.00	0.00
MgO	0.64	0.36	0.38	0.34	0.84	0.80	0.90	0.33	0.42	0.38	0.38	0.57	0.35	0.32
CaO	0.03	0.01	0.01	0.06	0.03	0.04	0.01	0.18	0.13	0.01	0.02	0.01	0.09	0.08
Na2O	0.87	0.85	0.94	1.02	0.73	0.78	0.71	1.01	1.33	0.72	0.97	0.83	0.80	1.02
K2O	8.92	8.37	8.74	8.42	8.73	8.91	9.01	8.22	8.21	8.86	8.31	8.86	8.24	8.25
F	0.00	0.00	0.14	0.00	0.00	0.00	0.00	0.00	0.00	0.00	0.04	0.00	0.00	0.00
Cl	0.01	0.00	0.01	0.01	0.01	0.00	0.01	0.00	0.01	0.00	0.00	0.00	0.00	0.01
Total	93.79	93.48	94.66	93.53	93.28	93.64	93.60	93.49	93.34	93.26	92.20	93.18	93.39	94.53
Si	3.13	3.18	3.14	3.15	3.20	3.19	3.20	3.14	3.14	3.14	3.17	3.14	3.20	3.18
Ti	0.00	0.00	0.00	0.00	0.00	0.01	0.00	0.00	0.00	0.00	0.00	0.00	0.00	0.00
Al	2.71	2.74	2.77	2.75	2.63	2.63	2.61	2.76	2.74	2.75	2.74	2.72	2.71	2.73
Fe2+	0.17	0.08	0.08	0.11	0.14	0.14	0.16	0.11	0.11	0.12	0.08	0.13	0.08	0.08
Mn	0.00	0.00	0.00	0.00	0.00	0.00	0.00	0.00	0.00	0.00	0.00	0.00	0.00	0.00
Mg	0.06	0.04	0.04	0.03	0.08	0.08	0.09	0.03	0.04	0.04	0.04	0.06	0.04	0.03
Ca	0.00	0.00	0.00	0.00	0.00	0.00	0.00	0.01	0.01	0.00	0.00	0.00	0.01	0.01
Na	0.11	0.11	0.12	0.13	0.10	0.10	0.09	0.13	0.17	0.09	0.13	0.11	0.10	0.13
K	0.77	0.71	0.74	0.72	0.75	0.77	0.78	0.70	0.71	0.76	0.72	0.76	0.70	0.69
F	0.00	0.00	0.03	0.00	0.00	0.00	0.00	0.00	0.00	0.00	0.01	0.00	0.00	0.00
Cl	0.00	0.00	0.00	0.00	0.00	0.00	0.00	0.00	0.00	0.00	0.00	0.00	0.00	0.00
Total	6.96	6.86	6.93	6.90	6.91	6.92	6.93	6.90	6.93	6.91	6.89	6.93	6.84	6.86
Prl	0.12	0.18	0.14	0.15	0.15	0.13	0.13	0.17	0.12	0.14	0.15	0.13	0.19	0.17
Par	0.11	0.11	0.12	0.13	0.10	0.10	0.09	0.13	0.17	0.09	0.13	0.11	0.10	0.13
Phl	0.07	0.04	0.04	0.04	0.06	0.05	0.06	0.05	0.04	0.05	0.03	0.05	0.03	0.03
Acel	0.02	0.01	0.01	0.01	0.05	0.07	0.07	0.00	0.04	0.00	0.02	0.02	0.02	0.02
Mus	0.69	0.67	0.70	0.67	0.65	0.65	0.65	0.68	0.64	0.71	0.67	0.69	0.66	0.65

PHENGITE FROM THE LYCIAN NAPPES (Ören area)

Sample	OREN001H	OREN001H	OREN001H	OREN001H	OREN001H	OREN001H	OREN001H	OREN001H	OREN001H	OREN001H	OREN001H	OREN001H	OREN001H	OREN001H
analysis	116	119	120	121	124	125	128	137	139	145	158	205	206	221
SiO2	48.60	47.18	47.61	47.60	47.13	47.50	47.64	46.97	48.00	46.89	45.94	48.65	48.07	47.06
TiO2	0.02	0.02	0.04	0.07	0.09	0.00	0.06	0.08	0.10	0.03	0.07	0.00	0.00	0.05
Al2O3	34.72	33.98	33.96	33.51	34.07	33.67	34.22	35.37	34.83	35.31	34.57	35.07	34.71	34.46
FeO Total	1.39	2.05	1.77	2.31	2.05	2.40	1.99	1.65	1.60	1.86	1.96	1.66	1.67	1.71
MnO	0.02	0.00	0.01	0.00	0.00	0.02	0.01	0.00	0.00	0.03	0.00	0.00	0.02	0.02
MgO	0.36	0.61	0.64	0.73	0.54	0.72	0.59	0.29	0.37	0.24	0.29	0.37	0.39	0.36
CaO	0.00	0.06	0.06	0.06	0.13	0.08	0.04	0.17	0.08	0.25	0.15	0.00	0.01	0.10
Na2O	0.94	1.10	1.25	0.91	0.95	0.92	1.12	1.15	0.88	1.57	1.07	0.91	0.90	1.14
K2O	8.19	8.48	8.27	8.77	8.76	8.98	8.34	8.38	8.62	7.37	8.16	8.41	8.39	8.04
F	0.00	0.04	0.00	0.00	0.00	0.01	0.00	0.00	0.01	0.00	0.00	0.00	0.00	0.00
Cl	0.01	0.00	0.00	0.01	0.01	0.00	0.01	0.02	0.01	0.00	0.00	0.02	0.02	0.01
Total	94.25	93.50	93.59	93.97	93.73	94.31	94.01	94.08	94.48	93.56	92.21	95.08	94.18	92.94
Si	3.21	3.17	3.19	3.19	3.17	3.18	3.18	3.13	3.18	3.13	3.13	3.20	3.19	3.17
Ti	0.00	0.00	0.00	0.00	0.00	0.00	0.00	0.00	0.00	0.00	0.00	0.00	0.00	0.00
Al	2.70	2.69	2.68	2.65	2.70	2.66	2.69	2.78	2.72	2.78	2.77	2.71	2.72	2.73
Fe2+	0.08	0.12	0.10	0.13	0.12	0.13	0.11	0.09	0.09	0.10	0.11	0.09	0.09	0.10
Mn	0.00	0.00	0.00	0.00	0.00	0.00	0.00	0.00	0.00	0.00	0.00	0.00	0.00	0.00
Mg	0.04	0.06	0.06	0.07	0.05	0.07	0.06	0.03	0.04	0.02	0.03	0.04	0.04	0.04
Ca	0.00	0.00	0.00	0.00	0.01	0.01	0.00	0.01	0.01	0.02	0.01	0.00	0.00	0.01
Na	0.12	0.14	0.16	0.12	0.12	0.12	0.15	0.15	0.11	0.20	0.14	0.12	0.12	0.15
K	0.69	0.73	0.71	0.75	0.75	0.77	0.71	0.71	0.73	0.63	0.71	0.70	0.71	0.69
F	0.00	0.01	0.00	0.00	0.00	0.00	0.00	0.00	0.00	0.00	0.00	0.00	0.00	0.00
Cl	0.00	0.00	0.00	0.00	0.00	0.00	0.00	0.00	0.00	0.00	0.00	0.00	0.00	0.00
Total	6.84	6.92	6.90	6.92	6.92	6.94	6.90	6.91	6.88	6.89	6.91	6.86	6.87	6.88
Prl	0.19	0.13	0.13	0.13	0.13	0.11	0.14	0.14	0.16	0.17	0.15	0.18	0.17	0.16
Par	0.12	0.14	0.16	0.12	0.12	0.12	0.15	0.15	0.11	0.20	0.14	0.12	0.12	0.15
Phl	0.03	0.04	0.03	0.04	0.04	0.04	0.04	0.03	0.03	0.04	0.05	0.04	0.04	0.04
Acel	0.02	0.05	0.07	0.07	0.06	0.08	0.04	0.02	0.04	0.00	0.00	0.02	0.02	0.02
Mus	0.64	0.64	0.62	0.64	0.67	0.66	0.63	0.68	0.67	0.62	0.68	0.65	0.66	0.64

PHENGITE FROM THE LYCIAN NAPPES (Ören area)

Sample	OREN001H	OREN001H	OREN001H	OREN001H	OREN001H	OREN001H	OREN001H	OREN001H	OREN001H	OREN001H	OREN001H	OREN001H	OREN001H	OREN001H
analysis	222	223	224	226	228	231	254	255	256	263	264	278	288	289
SiO2	47.47	48.18	47.66	47.13	45.86	48.07	46.92	47.62	46.78	47.46	46.73	48.09	46.32	47.01
TiO2	0.03	0.07	0.02	0.08	0.08	0.03	0.09	0.06	0.13	0.15	0.09	0.00	0.03	0.14
Al2O3	34.21	34.53	34.51	34.40	34.36	34.34	35.06	34.79	35.71	34.97	34.21	34.93	34.40	35.07
FeO Total	1.79	1.73	1.74	1.79	2.01	1.75	1.37	1.59	1.41	1.69	1.51	1.77	1.89	1.54
MnO	0.00	0.00	0.04	0.01	0.01	0.00	0.00	0.00	0.01	0.00	0.00	0.00	0.00	0.01
MgO	0.41	0.37	0.37	0.38	0.41	0.46	0.23	0.29	0.19	0.28	0.44	0.32	0.31	0.27
CaO	0.00	0.01	0.04	0.00	0.25	0.08	0.57	0.01	0.44	0.14	0.00	0.06	0.04	0.00
Na2O	0.90	0.79	0.90	0.91	1.25	0.78	1.51	0.94	1.67	1.04	0.81	0.86	0.93	0.83
K2O	8.66	8.29	8.55	8.39	8.02	8.47	7.46	8.34	7.09	8.37	8.44	8.42	8.38	8.86
F	0.00	0.00	0.00	0.01	0.00	0.00	0.00	0.00	0.00	0.04	0.00	0.00	0.00	0.00
Cl	0.01	0.00	0.00	0.00	0.01	0.01	0.03	0.00	0.00	0.00	0.01	0.00	0.00	0.00
Total	93.47	93.96	93.83	93.08	92.25	93.99	93.22	93.63	93.43	94.12	92.23	94.46	92.30	93.73
Si	3.18	3.20	3.18	3.17	3.12	3.20	3.14	3.18	3.12	3.16	3.17	3.18	3.15	3.15
Ti	0.00	0.00	0.00	0.00	0.00	0.00	0.00	0.00	0.01	0.01	0.00	0.00	0.00	0.01
Al	2.70	2.70	2.71	2.73	2.76	2.69	2.77	2.74	2.81	2.74	2.74	2.72	2.76	2.77
Fe2+	0.10	0.10	0.10	0.10	0.11	0.10	0.08	0.09	0.08	0.09	0.09	0.10	0.11	0.09
Mn	0.00	0.00	0.00	0.00	0.00	0.00	0.00	0.00	0.00	0.00	0.00	0.00	0.00	0.00
Mg	0.04	0.04	0.04	0.04	0.04	0.05	0.02	0.03	0.02	0.03	0.04	0.03	0.03	0.03
Ca	0.00	0.00	0.00	0.00	0.02	0.01	0.04	0.00	0.03	0.01	0.00	0.00	0.00	0.00
Na	0.12	0.10	0.12	0.12	0.16	0.10	0.20	0.12	0.22	0.13	0.11	0.11	0.12	0.11
K	0.74	0.70	0.73	0.72	0.70	0.72	0.64	0.71	0.60	0.71	0.73	0.71	0.73	0.76
F	0.00	0.00	0.00	0.00	0.00	0.00	0.00	0.00	0.00	0.01	0.00	0.00	0.00	0.00
Cl	0.00	0.00	0.00	0.00	0.00	0.00	0.00	0.00	0.00	0.00	0.00	0.00	0.00	0.00
Total	6.89	6.85	6.88	6.88	6.92	6.86	6.89	6.87	6.88	6.89	6.88	6.86	6.90	6.90
Prl	0.14	0.20	0.15	0.16	0.14	0.18	0.17	0.17	0.18	0.16	0.16	0.18	0.15	0.14
Par	0.12	0.10	0.12	0.12	0.16	0.10	0.20	0.12	0.22	0.13	0.11	0.11	0.12	0.11
Phl	0.03	0.04	0.03	0.04	0.04	0.04	0.01	0.03	0.03	0.03	0.04	0.04	0.04	0.03
Acel	0.04	0.01	0.03	0.01	0.03	0.03	0.06	0.01	0.01	0.03	0.01	0.01	0.01	0.02
Mus	0.66	0.65	0.67	0.66	0.66	0.66	0.64	0.66	0.63	0.67	0.68	0.67	0.68	0.71

PHENGITE FROM THE LYCIAN NAPPES (Ören area)

Sample	OREN001H	OREN001H	OREN001H	OREN001H	OREN001H	OREN001H	OREN001H	OREN001H	OREN001H	OREN001H	OREN001H	OREN001H	OREN001H	OREN001H
analysis	290	291	298	301	302	303	304	309	310	314	315	317	323	324
SiO2	47.26	46.46	48.00	48.44	48.68	48.39	48.28	46.66	46.93	47.92	48.18	46.28	48.44	48.43
TiO2	0.16	0.20	0.04	0.09	0.11	0.16	0.09	0.11	0.06	0.03	0.01	0.10	0.03	0.01
Al2O3	35.13	34.82	35.19	34.27	34.28	34.74	34.21	34.28	34.76	34.22	34.39	34.43	35.33	34.52
FeO Total	1.43	1.89	1.71	1.64	1.68	1.48	1.52	2.26	1.93	1.48	1.49	1.81	1.54	1.72
MnO	0.00	0.02	0.00	0.02	0.01	0.00	0.02	0.02	0.00	0.00	0.00	0.00	0.02	0.03
MgO	0.31	0.22	0.28	0.42	0.44	0.33	0.44	0.39	0.36	0.40	0.40	0.28	0.33	0.37
CaO	0.01	0.18	0.17	0.02	0.02	0.03	0.02	0.20	0.09	0.03	0.01	0.14	0.09	0.01
Na2O	0.90	1.12	1.67	0.73	0.83	1.13	0.96	1.17	1.08	1.00	0.83	1.17	1.32	0.85
K2O	8.53	8.22	7.36	8.50	8.35	8.23	7.97	7.98	8.18	8.20	8.27	7.82	7.63	8.37
F	0.00	0.00	0.00	0.04	0.00	0.01	0.00	0.00	0.00	0.00	0.00	0.00	0.00	0.00
Cl	0.00	0.02	0.00	0.00	0.00	0.01	0.02	0.00	0.00	0.01	0.01	0.02	0.00	0.01
Total	93.73	93.15	94.42	94.15	94.39	94.51	93.51	93.06	93.38	93.28	93.59	92.05	94.74	94.31
Si	3.15	3.13	3.17	3.21	3.22	3.20	3.22	3.15	3.15	3.21	3.21	3.15	3.18	3.21
Ti	0.01	0.01	0.00	0.00	0.01	0.01	0.00	0.01	0.00	0.00	0.00	0.01	0.00	0.00
Al	2.76	2.77	2.74	2.68	2.67	2.70	2.69	2.73	2.75	2.70	2.70	2.76	2.74	2.69
Fe2+	0.08	0.11	0.09	0.09	0.09	0.08	0.08	0.13	0.11	0.08	0.08	0.10	0.08	0.10
Mn	0.00	0.00	0.00	0.00	0.00	0.00	0.00	0.00	0.00	0.00	0.00	0.00	0.00	0.00
Mg	0.03	0.02	0.03	0.04	0.04	0.03	0.04	0.04	0.04	0.04	0.04	0.03	0.03	0.04
Ca	0.00	0.01	0.01	0.00	0.00	0.00	0.00	0.01	0.01	0.00	0.00	0.01	0.01	0.00
Na	0.12	0.15	0.21	0.09	0.11	0.14	0.12	0.15	0.14	0.13	0.11	0.15	0.17	0.11
K	0.73	0.71	0.62	0.72	0.70	0.69	0.68	0.69	0.70	0.70	0.70	0.68	0.64	0.71
F	0.00	0.00	0.00	0.01	0.00	0.00	0.00	0.00	0.00	0.00	0.00	0.00	0.00	0.00
Cl	0.00	0.00	0.00	0.00	0.00	0.00	0.00	0.00	0.00	0.00	0.00	0.00	0.00	0.00
Total	6.88	6.91	6.88	6.86	6.84	6.87	6.84	6.90	6.89	6.86	6.85	6.89	6.85	6.85
Prl	0.16	0.15	0.17	0.19	0.19	0.16	0.20	0.16	0.16	0.17	0.19	0.17	0.19	0.18
Par	0.12	0.15	0.21	0.09	0.11	0.14	0.12	0.15	0.14	0.13	0.11	0.15	0.17	0.11
Phl	0.04	0.04	0.03	0.03	0.03	0.02	0.04	0.05	0.05	0.03	0.03	0.04	0.04	0.04
Acel	0.01	0.02	0.03	0.04	0.04	0.05	0.02	0.02	0.01	0.04	0.02	0.00	0.00	0.03
Mus	0.69	0.68	0.58	0.65	0.64	0.63	0.62	0.64	0.66	0.64	0.65	0.65	0.61	0.65

PHENGITE FROM THE LYCIAN NAPPES (Ören, Gerit and Civril areas)

Sample	OREN001H	OREN001H	OREN001H	OREN001H	OREN001H	OREN001H	OREN001H	OREN001H	OREN001H	OREN001H	OREN001H	OREN001H	GERIT0101	civril001A1
analysis	325	326	334	341	345	347	348	349	354	355	365	369	83	9
SiO2	47.27	46.38	46.53	47.29	47.48	47.40	48.64	48.03	46.45	46.40	47.22	48.43	46.89	47.38
TiO2	0.08	0.04	0.11	0.10	0.03	0.04	0.10	0.12	0.05	0.02	0.11	0.04	0.00	0.11
Al2O3	35.26	34.14	34.69	35.23	34.96	34.66	34.85	34.57	34.99	34.62	34.77	34.42	36.50	35.22
FeO Total	1.64	1.76	1.97	1.61	1.87	1.97	1.32	1.37	1.58	1.96	1.77	1.41	0.42	1.81
MnO	0.02	0.00	0.00	0.01	0.02	0.00	0.01	0.00	0.01	0.03	0.00	0.00	0.07	0.07
MgO	0.27	0.37	0.28	0.22	0.34	0.32	0.33	0.30	0.29	0.32	0.32	0.40	0.30	0.52
CaO	0.36	0.05	0.04	0.04	0.09	0.03	0.01	0.01	0.15	0.15	0.04	0.03	0.03	0.01
Na2O	1.51	0.82	0.82	1.03	1.00	0.86	0.89	1.06	1.71	1.04	0.98	0.86	1.04	1.45
K2O	7.52	8.46	8.65	8.58	8.35	8.64	8.27	8.26	7.22	8.40	8.79	8.73	8.89	8.18
F	0.00	0.00	0.00	0.00	0.00	0.00	0.00	0.00	0.00	0.00	0.00	0.00	0.73	
Cl	0.01	0.03	0.01	0.01	0.01	0.00	0.01	0.00	0.01	0.02	0.01	0.01	0.01	0.00
Total	93.92	92.04	93.10	94.13	94.13	93.92	94.42	93.72	92.45	92.95	93.99	94.33	94.87	94.90
Si	3.14	3.16	3.14	3.15	3.16	3.17	3.21	3.20	3.13	3.14	3.16	3.21	3.11	3.13
Ti	0.00	0.00	0.01	0.00	0.00	0.00	0.00	0.01	0.00	0.00	0.01	0.00	0.00	0.01
Al	2.76	2.74	2.76	2.76	2.74	2.73	2.71	2.71	2.78	2.76	2.74	2.69	2.85	2.74
Fe2+	0.09	0.10	0.11	0.09	0.10	0.11	0.07	0.08	0.09	0.11	0.10	0.08	0.02	0.10
Mn	0.00	0.00	0.00	0.00	0.00	0.00	0.00	0.00	0.00	0.00	0.00	0.00	0.00	0.00
Mg	0.03	0.04	0.03	0.02	0.03	0.03	0.03	0.03	0.03	0.03	0.03	0.04	0.03	0.05
Ca	0.03	0.00	0.00	0.00	0.01	0.00	0.00	0.00	0.01	0.01	0.00	0.00	0.00	0.00
Na	0.19	0.11	0.11	0.13	0.13	0.11	0.11	0.14	0.22	0.14	0.13	0.11	0.13	0.19
K	0.64	0.74	0.74	0.73	0.71	0.74	0.70	0.70	0.62	0.72	0.75	0.74	0.75	0.69
F	0.00	0.00	0.00	0.00	0.00	0.00	0.00	0.00	0.00	0.00	0.00	0.00	0.15	0.00
Cl	0.00	0.00	0.00	0.00	0.00	0.00	0.00	0.00	0.00	0.00	0.00	0.00	0.00	0.00
Total	6.89	6.89	6.90	6.90	6.89	6.89	6.84	6.86	6.90	6.92	6.91	6.87	7.06	6.92
Prl	0.17	0.16	0.15	0.14	0.16	0.15	0.19	0.16	0.15	0.14	0.12	0.15	0.11	0.12
Par	0.19	0.11	0.11	0.13	0.13	0.11	0.11	0.14	0.22	0.14	0.13	0.11	0.13	0.19
Phl	0.03	0.04	0.05	0.03	0.04	0.04	0.03	0.02	0.04	0.04	0.03	0.02	0.02	0.04
Acel	0.03	0.01	0.00	0.02	0.01	0.02	0.02	0.04	0.00	0.02	0.04	0.06	0.00	0.04
Mus	0.63	0.69	0.70	0.68	0.67	0.68	0.65	0.64	0.60	0.68	0.68	0.66	0.74	0.64

PHENGITE FROM THE LYCIAN NAPPES (Güllük, Dilek-Selçuk klippen, and Ula areas)

Sample	GUL4F	GUL4F	GUL005c	KIRAZ1C	ULA3E	ULA1B	ULA1B	ULA1B	ULA1B	ULA1B	ULA1B	ULA1B	ULA1B	ULA1B
SiO2	47.15	46.93	45.77	47.25	47.26	48.06	47.26	47.71	48.18	47.98	47.88	47.93	47.42	48.11
TiO2	0.18	0.06	0.02	0.04	0.13	0.09	0.07	0.08	0.12	0.07	0.05	0.06	0.11	0.08
Al2O3	34.10	35.98	34.36	35.29	35.67	34.57	33.08	34.33	34.40	33.75	34.00	34.43	33.75	33.59
FeO Total	2.07	1.84	1.63	2.15	1.22	2.44	2.55	2.35	2.51	2.42	2.43	2.37	2.46	2.69
MnO	0.00	0.00	0.00	0.02	0.00	0.00	0.00	0.03	0.00	0.00	0.03	0.01	0.00	0.01
MgO	0.71	0.37	0.49	0.54	0.86	0.80	0.95	0.87	0.92	0.98	0.93	0.91	0.89	0.97
CaO	0.03	0.02	0.02	0.01	0.07	0.04	0.03	0.04	0.03	0.01	0.05	0.07	0.01	0.07
Na2O	0.79	1.14	1.29	0.80	1.17	1.77	0.77	1.11	0.95	0.77	1.00	0.96	0.73	0.72
K2O	8.56	8.97	8.29	9.17	8.86	7.91	8.43	8.24	8.42	8.93	8.64	8.41	8.75	8.96
F	0.00	0.00	0.00	0.00		0.00	0.00	0.00	0.00	0.00	0.00	0.00	0.00	0.00
Cl	0.00	0.01	0.04	0.01	0.00	0.01	0.01	0.00	0.02	0.00	0.00	0.00	0.00	0.00
Total	93.59	95.31	91.89	95.28	95.44	95.68	93.16	94.75	95.52	94.91	95.01	95.14	94.12	95.20
Si	3.16	3.10	3.13	3.13	3.11	3.16	3.19	3.16	3.17	3.19	3.17	3.17	3.17	3.19
Ti	0.01	0.00	0.00	0.00	0.01	0.00	0.00	0.00	0.01	0.00	0.00	0.00	0.01	0.00
Al	2.70	2.80	2.77	2.75	2.77	2.68	2.63	2.68	2.67	2.64	2.66	2.68	2.66	2.62
Fe2+	0.12	0.10	0.09	0.12	0.07	0.13	0.14	0.13	0.14	0.13	0.13	0.13	0.14	0.15
Mn	0.00	0.00	0.00	0.00	0.00	0.00	0.00	0.00	0.00	0.00	0.00	0.00	0.00	0.00
Mg	0.07	0.04	0.05	0.05	0.08	0.08	0.10	0.09	0.09	0.10	0.09	0.09	0.09	0.10
Ca	0.00	0.00	0.00	0.00	0.01	0.00	0.00	0.00	0.00	0.00	0.00	0.01	0.00	0.00
Na	0.10	0.15	0.17	0.10	0.15	0.23	0.10	0.14	0.12	0.10	0.13	0.12	0.09	0.09
K	0.73	0.76	0.72	0.77	0.74	0.66	0.73	0.70	0.71	0.76	0.73	0.71	0.75	0.76
F	0.00	0.00	0.00	0.00	0.00	0.00	0.00	0.00	0.00	0.00	0.00	0.00	0.00	0.00
Cl	0.00	0.00	0.00	0.00	0.00	0.00	0.00	0.00	0.00	0.00	0.00	0.00	0.00	0.00
Total	6.90	6.95	6.94	6.93	6.94	6.94	6.90	6.91	6.90	6.92	6.92	6.91	6.91	6.92
Prl	0.16	0.10	0.11	0.12	0.11	0.11	0.17	0.16	0.17	0.14	0.14	0.17	0.16	0.15
Par	0.10	0.15	0.17	0.10	0.15	0.23	0.10	0.14	0.12	0.10	0.13	0.12	0.09	0.09
Phl	0.06	0.04	0.04	0.06	0.03	0.05	0.07	0.07	0.07	0.06	0.06	0.07	0.07	0.06
Acel	0.01	0.01	0.02	0.01	0.05	0.06	0.03	0.01	0.01	0.05	0.04	0.01	0.02	0.05
Mus	0.67	0.71	0.66	0.71	0.70	0.56	0.63	0.62	0.63	0.65	0.63	0.64	0.66	0.65

PHENGITE FROM THE LYCIAN NAPPES (Ula area)

Sample	ULA1B	ULA1B	ULA1B	ULA1B	ULA1B	ULA1B	ULA1B2.	ULA1B2.	ULA1B2.	ULA1B2.	ULA1B2.	ULA1B2.	ULA1B2.	ULA1C1.	ULA1C1.
SiO2	47.66	48.06	47.74	50.27	47.88	47.34	49.68	47.24	48.37	47.89	47.20	47.94	47.56	47.47	47.30
TiO2	0.06	0.03	0.05	0.03	0.05	0.07	0.03	0.07	0.05	0.03	0.08	0.07	0.05	0.05	0.05
Al2O3	34.14	34.04	33.61	33.80	34.37	33.58	33.76	34.04	34.55	33.80	33.89	34.34	34.45	35.68	35.01
FeO Total	2.71	2.66	2.83	2.12	2.66	3.11	2.28	2.48	2.71	2.53	2.56	2.32	2.57	1.87	2.03
MnO	0.02	0.00	0.04	0.00	0.01	0.00	0.01	0.03	0.02	0.00	0.00	0.00	0.00	0.00	0.00
MgO	0.90	0.98	1.03	0.68	0.87	0.89	0.66	0.79	0.93	0.91	0.85	0.87	0.77	0.57	0.52
CaO	0.08	0.05	0.01	0.03	0.03	0.03	0.02	0.02	0.03	0.00	0.04	0.01	0.05	0.05	0.08
Na2O	0.86	0.75	0.75	0.84	0.99	0.84	1.02	1.01	1.01	0.71	0.80	0.98	0.88	1.29	1.20
K2O	8.46	8.61	9.07	8.27	8.49	8.92	7.67	9.04	8.54	8.93	8.65	8.26	9.13	8.36	8.37
F	0.00	0.00	0.00	0.00	0.00	0.00	0.00	0.00	0.00	0.00	0.00	0.00	0.00	0.00	0.00
Cl	0.00	0.00	0.01	0.00	0.00	0.01	0.01	0.02	0.01	0.02	0.02	0.00	0.02	0.00	0.03
Total	94.87	95.18	95.14	96.05	95.35	94.78	95.14	94.73	96.22	94.82	94.08	94.78	95.47	95.34	94.58
Si	3.16	3.18	3.17	3.27	3.16	3.16	3.26	3.15	3.17	3.18	3.16	3.17	3.15	3.12	3.14
Ti	0.00	0.00	0.00	0.00	0.00	0.00	0.00	0.00	0.00	0.00	0.00	0.00	0.00	0.00	0.00
Al	2.67	2.65	2.63	2.59	2.68	2.64	2.61	2.68	2.67	2.65	2.68	2.68	2.69	2.77	2.74
Fe2+	0.15	0.15	0.16	0.12	0.15	0.17	0.12	0.14	0.15	0.14	0.14	0.13	0.14	0.10	0.11
Mn	0.00	0.00	0.00	0.00	0.00	0.00	0.00	0.00	0.00	0.00	0.00	0.00	0.00	0.00	0.00
Mg	0.09	0.10	0.10	0.07	0.09	0.09	0.06	0.08	0.09	0.09	0.08	0.09	0.08	0.06	0.05
Ca	0.01	0.00	0.00	0.00	0.00	0.00	0.00	0.00	0.00	0.00	0.00	0.00	0.00	0.00	0.01
Na	0.11	0.10	0.10	0.11	0.13	0.11	0.13	0.13	0.13	0.09	0.10	0.13	0.11	0.16	0.15
K	0.72	0.73	0.77	0.69	0.72	0.76	0.64	0.77	0.71	0.76	0.74	0.70	0.77	0.70	0.71
F	0.00	0.00	0.00	0.00	0.00	0.00	0.00	0.00	0.00	0.00	0.00	0.00	0.00	0.00	0.00
Cl	0.00	0.00	0.00	0.00	0.00	0.00	0.00	0.00	0.00	0.00	0.00	0.00	0.00	0.00	0.00
Total	6.91	6.90	6.94	6.83	6.92	6.95	6.83	6.96	6.92	6.92	6.92	6.89	6.95	6.92	6.92
Prl	0.17	0.18	0.13	0.21	0.16	0.13	0.23	0.10	0.16	0.15	0.16	0.18	0.12	0.13	0.14
Par	0.11	0.10	0.10	0.11	0.13	0.11	0.13	0.13	0.13	0.09	0.10	0.13	0.11	0.16	0.15
Phl	0.08	0.08	0.07	0.04	0.07	0.07	0.05	0.05	0.08	0.07	0.07	0.07	0.06	0.05	0.05
Acel	0.00	0.01	0.04	0.06	0.01	0.04	0.03	0.06	0.01	0.03	0.01	0.00	0.04	0.00	0.02
Mus	0.64	0.65	0.65	0.59	0.63	0.65	0.56	0.66	0.63	0.66	0.66	0.63	0.68	0.66	0.65

PHENGITE FROM THE MENDERES MASSIF (Kavakbeleni and Kurudere areas)

Sample	KAVAKBEL0103	KAVAKBEL0103	KAVAKBEL0103	KAVAKBEL0103	KURU0101A	KURU0101A	KURU0101A	KURU0101A	KURU0101A	KURU0101A	KURU0107	KURU0108	KURU0109
analysis	57	65	66	74	39	40	43	44	69	71	55	32	35
SiO2	47.17	49.53	47.62	46.44	46.92	46.80	46.69	47.19	45.87	45.17	46.56	46.83	48.65
TiO2	0.07	0.16	0.11	0.00	0.13	0.13	0.21	0.13	0.00	0.02	0.16	0.23	0.35
Al2O3	32.36	32.61	33.75	32.79	34.66	35.22	35.76	34.32	35.55	35.98	32.60	29.76	30.14
FeO Total	2.33	2.14	2.30	2.18	1.93	1.98	2.36	2.32	1.76	1.81	2.81	4.46	3.56
MnO	0.11	0.00	0.00	0.00	0.00	0.00	0.07	0.02	0.01	0.00	0.03	0.03	0.00
MgO	1.05	1.06	0.98	1.00	0.70	0.79	0.70	1.01	0.75	0.80	1.09	1.50	1.88
CaO	0.05	0.00	0.01	0.04	0.03	0.00	0.02	0.04	0.05	0.82	0.03	0.03	0.02
Na2O	1.73	1.38	1.84	1.92	0.68	0.71	0.70	0.59	0.81	0.81	0.75	0.49	0.43
K2O	8.54	8.48	8.25	7.96	10.21	10.25	9.97	9.54	10.02	9.42	9.65	9.85	10.03
F	0.00	0.11	0.03	0.11	0.56	0.33	0.00	0.33	0.28	0.28	0.08	0.14	0.00
Cl	0.00	0.01	0.00	0.02	0.00	0.02	0.00	0.01	0.00	0.00	0.00	0.01	0.03
Total	93.40	95.49	94.87	92.45	95.81	96.21	96.47	95.51	95.08	95.10	93.75	93.32	95.09
Si	3.19	3.26	3.17	3.17	3.12	3.10	3.07	3.14	3.07	3.02	3.16	3.23	3.27
Ti	0.00	0.01	0.01	0.00	0.01	0.01	0.01	0.01	0.00	0.00	0.01	0.01	0.02
Al	2.58	2.53	2.64	2.64	2.72	2.75	2.78	2.69	2.80	2.84	2.61	2.42	2.39
Fe2+	0.13	0.12	0.13	0.12	0.11	0.11	0.13	0.13	0.10	0.10	0.16	0.26	0.20
Mn	0.01	0.00	0.00	0.00	0.00	0.00	0.00	0.00	0.00	0.00	0.00	0.00	0.00
Mg	0.11	0.10	0.10	0.10	0.07	0.08	0.07	0.10	0.07	0.08	0.11	0.15	0.19
Ca	0.00	0.00	0.00	0.00	0.00	0.00	0.00	0.00	0.00	0.06	0.00	0.00	0.00
Na	0.23	0.18	0.24	0.25	0.09	0.09	0.09	0.08	0.10	0.11	0.10	0.07	0.06
K	0.74	0.71	0.70	0.69	0.87	0.87	0.84	0.81	0.86	0.80	0.84	0.87	0.86
F	0.00	0.02	0.01	0.02	0.12	0.07	0.00	0.07	0.06	0.06	0.02	0.03	0.00
Cl	0.00	0.00	0.00	0.00	0.00	0.00	0.00	0.00	0.00	0.00	0.00	0.00	0.00
Total	6.99	6.93	6.98	7.01	7.10	7.07	6.99	7.03	7.07	7.07	7.01	7.04	6.98
Prl	0.04	0.11	0.06	0.05	0.05	0.04	0.07	0.11	0.04	0.09	0.07	0.07	0.08
Par	0.23	0.18	0.24	0.25	0.09	0.09	0.09	0.08	0.10	0.11	0.10	0.07	0.06
Phl	0.02	0.02	0.04	0.03	0.03	0.04	0.06	0.06	0.05	0.04	0.05	0.08	0.06
Acel	0.17	0.16	0.11	0.12	0.09	0.06	0.01	0.04	0.04	0.05	0.11	0.18	0.20
Mus	0.55	0.53	0.55	0.54	0.75	0.76	0.76	0.71	0.78	0.83	0.68	0.61	0.60

PHENGITE FROM THE MENDERES MASSIF (Kurudere and Nebiler areas)

Sample	KURU0110	KURU0111	KURU0112	KURU0113	NEBILER0101B	NEBILER0101B	NEBILER0101B	NEBILER0102A	NEBILER0102A
analysis	38	42	44	48	77	84	90	13	14
SiO2	47.00	46.44	47.39	47.34	46.46	45.52	45.78	45.77	46.26
TiO2	0.12	0.00	0.14	0.12	0.00	0.05	0.09	0.14	0.11
Al2O3	33.43	34.10	33.15	33.23	33.62	33.52	33.39	34.78	33.48
FeO Total	2.72	2.96	2.58	2.78	2.18	2.57	2.20	2.47	2.52
MnO	0.00	0.00	0.00	0.00	0.00	0.09	0.02	0.00	0.09
MgO	0.72	0.62	0.80	0.96	0.52	0.59	0.62	0.54	0.54
CaO	0.00	0.02	0.00	0.01	0.00	0.00	0.02	0.00	0.00
Na2O	1.26	1.51	1.24	0.80	0.91	1.09	0.88	0.95	0.96
K2O	9.73	8.93	9.38	9.93	9.79	9.91	9.66	9.98	9.36
F	0.14	0.00	0.17	0.03	0.00	0.33	0.41	0.20	0.20
Cl	0.00	0.00	0.02	0.01	0.00	0.00	0.00	0.00	0.03
Total	95.13	94.58	94.87	95.20	93.49	93.67	93.07	94.83	93.55
Si	3.15	3.12	3.18	3.17	3.15	3.11	3.14	3.08	3.15
Ti	0.01	0.00	0.01	0.01	0.00	0.00	0.00	0.01	0.01
Al	2.64	2.70	2.62	2.62	2.69	2.70	2.70	2.76	2.68
Fe2+	0.15	0.17	0.14	0.16	0.12	0.15	0.13	0.14	0.14
Mn	0.00	0.00	0.00	0.00	0.00	0.01	0.00	0.00	0.01
Mg	0.07	0.06	0.08	0.10	0.05	0.06	0.06	0.05	0.05
Ca	0.00	0.00	0.00	0.00	0.00	0.00	0.00	0.00	0.00
Na	0.16	0.20	0.16	0.10	0.12	0.14	0.12	0.12	0.13
K	0.83	0.76	0.80	0.85	0.85	0.86	0.84	0.86	0.81
F	0.03	0.00	0.03	0.01	0.00	0.07	0.09	0.04	0.04
Cl	0.00	0.00	0.00	0.00	0.00	0.00	0.00	0.00	0.00
Total	7.05	7.01	7.03	7.00	6.99	7.11	7.08	7.06	7.02
Prl	0.00	0.04	0.04	0.05	0.03	0.00	0.04	0.02	0.06
Par	0.16	0.20	0.16	0.10	0.12	0.14	0.12	0.12	0.13
Phl	0.02	0.05	0.03	0.04	0.02	0.03	0.03	0.04	0.04
Acel	0.15	0.08	0.15	0.12	0.12	0.12	0.11	0.07	0.09
Mus	0.65	0.64	0.63	0.68	0.71	0.71	0.71	0.75	0.68

PHENGITE FROM THE MENDERES MASSIF (Nebiler and Bahçeyaka areas)

Sample	NEBILER0102A	NEBILER0102A	NEBILER0102A	NEBILER0102A	NEBILER0103A	YAT0107B	YAT0107B	YAT0107B
analysis	22	25	26	8		107	108	109
SiO2	44.13	45.79	45.52	48.89	46.32	47.05	46.84	45.28
TiO2	0.11	0.09	0.07	0.02	0.13	0.00	0.00	0.09
Al2O3	33.08	33.81	33.68	33.13	35.21	36.07	34.31	36.47
FeO Total	4.39	2.49	2.36	2.06	2.22	1.64	1.83	1.96
MnO	0.04	0.00	0.00	0.00	0.00	0.02	0.09	0.00
MgO	0.50	0.66	0.60	0.46	0.37	0.49	0.48	0.48
CaO	0.00	0.02	0.02	0.05	0.01	0.08	0.01	0.05
Na2O	1.06	0.98	0.96	1.13	1.22	1.36	1.21	1.37
K2O	9.04	9.37	9.42	8.74	8.74	9.54	9.28	9.64
F	0.00	0.17	0.22	0.17	0.00	0.28	0.06	0.44
Cl	0.00	0.02	0.03	0.01	0.01	0.00	0.03	0.00
Total	92.34	93.38	92.87	94.65	94.22	96.52	94.14	95.77
Si	3.07	3.12	3.12	3.25	3.10	3.09	3.15	3.02
Ti	0.01	0.00	0.00	0.00	0.01	0.00	0.00	0.00
Al	2.71	2.71	2.72	2.59	2.78	2.79	2.72	2.86
Fe2+	0.26	0.14	0.14	0.11	0.12	0.09	0.10	0.11
Mn	0.00	0.00	0.00	0.00	0.00	0.00	0.01	0.00
Mg	0.05	0.07	0.06	0.05	0.04	0.05	0.05	0.05
Ca	0.00	0.00	0.00	0.00	0.00	0.01	0.00	0.00
Na	0.14	0.13	0.13	0.15	0.16	0.17	0.16	0.18
K	0.80	0.81	0.82	0.74	0.75	0.80	0.80	0.82
F	0.00	0.04	0.05	0.03	0.00	0.06	0.01	0.09
Cl	0.00	0.00	0.00	0.00	0.00	0.00	0.00	0.00
Total	7.04	7.03	7.04	6.93	6.95	7.06	6.99	7.14
Prl	0.06	0.06	0.05	0.11	0.10	0.03	0.05	0.00
Par	0.14	0.13	0.13	0.15	0.16	0.17	0.16	0.18
Phl	0.10	0.05	0.04	0.01	0.05	0.02	0.02	0.04
Acel	0.02	0.07	0.08	0.14	0.01	0.07	0.10	0.03
Mus	0.69	0.70	0.71	0.60	0.68	0.71	0.68	0.76

SODIC AMPHIBOLE FROM THE LYCIAN NAPPES (region of Karaböğütlen)

Sample	KARA2A4	KARA2C	KARA2C	KARA2C	KARA2C	KARA2C	KARA2C	KARA4B	KARA4B	KARA4B	KARA4B	KARA4B	KARAB0120B	KARAB0120B	KARAB0120B
Analysis	35	54	55	56	57	58	59	32	33	35	37	38	52	53	56
SiO2	54.00	55.04	55.14	54.30	54.82	54.99	55.46	54.61	53.78	55.43	55.42	56.51	54.17	54.20	54.18
TiO2	0.44	0.08	0.04	0.44	0.12	0.06	0.20	0.07	0.08	0.09	0.09	0.01	0.05	0.00	0.00
Al2O3	1.75	4.09	4.09	4.48	5.68	4.30	5.29	2.03	2.34	2.22	1.74	1.93	1.16	1.02	0.90
FeO	22.43	21.39	20.74	20.54	19.27	20.80	19.10	21.38	25.02	20.58	22.58	21.64	23.05	21.91	22.80
MnO	1.29	0.39	0.29	0.36	0.33	0.28	0.46	0.27	0.06	0.21	0.10	0.06	0.10	0.11	0.07
MgO	7.88	7.16	7.38	7.75	7.59	7.75	8.45	9.10	6.99	9.58	9.13	9.30	9.48	9.66	9.45
CaO	0.79	0.73	0.79	1.23	0.79	0.84	0.83	1.90	2.27	1.75	1.63	0.99	1.65	2.12	1.70
Na2O	6.39	6.71	6.62	6.53	5.71	6.57	6.64	6.04	5.90	6.14	6.44	6.89	6.28	6.06	6.03
K2O	0.02	0.06	0.01	0.05	1.25	0.04	0.00	0.06	0.11	0.04	0.04	0.00	0.00	0.03	0.03
F	0.03	0.04	0.18	0.13	0.03	0.04	0.08	0.00	0.00	0.00	0.01	0.00	0.00	0.28	0.09
Total	95.02	95.68	95.27	95.79	95.57	95.67	96.50	95.46	96.55	96.03	97.17	97.32	95.95	95.38	95.27
Si	7.98	8.06	8.09	7.94	7.98	8.01	7.94	8.00	7.95	8.03	8.00	8.09	7.91	7.99	7.96
Ti	0.05	0.01	0.00	0.05	0.01	0.01	0.02	0.01	0.01	0.01	0.01	0.00	0.01	0.00	0.00
Al	0.31	0.71	0.71	0.77	0.97	0.74	0.89	0.35	0.41	0.38	0.30	0.33	0.20	0.18	0.16
Al VI	0.28	0.71	0.71	0.71	0.95	0.74	0.83	0.35	0.35	0.38	0.29	0.33	0.10	0.16	0.12
Fe3+	1.55	1.00	0.89	0.96	0.94	1.10	1.05	1.31	1.25	1.28	1.38	1.28	1.69	1.32	1.62
Fe2+	1.23	1.62	1.66	1.55	1.40	1.44	1.24	1.31	1.84	1.21	1.35	1.31	1.13	1.38	1.18
Mn	0.16	0.05	0.04	0.04	0.04	0.03	0.06	0.03	0.01	0.03	0.01	0.01	0.01	0.01	0.01
Mg	1.74	1.56	1.61	1.69	1.65	1.68	1.80	1.99	1.54	2.07	1.96	1.98	2.06	2.12	2.07
Ca	0.13	0.11	0.12	0.19	0.12	0.13	0.13	0.30	0.36	0.27	0.25	0.15	0.26	0.33	0.27
Na	1.83	1.90	1.88	1.85	1.61	1.85	1.84	1.72	1.69	1.72	1.80	1.91	1.78	1.73	1.72
K	0.00	0.01	0.00	0.01	0.23	0.01	0.00	0.01	0.02	0.01	0.01	0.00	0.00	0.01	0.01
F	0.01	0.02	0.08	0.06	0.01	0.02	0.03	0.00	0.00	0.00	0.01	0.00	0.00	0.13	0.04
Total	13.00	13.00	13.00	13.00	13.00	13.00	13.00	13.00	13.00	13.00	13.00	13.00	13.00	13.00	13.00
X Mn	0.05	0.01	0.01	0.01	0.01	0.01	0.02	0.01	0.00	0.01	0.00	0.00	0.00	0.00	0.00
X Mg	0.59	0.49	0.49	0.52	0.54	0.54	0.59	0.60	0.46	0.63	0.59	0.60	0.65	0.61	0.64
X Fe2+	0.41	0.51	0.51	0.48	0.46	0.46	0.41	0.40	0.54	0.37	0.41	0.40	0.35	0.39	0.36
X Fe3+	0.85	0.59	0.56	0.57	0.50	0.60	0.56	0.79	0.78	0.77	0.83	0.80	0.94	0.89	0.93

SODIC AMPHIBOLE FROM THE MENDERES MASSIF (Civril area)

Sample	CIVRIL003A1.	CIVRIL003A1.	CIVRIL003A1.	CIVRIL003A1.	CIVRIL003A1.	CIVRIL003A1.	CIVRIL003A1.	CIVRIL003A1.	CIVRIL003A1.	CIVRIL003A1.	103-GLU-2	103-GLU-3	103-GLU-4
Analysis	1	2	3	4	5	6	7	8	9	10	70	71	73
SiO2	54.74	55.21	54.64	54.99	55.51	55.26	54.79	55.28	54.88	54.29	56.45	56.75	55.40
TiO2	0.16	0.14	0.12	0.10	0.26	0.12	0.13	0.14	0.21	0.13	0.00	0.09	0.31
Al2O3	1.29	1.37	1.35	1.37	1.36	1.29	1.29	1.26	1.29	1.34	1.40	1.66	1.18
FeO	20.27	21.88	20.78	21.55	21.06	20.31	21.49	21.17	21.00	21.57	21.59	21.14	20.90
MnO	0.00	0.01	0.00	0.05	0.07	0.09	0.05	0.00	0.00	0.09	0.08	0.01	0.00
MgO	9.70	9.39	9.62	9.86	9.88	9.84	9.49	9.34	9.59	9.68	10.15	10.41	10.59
CaO	0.47	0.42	0.51	0.62	0.43	0.49	0.45	0.44	0.48	0.53	1.87	2.24	1.95
Na2O	6.28	6.40	6.37	6.59	6.70	6.48	6.58	6.37	6.19	6.39	6.50	6.36	6.27
K2O	0.03	0.04	0.00	0.07	0.07	0.03	0.02	0.05	0.06	0.08	0.06	0.09	0.16
F	0.01	0.01	0.03	0.00	0.03	0.07	0.00	0.08	0.04	0.00	0.00	0.00	0.00
Total	92.95	94.87	93.41	95.19	95.37	93.99	94.29	94.13	93.74	94.09	98.10	98.74	96.76
Si	8.11	8.04	8.07	7.99	8.04	8.11	8.04	8.12	8.07	7.97	8.03	8.02	7.98
Ti	0.02	0.02	0.01	0.01	0.03	0.01	0.01	0.02	0.02	0.01	0.00	0.01	0.03
Al	0.22	0.23	0.23	0.23	0.23	0.22	0.22	0.22	0.22	0.23	0.23	0.28	0.20
Al VI	0.22	0.23	0.23	0.23	0.23	0.22	0.22	0.22	0.22	0.21	0.23	0.28	0.18
Fe3+	1.57	1.70	1.61	1.70	1.58	1.49	1.65	1.52	1.65	1.79	1.32	1.23	1.40
Fe2+	0.94	0.97	0.96	0.92	0.97	1.00	0.99	1.09	0.93	0.86	1.25	1.27	1.12
Mn	0.00	0.00	0.00	0.01	0.01	0.01	0.01	0.00	0.00	0.01	0.01	0.00	0.00
Mg	2.14	2.04	2.12	2.14	2.13	2.15	2.08	2.05	2.10	2.12	2.15	2.19	2.27
Ca	0.07	0.07	0.08	0.10	0.07	0.08	0.07	0.07	0.08	0.08	0.29	0.34	0.30
Na	1.80	1.81	1.82	1.86	1.88	1.84	1.87	1.81	1.76	1.82	1.79	1.74	1.75
K	0.01	0.01	0.00	0.01	0.01	0.01	0.00	0.01	0.01	0.02	0.01	0.02	0.03
F	0.01	0.00	0.01	0.00	0.01	0.03	0.00	0.04	0.02	0.00	0.00	0.00	0.00
Total	13.00	13.00	13.00	13.00	13.00	13.00	13.00	13.00	13.00	13.00	13.00	13.00	13.00
X Mn	0.00	0.00	0.00	0.00	0.00	0.00	0.00	0.00	0.00	0.00	0.00	0.00	0.00
X Mg	0.69	0.68	0.69	0.70	0.69	0.68	0.68	0.65	0.69	0.71	0.63	0.63	0.67
X Fe2+	0.31	0.32	0.31	0.30	0.31	0.32	0.32	0.35	0.31	0.29	0.37	0.37	0.33
X Fe3+	0.87	0.88	0.87	0.88	0.87	0.87	0.88	0.87	0.88	0.90	0.85	0.82	0.89

SODIC AMPHIBOLE FROM THE MENDERES MASSIF (Civril area)

Sample	103-GLU-5	103-GLU-6	103-GLU-8	103-GLU	103-GLU	103-GLU	103-GLU	103-GLU	103-GLU	103-GLU	97-17/3.	97-17/3.	97-17/3.	97-17/3.	97-17/3.	97-17/3.	97-17/3.	97-17/3.
Analysis	74	75	77	205	206	208	209	210	213	214	102	103	104	105	106	107	108	112
SiO2	55.63	55.27	55.22	55.86	55.78	56.12	55.54	54.13	55.21	55.64	56.23	54.71	56.25	56.16	55.74	55.88	55.48	56.53
TiO2	0.13	0.02	0.02	0.23	0.29	0.13	0.11	0.09	0.01	0.17	0.05	0.10	0.31	0.21	0.08	0.03	0.23	0.01
Al2O3	1.52	1.57	1.84	1.68	1.66	1.56	2.25	1.81	1.48	1.69	0.82	0.44	0.87	1.11	0.64	0.67	0.72	1.58
FeO	20.34	20.98	20.06	20.74	21.12	19.52	19.12	21.03	21.03	20.87	21.36	27.46	21.75	20.58	21.23	21.26	22.91	20.02
MnO	0.09	0.03	0.00	0.01	0.05	0.03	0.04	0.04	0.02	0.09	0.10	0.02	0.00	0.01	0.00	0.03	0.00	0.10
MgO	10.39	10.69	10.23	10.22	10.13	11.06	11.12	10.10	10.73	10.20	10.72	7.17	10.66	10.69	10.60	10.68	9.91	11.16
CaO	2.48	3.01	2.76	1.64	1.57	3.24	2.91	2.42	2.68	2.48	0.61	0.51	0.40	0.87	0.83	0.83	0.41	1.05
Na2O	6.09	5.63	5.97	6.56	6.43	5.44	5.73	6.28	5.88	6.18	6.41	6.59	6.70	6.80	6.93	6.73	7.22	6.64
K2O	0.07	0.09	0.09	0.10	0.11	0.08	0.31	0.05	0.07	0.14	0.06	0.06	0.04	0.11	0.02	0.07	0.05	0.04
F	0.00	0.00	0.00	0.00	0.00	0.00	0.00	0.00	0.00	0.00	0.00	0.00	0.00	0.00	0.00	0.00	0.00	0.00
Total	96.75	97.30	96.20	97.04	97.14	97.17	97.13	95.95	97.11	97.47	96.35	97.07	96.98	96.54	96.07	96.17	96.92	97.12
Si	8.03	7.93	8.03	8.02	7.99	8.03	7.94	7.91	7.93	7.99	8.02	7.99	7.98	8.04	8.04	8.03	7.98	8.00
Ti	0.01	0.00	0.00	0.02	0.03	0.01	0.01	0.01	0.00	0.02	0.00	0.01	0.03	0.02	0.01	0.00	0.02	0.00
Al	0.26	0.27	0.32	0.28	0.28	0.26	0.38	0.31	0.25	0.29	0.14	0.08	0.15	0.19	0.11	0.11	0.12	0.26
Al VI	0.26	0.19	0.32	0.28	0.27	0.26	0.32	0.22	0.18	0.28	0.14	0.07	0.13	0.19	0.11	0.11	0.10	0.26
Fe3+	1.18	1.37	1.07	1.29	1.39	1.14	1.17	1.31	1.42	1.18	1.85	1.88	1.85	1.51	1.59	1.67	1.73	1.59
Fe2+	1.28	1.15	1.37	1.20	1.14	1.20	1.12	1.26	1.10	1.33	0.70	1.48	0.73	0.96	0.97	0.89	1.03	0.78
Mn	0.01	0.00	0.00	0.00	0.01	0.00	0.01	0.01	0.00	0.01	0.01	0.00	0.00	0.00	0.00	0.00	0.00	0.01
Mg	2.23	2.29	2.22	2.19	2.16	2.36	2.37	2.20	2.30	2.18	2.28	1.56	2.26	2.28	2.28	2.29	2.12	2.35
Ca	0.38	0.46	0.43	0.25	0.24	0.50	0.45	0.38	0.41	0.38	0.09	0.08	0.06	0.13	0.13	0.13	0.06	0.16
Na	1.70	1.57	1.68	1.83	1.79	1.51	1.59	1.78	1.64	1.72	1.77	1.87	1.84	1.89	1.94	1.88	2.01	1.82
K	0.01	0.02	0.02	0.02	0.02	0.02	0.06	0.01	0.01	0.03	0.01	0.01	0.01	0.02	0.00	0.01	0.01	0.01
F	0.00	0.00	0.00	0.00	0.00	0.00	0.00	0.00	0.00	0.00	0.00	0.00	0.00	0.00	0.00	0.00	0.00	0.00
Total	13.00	13.00	13.00	13.00	13.00	13.00	13.00	13.00	13.00	13.00	13.00	13.00	13.00	13.00	13.00	13.00	13.00	13.00
X Mn	0.00	0.00	0.00	0.00	0.00	0.00	0.00	0.00	0.00	0.00	0.00	0.00	0.00	0.00	0.00	0.00	0.00	0.00
X Mg	0.64	0.67	0.62	0.65	0.66	0.66	0.68	0.64	0.68	0.62	0.76	0.51	0.75	0.70	0.70	0.72	0.67	0.75
X Fe2+	0.36	0.33	0.38	0.35	0.34	0.34	0.32	0.36	0.32	0.38	0.24	0.49	0.25	0.30	0.30	0.28	0.33	0.25
X Fe3+	0.82	0.88	0.77	0.82	0.84	0.81	0.78	0.86	0.89	0.81	0.93	0.96	0.93	0.89	0.94	0.94	0.95	0.86

SODIC AMPHIBOLE FROM THE MENDERES MASSIF (Gerit area)

Sample	GERIT0102E	GERIT0102E	GERIT0102E	GERIT0102E	GERIT0102E	GERIT0102E	GERIT0102B	GERIT0102B	GERIT0102B	GERIT0102B
Analysis	19	20	21	26	27	28	17	25	28	29
SiO2	55.88	56.11	56.03	55.97	56.85	55.52	55.83	56.98	56.56	56.24
TiO2	0.03	0.02	0.00	0.00	0.23	0.26	0.43	0.24	0.00	0.07
Al2O3	0.76	0.67	0.55	0.87	0.79	1.13	0.99	0.72	0.77	0.95
FeO	19.29	20.38	20.24	18.85	20.59	18.12	19.79	18.77	19.60	19.58
MnO	0.12	0.09	0.06	0.00	0.11	0.00	0.00	0.02	0.11	0.00
MgO	11.39	11.77	11.43	11.81	11.20	11.93	11.31	13.09	11.24	11.29
CaO	1.46	1.04	1.03	1.08	1.24	1.26	0.77	0.78	0.72	1.32
Na2O	6.49	6.37	6.51	6.43	6.48	6.12	6.10	5.91	6.47	6.16
K2O	0.11	0.06	0.13	0.08	0.10	0.03	0.09	0.09	0.12	0.13
F	0.00	0.19	0.17	0.00	0.30	0.09	0.28	0.05	0.37	0.00
Total	95.53	96.69	96.14	95.08	97.89	94.44	95.59	96.65	95.96	95.73
Si	8.07	7.97	8.03	8.05	8.04	8.02	8.00	7.94	8.11	8.07
Ti	0.00	0.00	0.00	0.00	0.02	0.03	0.05	0.03	0.00	0.01
Al	0.13	0.11	0.09	0.15	0.13	0.19	0.17	0.12	0.13	0.16
Al VI	0.13	0.08	0.09	0.15	0.13	0.19	0.17	0.06	0.13	0.16
Fe3+	1.43	1.79	1.62	1.61	1.45	1.56	1.67	2.07	1.45	1.54
Fe2+	0.90	0.63	0.81	0.66	0.99	0.63	0.70	0.11	0.90	0.80
Mn	0.01	0.01	0.01	0.00	0.01	0.00	0.00	0.00	0.01	0.00
Mg	2.45	2.49	2.44	2.53	2.36	2.57	2.42	2.72	2.40	2.41
Ca	0.23	0.16	0.16	0.17	0.19	0.19	0.12	0.12	0.11	0.20
Na	1.82	1.75	1.81	1.79	1.78	1.71	1.69	1.60	1.80	1.71
K	0.02	0.01	0.02	0.02	0.02	0.00	0.02	0.02	0.02	0.02
F	0.00	0.08	0.08	0.00	0.13	0.04	0.13	0.02	0.17	0.00
Total	13.00	13.00	13.00	13.00	13.00	13.00	13.00	13.00	13.00	13.00
X Mn	0.00	0.00	0.00	0.00	0.00	0.00	0.00	0.00	0.00	0.00
X Mg	0.73	0.80	0.75	0.79	0.71	0.80	0.77	0.96	0.73	0.75
X Fe2+	0.27	0.20	0.25	0.21	0.29	0.20	0.23	0.04	0.27	0.25
X Fe3+	0.92	0.96	0.95	0.92	0.92	0.89	0.91	0.97	0.92	0.91

SODIC AMPHIBOLE FROM THE MENDERES MASSIF (Gerit area)

Sample	GERIT0102B	GERIT0102B	GERIT0102B	GERIT0102B	GERIT0102B	GERIT0102B	GERIT0102B	GERIT0102B	GERIT0102B	GERIT0102B
Analysis	30	31	32	33	39	40	41	42	43	44
SiO2	56.57	56.70	56.23	57.25	55.93	55.54	56.11	56.79	56.84	56.19
TiO2	0.00	0.26	0.04	0.14	0.15	0.24	0.31	0.16	0.26	0.38
Al2O3	0.85	0.94	0.72	0.94	0.76	0.86	0.92	1.20	0.76	0.99
FeO	20.76	19.77	20.09	19.08	20.64	20.79	19.66	18.33	18.72	21.22
MnO	0.00	0.17	0.11	0.06	0.00	0.09	0.01	0.00	0.11	0.08
MgO	10.88	11.60	11.41	12.94	10.87	10.53	11.66	12.84	12.31	10.75
CaO	0.72	0.62	1.30	1.16	0.82	0.64	0.58	1.59	1.60	1.06
Na2O	6.84	6.70	6.41	5.72	6.54	6.21	6.06	6.04	6.14	6.54
K2O	0.03	0.08	0.11	0.09	0.05	0.01	0.06	0.13	0.12	0.05
F	0.19	0.00	0.09	0.00	0.05	0.23	0.14	0.38	0.29	0.28
Total	96.83	96.83	96.51	97.36	95.81	95.13	95.51	97.45	97.13	97.55
Si	8.07	8.01	8.03	7.94	8.04	8.03	7.99	7.96	8.03	7.98
Ti	0.00	0.03	0.00	0.01	0.02	0.03	0.03	0.02	0.03	0.04
Al	0.14	0.16	0.12	0.15	0.13	0.15	0.15	0.20	0.13	0.17
Al VI	0.14	0.16	0.12	0.09	0.13	0.15	0.15	0.16	0.13	0.15
Fe3+	1.52	1.72	1.57	2.04	1.65	1.69	1.87	1.55	1.45	1.52
Fe2+	0.95	0.61	0.83	0.17	0.83	0.83	0.47	0.60	0.77	1.00
Mn	0.00	0.02	0.01	0.01	0.00	0.01	0.00	0.00	0.01	0.01
Mg	2.31	2.45	2.43	2.67	2.33	2.27	2.48	2.68	2.59	2.28
Ca	0.11	0.09	0.20	0.17	0.13	0.10	0.09	0.24	0.24	0.16
Na	1.89	1.84	1.78	1.54	1.82	1.74	1.67	1.64	1.68	1.80
K	0.01	0.01	0.02	0.02	0.01	0.00	0.01	0.02	0.02	0.01
F	0.08	0.00	0.04	0.00	0.02	0.11	0.06	0.17	0.13	0.13
Total	13.00	13.00	13.00	13.00	13.00	13.00	13.00	13.00	13.00	13.00
X Mn	0.00	0.01	0.00	0.00	0.00	0.00	0.00	0.00	0.00	0.00
X Mg	0.71	0.80	0.75	0.94	0.74	0.73	0.84	0.82	0.77	0.70
X Fe2+	0.29	0.20	0.25	0.06	0.26	0.27	0.16	0.18	0.23	0.30
X Fe3+	0.91	0.92	0.93	0.96	0.93	0.92	0.93	0.91	0.92	0.91

CALCIC AMPHIBOLE FROM THE LYCIAN NAPPES (region of Karaböğütlen)

Sample	KARA2C	KARA4A	KARA4A	KARA4D	KARA4D	KARAB0102B	KARAB1-15C	KARAB1-15C	KARAB1-15C
Analysis	53	87	88	99	100	24	79	80	81
SiO2	53.45	54.23	53.32	56.09	54.13	53.71	52.57	53.20	52.87
TiO2	0.11	0.11	0.03	0.03	0.22	0.13	0.09	0.14	0.05
Al2O3	2.85	3.76	3.46	1.98	4.20	4.12	0.90	0.85	0.87
FeO	9.89	12.09	12.58	4.98	5.75	2.09	17.87	16.87	19.03
MnO	0.38	0.26	0.25	0.13	0.07	0.41	0.53	0.60	0.61
MgO	16.29	13.59	14.49	21.28	19.33	21.47	12.05	12.54	11.36
CaO	11.74	8.93	9.52	12.54	12.78	12.46	11.28	10.96	11.24
Na2O	0.93	1.29	1.44	0.09	0.13	0.91	0.59	0.77	0.54
K2O	0.15	1.07	0.66	0.00	0.00	0.05	0.18	0.16	0.20
F	0.00	0.00	0.03	0.11	0.06	0.17	0.00	0.00	0.00
Total	95.77	95.33	95.78	97.22	96.67	95.51	96.04	96.08	96.78
Si	7.74	7.89	7.72	7.72	7.57	7.53	7.85	7.89	7.87
Ti	0.01	0.01	0.00	0.00	0.02	0.01	0.01	0.02	0.01
Al	0.49	0.65	0.59	0.32	0.69	0.68	0.16	0.15	0.15
Al VI	0.23	0.54	0.31	0.04	0.26	0.21	0.01	0.04	0.03
Fe3+	0.08	0.20	0.46	0.46	0.22	0.16	0.31	0.30	0.31
Fe2+	1.12	1.27	1.06	0.11	0.45	0.08	1.92	1.79	2.06
Mn	0.05	0.03	0.03	0.01	0.01	0.05	0.07	0.08	0.08
Mg	3.52	2.95	3.13	4.37	4.03	4.49	2.68	2.77	2.52
Ca	1.82	1.39	1.48	1.85	1.92	1.87	1.80	1.74	1.79
Na	0.26	0.36	0.40	0.02	0.03	0.25	0.17	0.22	0.16
K	0.03	0.20	0.12	0.00	0.00	0.01	0.03	0.03	0.04
F	0.00	0.00	0.01	0.05	0.03	0.08	0.00	0.00	0.00
Total	13.00	13.00	13.00	13.00	13.00	13.00	13.00	13.00	13.00

CALCIC AMPHIBOLE FROM THE MENDERES MASSIF (Civril area and Gerit area)

Sample	97-17/3.	97-17/3.	97-17/3.	97-17/3.	97-17/3.	97-17/3.	97-17/3.	97-17/3.	GERIT0102B	GERIT0102B	GERIT0102B	GERIT0102B	GERIT0102B	GERIT0102F	GERIT0102F	GERIT0102F	GERIT0102F
Analysis	123	124	125	126	127	202	203	204	1	2	3	4	14	25	26	27	29
SiO2	52.74	53.73	54.98	56.76	55.18	55.79	57.37	57.63	53.17	55.15	55.36	55.42	53.65	58.53	58.97	58.02	58.40
TiO2	0.92	0.65	0.66	0.20	0.36	0.36	0.10	0.18	0.00	0.02	0.00	0.00	0.14	0.06	0.03	0.10	0.02
Al2O3	4.25	3.63	2.57	1.64	2.59	3.20	1.15	1.16	1.31	1.91	1.50	1.70	3.04	0.40	0.17	0.79	0.51
FeO	6.06	4.12	4.57	3.07	5.42	6.02	3.95	4.34	11.59	12.53	11.35	11.43	12.60	5.30	3.93	5.81	4.56
MnO	0.01	0.10	0.06	0.13	0.06	0.12	0.04	0.09	0.13	0.17	0.32	0.27	0.25	0.15	0.14	0.11	0.11
MgO	18.34	20.69	20.21	21.69	20.07	19.85	20.91	21.06	15.00	16.33	17.13	16.68	15.87	21.49	22.32	21.31	21.83
CaO	10.90	11.63	11.60	11.82	10.39	10.71	11.74	11.88	10.04	10.80	11.48	11.05	11.14	12.10	13.54	11.86	13.19
Na2O	1.72	1.08	0.87	0.49	1.23	1.27	0.72	0.78	1.16	1.23	0.92	1.11	1.46	0.46	0.04	0.75	0.13
K2O	0.03	0.03	0.00	0.00	0.01	0.01	0.03	0.00	0.07	0.17	0.06	0.11	0.09	0.03	0.00	0.00	0.00
F	0.00	0.00	0.00	0.00	0.00	0.00	0.00	0.00	0.21	0.26	0.05	0.00	0.16	0.00	0.00	0.00	0.00
Total	94.97	95.66	95.52	95.80	95.31	97.32	95.99	97.11	92.68	98.57	98.16	97.78	98.40	98.53	99.15	98.75	98.74
Si	7.55	7.52	7.73	7.86	7.71	7.67	7.99	7.95	7.96	7.76	7.79	7.82	7.60	7.96	8.00	7.88	7.95
Ti	0.10	0.07	0.07	0.02	0.04	0.04	0.01	0.02	0.00	0.00	0.00	0.00	0.02	0.01	0.00	0.01	0.00
Al	0.72	0.60	0.43	0.27	0.43	0.52	0.19	0.19	0.23	0.32	0.25	0.28	0.51	0.06	0.03	0.13	0.08
Al VI	0.26	0.12	0.15	0.13	0.14	0.19	0.18	0.14	0.19	0.08	0.04	0.11	0.11	0.02	0.02	0.00	0.03
Fe3+	0.17	0.43	0.25	0.33	0.63	0.57	0.10	0.15	0.19	0.42	0.43	0.40	0.39	0.36	0.03	0.45	0.13
Fe2+	0.56	0.05	0.29	0.03	0.01	0.12	0.36	0.35	1.26	1.06	0.90	0.95	1.11	0.24	0.42	0.21	0.39
Mn	0.00	0.01	0.01	0.02	0.01	0.01	0.00	0.01	0.02	0.02	0.04	0.03	0.03	0.02	0.02	0.01	0.01
Mg	3.91	4.32	4.23	4.48	4.18	4.07	4.34	4.33	3.35	3.43	3.59	3.51	3.35	4.35	4.51	4.31	4.43
Ca	1.67	1.74	1.75	1.75	1.56	1.58	1.75	1.76	1.61	1.63	1.73	1.67	1.69	1.76	1.97	1.73	1.92
Na	0.48	0.29	0.24	0.13	0.33	0.34	0.19	0.21	0.34	0.33	0.25	0.30	0.40	0.12	0.01	0.20	0.03
K	0.00	0.01	0.00	0.00	0.00	0.00	0.00	0.00	0.01	0.03	0.01	0.02	0.02	0.00	0.00	0.00	0.00
F	0.00	0.00	0.00	0.00	0.00	0.00	0.00	0.00	0.10	0.12	0.02	0.00	0.07	0.00	0.00	0.00	0.00
Total	13.00	13.00	13.00	13.00	13.00	13.00	13.00	13.00	13.00	13.00	13.00	13.00	13.00	13.00	13.00	13.00	13.00

CALCIC AMPHIBOLE FROM THE MENDERES MASSIF (Gerit area)

Sample	GERIT0102F	GERIT0102F	GERIT0102F	GERIT0102F	GERIT0102F	GERIT0102F	GERIT0102F	GERIT0102F	GERIT0102F
Analysis	30	31	32	33	34	35	36	37	38
SiO2	56.91	57.49	58.33	57.63	58.13	57.66	57.83	58.79	58.04
TiO2	0.09	0.09	0.04	0.08	0.05	0.11	0.05	0.03	0.05
Al2O3	1.82	1.30	0.53	1.25	1.02	0.89	0.99	0.23	0.94
FeO	4.62	4.74	4.75	4.32	5.64	6.37	5.15	4.21	4.52
MnO	0.08	0.15	0.15	0.10	0.12	0.14	0.10	0.19	0.12
MgO	21.48	22.02	21.97	22.02	21.31	21.12	21.49	22.06	21.58
CaO	13.17	12.79	12.98	13.11	12.08	11.41	12.40	13.32	12.98
Na2O	0.26	0.15	0.03	0.15	0.87	0.91	0.40	0.05	0.40
K2O	0.02	0.00	0.00	0.01	0.01	0.02	0.00	0.01	0.01
F	0.00	0.00	0.00	0.00	0.00	0.00	0.00	0.00	0.00
Total	98.45	98.73	98.79	98.67	99.21	98.62	98.40	98.87	98.62
Si	7.78	7.78	7.91	7.83	7.88	7.83	7.88	7.99	7.92
Ti	0.01	0.01	0.00	0.01	0.00	0.01	0.01	0.00	0.01
Al	0.29	0.21	0.08	0.20	0.16	0.14	0.16	0.04	0.15
Al VI	0.07	0.00	0.00	0.03	0.04	0.00	0.03	0.03	0.07
Fe3+	0.20	0.46	0.30	0.27	0.34	0.61	0.36	0.08	0.09
Fe2+	0.33	0.08	0.24	0.22	0.30	0.11	0.23	0.40	0.43
Mn	0.01	0.02	0.02	0.01	0.01	0.02	0.01	0.02	0.01
Mg	4.38	4.45	4.44	4.46	4.30	4.28	4.36	4.47	4.39
Ca	1.93	1.86	1.89	1.91	1.75	1.66	1.81	1.94	1.90
Na	0.07	0.04	0.01	0.04	0.23	0.24	0.10	0.01	0.11
K	0.00	0.00	0.00	0.00	0.00	0.00	0.00	0.00	0.00
F	0.00	0.00	0.00	0.00	0.00	0.00	0.00	0.00	0.00
Total	13.00	13.00	13.00	13.00	13.00	13.00	13.00	13.00	13.00

CALCIC AMPHIBOLE FROM THE MENDERES MASSIF (Milas klippen)

Sample	MK002B2C1-3.	MK002B2C1-4	MK002B2C1-5	MK002B2C1-9	MK002B2C1-10	MK002B2C1-11	MK002B2C1-12	MK002B2C1-13	MK002B2C2-28	MK002B2C2-30	MK002B2C2-31
Analysis											
SiO2	55.11	56.05	56.21	55.80	55.84	55.86	56.28	55.08	55.41	55.22	55.60
TiO2	0.06	0.01	0.03	0.14	0.08	0.12	0.03	0.32	0.03	0.04	0.01
Al2O3	1.95	1.37	1.11	1.76	1.78	1.64	1.20	2.30	1.78	1.93	1.76
FeO	14.34	12.59	12.67	13.20	13.41	12.98	12.10	13.86	14.49	14.74	13.54
MnO	0.36	0.39	0.34	0.41	0.44	0.41	0.53	0.38	0.44	0.34	0.39
MgO	14.44	16.05	16.08	15.58	15.51	15.42	16.19	15.11	14.88	14.85	15.59
CaO	8.97	9.94	9.86	9.48	9.37	9.00	10.44	9.04	8.95	8.80	10.01
Na2O	2.39	1.97	1.84	2.10	1.96	2.25	1.53	2.40	2.28	2.29	1.90
K2O	0.09	0.06	0.07	0.06	0.07	0.06	0.05	0.11	0.07	0.05	0.10
F	0.00	0.00	0.00	0.00	0.00	0.00	0.00	0.00	0.00	0.00	0.00
Total	97.70	98.43	98.22	98.53	98.47	97.73	98.34	98.60	98.32	98.25	98.91
Si	7.85	7.88	7.91	7.83	7.83	7.89	7.92	7.74	7.81	7.78	7.81
Ti	0.01	0.00	0.00	0.01	0.01	0.01	0.00	0.03	0.00	0.00	0.00
Al	0.33	0.23	0.18	0.29	0.29	0.27	0.20	0.38	0.30	0.32	0.29
Al VI	0.18	0.11	0.09	0.13	0.12	0.16	0.12	0.12	0.11	0.10	0.10
Fe3+	0.55	0.46	0.50	0.58	0.67	0.58	0.39	0.67	0.73	0.82	0.54
Fe2+	1.16	1.02	0.99	0.97	0.91	0.95	1.03	0.96	0.98	0.92	1.05
Mn	0.04	0.05	0.04	0.05	0.05	0.05	0.06	0.04	0.05	0.04	0.05
Mg	3.07	3.36	3.37	3.26	3.24	3.25	3.40	3.17	3.13	3.12	3.26
Ca	1.37	1.50	1.49	1.43	1.41	1.36	1.57	1.36	1.35	1.33	1.51
Na	0.66	0.54	0.50	0.57	0.53	0.61	0.42	0.65	0.62	0.63	0.52
K	0.02	0.01	0.01	0.01	0.01	0.01	0.01	0.02	0.01	0.01	0.02
F	0.00	0.00	0.00	0.00	0.00	0.00	0.00	0.00	0.00	0.00	0.00
Total	13.00	13.00	13.00	13.00	13.00	13.00	13.00	13.00	13.00	13.00	13.00

GARNET FROM THE LYCIAN NAPPES (region of Karaböğütlen)

Sample	KARAB-0104.	KARAB-0104.	KARAB-0104.	KARAB-0104.	KARAB-0104.	KARAB-0104.	KARAB-0104.	KARAB-0104.	KARAB-0104.	KARAB-0104.	KARAB-0104.	KARAB-0104.	KARAB-0114A
Garnet n°	G1	G1	G1	G1	G2	G2	G3	G3	G3	G3	G3	G3	G1
Comment	rim	rim	core	core	small garnet	small garnet	Atoll	Atoll	Atoll	Atoll	Atoll	core	
Analysis	82	83	84	85	88	89	94	95	96	97	98	99	1
SiO2	37.11	37.43	37.62	37.15	36.70	36.91	37.06	36.84	37.52	37.20	37.72	37.57	37.43
TiO2	0.22	0.03	0.12	0.08	0.43	0.33	0.07	0.12	0.13	0.08	0.05	0.25	0.12
Al2O3	21.19	21.39	21.42	20.62	19.23	20.14	21.37	21.44	20.83	20.95	21.01	20.98	21.40
FeO	13.52	18.72	8.99	11.04	19.01	17.99	16.25	17.86	15.88	16.81	16.58	12.32	7.12
MnO	17.56	14.19	21.37	21.10	15.07	15.15	16.40	15.63	16.08	16.27	15.53	19.20	23.68
MgO	4.49	4.23	4.71	4.17	3.40	3.55	4.28	3.70	4.03	4.14	3.44	3.64	6.05
CaO	6.13	4.77	6.43	6.31	6.59	6.04	4.95	4.79	5.79	5.10	6.50	7.03	4.73
Na2O	0.01	0.01	0.02	0.06	0.02	0.02	0.05	0.01	0.00	0.00	0.02	0.05	0.02
K2O	0.00	0.00	0.01	0.00	0.00	0.00	0.00	0.00	0.00	0.00	0.00	0.01	0.01
Total	100.22	100.77	100.68	100.53	100.44	100.12	100.42	100.38	100.26	100.55	100.85	101.04	100.55
Si	2.94	2.96	2.95	2.95	2.96	2.96	2.94	2.94	2.98	2.96	2.98	2.96	2.94
Ti	0.01	0.00	0.01	0.00	0.03	0.02	0.00	0.01	0.01	0.00	0.00	0.01	0.01
Al	1.98	1.99	1.98	1.93	1.83	1.90	2.00	2.01	1.95	1.96	1.96	1.95	1.98
Fe	0.90	1.24	0.59	0.73	1.28	1.21	1.08	1.19	1.05	1.12	1.10	0.81	0.47
Mn	1.18	0.95	1.42	1.42	1.03	1.03	1.10	1.06	1.08	1.09	1.04	1.28	1.57
Mg	0.53	0.50	0.55	0.49	0.41	0.42	0.51	0.44	0.48	0.49	0.40	0.43	0.71
Ca	0.52	0.40	0.54	0.54	0.57	0.52	0.42	0.41	0.49	0.43	0.55	0.59	0.40
Na	0.00	0.00	0.00	0.01	0.00	0.00	0.01	0.00	0.00	0.00	0.00	0.01	0.00
K	0.00	0.00	0.00	0.00	0.00	0.00	0.00	0.00	0.00	0.00	0.00	0.00	0.00

GARNET FROM THE LYCIAN NAPPES (region of Karaböğütlen)

Sample	KARAB-0114A	KARAB-0114A	KARAB-0114A	KARAB-0114A	KARAB-0114A	KARAB-0114A	KARAB-0114A	KARAB-0114A	KARAB-0114A	KARAB17D	KARAB17D	KARAB17D	KARAB17D
Garnet n°	G1	G2	G2	G2	G2	G3	G3	G4	G4	G1	G1	G2	G2
Comment						core	rim						
Analysis	2	8	9	10	12	15	16	20	21	27	28	29	30
SiO2	37.12	37.80	37.26	37.48	37.27	37.00	37.29	37.44	37.20	36.21	36.56	37.01	36.84
TiO2	0.08	0.25	0.03	0.02	0.21	0.08	0.00	0.00	0.08	0.30	0.25	0.00	0.12
Al2O3	21.35	21.46	20.99	21.20	21.01	21.73	21.86	21.51	21.24	21.05	21.01	21.07	21.32
FeO	7.64	7.28	7.23	8.18	7.59	7.51	7.62	7.31	7.42	20.02	19.73	20.55	20.17
MnO	23.89	23.39	23.08	23.14	23.07	23.82	23.12	23.22	24.12	14.24	14.18	13.63	13.26
MgO	5.91	6.19	6.20	6.30	6.30	5.96	5.92	6.06	6.00	3.06	3.00	3.30	3.35
CaO	4.73	4.38	4.28	4.48	4.36	4.39	4.57	4.29	4.07	5.48	5.43	4.81	4.80
Na2O	0.05	0.01	0.00	0.02	0.03	0.04	0.00	0.03	0.00	0.02	0.04	0.02	0.00
K2O	0.00	0.03	0.00	0.00	0.00	0.00	0.00	0.03	0.00	0.00	0.00	0.01	0.00
Total	100.77	100.79	99.09	100.80	99.83	100.53	100.38	99.87	100.13	100.37	100.19	100.39	99.85
Si	2.92	2.95	2.96	2.94	2.94	2.91	2.93	2.95	2.94	2.91	2.93	2.96	2.95
Ti	0.00	0.01	0.00	0.00	0.01	0.00	0.00	0.00	0.00	0.02	0.02	0.00	0.01
Al	1.98	1.97	1.96	1.96	1.96	2.01	2.02	2.00	1.98	1.99	1.99	1.99	2.01
Fe	0.50	0.47	0.48	0.54	0.50	0.49	0.50	0.48	0.49	1.35	1.32	1.37	1.35
Mn	1.59	1.55	1.55	1.54	1.54	1.59	1.54	1.55	1.61	0.97	0.96	0.92	0.90
Mg	0.69	0.72	0.73	0.74	0.74	0.70	0.69	0.71	0.71	0.37	0.36	0.39	0.40
Ca	0.40	0.37	0.36	0.38	0.37	0.37	0.38	0.36	0.34	0.47	0.47	0.41	0.41
Na	0.01	0.00	0.00	0.00	0.00	0.01	0.00	0.00	0.00	0.00	0.01	0.00	0.00
K	0.00	0.00	0.00	0.00	0.00	0.00	0.00	0.00	0.00	0.00	0.00	0.00	0.00

GARNET FROM THE LYCIAN NAPPES (region of Karaböğütlen)

Sample	KARAB17D	KARAB17D	KARAB18	KARAB18	KARAB18	KARAB18	KARAB18	KARAB18	KARAB0121C	KARAB0121C	KARAB0121C	KARAB0121C	KARAB0121C
Garnet n°	G3	G3	G1	G1	G1	G1	G1	G1	G1	G1	G2	G3	G4
Comment			rim	rim	rim	core	core	rim	big crystal	big crystal	small crystal	small crystal	small crystal
Analysis	31	32	41	42	43	44	45	46	55	56	57	58	59
SiO2	36.33	36.55	36.76	36.57	36.78	36.95	36.53	36.93	37.79	37.16	37.11	36.68	36.79
TiO2	0.03	0.00	0.22	0.12	0.00	0.28	0.25	0.23	0.00	0.38	0.23	0.05	0.10
Al2O3	21.42	21.30	20.35	20.50	20.56	20.21	20.01	20.52	21.40	21.06	20.62	21.60	20.88
FeO	21.58	21.27	11.73	11.72	12.05	11.34	11.40	11.25	9.80	10.01	9.63	8.92	8.95
MnO	11.51	11.48	21.29	21.45	21.25	21.80	21.61	21.55	24.64	24.16	26.92	27.14	26.78
MgO	3.39	3.55	2.07	2.09	2.23	1.77	1.91	2.06	5.03	4.83	3.64	3.75	3.58
CaO	4.26	4.66	7.74	7.54	7.88	8.02	7.82	8.04	2.71	3.12	2.55	2.02	2.46
Na2O	0.05	0.05	0.02	0.02	0.10	0.05	0.05	0.02	0.04	0.00	0.00	0.01	0.04
K2O	0.01	0.00	0.00	0.00	0.02	0.00	0.00	0.01	0.01	0.00	0.00	0.00	0.01
Total	98.57	98.86	100.18	100.01	100.88	100.41	99.58	100.60	101.43	100.71	100.70	100.17	99.59
Si	2.94	2.95	2.96	2.95	2.94	2.97	2.96	2.96	2.97	2.94	2.97	2.94	2.97
Ti	0.00	0.00	0.01	0.01	0.00	0.02	0.02	0.01	0.00	0.02	0.01	0.00	0.01
Al	2.05	2.03	1.93	1.95	1.94	1.92	1.91	1.94	1.98	1.97	1.94	2.04	1.98
Fe	1.46	1.44	0.79	0.79	0.81	0.76	0.77	0.75	0.64	0.66	0.64	0.60	0.60
Mn	0.79	0.79	1.45	1.47	1.44	1.48	1.48	1.46	1.64	1.62	1.82	1.84	1.83
Mg	0.41	0.43	0.25	0.25	0.27	0.21	0.23	0.25	0.59	0.57	0.43	0.45	0.43
Ca	0.37	0.40	0.67	0.65	0.68	0.69	0.68	0.69	0.23	0.26	0.22	0.17	0.21
Na	0.01	0.01	0.00	0.00	0.02	0.01	0.01	0.00	0.01	0.00	0.00	0.00	0.01
K	0.00	0.00	0.00	0.00	0.00	0.00	0.00	0.00	0.00	0.00	0.00	0.00	0.00

GARNET FROM THE LYCIAN NAPPES (region of Karaböğütlen)

Sample	KARAB0121C	KARAB0121C	KARAB0121C	KARAB0121C	KARAB0121C	KARAB0121C	KARAB0121C
Garnet n°	G5	G6	G7	G8	G8	G9	G9
Comment	small crystal	small crystal	big crystal	big crystal	big crystal	big crystal	big crystal
Analysis	60	61	62	66	67	70	71
SiO2	36.60	36.72	37.14	36.63	37.40	36.28	36.61
TiO2	0.11	0.00	0.15	0.05	0.13	0.16	0.00
Al2O3	20.63	21.61	21.28	21.32	21.56	21.42	21.31
FeO	9.41	9.03	9.54	10.08	9.84	9.35	9.53
MnO	26.36	26.76	24.73	25.43	25.78	25.58	25.30
MgO	3.87	4.43	4.73	4.21	4.13	4.55	4.66
CaO	2.61	2.02	2.36	2.66	2.80	2.10	2.17
Na2O	0.00	0.03	0.07	0.06	0.04	0.05	0.03
K2O	0.01	0.00	0.00	0.00	0.00	0.01	0.00
Total	99.59	100.60	100.00	100.44	101.67	99.50	99.60
Si	2.96	2.92	2.96	2.93	2.95	2.92	2.94
Ti	0.01	0.00	0.01	0.00	0.01	0.01	0.00
Al	1.96	2.03	2.00	2.01	2.00	2.03	2.01
Fe	0.64	0.60	0.64	0.67	0.65	0.63	0.64
Mn	1.80	1.81	1.67	1.72	1.72	1.74	1.72
Mg	0.47	0.53	0.56	0.50	0.48	0.55	0.56
Ca	0.23	0.17	0.20	0.23	0.24	0.18	0.19
Na	0.00	0.00	0.01	0.01	0.01	0.01	0.00
K	0.00	0.00	0.00	0.00	0.00	0.00	0.00